NOTE TO USERS

CRYSTALLOGRAPHIC, SPECTROSCOPIC AND THEORETICAL STUDIES OF

FLUORO- Kr(II), Xe(II), Au(V) AND HALOGEN(VII) COMPOUNDS;

AND NEW SYNTHETIC DEVELOPMENTS IN

BROMINE(VII) OXIDE FLUORIDE CHEMISTRY

By

JOHN F. LEHMANN, B.Sc.

A Thesis

Submitted to the School of Graduate Studies

in Partial Fulfillment of the Requirements

for the Degree

Doctor of Philosophy

McMaster University

© Copyright by John F. Lehmann 2004

NOBLE-GAS(II), GOLD(V) AND HALOGEN(VII) CHEMISTRY

DOCTOR OF PHILOSOPHY (2004) McMaster University

(Chemistry) Hamilton, Ontario

TITLE: Crystallographic, Spectroscopic and Theoretical Studies of Fluoro- Kr(II), Xe(II), Au(V) and Halogen(VII) Compounds; and New Synthetic Developments in Bromine(VII) Oxide Fluoride Chemistry

AUTHOR: John F. Lehmann, B.Sc.

SUPERVISOR: Professor G. J. Schrobilgen

NUMBER OF PAGES: xxii, 388

ABSTRACT

The structures of α-KrF₂, [KrF][MF₆] (M = As, Sb, Bi, Au) and several salts containing the $Kr_2F_3^+$ cation have been determined by use of low-temperature single-crystal X-ray diffraction. These structures account for nearly all of the crystallographic work reported for Kr(II) compounds, and represent the first studies of their kind for salts containing the KrF^+ and $Kr_2F_3^+$ cations. The crystallographic characterization of the strongly fluorine bridged [KrF][MF₆] ion pairs prompted a more comprehensive survey of XeF^+ salts, which included the X-ray structure determinations of [XeF][MF₆] (M = As, Sb, Bi), and [XeF][M₂F₁₁] (M = Sb, Bi). Variations in the Ng--F_b (Ng = Kr, Xe) bridge bond lengths of the NgF^+ salts were used to assess the relative fluoride ion acceptor strengths of AsF_5, SbF_5, BiF_5, AuF_5, Sb_2F_{10} and Bi_2F_{10} and the results were compared with a recently reported Lewis acidity scale derived from electronic structure calculations. The potent oxidizer properties of the KrF^+ cation have been used to synthesize [O₂][AuF₆] by the reaction of [KrF][AuF₆] with O₂. A previously unknown and ordered phase of [O₂][AuF₆] was identified by variable temperature Raman spectroscopy and by single-crystal X-ray diffraction, and resulted in the reassignment of the $v_2(E_g)$ vibrational mode of AuF_6^-.

The limited chemistry of Br(VII) has been extended in several respects. Accurate geometric parameters for the previously known BrF_6^+ cation and its chlorine and iodine analogues have been determined by single-crystal X-ray diffraction, allowing bond length trends among the late period 3 - 5 hexafluoro-species to be established. The octahedral geometries of the XF_6^+ (X = Cl, Br, I) cations in solution have been confirmed by the

measurement of their $^{35,37}Cl$, $^{79,81}Br$ and ^{127}I NMR spectra and spin-lattice relaxation times (T_1) in HF solution.

The previously unknown fluoride ion acceptor properties of BrO_3F have been established by its reactions with $[N(CH_3)_4][F]$, CsF, RbF, KF and NOF. The resulting $BrO_3F_2^-$ anion is only the fourth example of a Br(VII) species, with its predicted D_{3h} symmetry having been confirmed by vibrational spectroscopy, ^{19}F NMR spectroscopy, single-crystal X-ray diffraction and electronic structure calculations. The internal and symmetry force constants of $BrO_3F_2^-$ have been determined and are compared with the isostructural species XeO_3F_2, OsO_3F_2 and $ClO_3F_2^-$. The stronger fluoride ion acceptor properties of BrO_3F relative to those of ClO_3F have been demonstrated by use electronic structure calculations and have helped to explain failed attempts to prepare the $ClO_3F_2^-$ anion.

The fluoride ion donor properties of BrO_3F and ClO_3F were investigated by their reactions with $SbF_5(l)$. Whereas ClO_3F does not react with $SbF_5(l)$, BrO_3F undergoes reductive elimination of O_2 to form $[BrO_2][Sb_nF_{5n+1}]$. The geometric parameters of the BrO_2^+ cation have been obtained for the first time in the solid state by the X-ray structure determination of $[BrO_2][SbF_6]$. The contrasting reactivities of BrO_3F and ClO_3F towards $(SbF_5)_n$ have been addressed by use of thermochemical calculations.

Attempts to prepare BrO_2F_3 or salts containing the $BrO_2F_2^+$ cation by ligand exchange reactions with BrO_3F and oxidative fluorination of BrO_2F were unsuccessful, but have been accounted for by use of electronic structure calculations which were employed to evaluate the thermochemistries of the attempted reactions.

ACKNOWLEDGEMENTS

LIST OF ABBREVIATIONS AND SYMBOLS

General

ax	axial
CCD	charge coupled device
eq	equatorial
FEP	perfluoroethylene/perfluoropylene copolymer
LUMO	lowest unoccupied molecular orbital
IR	infrared
Kel-F	chlorotrifluoroethylene polymer
NMR	nuclear magnetic resonance
PTFE	tetrafluoroethylene polymer
VSEPR	valence shell electron pair repulsion

Nuclear Magnetic Resonance

ppm	part per million
δ	chemical shift
σ^p	paramagnetic shielding term
μ_B	Bohr magneton
μ_o	permeability of a vacuum
I	nuclear spin quantum number
J	scalar coupling constant, in Hertz
FID	free induction decay
SF	spectral frequency
SW	sweep width

TD	time domain
PW	pulse width
T_1	spin-lattice relaxation time
T_2	spin-spin relaxation time
P_i	imbalance of the valence electrons in the p-orbitals
D_i	imbalance of the valence electrons in the d-orbitals
$\Delta v_{1/2}$	line width at half height
τ_c	isotropic rotational correlation time
WF	width factor
Q	quadrupolar moment
eq	electric field gradient
η	asymmetry parameter of the electric field gradient

X-ray Crystallography

$a, b, c, \alpha, \beta, \gamma$	unit cell parameters
V	unit cell volume
Z	molecules per unit cell
V_m	molecular volume (V / Z)
Mol. mass	molecular mass
μ	absorption coefficient
R_1	conventional agreement index
wR_2	weighted agreement index
w	overall weight parameter

Computational and Thermochemical

HF	Hartree-Fock
LDF	local density functional

MP2	Møller Plesset, second order
ΔH°	difference in the standard enthalpy
ΔS°	difference in the standard entropy
ΔG°	difference in standard free energy
ΔH°_{vap}	standard enthalpy of vapourization
H°_{L}	standard lattice enthalpy
$\Delta H^{\circ}_{+F^{-}}$	standard enthalpy of fluoride ion attachment
$\Delta H^{\circ}_{-F^{-}}$	standard enthalpy of fluoride ion detachment
V_{m}	molecular volume $(V \div Z)$

TABLE OF CONTENTS

LIST OF TABLES

LIST OF FIGURES

CHAPTER 1

INTRODUCTION

1.1. Strong Oxidizing Agents

Reduction-oxidation (redox) reactions are a fundamentally important class of chemical reactions, which involve the transfer of electrons from a reducing agent to an oxidizing agent. Fluorine is undisputedly the strongest oxidizing agent among the elements as indicated by the high electron affinity of $F\cdot$ (eq 1.1)[1] and F_2 (eq 1.2),[2] its

$$F\cdot(g) + e^- \rightarrow F^-(g) \quad 3.401190(4) \text{ eV} \tag{1.1}$$

$$F_2(g) + e^- \rightarrow F_2^-(g) \quad 3.08(10) \text{ eV} \tag{1.2}$$

$$F_2 + 2e^- \rightarrow 2F^-(g) \quad 2.87 \text{ V} \tag{1.3}$$

large reduction potential (eq 1.3)[3] and low F-F bond dissociation energy (154.6(6) kJ mol^{-1}).[4] Despite these characteristics, thermodynamically favourable oxidations are occasionally kinetically controlled by the dissociation energy of fluorine, as illustrated by the high-temperature syntheses of XeF_2 (ΔH_f°, -162.8 kJ mol^{-1}),[5] XeF_4 (ΔH_f°, -267.1 kJ mol^{-1})[6] and XeF_6 (ΔH_f°, -338.2 kJ mol^{-1}).[7] The more potent oxidizing properties of the $F\cdot$ radical, which is the active oxidant in these cases, has also been utilized in the preparation of O_2F_2[8-10] and KrF_2,[11,12] however, cryogenic reaction conditions and novel methods of $F\cdot$ generation, such as photolysis,[13-18] electric discharge,[19-21] thermal gradients[16,22,23] and particle beams,[24,25] are required in these cases because the products are thermodynamically unstable.

The preparation of oxidative fluorinating agents that rival or exceed that of fluorine at low temperatures is of great importance for the preparation of thermally

1

unstable compounds that may be kinetically stable or stabilized by the entropy term of the Gibbs free energy term. However, overcoming the kinetic problems associated with molecular fluorine, while maintaining the thermodynamic viability of an oxidative fluorinating agent is a formidable challenge. To satisfy these requirements, the fluorinating agent must have M-F (M = central element) bonds that are weak but also significantly covalent in nature. The latter requirement serves to diminish the negative charge on the fluorine ligands, and contrasts with highly ionic M-F bonds where the fluorine ligands have a charge approaching -1 and are not expected to initiate redox reactions. The polarity of the M-F bond is strongly correlated to the effective electronegativity of the central element, which is dependent on both its position in the periodic table and formal oxidation state. As a consequence of the increasing trend in electronegativity on going from the bottom left hand corner to top right hand corner of the periodic table, and the accessibility of higher oxidation states as one proceeds from the left to the right across the periodic table, the halogens, noble gases, nitrogen and oxygen are expected to form the most covalent bonds with fluorine. Oxidizing strength also increases with net positive charge,[26-31] reflecting the higher electron affinities of cations and the further reduction of the M-F bond polarity. On the basis of these criteria, it is not surprising that cations derived from the high-valent fluorides and oxide fluorides of groups 17 and 18 rank among the strongest oxidative fluorinating agents known.[32]

The high chemical reactivities of fluorides, and in particular fluorocations, complicate the acquisition of reliable thermochemical data for these species by experimental methods. Given the scarcity of experimental thermochemical data, the oxidizer strengths of 36 main-group fluorocations have been assessed by calculations of their F^+ detachment enthalpies (eq 1.4) using the LDF method (Table 1.1).[32] Although

$$MF_{n+1} \rightarrow MF_n + F^+ \qquad (1.4)$$

2

Table 1.1. Calculated Enthalpies of F^+ Detachment for the Main-Group Fluorocations[a]

Species[b]	F^+ Detachment Enthalpy (kJ mol^{-1})[c]	Species[b]	F^+ Detachment Enthalpy (kJ mol^{-1})[c]
(π^3 HeF$^+$)	-67	ClO$_2$F$_2^+$	673.6
(F$^+$)	0	(IOF$_4^+$)	686.2
(π^3 NeF$^+$)	2.5	XeF$^+$	689.5
(F$_3^+$)	251.0	ClF$_2^+$	699.1
(ArF$^+$)	351.5	XeOF$_3^+$	724.3
KrF$^+$	484.9	BrF$_4^+$	728.0
(XeF$_7^+$)	488.3	IF$_6^+$	732.2
(OF$_3^+$)	511.3	NOF$_2^+$	733.5
(BrOF$_4^+$)	548.5	Cl$_2$F$^+$	749.4
(O$_2$F$^+$)	559.8	NF$_4^+$	753.5
(ClOF$_4^+$)	567.4	(XeOF$^+$)	763.2
N$_2$F$^+$	582.8	BrF$_2^+$	763.2
(XeOF$_5^+$)	584.9	ClO$_2$F$^+$	807.5
BrF$_6^+$	589.1	XeOF$_2^+$	817.1
(XeO$_2$F$_3^+$)	592.9	BrOF$_2^+$	838.9
ClF$_6^+$	616.3	IF$_4^+$	887.4
XeF$_3^+$	637.6	IF$_2^+$	893.3
ClF$_4^+$	664.0	(IOF$_2^+$)	962.3
XeF$_5^+$	664.8		

[a] From ref 32. [b] Cations shown in parentheses have not been isolated as stable salts. [c] The calculated F^+ detachment enthalpy of KrF$^+$ is anchored to the experimental value obtained using ΔH_f° (KrF$_2$), the appearance potential of KrF$^+$ from KrF$_2$, the first adiabatic I. P. of Kr, ΔH_f° (KrF$^+$) and the bond dissociation energy of KrF$^+$.

the detachment enthalpies are typically large, and there is no evidence that reactions involving these fluorocations proceed through a F^+ intermediate, the scale correlates well with the qualitative experimental oxidative fluorinating properties obtained for KrF^+,[33-36] BrF_6^+,[36] ClF_6^+,[37] NF_4^+,[33] N_2F^+,[38] $ClOF_2^+$,[33] XeF^+,[38] XeF_5^+,[35] and ClF_2^+.[38] The KrF^+ cation is the strongest oxidizer to be isolated on this scale, however, recent experimental results suggest that the oxidizing capabilities of NiF_3^+ and AgF_2^+ may exceed that of KrF^+.[31,39] It is noteworthy, however, that salts containing the NiF_3^+ and AgF_2^+ cations have yet to be isolated or characterized by spectroscopic methods and that evidence for the cation rests on its oxidizing capability when prepared *in situ*.

1.2. Methods for Assessing Lewis Acidity

The use of Lewis acids that behave as strong fluoride ion acceptors has had a dramatic impact on the development of strong oxidative fluorinating agents. This is particularly true for the noble-gas fluorides, which readily react with strong fluoride ion acceptors such as NbF_5, TaF_5, RuF_5, AsF_5 and SbF_5 to form the potent cationic oxidizing agents NgF^+, $Ng_2F_3^+$ ($Ng = Kr$, Xe), XeF_3^+, XeF_5^+ and $Xe_2F_{11}^+$ (eq 1.5 - 1.9).

$$NgF_2 + nMF_5 \rightarrow [NgF][M_nF_{2n+1}] \quad (Ng = Kr, Xe; n = 1, 2) \quad (1.5)$$

$$2NgF_2 + MF_5 \rightarrow [Ng_2F_3][MF_6] \quad (Ng = Kr, Xe) \quad (1.6)$$

$$XeF_4 + nMF_5 \rightarrow [XeF_3][M_nF_{2n+1}] \quad (n = 1, 2) \quad (1.7)$$

$$XeF_6 + nMF_5 \rightarrow [XeF_5][M_nF_{2n+1}] \quad (n = 1, 2) \quad (1.8)$$

$$2XeF_6 + MF_5 \rightarrow [Xe_2F_{11}][MF_6] \quad (1.9)$$
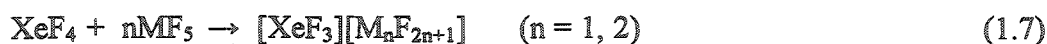
Until a recent report of a quantitative scale of Lewis acidities (*vide infra*), the strengths of strong Lewis acids were qualitatively determined by solution-based techniques such as cryoscopy, conductivity measurements, and Hammett acidity (H_o) measurements. In addition to these more traditional techniques, key stretching frequencies of the $[XeF][MF_6]$ (M = As, Sb, Bi) and $[XeF][Sb_2F_{11}]$ ion pairs have been

used to assess the relative Lewis acidities of the pnicogen pentafluorides. The latter method is based on the assumption that the $Ng-F_t$ (F_t, terminal fluorine) stretching frequency increases as the acidity of the acceptor species increases, resulting in a weaker cation-anion interaction.[40,41] This hypothesis is supported by simple 3c-4e and 2c-2e covalent bonding models of NgF_2 and NgF^+, respectively, which predict that Ng-F bond order increases from ½ to 1 upon the abstraction of fluoride from NgF_2. This method predicts the Lewis acidity of the pnicogen pentafluorides to increase in the order $BiF_5 \approx AsF_5 < SbF_5 < Sb_2F_{10}$,[40] and is in good agreement with relative Lewis acidities determined by cryoscopy in anhydrous HF solution ($PF_5 < AsF_5 < SbF_5$),[42] Hammet acidity (H_o) measurements in HSO_3F ($AsF_5 < SbF_5$)[43] and HF solutions ($PF_5 < AsF_5 < SbF_5$)[44] and conductivity measurements in HF ($PF_5 < AsF_5 < SbF_5$)[42] and HSO_3F solutions ($PF_5 < AsF_5 < BiF_5 < SbF_5$).[45] Although relative $Ng-F_t$ stretching frequencies are convenient, the method is complicated by the small $\nu(Ng-F_t)$ frequency range (*ca.* 30 cm^{-1}) of the salts studied and by the dependence of $\nu(Ng-F_t)$ on the solid-state morphologies of the salts as illustrated by the α- (607, 596 cm^{-1}) and β-phases (619, 615 cm^{-1}) of $[KrF][AsF_6]$.[40] In light of the very high Lewis acidity recently predicted for AuF_5 by theoretical methods,[46,47] the comparatively low $Kr-F_t$ stretching frequency of $[KrF][AuF_6]$ (597 cm^{-1})[35] in comparison to that of $[KrF][SbF_6]$ (621, 618 cm^{-1}) further emphasizes the caution that must be employed when using this approach, particularly when comparing species having vastly different electronic configurations. For these reasons, the development of additional experimental methods for the determination of relative Lewis acidities in the solid state continues to be of considerable interest.

The pH scale has been used extensively to quantitatively determine the strengths of protonic (Brönsted-Lowry) acids and bases and is one of the fundamental concepts of chemistry, however, a quantitative scale of Lewis acidity has only recently been reported

by Christe and coworkers.[46,48] This scale currently ranks 170 Lewis acids on the basis of their calculated fluoride ion affinities, which is defined as the negative enthalpy of eq 1.10, but is anchored to the experimental value obtained for COF_2.[49] The pF⁻ scale has

$$[LA] + F^- \rightarrow [LA]F^- \quad (LA = Lewis\ acid) \tag{1.10}$$

$$pF^- = \frac{F^-_{affinity}\ (kcal\ mol^{-1})}{10} \tag{1.11}$$

been defined according to eq 1.11 to emphasize the existence of a Lewis acidity scale, however, the definition fundamentally differs from the logarithmic-based pH scale. For this reason, and because the enthalpies of fluoride ion attachment in the present work are reported in SI units ($kJ\ mol^{-1}$), the unscaled enthalpies are used in the ensuing discussions instead of the pF⁻ scale. The F^+ cation is the strongest Lewis acid on this scale with a value of 1510 $kJ\ mol^{-1}$, however, the values estimated for common monomeric or polymeric Lewis acid fluoride ion acceptors (Table 1.2) generally do not exceed 551 kJ mol^{-1} (Sb_3F_{15}). It is noteworthy that the calculated scale shows a strong correlation with the qualitative results obtained by the experimental methods discussed above, despite the obvious neglect of solution and solid-state interactions. The significance of these latter effects is more obvious for the weaker Lewis acids, which generally do not behave as fluoride ion acceptors if their fluoride ion affinities are less than 125 to 150 $kJ\ mol^{-1}$.[46] This discontinuity can generally be accounted for by the competing fluoride ion affinity of the donor species, lattice enthalpies and solvent effects.

1.3. The Chemistry of the XeF⁺ and Xe₂F₃⁺ Cations

Xenon exhibits the most extensive and diverse chemistry of the noble gases, as illustrated by the accessibility of the 0, +½, +1, +2, +4, +6 and +8 oxidation states and the isolation of compounds in which it is bound to fluorine (XeF_2),[50] oxygen ($XeOF_4$),[50] nitrogen ($[HCNXeF][AsF_6]$),[51] chlorine ($[XeCl][Sb_2F_{11}]$),[52] gold ($[AuXe_4][Sb_2F_{11}]_2$),[53]

Table 1.2.   Fluoride ion Affinities and pF$^-$ Values of MF$_5$ (M = P, As, Sb, Bi, Au)
and M$_2$F$_{10}$ (M = Sb, Bi) and Sb$_3$F$_{15}$

Species	Fluoride Ion Affinity (kJ mol^{-1})	pF$^-$	Ref
PF$_5$	397.1	9.49	[46]
	352.7	8.43	[48]
AsF$_5$	443.1	10.59	[48]
	439.7	10.51	[46]
SbF$_5$	503.3	12.03	[48]
	472.8	11.30	[46]
BiF$_5$	456.5	10.91	[46]
AuF$_5$	590.8	14.12	[47]
	538.9	12.88	[46]
Sb$_2$F$_{10}$	530.9	12.69	[46]
Bi$_2$F$_{10}$	507.5	12.13	[46]
Au$_2$F$_{10}$	538.9	12.88	[47]
	602.9	14.41	[46]
Sb$_3$F$_{15}$	551.5	13.18	[46]

carbon ($[XeC_6F_5][B(C_6F_5)_3F]$),[54,55] mercury ($[XeHg][SbF_6][Sb_2F_{11}]$)[54] and to itself ($[Xe_2][Sb_4F_{21}]$).[57] Several comprehensive reviews on the chemistry of xenon have been published,[58-63] however, a full account of the chemistry of xenon is beyond the scope of this work, which has focused on the fluoride ion donor properties of XeF_2 and, more specifically, on the crystallographic characterization of salts containing the XeF^+ cation.

The accessibility of the positive oxidation states of xenon was first demonstrated by the reaction of xenon gas with PtF_6, which was originally reported to proceed through a one-electron redox reaction to form $[Xe][PtF_6]$,[64,65] however this compound has recently been reformulated as the xenon(II) salt, $[XeF][PtF_5]$ (eq 1.12).[66] In the presence

$$PtF_6 \ + \ Xe(\text{excess}) \ \xrightarrow{\ SF_6(g)\ } \ [XeF][PtF_5] \qquad (1.12)$$

$$[XeF][PtF_5] + PtF_6 \ \longrightarrow \ [XeF][PtF_6] + PtF_5 \ \xrightarrow{\ PtF_6, \ <60^\circ C\ } \ [XeF][Pt_2F_{11}] \quad (1.13)$$

of excess PtF_6, the Pt(V) salts, $[XeF][PtF_6]$ and $[XeF][Pt_2F_{11}]$, are formed (eq 1.13), with their relative amounts being dependant upon the experimental conditions used.[65,66] Salts containing the XeF^+ cation are more conveniently prepared by the reaction of XeF_2 with a suitable fluoride ion acceptor (eq 1.5). This method is advantageous because XeF_2 can be prepared in high yield and purity, and because it avoids the preparation and use of transition metal hexafluorides such as PtF_6,[64,65] RhF_6[67] and RuF_6,[30] which react rapidly with oxygen at room temperature to form dioxygenyl (O_2^+) salts.

Salts containing the XeF^+ cation have been extensively characterized by vibrational and ^{19}F NMR spectroscopy. The Raman spectra of the $[XeF][MF_6]$ (M = As,[68,69] Sb,[68] Bi,[41] Ru,[69] Os,[69] Ir,[69] Pt,[69] Au[70]) salts are considerably more complex than expected for a XeF^+ cation and an octahedral MF_6^- anion. The spectral complexity results from a strong interaction between the cation and the anion by means of a fluorine bridge. The bend in the $Xe\text{--}F_b\text{--}M$ bridge, which reflects the partial covalent nature of

8

the cation-anion interaction and the two lone electron pairs on F_b, serves to remove the degeneracy of the $\nu_2(E_g)$, $\nu_5(F_{2g})$, $\nu_3(F_{1u})$, $\nu_4(F_{1u})$ and $\nu_6(F_{2u})$ modes of the octahedral anion and introduces stretching and bending modes involving the bridging fluorine atom. A similar increase in complexity is also observed in the vibrational spectra of the $[XeF][M_2F_{11}]$ (M = Sb,[68,69] Ru,[69] Ir,[69] Nb,[68] Ta,[68] Bi,[41] Pt[64]) salts, however, these spectra are further complicated by the low symmetry of the anion. The strong ion pairing in the $[XeF][MF_6]$ (Structure I) and $[XeF][M_2F_{11}]$ (Structure II) salts has been verified by single

I   II
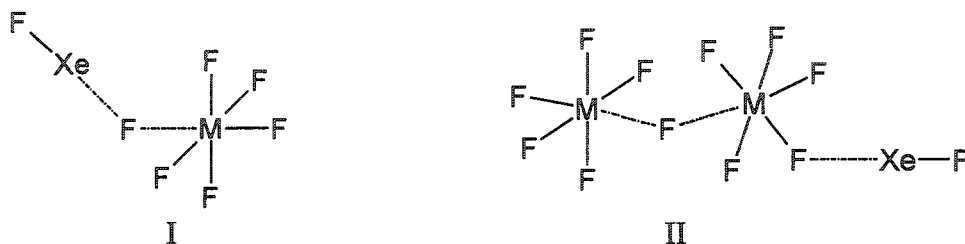
crystal X-ray diffraction studies of $[XeF][MF_6]$ (M = Ru,[71] As[72]) and $[XeF][Sb_2F_{11}]$.[73] The average $Xe-F_t$ (1.86(2) Å) bond length in these structures is significantly shorter than the average $Xe--F_b$ (2.24(8) Å) bond length, with the two values bracketing the Xe-F bond lengths of XeF_2 (2.00(1) Å) determined by single crystal X-ray diffraction.[74,75] The ionic formulation commonly used for the XeF^+ salts is consistent with the low-temperature (-115 °C) ^{19}F NMR spectra of $[XeF][MF_6]$ (M = As, Sb) in HSO_3F, which exhibit a single cation resonance (-243 ppm) with ^{129}Xe satellites in addition to a single anion resonance,[76] indicating that the fluorine bridge interaction is disrupted in solution. The lability of the $Xe--F_b$ bond has also been noted for XeF^+ in SbF_5 solvent at 26 °C. In this instance the ^{19}F resonance is even more shielded, occurring at -290 ppm.[77] The ^{129}Xe resonance of the low-coordinate XeF^+ cation exhibits a strong solvent dependence, occurring at -574 ppm for $[XeF][Sb_nF_{5n+1}]$ in SbF_5 solution[78,79] and -991 ppm for $[XeF][AsF_6]$ dissolved in HSO_3F.[80]

In contrast to the highly ionic $[XeF][MF_6]$ and $[XeF][M_2F_{11}]$ ion pairs obtained by the reactions of XeF_2 with strong fluoride ion acceptors, the products obtained by the reactions of XeF_2 with moderately strong Lewis acids are best described as molecular adducts. The fluorine-bridged $XeF_2 \cdot (MOF_4)_n$ (M = Mo, W; n = 1 - 4)[81,82] adducts were the first such species identified and characterized, exhibiting terminal Xe-F stretching frequencies (n = 1, 2; 566 - 581 cm^{-1}) that are intermediate with respect to those of the more ionic XeF^+ salts (602 - 620 cm^{-1})[41,68,69] salts and the parent covalent species, XeF_2 ($\nu_1(\Sigma_g^+)$, 514.5; $\nu_3(\Sigma_u^+)$, 555 cm^{-1}).[75,83] In contrast to the more ionic XeF^+ salts (*vide supra*), the low-temperature ^{19}F NMR spectra of these species in BrF_5 and SO_2ClF solvent exhibit two resonances flanked by ^{129}Xe satellites, which are indicative of non-labile Xe--F_b--M interactions.[82] The retention of the bridging interaction is further supported by the ^{129}Xe NMR spectra of these species, which exhibit AMX spin systems.[82] Interestingly, the ^{19}F NMR spectra of the $XeF_2 \cdot (WOF_4)_n$ systems provide evidence for Xe--F $\rightleftharpoons$ Xe--O bond isomerization, with the relative concentration of the oxygen bridged species being negligible for n = 1, intermediate for n = 2 and large for n = 3.[82] The low ionic nature of these adducts is also reflected in the Xe-F bond lengths of $XeF_2 \cdot WOF_4$ (F_t, 1.89(3); F_b 2.04(3) Å),[84] which are similar to those of XeF_2. The crystal structures of several $XeF_2 \cdot M^{n+}$ adducts (M^{n+} = Pb^{2+},[85] Sr^{2+},[85] Ca^{2+},[86] Ag^+,[87] Ba^{2+},[88] Mg^{2+},[89] Cd^{2+}[90]) have recently been reported. In these species, the Xe-F bond lengths are symmetric and comparable to those of the parent difluoride when bridged between two cations, but slightly distorted when coordinated to a single cation.

Salts containing the $Xe_2F_3^+$ cation are readily prepared by the reaction of XeF_2 with a suitable fluoride ion acceptor in 2:1 molar ratio (eq 1.6). The stabilities of these salts with respect to dissociation to XeF_2 and $[XeF][MF_6]$ is accounted for by the strong Lewis acidity of the XeF^+ cation, which favours coordination by means of a fluorine

bridge to the moderate Lewis base XeF_2, rather than to the MF_6^- anion which is derived from the strong Lewis acid MF_5. The stronger and symmetric $Xe\text{--}F_b$ interactions in the $Xe_2F_3^+$ cation are apparent from the ^{19}F NMR spectrum of $[Xe_2F_3][AsF_6]$ in BrF_5, which exhibit AX_2 spin systems with ^{129}Xe satellites.[40,76] The vibrational spectra of the $[Xe_2F_3][MF_6]$ (M = As,[68,69,91] Sb,[68] Ru,[69] Ir,[69] Os,[69] Au[35]) salts have been interpreted in terms of a V-shaped cation (Structure III) and an octahedral MF_6^- anion, contrasting with

$$\left. \begin{array}{c} \text{F} \qquad\qquad \text{F} \\ \diagdown \qquad\qquad \diagup \\ \text{Xe} \qquad \text{Xe} \\ \diagdown \qquad \diagup \\ \text{F} \end{array} \right]^{+}$$
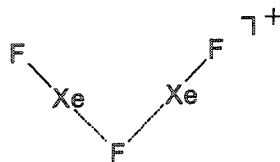
III

the strong ion pairing observed for the $[XeF][MF_6]$ and $[XeF][M_2F_{11}]$ salts (*vide supra*). The absence of significant fluorine bridging between the cation and the anion in the $Xe_2F_3^+$ salts is attested to by the crystal structures of $[Xe_2F_3][MF_6]$ (M = As,[91-93] Sb[91]), which have $Xe\text{-}F_t$ and $Xe\text{--}F_b$ bond lengths ranging from 1.908(6) to 1.929(6) Å and 2.09(9) to 2.26(2) Å, respectively.[91]

The Lewis acidity of the XeF^+ cation is further demonstrated by the cationic Xe-N bonded adducts formed by the reaction of $[XeF][MF_6]$ with oxidatively resistant nitrogen base centres, such as nitriles (eq 1.14),[94,95] pyridines (eq 1.15),[96] diazenes (eq 1.16)[97] and s-trifluoro-triazene (eq 1.17),[98] in HF and/or BrF_5 solvents. The high first adiabatic

$$[XeF][AsF_6] + RCN \rightarrow [RCN\text{-}XeF][AsF_6] \qquad (1.14)$$

$$[XeF][AsF_6] + C_5YF_4N \rightarrow [C_5YF_4NXeF][AsF_6] \qquad (1.15)$$

$$[XeF][AsF_6] + (o\text{ or }m)\text{-}C_4F_4N_2 \rightarrow [C_4F_4NN\text{-}XeF][AsF_6] \qquad (1.16)$$

$$[XeF][AsF_6] + s\text{-}C_3F_3N_3 \rightarrow [C_3F_3N_2N\text{-}XeF][AsF_6] \qquad (1.17)$$

ionization potentials of these nitrogen bases allows for a diverse range of derivatives (R = H, CH_3, CH_2F, C_2H_5, C_2F_5, C_3F_7, C_6F_5; Y = F, CF_3; Z = H, F) to be prepared by these

reactions. The retention of the Xe-N bond in solution has been confirmed by multi-NMR spectroscopy (^{1}H, ^{129}Xe, ^{13}C, ^{14}N),[94-96] and the nature of the Xe-N bond in the solid state has been investigated in detail by Raman spectroscopy[95,99] and X-ray structure determinations of [RCN-XeF][AsF$_6$] (R = H, C(CH$_3$)$_3$),[99] 1,3-[C$_4$F$_4$NN-XeF][AsF$_6$],[97] [s-C$_3$F$_3$N$_2$N-XeF][AsF$_6$],[99] [CH$_3$N-XeF][AsF$_6$]·HF,[99] [1,2-C$_4$F$_4$NN-XeF][AsF$_6$][99] and [C$_5$F$_5$N-XeF][AsF$_6$].[99]

1.4. The Chemistry of Krypton

The chemistry of krypton was first comprehensively reviewed by Bartlett and Sladky in 1973,[59] and various aspects of this field have been addressed in general reviews pertaining to the noble gases.[61-63,100-110] A more comprehensive review of the historical, synthetic, physiochemical, spectroscopic, crystallographic and theoretical aspects of the chemistry of krypton(II), including synthetic applications, has recently been published and represents the most current account of the field.[111]

With the exception of the argon-containing species HArF and DArF, which have recently been trapped in argon matrices and characterized by infrared spectroscopy,[112,113] krypton is the lightest noble gas known to form compounds in significant quantities. Unlike xenon, which forms compounds in the +½, +1, +2, +4, +6 and +8 oxidation states, the chemistry of krypton is currently limited to the +1 and +2 oxidation states. The chemistry of krypton(I) is currently limited to the KrF· radical, which is highly unstable but reported to have a purple colour when trapped in crystalline KrF$_2$.[114] The inherent instability of KrF· prevents it from being isolated in bulk quantities, however, the high-energy ultraviolet lasing (222, 248 nm)[115] properties of this radical are routinely exploited for resonance Raman spectroscopy, laser ablation, and semiconductor lithography.

The chemistry of krypton(II) is similar to that of xenon(II), but is much less extensive owing to the strong oxidizing properties of its compounds, which limit its

chemistry to bond formation with the most electronegative elements (*i.e.*, F, N, O) and renders all of its compounds thermodynamically unstable.

The efficient synthesis of KrF_2 is of considerable interest as a consequence of its thermodynamic instability (ΔH_f°, 60.2(3.4) kJ mol^{-1})[11,12] and because it is the sole precursor to all other Kr(II) compounds. In contrast to the fluorides of xenon, which are prepared, for kinetic reasons, by reaction of xenon with F· radicals, the synthesis of KrF_2 requires F· to be generated at low-temperatures because the product is thermodynamically unstable. The generation of the F· radical under cryogenic conditions is problematic but has been overcome by use of several synthetic methods. Krypton difluoride was first synthesized in 1963 by means of electric discharge, but was initially and incorrectly identified as KrF_4.[116,117] The difluoride was first correctly identified by infrared spectroscopy, which was used to monitor the reaction of krypton and fluorine in an argon matrix following irradiation with ultraviolet light.[118,119] In addition to the ultraviolet photolysis,[13-18] and high voltage discharge[19-21] methods noted above, KrF_2 has also been prepared by small particle (e$^-$, p$^+$) bombardment,[24,25] and low-temperature hot-wire thermolysis.[16,22,23] Of these methods, the ultraviolet photolysis of krypton in liquid fluorine and hot-wire thermolysis methods are the most widely used and have been optimized to provide yields of 1.22[16] and 6 g hr^{-1},[22] respectively. Krypton difluoride has been extensively characterized by infrared,[120-122] Raman,[120,123] ^{19}F NMR[40,124] and Mössbauer[125,126] spectroscopy, with the results of these studies being consistent with a linear and centrosymmetric geometry. The Kr-F bond length has been accurately determined in the gas phase by electron diffraction (1.889(10) Å)[127] and roto-vibrational spectroscopy of $^{84}KrF_2$ (1.882821(9) Å; $^{86}KrF_2$ (1.882766(8) Å).[128] These values are in good agreement with that determined for β-KrF_2 (1.89(2) Å),[129] which, until recently, was the only Kr(II) compound that had been characterized by crystallographic methods.

The fluoride ion donor properties of KrF_2 are analogous to those of XeF_2 (*vide supra*), and salts containing the KrF^+ and $Kr_2F_3^+$ cations can be prepared by the reaction of KrF_2 with strong Lewis acids (eq 1.5, 1.6). The formal bond order of the KrF^+ (1.0) cation is greater than that of KrF_2 (0.5) and consistent with the greater thermal stability associated with these salts, however, the KrF^+ and $Kr_2F_3^+$ cations are extremely potent oxidizing agents (see section 1.1) and must be handled with the rigorous exclusion of air because of their sensitivity towards moisture and oxygen (eq 1.18).[40,130] In the absence of

$$[KrF][MF_6] + O_2 \rightarrow [O_2][MF_6] + Kr + \frac{1}{2}F_2 \qquad (1.18)$$
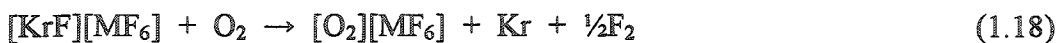
crystallographic studies, the structural characterization of $[KrF][MF_6]$, $[KrF][M_2F_{11}]$ and $[Kr_2F_3][MF_6]$ salts have been heavily reliant upon spectroscopic methods, and, in particular, on low-temperature Raman and ^{19}F NMR spectroscopy. As in the case of the XeF^+ salts (see section 1.3), the Raman spectra of the $[KrF][MF_6]$ (M = As, Sb, Bi, Au, Pt, Ta) and $[KrF][M_2F_{11}]$ (M = Sb, Nb, Ta) salts are consistent with structures in which the KrF^+ cation and fluoro-anions interact by means of a bent Kr--F_b--M fluorine bridge that results in significantly distorted anion geometries (Structures I, II). The ^{19}F NMR spectrum of $[KrF][Sb_2F_{11}]$ in HF exhibits a single resonance for the cation at -22.6 ppm (-40 °C),[40] reflecting the lability of the bridging interaction in solution.

The Raman spectra of the $[Kr_2F_3][MF_6]$ (M = As, Sb)[40] salts have been interpreted in terms of a V-shaped cation[40] and an octahedral anion by analogy with the $Xe_2F_3^+$ cations (Structure III), although excess KrF_2 is often associated with these systems.[40] The ^{19}F NMR spectra of $[Kr_2F_3][MF_6]$ (M = As, Sb) in BrF_5 solution at -65 and -66 °C, respectively, exhibit the anticipated AX_2 splitting pattern for the cation,[40] confirming the retention of the Kr--F_b--Kr bridge in solution.

Krypton difluoride forms molecular adducts with a number of moderate Lewis acids including VF_5, $CrOF_4$, $MoOF_4$, WOF_4, and MnF_4. The vibrational frequencies of

the $Kr-F_t$ and $Kr--F_b$ stretches in the $KrF_2 \cdot MOF_4$ (M = Cr,[124] Mo,[81] W[81]) adducts are consistent with a high degree of covalency, but the increasing separation of these modes with increasing atomic number of M (Cr, 64 cm^{-1}; Mo, 102 cm^{-1}; W, 117 cm^{-1}) suggests that the ionic character increases down the group. This hypothesis is in agreement with the ^{19}F NMR spectra of these adducts in SO_2ClF at -121 °C, where the $Kr--F_b--M$ bridge is retained for Mo and W,[81] but is labile for Cr where only KrF_2 and $CrOF_4$ can be identified.[124] The adducts $KrF_2 \cdot (MoOF_4)_2$ and $KrF_2 \cdot (MoOF_4)_3$ have also been identified by low-temperature (-121 °C) ^{19}F NMR spectroscopy in SO_2ClF solvent.[81] The tungsten analogues of these species are highly unstable with respect to WF_6 formation, which may be a result of isomerization between Kr-F--W and Kr-O--W bridging interactions,[81] which have been previously demonstrated for the $XeF_2 \cdot (MoOF_4)_2$ and $XeF_2 \cdot (MoOF_4)_3$ analogues.[82] The $KrF_2 \cdot MnF_4$ adduct has not been characterized in detail, but decomposes at ambient temperature to give high purity MnF_4.[131]

Compounds containing Kr-N or Kr-O bonds are significantly less stable than those containing only Kr-F bonds. Despite the thermal and kinetic instabilities of $[RCNKrF][AsF_6]$ (R = H, CF_3, C_2F_5, n-C_3F_7) above -40 °C, these cations have been characterized by ^{19}F NMR spectroscopy,[51,98] with $HCNKrF^+$ also having been characterized by ^1H and ^{15}N NMR spectroscopy.[51] The instabilities of these compounds above -50 °C have complicated their characterization by vibrational spectroscopy, however, the Kr-F and Kr-N stretching frequencies have been obtained for $[HCNKrF][AsF_6]$ under frozen HF solution by use of Raman spectroscopy[51] and correlate well with those estimated by theoretical methods.[132-135] In contrast to KrF_2, which exhibits moderate stability at ambient temperature, the -$OTeF_5$ analogue, $Kr(OTeF_5)_2$, decomposes rapidly to $F_5TeO-OTeF_5$ and krypton at temperatures as low as -78 °C and has only been characterized by ^{19}F and ^{17}O NMR spectroscopy at -110 °C.[136]

The use of the oxidizing properties of KrF_2, KrF^+ and $Kr_2F_3^+$ for the preparation of a broad range of high-valent fluorides and oxide fluorides has recently been reviewed.[111] In the context of the present work, these Kr(II) species have had a significant impact on the chemistries of Au(V) and Br(VII), which are discussed in the following sections, by providing efficient synthetic routes to high purity AuF_6^- [35] and BrF_6^+ salts.[36,137]

1.5. The Chemistry of Gold(V)

The reluctance of gold to undergo oxidation is well known and is clearly illustrated by the inability of HCl, H_2SO_4 or HNO_3 to dissolve the metal.[138] The inertness of gold metal has been attributed to relativistic effects, which contract and energetically stabilize atomic orbitals of the heavy elements.[139] Because these effects are strongest at the nucleus, the valence p-, d- and f-orbitals, which are more spatially extensive and have nodes at the nucleus, are not as strongly affected as the s-orbitals, which have finite probabilities at the nucleus. The contraction of the filled valence s-orbital also has the effect of shielding the nucleus and consequently destabilizes the valence 5d-orbitals. The relativistic stabilization of the 6s orbital of gold is in agreement with the higher first ionization potential of gold (9.225 eV)[140] relative to that of silver (7.576 eV)[140] and the general reluctance for gold to undergo oxidation. The increase in the 5d orbital energy of gold is apparent from the inversion of the second ionization potentials of gold (20.5 eV)[140] and silver (21.49 eV)[140] when compared with their first ionization potentials and accounts for the attainability of the +5 oxidation state of gold, which contrasts with the highest attained oxidation state of silver (i.e., +3).

The low-valent halogen chemistry of gold has been reviewed by Puddephatt[141] and will not be discussed in detail here. In contrast to the lower oxidation states, where the existence of AuX (X = Cl, Br, I), AuX_2^- (X = Cl, Br, I) Au_2X_6 (X = Cl, Br), AuX_4^- (Cl,

16

Br, I) and Au_2O_3 demonstrates the ability of gold to form bonds with the heavier halogens and oxygen, the only element known to stabilize the Au(V) oxidation state is fluorine. Consequently, the chemistry of Au(V) is limited to AuF_5[142,143] and to complex salts of the AuF_6^- anion,[35,70,144-149] and is indicative of the strong oxidizing properties of Au(V), which have previously been discussed by Bartlett and Leary.[146]

The AuF_6^- anion was first prepared as its $Xe_2F_{11}^+$ salt by the oxidation of AuF_3 with excess XeF_6 at 110 °C.[144] Salts of AuF_6^- have since been prepared by the oxidation of gold (eq 1.19)[143] or AuF_4^- salts (eq 1.20)[146] with fluorine at high temperature, and by

$$Au + 3F_2 + O_2 \rightarrow [O_2][AuF_6] \tag{1.19}$$

$$[M][AuF_4] + F_2 \rightarrow [M][AuF_6] \tag{1.20}$$

$$7KrF_2 + Au \xrightarrow{\text{HF, RT}} 2[KrF][AuF_6] + 5Kr \tag{1.21}$$
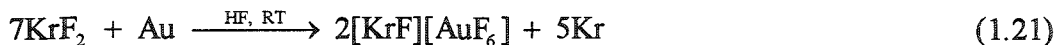
the oxidation of gold with KrF_2 (eq 1.21).[35] Although the preparation of $[KrF][AuF_6]$ is challenging because the preparation of KrF_2 is difficult, the strong oxidant properties (eq 1.22),[35] moderate Lewis acidity (eq 1.23),[150] and thermodynamic instability (eq 1.24)[35] of

$$2[KrF][AuF_6] + 2O_2 \xrightarrow{> -78\,°C} 2[O_2][AuF_6] + Kr + F_2 \tag{1.22}$$

$$[KrF][AuF_6] + CsF \xrightarrow{\text{HF, 20\,°C}} [Cs][AuF_6] + KrF_2 \tag{1.23}$$

$$2[KrF][AuF_6] \xrightarrow{60\,°C} 2AuF_5 + 2Kr + F_2 \tag{1.24}$$
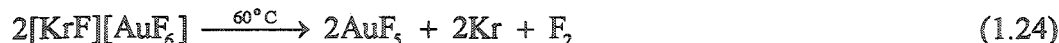
the KrF^+ cation make it a highly versatile precursor for the synthesis of other Au(V) compounds.

Ligand field theory predicts that the five valence d-orbitals of gold will be split into a lower energy set of t_{2g} orbitals and a higher energy set of e_g orbitals when octahedrally coordinated. The occupation of these orbitals by the six valence electrons of Au(V) in AuF_6^- results in a completely spin-paired and stable $t_{2g}^6 e_g^0$ electronic configuration. Consequently, AuF_6^- is expected to be devoid of Jahn-Teller distortion and to exhibit a regular octahedral geometry in the absence of strong cation-anion

interactions. The $t_{2g}^6 e_g^0$ electron configuration of AuF_6^- also accounts for the present inability to oxidize the anion to AuF_6,[30] and casts suspicion[139] on the reported preparation of AuF_7.[151] With the exception of the KrF^+,[35] XeF^+,[70] XeF_5^+ [70] and $Xe_2F_{11}^+$ [35] salts of AuF_6^-, where the splittings of the degenerate Raman-active bands of the AuF_6^- anion ($v_1(A_{1g})$, $v_2(E_g)$, $v_5(F_{2g})$) are indicative of a distorted octahedral geometry, the Raman-active and infrared-active ($v_3(F_{1u})$, $v_4(F_{1u})$) bands of salts containing the AuF_6^- anion have been assigned under O_h symmetry.[145,146] The Au-F bond lengths of the AuF_6^- anion have been determined from the X-ray powder diffraction patterns of [Li][AuF_6] (1.874(6) Å),[152] [Ca][AuF_6]$_2$ (1.86 Å)[153] and [Ba][AuF_6]$_2$ (1.86 Å),[153] and the single crystal X-ray structure determinations of [Xe_2F_{11}][AuF_6] (1.85(1) - 1.90(1) Å),[148,154] [O_2][AuF_6] (1.875(9) - 1.895(9) Å),[47,155] with these studies providing further confirmation of the octahedral (or near octahedral) geometry of the anion. Interestingly, the ^{19}F NMR spectra of [Xe_2F_{11}][AuF_6] in BrF_5 solution[146,156] and [XeF_5][AuF_6] in HF solution[35] do not exhibit $^1J(^{19}F-^{197}Au)$ spin-spin coupling (^{197}Au, 100% natural abundance, $I = ^3/_2$). Failure to observe the anticipated 1:1:1:1 line spectrum has been attributed to quadrupolar collapse induced by ion pairing, but may also reflect the small magnitude of the $^1J(^{19}F-^{197}Au)$ coupling that is anticipated as a consequence of the low gyromagnetic ratio (0.4692 × 10^7 rad s^{-1} T^{-1}) and the large line width factor (4.03 × 10^{-57} m^4) of ^{197}Au.[157]

Gold pentafluoride can be prepared in high purity by the thermal decomposition of [KrF][AuF_6] (eq 1.24), but can also be prepared by heating [O_2][AuF_6] under vacuum at 180 °C and collecting the product on a cold finger.[47,143] The vibrational spectrum of AuF_5 has been reported by several authors,[35,70,143,158,159] but has not been assigned in great detail because of the complexity introduced by the fluorine bridged structure. Mass spectrometry[143] and gas-phase electron diffraction[160] have been used to identify (AuF_5)$_2$ and (AuF_5)$_3$ in the gas phase, with the pseudo-octahedrally coordinated gold centres of

18

the dimer (D_{2h} symmetry) and the trimer (D_{3h} symmetry) being fluorine bridged through fluorine ligands lying *cis* to each other.[160] The solid-state structure of AuF_5 has recently been determined by single crystal X-ray diffraction, and is in accord with the dimeric structure determined by gas-phase electron diffraction.[47] The use of AuF_5 as a fluoride ion acceptor is generally deterred by its difficult preparation, however, interest in this pentafluoride has recently been revived by calculations that indicate that the Lewis acidity of AuF_5 significantly exceeds that of SbF_5 (Table 1.2).[46,47] Experimental evidence for this claim is currently limited, but a failed attempt to displace AuF_5 from $[Xe_2F_{11}][AuF_6]$ using SbF_5 is consistent with this prediction.[146]

1.6. The Chemistry of Bromine(VII)

The known and predicted Br(VII) species that can be derived from oxygen and fluorine are summarized in Table 1.3 along with their known or predicted geometries. Of these species, only BrO_4^-,[161] BrO_3F[162] and BrF_6^+ [137] have been isolated in significant quantities, whereas the $BrO_2F_2^+$,[163] $BrO_2F_3^+$ [163] and BrO_3^+ [162] cations have only been detected by positive ion mass spectrometry.

The limited chemistry of bromine(VII) is in accord with the general reluctance of late period 4 elements to form compounds in their highest oxidation states when compared with their period 3 and 5 analogues.[164,165] Prior to the discovery of the perbromate anion and $HBrO_4$, this anomaly was believed to be a consequence of poor 2p-4d π-orbital overlap between the oxygen ligands and the central element, which served to destabilize the period 4 peroxo-anions (*i.e.*, GeO_4^{4-}, AsO_4^{3-}, SeO_4^{2-} and BrO_4^-).[178] Although 2p-5d π-orbital overlap between oxygen and the late period 5 elements was also expected to be poor, the stabilities of $H_3IO_6^{2-}$ and IO_4^- had been accounted for by the involvement of the 4f orbitals in the form of d^2sf^3 and $sp^{3-\varepsilon}f^\varepsilon$ hybridization, respectively, where magnitude of ε was expected to be small.[179] These rationals have been viewed

19

Table 1.3. Known and Unknown Bromine(VII) Species; Their Geometries and Methods of Characterization
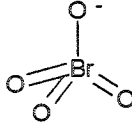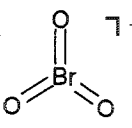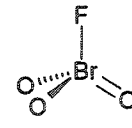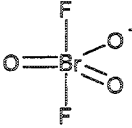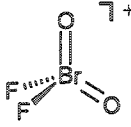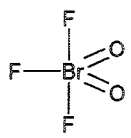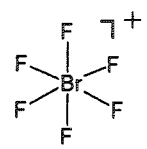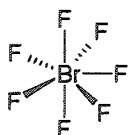
Species	VSEPR Arrangement Symmetry and Geometry	Methods of Characterization	Reference
BrO_4^-	AX_4 (T_d) tetrahedral	$^{79,81}Br$, ^{17}O NMR spectrosc. Infrared spectrosc. Raman spectrosc. UV-vis spectrosc. Calorimetry X-ray diffraction (single cryst.) (powder)	[166] [167, 168] [167, 168] [167] [169] [170] [171]
BrO_3^+	AX_3 (D_{3h}) trigonal planar	Positive ion mass spectrom.	[162, 163]
BrO_3F	AX_3Y (C_{3v}) trigonal pyramidal	Positive ion mass spectrom. Infrared spectrosc Raman spectrosc. ^{19}F, ^{81}Br NMR spectrosc. Electron diffraction Calorimetry	[162] [172, 173] [172] [166] [174] [175]
$BrO_3F_2^-$	AX_3Y_2 (D_{3h}) trigonal bipyramidal	Raman spectrosc. X-ray diffraction (single cryst.)	[This work] [This work]
$BrO_2F_2^+$	AX_2Y_2 (C_{2v}) distorted-tetrahedral	Positive ion mass spectrom.	[163]

Table 1.3.   (continued)

Species	VSEPR Arrangement Symmetry and Geometry	Methods of Characterization	Reference
BrO_2F_3	AX_3Y_2 (C_{2v}) distorted-trigonal bipyramidal	Positive ion mass spectrom.	[163]
BrF_6^+	AX_6 (O_h) octahedral	^{19}F NMR spectrosc. [79,81]Br NMR spectrosc. Infrared spectrosc. Raman spectrosc. X-ray diffraction (powder) (single cryst.)	[31, 36, 137] [this work] [176] [36, 177] [176] [this work]
BrF_7	XF_7 (D_{5h}) Pentagonal bipyramidal	Unknown	[36, 177]

with skepticism,[180] and the anomalous behaviour of the period 4 elements is now more commonly attributed to thermodynamic[181,182] and kinetic factors.[167]

With few exceptions, the thermodynamic arguments are supported by the enthalpies of oxidation (Table 1.4) calculated from the standard experimental enthalpies of formation for MF_n (n = 3, 5; M = P, As, Sb), MF_n (n = 4, 6; M = S, Se, Te), MO_n (n = 2, 3; M = S, Se, Te) and XO_n^- (n = 3, 4; X = Cl, Br, I). A comparison of the enthalpies of oxidative fluorination for MF_3 (eq 1.25) and MF_4 (eq 1.26) reveals that these reactions

$$MF_3 + F_2 \rightarrow MF_5 \quad (M = P, As, Sb) \tag{1.25}$$

$$MF_4 + F_2 \rightarrow MF_6 \quad (M = S, Se, Te) \tag{1.26}$$

are all exothermic, but that the reactions involving species of periods 4 and 5 are approximately 200 kJ mol^{-1} less exothermic than their period 3 analogues. The oxidations of MO_2 (eq 1.27) and XO_3^- (eq 1.28) by O_2 also illustrate this general trend,

$$MO_2 + \frac{1}{2}O_2 \rightarrow MO_3 \quad (M = S, Se, Te) \tag{1.27}$$

$$XO_3^- + \frac{1}{2}O_2 \rightarrow XO_4^- \quad (M = Cl, Br, I) \tag{1.28}$$
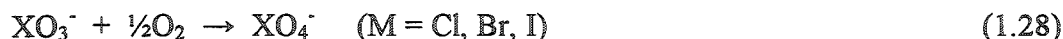
however, the high-valent species SeO_3, BrO_4^- and IO_4^- are unstable with respect to the lower oxidation state species. The greater stabilities of the intermediate oxidation states for the period 4 elements have been accounted for by the shielding effect the filled 3d-orbitals of the first transition metal series have on the valence 4s-orbitals.[183,184] Stabilization of the 4s orbital in molecular systems is apparent from the slightly higher first adiabatic ionization potential of $AsCl_3$ (11.2 eV) when compared with those of PCl_3 (10.2 eV) and $SbCl_3$ (11.0 eV),[192] and the instability of $AsCl_5$ towards Cl_2 elimination to give $AsCl_3$.[183,193] Early failures to prepare perbromates by the thermolysis of BrO_3^-,[194-197,180] or by the use of $HClO_4$ (eq 1.29),[198-202] $HClO_3$ (eq 1.30),[202] ClO_2 (eq 1.31)[202] or $NaIO_4$ (eq 1.32)[203] as oxidants, are consistent with the thermodynamic instability and higher reduction potential of BrO_4^- (eq 1.33),[175] however, a similar argument cannot be

Table 1.4. Standard Enthalpies of Reaction Calculated for the Fluorinations of MF_3 (M = P, As, Sb) and MF_4 (M = S, Se, Te) and the Oxidations of XO_3^- (X = Cl, Br, I)[a]

Reactant	$\Delta H^o_{f,\text{reactant}}$ (kJ mol-1)	Ref	Product	$\Delta H^o_{f,\text{product}}$ (kJ mol-1)	Ref	$\Delta H^o_{f,\text{product}} - \Delta H^o_{f,\text{reactant}} = \Delta H^o_{\text{oxidation}}$ (kJ mol-1)b
PF_3	-958.4	[185]	PF_5	-1594.4	[185]	-636.0
AsF_3	-852.4	[186]	AsF_5	-1234.2	[187]	-381.8
SbF_3	-915.5	[185]	SbF_5	-1327.9	[188]	-412.4
SF_4	-763.2	[185]	SF_6	-1220.5	[185]	-457.3
SeF_4	-849.4	[189]	SeF_6	-1117.0	[185]	-267.6
TeF_4	-1038.9	[190]	TeF_6	-1318.0	[185]	-279.1
SO_2	-296.8	[185]	SO_3	-395.7	[185]	-98.9
SeO_2	-225.4	[185]	SeO_3	-166.9	[185]	58.5
TeO_2	-320.4	[185]	TeO_3	-416	[191]	-95.6
ClO_3^-	-104.1	[169]	ClO_4^-	-128.4	[169]	-24.3
BrO_3^-	-66.7	[169]	BrO_4^-	13.3	[169]	80.0
IO_3^-	-219.7	[169]	IO_4^-	-144.6	[169]	75.1

[a] Enthalpies of formation and oxidation have been used in place of free energies, because complete thermochemical data are not available in the literature and for consistency. [b] The oxidation reactions correspond to $MF_3 + F_2 \rightarrow MF_5$ (M = P, As, Sb), $MF_4 + F_2 \rightarrow MF_6$ (M = S, Se, Te) and $XO_3^- + \frac{1}{2}O_2 \rightarrow XO_4^-$ (X = Cl, Br, I) where ΔH^o_f (F_2, O_2) are equal to zero.

$$HClO_4 + H^+ + 2e^- \rightarrow ClO_3^- + H_2O \qquad E^\circ = +1.19 \text{ V} \qquad (1.29)$$

$$HClO_3 + 2H^+ + 2e^- \rightarrow HClO_2 + H_2O \qquad E^\circ = +1.15 \text{ V} \qquad (1.30)$$

$$ClO_2 + H^+ + e^- \rightarrow HClO_2 \qquad E^\circ = +1.275 \text{ V} \qquad (1.31)$$

$$IO_4^- + 2H^+ + 2e^- \rightarrow IO_3^- + H_2O \qquad E^\circ = +1.64 \text{ V} \qquad (1.32)$$

$$BrO_4^- + 2H^+ + 2e^- \rightarrow BrO_3^- + H_2O \qquad E^\circ = +1.76 \text{ V} \qquad (1.33)$$

$$S_2O_8^{2-} + 2e^- \rightarrow 2SO_4^{2-} \qquad E^\circ = +2.07 \text{ V} \qquad (1.34)$$

$$O_3 + 2H^+ + 2e^- \rightarrow O_2 + H_2O \qquad E^\circ = +2.01 \text{ V} \qquad (1.35)$$
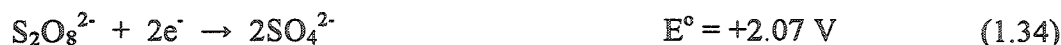
made for the inability of $S_2O_8^{2-}$ (eq 1.34)[204] or ozone (eq 1.35)[204] to oxidize BrO_3^-. The failure of these latter synthetic approaches suggests a significant kinetic barrier to the formation of BrO_4^- and is supported by the sluggish oxidizing properties of BrO_4^- when compared with those of IO_4^-.[167,169]

Several methods for the preparation of BrO_4^- salts have been devised to overcome the thermodynamic and kinetic barriers associated with the +7 oxidation state of bromine. The BrO_4^- anion was first prepared by the nuclear decay of $^{83}SeO_4^{2-}$ (eq 1.36), but was

$$^{83}SeO_4^{2-} \rightarrow {}^{83}BrO_4^- + \beta^- \qquad (1.36)$$

only identifiable by the decay of ^{83}Br ($t_{1/2}$ = 2.4 hr) in a [Rb][ClO$_4$] coprecipitate.[161] Alkali metal salts of BrO_4^- were subsequently prepared in low yield from BrO_3^- by means of electrolysis (2%, eq 1.37),[161] ^{60}Co γ-irradiation (eq 1.38)[168] and oxidation by XeF_2 in

$$BrO_3^- + H_2O \rightarrow BrO_4^- + 2H^+ + 2e^- \qquad (1.37)$$

$$2BrO_3^- \xrightarrow{\ ^{60}Co\ } BrO_4^- + BrO_4^- \qquad (1.38)$$

$$BrO_3^- + XeF_2 + H_2O \rightarrow BrO_4^- + Xe + 2HF \qquad (1.39)$$

aqueous solution (10% yield, eq 1.39).[161] Perbromate salts are currently prepared in highest yield and in multi-gram quantities by the reaction of fluorine gas with an aqueous alkaline solution of an alkali metal bromate salt (20% yield, eq 1.40).[167,205] The expected

$$BrO_3^- + F_2 + 2OH^- \rightarrow BrO_4^- + 2F^- + H_2O \qquad (1.40)$$

24
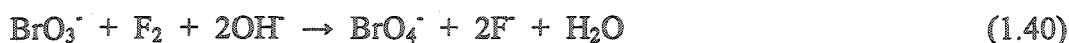
tetrahedral geometry of BrO_4^- has been verified by vibrational (Raman, Infrared)[167,168] and NMR spectroscopy (^{17}O, $^{79,81}Br$),[166] and the Br-O bond length (1.610(12) Å) has been determined by single crystal X-ray diffraction of $[K][BrO_4]$.[170]

In contrast to the other known Br(VII) species, which are prepared in low to moderate yield by the oxidation of Br(V) species, BrO_3F can be synthesized in nearly quantitative yield (eq 1.41)[162] by the method used for the preparation of ClO_3F,[206] and

$$[K][BrO_4] + 2SbF_5 + 3HF \rightarrow BrO_3F + [H_3O][SbF_6] + [K][SbF_6] \qquad (1.41)$$
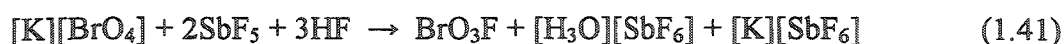
similar syntheses have since been devised using AsF_5,[207] BrF_5[207] $[BrF_6][AsF_6]$[207] and XeF_6[208] in place of SbF_5. Perbromyl fluoride undergoes rapid hydrolysis in water and in aqueous base, and has been shown to etch glass and react with metal surfaces that have not been pretreated with fluorine.[175] For these reasons, BrO_3F is typically handled at low temperatures in fluoroplastic apparatus constructed of Kel-F, FEP or Teflon plastics, with transfers of the material being carried out under static or dynamic vacuum. The structure of BrO_3F has been investigated by vibrational spectroscopy (Raman,[172,209] infrared[172,173]), NMR spectroscopy (^{19}F,[209] ^{81}Br[166]), and gas-phase electron diffraction.[174] These studies have shown that BrO_3F has C_{3v} symmetry with the Br-O (1.582(1) Å) and Br-F (1.708(3) Å) bond lengths having been determined in the latter study. Although BrO_3F exhibits stronger fluorinating properties than ClO_3F, the difficult synthesis and purification of the $[K][BrO_4]$ precursor and the thermodynamic instability of BrO_3F, have prevented its routine use as a fluorinating agent. Consequently, beyond its synthesis, physical properties and structure, little is known about the chemistry of BrO_3F.

Attempts to prepare salts containing the BrO_3^+ cation by the reaction of BrO_3F with the strong Lewis acids AsF_5 and SbF_5 in anhydrous HF have been unsuccessful,[207,209] and indicate that BrO_3F is a poor fluoride ion donor. This is in contrast to the well-known donor properties of the lower fluorides (BrF_5, BrF_3) and oxide

fluorides (BrO_2F, $BrOF_3$) of bromine, which allow for the syntheses of salts containing the BrF_4^+,[210] BrF_2^+,[211,212] BrO_2^+ [213,214] and $BrOF_2^+$ [215,216] cations, respectively. Despite the present inability to prepare salts containing the BrO_3^+ cation, the observation of this cation in the mass spectrum of BrO_3F[162] suggests that it has some inherent stability. The Lewis acidity of BrO_3F has not been specifically addressed, although the ease by which it can be recovered from NaF,[162] and the inability to prepare $ClO_3F_2^-$ salts by the reaction of CsF or NO_2F with ClO_3F,[217] has lead to the prediction that BrO_3F is a poor fluoride ion acceptor.[207] The moderate enthalpy of fluoride ion attachment of BrO_3F (-292.5 kJ mol^{-1}) calculated by Christe and Dixon[46] during the course of the present work contradicts this prediction, implying that the isolation of $BrO_3F_2^-$ salts may simply require a fluoride ion source that is stronger than NaF.

The synthesis of salts containing the BrF_6^+ cation is complicated by the saturated coordination of the bromine centre and the difficulty of oxidizing bromine to its +7 oxidation state (*vide supra*). Consequently, the BrF_6^+ cation cannot be prepared by the abstraction of fluoride ion from the non-existent heptafluoride, which is the preferred synthesis for salts containing the IF_6^+ cation (eq 1.42),[218,219] or by the oxidation of lower fluorides or oxide fluorides with PtF_6, which has been employed for the preparation of $[ClF_6][PtF_6]$ (eq 1.43 - 1.45).[220-222] Salts containing the BrF_6^+ [137,219] and ClF_6^+ [37] cations

$$IF_7 + 3SbF_5 \rightarrow [IF_6][Sb_3F_{16}] \qquad (1.42)$$

$$2ClF_5 + 2PtF_6 \xrightarrow{\text{unfiltered UV}} [ClF_6][PtF_6] + [ClF_2][PtF_6] + F_2 \qquad (1.43)$$

$$2ClF_5 + 2PtF_6 \xrightarrow{\text{filtered UV}} [ClF_6][PtF_6] + [ClF_4][PtF_6] \qquad (1.44)$$

$$6ClO_2F + 6PtF_6 \xrightarrow{-78\,°C} [ClF_6][PtF_6] + 5[ClO_2][PtF_6] + O_2 \qquad (1.45)$$
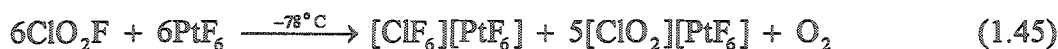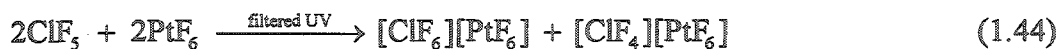
can be prepared in moderate yield (<20 and 11%, respectively) and in high purity using the potent oxidizing properties of the KrF^+ (eq 1.46) and $Kr_2F_3^+$ cations (eq 1.47).

$$[KrF][AsF_6] + XF_5 \rightarrow [XF_6][AsF_6] + Kr \quad (X = Cl, Br) \qquad (1.46)$$

$$[Kr_2F_3][AsF_6] + XF_5 \rightarrow [XF_6][AsF_6] + KrF_2 + Kr \quad (X = Cl, Br) \quad (1.47)$$
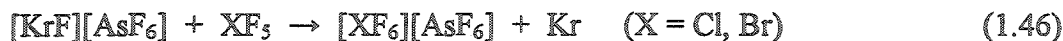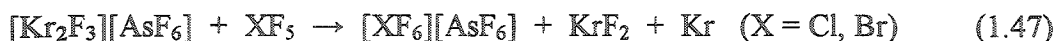
Higher yields of $[BrF_6][AsF_6]$ (42 %) and $[ClF_6][AsF_6]$ (32 %) have recently been reported using NiF_3^+ as the active oxidizing agent, however, the salts isolated using this method are typically contaminated with the paramagnetic side product, $[Ni][AsF_6]_2$ (eq 1.48).[31] The vibrational spectrum of the BrF_6^+ cation exhibits the three Raman-active

$$[K]_2[NiF_6] + 5AsF_5 + BrF_5 \rightarrow$$

$$[XF_6][AsF_6] + 2[K][AsF_6] + [Ni][AsF_6]_2 \quad (X = Cl, Br) \quad (1.48)$$
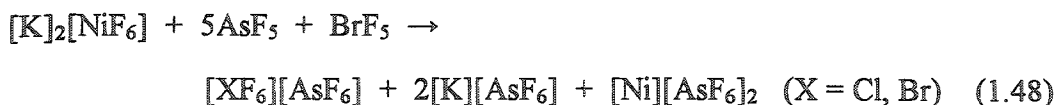
($\nu_1(A_{1g})$, $\nu_2(E_g)$, $\nu_5(F_{2g})$) and two infrared-active ($\nu_3(F_{1u})$, $\nu_4(F_{1u})$) modes expected for a cation having O_h symmetry,[31,36,176] but the most compelling evidence for this ideal geometry comes from the ^{19}F NMR spectra of $[BrF_6][AsF_6]$ and $[BrF_6][SbF_6]$ in anhydrous HF, which exhibit well-resolved one bond couplings to the central quadrupolar ^{79}Br (1575 - 1587 Hz) and ^{81}Br (1697 - 1709 Hz) nuclei.[36] The octahedral geometry of BrF_6^+ is further supported by the cubic morphology of $[BrF_6][AsF_6]$ determined by X-ray powder diffraction (space group, $Pa3$),[176] however, the bond lengths of the cation have not been determined. The chemical properties of the BrF_6^+ cation have not been extensively investigated, however its ability to oxidize O_2 (eq 1.49) and Xe (eq 1.50)[36] indicates that it is a stronger oxidant than ClF_6^+ and IF_6^+, which do not exhibit analogous

$$[BrF_6][AsF_6] + O_2 \rightarrow [O_2][AsF_6] \quad (1.49)$$

$$[BrF_6][AsF_6] + Xe \rightarrow [XeF][AsF_6] + BrF_5 \quad (1.50)$$
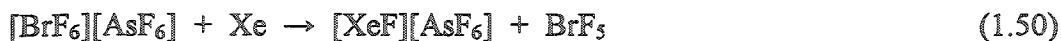
behaviours, and is consistent with the oxidizer strength scale (Table 1.1) reported by Christe and Dixon.[32] The fluoride-ion acceptor properties of BrF_6^+ have been investigated at -78 °C using NOF as the fluoride ion source, however, this reaction failed to provide evidence for the formation of BrF_7 and instead resulted in the reduction of the bromine(VII) centre with the evolution of fluorine (eq 1.51).[36] The inability to prepare

$$2NOF + [BrF_6][AsF_6] \rightarrow [NO][BrF_6] + [NO][AsF_6] + F_2 \quad (1.51)$$
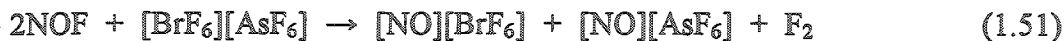
BrF$_7$ by this route suggests that BrF$_7$ is unstable and casts serious doubt on a patented high-temperature synthesis.[177]

Of the remaining neutral and cationic oxide fluorides of bromine(VII) listed in Table 1.3, only BrO$_2$F$_3$ and BrO$_2$F$_2^+$ have been identified experimentally by mass spectrometry.[163] Although these species originated from a hydrolyzed sample of BrF$_5$, the isolation of BrO$_2$F$_3$ or BrO$_2$F$_2^+$ salts by this method is likely to be problematic because the hydrolysis of BrF$_5$ (eq 1.52) results in nearly quantitative yields of BrO$_2$F

$$BrF_5 + 2H_2O \rightarrow BrO_2F + 4HF \qquad (1.52)$$

(>90%)[223] and is extremely hazardous (see section 2.2.10).[150] An attempt to prepare [BrO$_2$F$_2$][PtF$_6$], by analogy with [ClO$_2$F$_2$][PtF$_6$] (eq 1.53),[224,225] has been unsuccessful, resulting in the formation of [BrOF$_2$][PtF$_6$] (eq 1.54) and [BrO$_2$][PtF$_6$] (eq 1.55).[215] The

$$2ClO_2F + 2PtF_6 \rightarrow [ClO_2F][PtF_6] + [ClO_2][PtF_6] \qquad (1.53)$$

$$BrO_2F + {}^5\!/_2PtF_6 \rightarrow [BrOF_2][PtF_6] + \tfrac{1}{2}[O_2][PtF_6] + PtF_5 \qquad (1.54)$$

$$BrO_2F + PtF_6 \rightarrow [BrO_2][PtF_6] + \tfrac{1}{2}F_2 \qquad (1.55)$$
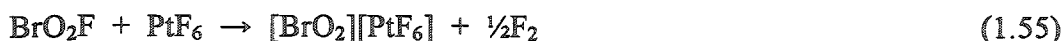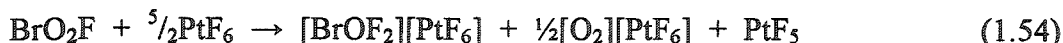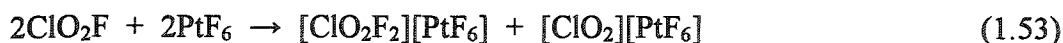
contrast between the oxidizing abilities of PtF$_6$ towards ClO$_2$F and BrO$_2$F is not surprising when one considers that PtF$_6$ is capable of oxidizing ClF$_5$ and ClO$_2$F to the ClF$_6^+$ cation, but is incapable of oxidizing BrF$_5$, even when assisted with UV irradiation.[226] The problematic oxidation of an oxygen ligand when attempting to oxidize the Br(V) centre of BrO$_2$F is also apparent when KrF$_2$ is used as the oxidant, resulting in O$_2$ evolution and the formation of BrOF$_3$ followed by further oxidation of BrOF$_3$ to give BrF$_5$ (eq 1.56).[227] Oxygen-fluorine metathesis reactions, such as that used to prepare

$$BrO_2F + KrF_2 \xrightarrow{2\,^\circ C} BrOF_3 + Kr + \tfrac{1}{2}O_2 \xrightarrow{\text{excess } KrF_2} BrF_5 + Kr + \tfrac{1}{2}O_2 \quad (1.56)$$

BrO$_3$F from [K][BrO$_4$], have been attempted on BrO$_3$F with the hope of circumventing the need to oxidize Br(V). The interaction of SbF$_5$ with BrO$_3$F in HF solvent does not result in ligand exchange to form BrO$_2$F$_3$ and SbOF$_3$,[209] however, there is some

preliminary evidence that ligand exchange occurs between XeF_6 and BrO_3F in HF solution (eq 1.57).[208]

$$XeF_6 + BrO_3F \rightarrow BrO_2F_3 + XeOF_4 \qquad (1.57)$$

There is currently no experimental evidence for the existence of $BrOF_5$, however, its synthesis has been attempted by the hydrolysis of $[BrF_6][AsF_6]$, the metathesis of $[BrF_6][AsF_6]$ and $[K][BrO_4]$, the high temperature (175 °C) oxidation of BrF_5 with O_2/F_2,[209] and the ultraviolet photolysis of BrF_5/O_2.[226] Instead of producing the desired $BrOF_5$ product, the hydrolysis and metathesis reactions proceeded according to eq 1.58 and eq 1.59, respectively, whereas those involving BrF_5 and O_2 did not react.

$$[BrF_6][AsF_6] + H_2O \rightarrow BrF_5 + \tfrac{1}{2}O_2 + 2HF + AsF_5 \qquad (1.58)$$

$$[BrF_6][AsF_6] + [K][BrO_4] \rightarrow BrF_5 + \tfrac{1}{2}O_2 + BrO_3F + [K][AsF_6] \qquad (1.59)$$
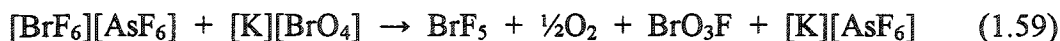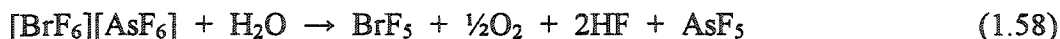
1.7. Purpose and Scope of the Present Work

Prior to the commencement of the present work, the structural characterization of many of the strongest oxidative fluorinating agents known was limited to spectroscopic methods. Although solution and solid-state spectroscopic methods have been used to determine the structures of these species with little ambiguity, they have rarely been able to provide detailed geometric data. The interest in structural characterization of fluorocations containing krypton is further emphasized by the observation that KrF_2 is the only krypton compound for which bond lengths have been determined experimentally. Therefore, one of the primary objectives of the present work was to obtain, for the first time, accurate geometric parameters for the KrF^+, $Kr_2F_3^+$, ClF_6^+, BrF_6^+ and IF_6^+ cations by determination of the single crystal X-ray structures of their salts at low-temperature. The X-ray crystallographic characterization of salts containing the XeF^+ cation have been revisited to obtain more precise geometric parameters for two of the salts reported earlier, and to characterize several additional salts. In cases such as the $[NgF][MF_6]$ (Ng = Kr,

29

Xe) ion pairs, where vibrational spectroscopy has previously been used to access the Lewis acidity of the parent MF_5 species, correlations between the terminal and bridge Ng-F bond lengths and the fluoride ion acceptor strengths of the MF_5 species have been investigated. The KrF^+ and $Kr_2F_3^+$ salts are known to react spontaneously with oxygen to form salts containing the O_2^+ cation. The vibrational frequency of the O_2^+ cation (1801 - 1865 cm^{-1})[142,228-230] exhibits a strong anion dependence, however, this dependence has not been correlated to the bond length of the cation, which is difficult to determine on account of the cation disorders typical of the O_2^+ salts.[67,231] A secondary objective the current work was therefore to measure the bond length of the O_2^+ cation to greater precision in an ordered salt and to correlate its bond length to its stretching frequency.

The general reluctance of bromine to form compounds in the +7 oxidation state was not overcome until Appelman reported the preparation of perbromates,[161,167] perbromic acid,[167] and perbromyl fluoride in 1968.[162] These discoveries were followed by the syntheses of BrF_6^+ salts in 1974,[36,137] however, no new Br(VII) species have been isolated since. The syntheses of new Br(VII) compounds is revisited in the present work, with the goal of isolating species such as BrO_3^+, $BrO_3F_2^-$, BrO_2F_3, and $BrO_2F_2^+$.

Electronic structure calculations have become a powerful tool for the experimental chemist, however, their correlation to experimental results are strongly dependent on the method and basis sets used and to the nature of the species investigated. One of the objectives of the present work was therefore to assess the accuracy to which several common computation methods could predict the molecular geometries and vibrational frequencies of the species studied by experiment. The development of such correlations between theory and experiment provides a basis for the identification and characterization of new species, and allows molecular properties that are not quantifiable by experimental methods (*i.e.*, atomic charges, bond orders) to be investigated.

CHAPTER 2

EXPERIMENTAL SECTION

2.1. Standard Techniques

The majority of the precursors and products discussed in this work are air and/or moisture sensitive, and were therefore prepared and handled under conditions that rigorously excluded oxygen and moisture.

Non-volatile solids were routinely handled under the nitrogen atmosphere (< 0.1 ppm H_2O) of a Vacuum Atmospheres dry box. Thermally sensitive materials could be introduced into the dry box through a liquid nitrogen cooled glass cryowell, located on the base of the dry box, and could be handled at approximately -160 °C for extended periods of time (*ca.* 1 hr) in a stainless steel Dewar filled with pre-cooled 4.5 mm o.d. metal spheres (copper plated iron air-riffle shots).

Volatile reagents and solvents that did not attack glass were transferred on a Pyrex glass vacuum line equipped with grease-free J-Young glass stopcocks and PTFE barrels (Figure 2.1). The vacuum (*ca.* 10^{-5} Torr) was achieved and maintained by means of a two-stage direct drive vacuum pump (Edwards E2M8). The quality of the vacuum in the glass manifold was monitored prior to the transfer of reagents by use of a high-frequency Tesla coil. Pressures in the glass manifold ranging from <1 to 800 Torr could be measured to an accuracy of ±0.5 Torr using a mercury manometer.

Volatile reagents and solvents that were corrosive towards glass or mercury (*i.e.*, F_2, HF, KrF_2, BrF_5, etc.) were transferred on a vacuum line constructed from nickel and 316-stainless steel (Figure 2.2). All components of this vacuum line, including the
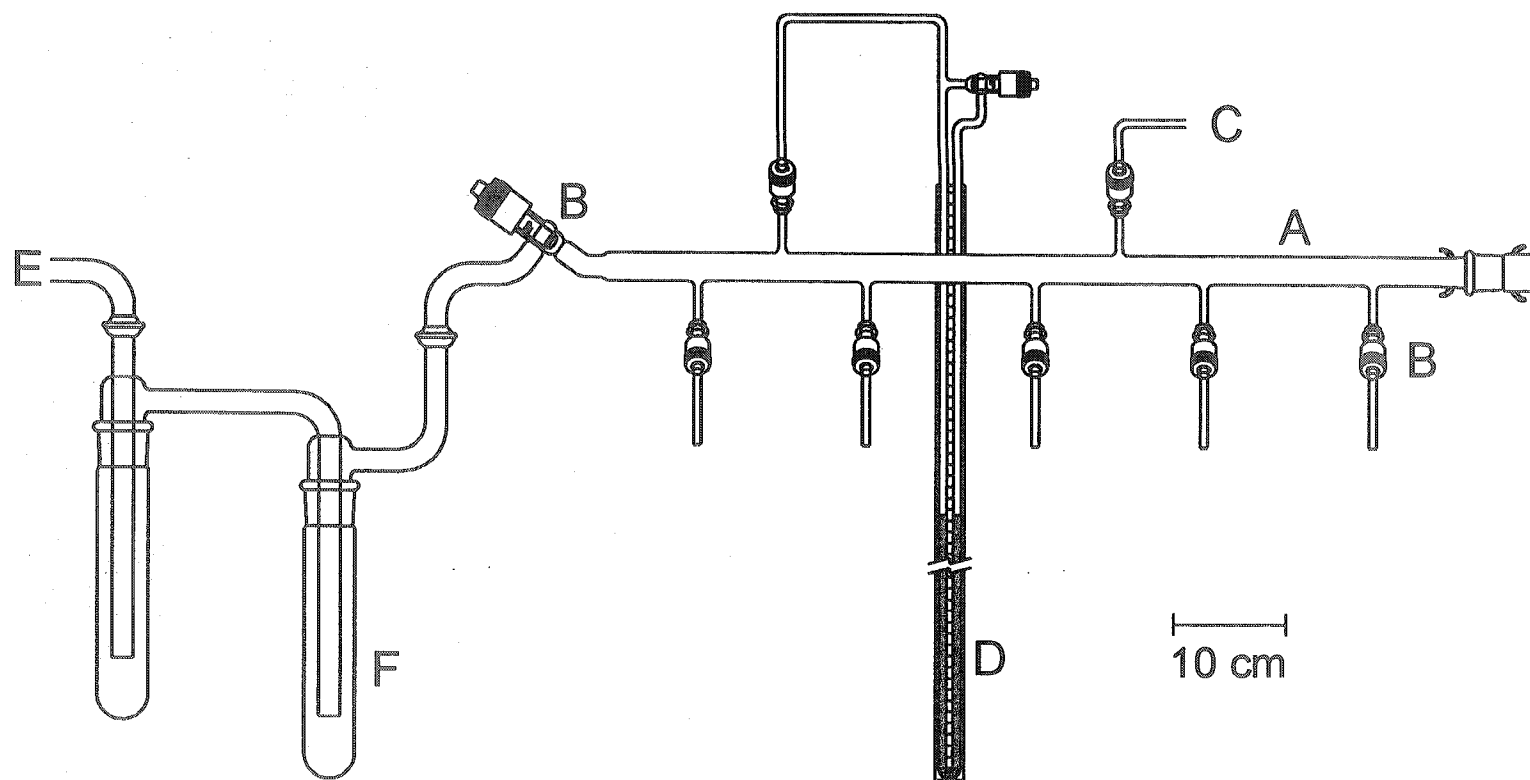
Figure 2.1. A glass vacuum line used to handle non-corrosive materials. (A) Glass manifold. (B) J-Young valve with PTFE barrel. (C) Dry N_2 inlet. (D) Mercury manometer. (E) Outlet to vacuum pump. (F) Glass cryo-trap (submersed in liquid nitrogen).
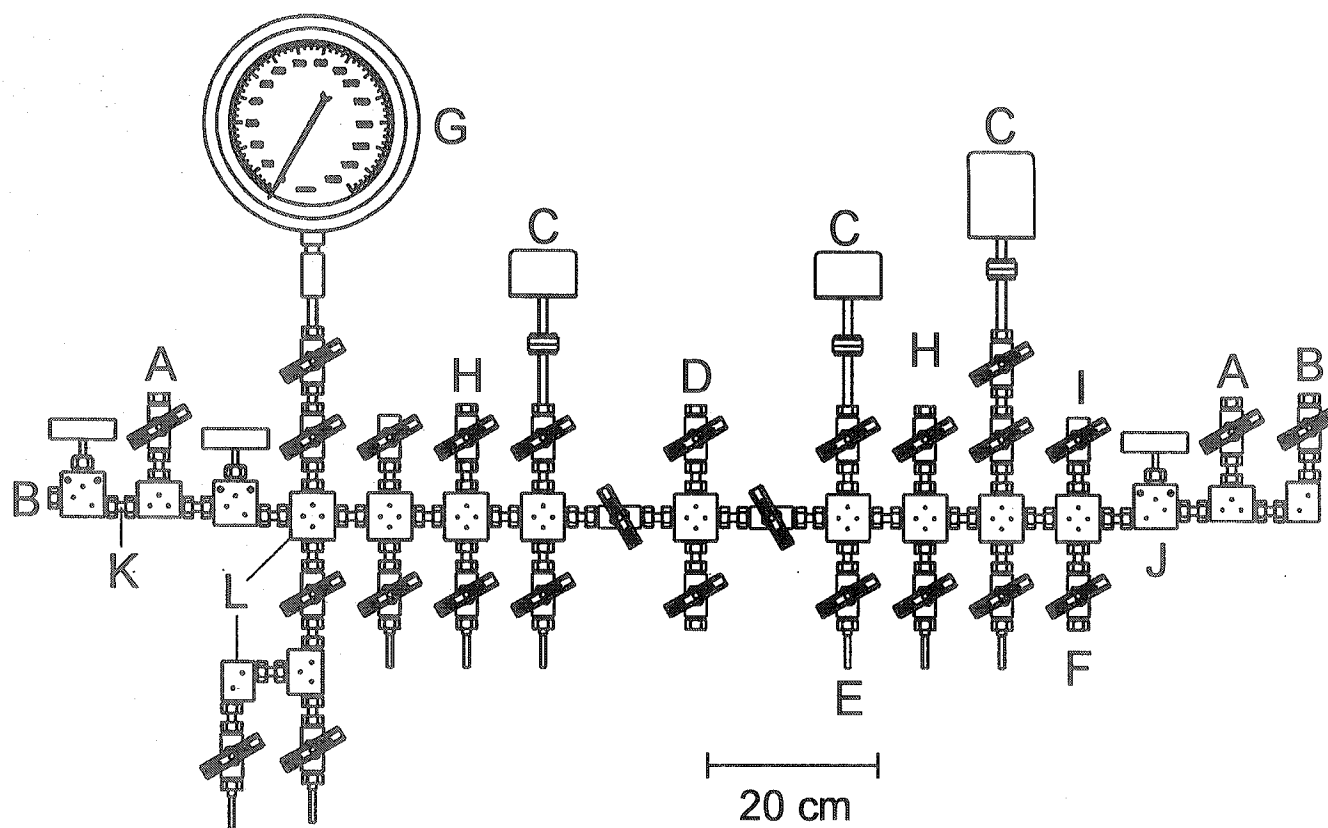
Figure 2.2. The metal vacuum line used to handle corrosive materials. (A) Outlet to primary (corrosives) vacuum pump. (B) Outlet to secondary (non-corrosives) vacuum pump. (C) Pressure gauge (0 - 1500 Torr). (D) Fluorine inlet. (E) Nickel port for reaction vessel. (F) Vacuum port for KrF_2 reactor (see Figure 2.4). (G) Pressure transducer (MKS). (H) Dry nitrogen inlet. (I) Ultra-high-purity argon inlet. (J) High-pressure stainless steel valve (Autoclave Engineers). (K) Nickel tubing. (L) High-pressure stainless steel T- and L-connections.

stainless steel valves (Autoclave Engineers Inc.) were thoroughly degreased prior to use. Two pumps (Edwards E2M8), operating in parallel to each other, maintained the vacuum on the metal vacuum lines and could be used to retain pressures of approximately 10^{-4} Torr. The first of these pumps was preceded by a fluoride/fluorine trap, constructed from a stainless steel barrel (75 cm long, 15 cm o.d.) and packed with soda lime (Fisher Scientific, 4-8 mesh), followed by a glass cryo-trap (-196 °C). This pump was used to evacuate the majority of the corrosive materials from the vacuum line. The second pump was used to remove non-corrosive materials from the line, and provided a superior vacuum because of positioning of its smaller precautionary soda lime trap (*ca.* 1 L) after a glass cryo-trap (-196 °C). The pressure in the metal vacuum line was monitored using MKS pressure transducers, which had dynamic ranges of 0.1 to 1100 and 0.1 to 100 Torr.

The aggressive oxidizing and fluorinating properties of the compounds described in this work required that they be prepared and stored in vessels constructed from FEP tubing (St. Gobain). Vessels constructed from this material could be sealed or joined by gently fusing the material within a glass form constructed of standard wall glass tubing using a Bunsen burner, and could be further shaped by gentle heating with a heat gun. The tube openings were maintained during this process by insertion of standard size glass rods, which were withdrawn after the fused tubes had re-solidified upon cooling. A combination of these techniques allowed for the construction of vessels having various configurations (straight, T-, U-, Y-, etc.) and functionalities (see figures that follow for examples). The tube ends were then heat-sealed and the resulting vessels were usually compression sealed to Kel-F valves by flaring the open end of the tube to 40°. Vessels that were used to handle salts of KrF^+, $Kr_2F_3^+$, XeF_3^+, XeF_5^+ or $Xe_2F_{11}^+$ were compression sealed to thoroughly degreased stainless steel valves (Whitey ORF2), because these cations are capable of oxidizing and cracking Kel-F. Each FEP vessel was

dried under dynamic vacuum on a glass vacuum line for a minimum of 8 hr, prior to being transferred to the metal vacuum line, where they were passivated with fluorine gas for a minimum of 8 hr. The fluorine and other volatile contaminants were then removed under vacuum and the vessel was backfilled with 1000 Torr of argon until used.

The glass vessels used to handle less corrosive materials were dried under dynamic vacuum for a minimum of 8 hr and periodic heating with a Bunsen burner.

2.2. Sources, Preparation and Purification of Starting Materials

Caution: Anhydrous HF must be handled using appropriate protective gear and immediate access to proper treatment procedures[232-234] in the event of contact with liquid or gaseous HF. The compounds of Kr(II), Br(V, VII), Cl(V, VII), I(V,VII) and Au(V) are potent oxidizing agents and may react explosively with water and/or organic materials. Extreme caution should be used when handling and disposing of these compounds to avoid violent detonations. Small quantities of these species as HF solutions (ca. 1 mL or less) or as solids (ca. 100 mg) should be disposed of by slowly pouring the cold compound into several litres of cold and dilute NaOH(aq) inside a properly shielded fume hood. During the disposal, the vessels should be handled with long metal tongs and appropriate safety apparel should be worn (i.e., goggles, lab coat, heavy rubber gloves).

2.2.1. Gases; N_2, F_2, O_2, Ar, Kr, and Xe

The nitrogen routinely used to backfill reaction vessels on the glass vacuum lines was generated from a liquid nitrogen boil off and redried by passing it through a freshly regenerated bed of type 4A molecular sieves. Technical grade F_2 (Air Products) was used without further purification, unless otherwise noted. Ultra-high purity Ar (Air Liquide; cert. 99.999%, <2ppm O_2, <3ppm H_2O), O_2 (Air Liquide, 99.8%), Xe (Air Products, 99.995%) and Kr (Air Products, 99.995%) were used without further

purification. High-purity+ nitrogen (Air Liquide; 99.998%, <5 ppm H_2O, <5ppm O_2) was used for the gas flows during the crystal mounting procedure (see section 2.10.2).

2.2.2. Solvents; HF and CH_3CN

Anhydrous hydrogen fluoride (Harshaw Chemical Co.) was purified by the literature method[95] and stored over BiF_5 in a Kel-F storage vessel. Acetonitrile (Caledon, HPLC grade) was purified by the literature method[235] and stored in a glass vessel. These solvents were transferred under static vacuum on the metal and glass vacuum lines, respectively, as illustrated for HF (Figure 2.3).

2.2.3. Fluoride Ion Sources; NaF, KF, RbF, CsF, $[N(CH_3)_4][F]$ and NOF

Finely ground NaF (J. T. Baker Chemical Co., 99%) and KF (J. T. Baker Chemical Co., 99%) were dried under dynamic vacuum while being heated (250 - 300 °C) in a glass vessel for a minimum of 3 days. The fluorides were kept in the glass drying apparatus, which was stored in a dry box until used.

Rubidium fluoride (ICN-KCK Laboratories Inc., 99.9%) and CsF (Aldrich, 99.9%) were dried by fusion in a platinum crucible. The molten fluorides were allowed to cool under vacuum in the evacuation port of the dry box, and then coarsely ground with a mortar and pestle inside the dry box. The highly hygroscopic salts were stored in sealed FEP containers within the dry box, where they could be transferred as necessary.

Tetramethylammonium fluoride was prepared according to the literature method by titration of $[N(CH_3)_4][OH]$ with 47% aqueous HF to its equivalence point.[236] After drying the product under dynamic vacuum at 150 °C, the remaining traces of water were removed by dissolving the salt in isopropanol and abstracting the water / isopropanol azeotrope under dynamic vacuum at room temperature and then 150 °C. This latter process was repeated until the infrared adsorption bands of $[N(CH_3)_4][F]\cdot H_2O$ at 822 and 895 cm^{-1} were comparable in intensity to the $N(CH_3)_4^+$ band at 1203 cm^{-1}.

vacuum

B

10 cm

C

D

B

A
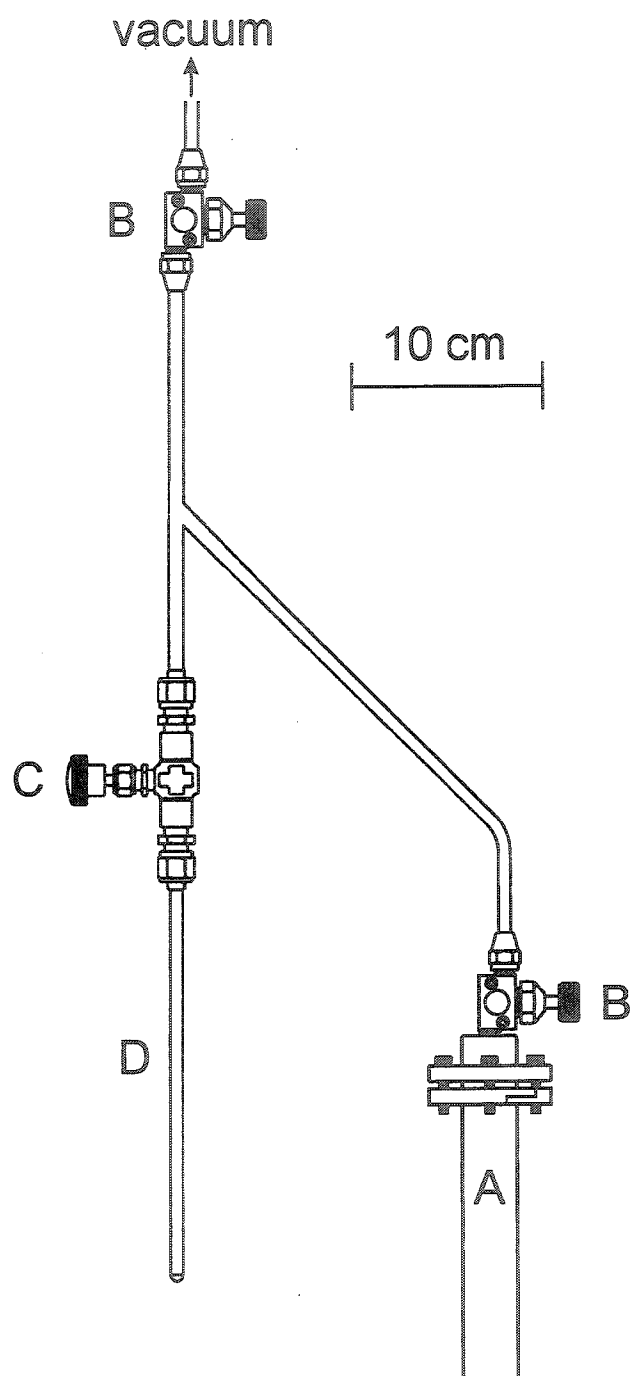
Figure 2.3. The anhydrous HF distillation apparatus. (A) Kel-F storage vessel containing BiF$_5$ (*ca.* 1 g). (B) Kel-F valve. (C) Stainless steel valve. (D) Reaction vessel constructed from FEP.

Nitrosyl fluoride was prepared and purified as previously described[222] by the direct reaction of NO with a 20 mol% excess of F_2 in a 30-mL nickel canister at ambient temperature. The excess F_2 was removed under dynamic vacuum (-183 °C) and the NOF was stored in the nickel canister without further purification. Only small amounts of NO_2F (0.5%) and NOF_3 (0.4%) were detectible in the ^{19}F NMR spectrum of the product.

2.2.4. SbF_3, BiF_5, SbF_5, PF_5 and AsF_5

Antimony trifluoride[237] (Aldrich, 98%) and BiF_5[41] (Ozark Mahoning Co.) were purified as previously described by sublimation of the heated crude material under dynamic vacuum in a glass vessel equipped with a PTFE stopcock. The freshly sublimed fluorides were colourless crystalline solids, and were stored in sealed FEP tubes inside a dry box where they could be weighed and transferred as necessary.

Antimony pentafluoride (Ozark Mahoning) was purified by vacuum distillation as previously described,[76] and stored in a glass vessel inside a desiccator until used. Solutions of SbF_5 in anhydrous HF were prepared by the oxidation of SbF_3 with F_2 in the solvent at room temperature. A positive pressure of F_2 (*ca.* 1000 Torr) was maintained in the vessel during the oxidation by periodically cooling the vessel to -78 °C and re-pressurizing the system. This process was repeated until the last traces of the insoluble SbF_3 had disappeared. The excess F_2 was removed under dynamic vacuum at -196 °C.

Phosphorus pentafluoride (Ozark Mahoning) was purified by distilling the crude material through an FEP U-tube (-117 °C) under dynamic vacuum to trap HF and POF_3, and through a second U-tube (-196 °C) to collect the product. The process was repeated a second time prior to storing the PF_5 in a stainless steel cylinder. Only a trace amount of POF_3 was detected in the infrared spectrum of the purified PF_5.

Arsenic pentafluoride was prepared by the direct fluorination of AsF_3 with F_2.[5] In a typical reaction, 30 g of AsF_3 (shown to contain 9 mol% HF by ^{19}F NMR) was

condensed into a 2-L nickel canister containing eight-fold molar excess of NaF and allowed to stand at ambient temperature for 24 hr. A sample of the treated AsF_3 was condensed into a 4-mm o.d. FEP tube and the ^{19}F NMR spectrum was recorded to confirm the absence of HF. The purified AsF_3 was condensed into a 1-L nickel canister (¼-in thick walls) that had been pretreated with F_2. Hydrogen fluoride and other condensable impurities were removed from the technical grade fluorine by condensing the F_2 into a 30-mL nickel canister at -196 °C. This vessel was then warmed to -183 °C, at which temperature the F_2 was allowed to expand into the metal vacuum line and was recondensed into the AsF_3 containing canister. The F_2 was added to the AsF_3 in three equal amounts, such that a 50% stoichiometric excess of fluorine was used in total. After each addition, the reactor was warmed to ambient temperature behind a blast shield. After the final addition, the canister was warmed to room temperature for one day and then heated to 100 °C for 8 hr to ensure that the reaction had proceeded to completion. The canister was cooled to -196 °C and excess F_2 was removed under vacuum. **Caution:** The use of larger quantities of AsF_3 (*i.e.*, 50 - 85 g) proceeded explosively on two occasions when the F_2 was added in a single step. For this reason, the preparation of AsF_5 should be carried out by stepwise addition of F_2, as described above, and on a limited scale. An alternative preparation of AsF_5, utilizing As_2O_3 in place of AsF_3, has recently been reported and may provide a safer synthetic route to this reagent.[238]

2.2.5. ClF_5 and BrF_5

Spectroscopically pure ClF_5 (infrared spectroscopy) was obtained in a stainless steel cylinder from Prof. K. O. Christe (University of Southern California) and was used without further purification.

Bromine pentafluoride (Ozark-Mahoning Co.) was purified in an FEP vessel equipped with a Kel-F valve and loaded with 20 g of KF (to complex HF as

[K][HF$_2$·nHF]). Bromine and BrF$_3$ impurities were eliminated by the direct fluorination of these species to BrF$_5$ at ambient temperature as previously described.[40] The product was stored in the purification vessel under 1000 Torr of a 1:1 mixture of N$_2$ (or Ar) and F$_2$ at -78 °C and transferred under dynamic vacuum when required.

2.2.6. KrF$_2$

Krypton difluoride was prepared by use of a 316 stainless steel hot-wire reactor (Figure 2.4) equipped with a nickel filament, similar to that originally described by Bezmel'nitsyn et al.[7] and subsequently modified by Kinkead et al.[9] The filament was fabricated from a $^1/_{16}$-in nickel rod tightly wound about a second length of $^1/_{16}$-in rod that was, in turn, coiled and stretched into a helix. In a typical preparation, the hot-wire reactor was pressurized with 1000 Torr (50 mmol) of krypton and then cooled to -196 °C in a 20-L Dewar. After reaching thermal equilibrium, the reactor was pressurized with 25 Torr of F$_2$ and the DC power supply for the nickel filament was adjusted to ca. 6 V and 30 A (the filament was dull red in colour under these conditions). The F$_2$ pressure increased to ca. 45 Torr after the power supply was turned on and was regulated between 25 and 45 Torr by the periodic addition of F$_2$ during the synthesis. The declining F$_2$ pressure was used to qualitatively monitor the production of KrF$_2$, and additional Kr (1.0 to 2.0 mmol) was condensed into the reactor when the rate of KrF$_2$ production slowed or ceased. Upon completion of the reaction (ca. 12 hr), excess F$_2$ was removed under dynamic vacuum at -196 °C. The excess Kr and crude KrF$_2$ were recovered as a pink solid (the colouration arises from chromium oxide fluoride contamination) by allowing the reactor to slowly warm to room temperature while dynamically pumping the volatile contents through a ½-in o.d. FEP U-trap (-196 °C). The Kr/KrF$_2$ mixture was then warmed to -78 °C under dynamic vacuum to remove the unreacted Kr. The crude KrF$_2$ was purified by briefly warming the sample to 0 °C and flash distilling off the more

a

6.7 in.

AgCl or Saphire
Window Viewport

Permissable Coolant
Level Variation (1.5 in.)

Gas
Inlet

2.75-in. Blind
Flanges (3)

1.33-in. Medium Current
Solid Conductor
Electrical Feedthroughs

Copper or
Stainless Steel
Cooling Fins (6)

18.0 in.

11.0 in.

b

Coiled Nickel
Filament
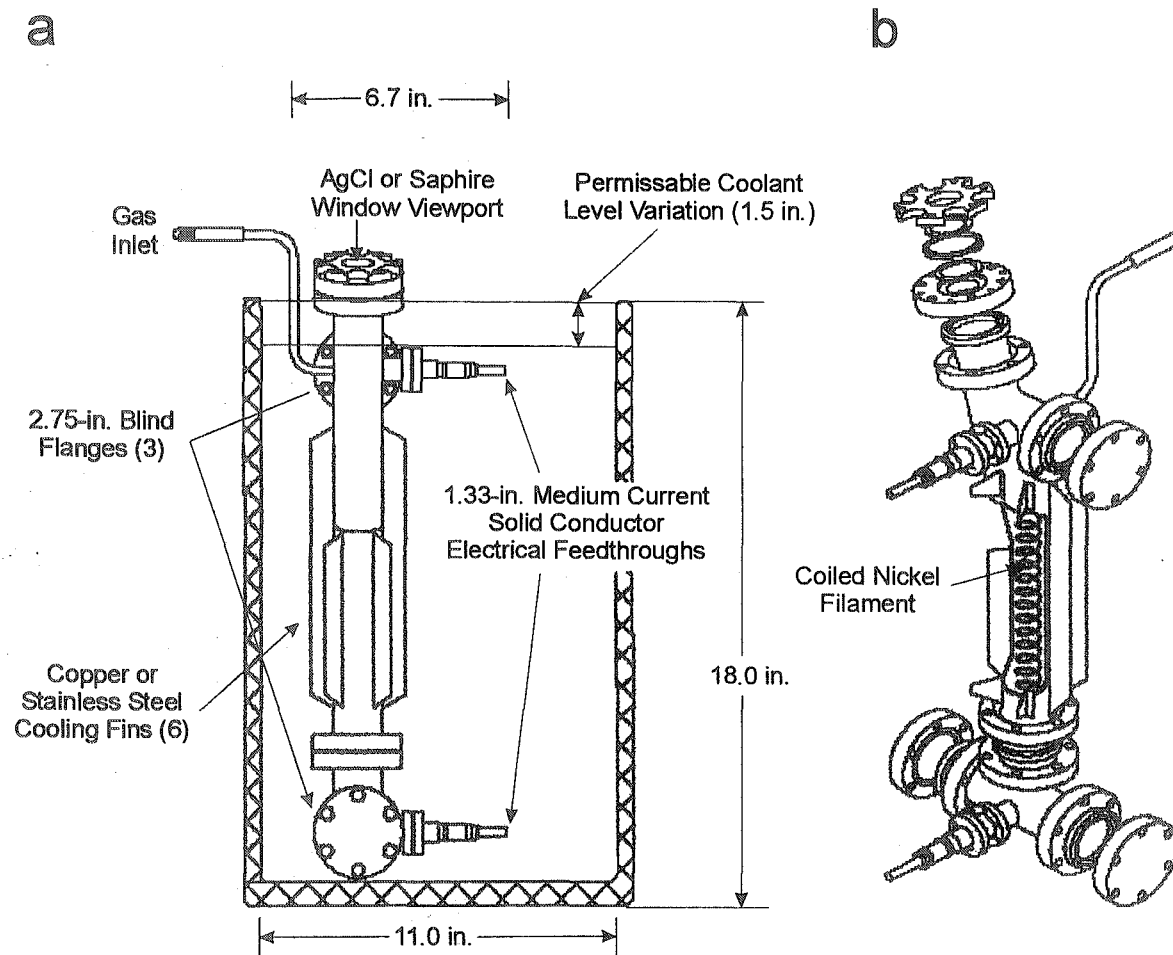
Figure 2.4. The stainless steel hot-wire reactor used for the preparation of KrF_2. (a) External view and dimensions of a hot-wire reactor submerged in a liquid nitrogen coolant bath. (b) A perspective drawing of the hot-wire reactor showing the flange assembly and nickel filament (cut away region). Reproduced with permission from ref 239.

volatile chromium oxide fluorides. The remaining colourless KrF_2 was finally warmed to room temperature and rapidly sublimed into a $^3/_8$-in o.d. FEP tube equipped with a Kel-F valve, where it was stored under 1000 Torr of N_2 or Ar at -78 °C until used. This synthesis is highly reproducible and typically yields 2.5 to 3.0 g of purified KrF_2 over a 12 hr period.

2.2.7. XeF_2, XeF_4 and XeF_6

Xenon difluoride,[5] and XeF_4[6] were prepared by the literature methods and stored in sealed Kel-F tubes at ambient temperature within a dry box, where they were weighed and transferred as required.

Xenon hexafluoride was prepared by a method similar to that described by Chernick and Malm,[240] and stored at ambient temperature in an FEP vessel equipped with stainless steel valve. Sharp Raman bands at 503 and 543 cm^{-1} identified XeF_4 as an impurity. The XeF_4 was converted to XeF_6 by reaction with small amounts of KrF_2 at the melting point of the mixture (*ca.* 45 °C). Xenon hexafluoride is highly volatile and was transferred under static vacuum on a sub-manifold of the metal vacuum line.

2.2.8. [K][BrO$_4$]

Potassium perbromate was prepared by the method described by Appelman.[167] A 600 mL aqueous solution of NaOH (5 M) and [Na][BrO$_3$] (1 M) was prepared in a 1-L Nalgene-FEP bottle equipped with a PTFE screw-cap. The PTFE cap contained a gas inlet, consisting of a thick-walled ¼-in o.d. PTFE tube, which acted as a bubbler and was immersed in the bromate solution, and thick-walled ¼-in o.d. PTFE outlet tube, which exhausted any unreacted F_2 into a soda-lime trap. Fluorine was bubbled through the chilled (0 °C) bromate solution for 8 hr by pressurizing the metal vacuum manifold with 1000 Torr of F_2 and leaking this gas into the vessel through the PTFE gas inlet. The resulting pale yellow solution was reduced in volume by gently warming it under an

infrared heat lamp, and the insoluble components (*i.e.*, [Na][BrO$_3$], NaF) were removed by centrifugation. The remaining bromate, was precipitated from the solution as [Ag][BrO$_3$] by the addition AgF (Aldrich, 99.9+%), and removed by centrifugation. The residual Ag$^+$ and F$^-$ were precipitated as AgO and CaF$_2$ by the addition of CaO. These solids were removed by centrifugation, leaving behind a clear solution of [Na][BrO$_4$].

The acid form of the cation exchange resin Dowex-50W, 50X8-50 (Sigma) was prepared by treating it first with HCl (1M), followed by distilled and deionized water to remove any traces of chloride. The [Na][BrO$_4$] solution was eluted through the 32-cm resin column to produce a dilute solution of HBrO$_4$. Diatomaceous earths (*ca.* 12 g) were added to the HBrO$_4$ solution, and the acid was filtered through a fine glass frit. The solution was titrated with 0.1 M KOH to its equivalence point, which was determined with the aid of a pH meter. Crude [K][BrO$_4$] was obtained by slowly evaporating the solvent under an infrared heat lamp, and was purified by recrystallization from HPLC-grade deionized water (Caledon). The recrystallized [K][BrO$_4$] was dried under dynamic vacuum for one week in a glass vessel, prior to storing it in an FEP tube inside a dry box. No impurities were detectable in the Raman spectrum of the product.[167]

2.2.9. BrO$_3$F

Perbromyl fluoride was prepared as described in the literature by the reaction of AsF$_5$ with [K][BrO$_4$] in anhydrous HF (eq 2.1).[162,207] In a typical reaction, 110 mg (0.601

$$[K][BrO_4] + AsF_5 + 3HF \rightarrow BrO_3F + [H_3O][AsF_6] + [K][AsF_6] \qquad (2.1)$$
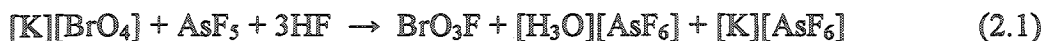
mmol) of [K][BrO$_4$] was dissolved in ¾ mL of anhydrous HF in a ¼-in o.d. FEP vessel equipped with a Kel-F valve. Arsenic pentafluoride (0.306 g, 1.80 mmol) was then condensed into the vessel at -196 °C, and the vessel was backfilled with argon after allowing the AsF$_5$ to dissolve in the HF at -78 °C. The contents of the vessel were warmed to ambient temperature for 45 to 60 min with periodic mixing to ensure complete

reaction. After this period, the solution was cooled again to -78 °C and the volatile components were distilled under dynamic vacuum into a U-tube (-196 °C) containing 3 g of pre-dried NaF. The non-volatile products, $[K][AsF_6]$ and $[H_3O][AsF_6]$, were generally colourless, but occasionally contained a lemon-yellow coloured impurity that evolved bromine rapidly when thoroughly dried and warmed to room temperature. This byproduct was not produced in large enough quantities to be observed by Raman spectroscopy, but its colour and stability are similar to those reported for Br_2O_3.[241] The U-tube containing the volatile products was isolated under static vacuum and warmed to ambient temperature using a water bath, which helped regulate the temperature of the tube during the exothermic reactions of HF and AsF_5 with NaF. After 5 to 10 min, the U-tube was recooled to -196 °C and the vacuum in the tube was refreshed. The purified BrO_3F was transferred by rapidly warming the U-tube to ambient temperature using a water bath, and condensing the volatile product into an awaiting vessel at -196 °C.

2.2.10. ClO_2F and BrO_2F

Chloryl fluoride was prepared as described in the literature,[242] by the reaction of $[Na][ClO_3]$ with ClF_3 (eq 2.2) in a stainless steel vessel. Chlorine and ClF_3 impurities

$$6[Na][ClO_3] + 4ClF_3 \rightarrow 6NaF + 2Cl_2 + 3O_2 + 6ClO_2F \tag{2.2}$$
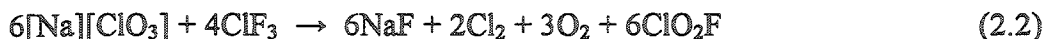
were removed by vacuum distillation through an FEP U-tube cooled to -112 °C, with the ClO_2F product being trapped in a second U-tube cooled to -196 °C. The purification process was repeated until the ClF_3 bands were no longer visible in the Raman spectrum of the product. The colourless product was stored in an FEP vessel under Ar at -78 °C.

Bromyl fluoride was prepared by a method similar to that described by Jacob[223] (eq 2.3), but on $1/20^{th}$ of the scale. In a typical reaction, 136 mg (7.72 mmol) of deionized

$$BrF_5(s) + 2H_2O \xrightarrow{\text{excess } BrF_5} BrO_2F + 4HF \tag{2.3}$$
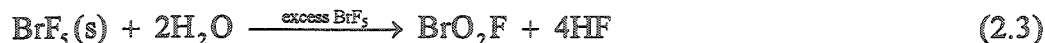
water (Caledon, HPLC grade) was preweighed into an FEP vessel and then condensed into the primary FEP vessel (1.2 cm o.d.) at -196 °C, such that the ice was evenly distributed over a 7 cm high region of the walls. A six-fold molar equivalent of BrF_5 (8.28 g, 47.3 mmol), measured by volume in a ¼-in o.d. FEP tube and statically distilled into the upper region of the primary reactor at -196 °C and periodically knocked into lower region of the tube. The excess BrF_5 was required to ensure that further hydrolysis of the BrO_2F product to $HBrO_3$ did not occur.[223] The reactor was warmed to -100 °C for 20 min using an ethanol slush prepared in a stainless steel Dewar while being kept under dynamic vacuum. The reactor was then isolated under static vacuum and warmed to -55 °C (dry ice / acetone bath in a stainless steel Dewar) to melt the BrF_5. The excess BrF_5 and HF by-products were removed under dynamic vacuum at this temperature and trapped in an FEP U-tube at -196 °C for subsequent disposal. The product was purified by distilling it under dynamic vacuum at 0 °C and trapping it in a U-tube (-50 °C). The Raman spectrum of the colourless product was in agreement with that reported earlier,[243,244] and no impurities were observed. The product was stored under Ar at -78 °C, but decomposes slowly over the course of several weeks at this temperature as indicated by the evolution of bromine. The decomposition products were removed by flash pumping the discoloured product at 0 °C until it became colourless. **Caution:** Although this synthesis is advantageous because of the high yields (*ca.* 90% with respect to H_2O) and the feasibility of producing [17]O- and ^{18}O-enriched samples of BrO_2F, a subsequent attempt to prepare BrO_2F by this method resulted in a violent explosion and ignition of the ethanol slush bath during the first warming period (-100 °C). Attempts to prepare BrO_2F by the reaction of $KBrO_3$ and BrF_5 with a catalytic amount of HF[243,244] were less than satisfactory. In one instance, the reaction rapidly evolved Br_2 and ended with a small explosion, while a poor yield (*ca.* 5 mg) was obtained in a second attempt.

45

2.3. Syntheses of Salts Containing the KrF^+, $Kr_2F_3^+$ and XeF^+ Cations

2.3.1. $[KrF][MF_6]$ (M = As, Sb, Bi, Au), $[Kr_2F_3][SbF_6]\cdot KrF_2$, $[Kr_2F_3]_2[SbF_6]_2\cdot KrF_2$ and $[Kr_2F_3][AsF_6]\cdot[KrF][AsF_6]$

The salt, $[KrF][AsF_6]$, was prepared by the literature method.[40] In a typical preparation, KrF_2 (100 mg, 0.821 mmol) was condensed into a ¼-in o.d. T-shaped FEP vessel equipped with a stainless steel valve at -196 °C. An excess of AsF_5 (ca. 0.5 mL, 23 mmol) was condensed into the vessel, and the reaction vessel was cycled between -78 and -53 °C for 1 hr with periodic agitation to ensure that the reaction was complete. The excess AsF_5 was removed under dynamic vacuum at -78 °C and the vessel was backfilled with dry nitrogen or argon. Raman spectroscopy (-78 °C) confirmed the coexistence of α-$[KrF][AsF_6]$ and β-$[KrF][AsF_6]$[40] in the sample and the absence of $[O_2][AsF_6]$. The $[Kr_2F_3][AsF_6]\cdot[KrF][AsF_6]$ adduct was prepared by condensing a small stoichiometric excess of KrF_2 onto a sample of $[KrF][AsF_6]$. Anhydrous HF (0.5 mL) was condensed into the reaction vessel, such that the product was completely soluble at -10 °C. The product was stored at -78 °C under a positive atmosphere of argon and subsequently identified by single crystal X-ray diffraction.

The salts, $[KrF][SbF_6]$[40] and $[KrF][BiF_6]$,[41] were prepared by the literature methods. In a typical experiment, 100 mg of the pentafluoride was dissolved (BiF_5) or prepared (SbF_5) in 1 mL of anhydrous HF. A stoichiometric excess of KrF_2 (ca. 10 mol% to account for the passivation of the stainless steel valve by KrF_2) was then condensed into the vessel at -196 °C prior to warming the vessel to -78 °C and backfilling it with argon. The vessel was warmed to 0 °C for 10 min with gentle agitation prior to storing it at -78 °C until crystals could be grown.

The $[Kr_2F_3][SbF_6]\cdot KrF_2$ and $[Kr_2F_3]_2[SbF_6]_2\cdot KrF_2$ salts were prepared in the same fashion as $[KrF][SbF_6]$ with minor modifications. The salt, $[Kr_2F_3][SbF_6]\cdot KrF_2$, was

synthesized using a large excess of KrF_2 ($3.5KrF_2$:SbF_5; 75 mol% excess with respect to $Kr_2F_3^+$), whereas $[Kr_2F_3]_2[SbF_6]_2 \cdot KrF_2$ was isolated when a 0.6 mol% stoichiometric excess of KrF_2 was used. Unit cell determinations obtained by single crystal X-ray diffraction verified the presence of $[KrF][SbF_6]$ in crystalline samples of $[Kr_2F_3]_2[SbF_6]_2 \cdot KrF_2$ and $[Kr_2F_3][SbF_6] \cdot KrF_2$, however, the ratios of these salts were not assessed.

2.3.2. $[Kr_2F_3][PF_6] \cdot nKrF_2$ (n > 0)

In a typical experiment, 0.777 mmol of PF_5 was condensed into an FEP vessel containing 0.821 mmol of KrF_2 at -196 °C, and then warmed to -78 °C to melt the PF_5. The progress of the reaction was monitored on weekly to biweekly basis using Raman spectroscopy, and additional aliquots of PF_5 were added as necessary. The reaction was determined to be complete when the changes in the Raman spectrum ceased (ca. 7 weeks) and the intense $\nu_1(\Sigma^+_g)$ vibration of KrF_2 was barely visible at 465 cm^{-1}. The $[Kr_2F_3][PF_6] \cdot nKrF_2$ (n > 0) produced by this method did not react with excess PF_5 at -78 °C to produce $[Kr_2F_3][PF_6]$ or $[KrF][PF_6]$. The product was also monitored for $[O_2][PF_6]$ impurities arising from the reaction of $Kr_2F_3^+$ with O_2 or H_2O, however, only trace amounts of this salt could be identified by the $\nu(O_2^+)$ modes observed at 1859 and 1863 cm^{-1} after 7 weeks.

2.3.3. $[KrF][AuF_6]$

The salt, $[KrF][AuF_6]$, was prepared as previously described.[35] In a typical preparation, 100 mg of gold powder (Aldrich, cert. 99.99%) was weighed and transferred to an FEP vessel in a dry box. Anhydrous HF (½ mL) was distilled into the vessel, followed by a stoichiometric excess of KrF_2 (ca. 50 mol%) at -196 °C. The contents of the vessel were carefully warmed towards 0 °C, where the oxidation of gold by KrF_2 becomes rapid. During the early phases of the oxidation, the reaction was periodically

quenched with liquid nitrogen to slow its rate and prevent the displacement of the gold and KrF_2 into the upper region of the vessel where the reaction could become uncontrollable. The contents of the vessel were also periodically cooled to -78 °C to allow the accumulating krypton gas to be vented into the metal vacuum line, which was prepressurized with 800 Torr of argon. The synthesis of $[KrF][AuF_6]$ was determined to be complete when the solid in the bottom of the tube had a uniform canary-yellow colour and the release of Kr and F_2 gas from the sample had ceased. Although $[Kr_2F_3][AuF_6]$ has been prepared from gold and excess KrF_2,[70] it is not kinetically stable in HF at ambient temperature and results in the rapid decomposition of the excess KrF_2, yielding only $[KrF][AuF_6]$. The high purity of the product was verified by Raman spectroscopy, however, samples stored for appreciable periods of time (>1 day) frequently became contaminated with $[O_2][AuF_6]$ despite being stored under argon at -78 °C.

2.3.4. $[XeF][MF_6]$ (M = As, Sb, Bi) and $[XeF][M_2F_{11}]$ (M = Sb, Bi)

The salt, $[XeF][AsF_6]$, was prepared by the reaction of XeF_2 with AsF_5, as previously described.[68] In a typical preparation, anhydrous HF (0.5 mL) was condensed into a T-shaped FEP vessel containing a pre-weighed amount of XeF_2 (24.0 mg, 0.142 mmol). A stoichiometric excess of AsF_5 (0.177 mmol) was condensed into the vessel and the contents were warmed to ambient temperature and allowed to react. The colourless product was stored under argon at -78 °C until crystals could be grown.

The salt, $[XeF][SbF_6]$, was prepared according to the literature method[68] by the reaction of XeF_2 with SbF_5 in HF solvent. In a typical preparation, XeF_2 (31.5 mg, 0.186 mmol) was transferred into a T-shaped FEP vessel containing 0.194 mmol of SbF_5 dissolved in anhydrous HF at -160 °C in a dry box. The solution was warmed to ambient temperature to completely dissolve the reagents and allow them to react. The product was stored under Ar at -78 °C until crystals could be grown.

The salt, [XeF][BiF$_6$], was prepared according to the literature method.[41] In a typical reaction, XeF$_2$ (10.6 mg, 80.6 μmol) and BiF$_5$ (25.4 mg, 80.6 μmol) were weighed into a T-shaped FEP vessel in a dry box. Anhydrous HF (0.5 mL) was distilled into the vessel at -196 °C and the vessel was warmed to ambient temperature to completely dissolve the reagents. The pale yellow product was stored under Ar at -78 °C until crystals could be grown.

The salt, [XeF][Sb$_2$F$_{11}$], was prepared according to the literature method by the reaction of XeF$_2$ with neat SbF$_5$.[245] Antimony pentafluoride (ca. 1 mL) was condensed into an FEP vessel containing a pre-weighed amount of XeF$_2$ (250 mg, 1.48 mmol). The XeF$_2$ was completely dissolved in the SbF$_5$ solvent by warming the vessel to 45 °C in a hot water bath. The contents of the vessel were cooled to ambient temperature over the course of several days, during which time crystals of [XeF][Sb$_2$F$_{11}$] formed in the solution. The excess SbF$_5$ was removed under dynamic vacuum at ambient temperature, leaving behind pale yellow crystals of [XeF][Sb$_2$F$_{11}$].

The salt [XeF][Bi$_2$F$_{11}$] was prepared according to the literature method.[41] Crystalline [XeF][Bi$_2$F$_{11}$] was obtained from a 1:2 molar ratio XeF$_2$ and BiF$_5$ in HF, by slowly removing the solvent under dynamic vacuum at -48 °C. Attempts to isolate [XeF][Bi$_2$F$_{11}$] by slowly cooling 1:2 molar solutions of XeF$_2$ and BiF$_5$ in HF and decanting off the HF solvent as described for the crystallization of the [NgF][MF$_6$] (Ng = Kr, Xe) salts (see section 2.10.1.2), resulted in the formation of crystalline [XeF][BiF$_6$], suggesting that the increasing acidity of the concentrated solutions during the slow evaporation of the solvent plays an important role in the isolation of [XeF][Bi$_2$F$_{11}$].

2.4. Synthesis of [O$_2$][AuF$_6$]

In a typical reaction, a vessel containing [KrF][AuF$_6$] (see section 2.3.3) under 0.5 mL anhydrous HF was pressurized with oxygen at -78 °C, and then warmed to ambient

temperature. The vessel was periodically evacuated at -78 °C and repressurized with fresh O_2 to ensure the complete conversion of [KrF][AuF$_6$] to [O$_2$][AuF$_6$]. No impurities were observed in the Raman spectrum[146,230] of the product after the removal of the HF solvent under vacuum at -78 °C. The product was stored under argon at -78 °C.

2.5. Syntheses of Salts Containing the ClF$_6^+$, BrF$_6^+$ and IF$_6^+$ Cations

2.5.1. [ClF$_6$][AsF$_6$] and [BrF$_6$][AsF$_6$]

The salts, [ClF$_6$][AsF$_6$][37] and [BrF$_6$][AsF$_6$],[36] were prepared in FEP reaction vessels equipped with stainless steel valves by allowing the oxidant [KrF][AsF$_6$] (0.5 g) to react with approximately 0.5 mL of ClF$_5$ and BrF$_5$, respectively, at room temperature. Excess ClF$_5$, BrF$_5$, and volatile side products (*i.e.*, [ClF$_4$][AsF$_6$] and [BrF$_4$][AsF$_6$]) were removed under dynamic vacuum at ambient temperature, and the product purities were checked by Raman spectroscopy. The products were stored under Ar at -78 °C until used, and transferred inside a dry box.

2.5.2. [ClF$_6$][Sb$_2$F$_{11}$] and [BrF$_6$][Sb$_2$F$_{11}$]

The salts, [ClF$_6$][Sb$_2$F$_{11}$] and [BrF$_6$][Sb$_2$F$_{11}$], were prepared by transferring the AsF$_6^-$ salts of ClF$_6^+$ and BrF$_6^+$ into solutions containing a slight excess of SbF$_5$ (*i.e.*, > 2SbF$_5$:AsF$_6^-$) in anhydrous HF in a T-shaped FEP vessel equipped with a stainless steel valve. The AsF$_5$ and excess SbF$_5$ were removed by decanting the cold supernatant into the sidearm of the vessel, which was cooled to -196 °C and sealed off under vacuum. The product was dried under dynamic vacuum at -70 °C.

2.5.3. [IF$_6$][Sb$_3$F$_{16}$] and [IF$_6$][Sb$_2$F$_{11}$]

The salt, [IF$_6$][Sb$_3$F$_{16}$], was prepared by condensing IF$_7$ (1.871 g, 7.199 mmol) at -196 °C directly onto neat SbF$_5$ (*ca.* 10 g) in a Kel-F reaction vessel followed by the addition of 5 mL of anhydrous HF. The reaction mixture was warmed to -78 °C followed by slow warming over a period of 30 min to room temperature, whereupon the reaction

mixture was agitated and allowed to stand for several hours. The HF solvent and excess SbF_5 were removed under dynamic vacuum at -78 °C and ambient temperature respectively. The stoichiometry of the $[IF_6][Sb_3F_{16}]$ salt was determined by the mass of the product (expt., 6.415 g; theoretical, 6.550 g).

The salt, $[IF_6][Sb_2F_{11}]$, was prepared in a T-shaped FEP vessel by dissolving $[IF_6][Sb_3F_{16}]$ (113.2 mg) in anhydrous HF (0.5 mL) and slowly cooling the solution from 0 to -70 °C. The HF solvent and residual SbF_5 were decanted into the sidearm of the vessel, which was cooled to -196 °C and sealed off under vacuum. The product was dried under dynamic vacuum at -70 °C and stored under 1000 Torr of nitrogen at -78 °C.

2.6. Fluoride Ion Acceptor Properties of BrO_3F and ClO_3F

2.6.1. Syntheses of $[M][BrO_3F_2]$ (M = K, Rb, Cs, $N(CH_3)_4$) and $[NO]_2[BrO_3F_2][F]$

Caution: On occasion, solutions of BrO_3F and CH_3CN detonated violently. These detonations were usually initiated by rapid warming of the mixtures from -50 to 0 °C or rapid freezing of the solutions in liquid nitrogen. For this reason, it is recommended that $[M][BrO_3F_2]$ (M = K, Rb, Cs) and $[N(CH_3)_4][BrO_3F_2]$ only be prepared on small scales (< 100 mg) when CH_3CN is used as a solvent.

Salts containing the $BrO_3F_2^-$ anion were prepared by the reaction of BrO_3F with strong fluoride ion donors (eq 2.4). In a typical experiment, CH_3CN solvent (0.25 mL)

$$BrO_3F + F^- \rightarrow BrO_3F_2^- \tag{2.4}$$
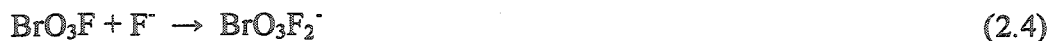
was condensed into a 4-mm or ¼-in o.d. FEP vessel containing 0.1 to 0.2 mmol of finely ground MF (M = Cs, Rb, K) or $[N(CH_3)_4][F]$. The vessel was backfilled with nitrogen and temporarily stored at -78 °C to prevent the alkali metal fluorides, and particularly $[N(CH_3)_4][F]$[236,246] from reacting with the solvent. A stoichiometric excess of BrO_3F (*ca.* 0.6 mmol), that had been prepared *in situ* 2.2.9), was condensed into the vessel at -196 °C and the vessel was backfilled with 1000 Torr of argon at -78 °C. The mixture was

warmed above the melting point of the CH_3CN (-46 °C) solvent for 1 hr before isolation of the colourless salts by removal of the solvent under dynamic vacuum. The ideal reaction temperature varied from salt to salt, likely reflecting the relative lattice energies and solubilities of the fluoride ion donors. Cesium fluoride readily reacts with BrO_3F in CH_3CN at -40 to -48 °C to produce the α-$[Cs][BrO_3F_2]$, but forms β-$[Cs][BrO_3F_2]$ when the solution is warmed to -35 °C. The higher temperature β-phase can also be prepared by warming α-$[Cs][BrO_3F_2]$ to 0 °C in the absence of a solvent and monitoring the phase transition by Raman spectroscopy. Complete conversion of a 100 mg sample of α-$[Cs][BrO_3F_2]$ to β-$[Cs][BrO_3F_2]$ by the latter method requires *ca.* 35 hr. The reactions of KF and RbF with BrO_3F proceed very slowly below -40 °C, but at an acceptable rate when warmed to between -30 and -35 °C. The Raman spectra of $[K][BrO_3F_2]$ and $[Rb][BrO_3F_2]$ closely resembled that of β-$[Cs][BrO_3F_2]$ and no evidence for a lower temperature phase of these salts was obtained. The reaction of $[N(CH_3)_4][F]$ with BrO_3F proceeds at -40 °C, however, warming these solutions above 0 °C should be avoided because $[N(CH_3)_4][BrO_3F_2]$ reacts slowly with CH_3CN to produce NO_2F and CH_3COF.

The salt, $[NO]_2[BrO_3F_2][F]$, was prepared by the direct reaction of BrO_3F with liquid NOF at -78 °C in the absence of a solvent. In a typical reaction, BrO_3F (*ca.* 0.6 mmol) was prepared *in situ* and condensed into a ¼-in. o.d. FEP vessel containing 0.1 mL of NOF (*ca.* 0.13 g, 2.7 mmol). The mixture was warmed to -78 °C, resulting in the formation of a colourless solid. The vessel was briefly (*ca.* 30 s) evacuated at this temperature until the last traces of the liquid reagents had evaporated, but was not rigorously pumped on because the salt rapidly dissociates and is readily pumped off under these conditions. The Raman spectra of the bulk and sublimed materials were identical, and the product was subsequently identified as $[NO]_2[BrO_3F_2][F]$ by single crystal X-ray diffraction.

2.6.2. Attempted Synthesis of $[N(CH_3)_4]_2[BrO_3F_3]$

The preparation of $[N(CH_3)_4]_2[BrO_3F_3]$ was attempted by the reaction of $[N(CH_3)_4][BrO_3F_2]$ with $[N(CH_3)_4][F]$ (eq 2.5). A sample of $[N(CH_3)_4][BrO_3F_2]$ was

$$[N(CH_3)_4][BrO_3F_2] + [N(CH_3)_4][F] \rightarrow [N(CH_3)_4]_2[BrO_3F_3] \qquad (2.5)$$
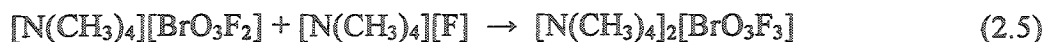
prepared from $[N(CH_3)_4][F]$ (6.48 mg, 69.6 μmol) and a stoichiometric excess of BrO_3F, as described above. After removal of the CH_3CN solvent by pumping under vacuum at 0 °C, $[N(CH_3)_4][F]$ (6.98 mg, 74.9 μmol) was weighed into the reaction vessel at -160 °C. A small amount of CH_3CN (0.1 mL) was then condensed into the vessel and the solution was warmed to 0 °C for 5 min to partially dissolve the reagents. The Raman spectrum of the colourless solid remaining after the removal of the solvent under dynamic vacuum at -40 °C did not exhibit significant differences in the anion bands when compared with $[N(CH_3)_4][BrO_3F_2]$, indicating that the transfer of a second fluoride ion to BrO_3F to form $[N(CH_3)_4]_2[BrO_3F_3]$ had not occurred.

2.6.3. Attempted Syntheses of $O_3Br-OTeF_5$ and $[N(CH_3)_4][BrO_3F(OTeF_5)]$

The preparation of the -$OTeF_5$ derivative of BrO_3F was attempted by the direct reaction of BrO_3F with $B(OTeF_5)_3$, with the anticipation that the reaction may proceed by eq 2.6. Perbromyl fluoride (*ca.* 0.77 mmol) was prepared *in situ* and condensed into an

$$3BrO_3F + B(OTeF_5) \rightarrow 3BrO_3(OTeF_5) + BF_3 \qquad (2.6)$$
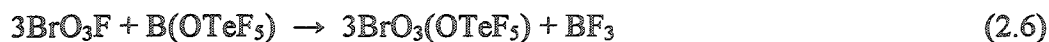
FEP reaction vessel containing 9.73 mg (0.013 mmol) of $B(OTeF_5)_3$. The contents of the vessel were monitored by Raman spectroscopy (-90 °C) after warming the sample to -75, -52, -40 and 0 °C. Although $B(OTeF_5)_3$ exhibited limited solubility at the lower temperatures, it was completely soluble at 0 °C which should have provided an excellent opportunity for the reagents to react. Perbromyl fluoride and $B(OTeF_5)_3$ were the only species observed in the Raman spectra.

The preparation of $[N(CH_3)_4][F_5TeO\text{-}BrO_3F]$ was attempted by the direct reaction of $[N(CH_3)_4][OTeF_5]$ (22.9 mg; 0.073 mmol) with BrO_3F (*ca.* 0.1 mL, 0.68 mmol) according to (eq 2.7). The low solubility of $[N(CH_3)_4][OTeF_5]$ in BrO_3F at 0 °C did not

$$BrO_3F + [N(CH_3)_4][OTeF_5] \rightarrow [N(CH_3)_4][BrO_3F(OTeF_5)] \qquad (2.7)$$

permit the reaction of these reagents in the absence of a solvent over the course of 15 min as determined by Raman spectroscopy (-163 °C), however, the addition of 0.02 mL of CH_3CN was sufficient to solubilize the $[N(CH_3)_4][OTeF_5]$ at -32 °C. The Raman spectrum of a CH_3CN solution of $[N(CH_3)_4][OTeF_5]$ and BrO_3F was acquired at -42 °C, however, only bands which could be assigned to BrO_3F and CH_3CN were observed. The colourless solid remaining after the removal of the volatile components of the mixture under dynamic vacuum at -40 °C was identified as $[N(CH_3)_4][OTeF_5]$ by use of low-temperature (-163 °C) Raman spectroscopy, indicating that $[N(CH_3)_4][BrO_3F(OTeF_5)]$ is not formed or readily dissociates to its starting reagents at -40 °C.

2.6.4. Attempted Synthesis of $[N(CH_3)_4][ClO_3F_2]$

The synthesis of $[N(CH_3)_4][ClO_3F_2]$ was attempted by analogy with the synthesis of $[N(CH_3)_4][BrO_3F_2]$ (see section 2.6.1). Perchloryl fluoride (80.6 μmol) was condensed into an FEP vessel (4-mm o.d.) containing a pre-weighed amount of $[N(CH_3)_4][F]$ (7.51 mg, 80.6 μmol) dissolved in 0.3 mL of CH_3CN. The vessel was backfilled with nitrogen and then warmed to -40 °C for 1 hr with gentle agitation before removal of the solvent at -40 °C under dynamic vacuum. The Raman spectrum of the remaining colourless solid, recorded at -40 °C, did not differ significantly from that of $[N(CH_3)_4][F]$,[246] and did not exhibit bands that could be attributed to the formation of $[N(CH_3)_4][ClO_3F_2]$.

The synthesis of $[N(CH_3)_4][ClO_3F_2]$ was also attempted by the direct reaction of $[N(CH_3)_4][F]$ (28.5 mg; 306 μmol) with a large excess of ClO_3F (0.11 mL; 1.5 mmol) in a 4-mm o.d. FEP vessel. The combined reagents were warmed to -40 °C for 2 hr with

54

periodic agitation. The Raman spectrum (-163 °C) of the colourless solid under the ClO_3F was consistent with a mixture of $[N(CH_3)_4][F]$ and ClO_3F and provided no evidence for the formation of $[N(CH_3)_4][ClO_3F_2]$. The Raman spectrum (-163 °C) of the solid remaining after the removal of the ClO_3F at -120 °C was that of $[N(CH_3)_4][F]$.

2.7. Fluoride Ion Donor Properties of BrO_3F and ClO_3F

2.7.1. Attempted Syntheses of $[BrO_3][SbF_6 \cdot nSbF_5]$ (n $\geq$ 0); Synthesis and Purification of $[BrO_2][SbF_6]$

The synthesis of $[BrO_3][Sb_nF_{5n+1}]$ (n $\geq$ 1) was attempted by the reaction of BrO_3F with excess SbF_5 (eq 2.8). In a typical experiment, BrO_3F (0.55 mmol) was prepared *in*

$$BrO_3F + nSbF_5 \xrightarrow{\text{SbF}_5 \text{ solvent}} [BrO_3][Sb_nF_{5n+1}] \ (n \geq 1) \qquad (2.8)$$

situ and condensed into a Y-shaped FEP vessel containing a large excess of neat SbF_5 (*ca.* 0.5 mL, 7 mmol), which had previously been distilled into the vessel under dynamic vacuum. The vessel was backfilled with argon, and the reagents were warmed to 0 °C in an ice bath. Perbromyl fluoride reacted vigorously at the surface of the SbF_5 with the evolution of a colourless gas, producing an orange-red solid. The Raman spectrum (-110 °C) of the product exhibited two sharp Br-O stretches at 937 and 870 cm^{-1}, which were similar to those reported for $[BrO_2][Sb_{2.24}F_{12.2}]$ (932, 865 cm^{-1}).[213] The excess SbF_5 was removed under dynamic vacuum at ambient temperature and the contents of the vessel were transferred to a T-shaped FEP vessel, followed by the addition of anhydrous HF solvent (0.5 mL). The salt, $[BrO_2][SbF_6]$, was isolated in high purity by slowly cooling the pale orange solution form 0 to -70 °C over a period of several hours and decanting the supernatant into the sidearm of the vessel, which had been precooled to -196 °C. The block-shaped crystals were dried under dynamic vacuum and the sidearm of the vessel was heat-sealed off prior to backfilling the vessel with dry nitrogen. The product was identified as $[BrO_2][SbF_6]$ by Raman spectroscopy and single crystal X-ray diffraction.

In light of the possibility that the BrO_3^+ cation may be unstable at temperatures above 0 °C, the abstraction of fluoride from BrO_3F was also attempted using neat AsF_5 and SbF_5 dissolved in AsF_5. Perbromyl fluoride did not react with AsF_5 at -78 °C, but reacted slowly with SbF_5 dissolved in AsF_5 at -45 °C to produce $[BrO_2][Sb_nF_{5n+1}]$ ($n \geq 1$), which was identified by Raman spectroscopy.

2.7.2. Attempted Synthesis of $[ClO_3][SbF_6 \cdot nSbF_5]$ ($n \geq 1$)

The synthesis of $[ClO_3][Sb_nF_{5n+1}]$ ($n \geq 1$) was attempted by the reaction of ClO_3F with neat SbF_5. Perchloryl fluoride (2.04 mmol) was condensed into an FEP vessel containing 0.5 mL of neat SbF_5 (*ca.* 7 mmol). The vessel was backfilled with argon and warmed to ambient temperature overnight. The Raman spectrum of the mixture exhibited a sharp Cl-O stretch at 1058 cm^{-1}, which is similar to that reported for ClO_3F (1063 cm^{-1}). The failure of ClO_3F to react with SbF_5 to form ionic salts containing the ClO_3^+ or ClO_2^+ cations was further confirmed by the volatilities of all of the components of this mixture under dynamic vacuum at ambient temperature.

2.8. Synthesis and Purification of $[ClO_2][SbF_6]$

The salt, $[ClO_2][SbF_6]$, was prepared in a ¼-in o.d. FEP reaction vessel equipped with a Kel-F valve. Chloryl fluoride (4.16 mmol) was condensed into a vessel containing SbF_5 (3.64 mmol) dissolved in anhydrous HF (0.75 mL). The vessel was warmed to ambient temperature for 30 min to allow the reagents to completely react (eq 2.9) and

$$ClO_2F + SbF_5 \xrightarrow{\text{HF}} [ClO_2][SbF_6] \qquad (2.9)$$

then cooled to 0 °C, at which temperature the HF solvent and excess ClO_2F were removed under dynamic vacuum. A portion of the crude product (*ca.* 200 mg) was transferred into a T-shaped FEP vessel and completely dissolved in HF (1 mL) at ambient temperature. This solution was slowly cooled to -65 °C to recrystallize the $[ClO_2][SbF_6]$ salt. The HF solvent was decanted into the side arm of the vessel, which was

subsequently removed under dynamic vacuum at -196 °C. The product was dried under dynamic vacuum at -65 °C and stored under dry nitrogen at -78 °C. No significant impurities were detected in the Raman spectrum (-163 °C) of the pale yellow product.

2.9. Attempts to Prepare BrO_2F_3 and Salts Containing the $BrO_2F_2^+$ Cation

2.9.1. Reaction of XeF_6 with $[K][BrO_4]$

The metathesis reaction between XeF_6 and BrO_4^- was attempted in anhydrous HF with anticipation that the reaction may go beyond the formation of BrO_3F (eq 2.10)[208] in the presence of excess XeF_6 (eq 2.11). Xenon hexafluoride (33.3 mg, 0.136 mmol; 9.81

$$2[K][BrO_4] + XeF_6 \xrightarrow{\text{HF}} BrO_3F + XeOF_4 + 2KF \qquad (2.10)$$

$$BrO_3F + XeF_6 \xrightarrow{\text{HF}} BrO_2F_3 + XeOF_4 \qquad (2.11)$$
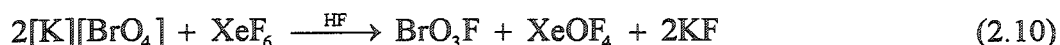
mg, 0.401 mmol), that had been treated with KrF_2 to remove XeF_4 and $XeOF_4$ impurities, was distilled into a 4-mm o.d. FEP reaction vessel. Potassium perbromate was weighed into the vessel in the dry box at -160 °C, such that $[K][BrO_4]:XeF_6$ molar ratios were 1:2.3 and 1:5.2, respectively. Anhydrous HF was condensed into the vessels and the samples were sealed under dynamic vacuum. Both samples were monitored by ^{19}F NMR spectroscopy at -80 °C after each of several warming cycles. The $[K][BrO_4]:2.3XeF_6$ sample was shown to contain BrO_3F, $XeOF_4$ and XeF_4 after warming to -78 (2 hr), -60 (30 min) and 0 °C (5 min). The $[K][BrO_4]: 5.24XeF_6$ sample was shown to contain BrO_3F, $XeOF_4$ and XeF_6 after warming to -78 (2 hr), -60 (30 min), 0 (2, 8, 35 min) and 23 °C (20 min). There was no evidence to suggest that fluorine-oxygen exchange proceeds beyond the formation of BrO_3F and $XeOF_4$.

2.9.2. Reactions of BrO_2F with XeF_4 and XeF_4/AsF_5

Approximately 0.75 mL of anhydrous HF solvent was distilled into a Y-shaped ¼-in o.d. FEP vessel equipped with stainless steel valves containing a pre-weighed amount of XeF_4 (108.75 mg, 0.52462 mmol). Bromyl fluoride was dynamically distilled

into the vessel by trapping the material at the Y-connection of the tube at -196 °C. The mass of the BrO_2F transferred to the vessel could not be accurately determined because of continuous decomposition of liquid BrO_2F during the distillation[244,247] and the comparatively large mass of the two metal valves on the vessel, but was estimated to be approximately 75 mg (0.57 mmol) based on the volume of the condensed solid. The BrO_2F was freed from the upper walls of the vessel by tapping the frozen solid to the lower region of the tube. The mixture was then warmed to -78 °C and agitated for 4 hr. The solid material remaining after this period was identified as a mixture of XeF_4 and BrO_2F using Raman spectroscopy. The mixture was warmed to -30 °C to completely dissolve the reagents and was agitated for an additional hour. The Raman spectrum of the solid precipitated from this solution at -78 °C was again consistent with the presence of XeF_4 and BrO_2F, and provided no evidence for the oxidation of BrO_2F to BrO_2F_3.

A stoichiometric amount of AsF_5 (0.5246 mmol) was condensed into the vessel containing the $XeF_4/BrO_2F/HF$ mixture described above. After warming the mixture to -60 °C, the HF solution became pale orange in colour and an orange precipitate settled to the bottom of the tube. The Raman spectrum (-163 °C) of the precipitated product exhibited bands consistent with those of XeF_4 and BrO_2F in addition to two new bands (863, 931 cm^{-1}) in the Br-O stretching region. The latter modes are consistent with those reported earlier for $[BrO_2][AsF_6]$ (862, 931 cm^{-1}),[207] suggesting that BrO_2F is a better fluoride ion donor than XeF_4 (eq 2.12).

$$BrO_2F + XeF_4 + AsF_5 \rightarrow [BrO_2][AsF_6] + XeF_4 \qquad (2.12)$$
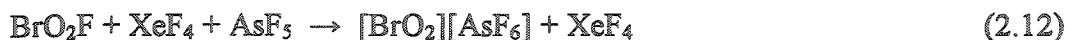
In light of the inability of XeF_4 to oxidize BrO_2F and the unlikelihood that XeF_4 would oxidize the BrO_2^+ cation, an additional aliquot of AsF_5 (0.5246 mmol) was condensed into the vessel at -196 °C to convert the XeF_4 to the more potent oxidizer $[XeF_3][AsF_6]$. The Raman spectra (-163 °C) of the solids precipitated after warming the

solution to -35 (1 hr), 0 (3 hr), 23 (24 hr) and 40 °C (6 hr), were consistent with mixtures of $[BrO_2][AsF_6]^{207}$ and $[XeF_3][AsF_6]^{248}$ and no new Br-O containing species (*i.e.*, $BrO_2F_2^+$, BrO_2F_3) were observed.

2.9.3. Reactions of $[BrO_2][SbF_6]$ with KrF_2; and BrO_2F with $[KrF][AsF_6]$

A small amount of KrF_2 (19.70 mg, 0.1617 mmol) was condensed into a preweighed ¼-in o.d. FEP reaction vessel under static vacuum. The vessel, and a sample of recrystallized $[BrO_2][SbF_6]$ were then transferred into the dry box through the cyrowell of the dry box. While frozen (*ca.* -160 °C), a small quantity of $[BrO_2][SbF_6]$ (43.93 mg, 0.1436 mmol) was weighed into the reaction vessel. The vessel was removed from the dry box and temporarily stored at -78 °C until HF solvent (0.5 mL) could be condensed into the vessel. The contents of the vessel were warmed to -30 °C for 2 min to completely dissolve the $[BrO_2][SbF_6]$, before cooling the solution to -78 °C. The warming and cooling cycle was repeated four more times and was accompanied by vigorous evolution of a colourless gas at -30 °C. The Raman spectrum product was obtained at -163 °C and the product was shown to be a mixture of salts containing the BrO_2^+ (372, 878, 942 cm^{-1}), O_2^+ (1865 cm^{-1}), $BrOF_2$ (318, 657, 1059 cm^{-1}) and BrF_4^+ (713, 718 cm^{-1}) cations. The counter-anions corresponding the O_2^+, BrO_2^+ and $BrOF_2^+$ cations could not be specifically determined, however, the complexity of the Sb-F stretching region indicates the presence of the SbF_6^- and $Sb_2F_{11}^-$ anions.[248]

Bromyl fluoride (*ca.* 75 mg; 0.57 mmol) was dynamically distilled into a ¼-in o.d. Y-shaped FEP vessel equipped with stainless steel valves, followed by condensation of 0.75 mL of BrF_5 solvent into the vessel. Krypton difluoride (0.821 mmol) was statically distilled into vessel, and the solution was acidified by the addition of AsF_5 (1.067 mmol). When warmed to -30 °C, the BrF_5 solution turned orange-brown in colour and slowly began to evolve gas. After the evolution of gas ceased (*ca.* 30 min), the

contents of the vessel were cooled to -50 °C and the BrF_5 solvent was removed under dynamic vacuum leaving behind a pale orange solid. The Raman spectrum of this solid exhibited bands consistent with those of $[BrO_2][AsF_6]$,[207] $[BrOF_2][AsF_6]$,[215,216] and $[O_2][AsF_6]$,[230] but did not exhibit new features in the Br-O stretching region. A second Raman spectrum of the solid was obtained after the removal of the volatile products under dynamic vacuum at ambient temperature (45 min), and the remaining solid was $[BrOF_2][AsF_6]$.

2.9.4. Reaction of BrO_2F with $[Xe_2F_{11}][AsF_6]$

Xenon hexafluoride (5.39 mg, 0.2197 mmol) was statically distilled into a Y-shaped ¼-in o.d. diameter FEP reaction vessel equipped with stainless steel valves. The XeF_6 that had been transferred to the reaction vessel was shown, by Raman spectroscopy, to contain a small amount of XeF_4 as a consequence of contact with and reduction by the steel valves and was treated with KrF_2 at ambient temperature overnight. After the absence of XeF_4 and KrF_2 in the purified XeF_6 sample was confirmed by Raman spectroscopy, anhydrous HF (0.75 mL) was distilled into the reaction vessel. Bromyl fluoride (ca. 75 mg, 0.57 mmol) was distilled under dynamic vacuum into the reaction vessel by trapping it in the Y-connection of the vessel at -196 °C and then tapped into the lower region of the tube. A one-half molar equivalent of AsF_5 (0.110 mmol) with respect to XeF_6 was then condensed into vessel at -196 °C and the vessel was backfilled with argon at -78 °C. The resulting pale yellow solution was warmed to -50 °C for 6 hr, at which point a Raman spectrum of the solid material was acquired at -73 °C. The spectrum confirmed the presence of BrO_2F,[243,244] $[Xe_2F_{11}][AsF_6]$[249] and a small amount of XeF_4,[250] however, additional bands in the Br-O stretching region, arising from $[BrO_2][AsF_6]$, $[BrOF_2][AsF_6]$ or new compounds of bromine(VII) were not observed. The solution was warmed to -40 (6 hr), and -30 (6, 12, 20 hr), during which time a

colourless gas evolved and the solution took on a pale yellow colour. The Raman spectrum of the colourless precipitate was monitored after each period of warming and was shown to exhibit XeF_4 bands that progressively increased in intensity, while those of $[Xe_2F_{11}][AsF_6]$ decreased and had all but disappeared after a total of 20 hr at -30 °C. The only oxygen-containing bromine species observed in the Raman spectrum after this period was BrO_2F, indicating that the bromine species produced during the reduction of $Xe_2F_{11}^+$ is very soluble and a better fluoride ion donor than XeF_4 and BrO_2F.

The reaction between BrO_2F and $[Xe_2F_{11}][AsF_6]$ was also monitored by ^{19}F NMR spectroscopy. Bromyl fluoride (*ca.* 10 mg; 76 μmol) was distilled under dynamic vacuum into a Y-shaped FEP (4-mm o.d.) vessel. A stoichiometric excess of XeF_6 (181.4 mg; 739.5 μmol) was then condensed into the vessel and the contents of the vessel were temporarily stored at -78 °C. Anhydrous HF solvent was distilled into the vessel to a depth of 5 mm, followed by the addition of 370 μmol of AsF_5 at -196 °C. The contents of the vessel were warmed to -78 °C for 5 min to allow the AsF_5 to react with the XeF_6, prior to sealing the vessel under dynamic vacuum at -196 °C. A Raman spectrum of the colourless solid at the bottom of the tube confirmed the coexistences of $[Xe_2F_{11}][AsF_6]$, XeF_6 and the absence of XeF_4. The fluorine ^{19}F NMR spectrum of the mixture was acquired at -70 °C prior to further warming, and then again after allowing the solution to stand at -30 °C for 1.5 and 18 hr. A colourless gas was evolved during the first five minutes of warming and coincided with increased quantities of XeF_4 and $XeOF_4$ in the ^{19}F NMR spectrum. The bromine-containing product was not observed in the ^{19}F NMR spectrum but is speculated to be $BrOF_3$, which is known to undergo rapid exchange in HF solution.[247] The ^{19}F NMR spectrum acquired after warming the sample to -30 °C for 18 hr did not exhibit significant changes in the quantities of XeF_4 or $XeOF_4$, indicating that the reaction had proceeded to completion during the first warming period.

2.10. Structural Characterization by Single Crystal X-ray Diffraction

2.10.1. Growth of Single Crystals

2.10.1.1. KrF$_2$

Approximately 50 mg of KrF$_2$ was distilled into one arm of an h-shaped FEP vessel equipped with a Kel-F valve (Figure 2.5). The vessel was evacuated at -78 °C on a metal vacuum line and allowed to stand under static vacuum during the crystallization process. The arm containing the KrF$_2$ was warmed from -78 to -40 °C using a dry ice acetone bath, while the vacant arm was cooled to -78 °C. Over the course of a 4 hr period, nearly cubic crystals of KrF$_2$ were deposited in the colder side of the tube just above the level of the acetone / dry ice coolant. When the sublimation was complete, the vessel was backfilled with nitrogen at stored at -78 °C until a crystal could be mounted on the X-ray diffractometer.

2.10.1.2. XeF$_2$, [NgF][MF$_6$] (Ng = Kr, Xe; M = As, Sb, Bi), [KrF][AuF$_6$], [Kr$_2$F$_3$][SbF$_6$]·KrF$_2$, [Kr$_2$F$_3$]$_2$[SbF$_6$]$_2$·KrF$_2$, [O$_2$][AuF$_6$], [Kr$_2$F$_3$][AsF$_6$]·[KrF][AsF$_6$], [XF$_6$][Sb$_2$F$_{11}$] (X = Cl, Br, I) and [XO$_2$][SbF$_6$] (X = Cl, Br).

Anhydrous HF solutions of the title compounds were prepared in T-shaped FEP vessels such that the salts were completely soluble at -10 to -20 °C. This degree of solubility allowed thermally sensitive salts, such as those containing the KrF$^+$ and Kr$_2$F$_3^+$ cations to be handled with minimal decomposition. The crystals were obtained by slowly cooling these solutions from -10 to -80 °C in a vacuum jacketed glass tube using a cold flow of nitrogen gas obtained by boiling liquid nitrogen (Figure 2.6). The rate of cooling was controlled by a resistive heater residing within the liquid nitrogen and could be regulated (±0.2 °C) between room temperature and -90 °C. After the crystals had been deposited from the solution and the temperature had reached -70 to -80 °C, the supernatant was decanted into the sidearm of the vessel, which had been emmersed in
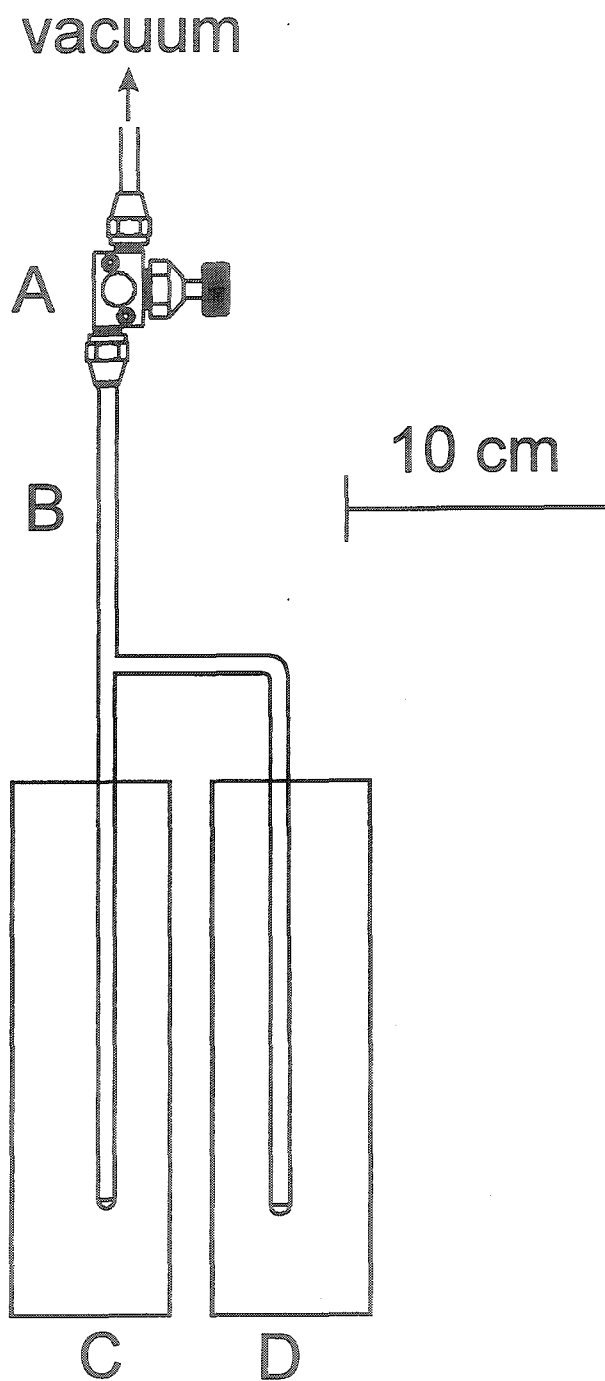
Figure 2.5. The apparatus used for the growth of crystalline KrF_2; (A) Kel-F valve. (B) h-shaped FEP vessel. (C) Dewar containing an acetone bath (-40 °C). (D) Dewar containing a dry ice / acetone slush (-78 °C).
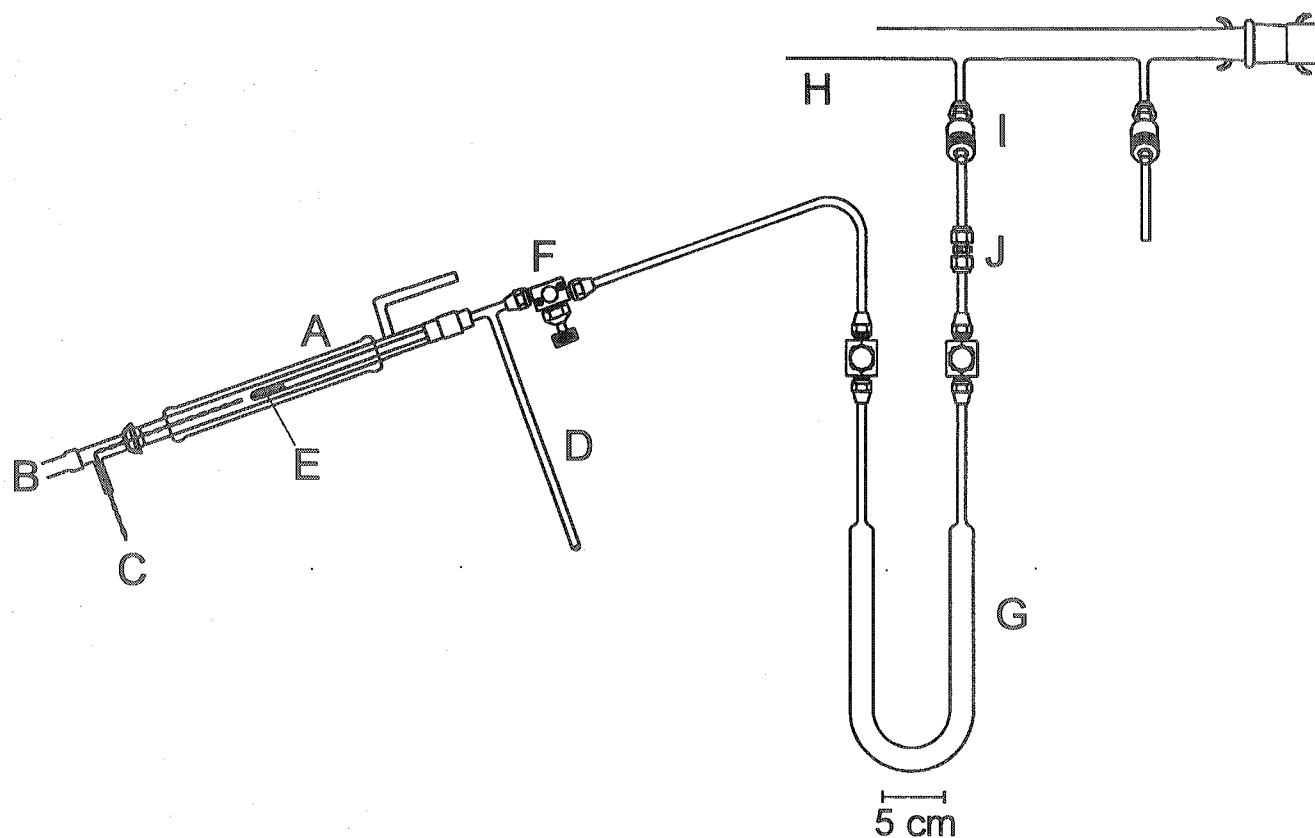
Figure 2.6. The low-temperature crystal growing apparatus. (A) Glass jacketed Dewar (not silvered). (B) Cold flow of N_2, generated by resistively heating $N_2(l)$. (C) Thermocouple. (D) T-shaped FEP vessel. (E) Compound dissolved in solvent. (F) Kel-F valve. (G) FEP U-trap (submersed in liquid nitrogen). (H) Glass vacuum manifold. (I) Greaseless J-Young valve with a PTFE barrel. (J) PTFE Swagelok® or stainless steel Cajon Ultra-Torr connector.

liquid nitrogen. The sidearm was then heat sealed off and removed under dynamic vacuum using a heat-sealing device. The residual HF was removed from the surface of the crystals by pumping under dynamic vacuum and the crystals were stored under dry nitrogen at -78 °C until they could be mounted on the X-ray diffractometer.

2.10.1.3. [XeF][M$_2$F$_{11}$] (M = Sb, Bi)

Suitable crystals of [XeF][Sb$_2$F$_{11}$] and [XeF][Bi$_2$F$_{11}$] were obtained during the course of the syntheses of these salts (see section 2.3.4) and were not re-grown prior to their characterization by single crystal X-ray diffraction.

2.10.1.4. [N(CH$_3$)$_4$][BrO$_3$F$_2$] and [NO]$_2$[BrO$_3$F$_2$][F]

A sample of [N(CH$_3$)$_4$][BrO$_3$F$_2$] (19.5 mg, 81.3 μmol) was dissolved in 0.75 mL of CH$_3$CN at 10 °C. The solution was cooled to -25 °C over the course of several hours using the crystal growing apparatus described in section 2.10.1.2. The majority of the solvent was decanted into the sidearm of the vessel, which was sealed off under dynamic vacuum. The colourless crystals were rigorously dried under dynamic vacuum at -25 °C and then stored under dry N$_2$ until they could be mounted on the X-ray diffractometer.

Crystals of [NO]$_2$[BrO$_3$F$_2$][F] were grown by sublimation of the crude product under 1000 Torr of argon over the course of several weeks while being stored in a Dewar filled with solid dry ice. The colourless block-shaped crystals accumulated in the upper region of the FEP vessel where the fresh dry ice was added to the Dewar on a daily basis. The resulting crystals were kept cold (*i.e.*, $\leq$ -78 °C) under an Ar atmosphere because of the significant volatility of this salt at temperatures as low as -120 °C (see section 2.10.2).

2.10.2. Mounting of Single Crystals at Low-Temperature

Each of the crystals investigated in this work was mounted at low-temperature using the apparatus shown in Figures 2.7 and 2.8. Prior to transferring the crystals, the aluminum tray was cooled to -110 (±5) °C by regulating the dry N$_2$ (HP+) flow that was
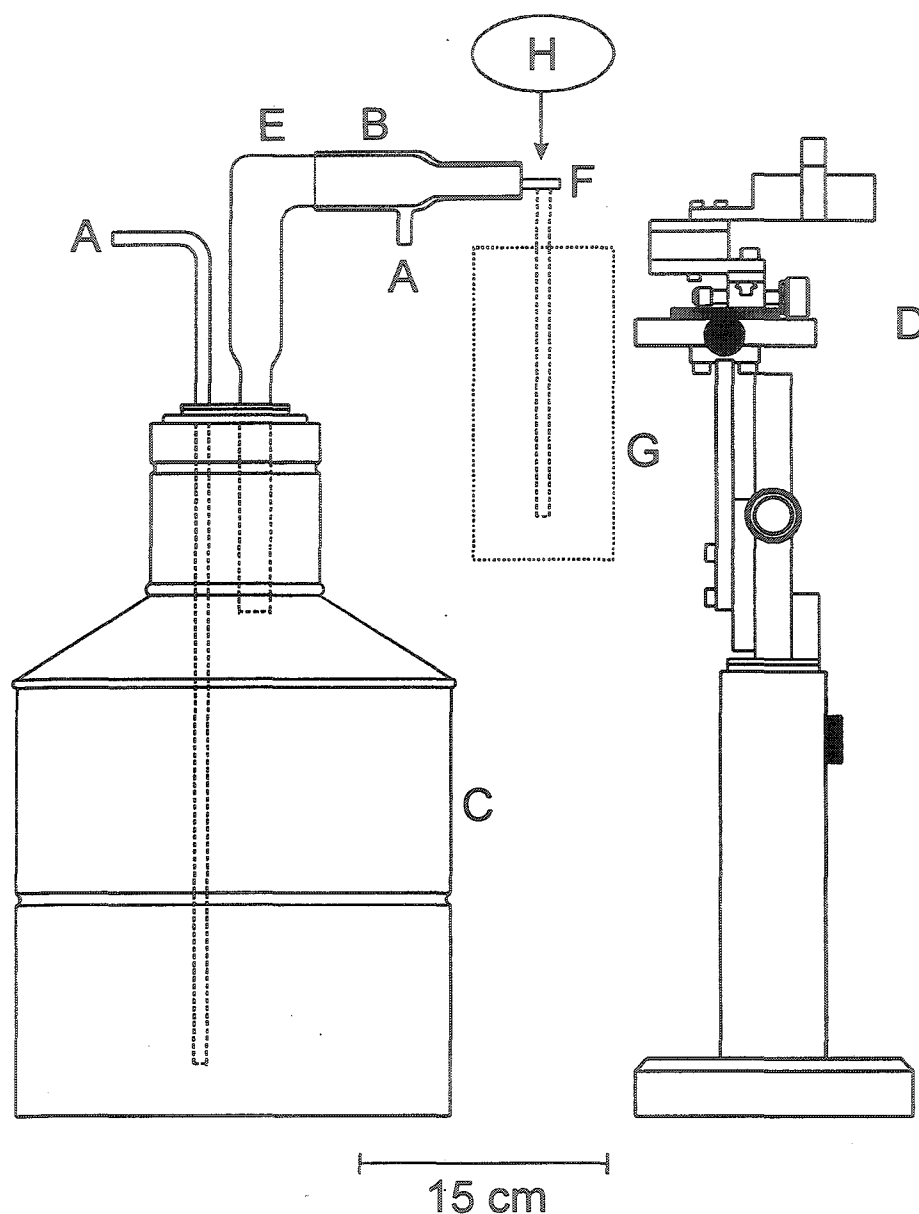
Figure 2.7. The low-temperature crystal mounting apparatus. (A) Nitrogen (HP+) inlet. (B) Glass sleeve for room temperature nitrogen (HP+) flow. (C) Dewar filled with $N_2(l)$. (D) Adjustable stage used to hold mounted crystals prior to transferring them to the diffractometer. (E) Glass jacketed Dewar (silvered). (F) Aluminum tray used to hold the crystals during the mounting process. The aluminum tray was replaced with a copper tray and cooling rod (dashed), which was immersed in a Dewar of liquid nitrogen (G), when mounting crystals of $[NO]_2[BrO_3F_2][F]$. (H) Stereo-zoom microscope.

66

E   B

I

D   G   F

A

H

C

10 cm
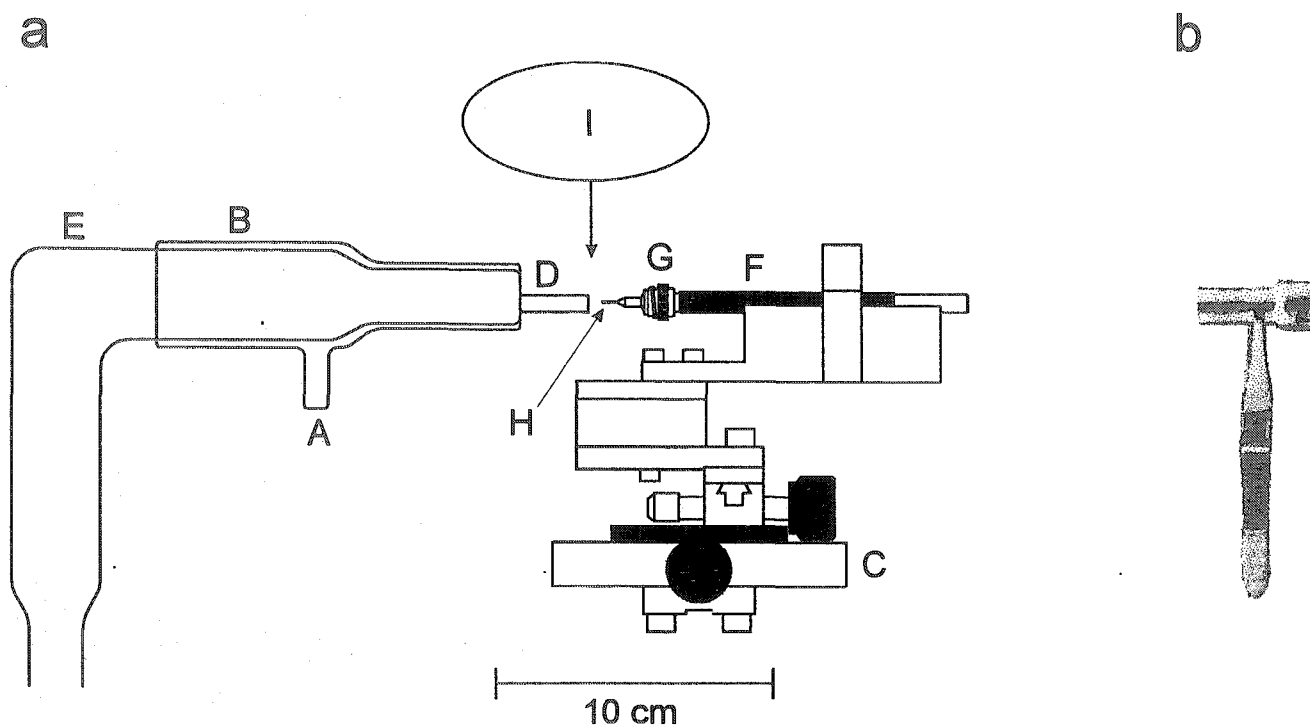
Figure 2.8. (a) Enlarged view of the crystal mounting apparatus illustrating how a mounted crystal could be maintained under inert conditions during visual inspection prior to being transferred to the goniometer; (A) Nitrogen (HP+) inlet. (B) Glass sleeve for room temperature nitrogen (HP+) flow. (C) Adjustable stage used to hold mounted crystals prior to transferring them to the diffractometer. (D) Aluminum tray used to hold the crystals during the mounting process. (E) Glass jacketed Dewar (silvered). (F) Magnetic-based wand used to manipulate the magnetic-based copper pin assembly (G) during the selection of a crystal. (H) Glass fibre. (I) Stereo-zoom microscope. (b) Cryotongs (-196 °C) used to transfer the copper pin assembly and mounted crystal from the magnetic wand to the goniometer of the X-ray diffractometer.

bubbled through the Dewar of liquid nitrogen. With the aid of a glass sleeve, dry N_2 (HP+) was flowed around the region surrounding the cold nitrogen flow to produce a laminar flow and to limit the accumulation of ice on the tray from moisture in surrounding atmosphere. The crystals were transferred from their FEP storage vessel by cutting the tube below the valve under a flow of dry N_2 (HP+) while maintaining the bottom of the vessel at -78 °C. The vessel was inverted over the aluminum tray and gently tapped to dislodge any crystals that were attached to its walls. Suitable crystals were selected with the aid of a stereo-zoom microscope and were mounted on a glass fiber using a perfluorinated polyether oil adhesive (Ausimont Inc., Fomblin Z15 or Z25). The glass fiber had previously been affixed to a copper pin with a magnetic base and could be manipulated with precision when attached to a magnetic wand (Hampton Research). The magnetic wand could be rested on the adjustable support stage such that the quality of the mounted crystal could be assessed visually prior to transferring the magnetic-based pin assembly and the attached crystal to the goniometer (Figure 2.8a). The mounted crystal and brass pin were quickly transferred (*ca.* 5 s) from the wand to the magnetic base of the goniometer using a cryotongs (Figure 2.8b; Hampton Research) that had been pre-cooled in liquid nitrogen. Once on the diffractometer, the crystals were maintained at -173.3(1) °C or *ca.* -120(1) °C using a cold stream of N_2 generated from an Oxford Cryosystems or Molecular Structure Corporation cryostat system, respectively. Each crystal was centred on the goniometer and screened for quality by checking the intensities and shape of the diffraction spots obtained at several random orientations.

The crystals of $[NO]_2[BrO_3F_2][F]$ sublimed rapidly (< 15 min) in the cold flow of the aluminum tray even when cooled to -120 °C. To extend the lifetime of $[NO]_2[BrO_3F_2][F]$, the aluminum tray was replaced by a copper tray that had a solid copper rod (20 cm long, 0.95 cm o.d.) silver-soldered to its base (Figure 2.7). Prior to

transferring the crystals into the copper tray and during the mounting procedure, the copper rod was immersed in a Dewar of liquid nitrogen. The temperature of the cold stream passing over the tray was -125(5) °C, however, the temperature of the copper tray could be maintained at *ca.* -150 °C by immersing the rod in liquid nitrogen to a depth of 15 cm. Using this configuration, crystals of $[NO]_2[BrO_3F_2][F]$ could be screened for durations in excess of 1 hr, however, frosting on the tray was significantly more problematic as a consequence of the additional turbulence produced by the cooling rod.

2.10.3. Collection of X-ray Crystallographic Data

The crystallographic data was collected using a Siemens P4 diffractometer controlled by SMART[251] and equipped with a rotating molybdenum anode and a Siemens SMART 1k CCD area detector. The Mo K_α X-rays ($\lambda = 0.71073$ Å) were filtered using a graphite monochromator and a collimator was used to limit the incident X-rays to a 0.3 mm beam. The 1k CCD detector was set to 512×512 pixel mode using 2×2 pixel binning. The intensities of the diffraction spots were integrated over three dimensions using SAINT,[252] which applied Lorentz and polarization corrections to the data. Empirical adsorption and decay corrections were applied to the data using SADABS,[253] which obtained these scaling factors from the intensities of redundant reflections. The acquisition parameters and refinement statistics of the crystals investigated are summarized in Table 2.1.

2.10.3. Solution and Refinement of X-ray Crystal Structures

The cell dimensions obtained by SMART were verified using XPREP,[254] which was also used to determine the space groups of the crystals based on the geometry of the unit cell and the presence of any systematic absences in the diffraction data. Direct methods were generally used to locate the positions of the heavier atoms in the asymmetric unit, however, the Patterson method was occasionally employed when heavy

Table 2.1. Summary of X-ray Data Collection Parameters

	α-KrF$_2$	β-[KrF][AsF$_6$]	[KrF][SbF$_6$]	[KrF][BiF$_6$]
detector dist. (cm)	4.987	4.987	4.987	4.987
T (°C)	-125	-120	-125	-130
morphology	block	needle	block	needle
cryst. dimen. (mm)	0.15×0.15×0.10	0.25×0.10×0.10	0.30×0.28×0.15	0.15×0.10×0.10
F(000)	108.0	528.0	600.0	728.0
h	-3 to 5	-6 to 6	-6 to 6	-6 to 6
k	-5 to 4	-12 to 12	-13 to 13	-13 to 13
l	-7 to 8	-13 to 13	-13 to 13	-14 to 14
max 2θ (deg)	54.93	54.93	55.08	55.10
no. of refl. measured	325	5224	5856	5231
no. refl. rejected	0	159	200	154
no. independ. refl.	55	1241	1287	1354
R_1	0.0231	0.0265	0.0266	0.0344
wR_2	0.0534	0.0652	0.0527	0.0912

	[KrF][AuF$_6$]	α-[O$_2$][AuF$_6$]	[Kr$_2$F$_3$][SbF$_6$]· KrF$_2$	[Kr$_2$F$_3$]$_2$[SbF$_6$]$_2$· KrF$_2$
detector dist. (cm)	4.987	4.992	4.987	4.987
T (°C)	-125	-122	-113	-125
morphology	plate	plate	plate	cubic
cryst. dimen. (mm)	0.15×0.15×0.04	0.30×0.20×0.04	0.20×0.15×0.08	0.10×0.10×0.10
F(000)	712.0	149.0	516.0	1848.0
h	-10 to 10	-6 to 6	-9 to 10	-10 to 10
k	-9 to 9	-6 to 6	-11 to 11	-39 to 39
l	-13 to 13	-6 to 6	-11 to 11	-10 to 10
max 2θ (deg)	54.97	61.22	55.23	55.10
no. of refl. measured	4374	1074	4218	18443
no. reflect. rejected	218	0	0	192
no. independ. reflect.	1099	451	1956	4033
R_1	0.0389	0.0481	0.0402	0.0376
wR_2	0.0911	0.1181	0.1039	0.0742

Table 2.1.   continued...

	$[Kr_2F_3][AsF_6] \cdot$ $[KrF][AsF_6]$	XeF_2	$[XeF][AsF_6]$	$[XeF][SbF_6]$
detector dist. (cm)	4.987	4.987	4.987	4.987
T (°C)	-120	-173	-173	-173
Morphology	needle	wedge	block	needle
cyst. Dimen. (mm)	0.20×0.04×0.02	0.14×0.08×0.08	0.18×0.08×0.08	0.20×0.06×0.06
$F(000)$	1272.0	144.0	600.0	672.0
h	-8 to 8	-6 to 5	-7 to 8	-6 to 6
k	-31 to 32	-6 to 5	-8 to 8	-14 to 13
l	-11 to 11	-10 to 11	-20 to 20	-14 to 13
max 2θ (deg)	55.17	71.64	54.97	54.98
no. of refl. measured	13312	1421	10636	11854
no. of refl. rejected	0	0	613	303
no. of independ. refl.	2926	107	1355	1454
R_1	0.0471	0.0160	0.0269	0.0169
wR_2	0.0936	0.0354	0.0646	0.0365

	$[XeF][BiF_6]$	$[XeF][Sb_2F_{11}]$	$[XeF][Bi_2F_{11}]$	$[ClF_6][Sb_2F_{11}]$
detector dist. (cm)	4.987	4.987	4.978	4.987
T (°C)	-173	-173	-173	-125
morphology	plate	needle	neddle	plate
cyst. Dimen. (mm)	0.20×0.04×0.02	0.31×0.20×0.04	0.12×0.04×0.04	0.04×0.04×0.02
$F(000)$	800.0	528.0	1312	1088.0
h	-6 to 6	-9 to 9	-10 to 12	-14 to 15
k	-12 to 12	-12 to 12	-12 to 14	-10 to 11
l	-15 to 15	-10 to 10	-18 to 21	-16 to 15
max 2θ (deg)	54.78	55.06	66.20	57.93
no. of refl. measured	8913	9493	24021	11208
no. of refl. rejected	247	22	81	486
no. of independ. refl.	1457	2402	3967	2899
R_1	0.0409	0.0219	0.0395	0.0488
wR_2	0.1076	0.0491	0.0759	0.1070

Table 2.1.   continued...

	[BrF$_6$] [Sb$_2$F$_{11}$]	[IF$_6$] [Sb$_2$F$_{11}$]	[N(CH$_3$)$_4$] [BrO$_3$F$_2$]	[NO]$_2$ [BrO$_3$F$_2$][F]
detector dist. (cm)	4.987	4.987	4.987	4.970
T (°C)	-130	-173	-173	-173
morphology	block	needle	block	block
cyst. Dimen. (mm)	0.20×0.08×0.08	0.15×0.15×0.08	0.10×0.10×0.04	0.10×0.10×0.10
F(000)	1300.0	1232.0	240.0	928.0
h	-15 to 14	-15 to 15	-14 to 13	-14 to 12
k	-11 to 11	-11 to 11	-14 to 10	-18 to 16
l	-15 to 14	-15 to 15	-9 to 7	-13 to 14
max 2θ (deg)	57.92	54.88	73.28	61.15
no. of refl. measured	11179	10775	11010	12910
no. of refl. rejected	341	525	390	240
no. of independ. refl.	2946	2722	615	1914
R$_1$	0.0707	0.0217	0.0314	0.0671
wR$_2$	0.1577	0.0601	0.0761	0.1813

	[ClO$_2$][SbF$_6$]	[BrO$_2$][SbF$_6$]
detector dist. (cm)	5.000	4.987
T (°C)	-173	-173
F(000)	276.0	312.0
morphology	needle	block
cyst. Dimen. (mm)	0.14×0.08×0.08	0.16×0.08×0.08
h	-11 to 11	-9 to 9
k	-7 to 9	-7 to 7
l	-11 to 9	-9 to 9
max 2θ (deg)	72.43	54.94
no. of refl. measured	4390	5308
no. of refl. rejected	196	226
no. of independ.	1310	704
R$_1$	0.0558	0.0142
wR$_2$	0.1385	0.0331

atoms such as Sb, Bi, or Au were present. The positions of the lighter atoms were determined using full-matrix least-squares refinements and successive difference Fourier syntheses of the atomic positions and the isotropic thermal parameters. Once the atomic positions were determined, the structure was refined with the addition of anisotropic thermal parameters and a weighting factor determined by the program.

2.11. Characterization by Spectroscopic Methods

2.11.1. Raman Spectroscopy

Raman spectra were recorded on a Bruker RFS 100 Fourier transform Raman spectrometer using the 1064-nm line of a Nd-YAG laser. The instrument was equipped with a quartz beam splitter and a liquid nitrogen cooled germanium diode detector configured to detect 180°-backscattered radiation. The Fourier transforms of the raw interferograms were processed using a Blackman Harris 4-term apodization and a zero-filling factor of 2. The spectral range of the instrument was -999 to +3510 cm^{-1} relative to the excitation line (0 cm^{-1}), which was filtered (-50 to +50 cm^{-1}) to prevent the detector from becoming saturated. Because the anti-Stokes Raman lines are intrinsically weak at low temperature and provide a limited amount of additional information, only the Stokes lines (*i.e.*, 50 to 3500 cm^{-1}) are reported in the present work. For routine measurements, the 300 mW laser was focused to a diameter of *ca.* 0.1 mm on the sample and 300 to 500 scans were acquired with 1 cm^{-1} resolution. To obtain the highest resolution, most of the spectra were acquired at the lower limit of the Bruker R495 low-temperature accessory (-163 °C), however, temperatures between +25 and -163 °C were used to investigate materials under liquid solvents, such as anhydrous HF, and the phase behaviour of $[O_2][AuF_6]$. Samples that were found to decompose or strongly fluorescence under these conditions were investigated at reduced laser powers.

2.11.2. Infrared Spectroscopy

Infrared spectra were obtained at ambient temperature using a Bio-Rad FTS-40 spectrometer. The spectra of gaseous samples (*i.e.*, PF_5) were acquired by pressurizing an FEP tube (1.9 cm o.d., 10 cm length) equipped with a Kel-F valve and AgCl windows with 10 to 20 Torr of the reagent. The spectra of solid materials (*i.e.*, $[Cs][BrO_3F_2]$) were acquired as AgCl pellets. The AgCl pellets were fabricated in three layers using a Wilks mini-press, with the external layers being composed of AgCl and the central layer being a mixture of the sample and AgCl. This sandwich configuration allowed air and moisture sensitive compounds to be handled with minimal contamination for short periods of time in the atmosphere.

2.11.3. NMR Spectroscopy

The samples investigated by NMR spectroscopy were prepared in sealed FEP vessels (4-mm o.d.), which were inserted into standard thin walled precision glass (5 mm i.d.) NMR tubes (Wilmad) during the data acquisition.

The spectra were acquired with a Bruker DRX-500 (11.7438 T) spectrometer operating in unlocked mode (field drift < 0.1 Hz hr^{-1}) using a 5-mm broad-band probe. The temperature of the sample region of the probe could be regulated to within ±0.1 °C and was calibrated using an external thermocouple prior to the insertion of the sample into the spectrometer. The spectra were externally referenced to neat $CFCl_3$ (^{19}F), neat $Si(CH_3)_4$ (^1H, ^{13}C) and aqueous KX (X = Cl, Br, I) extrapolated to infinite dilution ($^{35,37}Cl$, $^{79,81}Br$, ^{127}I) at 27 °C. The specific parameters used for acquisition of the NMR spectra are summarized in Table 2.2.

The T_1-relaxation times of the central halogens in the XF_6^+ cations were determined by the spin-inversion-recovery method with delay time (τ) ranges of 0.100 - 3.00 s ($^{35,37}Cl$), 0.100 - 100 ms ($^{79,81}Br$) and 0.100 - 30 ms (^{127}I). The remaining spectral

Table 2.2. Summary of NMR Spectroscopy Data Collection Parameters

Sample	Solvent	Temp (°C)	Nucleus	Pulse Width (μs)	Freq. (MHz)	Spectral Region (ppm)[a]	TD[b] (kHz)	SI[b] (kHz)	SW[b] (kHz)	Resolution[b] (Hz/pt)
$[ClF_6][AsF_6]$	HF	27	^{35}Cl	31.00	49.042	775 to 865	4	4	48.83	1.192
			^{37}Cl	29.25	40.823	775 to 855	4	4	32.55	0.795
$[BrF_6][AsF_6]$	HF	27	^{79}Br	13.00	125.561	2010 to 2150	8	8	20.00	2.441
			^{81}Br	13.00	135.348	2020 to 2130	8	8	50.00	6.104
$[IF_6][Sb_3F_{16}]$	HF	27	^{127}I	16.75	100.400	3000 to 3700	4	4	69.93	2.134
$[N(CH_3)_4][BrO_3F_2]$[c]	CH_3CN	-40	^{19}F	2.30	470.592	-500 to -300	32	32	94.34	2.879
					470.489	-320 to -120	32	32	94.34	2.879
					470.569	-140 to 40	32	32	84.75	2.586
					470.649	20 to 220	32	32	94.34	2.879
					470.733	200 to 400	32	32	94.34	2.879
					470.818	380 to 580	32	32	94.34	2.879
					470.705	220 to 260	16	16	18.80	1.147
			^1H	7.70	500.133	-1.00 to 20.0	32	32	10.50	0.321
			^{13}C	12.80	125.771	-9.25 to 221	32	32	28.99	0.885
$[N(CH_3)_4][BrO_3F_2]$[d]	CH_3CN	-40	^{19}F	2.30	470.545	-200 to 0	32	32	94.34	2.879
					470.616	-50 to 150	32	32	94.34	2.879
					470.686	100 to 300	32	32	94.34	2.879
					470.757	250 to 450	32	32	94.34	2.879
					470.827	400 to 600	32	32	94.34	2.879
			^1H	7.70	500.133	-1.3 to 12.2	32	32	6.78	0.207
			^{13}C	12.80	125.792	-21.6 to 180.2	32	32	81.30	2.481

Table 2.2.   continued...

Sample	Solvent	Temp (°C)	Nucleus	Pulse Width (µs)	Freq. (MHz)	Region[a] (ppm)	TD[b] (kHz)	SI[b] (kHz)	SW[b] (kHz)	Resolution[b] (Hz/pt)
XeF$_6$:[K][BrO$_4$] (5.2 : 1)	HF	-80	^{19}F	2.30	470.620	-0.0 to 120.0	32	32	56.50	1.724
					470.677	109.9 to 250.1	32	32	66.01	2.014
					470.721	210.0 to 340.0	32	32	61.16	1.867
					470.780	340.0 to 460.0	32	32	56.50	1.724
XeF$_6$:[K][BrO$_4$] (2.3 : 1)	HF	-80	^{19}F	2.30	470.604	-49.8 to 99.8	32	32	70.42	2.149
					470.651	50.1 to 199.8	32	32	70.42	2.149
					470.674	100.2 to 249.8	32	32	70.42	2.149
					470.710	200.0 to 300.3	32	32	47.17	1.440
[Xe$_2$F$_{11}$][AsF$_6$]:BrO$_2$F (4.76 : 1)	HF	-70	^{19}F	2.30	470.493	-260.1 to -159.9	32	32	47.17	1.440
					470.533	-170.0 to -80.0	32	32	42.37	1.293
					470.545	-160.0 to -40.0	32	32	56.50	1.724
					470.580	-85.0 to 35.0	32	32	56.50	1.724
					470.627	24.9 to 125.1	32	32	47.17	1.440
					470.655	90.0 to 180.0	32	32	42.37	1.293
					470.688	160.0 to 250.0	32	32	42.37	1.293
					470.708	206.4 to 288.4	32	32	40.00	1.221
					470.720	255.0 to 290.0	32	32	16.50	1.007
					470.749	270.0 to 400.0	32	32	61.16	1.867
					470.592	309.9 to 410.1	32	32	47.17	1.440

[a] All spectra are referenced to the standards references for the respective nuclei at 27 °C (^{19}F, CFCl$_3$; ^{1}H, Si(CH$_3$)$_4$; ^{13}C, Si(CH$_3$)$_4$; ^{m}X (X = Cl, Br, I), infinitely dilute aqueous K^{m}X).   [b] The size of the time domain, the size of the transformed spectrum and the spectral width are denoted as TD, SI and SW, respectively. The size of the raw FID is given by of TD + SI, with the resulting spectrum having a size of (TD + SI)/2 (Note: 1k = 1024). The spectral resolution is given by 2SW / (TD + SI).   [c] Spectrum recorded without warming the sample above -40 °C.   [d] Recorded after the sample had been warmed to 20 °C for approximately 2 hr.

parameters were identical to those used to acquire the 1-D spectra (*vide supra*). The T_1-relaxtion times were calculated by plotting the intensity of the central peak, I_c, of the septet versus τ, and fitting the data to the exponential relation, $I_c = a + be^{-\tau/T_1}$, where a, b and T_1 were refined as independent variables.

2.12. Electronic Structure Calculations

The local density functional level[255] calculations for KrF_2, KrF^+, $[KrF][MF_6]$ (M = P, As, Sb, Bi) and $Kr_2F_3^+$, were completed using the Dgauss[256-258] software package. The remaining calculations were completed using the Gaussian 98 software package,[259] and basis sets equipped with the program or available online.[260] The energy minimized geometries of the molecules and ions investigated were obtained using analytic gradient methods prior[261] to the determination of the molecular and ionic properties (*i.e.*, vibrational frequencies, atomic charges, bond orders, etc.). Highly accurate basis sets (6-311G(d) or DZVP) were utilized for systems composed entirely of light atoms (*i.e.*, periods 2 - 4), while basis sets with effective core potentials (ECP) were used for systems containing heavy atoms (I, Sb, Bi, Xe, Au). The basis sets used at each level of theory for the species investigated, and the level of theory from which the Mayer bond orders, Mayer valencies and atomic charges were derived are summarized in Table 2.3.

Table 2.3. Summary of the Levels of Theory and Basis Sets Used for the Calculation of Energy Minimized Geometries, Vibrational Spectra, Atomic Charges, Valencies and Bond Orders

Compound	HF	MP2	LDF
AuF_6^-	Stuttgart RLC ECP (Kr, F)	Stuttgart RLC ECP (Kr, F)	DZVP (Kr, F)
			Hay Wadt ECP (Au)*
ClF_6^+	DZVP*[‡]	DZVP*	DZVP*[‡]
ClO_2^+	6-311G(d)	6-311G(d)	DZVP
ClO_3F	6-311G(d)	6-311G(d)	DZVP*
$ClO_3F_2^-$	6-311G(d)	6-311G(d)	DZVP*
ClO_4^-	6-311G(d)	6-311G(d)	DZVP*
BrF_6^+	DZVP*[‡]	DZVP*	DZVP*[‡]
BrO_2^+	6-311G(d)	6-311G(d)	DZVP
BrO_3F	6-311G(d)	6-311G(d)	DZVP*
$BrO_3F_2^-$	6-311G(d)	6-311G(d)	DZVP*
$BrO_3F_3^{2-}$	6-311G(d)	6-311G(d)	DZVP*
BrO_4^-	6-311G(d)	6-311G(d)	DZVP*
IF_6^+	DZVP*[‡]	DZVP*	DZVP*[‡]
KrF_2	DZVP (F), Hay Wadt (Kr)[†]		DZVP*[†]
KrF^+	DZVP (F), Hay Wadt (Kr)[†]	6-311G(d)	DZVP*[†]
$Kr_2F_3^+$	DZVP (F), Hay Wadt (Kr)[†]		DZVP*[†]
[KrF][AsF_6]	DZVP (F), Hay Wadt (Kr, As)[†]		DZVP*[†]
[KrF][AuF_6]	Stuttgart RSC 1997 ECP (Au)	Stuttgart RSC 1997 ECP (Au)	DZVP (Kr, F) Stuttgart RLC ECP
(Kr, F)	Stuttgart RLC ECP (Kr, F)		Hay Wadt ECP (Au)*

Table 2.3. continued...

Compound	HF	MP2	LDF
[KrF][BiF$_6$]	DZVP (F), Hay Wadt (Kr, Bi)[†]		DZVP (Kr, F) Hay Wadt ECP (Bi)*[†]
[KrF][PF$_6$]	DZVP (F, P), Hay Wadt (Kr)[†]		DZVP*[†]
[KrF][SbF$_6$]	DZVP (F), Hay Wadt (Kr, Sb)[†]		DZVP*[†]
O$_2$	6-311G(d)	6-311G(d)	DZVP*
O$_2$$^+$	6-311G(d)	6-311G(d)	DZVP*
XeF$_2$	Stuttgart RLC ECP	Stuttgart RLC ECP	DZVP
XeF$^+$	Stuttgart RLC ECP	Stuttgart RLC ECP	DZVP*
[XeF][AsF$_6$]	Stuttgart RLC ECP	Stuttgart RLC ECP	DZVP*
[XeF][BiF$_6$]	Stuttgart RLC ECP	Stuttgart RLC ECP	Stuttgart RLC ECP*
[XeF][SbF$_6$]	Stuttgart RLC ECP	Stuttgart RLC ECP	DZVP*

[a] The standard 6-311G(d) basis set included in the Gaussian 98 software package was used without modification. The Stuttgart RSC 1997 ECP, Stuttgart RLC ECP, Hay Wadt[262-264] and DZVP[265] basis sets were obtained in electronic form from ref 260. [b] Calculations at the local density functional level of theory were performed using the potential fit described by Vosko, Wilk, and Nusair (SVWN),[266] or modified Perdew-Wang method (MPW1PW91) described by Adamo and Barone.[267] [c] Mayer bond orders, Mayer valencies and atomic charges were calculated using the levels of theory and basis sets denoted with asterisks. [d] Calculations marked with dagger (†) were performed by Dr. David Dixon (William R. Wiley Environmental Molecular Science Laboratory, Pacific Northwest National Laboratory). Calculations marked with a double dagger (‡) were performed by Dr. Reijo Suontamo (Department of Chemistry, University of Jyväskylä). All other calculations were performed by the author.

CHAPTER 3

STRUCTURAL CHARACTERIZATION OF α-KrF₂ AND THE PNICOGEN HEXAFLUORO-ANION SALTS OF THE KrF⁺ AND Kr₂F₃⁺ CATIONS[268]

3.1. Introduction

The compounds of krypton that have been isolated in macroscopic quantities are limited to the element's +2 oxidation state and currently include KrF_2,[13-15,19,22,24,119,269] $Kr(OTeF_5)_2$,[136] salts of the KrF^+,[21,35,40,41,62,270-272] $Kr_2F_3^+$,[21,40,62,137,271,272] and $RCN-KrF^+$ (R = H, CF_3, C_2F_5, $n-C_3F_7$) cations,[51,98] and the molecular adducts $KrF_2 \cdot MOF_4$ (M = Cr, Mo, W),[81,124] $KrF_2 \cdot nMoOF_4$ (n = 2, 3),[81] $KrF_2 \cdot VF_5$,[273] and $KrF_2 \cdot MnF_4$.[131] While the strong oxidizing character of KrF_2, KrF^+ and $Kr_2F_3^+$ provides clean, low temperature synthetic routes to $[BrF_6][AsF_6]$,[36,137] $[ClF_6][AsF_6]$,[37] OsO_2F_4,[274] AuF_5,[35] and $TcOF_5$,[275] it has also served as a significant impediment to their detailed structural characterization by single crystal X-ray diffraction. With the exception of KrF_2, no other krypton compound has been structurally characterized by X-ray or electron diffraction techniques. Of the two phases of KrF_2 identified by variable temperature Raman spectroscopy,[123] only the X-ray crystal structure of the high-temperature β-phase has been reported at -80 °C,[129] although an incorrect determination of the unit cell parameters at room temperature had been reported earlier.[276]

Krypton difluoride exhibits fluoride ion donor properties that are analogous to those established for XeF_2.[62,71-73,81,82] The reaction of KrF_2 with strong fluoride ion acceptors leads to the formation of KrF^+ and $Kr_2F_3^+$ salts, i.e., $[KrF][MF_6]$ (M = As,[40,137] Sb,[21,40,137,272] Bi,[41] Au,[35] Pt,[40,137] Ta[21,271]), $[KrF][M_2F_{11}]$ (M = Sb,[21,40,137,270] Ta,[21,271]

$Nb^{21,271}$) and $[Kr_2F_3][MF_6]$ (M = As,[40,137] Sb,[21,40,137,272] Ta[21]). The physical and spectroscopic (infrared, Raman, Mössbauer and ^{19}F NMR) properties of these salts have been the topic of two detailed reviews.[62,111] Unlike their xenon(II) analogues, krypton(II) compounds are thermodynamically unstable. The relative kinetic stabilities of their salts, however, show considerable variations as exemplified by $[KrF][SbF_6]$,[40,137,272] $[KrF][Sb_2F_{11}]$,[21,270] $[Kr_2F_3][SbF_6]$,[21,40,137] and $[KrF][AuF_6]$,[35] which can be stored at room temperature for appreciable periods of time without significant decomposition whereas other KrF^+ salts can only be handled at low temperatures.[21,271]

Structural characterization of the KrF^+ and $Kr_2F_3^+$ salts in the solid state using Raman spectroscopy has been most extensive.[21,35,40,41,137,271,272] The Raman spectra of KrF^+ salts indicate that the KrF^+ cation strongly interacts with the anion by formation of a fluorine bridge between krypton and a fluorine of the anion, as is the case for XeF^+ in the crystal structures of $[XeF][AsF_6]$,[72] $[XeF][Sb_2F_{11}]$,[73] and $[XeF][RuF_6]$.[71] Consequently, fluorine bridge modes and additional modes resulting from symmetry lowering of the octahedral anion have been reported and tentatively assigned.[21,35,40,41] The Raman spectra of $[Kr_2F_3][AsF_6]$, $[Kr_2F_3][SbF_6]$, $[Kr_2F_3][AsF_6] \cdot nKrF_2$ and $[Kr_2F_3][SbF_6] \cdot nKrF_2$, have been assigned on the basis of a symmetrical V-shaped fluorine bridged geometry for the cation,[40,137] analogous to that established by X-ray crystallography for $[Xe_2F_3][AsF_6]$[91,93,277] and $[Xe_2F_3][SbF_6]$.[91] In contrast to KrF^+, cation-anion interactions in the $Kr_2F_3^+$ salts appear to be weak, as indicated by retention of the octahedral anion symmetry.[21,40,137] Fluorine-19 NMR spectroscopy has also been used to study the KrF^+ cation in HF solution[40] and the $Kr_2F_3^+$ cation in BrF_5 solution,[40,137] with the latter study providing the first unambiguous structural characterization of the $Kr_2F_3^+$ cation.

The present study reports the first detailed X-ray crystallographic study of salts containing the KrF^+ and $Kr_2F_3^+$ cations and confirms the dimorphism of KrF_2 by

determination of the X-ray structure of the low-temperature, α-phase, of KrF_2. Theoretical calculations have been used to arrive at the energy-minimized, gas-phase geometries and to reassign or confirm earlier vibrational assignments of KrF_2, the $[KrF][MF_6]$ (M = P, As, Sb, Bi) ion pairs and the $Kr_2F_3^+$ cation in the gas phase. The effects of crystal packing on the geometries of the $[KrF][MF_6]$ ion pairs and the $Kr_2F_3^+$ cation are also assessed in light of their calculated gas-phase geometries.

3.2. Results and Discussion

3.2.1. Synthesis of KrF_2, $[KrF][MF_6]$ (M = As, Sb, Bi), $[Kr_2F_3][SbF_6]\cdot KrF_2$, $[Kr_2F_3]_2[SbF_6]_2\cdot KrF_2$, $[Kr_2F_3][AsF_6]\cdot[KrF][AsF_6]$, and $[Kr_2F_3][PF_6]\cdot nKrF_2$ (n $\geq$ 0)

Krypton difluoride was prepared by the reaction of solid krypton with fluorine radicals in a hot wire reactor. The highly volatile chromium oxide fluoride impurities produced in the stainless steel reactor were removed by their flash distillation from the product under dynamic vacuum at 0 °C.

The $[KrF][MF_6]$ (M = P, As, Sb, Bi), $[Kr_2F_3][SbF_6]\cdot KrF_2$, $[Kr_2F_3]_2[SbF_6]_2\cdot KrF_2$ and $[Kr_2F_3][AsF_6]\cdot[KrF][AsF_6]$ salts were synthesized by the fluoride ion transfer reactions of KrF_2 with MF_5 in 1:1 (eq 3.1), 2.06:1 (eq 3.2), 3.5:1 (eq 3.3) and 2:1 (eq 3.4)

$$KrF_2 + MF_5 \rightarrow [KrF][MF_6] \tag{3.1}$$

$$2.06KrF_2 + SbF_5 \rightarrow [Kr_2F_3][SbF_6]\cdot KrF_2 + ([KrF][SbF_6] + Kr + F_2) \tag{3.2}$$

$$3.5KrF_2 + SbF_5 \rightarrow [Kr_2F_3]_2[SbF_6]_2\cdot KrF_2 + ([KrF][SbF_6] + Kr + F_2) \tag{3.3}$$

$$4KrF_2 + 2AsF_5 \rightarrow [Kr_2F_3][AsF_6]\cdot[KrF][AsF_6] \tag{3.4}$$

molar ratios, respectively, in anhydrous HF solvent. The salts, $[Kr_2F_3][SbF_6]\cdot KrF_2$, $[Kr_2F_3]_2[SbF_6]_2\cdot KrF_2$, and $[Kr_2F_3][AsF_6]\cdot[KrF][AsF_6]$, were obtained while attempting to crystallize the stoichiometric $[Kr_2F_3][MF_6]$ (M = As, Sb) salts. The excess KrF_2 used in reactions leading to the formation of $[Kr_2F_3][SbF_6]\cdot KrF_2$ and $[Kr_2F_3]_2[SbF_6]_2\cdot KrF_2$ were required in order to compensate for the slow auto-decomposition of $[Kr_2F_3][SbF_6]$ in HF

82

solution at temperatures as low as -40 °C (eq 3.5), which resulted in the products being

$$[Kr_2F_3][SbF_6] \rightarrow [KrF][SbF_6] + Kr + F_2 \qquad (3.5)$$

contaminated with $[KrF][SbF_6]$. A similar decomposition accounts for the crystallization

of $[Kr_2F_3][AsF_6]\cdot[KrF][AsF_6]$ from stoichiometric solutions of $[Kr_2F_3][AsF_6]$.

In contrast to $[Kr_2F_3][MF_6]\cdot nKrF_2$ (M = As, Sb; $n \geq 0$), which reacts with excess

AsF_5 and SbF_5 to produce $[KrF][MF_6]$ (M = As, Sb) or $[KrF][Sb_2F_{11}]$, the reaction of

KrF_2 with a stoichiometric excess of neat PF_5 at -78 °C produced only $[Kr_2F_3][PF_6]\cdot nKrF_2$

(eq 3.6) where n is unspecified but may take on values of ½ or 1 as determined for the

$$(2 + n)KrF_2 + PF_5 \rightarrow [Kr_2F_3][PF_6]\cdot nKrF_2 \qquad (3.6)$$

SbF_6^- analogues (see section 3.2.2.3.).

3.2.2. X-ray Crystal Structures of α-KrF$_2$ and Salts of the KrF$^+$ and Kr$_2$F$_3$$^+$ Cations
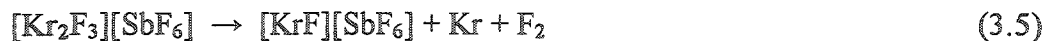
Suitable single crystals of KrF_2 were grown by sublimation of the difluoride under

static vacuum from -40 to -78 °C. Single crystals of $[KrF][MF_6]$ (M = P, As, Sb, Bi),

$[Kr_2F_3][SbF_6]\cdot KrF_2$, $[Kr_2F_3]_2[SbF_6]_2\cdot KrF_2$ and $[Kr_2F_3][AsF_6]\cdot[KrF][AsF_6]$ were obtained

by slowly cooling their anhydrous HF solutions. The unit cell parameters and refinement

statistics for KrF_2, $[KrF][MF_6]$ (M = P, As, Sb, Bi), $[Kr_2F_3][AsF_6]\cdot[KrF][AsF_6]$,

$[Kr_2F_3][SbF_6]\cdot KrF_2$, and $[Kr_2F_3]_2[SbF_6]_2\cdot KrF_2$ are summarized in Table 3.1. With the

exception of $[Kr_2F_3][AsF_6]\cdot[KrF][AsF_6]$, which was refined as a merohedral twin, the all

of the structures were solved and refined as single crystals.

3.2.2.1. α-KrF$_2$

The crystal structure of KrF_2 was redetermined to obtain more precise structural

parameters, which are important for comparison with other Kr-F bond lengths, and to

establish the structural basis for the dimorphism of KrF_2. The dimorphism of KrF_2 was

originally studied by Raman spectroscopy in conjunction with a factor-group analysis.

The study indicated that the low-temperature phase (α) of KrF_2 (Figure 3.1a) is

Table 3.1. Crystal Data and Refinement Results for α-KrF₂, [KrF][MF₆] (M = As, Sb, Bi), [Kr₂F₃][SbF₆]·KrF₂, [Kr₂F₃]₂[SbF₆]₂·KrF₂, and [Kr₂F₃][AsF₆]·[KrF][AsF₆]

	α-KrF₂	β-[KrF][AsF₆]	[KrF][SbF₆]	[KrF][BiF₆]	[Kr₂F₃]₂[SbF₆]₂· KrF₂	[Kr₂F₃][SbF₆]· KrF₂	[Kr₂F₃][AsF₆]· [KrF][AsF₆]
Space Group	$I4/mmm$	$P2_1/c$	$P2_1/c$	$P2_1/c$	$P2_1/c$	$P\bar{1}$	$P2_1/c$
a (Å)	4.1790(6)	5.1753(2)	5.2922(6)	5.336(1)	8.042(2)	8.032(3)	6.247(1)
b (Å)	4.1790(6)	10.2019(7)	10.444(1)	10.513(2)	30.815(6)	8.559(4)	24.705(4)
c (Å)	6.489(1)	10.5763(8)	10.796(1)	11.046(2)	8.137(2)	8.948(4)	8.8616(6)
α (deg)	90	90	90	90	90	69.659(9)	90
β (deg)	90	95.298(2)	94.693(4)	94.79(3)	111.945(3)	63.75(1)	90.304(6)
γ (deg)	90	90	90	90	90	82.60(1)	90
V (Å³)	113.32(3)	556.02(6)	594.73(1)	617.6(2)	1870.1(7)	517.1(4)	1367.6(3)
Z	2	4	4	4	4	2	4
mass (g mol⁻¹)	121.80	291.72	338.55	425.78	1042.47	582.15	705.24
ρ_{calcd} (g cm⁻³)	3.570	3.485	3.781	4.579	3.703	3.739	3.425
T (°C)	-125	-120	-113	-130	-125	-113	-120
μ (mm⁻¹)	19.60	14.09	12.09	35.72	14.82	15.54	14.70
R_1[a]	0.0231	0.0265	0.0266	0.0344	0.0376	0.0402	0.0471
wR_2[b]	0.0534	0.0652	0.0526	0.0912	0.0742	0.1039	0.0958

[a] $R_1 = \dfrac{\sum\left\|F_o|-|F_c\right\|}{\sum|F_o|}$ for $I > 2\sigma(I)$. [b] $wR_2 = \dfrac{\sum\left|(|F_o|-|F_c|)w^{1/2}\right|}{\sum(|F_o|w)}$ for $I > 2\sigma(I)$.
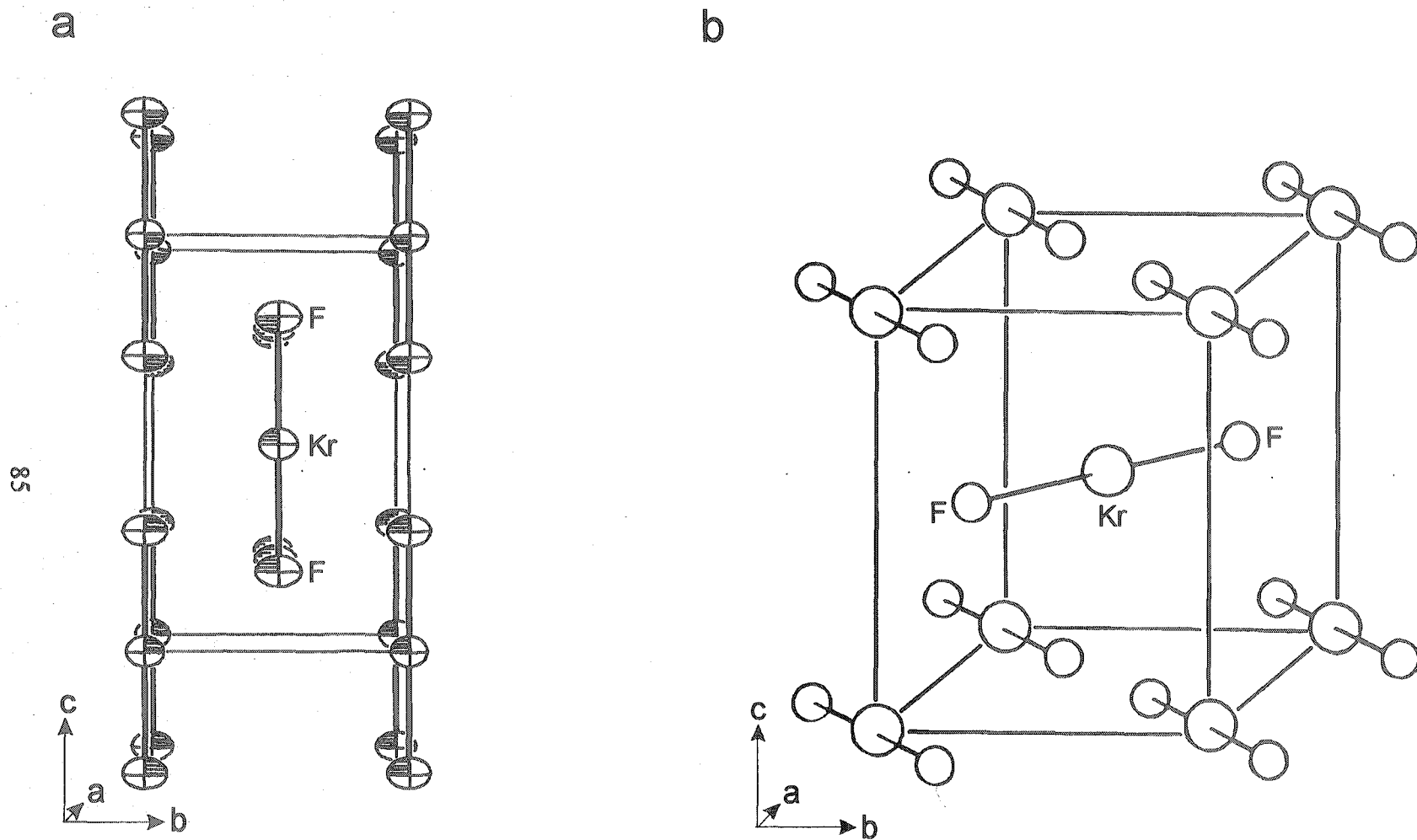
Figure 3.1. Packing diagram of (a) α-KrF_2 viewed along the a-axis and (b) β-KrF_2 viewed along the a-axis (reproduced with permission from ref 129).

isomorphous with XeF_2, which crystallizes in the tetragonal space group *I4/mmm* at room temperature.[278] The present study confirms the dimorphism of KrF_2 and the correctness of the earlier vibrational analysis and space group assignment. The crystal structure of β-KrF_2 (Figure 3.1b) has been previously determined at -80 °C and the α→β phase transition has been shown by variable temperature Raman spectroscopy to occur below this temperature.[123] The observation that crystals of β-KrF_2 were initially grown by sublimation at -78 °C in the present study and then cooled to -125 °C during X-ray data collection on the α-phase, indicates that the β→α phase transition occurs without loss of crystallinity. The crystal packing of α-KrF_2 (Figure 3.1a) is analogous to that of XeF_2,[278] and consists of a body centred arrangement of KrF_2 molecules lying parallel to each other and to the *c*-axis. This is in contrast to the β-phase (Figure 3.1b),[129] in which the molecules centred at the origin and the centre of the cell lie parallel to the *ab*-plane, but are rotated 90° with respect to each other and 45° to the *a*- and *b*-axes. The interconversion between the β- and α-phases may therefore occur by means of a 45° rotation of the molecules occupying the corner sites, such that they become aligned with the *a*-axis of the β-phase, and a 45° rotation of the central molecule in the opposite direction, such that it also lies parallel to the *a*-axis. Consequently, the unit cell axes of the β-phase transform into those of the α-phase as follows: $a \rightarrow c$ and $b,c \rightarrow a,b$ or b,a.

The Kr-F bond length in α-KrF_2 is 1.894(5) Å and is in excellent agreement with those determined for β-KrF_2 (1.89(2) Å, -80 °C) by X-ray diffraction,[129] and gaseous KrF_2 by electron diffraction (1.889(10) Å, -40 °C),[127] infrared spectroscopy (1.875(2) - 1.882821(9) Å)[128,279] and theoretical calculations (1.822 - 1.933 Å)[23,280-283] (Table 3.2). As observed for β-KrF_2, α-KrF_2 is linear and centrosymmetric by symmetry. Despite the modest contraction in the unit cell volume for the α-phase (113.32(3) Å^3, -125 °C) relative to that of the β-phase (122.5 Å^3, -80 °C) and reorientation of KrF_2 molecules

Table 3.2.   Experimental and Calculated Kr-F Bond Lengths for KrF_2

State	Bond Length	Method	Reference
Gas	1.889(1)[a]	Electron diffraction	[127]
	1.875(2) - 1.867(2)[b]	High-resolution IR	[279]
	1.882821(9)[b]	High-resolution IR	[128]
	1.882766(8)[c]	High-resolution IR	[128]
Solid	1.894(5)[d]	X-ray diffraction	This work
	1.89(2)[e]	X-ray diffraction	[129]
	1.881(4) - 1.887(4)[f]	X-ray diffraction	This work
	1.868(4) - 1.888(4)[g]	X-ray diffraction	This work
Theory (Gas)	1.822	HF	[23]
	1.826	HF	[280]
	1.910	LDF	[23]
	1.919	MP2/SBK+(D)	[281]
	1.933	CCSD/SBK+(D)	[281]
	1.88	NDDO-2 (α,β)	[282]
	1.91	Xα-Sw	[283]

[a] Determined in the gas-phase at -40 °C. [b] Calculated from the rotational fine structure of the ν_2 vibration of $^{84}KrF_2$. [c] Calculated from the rotational fine structure of the ν_3 vibration of $^{86}KrF_2$. [d] Low-temperature (-125 °C) α-phase; space group, *I4/mmm*. [e] High-temperature (-80 °C) β-Phase; space group, *P4_2/mnm*. [f] $[Kr_2F_3]_2[SbF_6]_2 \cdot KrF_2$; -125 °C. [g] $[Kr_2F_3]_2[SbF_6]_2 \cdot KrF_2$; -113 °C.

within the cell, the intermolecular F···F distances between the collinearly orientated KrF_2 molecules is 2.71 Å in both structures.

3.2.2.2. β-[KrF][AsF₆], [KrF][SbF₆] and [KrF][BiF₆]

The title compounds form an isomorphous and isostructural series (Figures 3.2 - 3.4) in which the KrF^+ cation strongly interacts with the anion by formation of a fluorine bridge with the MF_6^- anion that is bent about F_b. The important bond lengths and bond angles in these salts are summarized in Table 3.3 where they are also compared with those of the [KrF][AsF₆] unit of [Kr₂F₃][AsF₆]·[KrF][AsF₆].

The [KrF][MF₆] ion pairs pack in columns along the a-axis of the unit cell and are tilted such that alternating cation and anion planes are parallel to the b-c face (Figures 3.2b, 3.3b, 3.4b). The point group symmetries of the [KrF][MF₆] ion pairs are C_1 because the F_b--Kr-F_t group is skewed with respect to a plane defined by F_a, the axial fluorine trans to F_b, and two equatorial fluorines, F_e, trans to each other. The smallest F_e-M--F_b--Kr dihedral angles are 22.1°, 22.2°, 19.7° and 28.1° for β-[KrF][AsF₆], [KrF][SbF₆], [KrF][BiF₆] and [Kr₂F₃][AsF₆]·[KrF][AsF₆], respectively.

As inferred from the Raman spectra, the Kr-F_t bond lengths (1.765(3) - 1.774(6) Å) in these salts are significantly shorter and the Kr--F_b bridge bond lengths are significantly longer (2.090(6) - 2.140(3) Å) than that of α-KrF_2 (1.894(5) Å). The MF_6^- octahedra are distorted and have local C_{4v} symmetries that result from strong bridging to the cation, giving rise to a long M--F_b bond. There is no clear distinction between the M-F_e and the M-F_a bond lengths in these compounds. Despite the strong fluorine bridge interactions and variations in the fluoride ion acceptor strengths of AsF_5, SbF_5, and BiF_5, the Kr-F_t bond lengths in all three salts and the Kr--F_b bond distances in β-[KrF][AsF₆] (2.131(2) Å) and [KrF][SbF₆] (2.140(3) Å) exhibit no crystallographically significant difference at the ±3σ limit. The Kr--F_b bridge bond length is, however, significantly
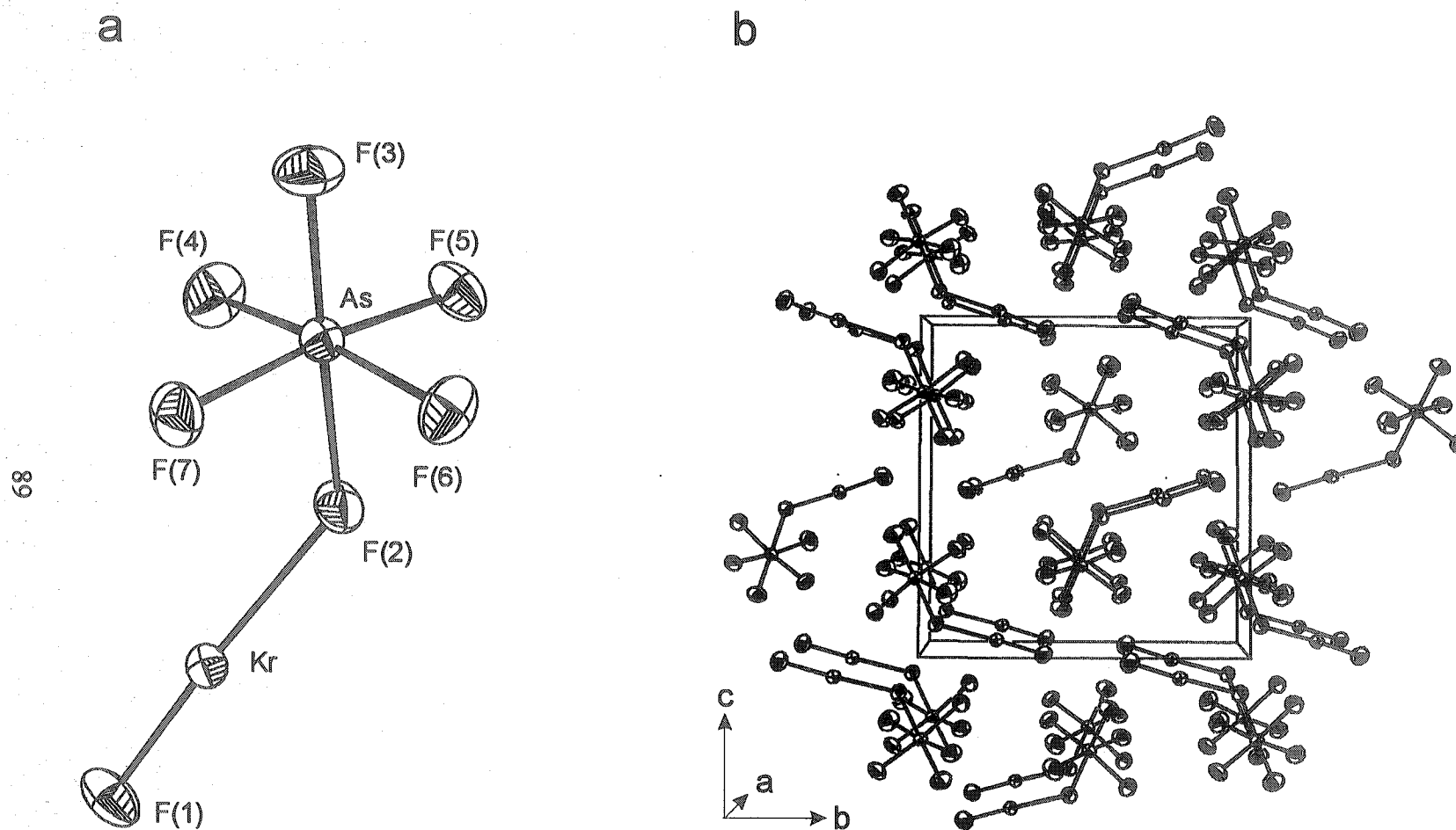
Figure 3.2. The X-ray crystal structure of (a) β-[KrF][AsF$_6$] at -120 °C and (b) its packing diagram viewed along the *a*-axis. The thermal ellipsoids are shown at the 50% probability level.
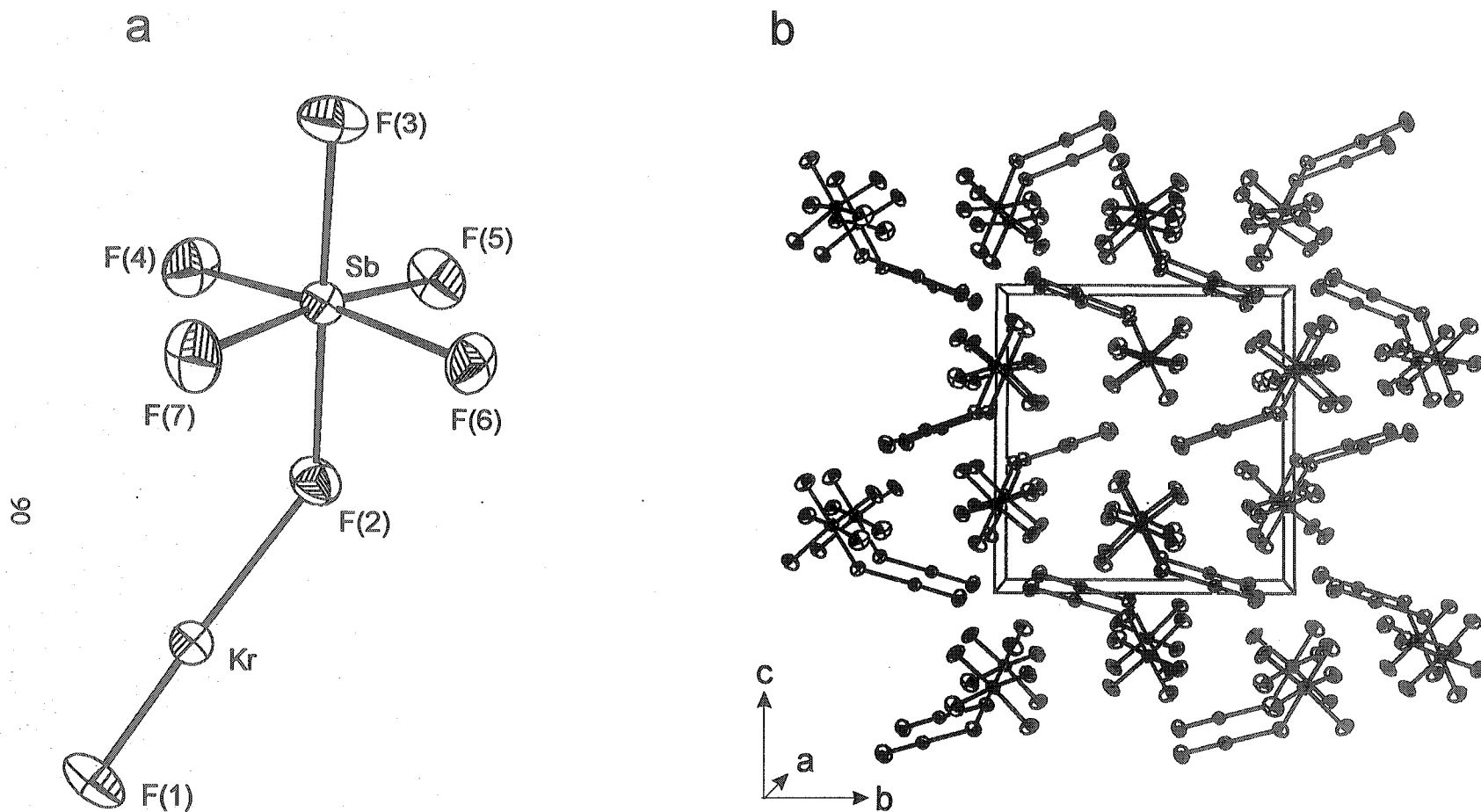
Figure 3.3. The X-ray crystal structure of (a) [KrF][SbF$_6$] at -113 °C and (b) its packing diagram viewed along the *a*-axis. The thermal ellipsoids are shown at the 50% probability level.
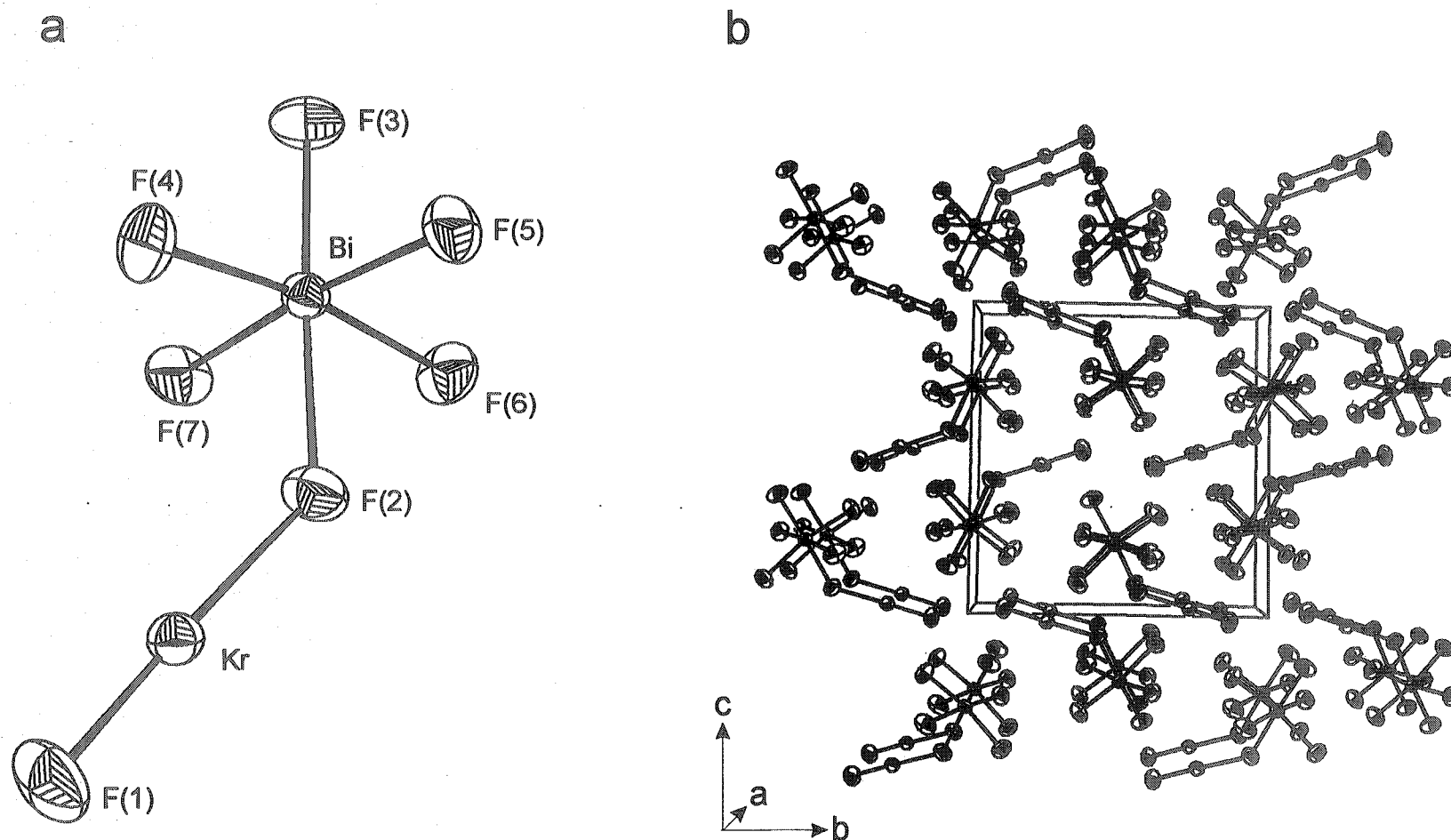
Figure 3.4. The X-ray crystal structure of (a) [KrF][BiF₆] at -130 °C and (b) its packing diagram viewed along the *a*-axis. The thermal ellipsoids are shown at the 50% probability level.

Table 3.3. Experimental (M = As, Sb, Bi) and Calculated (M = P, As, Sb, Bi) Geometric Parameters for [KrF][MF₆]

	β-[KrF][AsF₆]			[Kr₂F₃][AsF₆]·[KrF][AsF₆] [a]	[KrF][SbF₆]			[KrF][BiF₆]			[KrF][PF₆]	
	expt. LDFT	HF	LDFT	expt.	expt.	HF	LDFT	expt.	HF	LDFT	HF	
Kr-F(1)	1.765(2)	1.867	1.746	1.783(6)	1.765(3)	1.857	1.739	1.774(6)	1.859	1.745	1.877	1.789
Kr--F(2)	2.131(2)	1.998	2.002	2.106(6)	2.140(3)	2.017	2.038	2.090(6)	2.012	2.003	1.972	1.873
M--F(2)	1.845(2)	2.096	1.972	1.878(6)	1.963(3)	2.185	2.049	2.106(6)	2.266	2.194	2.176	2.493
M-F(3)	1.691(2)	1.709	1.659	1.686(6)	1.856(3)	1.898	1.813	1.944(6)	1.948	1.950	1.561	1.526
M-F(4)	1.698(2)	1.729	1.672	1.711(6)	1.847(3)	1.907	1.821	1.957(6)	1.977	1.969	1.588	1.533
M-F(5)	1.710(2)	1.752	1.700	1.684(7)	1.859(3)	1.907	1.821	1.962(6)	1.977	1.969	1.609	1.572
M-F(6)	1.703(2)	1.734	1.681	1.720(6)	1.861(3)	1.925	1.841	1.938(6)	1.957	1.958	1.592	1.556
M-F(7)	1.703(2)	1.734	1.681	1.685(7)	1.857(3)	1.925	1.841	1.941(6)	1.957	1.959	1.592	1.556
Bond Angles (deg)												
F(1)-Kr--F(2)	176.8(1)	177.7	178.3	177.3(3)	177.9(2)	177.4	178.6	177.0(4)	177.2	178.7	178.3	179.3
Kr-F(2)--M	133.7(1)	120.0	128.3	124.6(3)	139.2(2)	114.1	124.9	138.3(3)	113.8	131.2	119.1	117.2

[a] The fluorine atom labels F(4), F(5), F(6), F(7), F(8), F(9), and F(10) for the [KrF][AsF₆] unit in [Kr₂F₃][AsF₆]·[KrF][AsF₆] (see Figure 3.7) are given as F(1), F(2), F(3), F(4), F(5), F(6) and F(7), respectively, in this table.

shorter in the BiF_6^- salt (2.089(6) Å) than in the AsF_6^- and SbF_6^- analogues, suggesting BiF_5 is a weaker fluoride ion acceptor than AsF_5 and SbF_5. Comparison of the Xe--F_b bonds for β-[XeF_3][SbF_6] and [XeF_3][BiF_6] reveals the same trend.[284,285] The Kr--F_b bond lengths of the three salts are significantly less than the sum of the fluorine (1.47,[286] 1.35 Å[287]), and krypton (2.02 Å[286]) van der Waals radii and are indicative of significant covalent bond character that is also reflected in the nonlinearity of the Kr--F_b-M bridge angles (*vide infra*).

Variable temperature Raman spectroscopy has previously shown that [KrF][AsF_6] exhibits a phase transition between 25 and -78 °C. It was expected that [KrF][SbF_6] and the low-temperature β-phase of [KrF][AsF_6] would prove to be isomorphous and isostructural because their Raman spectra exhibit the same Kr-F_t stretching frequency and splitting (615, 619 cm^{-1}) and similar Kr-F_b stretching frequencies (see section 3.3.2.3).[40] The structural relationship has now been verified by the crystal structures of these compounds and their near-identical Kr-F_t and Kr--F_b bond lengths. Although significant lengthening of the Kr-F_t bond is not observed for [KrF][BiF_6], the split Kr-F_t stretching frequency is shifted to lower frequency (604, 610 cm^{-1}) and is consistent with a shortening of the Kr--F_b bond length relative to those of the arsenic and antimony analogues. The effect on the Kr--F_b stretch cannot be directly assessed for [KrF][BiF_6] because the experimental frequency of this vibration has not been reported, however, the frequency of this mode has been calculated (see section 3.3.2.3) and is predicted to have a value similar to that of [KrF][AsF_6]. The splitting of the Kr-F_t stretch in all three compounds is readily understood in terms of their crystal structures and arises from vibrational coupling among the four equivalent structural units in each of their unit cells. A factor-group analysis correlates the C_1 symmetry of the four free ion pairs to their site-symmetry, C_1. Correlation of the C_1 site-symmetry to the unit cell symmetry, C_{2h}, reveals

that each vibrational mode is split into two Raman-active components having A_g and B_g symmetries and into two infrared-active components having A_u and B_u symmetries.[288]

The F_t-Kr--F_b bond angle in the [KrF][MF_6] salts is bent slightly (176.8(1) - 177.9°) away from the anion, with these deviations from linearity also being reproduced in the calculated structures (see section 3.3.1.2). This small bend may arise as a consequence of a weak but repulsive interaction between the two lone electron pairs on F_b and the three lone electron pairs of krypton. The Kr--F_b--M bridge bond angles exhibit minor variations over the series of structures of β-[KrF][AsF_6] (133.7(1)°), [KrF][SbF_6] (139.2(2)°), and [KrF][BiF_6] (138.3(3)°), but are otherwise consistent with the bent geometry predicted for an $AXYE_2$ (A = F_b, X = Kr, Y = M) VSEPR arrangement.

The structure of the [KrF][AsF_6] ion pair in [Kr_2F_3][AsF_6]·[KrF][AsF_6] differs from that of β-[KrF][AsF_6] in that the dihedral F_e-M--F_b--Kr angle (28.1°) in the double salt is larger than that of β-[KrF][AsF_6] (22.1°) and indicates that the geometry of the ion pair is significantly influenced by the crystal packing. The Kr--F_b bond length in the double salt is significantly shorter (2.106(6) Å) than in β-[KrF][AsF_6], while the Kr-F_t bond length (1.783(6) Å) shows no significant change.

The contributions from individual contacts in the structures of [KrF][MF_6] (M = As, Sb, Bi) and [Kr_2F_3][AsF_6]·[KrF][AsF_6] are difficult to assess. Each isomorphous [KrF][MF_6] structure has eight secondary intermolecular Kr···F contacts (2.980 - 3.480 Å) that are less than or equal to the sum of the krypton and fluorine van der Waals radii, while the krypton atom of KrF^+ in [Kr_2F_3][AsF_6]·[KrF][AsF_6] has seven such contacts (3.076 - 3.489 Å). Intramolecular contacts between krypton and a non-bridging fluorine in the anion (*i.e.*, an equatorial fluorine) are only observed in [KrF][AsF_6] (3.301 Å) and [Kr_2F_3][AsF_6]·[KrF][AsF_6] (3.061, 3.449 Å). The absence of such contacts in the antimony and bismuth analogues may be attributed to their longer M-F_e bond lengths.

3.2.2.3. $[Kr_2F_3][SbF_6] \cdot KrF_2$, $[Kr_2F_3]_2[SbF_6]_2 \cdot KrF_2$ and $[Kr_2F_3][AsF_6] \cdot [KrF][AsF_6]$

The X-ray crystal structures of the title compounds along with their packing diagrams are depicted in Figures 3.5, 3.6 and 3.7, respectively. The important bond lengths and bond angles of these salts are summarized in Table 3.4, with the exception of those for the $[KrF][AsF_6]$ portion of $[Kr_2F_3][AsF_6] \cdot [KrF][AsF_6]$, which are summarized and compared with those of $[KrF][MF_6]$ (M = As, Sb, Bi) in Table 3.3.

When viewed along the a-axis, the crystal packing of $[Kr_2F_3][SbF_6] \cdot KrF_2$ consists of alternating cation and equally populated anion/KrF_2 layers (Figure 3.5b). Columns of eclipsed $Kr_2F_3^+$ cations run parallel to the a-axis, whereas the KrF_2 molecules in the anion/KrF_2 columns are off centre with respect to the anion.

The packing of $[Kr_2F_3]_2[SbF_6]_2 \cdot KrF_2$ (Figure 3.6b) is significantly more complex than that of $[Kr_2F_3][SbF_6] \cdot KrF_2$. When viewed along the c-axis, a layered structure is not evident, however, a complex system of columns can be identified. Half of the $Kr_2F_3^+$ cations form columns in which the cations eclipse one another, while the other half are shifted off center and alternate with the SbF_6^- anions of an adjacent column, which also runs parallel to the c-axis. The remaining anions and KrF_2 molecules are arranged in columns in which the KrF_2 molecules are off centre with respect to the anion, similar to that observed in $[Kr_2F_3][SbF_6] \cdot KrF_2$. The view along the a-axis, is similar to that observed along the c-axis.

Of the solid-state structures investigated in this study, only $[Kr_2F_3][AsF_6] \cdot [KrF][AsF_6]$ exhibited crystal twinning. The twinning is not surprising in light of the near-orthorhombic unit cell ($\beta = 90.304(6)°$), which can allow a 90° reorientation of the crystal growth along the b-axis. The refined structure has a 0.489:0.511 population ratio for the two orientations. When viewed along the a-axis, distinct columns of $Kr_2F_3^+$ cations, AsF_6^- anions and $[KrF][AsF_6]$ ion pairs are observed (Figure 3.7b).

a
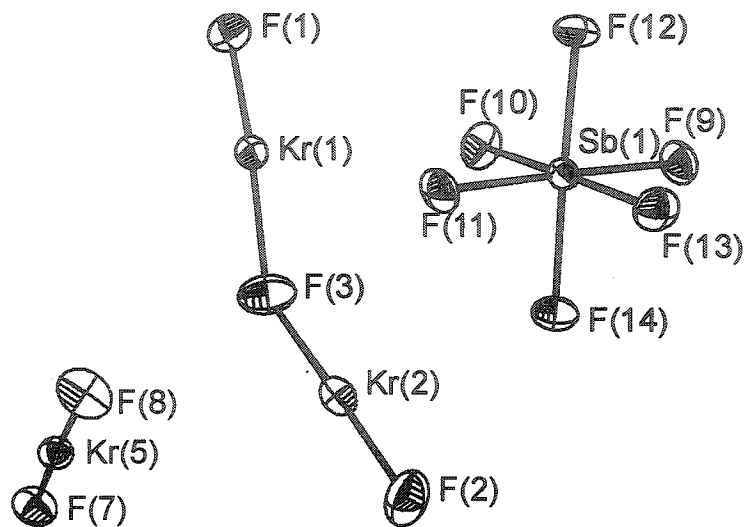
b
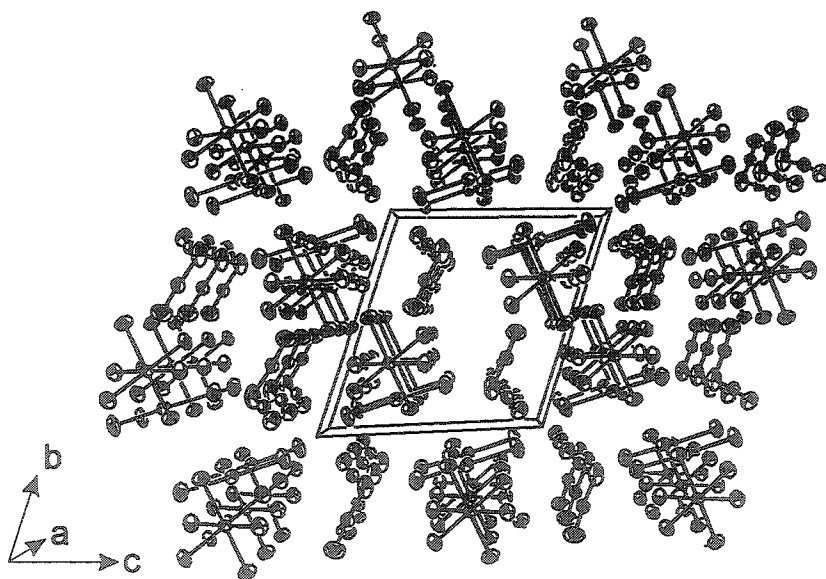
Figure 3.5. The X-ray crystal structure of (a) [Kr$_2$F$_3$][SbF$_6$]·KrF$_2$ at -113 °C and (b) its packing diagram viewed along the a-axis. The thermal ellipsoids are shown at the 50% probability level.

a
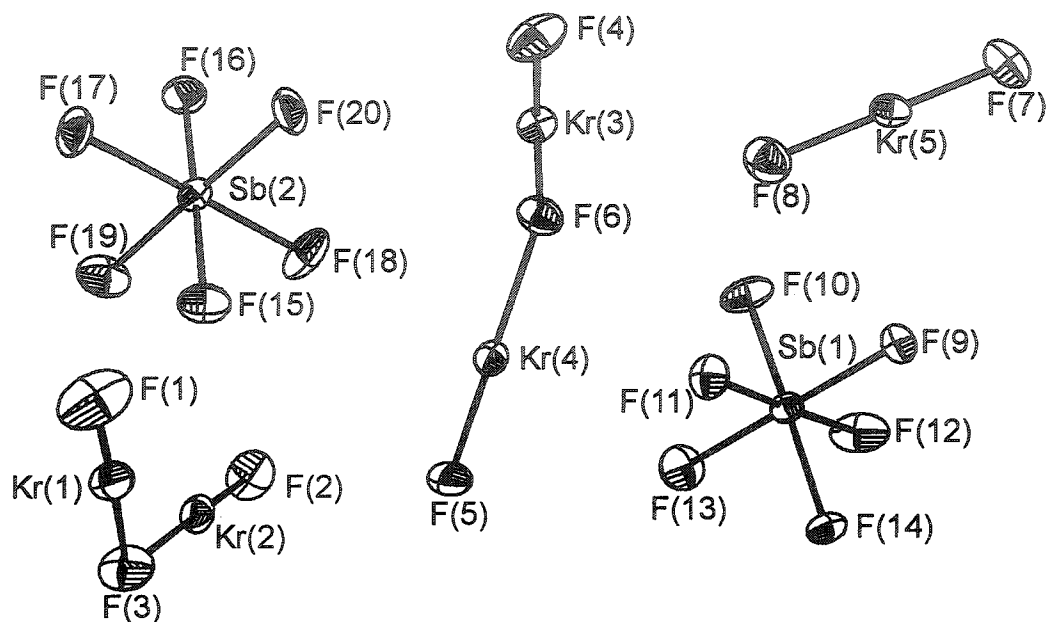
b
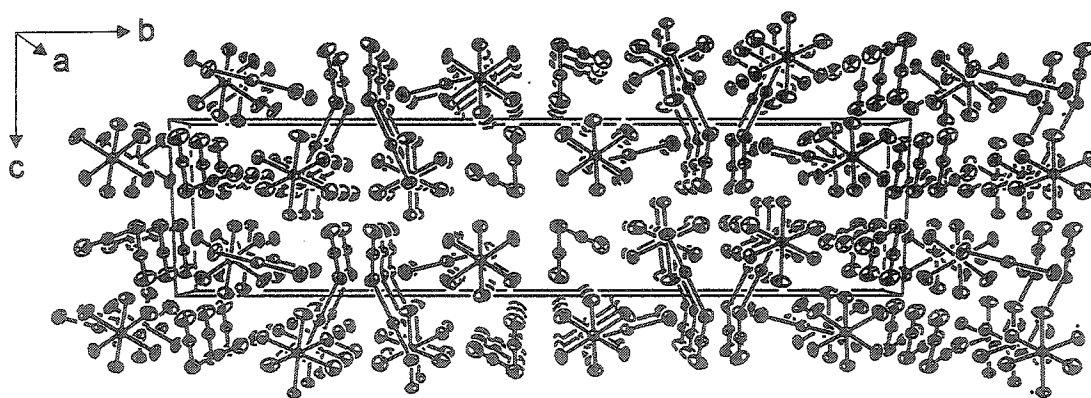
Figure 3.6. The X-ray crystal structure of (a) $[Kr_2F_3]_2[SbF_6]_2 \cdot KrF_2$ at -125 °C and (b) its packing diagram viewed along the a-axis. The thermal ellipsoids are shown at the 50% probability level.

a

b
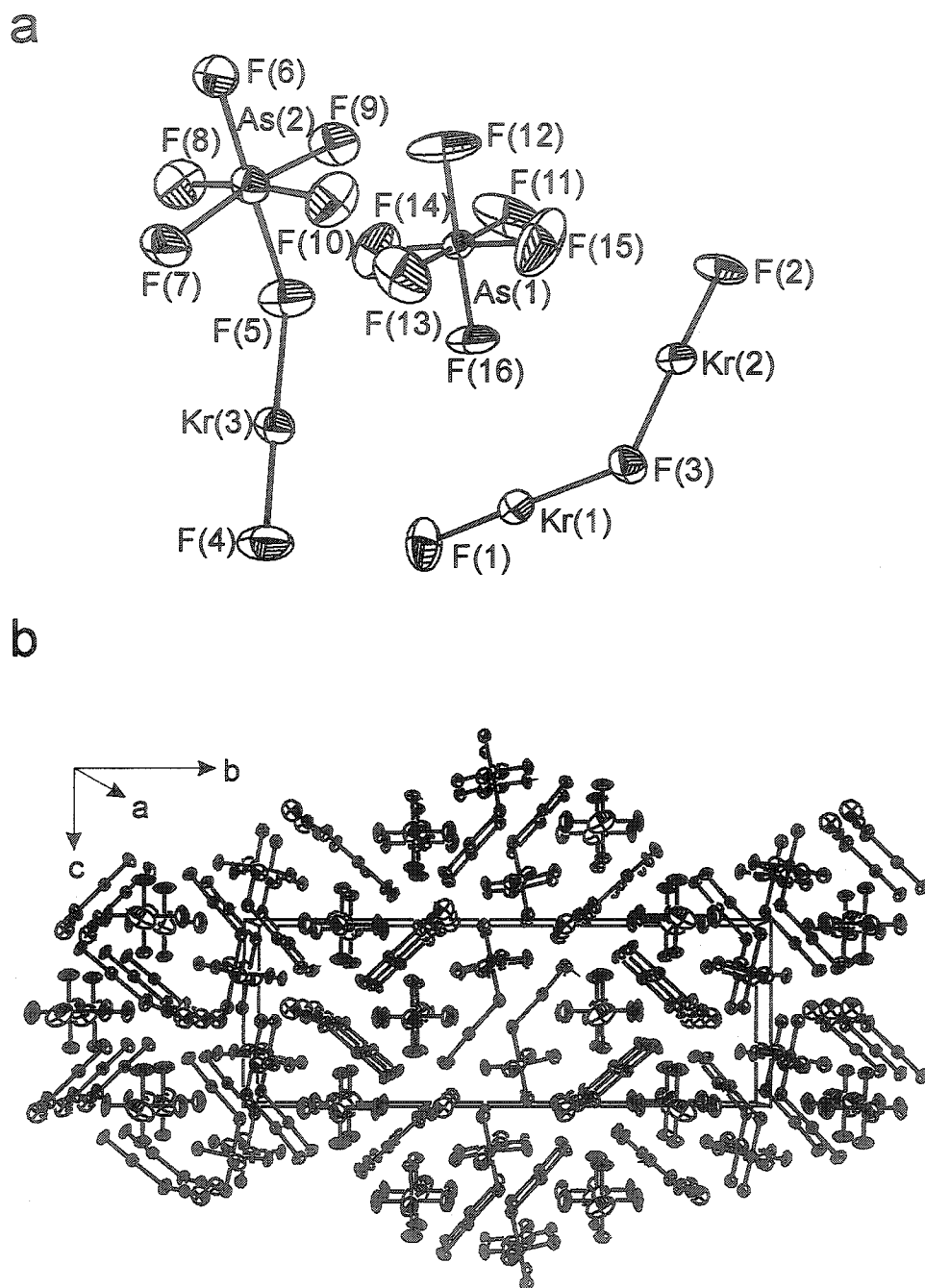
Figure 3.7. The X-ray crystal structure of (a) [Kr$_2$F$_3$][AsF$_6$]·[KrF][AsF$_6$] at -120 °C and (b) its packing diagram viewed along the a-axis. The thermal ellipsoids are shown at the 50% probability level.

Table 3.4. Experimental Bond Lengths and Bond Angles for $[Kr_2F_3][SbF_6]\cdot KrF_2$, $[Kr_2F_3]_2[SbF_6]_2\cdot KrF_2$ and $[Kr_2F_3][AsF_6]\cdot[KrF][AsF_6]$[a]

	$[Kr_2F_3]_2[SbF_6]_2\cdot$ KrF$_2$	$[Kr_2F_3][SbF_6]\cdot$ KrF$_2$	$[Kr_2F_3][AsF_6]\cdot$ [KrF][AsF$_6$]	LDFT (C_{2v})	HF ($D_{\infty h}$)
Bond Lengths (Å)					
Kr(1)-F(1)	1.805(5)	1.800(5)	1.780(7)	1.826	1.730
Kr(2)-F(2)	1.799(4)	1.790(5)	1.803(6)	1.826	1.730
Kr(1)--F(3)	2.041(4)	2.027(5)	2.061(6)	2.081	2.082
Kr(2)--F(3)	2.065(4)	2.046(5)	2.049(6)	2.081	2.082
Kr(3)-F(4)	1.797(5)				
Kr(4)-F(5)	1.787(4)				
Kr(3)--F(6)	2.052(5)				
Kr(4)--F(6)	2.056(4)				
Kr(5)--F(7)	1.881(4)	1.868(4)			
Kr(5)--F(8)	1.887(4)	1.888(4)			
M-F(9)	1.872(4)	1.875(4)			
M-F(10)	1.880(4)	1.874(4)			
M-F(11)	1.876(4)	1.872(4)	1.689(7)		
M-F(12)	1.879(4)	1.861(4)	1.701(7)		
M-F(13)	1.873(4)	1.875(4)	1.719(7)		
M-F(14)	1.872(4)	1.886(4)	1.710(8)		
M-F(15)	1.882(4)		1.674(9)		
M-F(16)	1.874(4)		1.712(6)		
M-F(17)	1.882(4)				
M-F(18)	1.876(4)				
M-F(19)	1.879(4)				
M-F(20)	1.872(4)				
MF$_6$ (mean)	1.876(4)	1.874(8)	1.701(17)		
Bond Angles (°)					
F(1)-Kr(1)--F(3)	177.9(2)	175.1(2)	178.2(3)	177.4	180.0
F(2)-Kr(2)--F(3)	177.8(2)	176.8(2)	178.6(3)	177.4	180.0
F(4)-Kr(3)--F(6)	178.7(2)				
F(5)-Kr(4)--F(6)	178.3(2)				
Kr(1)--F(3)--Kr(2)	126.0(2)	142.5(3)	127.5(3)	135.2	180.0
Kr(3)--F(6)--Kr(4)	128.0(2)				
F(7)-Kr(5)-F(8)	179.1(2)	178.0(2)			

[a] The geometric parameters for the [KrF][AsF$_6$] component of $[Kr_2F_3][AsF_6]\cdot[KrF][AsF_6]$ salt are summarized in Table 3.3.

The $Kr-F_t$ bond lengths of $Kr_2F_3^+$ exhibit no crystallographically significant variations among the structures of $[Kr_2F_3][SbF_6] \cdot KrF_2$ (Figure 3.5a), $[Kr_2F_3]_2[SbF_6]_2 \cdot KrF_2$ (Figure 3.6a) and $[Kr_2F_3][AsF_6] \cdot [KrF][AsF_6]$ (Figure 3.7a), ranging from 1.780(7) to 1.805(5) Å with a mean value of 1.796(9) Å. The longer and more polar $Kr--F_b$ bonds are more sensitive to the surrounding environment and range from 2.027(5) to 2.065(4) Å with an average value of 2.048(14) Å. Long $Kr \cdots F$ interionic contacts are likely responsible for the variability of $Kr--F_b$ bond lengths and $Kr--F_b--Kr$ bond angles in the salts investigated. Half of the $Kr_2F_3^+$ cations in $[Kr_2F_3]_2[SbF_6]_2 \cdot KrF_2$ are asymmetric as a result of the small, but significant, bond length difference between $Kr(1)-F_b(3)$ (2.041(4) Å) and $Kr(2)-F_b(3)$ (2.065(4) Å). This is the first example of an asymmetric $Ng_2F_3^+$ (Ng = Kr, Xe) cation that has been documented crystallographically, although the possibility of an asymmetric $Kr_2F_3^+$ cation in $[Kr_2F_3][SbF_6]$ had been previously proposed based on Raman spectroscopic evidence.[21,40,137] In all other cases, $Ng_2F_3^+$ cations have been described as symmetric having C_{2v} symmetries.

The bent geometry of the $Kr_2F_3^+$ cation is readily explained by the VSEPR model, for which the two lone electron pairs on the bridge fluorine account for the large $Kr--F_b--Kr$ bond angle, and the three lone pairs on the krypton centres account for the near linear $F_t-Kr--F_b$ bond angles. The large variation of the $Kr--F_b--Kr$ bond angles in the structures of $[Kr_2F_3]_2[SbF_6]_2 \cdot KrF_2$ (126.0(2) - 128.0(2)°), $[Kr_2F_3][AsF_6] \cdot [KrF][AsF_6]$ (127.5(3)°) and $[Kr_2F_3][SbF_6] \cdot KrF_2$ (142.5(3)°) is attributed to long interionic/intermolecular $Kr \cdots F$ contacts[289] and to the effects of crystal packing on the highly deformable fluorine bridge. The distortion of the $F_t-Kr--F_b$ bond angle from linearity in the structures of $[Kr_2F_3]_2[SbF_6]_2 \cdot KrF_2$ (177.8(2) - 178.7(2)°), $[Kr_2F_3][SbF_6] \cdot KrF_2$ (175.1(2) - 176.8(2)°) and $[Kr_2F_3][AsF_6] \cdot [KrF][AsF_6]$ (178.2(3) - 178.6(3)°) gives the $Kr_2F_3^+$ cation a shallow W-shape. The persistence of this distortion in the calculated structure of the cation (LDF,

see section 3.3.1.3),[23] implies that it cannot be entirely attributed to interionic or intermolecular Kr···F contacts. As previously discussed for the [KrF][MF$_6$] salts (see section 3.2.2.2), the non-linear F$_t$-Kr--F$_b$ bond angles are suspected to arise from a distortion of the toroidal lone electron pair distributions on the krypton atoms by the two lone electron pairs on the adjacent bridging fluorine atom.

Unlike the KrF$_2$ molecules in α-KrF$_2$ and β-KrF$_2$, which are linear by symmetry, the KrF$_2$ molecules in [Kr$_2$F$_3$][SbF$_6$]·KrF$_2$ and [Kr$_2$F$_3$]$_2$[SbF$_6$]$_2$·KrF$_2$ are slightly bent (178.0(2) and 179.1(2)°) with Kr-F bond lengths of 1.868(4), 1.888(4) Å and 1.881(4), 1.887(4) Å, respectively. The small bond length differences and angle distortions are attributed to long Kr···F contacts[289] and to crystal packing, and do not persist in the gas-phase energy-minimized geometry. The X-ray structure determinations of [Kr$_2$F$_3$]$_2$[SbF$_6$]$_2$·KrF$_2$ and [Kr$_2$F$_3$][SbF$_6$]·KrF$_2$ confirm earlier Raman spectroscopic studies of the KrF$_2$/SbF$_5$ and KrF$_2$/AsF$_5$ systems in which an undetermined excess of KrF$_2$ was shown to associate with [Kr$_2$F$_3$][SbF$_6$][21,40,137] and [Kr$_2$F$_3$][AsF$_6$].[40,137] The symmetric stretch of the associated KrF$_2$ was shifted to higher frequency than that of free KrF$_2$ by approximately 10 cm^{-1} in these studies.

3.2.2.4. Structural Trends Among KrF$_2$, KrF$^+$ and Kr$_2$F$_3$$^+$

The experimental trends in bond lengths and bond angles among NgF$_2$, Ng$_2$F$_3$$^+$ and the [NgF][MF$_6$] ion pairs (Ng = Kr, Xe) are analogous for krypton and xenon. The Kr-F$_t$ bond exhibits a considerable variation in length among the solid-state krypton fluoride structures that are now known. The Kr-F$_t$ bonds show no crystallographically significant differences among their respective KrF$^+$ (1.765(3) - 1.783(6) Å) and Kr$_2$F$_3$$^+$ (1.780(7) - 1.805(5) Å) salts, and are shorter than those determined for KrF$_2$ (1.868(4) - 1.889(10) Å) in the solid state. This trend is consistent with the simple valence bond (Structures I - II) and 3c-4e descriptions, for which the averaged structure of "KrF$_2$" is

$$F\text{-}Kr^+ \; F^- \quad \leftrightarrow \quad F^- \; {}^+Kr\text{-}F$$

$$I \qquad\qquad\qquad II$$

predicted to have a bond order of ½, whereas the bond order for KrF^+ is 1.

The $Kr\text{-}F_t$ bond length in $Kr_2F_3^+$ is intermediate with respect to those of KrF_2 and KrF^+, and reflects the dominant roles KrF^+ and "KrF_2" play in the resonance description of $Kr_2F_3^+$ (Structures III - V). Moreover, the $Kr\text{--}F_b$ bond (2.027(5) - 2.065(4) Å), though

$$\text{"F-Kr-F"} \; {}^+Kr\text{-}F \quad \leftrightarrow \quad F\text{-}Kr^+ \; F^- \; {}^+Kr\text{-}F \quad \leftrightarrow \quad F\text{-}Kr^+ \; \text{"F-Kr-F"}$$

$$III \qquad\qquad\qquad IV \qquad\qquad\qquad V$$

significantly longer than that of KrF_2, has substantial covalent character and is approximately 1.4 Å shorter than the sum of the krypton and fluorine van der Waals radii. The covalency of the $Kr\text{--}F_b$ bond is also supported by the significantly bent $Kr\text{--}F_b\text{--}Kr$ bond angles observed for the $Kr_2F_3^+$ cation, which is consistent with the AX_2E_2 VSEPR arrangement at the fluorine bridge. The upper limit of the $Kr\text{--}F_b\text{--}Kr$ bond angle (range, 126.0(2) - 142.4(3)°) is in good agreement with the $Xe\text{--}F_b\text{--}Xe$ bond angles observed in the monoclinic (148.6(4)°) and trigonal (139.8(8)°) phases of $[Xe_2F_3][AsF_6]$, but is considerably smaller than the angle observed in $[Xe_2F_3][SbF_6]$ (160.3(3)°).[91,92] The X-ray crystal structures and energy-minimized structures derived from electronic structure calculations for the $Xe_2F_3^+$ cation[91] and the $Kr_2F_3^+$ cation in this work show that they have a shallow W-shape (see section 3.3.1.3), with the $F_t\text{-}Xe\text{--}F_b$ angles distorted from linearity by similar amounts (expt., 2.4(3)° [As] and 1.4(4)° [Sb]; calc. 2.3°) when compared with those of $Kr_2F_3^+$ (expt. 3.2(1) - 2.1(2)°; calc. 2.6°).

Although the crystal structures of $[XeF][AsF_6]$,[73] $[XeF][Sb_2F_{11}]$,[71] and $[XeF][RuF_6]$[72] have been previously reported, the uncertainties in the $Xe\text{-}F_t$ and $Xe\text{--}F_b$ bond lengths for the $Sb_2F_{11}^-$ and RuF_6^- salts were relatively large (0.03 and 0.02 Å, respectively) and do not permit meaningful bond length comparisons to be made. To

remedy this problem the crystal structures of the [XeF][MF$_6$] (M = As, Sb, Bi) and [XeF][M$_2$F$_{11}$] (M = Sb, Bi) salts have been determined with greater precision and at low temperature (see section 5.2.2). In contrast to the [KrF][MF$_6$] salts, in which no significant variations of the Kr-F$_t$ bond length were observed, the Xe-F$_t$ bond length of [XeF][BiF$_6$] (1.913(7) Å) is significantly longer than those of [XeF][AsF$_6$] (1.888(3) Å) and [XeF][SbF$_6$] (1.885(2) Å) which are similar. Interestingly, the Xe-F$_t$ bond lengths of the [XeF][M$_2$F$_{11}$] (Sb, 1.884(4); Bi, 1.909(6) Å) salts are comparable to those of their MF$_6^-$ analogues, with the Bi$_2$F$_{11}^-$ salt again exhibiting a longer bond length than its antimony counterpart. In contrast to the krypton salts where the Xe--F$_b$ bond length is comparable in the AsF$_6^-$ (2.131(2) Å) and SbF$_6^-$ (2.140(3) Å) salts, but shorter in the BiF$_6^-$ (2.090(6) Å) salt, the xenon series exhibits comparable Xe--F$_b$ bond lengths for the AsF$_6^-$ (2.208(3) Å) and BiF$_6^-$ (2.204(7) Å) salts but a longer bond for the SbF$_6^-$ (2.278(2) Å) salt. The trends observed for the [XeF][MF$_6$] salts are in better agreement with the stronger Lewis acidity of SbF$_5$ when compared with AsF$_5$ and BiF$_5$, and are also reflected in the M$_2$F$_{11}^-$ salts where the Xe--F$_b$ bond length of [XeF][Sb$_2$F$_{11}$] (2.343(4) Å) is longer than that of [XeF][Bi$_2$F$_{11}$] (2.253(5) Å). As noted for the [KrF][MF$_6$] salts, the [XeF][MF$_6$] and [XeF][M$_2$F$_{11}$] salts exhibit minor distortions of their F$_t$-Xe--F$_b$ bond angles from linearity (177.94(9) - 179.3(2)°), which further supports the postulate that these bends result from asymmetric bonding to the xenon atom and are not simply solid state effects. The Xe--F$_b$--M bond angles [XeF][AsF$_6$] (133.6(2)°) and [XeF][SbF$_6$] (136.9(1)°) are within 2.3° of their krypton analogues, however, this bond angle is significantly larger in [XeF][BiF$_6$] (156.1(4)°) than it is in [KrF][BiF$_6$] (138.3(3)°). Although the larger Xe--F$_b$--M bond angle in [XeF][BiF$_6$] could result from its electronic structure, a similar variation is noted among the Kr--F$_b$--As bond angles of [KrF][AsF$_6$]

(133.7°) and $[Kr_2F_3][AsF_6]\cdot[KrF][AsF_6]$ (124.6°), suggesting this bond angle is highly deformable and is easily distorted by solid state packing effects.

3.2.3. Characterization of $[Kr_2F_3][PF_6]\cdot nKrF_2$ by Raman Spectroscopy

Neither $[KrF][PF_6]$ and $[Kr_2F_3][PF_6]$ nor their xenon(II) analogues have been reported previously. Attempts, in the present work, to synthesize $[KrF][PF_6]$ or $[Kr_2F_3][PF_6]$ by reaction of KrF_2 with excess PF_5 in anhydrous HF solvent at -78 °C were unsuccessful. The reaction of KrF_2 with liquid PF_5 at -78 °C, however, yielded $[Kr_2F_3][PF_6]\cdot nKrF_2$, where n is unspecified. The complete conversion to $[Kr_2F_3][PF_6]\cdot nKrF_2$ required nearly two months and was deemed complete upon the disappearance of the intense $v_1(\Sigma^+_g)$ vibrational mode of free KrF_2 at 465.5 cm^{-1} (α-phase) or 468.6 and 469.5 cm^{-1} (β-phase) in the Raman spectrum, during which time, modes consistent with $Kr_2F_3^+$ and PF_6^- grew in. Further addition of fresh aliquots of PF_5 to $[Kr_2F_3][PF_6]\cdot nKrF_2$ did not result in $[KrF][PF_6]$ formation or any further changes in the Raman spectrum over an period of two months at -78 °C. The $[Kr_2F_3][PF_6]\cdot nKrF_2$ adduct was isolated at -78 °C as a white solid under 1000 Torr of PF_5(g), but dissociated to KrF_2 and PF_5 under reduced PF_5 pressures at this temperature.

The Raman spectrum of $[Kr_2F_3][PF_6]\cdot nKrF_2$ (Figure 3.8) was acquired under 1000 Torr of PF_5 at -80 °C after seven weeks contact between KrF_2 and PF_5 at -78 °C and closely resembles the spectra of the $[Kr_2F_3][MF_6]\cdot nKrF_2$ (M = As, Sb) salts (Table 3.5). Consequently, the assignments of the $Kr_2F_3^+$ cation for $[Kr_2F_3][PF_6]\cdot nKrF_2$ were initially based on those of the AsF_6^- and SbF_6^- analogues and were refined with the aid of theoretical calculations (see section 3.3.2.2). The PF_6^- anion was identified by the $v_1(A_{1g})$ (748 cm^{-1}), $v_2(E_g)$ (572, 581 cm^{-1}) and $v_5(F_{2g})$ (464, 469, 475 cm^{-1}) bands, which are consistent with an octahedral anion, for which site-symmetry lowering apparently results in removal of the degeneracies of the E_g and F_{2g} modes.[290] The intense bands at 555 and

Figure 3.8. Raman spectrum of powdered $[Kr_2F_3][PF_6]\cdot nKrF_2$, where n is unspecified, recorded at -80 °C using 514.5 nm excitation. Peaks arising from the FEP sample tube are denoted by asterisks (*), while that resulting from residual PF_5 is denoted by a dagger (†).

Table 3.5. Experimental Raman and Calculated Vibrational Frequencies, Assignments and Mode Descriptions for $Kr_2F_3^+$

$[Kr_2F_3][AsF_6]^{a,b}$	$[Kr_2F_3][SbF_6]^{a,b}$	$[Kr_2F_3][PF_6]\cdot nKrF_2^{b,c}$	$[Kr_2F_3][AsF_6]\cdot nKrF_2^{a,b}$	$[Kr_2F_3][SbF_6]\cdot nKrF_2^{a,b}$	$LDFT^d$	Assignments for $Kr_2F_3^+$ under C_{2v} symmetry^e
610(43)		605(100)	602(100)	599(100)	628[12]	$\nu_1(A_1)$ $\nu(KrF_t + KrF_t)$
600(80)	603(100)					
594(100)	594(89)					
570(4)	555(34)	555(52)	575(23)	557(50)	608[273]	$\nu_6(B_1)$ $\nu(KrF_t - KrF_t)$
567(31)			553(50)			
437(sh)	456(4)	462(11)	462	466(60)	441[212]	$\nu_7(B_1)$ $\nu_{as}(KrF_b)$
336(17)	330(18)	358(19)	355(19)	340(14)	313[11]	$\nu_2(A_1)$ $\nu_s(KrF_b)$
183(15)	186(16)	191(11)	190(10)	200(2)	196[14]	$\nu_9(B_2)$ $\delta(F_t\text{-}Kr\text{--}F_b)$ o.o.p. antisym. comb.
174(13)	180(sh)	185(7)	184(sh)	188(10)	168[1]	$\nu_3(A_1)$ $\delta_s(F_t\text{-}Kr\text{--}F_b)$ i.p. sym. comb.
158(2)	176(sh)	176(5)	177(sh)	122(46)	159[0]	$\nu_5(A_2)$ $\delta(F_t\text{-}Kr\text{--}F_b)$ o.o.p. sym. comb.
					155[0]	$\nu_8(B_1)$ $\delta(F_t\text{-}Kr\text{--}F_b)$ i.p. antisym. comb.
					41[0]	$\nu_4(A_1)$ $\delta(Kr\text{--}F_b\text{--}Kr)$ bend

[a] From ref 40. [b] Values in parentheses denote relative Raman intensities. [c] Frequencies observed for PF_6^-: 748(7), $\nu_1(A_{1g})$; 581(7) and 572(13), $\nu_2(A_{1g})$; 475(12), 469(35), and 464(11), $\nu_5(F_{2g})$. Spectrum recorded on a powder in a ¼-in. FEP sample tube at -80 °C using 514.5 nm excitation. Values in parentheses denote relative Raman intensities. Additional weak bands observed at 1859(0.20) at 1863(0.15) cm^{-1} are assigned to O_2^+. [d] Infrared intensities in $km \cdot mol^{-1}$, are given in brackets. The abbreviations o.o.p. and i.p. denote out-of-plane and in-plane bends, respectively.

605 cm^{-1}, are assigned under C_{2v} symmetry, to the asymmetric and symmetric Kr-F$_t$ stretches, $v_6(B_1)$ and $v_1(A_1)$, respectively, of the Kr$_2$F$_3$$^+$ cation. It is noteworthy that, like [Kr$_2$F$_3$][AsF$_6$]·nKrF$_2$ and [Kr$_2$F$_3$][SbF$_6$]·nKrF$_2$, the 605 cm^{-1} band is not factor-group split, but is split in [Kr$_2$F$_3$][AsF$_6$] and [Kr$_2$F$_3$][SbF$_6$]. The weak band at 358 cm^{-1} is assigned to $v_2(A_1)$, the symmetric Kr--F$_b$--Kr stretch, and the coupled in-plane and out-of-plane bends associated with the F$_t$-Kr--F$_b$ groups are assigned to medium intensity bands at 191 ($v_9(B_2)$), 185 ($v_3(A_1)$) and 176 cm^{-1} ($v_5(A_2)$). The aforementioned show negligible dependence on the counter anion, which is also true for the AsF$_6$$^-$ and SbF$_6$$^-$ salts,[40,137] and is consistent with a Kr$_2$F$_3$$^+$ cation that interacts weakly with the PF$_6$$^-$ anion. The Raman spectrum (Figure 3.8) also revealed a trace impurity in the sample, which exhibits weak vibrational frequencies at 1859 and 1863 cm^{-1}. The bands are assigned to the O$_2$$^+$ cation and are in good agreement with the O$_2$$^+$ frequencies observed for [O$_2$][MF$_6$] (M = As, Sb, Bi, Ru, Rh, Pd, Pt, Au).[230] The [O$_2$][PF$_6$] contaminant arises from the oxidation of trace amounts of H$_2$O and/or O$_2$ by Kr$_2$F$_3$$^+$. The splitting of the O$_2$$^+$ band is likely attributable to a mixture of α- and β-[O$_2$][PF$_6$], which apparently coexist near the phase transition temperature as noted for [O$_2$][AsF$_6$][291,292] and [O$_2$][AuF$_6$] (see section 4.2.3).[130]

3.3. Computational Results

Dixon *et al* have previously used *ab initio* calculations at the HF level of theory to investigate the structures and electronic structures of Xe$_2$F$_3$$^+$ and the isoelectronic analogue, XeIF$_3$.[277] In these studies the HF method predicted a linear geometry for Xe$_2$F$_3$$^+$, contrasting with the bent geometries obtained by single crystal X-ray diffraction. The LDF method has recently been used to calculate the energy minimized geometry of Xe$_2$F$_3$$^{+,91}$ and was shown to reproduce the highly distortable Xe--F$_b$--Xe bond angle with reasonable accuracy (LDF, 146.9°; expt., 139.8(8) - 160.3(3)°[91,92]).

In a recent collaboration with Dr. David Dixon (Pacific Northwest National Laboratory), the energy-minimized geometries, vibrational frequencies and, atomic charges, Mayer bond orders and Mayer valencies of KrF_2, KrF^+, $Kr_2F_3^+$ and the [KrF][MF_6] (M = P, As, Sb, Bi) ion pairs have been calculated at the HF and LDF methods to assist in the description of these species.[23] The results of this collaborative work are summarized in sections 3.3.1 through 3.3.3.3.

3.3.1. Geometries

3.3.1.1. KrF_2

The calculated geometries of KrF_2 (Table 3.2) are linear with Kr-F bond lengths of 1.822 (HF) and 1.910 Å (LDF), with the LDF method providing better agreement with the experimental values.

3.3.1.2. KrF^+ and [KrF][MF_6]

Two conformers having C_s point symmetry are found for the energy minimized gas phase structures of the [KrF][MF_6] ion pairs (Table 3.3). The structures calculated for [KrF][PF_6] and [KrF][AsF_6] have the F_t-Kr-F_b moiety in an MF_3 plane (Structure VI)

VI   VII
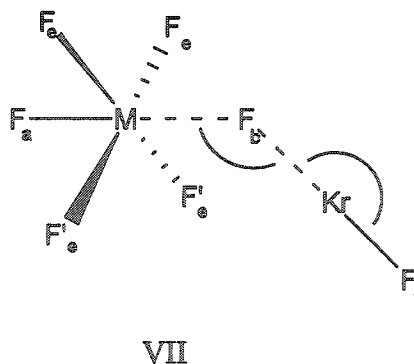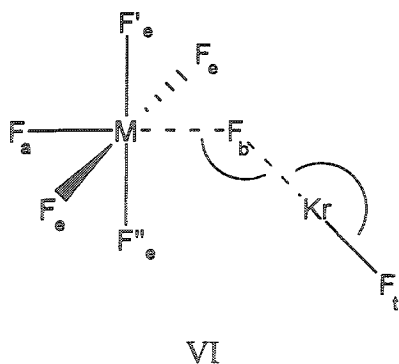
whereas for [KrF][SbF_6] and [KrF][BiF_6], the F_t-Kr-F_b moiety is rotated by 45° so that it is staggered and lying in the mirror plane that bisects the angle subtended by two equatorial fluorine atoms of the axially distorted MF_6^- anion (Structure VII). In contrast,

this angle ranges from 19.7 to 28.1° in the experimental structures and, consequently, their differences from the calculated values are attributed to crystal packing.

The bond length of free KrF^+ was calculated to be 1.780 Å (LDF) and 1.717 Å (HF). Very little variation of the $Kr-F_t$ bond length was observed among the $[KrF][MF_6]$ (M = P, As, Sb, Bi) ion pairs with the LDF method. This contrasts with the HF calculations, where the $Kr-F_t$ bond lengths for $[KrF][AsF_6]$ (1.746 Å), $[KrF][SbF_6]$ (1.739 Å), and $[KrF][BiF_6]$ (1.739 Å) were similar, but were significantly shorter than the $Kr-F_t$ bond length determined for $[KrF][PF_6]$ (1.789 Å). Surprisingly, the experimental $Kr-F_t$ bond lengths are most accurately approximated by the bond length of free KrF^+, which is overestimated by roughly the same amount (*ca.* 0.01 Å) as those calculated for KrF_2 and the $Kr-F_t$ bond lengths of $Kr_2F_3^+$ using LDF. It should be noted that the LDF $Kr-F_t$ bond lengths for the ion pairs are longer than the bond length of free KrF^+ by approximately 0.09 Å, and are also predicted to be longer than the $Kr-F_t$ bond lengths of $Kr_2F_3^+$.

The LDF method predicts that the KrF_2 interaction with the weak fluoride ion acceptor, PF_5, is better described as a $KrF_2 \cdot PF_5$ adduct than as an ionic complex, $[KrF][PF_6]$. The KrF_2 moiety is asymmetric, having a $Kr--F_b$ bond length of 1.972 Å and a $Kr-F_t$ bond length of 1.877 Å. The $Kr--F_b$ bond is 0.06 Å longer and the $Kr-F_t$ bond is 0.03 Å shorter than the calculated bond distance in KrF_2, while $Kr-F_t$ in $KrF_2 \cdot PF_5$ is 0.10 Å longer than the bond in free KrF^+. The $P--F_b$ bond distance of 2.176 Å is lengthened by 36% when compared with the average bond length of the equatorial P-F bonds (1.595(9) Å). The $M--F_b$ bridge distances for the heavier pnicogens in $[KrF][MF_6]$ are 2.096 (As), 2.185 (Sb) and 2.266 (Bi) Å and the $Kr--F_b$ bridge bond distances are 1.998 (As), 2.017 (Sb), and 2.012 (Bi) Å with moderately shorter terminal $Kr-F_t$ bond distances of 1.867 (As), 1.857 (Sb), and 1.859 (Bi) Å. As noted for the experimental structures, a clear correlation between the Lewis acidity of the $Kr-F_t$ bond lengths and the Lewis

acidity of the parent pentafluorides is also not apparent from the calculated geometries. The calculated $M-F_b$ distances are 21 (As), 14 (Sb), and 15% (Bi) longer than the average of the equatorial M-F bond lengths; 1.737(10) (As), 1.916(10) (Sb), and 1.967(12) (Bi) Å. The comparison of the $M-F_b$ and $M-F_e$ bond lengths is particularly noteworthy for the PF_6^- and AsF_6^- ion pairs, for which the degree of fluoride ion transfer from KrF_2 to the strong fluoride ion acceptor, AsF_5, is considerably greater than that for PF_5. The $M-F_b$ interactions and degrees of F^- transfer are greatest for SbF_5 and BiF_5, where the $M-F_b$ bond lengths are approximately 15% longer than the average equatorial M-F bond length. This trend is consistent with the fluoride ion affinities of the parent MF_5 molecules, which have most recently been calculated to increase in the order $PF_5 <$ $AsF_5 < BiF_5 < SbF_5$ (Table 1.2).[48] The calculated structures contrast to the experimental results for which the $M-F_b$ bond lengths are only 8 (As), 6 (Sb) and 8% (Bi) longer than the $M-F_e$ bond lengths and indicate a greater degree of fluoride ion transfer from KrF_2 to MF_5. The F_t-Kr-F_b angles in the [KrF][MF_6] ion pairs are calculated to be slightly distorted from linearity (177.2 - 178.3°), with similar distortions being observed in the experimental structures (As, 176.8(1); Sb, 177.9(2); Bi, 177.0(4)°). The $Kr-F_b-M$ angles (113.8 - 120.0°) are calculated to be considerably more closed than in the experimental structures (As, 133.7(1); Sb, 139.2(2); Bi, 138.3(3)°) where the similar but larger bond angles are likely a consequence of the isomorphous packing arrangements. The significance of the solid-state packing effects on the bond angle is supported by the observation that the $Kr-F_b-As$ angle (124.6(3)°) in the [KrF][AsF_6] portion of [Kr_2F_3][AsF_6]·[KrF][AsF_6], is considerably more closed than in β-[KrF][AsF_6] and in better agreement with the theoretical value. The deformability of this angle is not surprising considering the low frequencies calculated for the $Kr-F_b-M$ bending modes (73 - 80 cm^{-1}; see section 3.3.2.3).

3.3.1.3. $Kr_2F_3^+$

As previously determined for $Xe_2F_3^+$,[91] the LDF method predicts a bent structure for $Kr_2F_3^+$, in agreement with experiment, whereas the HF method predicts a linear geometry (Table 3.4). As expected from the bond lengths determined for KrF_2 (*vide supra*), the $Kr-F_t$ bond length is slightly overestimated (*ca.* 0.03 Å) by the LDF method and overestimated by a greater amount (*ca.* 0.07 Å) by the HF method. This is in contrast to the $Kr--F_b$ bond lengths, for which the values determined by the LDF (2.081 Å) and HF (2.082 Å) methods were similar to each other but 0.02 to 0.05 Å longer than those observed experimentally.

The LDF method predicts $F_t-Kr--F_b$ and $Kr--F_b--Kr$ bond angles of 177.4 and 135.2°, respectively, which lie within the experimental bond angle ranges of 175.1(2) - 178.6(3) and 126.0(2) - 142.4(3)°, and is in contrast to the completely linear geometry predicted by the HF method. The persistence of bent $F_t-Kr--F_b$ and $Kr--F_b--Kr$ bond angles in the LDF structure implies that they are intrinsic to the cation and do not arise as a consequence of solid-state packing effects. Although the non-linear $F_t-Kr--F_b$ bond angle, which give rise to a shallow W-shaped geometry, is hypothesized to arise as a consequence of the interaction between the lone electron pairs associated with the krypton and bridging fluorine atoms, the low $F_t-Kr--F_b$ bending frequencies calculated for $Kr_2F_3^+$ (155 - 168 cm^{-1}) suggest that these interactions are weak.

3.3.2. Vibrational Frequencies

The vibrational frequencies of KrF_2, KrF^+, $Kr_2F_3^+$, and the $[KrF][MF_6]$ ion pairs have been calculated by use of the HF and LDF methods. Comparison of the two methods reveals that the vibrational frequencies predicted by the LDF method are more accurate than those predicted by the HF method. The HF method overestimated the vibrational frequencies by 12 to 143 cm^{-1}, in accord with the shorter bond lengths

predicted by this method. Moreover, the geometry of $Kr_2F_3^+$ calculated at the HF level is linear, and not bent as predicted by the LDF method and observed experimentally. Despite the significant difference in the LDF and HF bond lengths and bond angles, the frequency orderings are essentially identical using both methods. Only the vibrational frequencies predicted by LDF method are compared in the ensuing discussion.

3.3.2.1. KrF_2 and KrF^+

The LDF method predicts the vibrational modes of KrF_2 to occur at $\nu_1(\Sigma_u^+)$ 623, $\nu_2(\Sigma_g^+)$ 504 and $\nu_3(\Pi_u)$ 228 cm^{-1}, which are in good agreement with the experimental values (596/580, 449 and 233 cm^{-1}).[120] The stretching frequency of the free KrF^+ cation is calculated to be 686 cm^{-1} and is significantly higher than the symmetric stretching frequency of KrF_2. The difference is consistent with the 2c-2e and 3c-4e bonding descriptions of KrF^+ and KrF_2 and their valence bond descriptions (Structures I - II), which lead to formal bond orders of 1 and ½, respectively. The experimental Kr-F stretching frequencies for the KrF^+ salts considered in the present work range from 607 to 619 cm^{-1}. The high value of the calculated stretching frequency of the free KrF^+ cation relative to those observed and calculated (see section 3.3.2.3) for the $[KrF][MF_6]$ (M = As, Sb, Bi) salts is consistent with a significant fluorine bridge interaction between the cation and anion, which leads to longer and less ionic $Kr-F_t$ bonds in the ion pairs.

3.3.2.2. $Kr_2F_3^+$

The symmetric and asymmetric $Kr-F_t$ stretching frequencies of $Kr_2F_3^+$ (Table 3.5) are also significantly lower than those of free KrF^+ and are in accord with significant bonding interactions between the terminal KrF^+ cations and the bridging F^- anion described in Structure IV. The calculated values are in reasonable agreement with the experimental frequencies, and allow for the assignment of the vibrational modes of $Kr_2F_3^+$. With the exception of the $\nu_1(A_1)$ and $\nu_6(B_1)$ stretches, whose assignments have

been reversed on the basis of the calculated frequencies, the present assignments are in accord with those made previously from the experimental spectra. The $v_4(A_1)$ and $v_8(B_1)$ bending modes, which have not been observed experimentally, are predicted to occur at 41 and 155 cm^{-1}, respectively. The low frequency of $v_4(A_1)$, which is assigned to the symmetric Kr--F_b--Kr bending mode, is consistent with the deformability of the $Kr_2F_3^+$ cation about this bond angle. Similar deformabilities have been noted for the Xe--F_b--Xe angles in several $Xe_2F_3^+$ salts when compared with their calculated values.[91,92]

3.3.2.3. [KrF][MF₆]

A difficulty arises when assigning the vibrational spectra of fluoride and oxide fluoride complexes with strong pentafluoride acceptors. In the idealized case of complete fluoride ion transfer, an octahedral MF_6^- anion results, and only the Raman-active $v_1(A_{1g})$, $v_2(E_g)$ and $v_5(F_{2g})$ modes and the infrared-active $v_3(F_{1u})$ and $v_4(F_{1u})$ modes are observed in addition to $v(Kr-F)$ of the cation. Because complete fluoride ion transfer is never achieved in the solid state, except when the cation is coordinatively saturated as in $Kr_2F_3^+$ salts, the anion symmetry is primarily distorted by the elongation of M--F_b bond. Consequently, the bridging interaction lowers symmetry of the anion and results in the observation of additional bands in the vibrational spectra. The symmetry of the anion is often approximated as C_{4v}[2135,40,41,69,248] and the vibrational spectra are assigned under this or a lower point symmetry such as C_s symmetry[69] to allow for the bent nature of the E--F_b--M bridge (where E is the central atom of the cation). Along with the tentative assignments and approximate mode descriptions for the fluorine bridged anion, previous attempts have been made to assign the vibrational modes associated with the E--F_b--M bridge.[35,40,137,248] In the present work, the mode descriptions and the frequency assignments derived from LDF and HF calculations for the fluorine bridged [KrF][MF₆] ion pairs are given in Tables 3.6, 3.7, 3.8 and 3.9 for M = P, As, Sb, and Bi, respectively).

Table 3.6. Calculated Vibrational Frequencies, Assignments and Mode Descriptions for [KrF][PF₆]

LDF[a]	HF[a]	Assignments for [KrF][PF$_6$] under C_s Symmetry[b]	
951(358)	1085(437)	A"	$\nu_{as}(PF_{2e})$
937(305)	1071(413)	A'	$\nu(PF'_e)$
917(375)	1052(382)	A'	$\nu(PF_a)$
735(8)	859(8)	A'	$\nu_s(PF_5)$
616(71)	694(5)	A'	$\nu_s(PF_{2e}) - \nu_s(PF'_e) - \nu_s(PF''_e) + \nu(KrF_t)$
613(100)	676(250)	A'	$\nu_s(PF_{2e}) - \nu_s(PF'_e) - \nu_s(PF''_e) - \nu(KrF_t)$
515(32)	598(109)	A'	$\delta(PF_{2e}) + \delta(F_aPF'_e - F_aPF''_e)$
511(38)	592(57)	A"	$\delta(F'_ePF''_e) + \delta(F_aPF_e - F_aPF_e)$
499(1)	587(5)	A"	$\delta(F''_ePF_e) + \delta(F'_ePF_e)$
497(21)	580(27)	A'	$\delta(PF_{2e}) + \delta(PF'_eF''_e)$ o.o.p. + $\nu_s(KrF_2)$
436(113)	505(283)	A'	$\nu(KrF''_e) + \nu(KrF_b) + \delta(PF_{2e}F'_eF''_e)$ o.o.p.
358(0)	402(6)	A"	$\delta(F_ePF_a) - \delta(F_aPF_e) + \delta(F_ePF_b) - \delta(F_ePF_b)$
341(20)	387(0)	A'	$\delta(F_aPF''_e)$ i.p. - $\delta(F_aPF'_e)$ i.p.
278(117)	312(83)	A'	$\nu(KrF_b) + \delta(F_tKrF_b)$ i.p.
247(6)	304(20)	A"	$\delta(F_tKrF_b)$ o.o.p.
190(0)	149(0)	A'	$\delta(F'_ePF''_e)$ i.p. - $\delta(F_ePF_e)$ along F_a-P-F_b
164(3)	145(5)	A"	$\delta(F_tKrF''_e)$ o.o.p. + torsion about PF''_e
155(6)	112(5)	A'	$\delta(F'_ePF''_e) - \delta(F_tKrF''_e)$ i.p.
127(17)	75(10)	A'	$\nu(P-F_b)$
81(0)	52(3)	A'	$\delta(PF_bKr) + \nu(KrF''_e)$
23(0)	10i(0)	A"	Torsion of KrF$_2$ group about the P-F$_b$ bond + rock of PF$_5$ group towards KrF$_2$

[a]Infrared intensities, in km mol^{-1} are given in parentheses. [b] The atom labeling scheme is given in Structure VI; o.o.p. and i.p. denote out-of-plane and in-plane bends, respectively.

Table 3.7. Experimental Raman Frequencies and Calculated Vibrational Frequencies, Assignments, and Mode Descriptions for β-[KrF][AsF$_6$]

LDF[a]	HF[a]	Experimental[b]	Assignments for [KrF][AsF$_6$] under C_s Symmetry[c]
745(152)	824(199)		A" $\nu_{as}(AsF_{2e})$
737(129)	819(192)		A' $\nu(AsF'_e) - \nu(AsF''_e) - \nu(AsF_a)$
730(123)	813(114)	716(16)	A' $\nu(AsF'_e) - \nu(AsF''_e) + \nu(AsF_a)$
652(16)	745(57)	676(13)	A' $\nu_s(AsF_5) + $ small $\nu(AsF_a)$
611(179)	735(113)	615(100), 619(72)	A' $\nu(KrF_t)$
601(0)	650(4)		A' $\nu(AsF''_e + AsF'_e) - \nu(AsF_{2e})$
454(23)	498(128)	464(3)	A' $\nu(KrF_b) + \nu(KrF_t)$
361(16)	447(63)	384(4)	A" $\delta(F_eAsF''_e) - \delta(F_eAsF''_e)$
356(14)	434(52)	366(9)	A' $\delta(F_bAsF''_e) + \delta(F_eAsF_e)$ along F'_e-As-F''_e
340(25)	425(35)	338(16)	A" $\delta(F'_eAsF_e) - \delta(F'_eAsF_e)$
335(24)	406(13)		A' $\delta(F_{eAsFe}) + \delta(F''_eAsF_b)$ along F'_e-As-F''_e
289(199)	365(0)	273(1)	A' $\nu(AsF_b) + \delta(AsF_{2e}F'_eF_e)$ o.o.p.
280(0)	315(157)		A" $\delta(F_bAsF_e) + \delta(F_aAsF_e)$
249(7)	299(376)		A' $\delta(F''_eAsF_a) + \delta(F'_eAsF_b) + \nu(F_bKr)$
225(5)	282(5)		A" $\delta(F_tKrF_b)$ o.o.p. $+ \delta(F_bKrF_a)$
171(1)	222(1)	173(10)	A' $\nu(KrF''_e) + \nu(KrF_b)$ along F_a-As-F_b
155(6)	197(3)	162(11)	A' $\delta(F_tKrF''_e)$ i.p. $+ \nu(AsF_b)$
149(1)	185(41)		A" $\delta(F_tKrF_b)$ o.o.p. $+ (AsF_5)$ rock o.o.p.
137(1)	168(9)		A' $\delta(F''_eAsF_b) - \delta(F'_eAsF_b)$
73(0)	70(0)		A' $\delta(KrF_bAs)$
4(0)	21i(0)		A" Torsion of KrF$_2$ group about the As-F$_b$ bond + rock of AsF$_5$ group towards KrF$_2$

[a] Infrared intensities, in km mol^{-1} are given in parentheses. [b] Experimental values are taken from ref 40. Values in parentheses denote relative Raman intensities. [c] The atom labeling scheme is given in Structure VI; o.o.p. and i.p. denote out-of-plane and in-plane bends, respectively.

Table 3.8. Experimental Raman Frequencies and Calculated Vibrational Frequencies, Assignments, and Mode Descriptions for [KrF][SbF$_6$]

LDF[a]	HF[a]	Experimental[b]	Assignments for [KrF][SbF$_6$] under C_s Symmetry[c]
668(94)	748(72)	682(3)	A' ν_{as}(SbF$_e$ - SbF'$_e$) + ν_{as}(SbF$_a$) + ν_{as}(SbF'$_e$ - SbF$_e$)
666(94)	727(134)	664(45)	A" ν(SbF'$_e$ - SbF$_e$) + ν(SbF$_e$ - SbF'$_e$)
661(72)	725(139)	642(10)	A' ν(SbF$_a$) - ν(SbF'$_e$ + SbF$_e$)
616(170)	719(113)	615(100), 619(74)	A' ν(KrF$_t$) + ν(SbF$_{2e}$ + SbF'$_{2e}$)
600(5)	677(38)		A' ν(KrF$_t$) - ν_s(SbF$_5$)
581(4)	613(4)	586(5)	A' ν(SbF$_e$ + SbF'$_e$) - ν(SbF$_e$ + SbF'$_e$)
439(64)	439(239)	462(8), 480(4)	A' ν(KrF$_b$) + ν(KrF$_t$)
357(43)	413(31)	338(4)	A' ν(SbF$_b$)
253(47)	331(82)	288(9)	A' δ(F'$_e$SbF'$_e$)
246(44)	327(12)	266(6)	A" δ(F$_b$SbF$_a$) o.o.p. δ(F$_t$KrF$_b$)
236(60)	311(78)	255(6)	A' δ(F$_e$SbF$_e$)
231(41)	300(19)	255(6)	A' δ(F$_a$SbF$_b$) i.p. + δ(F$_e$SbF$_e$) - δ(F'$_e$SbF'$_e$)
226(5)	294(268)	214(2)	A" δ(F$_t$KrF$_b$) o.o.p. - δ(F$_a$SbF$_b$) o.o.p.
179(4)	236(35)	169(5)	A" δ(F$_t$KrF$_b$) - δ(F$_b$SbF$_a$)
176(2)	227(2)	162(7)	A" δ(F$_a$SbF$_e$) - δ(F$_e$SbF'$_e$) + δ(F$_t$KrF$_b$) o.o.p.
165(1)	194(2)	145(3)	A' δ(F$_t$KrF$_b$) i.p.
139(0)	173(1)		A" δ(F$_a$SbF$_b$) o.o.p. + δ(F$_e$SbF'$_e$) + δ(F$_e$SbF'$_e$)
109(2)	152(0)		A' δ(F$_b$SbF$_a$) i.p. - δ(SbF$_b$Kr)
91(0)	141(11)		A" δ(F'$_e$SbF$_e$) o.o.p. - δ(F'$_e$SbF$_e$)
80(0)	53(1)		A' δ(SbF$_b$Kr) + δ(F$_b$SbF$_a$)
54(0)	22(0)		A" KrF$_t$ torsion about SbF$_b$ + (SbF$_5$) rock

[a] Infrared intensities, in km mol^{-1} are given in parentheses. [b] Experimental values are taken from ref 40. Values in parentheses denote relative Raman intensities. [c] The atom labeling scheme is given in Structure VII; o.o.p. and i.p. denote out-of-plane and in-plane bends, respectively.

Table 3.9. Experimental Raman Frequencies and Calculated Vibrational Frequencies, Assignments, and Mode Descriptions for [KrF][BiF$_6$]

LDF[a]	HF[a]	Experimental[b]	Assignments for [KrF][BiF$_6$] under C_s Symmetry[c]
616(149)	737(106)	604(11), 610(100)	A' ν(KrF$_t$) - small ν(KrF$_b$)
578(68)	691(83)	592(35), 600(11)	A' ν(BiF$_a$)
567(60)	690(119)	580(40)	A" ν_{as}(BiF$_{2e}$) - ν(BiF'$_e$)
566(64)	689(93)	580(40)	A" ν_{as}(BiF$_{2e}$) - ν(BiF'$_e$)
537(6)	668(48)	547(3)	A' ν_s(BiF$_{2e}$ + BiF'$_{2e}$)
527(8)	614(8)	541(9)	A" ν_{as}(BiF$_{2e}$) + ν_{as}(BiF'$_{2e}$)
436(75)	446(368)		A' ν(KrF$_b$)
342(43)	374(31)	316(6)	A' ν(BiF$_b$)
234(22)	293(44)	244(5)	A" δ(F$_b$KrF$_t$) o.o.p. - δ(F$_b$KrF$_a$)
230(30)	258(0)	233(3)	A' δ(BiF'$_{2e}$)
213(65)	237(203)	225(1)	A' δ(BiF$_{2e}$)
205(33)	236(67)	209(5)	A" δ(F'$_e$BiF$_a$) - δ(F'$_e$BiF$_e$) - δ(F'$_e$BiF$_e$)
201(35)	234(52)	203(3)	A' δ(F$_e$BiF'$_e$) + δ(F$_a$BiF$_b$) i.p.
166(1)	199(1)	193(4)	A" δ(F$_e$BiF$_a$) + δ(F$_t$KrF$_b$) o.o.p.
163(8)	193(6)	184(5)	A" δ(F$_e$BiF$_a$) - δ(F$_e$BiF$_e$)
159(1)	184(15)		A' δ(F$_t$KrF$_b$) i.p. + ν(F$_b$Bi) + small δ(F$_b$BiF$_a$)
127(0)	134(0)	117(4)	A" δ (F$_b$BiF$_a$) o.o.p.
100(1)	127(2)		A' δ(F$_b$BiF$_a$) i.p. + δ(KrF$_b$Bi)
84(0)	107(3)		A" δ(BiF$_b$Kr) o.o.p.
74(0)	51(1)		A' δ(BiF$_b$Kr) i.p.
43(0)	6i(0)		A" KrF$_t$ torsion about Bi-F$_b$ + (BiF$_5$) rock

[a] Infrared intensities, in km mol^{-1} are given in parentheses. [b] Experimental values are taken from ref 41. Values in parentheses denote relative Raman intensities. [c] The atom labeling scheme is given in Structure VII; o.o.p. and i.p. denote out-of-plane and in-plane bends, respectively.

Although the conformations of the ion pairs are skewed to give C_1 point symmetry in their crystal structures and not all of the predicted frequencies have been observed, the approach provides more complete assignments and more precise descriptions of the vibrational modes in these strongly coupled systems than have been available previously.[40] Assignments and descriptions of the vibrational modes of the MF_5 moiety are provided without further comment.

The calculated Kr-F_t stretches of the gas-phase [KrF][MF_6] ion pairs occur at 611 (As), 616 (Sb), and 616 (Bi) cm^{-1} and are in excellent agreement with the experimental values, which are also insensitive to the degree of F$^-$ ion transfer. The lower frequency Kr--F_b stretches, which are predicted at 454 (As), 357, 439 (Sb), and 436 (Bi) cm^{-1}, are in good agreement with the experimental values. Direct comparison of the Kr--F_b stretching modes is not possible because of coupling to Kr-F_t (As) and to the MF_5 modes (P and Sb). Only in [KrF][BiF_6] is the Kr--F_b stretch not strongly coupled. Likewise, the Kr-F_t and Kr--F_b stretches of $KrF_2 \cdot PF_5$, for which there are no experimental values, are strongly coupled to anion modes and cannot be compared with other members of the series.

3.3.3. Mayer Bond Orders and Valencies, and Atomic Charges

One way to gain insight into the types of interactions involved is to use Mayer valency and bond order indices.[293-296] The Mayer bond orders, Mayer valencies and atomic charges for KrF_2, KrF^+, $Kr_2F_3^+$ and the [KrF][MF_6] ion pairs have been estimated using the electronic structures derived from the LDF calculations (Table 3.10).

3.3.3.1. KrF_2 and KrF^+

The atomic charges of KrF_2 were calculated to be 0.72 on krypton and -0.36 on each of the fluorine centres. For KrF^+, the full positive charge resides on krypton with zero charge on the fluorine atom. The Mayer bond order calculated for KrF^+ (1.09) is notably larger than those of KrF_2 and in qualitative agreement with the 2c-2e and 3c-4e

Table 3.10. Atomic Charges, Mayer Valencies and Mayer Bond Orders for [KrF][MF$_6$] (M = P, As, Sb, Bi), Free KrF$^+$, Kr$_2$F$_3$$^+$ and KrF$_2$

	[KrF]·[PF$_6$]	[KrF][AsF$_6$]	[KrF][SbF$_6$]	[KrF][BiF$_6$]	KrF$^+$	Kr$_2$F$_3$$^+$	KrF$_2$
Atomic Charges and Valencies[a,b]							
Kr	+0.79 (1.32)	+0.80 (1.32)	+0.82 (1.31)	+0.82 (1.32)	+1.00 (1.09)	+0.85 (1.28)	+0.72 (1.35)
M	+1.16 (5.36)	+0.90 (5.60)	+1.45 (5.14)	+2.23 (3.15)			
F$_t$	-0.30 (0.95)	-0.27 (0.97)	-0.26 (0.98)	-0.26 (0.98)	0.00 (1.09)	-0.37 (1.04)	-0.36 (0.89)
F$_b$	-0.37 (0.99)	-0.31 (1.08)	-0.31 (1.08)	-0.41 (0.92)		-0.16 (1.03)	
F$_a$	-0.26 (1.14)	-0.20 (1.20)	-0.31 (1.08)	-0.47 (0.82)			
F$_e$	-0.26 (1.08)	-0.22 (1.15)	-0.32 (1.06)	-0.50 (0.76)			
F'$_e$	-0.24 (1.10)	-0.20 (1.18)	-0.36 (1.00)	-0.46 (0.81)			
F"$_e$	-0.30 (1.03)	-0.27 (1.10)					
Mayer Bond Orders[a]							
Kr-F$_t$	0.74	0.76	0.79	0.79	1.09	0.86	0.67
Kr-F$_b$	0.54	0.50	0.47	0.48		0.38	
F$_b$-F$_t$	0.19	0.18	0.17	0.18		0.14	0.22
M-F$_b$	0.23	0.37	0.42	0.18			
M-F$_a$	1.09	1.10	0.99	0.65			
M-F$_e$	1.02	1.04	0.96	0.61			
M-F'$_e$	1.03	1.05	0.90	0.55			
M-F"$_e$	0.97	0.98					

[a]Calculated values were obtained by the LDF method in conjunction with the DZVP basis set. [b]Mayer valencies are given in parentheses.

covalent bonding models of these species, which predict bond orders of 1 and ½, respectively. Interestingly, there is a considerable residual bond order between the two fluorine atoms in KrF_2 (0.22). Slightly smaller F$\cdots$F bond orders have been calculated for $Kr_2F_3^+$ and the $[KrF][MF_6]$ ion pairs (*vide supra*), however such interactions are negligible for the $[XeF][MF_6]$ analogues (see section 5.3.3) and $Xe_2F_3^+$.[297]

3.3.3.2. $Kr_2F_3^+$

The bond orders are similar for $Kr_2F_3^+$ and $Xe_2F_3^+$, however, the charges and valencies (values for $Xe_2F_3^+$ are taken from ref 91 and are given in square brackets), show some noteworthy variations. The Kr--F_b bridge bond order of $Kr_2F_3^+$ is 0.38 [0.40] while the Kr-F_t bond order of 0.86 [0.92] is intermediate with respect to that of free KrF^+ and KrF_2. The valencies of the krypton atoms are 1.28 [1.37], and are slightly reduced with respect to that of KrF_2. The valencies of F_t, 1.04 [1.03], and F_b, 1.03 [0.94], are also similar, but the fluorine charges; F_t, -0.37 [-0.24], and F_b, -0.16 [-0.46]; and Ng atom charges, 0.85 [0.96], indicate that, relative to $Xe_2F_3^+$, a significant amount of charge has shifted from the bridge fluorine onto the Kr-F_t group. The charge on F_t of $Kr_2F_3^+$ is very similar to those on the fluorines of KrF_2 (-0.36) and that of F_b (-0.16) is intermediate with respect to those of KrF^+ (0.00) and KrF_2. The charge distributions indicate that the bridge fluorine of $Kr_2F_3^+$ is, next to the fluorine of KrF^+, the most electrophilic fluorine site in the series under discussion. There is again a significant bond order for F_t--F_b (0.14) in the $Kr_2F_3^+$ cation, which is significantly reduced with respect to that of KrF_2 (0.22), but greater than that in $Xe_2F_3^+$ (0.08).[297]

The Mayer bond orders are in semiquantitative agreement with the simple valence bond descriptions of NgF^+, NgF_2 and $Ng_2F_3^+$, which predict Ng-F bond orders of ½ for NgF_2, a bond order of 1 for the free NgF^+ cation and a value somewhere between ½ and 1 for the terminal Ng-F_t bonds of $Ng_2F_3^+$.

3.3.3.3. The [KrF][MF$_6$] (M = P, As, Sb, Bi) Ion Pairs

Little variation and no clear pattern is apparent among the atomic charges and valencies calculated for the F$_t$-Kr--F$_b$ groups of the [KrF][MF$_6$] ion pairs. The negative charges on the F$_a$ and F$_e$ atoms of the MF$_5$ groups increase on descending group 15, a trend that is consistent with a corresponding increase in fluoride ion acceptor strength. The [KrF][MF$_6$] ion pairs containing the heavier pnicogens are also shown to be more ionic from the increasing ratios of their M--F$_b$ and average non-bridging bond orders (P, 0.23; As, 0.36; Sb, 0.45; Bi, 0.59). The Kr-F$_t$ bond orders (P, 0.74; As, 0.76; Sb, 0.79; Bi, 0.79) and F$_t$--F$_b$ bond orders (P, 0.19; As, 0.18; Sb, 0.17; Bi, 0.18) are intermediate with respect to those of Kr$_2$F$_3{}^+$ and KrF$_2$ (*vide supra*). The anomalously low M-F and M--F$_b$ bond orders calculated for [KrF][BiF$_6$] when compared to the lighter pnicogen species is believed to arise as a consequence of the effective core potential used for the bismuth atom. These results show that the degree of F$^-$ complexation increases as the size of the central atom increases and the coordination sphere around the pnicogen atom becomes less crowded, allowing MF$_5$ to more effectively compete with the KrF$^+$ cation for the bridge fluorine. Although comparisons among bond orders of different elements should be made with caution, the Kr--F$_b$ bond order of Kr$_2$F$_3{}^+$ is larger than that of the P--F$_b$ bond order for [KrF][PF$_6$], indicating that the inability to prepare the latter species is a result of KrF$^+$ having a higher fluoride ion affinity than PF$_5$.

3.4. Conclusion

Prior to the present work, the only Kr(II) compound for which accurate geometric parameters were known was KrF$_2$. The single crystal X-ray structure determinations of α-KrF$_2$, [KrF][MF$_6$] (M = As, Sb, Bi), [Kr$_2$F$_3$][SbF$_6$]·KrF$_2$, [Kr$_2$F$_3$]$_2$[SbF$_6$]$_2$·KrF$_2$, and [Kr$_2$F$_3$][AsF$_6$]·[KrF][AsF$_6$] in the present work, dramatically extends the structural characterization of Kr(II) compounds and represent the first bond length and bond angle

measurements for salts containing the KrF^+ and $Kr_2F_3^+$ cations. Single crystal X-ray structure determinations and theoretical calculations show that the solid state and gas-phase $[KrF][MF_6]$ ion pairs are strongly fluorine bridged. With the exception of the calculated $KrF_2 \cdot PF_5$ adduct the $Kr-F_t$ bond length is not strongly influenced by the MF_6^- anion. No significant difference in the $Kr--F_b$ bond length was observed in the AsF_6^- and SbF_6^- salts, although the bond length was found to be significantly shorter in the BiF_6^- salt, and contrasts with the theoretical results which predict that the fluoride ion affinities of the pnicogen pentafluorides increase in the order, $PF_5 < AsF_5 < BiF_5 < SbF_5$. The Raman spectra of the fluorine bridged $[KrF][MF_6]$ ion pairs have been assigned in greater detail by comparison with their calculated vibrational spectra.

The $Kr_2F_3^+$ cation is highly deformable in the solid state, specifically with regards to the $Kr--F_b$ bond distances, and the $Kr--F_b--Kr$ bridge bond angle. These deformations are attributed to long contacts between the krypton atoms in the cation and fluorine atoms associated with the anion in the crystal lattice and are not reproduced by theoretical calculations of the gas-phase geometries. The calculated vibrational frequencies of $Kr_2F_3^+$ show that the prior assignments of the terminal symmetric and asymmetric stretching modes were incorrect and their assignments should be interchanged.

Raman spectroscopic investigation of the KrF_2/PF_5 system indicates that the only existing species is $[Kr_2F_3][PF_6] \cdot nKrF_2$. This compound is characteristic of the $[Kr_2F_3][MF_6] \cdot nKrF_2$ (M = As, Sb, Bi) series and exhibits vibrational modes consistent with a weakly interacting $Kr_2F_3^+$ cation and an octahedral PF_6^- anion. Failure to synthesize $[KrF][PF_6]$ in the presence of excess PF_5 reflects the low fluoride ion affinity of PF_5 and conforms to the theoretical results, which predict an adduct in which PF_5 is weakly fluorine bridged to KrF_2.

CHAPTER 4

CHARACTERIZATION OF [KrF][AuF$_6$] AND [O$_2$][AuF$_6$] BY SINGLE CRYSTAL X-RAY DIFFRACTION, RAMAN SPECTROSCOPY AND THEORETICAL METHODS[298]

4.1. Introduction

The chemistry of gold(V) is currently limited to salts containing the AuF$_6^-$ anion and AuF$_5$. Despite the limitation to compounds containing only Au-F bonds, interest in the chemistry of gold(V) has recently been renewed by the calculated fluoride ion affinity of AuF$_5$ (591,[47] 539 kJ mol^{-1} [46]), which exceeds that of SbF$_5$ (503,[48] 473 kJ mol^{-1} [46]) and is currently only predicted to be weaker than that of Sb$_3$F$_{15}$ (552 kJ mol^{-1}).[46]

Salts containing the AuF$_6^-$ anion have been extensively characterized by vibrational spectroscopy and, in particular, by Raman spectroscopy. By analogy with the salts containing the pnicogen hexafluoride anions (see Chapters 3 and 5), the vibrational spectra of salts having strong cation-anion interactions are complex as a consequence of the symmetry lowering and removal of the degeneracies of the E$_g$, F$_{2g}$, F$_{2u}$ and F$_{1u}$ modes of the otherwise octahedral AuF$_6^-$ anion. While the majority of AuF$_6^-$ salts have weakly interacting counter-cations, which include those of group 1[70,144,146,154,299] and group 2,[147] NO$^+$,[35,146] O$_2^+$,[35,70,142,143,230] ClF$_2^+$,[145] ClF$_4^+$,[145] ClF$_6^+$ [145] ClO$_2^+$,[145] ClOF$_2^+$,[145] ClF$_6^+$,[145] BrF$_6^+$,[70,158] IF$_6^+$,[146] and ReF$_6^+$,[300,301] the Raman spectra of the KrF$^+$,[35,70,158] XeF$^+$,[70] XeF$_5^+$ [70,146,158,249] and Xe$_2$F$_{11}^+$ [35,70,158] salts indicate relatively strong cation-anion interactions. The only detailed crystal structure reported in which the AuF$_6^-$ anion exhibits strong fluorine bridge interactions is [Xe$_2$F$_{11}$][AuF$_6$].[154] Unfortunately, extraction of qualitative

information relating to the fluoride ion affinity of AuF_5 from this structure is complicated by two fluorine bridges between the cation and anion that involve two fluorines of AuF_6^- that are cis to each other, the asymmetry of the fluorine bridge in the cation, and the relatively large uncertainties in the geometric parameters.

In the present study, the single crystal X-ray structure of $[KrF][AuF_6]$ was investigated with the hope of obtaining qualitative experimental evidence to support the high fluoride ion affinity reported for AuF_5. Structural characterization of $[KrF][AuF_6]$ is of particular interest because the $Kr-F_t$ stretching frequency of this salt (597 cm^{-1})[35] is anomalously low in comparison to α-$[KrF][AsF_6]$ (607, 596 cm^{-1}),[40] β-$[KrF][AsF_6]$ (619, 615 cm^{-1}),[40] $[KrF][SbF_6]$ (619, 615 cm^{-1}),[40] $[KrF][BiF_6]$ (610, 604 cm^{-1})[41] and $[KrF][Sb_2F_{11}]$ (624 cm^{-1})[40] and contradicts the prediction that the frequency of this mode increases as the fluoride ion acceptor strength of the parent pentafluoride increases.[41,68] Moreover, the interaction between the cation and the anion is expected to be limited to a single fluorine bridge, which simplifies the assessment of the fluoride ion acceptor properties of AuF_5 when compared with $[Xe_2F_{11}][AuF_6]$. Although the crystal structures of $[NgF][MF_6]$ (Ng = Kr,[23] Xe; M = As, Sb, Bi) (see sections 3.2.2.2 and 5.2.2.2) have indicated that the $Ng-F_t$ bond length is generally insensitive to the fluoride ion acceptor properties of MF_5, the $Ng--F_b$ bond lengths appear to be more sensitive to the nature of the counter anion and may permit a more representative evaluation of Lewis acidity of AuF_5 than is obtainable from the vibrational spectra. The structural characterization of $[KrF][AuF_6]$ is of additional interest because the salt can be used a precursor to nearly every known compound of Au(V). The versatility of $[KrF][AuF_6]$ results from the easy displacement of KrF_2 by stronger fluoride ion donors (eq 4.1)[150] and the potent oxidizing

$$[KrF][AuF_6] + CsF \xrightarrow{\text{HF, 20°C}} [Cs][AuF_6] + KrF_2 \qquad (4.1)$$

properties of the KrF^+ cation, which can be used to prepare salts such as $[O_2][AuF_6]$ *in situ* (eq 4.2).[35,70] The thermal instability of $[KrF][AuF_6]$ also makes it an ideal precursor to high purity AuF_5 (eq 4.3).[35,70]

$$2[KrF][AuF_6] + 2O_2 \xrightarrow{-78°C} 2[O_2][AuF_6] + Kr + F_2 \qquad (4.2)$$

$$2[KrF][AuF_6] \xrightarrow{60°C} 2AuF_5 + 2Kr + F_2 \qquad (4.3)$$
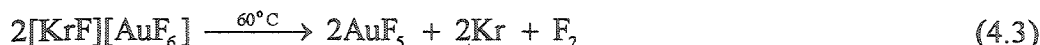
During the course of this work, a low-temperature modification of $[O_2][AuF_6]$ obtained by the reaction of $[KrF][AuF_6]$ with O_2 has also been identified[302] and has subsequently been reported by Seppelt and Hwang.[47] Crystallographic characterization of this fully ordered phase is of fundamental interest because the majority of the dioxygenyl salts investigated to date exhibit disordering of the cation,[67,231,303,304] which is attributed to the positioning of the cation in the large interstitial sites produced by the oxidatively resistant fluoro-anion host lattice. The accurate determination of the O_2^+ bond length in $[O_2][AuF_6]$, and eventually other salts, may also provide insight into the salt-dependent shifts of the O_2^+ vibrational frequency.[35,67,70,142,229,230,291,292,307-307] Variable temperature Raman spectroscopy has been used to identify the temperature at which the α-β phase transition occurs and has also been used to reassign the $v_2(E_g)$ vibrational band of the AuF_6^- anion with the aid of electronic structure calculations.

4.2. Results and Discussion

4.2.1. Syntheses of [KrF][AuF₆] and [O₂][AuF₆]

Samples of $[KrF][AuF_6]$ were prepared as previously described[35] by the oxidation of gold powder with KrF_2 (eq 4.4). The salt, $[O_2][AuF_6]$, was prepared by the reaction of

$$Au + \tfrac{1}{2}KrF_2 \xrightarrow{HF, 20°C} [KrF][AuF_6] + \tfrac{1}{2}Kr \qquad (4.4)$$

$$[KrF][AuF_6] + O_2 \rightarrow [O_2][AuF_6] + Kr + \tfrac{1}{2}F_2 \qquad (4.5)$$
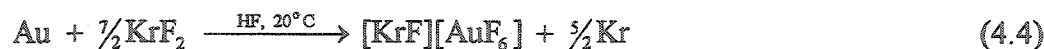
O_2 with $[KrF][AuF_6]$ in the presence of a small excess of KrF_2 in anhydrous HF at room temperature (eq 4.5).[35] The purities of both salts were verified by Raman spectroscopy.

4.2.2. X-Ray Crystal Structures

The unit cell parameters and refinement statistics for [KrF][AuF$_6$] at -125 °C and

α-[O$_2$][AuF$_6$] at -122 °C are given in Table 4.1, where they are compared with those of β-

[O$_2$][AuF$_6$][155] at ambient temperature and α-[O$_2$][AuF$_6$] at -169 °C.[47]

4.2.2.1. [KrF][AuF$_6$]

Despite the acquisition of high-angle diffraction data at low temperatures and

clean diffraction patterns observed during the data acquisition, the bond length

uncertainties in the structure of [KrF][AuF$_6$] are rather high (Table 4.2). The thermal

parameters of the refined structure (Figure 4.1a) are consistent with a correlated

librational anion rock in the plane containing the F(2), F(3) F(5), F(7) and Au atoms.

Because motions of this type are known to alter the apparent bond lengths and angles, a

librational correction was applied.[308] In contrast to the [KrF][MF$_6$] (M = As, Sb, Bi) salts

(see section 3.2.2.2),[23] which crystallize in the space group $P2_1/c$, the isostructural

[KrF][AuF$_6$] salt crystallizes in the non-centrosymmetric space group Cc with the ion

pairs packing in columns along the b-axis (Figure 4.1b).

Similar to the [KrF][MF$_6$] (M = As, Sb, Bi) series, [KrF][AuF$_6$] consists of a KrF$^+$

cation that interacts strongly with the AuF$_6^-$ anion by means of a fluorine bridge (F$_b$).

Despite the higher fluoride ion affinity of AuF$_5$ (591,[47] 539 kJ mol^{-1} [46]) relative to SbF$_5$

(503,[48] 473 kJ mol^{-1} [46]), BiF$_5$ (457 kJ mol^{-1})[46] and AsF$_5$ (443,[48] 440 kJ mol^{-1} [46]), the Kr-F$_t$

(F$_t$, terminal fluorine) bond length in [KrF][AuF$_6$] (1.76(1) Å) does not differ by more

than ±3σ from those of [KrF][MF$_6$] (M = As, Sb, Bi), which range from 1.765(3) to

1.783(6) Å (see section 3.2.2.2).[23] Although there is no experimental value available for

the bond length of gaseous KrF$^+$, the insensitivity of the Kr-F$_t$ bond length in the

[KrF][MF$_6$] (As, Sb, Bi, Au) salts to the fluoride ion basicities of AsF$_6^-$,[46,48] SbF$_6^-$,[46,48]

BiF$_6^-$ [46] and AuF$_6^-$ [46,47] suggests that all four salts have achieved the minimal KrF$^+$ bond

Table 4.1. Crystal Data a Refinement Results for $[KrF][AuF_6]$ and $[O_2][AuF_6]$

	$[KrF][AuF_6]$[a]	$\alpha\text{-}[O_2][AuF_6]$[a]	$\alpha\text{-}[O_2][AuF_6]$[b]	$\beta\text{-}[O_2][AuF_6]$[c]
Space Group	Cc	$P\bar{1}$	$P\bar{1}$	$P\bar{3}$
a (Å)	7.993(3)	4.935(6)	4.933(1)	7.742(1)
b (Å)	7.084(3)	4.980(6)	4.973(2)	7.742(1)
c (Å)	10.721(4)	5.013(6)	5.006(2)	7.089(2)
α (deg)	90	101.18(1)	101.32(1)	90
β (deg)	105.58(1)	90.75(2)	90.63(1)	90
γ (deg)	90	101.98(2)	102.09(1)	120
V (Å^3)	584.8(4)	118.0(2)	117.6(1)	368.0(1)
Z	4	1	2[d]	3
Mol. mass (g mol^{-1})	413.77	342.97	342.97	342.97
ρ_{calcd} (g cm^{-3})	4.700	4.825	4.84	4.182
T (°C)	-125	-122	-169	N/A
μ (mm^{-1})	32.74	31.24	N/A	N/A
R_1[e]	0.0389	0.0481	0.0556	0.0221
wR_2[f]	0.0911	0.1181	0.1406	0.045

[a] This work. [b] Values taken from ref 47. [c] Values taken from ref 155. [d] The value of Z is incorrectly reported, and should have a value of 1 (see section 4.2.2.2).

[e] $R_1 = \dfrac{\sum \left\| F_o \right| - \left| F_c \right\|}{\sum \left| F_o \right|}$ for $I > 2\sigma(I)$. [f] $wR_2 = \dfrac{\sum \left| \left(\left| F_o \right| - \left| F_c \right| \right) w^{\frac{1}{2}} \right|}{\sum \left(\left| F_o \right| w \right)}$ for $I > 2\sigma(I)$.

Table 4.2. Experimental and Calculated Bond Lengths and Bond Angles for [KrF][AuF$_6$]

	Experimental		Calculated		
	uncorrected	corrected[a]	HF	MP2	MPW1PW91
Bond Lengths (Å)					
Kr-F(1)	1.76(1)	1.76(1)	1.715	1.817	1.830
Kr--F(2)	2.16(1)	2.15(1)	2.064	2.015	2.063
Au--F(2)	1.93(1)	1.96(1)	1.982	2.047	2.060
Au-F(3)	1.87(1)	1.90(1)	1.825	1.891	1.886
Au-F(4)	1.90(1)	1.92(1)	1.880	1.940	1.939
Au-F(5)	1.90(1)	1.89(1)	1.880	1.940	1.939
Au-F(6)	1.90(1)	1.90(1)	1.858	1.925	1.923
Au-F(7)	1.88(1)	1.90(1)	1.858	1.925	1.923
Bond Angles (°)					
F(1)-Kr---F(2)	175.4(7)		181.7	180.0	177.0
Kr--F(2)--Au	125.3(7)		117.4	111.4	115.3
F(4)-Au-F(2)-F(5)	13.6		44.3	44.1	44.2

[a] The bond lengths and bond angles of [KrF][AuF$_6$] have been corrected for a librational rock (ref 308), which occurs along the plane of the F(2), F(3) F(5), F(7) and Au atoms (Figure 4.1a).

a

b
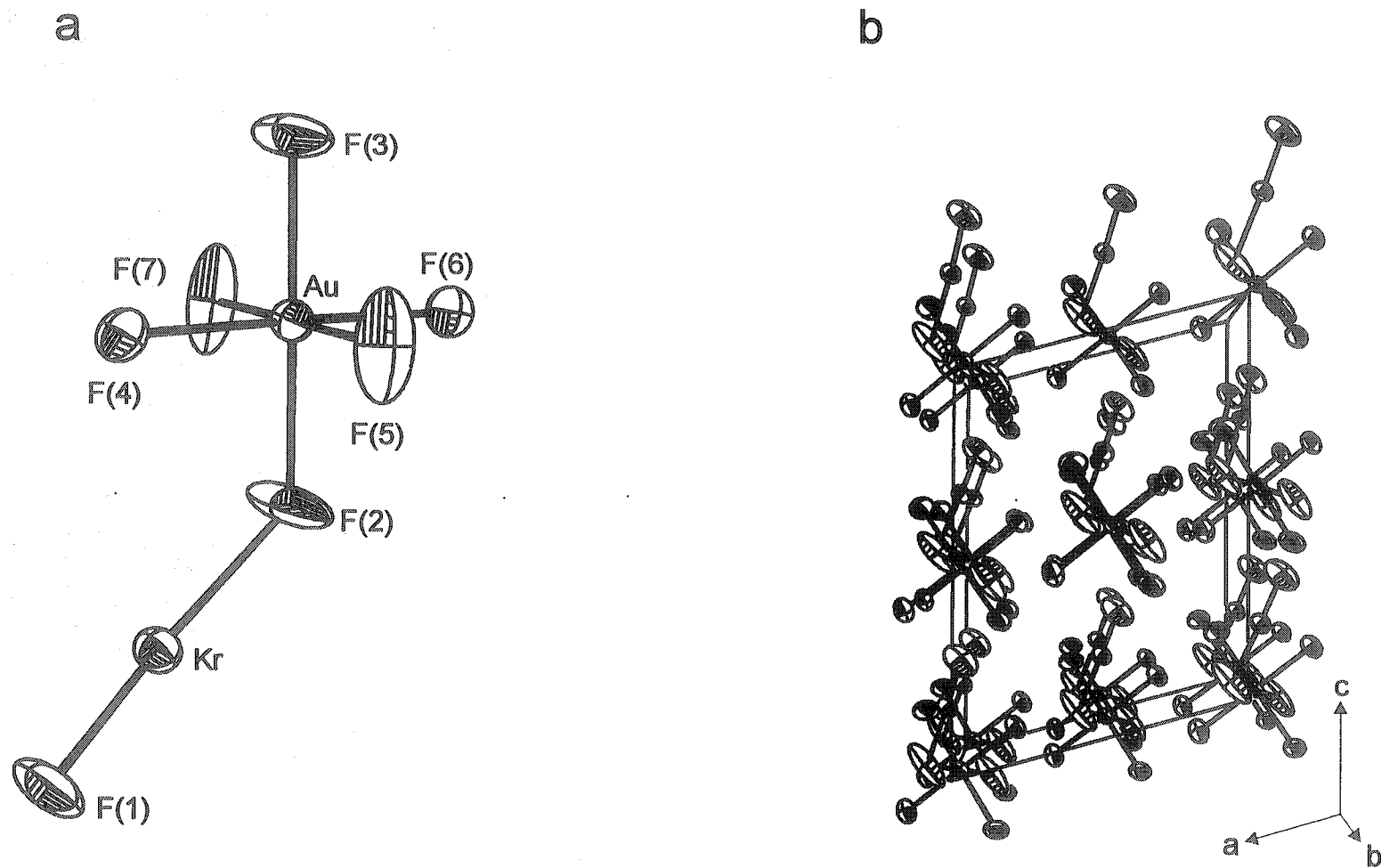
Figure 4.1 The X-ray crystal structure of (a) [KrF][AuF$_6$] at -125 °C and (b) its packing diagram viewed along the b-axis. The thermal ellipsoids are shown at the 50% probability level.

length associated with the dominant contributing valence bond Structure III. The only

$$F^- \ ^+Kr\text{-}F \ MF_5 \ \leftrightarrow \ F\text{-}Kr^+ \ F^- \ MF_5 \ \leftrightarrow \ F\text{-}Kr^+ \ F\text{-}MF_5^-$$
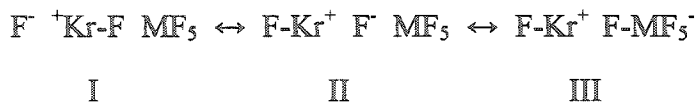
$$I \qquad\qquad\qquad II \qquad\qquad\qquad III$$

known salt of KrF^+ that may more closely approximate the free KrF^+ cation in Structure III is $[KrF][Sb_2F_{11}]$, which exhibits the highest known $Kr\text{-}F_t$ stretching frequency (627 cm^{-1}),[21] however, the crystal structure of this salt has not been determined.

The $Kr\text{--}F_b$ bond length in the AuF_6^- salt is 2.16(1) Å, and is similar to those reported for $[KrF][AsF_6]$ (2.131(2) Å) and $[KrF][SbF_6]$ (2.140(3) Å), but significantly longer than that determined for $[KrF][BiF_6]$ (2.090(6) Å).[23] The similarities among the $Kr\text{--}F_b$ bond lengths of $[KrF][MF_6]$ (M = As, Sb, Au) prevent the greater fluoride ion affinity predicted for AuF_5 from being verified on the basis of the crystal structures of these salts, but suggest that AsF_5, SbF_5 and AuF_5 are stronger fluoride ion acceptors than BiF_5. With the exception of the X-ray structures of $[XeF][AsF_6]$ and $[XeF][BiF_6]$, for which the $Xe\text{--}F_b$ bond lengths are comparable, the trend is also observed for the crystal structures of the $[XeF][MF_6]$ (M = As, Sb, Bi),[72,309] $[XeF_3][MF_6]$ (M = Sb, Bi)[284,285] and $[XeF][M_2F_{11}]$ (M = Sb,[73] Bi; see section 5.2.2.2) salts. Overall, the comparison of the $Ng\text{--}F_b$ bond lengths among these species implies that the fluoride ion affinities of the pentafluorides under investigation increases in the order: $BiF_5 < AsF_5 < SbF_5 \approx AuF_5$, which is in reasonable agreement with the ordering predicted by the gas-phase electronic structure calculations (*i.e.*, $AsF_5 < BiF_5 < SbF_5 < AuF_5$).[46,48]

Although a *trans*-influence resulting from the long $Au\text{--}F_b$ bond (1.96(1) Å) may be expected to contract the $Au\text{-}F(3)$ bond, this effect was not observed because bond length uncertainties prevent discrimination among the non-bridging $Au\text{-}F$ bonds (range, 1.89(1) - 1.92(1) Å). Moreover, failure to observe a *trans*-influence in $[KrF][AuF_6]$ is not surprising because there is no significant contraction of the $M\text{-}F(3)$ bond in the MF_6^- (M

= As, Sb, Bi) analogues, where the bond length uncertainties are lower (see section 3.2.2.2).[23] The fluorine bridge in $[KrF][MF_6]$ salts can be thought of in terms of a competition between the Lewis acids KrF^+ and MF_5 for the fluoride ion (Structures I - III). Thus, the ion-pair has a significant amount of covalent character, which is reflected in the F_t-Kr--F_b and Kr--F_b--M bond angles. The F(1)-Kr-F(2) bond angle was determined to be 175.4(7)° and the deviation of this angle from the expected linear AX_2E_3 geometry is consistent with the pnicogen analogues where this angle ranges from 176.8(1) to 177.9(2)° (Table 3.3).[23] Of the $[KrF][MF_6]$ species investigated by single crystal X-ray diffraction, $[KrF][AuF_6]$ most closely resembles an eclipsed geometry having C_s symmetry with a F(4)-Au-F(2)--Kr torsion angle of 13.6°, when compared with those of $[KrF][AsF_6]$ (22.1°), $[Kr_2F_3][AsF_6]\cdot[KrF][AsF_6]$ (28.1°), $[KrF][SbF_6]$ (22°) and $[KrF][BiF_6]$ (19.7°).[23] The variations among the Kr--F_b--M bond angles and the torsion angles may have some anion dependence, however, the observed variations are more likely a result of long inter-ionic contacts in the solid state as inferred from the differences observed among the ion pairs in $[KrF][AsF_6]$ and $[Kr_2F_3][AsF_6]\cdot[KrF][AsF_6]$. The solid-state effect on the dihedral angle is also apparent from the calculated structures of these ion pairs, which demonstrate preferences for eclipsed ($[KrF][MF_6]$ (M = P, As); Structure IV) or staggered ($[KrF][MF_6]$ (M = Sb, Bi, Au); Structure V) conformations rather than gauche conformations (see sections 3.3.1.2 and 4.3.1.1). The Kr--F_b--Au
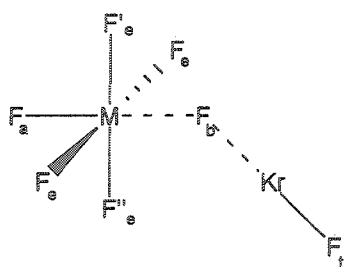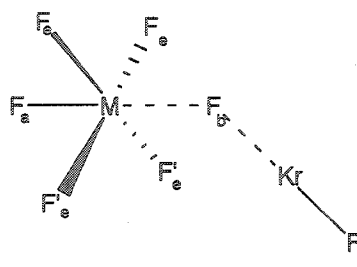
IV   V

bond angle is 125.3(7)° and is intermediate with respect to those determined for [KrF][AsF$_6$] (133.7(1)°), [Kr$_2$F$_3$][AsF$_6$]·[KrF][AsF$_6$] (124.6(3)°), [KrF][SbF$_6$] (139.2(2)°) and [KrF][BiF$_6$] (138.3(3)°).[23] This bond angle is also consistent with the considerable covalent character for the Kr--F$_b$ and F$_b$--M bridge bonds and a bent AX$_2$E$_2$ geometry predicted by the VSEPR model. The calculated Kr--F$_b$--M bond angles in [KrF][MF$_6$] (M = As, Sb, Bi, Au) are found to be sensitive to the computational method used, and as a result, the relationship of the anion or crystal packing to this angle cannot be readily assessed. Moreover, the low Kr--F$_b$--M bending frequencies (see sections 3.3.2.3 and 4.3.2.1) imply that these bond angles may be easily distorted by inter-molecular interactions in the solid state.

4.2.2.2. α-[O$_2$][AuF$_6$]

The room temperature phase (β-) of [O$_2$][AuF$_6$] was previously determined to crystallize in the rhombohedral space group $R\bar{3}$,[155] contrasting with [O$_2$][MF$_6$] (M = As,[291,310,311] Sb,[142,229,310-312] Bi,[142] Ru,[67,155] Pt,[155,231,304,313] Rh[67]), which have cubic morphologies at or below room temperature as a result of cation and/or anion disorders. Detailed investigation of the [O$_2$][AsF$_6$] system by X-ray powder diffraction, calorimetry and by Raman, infrared and ^{19}F wide-line NMR spectroscopy revealed phase transitions at -3 and -82 °C which are believed to represent transitions to monoclinic and/or triclinic phases.[291] Although a cubic phase of [O$_2$][AuF$_6$] is currently unknown, it would likely only exist at elevated temperatures based on the structures of other [O$_2$][MF$_6$] salts and the trend of decreasing crystallographic order with increasing temperature observed for [O$_2$][AsF$_6$]. A low-temperature rhombohedral phase of [O$_2$][PtF$_6$] is also known and is consistent with this hypothesis.[304]

The structure of α-[O$_2$][AuF$_6$] was determined at -122 °C,[314] and was determined to crystallize in the triclinic space group $P\bar{1}$ (Figure 4.2). The unit cell dimensions
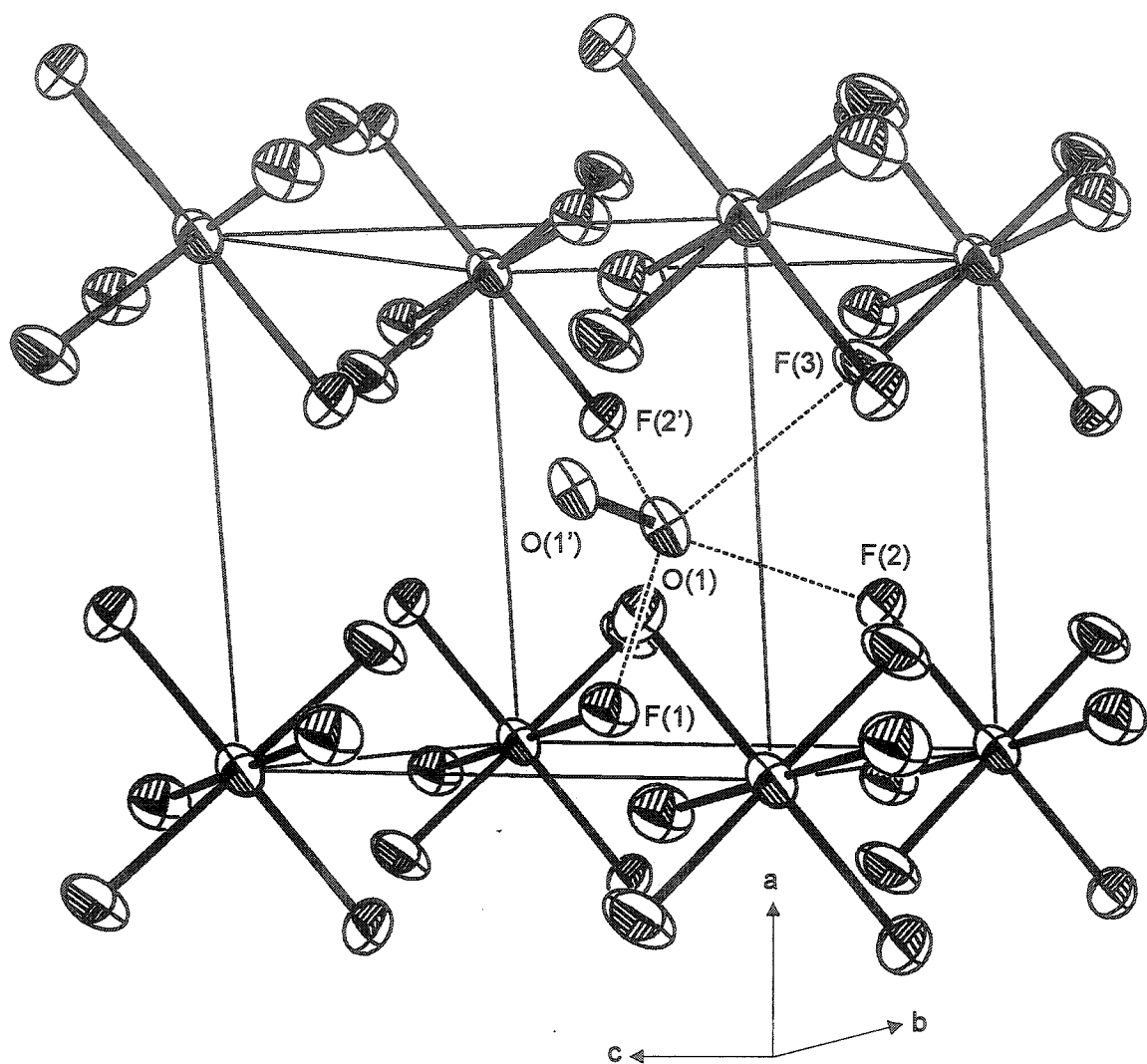
Figure 4.2. The unit cell diagram of α-$[O_2][AuF_6]$ at -122 °C showing the shortest O···F contacts (dotted lines). The thermal ellipsoids are shown at the 50% probability level.

(Table 4.1) are comparable with those recently reported at -169 °C,[47] with the small differences in the α-, β- and γ-angles being attributed to the different acquisition temperatures. The value of 2 reported for Z in the -169 °C study is incorrect and should be 1, which is consistent with the unit cell volume of this salt (118.(2) $Å^3$) and the formula unit volumes of [Li][AuF_6] (98.1 $Å^3$),[299] [Na][AuF_6] (119.1 $Å^3$),[299] [K][AuF_6] (112.2 $Å^3$),[299] [Rb][AuF_6] (128.1 $Å^3$),[299] and [Cs][AuF_6] (137.0, 141 $Å^3$).[144,299]

The geometric parameters for α-[O_2][AuF_6] are listed in Table 4.3. In contrast to the rhombohedral β-phase, the O_2^+ cations in the α-phase are not disordered within the octahedral interstitial sites produced by the anions. The ordering of the O_2^+ cations is accompanied by minor distortions of the AuF_6^- anion, which are also reflected in the low-temperature Raman spectrum of this salt (see section 4.2.3). The three crystallographically unique Au-F bond lengths (1.86(1), 1.89(1), 1.90(1) Å), are not significantly different at the ±3σ confidence limit, however, the anion is clearly distorted because the cis-F-Au-F bond angles (86.7(6), 93.3(5), 91.4(6)°) are different at the ±3σ confidence limit. The Au-F bond lengths are in agreement with those determined for other AuF_6^- salts, where the anion is not strongly bridged to the cation (e.g. [Li][AuF_6], 1.874(6) Å)[315] and the non-bridging Au-F bond lengths in [KrF][AuF_6] (1.89(1) - 1.92(1) Å)[23] and [Xe_2F_{11}][AuF_6] (1.85(1) - 1.86(1) Å).[148,154] The O-O bond length (1.068(30) Å) is in good agreement with the bond lengths determined in the ordered structures of [O_2][Mn_2F_9] (1.10 Å),[316] α-[O_2][AuF_6] (1.079(27) Å, -169 °C),[47] and in the disordered structures of [O_2][PtF_6] (1.21(17) Å)[231] and [O_2][RuF_6] (1.125(17) Å, -127 °C; 1.12(4) Å, 20 °C),[67] where the cation has been treated for a three-fold disorder. With the exception of [O_2]_2[Ti_7F_{30}], which has an anomalously short O-O bond length (0.96 Å) and an unreported uncertainty,[303] all of the crystallographic values are in good agreement with the value determined for the gas-phase O_2^+ cation (1.1227 Å).[317] Each oxygen atom in α-

Table 4.3.　Experimental and Calculated Bond Lengths for $[O_2][AuF_6]$

	Experimental	Calculated[a]		
	$[O_2][AuF_6]$	HF	MP2	MPW1PW91
		Stuttgart ECP	Stuttgart ECP	Hay-Wadt/DZVP
Bond Lengths (Å)				
O-O	1.068(30)	1.061[b]	1.156[b]	1.117
Au-F(1)	1.885(11)	1.873	1.938	1.937
Au-F(2)	1.863(10)	1.873	1.938	1.937
Au-F(3)	1.894(11)	1.873	1.938	1.937
F(1)⋯O	2.492, 2.865, 3.069, 3.161			
F(2)⋯O	2.673, 2.724, 2.982, 3.790			
F(3)⋯O	2.430, 2.868, 2.964, 3.459			
Bond Angles (°)				
F(1)-Au-F(2)	93.3(5)	90.0	90.0	90.0
F(1)-Au-F(3)	91.4(6)	90.0	90.0	90.0
F(2)-Au-F(3)	88.7(6)	90.0	90.0	90.0

[a] The calculated values are for the free gas-phase O_2^+ and AuF_6^- ions and not their ion pair.　[b] The 6-311G(d) basis set was used for the geometry optimization of the O_2^+ cation.

[O_2][AuF_6] has four contacts to different anions that are within the sum of the van der Waals radii of oxygen (1.40,[287] 1.50 Å[286]) and fluorine (1.35,[287] 1.47 Å[286]). The longest O$\cdots$F(2) contact (2.724 Å) is at the van der Waals limit and is nearly collinear with the O-O bond axis ($\angle$OOF, 175.3°), while the contact distances to F(1) (2.492 Å), F(2) (2.673 Å) and F(3) (2.430 Å) are shorter and are approximately perpendicular to the O-O bond axis ($\angle$OOF, 112.8, 96.1 and 109.6°, respectively). These shorter O$\cdots$F contact distances are comparable to the three contacts noted in the low-temperature cubic (space group *Ia3*) structure of [O_2][RuF_6] (2.36(3), 2.36(2), 2.61(1) Å).[67]

4.2.3. Variable Temperature Raman Spectroscopy of [O_2][AuF_6]

The vibrational spectra of salts containing the AuF_6^- anion have been mainly investigated by Raman spectroscopy because compounds of Au(V) readily react with materials commonly used for infrared cells. Raman spectroscopy is also favoured because the $v_1(A_{1g})$, $v_2(E_g)$, and $v_5(F_{2g})$ vibrations are Raman active, whereas only the $v_3(F_{1u})$ and $v_4(F_{1u})$ are infrared active. Furthermore, the lower frequency $v_4(F_{1u})$ bend occurs at *ca.* 259 cm^{-1},[158] making it difficult to observe by infrared spectroscopy, and the $v_6(F_{2u})$ bend is predicted to be both Raman and infrared inactive. Based on the Raman spectra of the [M][AuF_6] (M = Li,[299] Na,[70,299] K,[146,299] Rb,[299] Cs,[144,146,154,299] NO,[335,146] O_2,[35,70,142,146,230] BrF_6,[70,158] IF_6,[146] XeF,[70] Xe_2F_3,[35,70,158] Xe_2F_{11},[70,144,146,154] XeF_5,[70,146,158,249] KrF,[35] ClF_2,[145] ClO_2,[145] $ClOF_2$,[145] ClF_4,[145] ClF_6,[145] ReF_6[300,301]) and [M][AuF_6]$_2$ (M = Mg, Ca, Sr, Ba)[147] salts, the distortion of the anion is generally minimal, except in cases where a strong fluorine bridge interaction exists between the cation, *i.e.*, KrF^+, XeF^+, XeF_5^+, $Xe_2F_{11}^+$, and the anion. For the salts mentioned above, the Raman-active bands of AuF_6^- have been reported to occur in the ranges 583 - 612 cm^{-1} (A_{1g}), 513 - 531 cm^{-1} (E_g), and 218 - 233 cm^{-1} (F_{2g}) depending on the cation and whether the spectrum of AuF_6^- was acquired as a solid or in HF solution. In each case, the symmetric $v_1(A_{1g})$ band of the

cation is reported to be most intense, followed by the $\nu_5(F_{2g})$ band, which exhibits an intensity ranging from 16 to 50% that of the $\nu_1(A_{1g})$ mode. With the exception of $[Xe_2F_3][AuF_6]$ and $[Cs][AuF_6]$, where the relative intensity of the $\nu_2(E_g)$ band is reported to be as large as 12[35] and 28%,[144] respectively, this band has not been reported to have a relative intensity exceeding 5%. The $\nu_2(E_g)$ band is completely absent in the Li^{+},[299] Na^{+},[70,299] K^{+},[146,299] Rb^{+},[299] Mg^{2+},[147] Ca^{2+},[147] Sr^{2+},[147] Ba^{2+},[147] NO^{+},[35,146] BrF_6^{+},[58,70] IF_6^{+},[146] $Xe_2F_{11}^{+}$,[70,144,146,154] XeF_5^{+},[70,146,158] $Kr_2F_3^{+}$,[70] ReF_6^{+}[300,301] and ClO_2^{+}[145] salts despite the otherwise simple nature of their spectra in this region, although it has been postulated that this band is inherently weak as a consequence of the infringement of adiabatic conditions for many electron systems by analogy with the UCl_6^{2-} and $CeCl_6^{2-}$ anions.[318,319] This anomaly, along with the discovery of α-$[O_2][AuF_6]$, prompted the reinvestigation of the AuF_6^{-} anion as its O_2^{+} salt by use of variable-temperature Raman spectroscopy.

The Raman spectra of $[O_2][AuF_6]$ at temperatures between 25 and -163 °C are shown in Figure 4.3. The spectrum of β-$[O_2][AuF_6]$ at 25 °C agrees well with that reported earlier and the $\nu_2(E_g)$ band of AuF_6^{-} is not observed near 530 cm^{-1}.[35,70,142,146,230] The band at 597 cm^{-1} is broad and asymmetric with weak shoulders at 592 and 594 cm^{-1} and the band at 229 cm^{-1} has a pronounced shoulder at 220 cm^{-1}. Cooling the sample from 25 to -114 °C resulted in a monotonic shift of the O_2^{+} vibrational frequency from 1835 to 1831 cm^{-1}, which was accompanied by broadening and splitting of the peaks at 229 and 595 cm^{-1}. The shift in the O_2^{+} frequency upon cooling is consistent with contraction of the unit cell volume, which brings the anion and cation closer together and presumably has the effect of transferring electron density from the surrounding anions into the π^{*} molecular orbital of O_2^{+}. At temperatures between -114 and -118 °C, the α- and β-phases coexist as indicated by the presence of two peaks in the O_2^{+} stretching region (1831 and 1837 cm^{-1}) and the increased complexity of the regions around 229 and
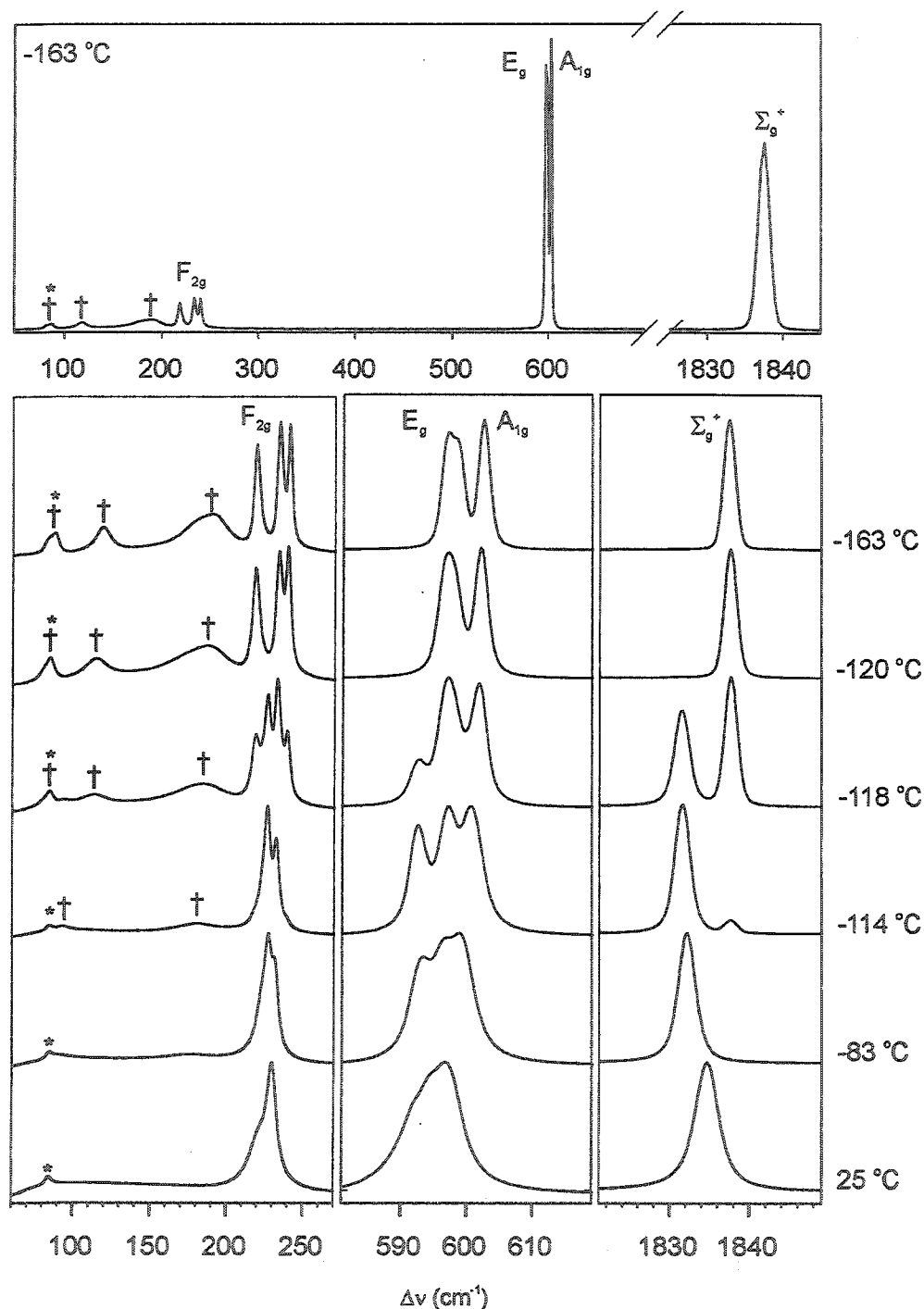
Figure 4.3. Variable temperature Raman spectra of $[O_2][AuF_6]$ recorded using 1064-nm excitation. Daggers (†) indicate lattice modes and asterisks (*) denote an instrumental artifact.

595 cm^{-1}. In addition, lattice modes associated with the low-temperature α-phase emerge at 85(4), 118(6) and 189(20) cm^{-1}. Further cooling of the sample to -163 °C simplifies the spectrum considerably, with the O_2^+ stretching band returning to a single peak at higher frequency (1838 cm^{-1}). This is indicative of the re-emergence of a single low-temperature phase where the transfer of electron density into the π^* orbital may be geometrically less favoured as a consequence of the cation having a fixed orientation. The anion band, originally at 597 cm^{-1}, is split into two sets of peaks at -163 °C, with the one at higher frequency (603 cm^{-1}) appearing as a singlet and the one at lower frequency showing evidence of further splitting (597, 598 cm^{-1}). The peak assigned to the $\nu_5(F_{2g})$ band of AuF$_6^-$ at ambient temperature splits into three well-resolved bands at 219, 234, and 241 cm^{-1}. The changes in the Raman spectrum at low temperature are consistent with the triclinic α-phase, which was shown to be stable at temperatures between -122 and -169 °C[47] by X-ray crystallography. The lowering of the anion symmetry from O_h to C_i site symmetry in the solid state at -163 °C results in splitting of the degenerate vibrational modes, i.e., A_{1g} (595 cm^{-1}) → A_g (603 cm^{-1}), E_g (595 cm^{-1}) → 2A_g (598, 597 cm^{-1}) and F_{2g} (229 cm^{-1}) → 3A_g (219, 234, 241 cm^{-1}). In contrast to earlier studies, which assigned the $\nu_2(E_g)$ band to ca. 530 cm^{-1}, the splitting observed in α-[O_2][AuF$_6$] suggests that the $\nu_1(A_{1g})$ and $\nu_2(E_g)$ bands of the octahedral AuF$_6^-$ anion are very similar in frequency, accounting for the apparent absence of the $\nu_2(E_g)$ band in many AuF$_6^-$ salts. Attempts to verify the accidental coincidence of the $\nu_1(A_{1g})$ and $\nu_2(E_g)$ bands of [O_2][AuF$_6$] in HF solution by determining the depolarization ratio of $A_{1g} + E_g$ versus F_{2g} were unsuccessful because of the low solubility of [O_2][AuF$_6$] at ambient temperature. The published spectra of many AuF$_6^-$ salts in the solid state also exhibit relatively intense (77 to 93%) bands lying between the 581 cm^{-1} and the $\nu_1(A_{1g})$ bands, however, these lower frequency bands have frequently been attributed to factor-group splitting of the $\nu_1(A_{1g})$ band.

Although factor-group splitting of the $\nu_1(A_{1g})$ band may be anticipated for salts in which the crystallographic unit cell contains more than one asymmetric unit, it will not occur for crystal morphologies where $Z = 1$, such as α-$[O_2][AuF_6]$. Under C_i symmetry, the infrared-active $\nu_3(F_{1u})$ and $\nu_3(F_{1u})$ bands and the Raman- and infrared-inactive $\nu_6(F_{2u})$ band would likewise be reduced in symmetry to give nine A_u bands, all of which are infrared active but Raman-inactive as a consequence of the rule of mutual exclusion.

Another feature which supports the re-assignment of the $\nu_2(E_g)$ band is the relative intensities of the three Raman-active bands. The integrated intensity ratio $A_{1g}:E_g:F_{2g}$ is 66:100:28 for α-$[O_2][AuF_6]$ and can be compared with that of the previously assigned bands where the A_{1g} band was most intense, and the $\nu_2(E_g)$ band intensity generally did not exceed 5%. Although the relative intensities of the Raman-active bands of AuF_6^- contrast those of $[NO][OsF_6]$ (100:24:31),[320] $[NO][IrF_6]$ (100:26:62)[320] and $[NO][PtF_6]$ (100:37:54),[320] in which the anions are expected to have similar polarizabilities, the latter anions demonstrate that the $\nu_2(E_g)$ band of AuF_6^- is expected to have a significant intensity and that the $\nu_2(E_g)$ band intensity may increase along the fifth row of the periodic table. This contradicts an earlier hypothesis that the intensity of the $\nu_2(E_g)$ band is weakened by infringement of adiabatic conditions.[318,319]

4.3. Computational Results

The energy-minimized geometries, vibrational frequencies and electronic properties of KrF_2, KrF^+, $Kr_2F_3^+$ and the $[KrF][MF_6]$ ion pairs (M = P, As, Sb, Bi) have been investigated by use of the HF and LDF methods (see section 3.3).[23] These calculations have been extended, to include the $[KrF][AuF_6]$ ion pair, the AuF_6^- anion and the O_2^+ cation by use of the HF, MP2 and LDF methods. The SVWN, B3LYP and MPW1PW91 combinations of exchange and correlation functionals were investigated for $[KrF][AuF_6]$ and AuF_6^- with the MPW1PW91 method providing the best agreement with

the experimental results, particularly for the vibrational frequencies and Raman intensities of the [KrF][AuF$_6$] ion pair. Consequently, the LDF results referred to in the following discussion were determined by use of the MPW1PW91 method.

4.3.1. Geometries

4.3.1.1. The [KrF][AuF$_6$] Ion Pair

The energy-minimized geometries of [KrF][AuF$_6$] determined by use of the HF, MP2 and MPW1PW91 methods are summarized in Table 4.2, where they are compared with the structure of the ion pair determined by experiment. The [KrF][AuF$_6$] ion pair has a staggered conformation similar to those calculated for [KrF][MF$_6$] (M = Sb, Bi), where the F$_e$'-M--F$_b$--Kr dihedral angles are 45° (Structure IV).[23] The Kr-F$_t$ bond lengths determined by the HF (1.715 Å), MP2 (1.817 Å) and MPW1PW91 (1.830 Å) methods bracket the experimental value of 1.76(1) Å, with no one method clearly out-performing the others. Interestingly, the Kr-F$_t$ bond length in [KrF][AuF$_6$] determined by use of the HF method is significantly shorter than those estimated for [KrF][MF$_6$] (M = As, Sb, Bi), where this value ranged from 1.739 to 1.746 Å, and more closely resembles the value determined for the gas-phase free KrF$^+$ (1.717 Å).[23] The opposite was true for the MPW1PW91 method, for which the Kr-F$_t$ bond length more closely resembles the values calculated for the pnicogen series (1.857 - 1.867 Å) than for free KrF$^+$ (1.780 Å). For comparison, the free KrF$^+$ cation has a bond length of 1.774 Å at the MP2 level of theory, and is elongated by approximately 0.04 Å in the [KrF][AuF$_6$] ion pair, resembling the trends obtained when the LDF method is used. The Kr--F$_b$ bond lengths determined by the HF (2.064 Å), MP2 (2.015 Å) and MPW1PW91 (2.063 Å) methods are significantly shorter than the experimental value (2.15(1) Å), but are generally longer than those calculated for the [KrF][MF$_6$] (M = As, Sb, Bi) ion pairs (HF, 2.002 - 2.038 Å; MPW1PW91, 1.998 - 2.017 Å). The contracted Kr-F$_t$ and elongated Kr-F$_b$ bond lengths

determined for [KrF][AuF$_6$] relative to those of [KrF][MF$_6$] (M = As, Sb, Bi) are consistent with a greater fluoride ion affinity for AuF$_5$ than for AsF$_5$, SbF$_5$ and BiF$_5$. With the exception of the Au--F$_b$ bond length, which is overestimated by all three methods, the experimental Au-F bond lengths (1.869(13) - 1.902(11) Å) are bracketed by the shorter values obtained by use of the HF method (1.825 - 1.880 Å) and the longer values obtained from the MP2 (1.891 - 1.940 Å) and LDF (1.886 - 1.939 Å) calculations. All three methods are consistent in the ordering of the axial, equatorial and bridging Au-F bond lengths, which increase in the order: Au-F$_a$ < Au-F$_e$ < Au-F$_e$' < Au--F$_b$. The shorter Au-F$_a$ bond length is accounted for by the *trans*-influence of the fluorine bridge, and the elongation of F$_e$' with respect to F$_e$ (0.015 to 0.022 Å) may result from the Kr-F$_b$-Au bend, which brings the positively charged krypton atom in closer proximity to F$_e$' than to F$_e$. These differences could not be observed experimentally because the bond length uncertainties are relatively large and the ion-pair symmetry is lower (C_1). Intermolecular contacts may also affect the Au-F bond lengths to a minor extent, as inferred from their influence on the Kr--F$_b$--Au-F$_e$' torsion angle, which distorts the ion pair from its ideal eclipsed or staggered conformation.

The small deviation of the F$_t$-Kr--F$_b$ bond angle from linearity (175.4(7)°) is also found for the calculated geometries (175.4 - 177.1°), indicating that the bend is not solely a consequence of crystal packing. The underestimation of the experimental Kr--F$_b$--Au bond angle (125.3(7)°) by the HF (117.4°), MP2 (111.4°), and MPW1PW91 (115.3°) methods is consistent with the trends observed for [KrF][MF$_6$] (M = As, Sb, Bi).[23]

4.3.1.2. The AuF$_6^-$ Anion

The energy-minimized geometries of AuF$_6^-$ determined by use of the HF, MP2 and MPW1PW91 methods are summarized in Table 4.3, where they are compared with the structures of the anion determined in α- and β-[O$_2$][AuF$_6$]. In contrast to α-

$[O_2][AuF_6]$, where the anion exhibits a small distortion from octahedral geometry, the calculated structures of this anion were octahedral. This is consistent with the electronic t_{2g}^6 ground state of AuF_6^-, which is not expected to be stabilized by a Jahn-Teller distortion, and indicates that the distortion observed in the crystal structure of $[O_2][AuF_6]$ is induced by cation-anion or anion-anion interactions in the solid state. The average experimental Au-F bond length in α-$[O_2][AuF_6]$ (1.88(2) Å) was most accurately reproduced with the HF method (1.873 Å), whereas the values determined by the MP2 (1.938 Å) and MPW1PW91 (1.937 Å) methods were overestimated by *ca.* 0.05 Å.

4.3.1.3. The O_2^+ cation and O_2

Unlike $[KrF][AuF_6]$, KrF^+ and AuF_6^-, which have singlet ground state electronic configurations and are adequately treated using common theoretical methods (e.g. HF, MP2, LDF), O_2 and O_2^+ have triplet and doublet ground states, respectively, which reduce the reliability of these methods as a consequence of spin contamination. While this is not obvious, based on the reasonable bond lengths obtained for O_2 and O_2^+ (Table 4.4) when compared with experimental values (O_2, 1.20740(4);[321] O_2^+ 1.227 Å[317]), the calculated vibrational frequencies of these species clearly demonstrate the inadequacy of the HF, MP2 and LDF methods for these small open shell systems (see section 4.3.2.3). Symmetry breaking and electron correlation have been investigated for O_2^n (n = -1, 0, 1) using coupled cluster (CCSD) and quadratic configuration interaction (QCISD) techniques.[322] The CCSD and QCISD techniques predict O-O bond lengths ranging from 1.2016 to 1.2214 Å and 1.1083 to 1.1270 Å for O_2 and O_2^+, respectively, depending on the method and the basis set used, and are also consistent with the experimental values.

4.3.2. Vibrational Frequencies

The gas-phase vibrational frequencies of O_2^+, AuF_6^-, and the ion pair, $[KrF][AuF_6]$, have been determined by use of the HF, MP2, and MPW1PW91 methods.

Table 4.4. Calculated Bond Lengths and Vibrational Frequencies for O_2 and O_2^+

	O_2	O_2^+
Bond Lengths (Å)		
HF	1.157	1.061
MP2	1.224	1.156
MPW1PW91	1.208	1.117
CCSD/QCISD[b]	1.202 - 1.221	1.108 - 1.127
Experimental	1.20740(4)[c]	1.227[d]
Frequencies (cm^{-1})		
HF	2000	2536
HF (scaled)[a]	1791	2270
MP2	1452	1480
MPW1PW91	1709	2128
CCSD/QCISD[b]	1519 - 1672	1923 - 2028
Experimental	1580[e]	1801 - 1865[f]

[a] Multiplied by 0.8953 as suggested in ref 323. [b] The range of values was obtained from ref 322, which investigated the use of unconstrained electronic configurations. [c] From ref 321. [d] From ref 317. [e] From ref 321. The lower and upper limits of the O_2^+ vibrational frequency are defined by $[O_2]_2[NiF_6]$ (ref 228) and $[O_2][Sb_2F_{11}]$ (ref 142, 229, 230), respectively.

The frequencies discussed in the following sections are unscaled unless otherwise noted. For comparison, the stretching frequency of the free KrF^+ cation has been determined to be 651 cm^{-1} by the MP2 method and is lower than those obtained by both the HF (726 cm^{-1}) and MPW1PW91 (686 cm^{-1}) methods.[23]

4.3.2.1. The [KrF][AuF$_6$] Ion Pair

As previously observed for [KrF][MF$_6$] (M = As, Sb, Bi),[23] the strong bridging interaction between the cation and anion distorts the anion symmetry, which in turn, removes the two-fold and three-fold degeneracies of the E_g, F_{2g}, F_{1u} and F_{2u} vibrational modes of the octahedral anion and also introduces vibrational modes associated with the Kr--F$_b$--M bridge. This is also the case for [KrF][AuF$_6$], and with the use of optimized geometries determined by the HF, MP2 and MPW1PW91 methods, the vibrational mode descriptions of this ion pair are now interpreted in greater detail than in earlier reports (Table 4.5).[35,70] The optimized geometry of [KrF][AuF$_6$] is comparable with those of [KrF][SbF$_6$] and [KrF][BiF$_6$] in that the F$_e$-Au-F$_b$-Kr torsion angle is approximately 45°, *i.e.*, the cation assumes a staggered conformation (Structure IV) with respect to the equatorial fluorine atoms of the anion.[23] This is in contrast to the gauche conformation observed experimentally, which has a torsion angle of 13.6° and more closely resembles an eclipsed conformation. The eclipsed (Structure V) and staggered conformations both have C_s symmetry and 21 vibrational modes, all of which are expected to be Raman-active. The two C_s conformations differ in that the eclipsed conformation should exhibit 14 A' and 7 A" modes, whereas the staggered conformation should exhibit 13 A' and 8 A" modes. The dihedral angle is not expected to significantly affect the vibrational frequencies of the ion pair with, perhaps, the exception of the low-frequency torsional wagging of the F$_b$--Kr-F$_t$ group about the Au--F$_b$ bond.

Table 4.5. Experimental and Calculated Vibrational Frequencies[a] and Assignments for [KrF][AuF$_6$].

Expt[c,d]	HF[c]	Scaled HF	MP2	MPW1PW91	Assignments (C_s symmetry)[b]
672.0(1)	770.3(100)[26.3]	689.6	627.3(55.6)[25.5]	659.3(98.4)[22.0]	A' ν(AuF$_a$) + small ν(KrF$_t$)
650.3(31)	720.3(32.9)[163.8]	644.9	626.7(6.9)[96.3]	642.0(3.0)[116.8]	A' ν_s(AuF$_e$ – AuF'$_e$) + ν_s(AuF$_e$ – AuF'$_e$)
	720.2(19.5)[145.4]	644.8	624.8(2.4)[75.3]	640.2(3.6)[92.6]	A" ν_{as}(AuF'$_e$ – AuF$_e$) + ν_{as}(AuF$_e$ – AuF'$_e$)
600.2(100)	753.3(67.5)[115.9]	674.4	583.2(84.8)[124.5]	613.8(100)[150.6]	A" ν_s(KrF$_t$) – small ν(KrF$_b$)
595.6(92)	682.0(56.9)[77.5]	610.6	549.8(100)[0.4]	573.0(63.3)[3.0]	A' ν_s(AuF$_{2e}$ + AuF'$_{2e}$)
528.3(4)	679.2(30.9)[70.2]	608.1	556.5(84.0)[1.3]	566.0(47.7)[4.1]	A" ν_{as}(AuF$_e$ + AuF'$_e$) – ν_{as}(AuF$_e$ + AuF'$_e$)
391.9(1)	517.5(10.3)[308.6]	463.3	495.2(7.9)[297.9]	444.9(5.9)[248.3]	A' ν(AuF$_b$) – small ν(KrF$_b$)
391.9(1)	393.4(1.2)[205.9]	352.2	434.9(57.0)[9.5]	400.9(34.4)[17.0]	A' ν(KrF$_b$) – small ν(KrF$_t$)
277.0(1)	308.1(0.7)[2.8]	275.8	249.4(7.1)[7.9]	259.1(2.5)[9.1]	A' δ(F$_e$AuF$_e$) – δ(F'$_e$AuF'$_e$) pucker + δ(F$_t$KrF$_b$) i.p.
264.0(1)	301.3(0.0)[5.8]	269.8	247.3(0.4)[5.2]	252.5(0.2)[7.3]	A" δ (F$_t$KrF$_b$) o.o.p. + δ(F$_a$AuF$_b$) o.o.p. + δ(F$_e$AuF$_e$) – δ(F'$_e$AuF'$_e$)
	291.7(0.2)[3.3]	261.2	232.5(0.8)[2.3]	245.5(0.2)[3.1]	A' δ(F$_e$AuF$_e$) – δ(F'$_e$AuF'$_e$)
	272.2(0.2)[0.4]	243.7	226.2(0.6)[0.1]	231.0(0.8)[0.2]	A" δ(F$_t$KrF$_b$) o.o.p. + δ(F$_a$AuF$_b$) o.o.p. + δ(F$_e$AuF'$_e$) – δ(F$_e$AuF'$_e$)
	251.1(0.9)[0.5]	224.8	205.3(0.2)[0.2]	207.5(0.6)[0.3]	A" δ(F$_e$AuF$_e$') – δ(F$_e$AuF'$_e$) i.p. scissor + δ(F$_t$KrF$_b$) o.o.p.

Table 4.5. continued...

Expt[c,d]	HF[c]	Scaled HF	MP2	MPW1PW91	Assignments (C_s symmetry)[b]
232.1(12)	250.8(4.3)[2.0]	224.5	199.4(7.5)[1.2]	199.9(6.6)[0.7]	A' $\delta(F_aAuF_b)$ i.p. + (F_eAuF_e) + $\delta(F'_eAuF_e')$
225.0(21)	246.3(3.8)[0.8]	220.5	193.3(7.3)[0.6]	195.8(5.6)[0.5]	A" $\delta(F_tKrF_b)$ o.o.p. + (F_bAuF_a) o.o.p.
218.1(13)	244.1(4.9)[0.3]	218.5	189.0(10.7)[0.1]	192.2(7.3)[0.1]	A' $\delta(F_bAuF_a)$ i.p. + $\delta(F_eAuF_e)$ + $\delta(F'_eAuF'_e)$
163.0(2)	189.8(1.3)[6.1]	169.9	179.1(3.0)[4.0]	170.3(2.5)[3.5]	A' $\delta(F_tKrF_b)$ i.p.
	167.9(0.9)[2.2]	150.3	140.9(3.0)[1.3]	141.9(1.9)[1.7]	A" $\delta(F_tKrF_b)$ o.o.p.
133.3(4)	140.5(1.7)[8.3]	125.8	119.6(10.9)[1.9]	121.2(8.9)[2.1]	A' $\delta(F_tKrF_b)$ i.p. + $\delta(F_bAuF_a)$ i.p.
	63.5(0.4)[1.3]	56.9	74.9(1.6)[0.8]	62.4(1.6)[1.0]	A' $\delta(AuF_bKr)$ i.p.
	32.8(0.5)[0.1]	29.4	46.3(2.0)[0.0]	33.1(1.6)[0.0]	A" KrF_t torsion about AuF_b + (AuF_5) rock

[a] Frequencies are in cm^{-1}. [b] The abbreviations i.p. and o.o.p. are used to designate in-plane and out-of-plane vibrations, respectively. [c] Values in parentheses are calculated Raman intensities scaled to the most intense peak, which is given a value of 100 and values in brackets are calculated infrared intensities (km mol^{-1}). [d] Spectrum recorded at -78 °C. [e] Original values were multiplied by 0.8953 as suggested in ref 323.

Despite overestimation of the $Kr-F_t$ bond length, the $Kr-F_t$ stretching frequencies predicted by the MP2 (583 cm^{-1}) and MPW1PW91 (614 cm^{-1}) methods are in good agreement with the experimental value of 600 cm^{-1}. The frequency predicted by use of the HF method (753 cm^{-1}) is significantly higher than the experimental value, even when a scaling factor of 0.8953 is applied,[323] and may be partially attributed to the shorter $Kr-F_t$ bond length obtained by this method. One of the more notable shortcomings of the calculated spectra is the inconsistency of the Raman intensities for the $[KrF][AuF_6]$ ion pair. This likely arises because vibrational modes involving Au-F stretches for the distorted anion are expected to be highly polarizable so that the intensities of these modes, when compared with those involving the Kr-F stretches are highly dependant on the predicted geometries and, in particular, on the interactions between F_b and the KrF^+ and AuF_5 moieties. The MPW1PW91 method was the only calculation to determine the highly polarizable $Kr-F_t$ stretch to be the most intense band in the spectrum, whereas the HF method predicted this band to be as weak as 68%. As expected, the calculated $Kr--F_b$ stretching frequency (HF, 393; MP2, 435; MPW1PW91, 401 cm^{-1}) is at lower frequency than the $Kr-F_t$ stretch, and is lower than comparable modes in $[KrF][MF_6]$ (M = As, Sb, Bi), which range from 436 to 498 cm^{-1} depending on the ion pair and method used. This weaker $Kr--F_b$ interaction is consistent with a stronger fluoride ion affinity for AuF_5, however, a quantitative comparison is difficult to make because of the varying degree of vibrational coupling observed for the $Kr-F_t$ and $Kr--F_b$ vibrational modes in the calculated spectra. In contrast with the $[KrF][MF_6]$ (M = As, Sb, Bi) series, where the $M--F_b$ stretching frequency is lower than the $Kr--F_b$ stretching frequency,[23] the $Au--F_b$ mode is calculated to be approximately 40 to 120 cm^{-1} higher than the $Kr--F_b$ mode in $[KrF][AuF_6]$ and is also consistent with a greater degree of fluoride ion abstraction.

4.3.2.2. The AuF$_6^-$ Anion

The vibrational frequencies determined for the AuF$_6^-$ anion by use of the HF, MP2 and MPW1PW91 methods are summarized in Table 4.6, where they are compared with the anion vibrational frequencies reported for α-[O$_2$][AuF$_6$], β-[O$_2$][AuF$_6$], [Na][AuF$_6$] and [ClF$_6$][AuF$_6$]. The vibrational frequencies calculated by the HF method are in excellent agreement with the experimental values for the octahedral AuF$_6^-$ anion after the recommended correction factor of 0.8953 is applied.[323] As anticipated from the longer bond lengths determined by the MP2 (1.938 Å) and LDF (1.937 Å) methods, these methods consistently underestimate the vibrational frequencies of the anion. The ordering of the vibrational frequencies is invariant among the methods used (ν_3(F$_{1u}$) > ν_1(A$_{1g}$) > ν_2(E$_g$) > ν_4(F$_{1u}$) > ν_6(F$_{2u}$) > ν_5(F$_{2g}$)), with the exception of the ν_1(A$_{1g}$) and ν_2(E$_g$) modes, which are reversed when the MP2 method is used. When compared with the original assignment of the ν_2(E$_g$) mode, in which the difference between the ν_1(A$_{1g}$) and ν_2(E$_g$) bands was approximately 70 cm^{-1}, the reassigned spectrum of the AuF$_6^-$ anion of α-[O$_2$][AuF$_6$] ($\nu_1 - \nu_2 = 5$ cm^{-1}) is in much better agreement with the differences determined by the HF (4 cm^{-1}), MP2 (-8 cm^{-1}) and LDF (8 cm^{-1}) methods. While it is possible that ordering of the ν_1(A$_{1g}$) and ν_2(E$_g$) bands could be reversed in some AuF$_6^-$ salts, spectroscopic differentiation of these bands is anticipated to be difficult (unless splitting of the ν_2(E$_g$) band can be observed) because the integrated intensity ratios of the ν_1(A$_{1g}$) and ν_2(E$_g$) bands in α-[O$_2$][AuF$_6$] and other AuF$_6^-$ salts are similar and the two bands are generally coincident in solution, making polarization measurements ineffective.

Reassignment of the E$_g$ band is further supported by the calculated relative Raman intensities. The HF, MP2 and LDF methods predict the relative A$_{1g}$:E$_g$:F$_{2g}$ intensity ratios to be 100:83:15, 80:100:43, and 92:100:26, respectively, which is in reasonable agreement with the integrated relative intensities measured for α-[O$_2$][AuF$_6$] at -163 °C

Table 4.6. Correlation Table for the Calculated and Experimental Vibrational Modes of the AuF_6^- Anion under O_h and C_i Symmetries

O_h	C_i	Experimental[a]				Theoretical[a]			
		α-[O$_2$][AuF$_6$][b] (-163 °C)	β-[O$_2$][AuF$_6$] (25 °C)	[Na][AuF$_6$][c]	[ClF$_6$][AuF$_6$][d]	HF	HF (scaled)[e]	MP2	LDF
Raman Active									
v_1 A$_{1g}$	A$_g$	603(100)	597(100)[f]	605(100)	598(100)	684.8(100)	613.1	539.6(80)	569.3(92)
v_2 E$_g$	A$_g$	598(76)	594(sh)[f]	598(100)	591(85)	679.9(83)	608.7	551.6(100)	561.2(100)
	A$_g$	597(76)	592(sh)[f]						
v_5 F$_{2g}$	A$_g$	241(14)	229(28)[f]	245(50)	231(sh)	245.8(15)	220.1	192.1(20)	196.1(26)
	A$_g$	234(14)		238(50)	226(33)				
	A$_g$	219(14)							
Infrared Active									
v_3 F$_{1u}$	3A$_u$			628	653(s)	688.4[785]	616.3	606.8[347]	623.0[383]
v_4 F$_{1u}$	3A$_u$			259		304.8[11]	272.9	241.9[9]	257.9[15]
Inactive									
v_6 F$_{2u}$	3A$_u$					261.5	234.1	210.8	217.8

[a] Frequencies are in cm^{-1}. Raman intensities are given in parentheses and scaled with respect to the highest intensity peak, which is given a value of 100. Infrared intensities are given in brackets in units of km mol^{-1}. [b] Lattice modes were also observed at 189(20), 118,(6) and 85(4) cm^{-1}. [c] Raman bands are from ref 299 and infrared bands are from ref 158. [d] Data are from ref 145, which reports a Raman band at 527(6) cm^{-1} assigned to the v_2(E$_g$) mode of AuF$_6^-$. [e] Original values were multiplied by 0.8953 as suggested in ref 323. [f] Relative intensities for β-[O$_2$][AuF$_6$] are with respect to A$_{1g}$ + E$_g$ = 100. The peak intensities and those of associated shoulders are included in the total integrated intensity reported in parentheses.

(65:100:28), and contradicts the weak Raman intensity originally assigned to the $v_2(E_g)$ band of this salt.[35] The $v_3(F_{1u})$ stretching frequency is predicted to occur at 612.7 (HF), 608.8 (MP2) and 623.0 cm^{-1} (MPW1PW91) and is in good agreement with the experimental values (637 - 653 cm^{-1}).[70,145,146,158] Excellent agreement is found for the $v_4(F_{1u})$ band, which has been assigned in [Na][AuF$_6$] (259 cm^{-1})[158] and is calculated to occur at 271 (HF), 242 (MP2) and 258 cm^{-1} (MPW1PW91). Although the infrared intensity of the $v_3(F_{1u})$ band varies considerably among the HF (785 km mol^{-1}), MP2 (347 km mol^{-1}) and MPW1PW91 (383 km mol^{-1}) methods, this band is consistently more intense than the $v_4(F_{1u})$ band, which was calculated to have an intensity range of 9 to 15 km mol^{-1}. These values are consistent with the qualitative results obtained from the infrared spectrum of [Na][AuF$_6$].[158] Although the Raman- and infrared-inactive $v_6(F_{2u})$ band has been predicted to occur at 160 cm^{-1},[324] the HF (262 cm^{-1}), MP2 (211 cm^{-1}), and MPW1PW91 (218 cm^{-1}) methods predict higher frequencies. The band reported at *ca.* 530 cm^{-1} in the Cs$^+$,[144,145,154] ClF$_2^+$,[145] ClOF$_2^+$,[145] ClF$_4^+$,[145] ClF$_6^+$ [145] and Xe$_2$F$_3^+$ [35,70,158] salts, which had been previously assigned to the E$_g$ mode, is possibly the $2v_6$ ($2F_{2u} = A_{1g}$ + E$_g$ + [F$_{1g}$] + F$_{2g}$) overtone. This overtone, which is expected to be Raman-active because the direct product, $F_{2u} \otimes F_{2u}$, contains the A$_{1g}$, E$_g$ and F$_{2g}$ representations, should occur at *ca.* 520 cm^{-1}, based on the infrared spectrum of [Na][AuF$_6$],[158] or at 484 to 610 cm^{-1}, based on the theoretical values obtained in this study (the upper limit, 610 cm^{-1}, determined with the HF method, is reduced to 543 cm^{-1} when scaled by 0.8953[323]). The low intensity of this band is consistent with the low intensities of overtones and combination bands that are normally encountered for Raman spectra. An alternative explanation for this band is that it results from an impurity, which would account for the intensity variations reported for [Xe$_2$F$_3$][AuF$_6$] (12% to weak)[35,70,158] and [Cs][AuF$_6$] (28% to very weak).[144,146,154,299]

4.3.2.3. The O_2^+ Cation and O_2

The O-O stretching frequencies of O_2 and O_2^+ are shown to be very sensitive to the computational method used, with the magnitude of the variation being so large that comparison with the experimental values provides little insight. For example, the stretching frequency of O_2 was calculated to be 2000, 1452 and 1709 cm^{-1} by use of the unrestricted HF, MP2 and MPW1PW91 methods, respectively, which are in poor agreement with the experimental value (1580 cm^{-1}).[321] Likewise, the values 2536 (HF), 1480 (MP2) and 2128 (MPW1PW91) cm^{-1} calculated for O_2^+ are inaccurate despite the large vibrational frequency range exhibited for O_2^+ salts (1801 - 1865 cm^{-1}). The difficulty in obtaining accurate vibrational frequencies is a consequence of electronic spin contamination arising from the triplet and doublet ground states of O_2 and O_2^+, respectively. Consequently, the CCSD and QCISD methods provide superior results, with O_2 and O_2^+ vibrational frequencies ranging from 1519 to 1672 cm^{-1} and 1923 to 2028 cm^{-1},[322] respectively, on account of their treatment of the spin contamination and symmetry relaxation.

4.4. Variations of the O_2^+ Stretching Frequency in the Solid State

The vibrational frequency of O_2^+, which ranges from 1801 cm^{-1} in $[O_2]_2[NiF_6]$[228] to 1865 cm^{-1} in $[O_2][Sb_2F_{11}]$,[142,229,230] is significantly higher than that of molecular O_2 (1580 cm^{-1})[321] because of the reduced anti-bonding contribution in the ground state of O_2^+ ($\sigma_g^2\sigma_u^{*2}\sigma_g^2\pi_u^4\pi_g^{*1}$) when compared with that of O_2 ($\sigma_g^2\sigma_u^{*2}\sigma_g^2\pi_u^4\pi_g^{*2}$). Although the higher formal bond order in O_2^+ (b.o., 2.5) relative to that of O_2 (b.o., 2) reduces the O-O bond length, the magnitude of this contraction may, like the O_2^+ vibrational frequency, have some dependence on the nature of the anion. It has recently been suggested that the range in the O_2^+ vibrational frequency results from incomplete charge transfer between the anion and the cation and that in highly coloured salts, such as $[O_2][RhF_6]$, the anion

charge may be reduced by up to 10% when compared with that of $[O_2][SbF_6]$, which was considered to be completely ionic.[67] Although the intense colours of some transition metal dioxygenyl salts may arise from incomplete charge transfer, a detailed survey of the vibrational frequencies of the known O_2^+ salts indicates that the frequency shifts are not a reliable measure of this phenomenon. This is best supported by the low-lying O_2^+ vibrational frequency in $[O_2][AuF_6]$ (1831 to 1837 cm^{-1}), which is intermediate with respect to those of the highly coloured O_2^+ salts of PtF_6^- (1838 cm^{-1}), RuF_6^- (1838 cm^{-1}), RhF_6^- (1825 cm^{-1}) and PdF_6^- (1819 cm^{-1}). Significant charge transfer to form the neutral constituents is unlikely for $[O_2][AuF_6]$ because the salt is pale yellow-green in colour, and the calculated electron affinity of the currently unknown radical, AuF_6 (> -753 kJ mol^{-1}),[325] is significantly greater than those of PtF_6 (-675(33) kJ mol^{-1}),[326] RuF_6 (-624(30) kJ mol^{-1}),[326] RhF_6 (-588 kJ mol^{-1} (calc.)),[327] PdF_6 (-588 kJ mol^{-1} (calc.)).[327] The intense colouration of $[O_2][MF_6]$ (M = Pt, Rh, Ru, Pd) may more appropriately reflect the ability of these charge transfer reactions to take place, yielding a neutral hexafluoride with appreciable stability. This is consistent with the thermal decompositions of $[O_2][MF_6]$ (M = Pt, Ru, Rh, As, Sb, Bi) and $[O_2][M_2F_{11}]$ (M = Sb, Nb, Ta, V), which have been shown by mass spectrometry to proceed by eq 4.6 - 4.8.[328,329] The observation of $O_2F\cdot$ above

$$[O_2][MF_6] \rightarrow O_2 + MF_6 \quad (M = Pt, Ru, Rh) \tag{4.6}$$

$$[O_2][MF_6] \rightarrow O_2 + \tfrac{1}{2}F_2 + MF_5 \quad (M = As, Sb, Bi) \tag{4.7}$$

$$[O_2][M_2F_{11}] \rightarrow O_2 + \tfrac{1}{2}F_2 + 2MF_5 \quad (M = Sb, Nb, Ta) \tag{4.8}$$
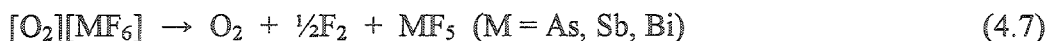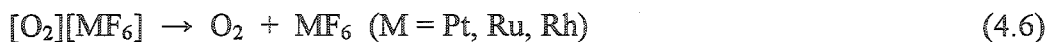
samples of $[O_2][AsF_6]$ by Raman spectroscopy at -142 to -7 °C,[330] suggests that interactions between O_2^+ and anions, which do not form neutral hexafluorides, proceed by fluoride ion transfer to form stable pentafluorides and the $O_2F\cdot$ radical (eq 4.9) before undergoing further decay to O_2 and F_2. The relative constancy of the O_2^+ stretching

$$[O_2][MF_6] \rightarrow O_2F\cdot + MF_5 \tag{4.9}$$

frequency in the MF_6^- (M = P, As, Sb, Bi).series (1849 - 1863 cm^{-1}) and the much lower frequency observed for $[O_2][AuF_6]$ also indicate that the stretching frequency is not influenced by the competing fluoride affinities of O_2^+ and the parent pentafluorides (PF$_5$, AsF$_5$, SbF$_5$, BiF$_5$), as illustrated by resonance Structures VI - VIII, and suggests that the contributions of Structures VII and VIII are minimal in the solid state.

$$O_2^+ \; MF_6^- \; \leftrightarrow \; O\text{-}O\text{---}F\text{---}MF_5 \; \leftrightarrow \; O\text{-}O\text{-}F \; MF_5$$

$$\text{VI} \qquad\qquad \text{VII} \qquad\qquad \text{VIII}$$
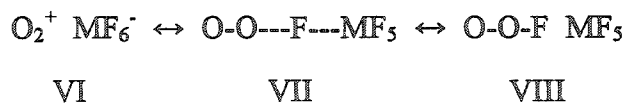
A detailed review of the vibrational frequencies of the dioxygenyl salts suggests that the O_2^+ vibrational frequency is strongly influenced by the valence electron configuration of the central atom of the anion and, to a lesser extent, by the electron affinity of the neutral fluoride species. In general, the O_2^+ vibrational frequency is highest when the central atom of the anion has a closed shell electron configuration (i.e., d^0 or p^0) as illustrated by the pentavalent group 5 (1853 - 1858 cm^{-1})[142,230] and group 15 (1849 - 1865 cm^{-1})[142,229,230,291,292] fluoro-anion salts, $[O_2][GeF_5]$ (1841-1849 cm^{-1}),[306] and $[O_2][BF_4]$ (1868, 1866 cm^{-1}).[307] As noted by Bartlett,[67] there appears to be a significant difference between the behaviour of the period 5 and period 6 transition metals, however, the O_2^+ vibrational frequency decreases systematically along both periods as the occupation of the d-orbitals increases (period 5: NbF$_6^-$, 1853 cm^{-1} [142,230] > RuF$_6^-$, 1838 cm^{-1} [142,230] > RhF$_6^-$, 1825 cm^{-1} [142,230] > PdF$_6^-$, 1819 cm^{-1} [230]; period 6: PtF$_6^-$, 1838 cm^{-1} [142,230] > AuF$_6^-$, 1835 cm^{-1} [35,70,142,230]). The similarity between the O_2^+ frequencies in the PtF$_6^-$ and AuF$_6^-$ salts can be attributed to the stability of the fully paired t_{2g}^6 electron configuration of AuF$_6^-$, which does not favour transfer of electron density to the cation. Unfortunately, the O_2^+ salts of OsF$_6^-$ and IrF$_6^-$ have not been synthesized, so a complete comparison of O_2^+ salts of both periods is not possible at this time. Likewise, the AgF$_6^-$ anion is unknown, so the effect of filling the t_{2g} molecular orbital in this period cannot be

assessed. The charge density on the anion also appears to have a pronounced effect on the O_2^+ vibrational frequency as demonstrated by the low values observed for the dianion salts of MnF_6^{2-} (1805 cm^{-1})[228] and NiF_6^{2-} (1801 cm^{-1}),[228] and the higher value observed for $[O_2]_2[Ti_7F_{30}]$ (1857 cm^{-1}),[303] where the anion is much larger and the charge more dispersed. The influence of anion charge density is also reflected, to a lesser extent, in a comparison among the singly charged MF_6^- and $M_2F_{11}^-$ salts (M = Sb, Nb), where the O_2^+ vibrational frequency is 3 to 5 cm^{-1} higher for the $M_2F_{11}^-$ salts.[142,230]

Although the electronic nature of the anion may be further influenced by the relative orientations of the cation and anion in the crystallographic unit cell, quantifying these effects is encumbered by the limited discussion of ion-contact distances and angles for the salts, which have been investigated crystallographically. The relevance of these contributions are demonstrated by the decrease in the O_2^+ vibrational frequency upon cooling β-$[O_2][AuF_6]$, which is consistent with unit cell contraction resulting in closer ion contacts, and the higher O_2^+ vibrational frequency observed in α-$[O_2][AuF_6]$, where the orientations of the two ions are fixed. A similar effect has been observed when cooling $[O_2][AsF_6]$, where a sharp increase in the O_2^+ vibrational frequency is observed at -3 °C (phase I $\rightarrow$ II transition) and a gradual decrease of this vibrational frequency is observed upon further cooling from -3 to -82 °C.[291,292]

4.5. Conclusions

The crystal structure of $[KrF][AuF_6]$ has been shown to be most similar to those of $[KrF][AsF_6]$ and $[KrF][SbF_6]$ with respect to the Kr-F$_t$ and Kr--F$_b$ bond lengths. The structure of the ion-pair was reproduced with reasonable accuracy by use of the HF, MP2 and MPW1PW91 methods, however, the MPW1PW91 results were clearly superior for the calculation of vibrational frequencies and intensities. Unfortunately, the comparison of the X-ray structures of $[KrF][MF_6]$ (M = As, Sb, Au) does not resolve the ordering of

the fluoride ion affinity strength of AsF_5, SbF_5 and AuF_5, however, analysis of the vibrational frequencies determined by the HF, MP2 and MPW1PW91 methods does support a fluoride ion affinity for AuF_5 that exceeds those of AsF_5 and SbF_5.

The α-β phase transition in $[O_2][AuF_6]$ has been shown, by Raman spectroscopy, to occur between -114 and -118 °C. The reduced crystallographic symmetry in the α-phase has the effect of ordering the O_2^+ cation and has allowed the determination of the O_2^+ bond length without recourse to a disorder model. The reduced crystallographic symmetry has also resulted in the reassignment of the $v_2(E_g)$ mode of AuF_6^-, and is supported by the frequencies and intensities obtained from electronic structure calculations. Comparison of the O_2^+ vibrational frequencies of known dioxygenyl salts reveals that this frequency generally decreases with increasing population of the valence d-orbitals of the central metal anion. Cation-anion contact distances and orientations are anticipated to play a minor, but significant, role in the O_2^+ vibrational frequency as indicated by the variable temperature studies of $[O_2][AuF_6]$ and $[O_2][AsF_6]$.

CHAPTER 5

STRUCTURAL CHARACTERIZATION OF XeF_2
AND THE XeF^+ CONTAINING SALTS
[XeF][MF$_6$] (M = As, Sb, Bi) AND [XeF][M$_2$F$_{11}$] (M = Sb, Bi)

5.1. Introduction

Xenon difluoride is a fluoride ion donor and reacts with a large number of strong Lewis acid fluoride ion acceptors. The latter mainly consist of transition metal and main-group pentafluorides, forming 1:1, 1:2 and 2:1 adducts that are best described as salts having the formulations [XeF][MF$_6$] (M = As,[68,69] Sb,[68] Bi,[41] Ru,[69] Os,[69] Ir,[69] Pt[69]), [XeF][M$_2$F$_{11}$] (M = Sb,[68,245] Bi,[41] Ru,[69] Ir,[69] Pt,[69] Nb,[68] Ta[68,245]) and [Xe$_2$F$_3$][M$_2$F$_{11}$] (M = As,[68,69,93] Sb,[69] Ru,[69] Os,[69] Ir,[69] Pt[69]).

The crystal structures of [Xe$_2$F$_3$][AsF$_6$][91,93,277] and [Xe$_2$F$_3$][SbF$_6$][91] have shown that the cations and anions are well separated in these salts, exhibiting only weak interactions that are similar to those observed between the Kr$_2$F$_3$$^+$ cation and its counter anions in [Kr$_2$F$_3$][SbF$_6$]·KrF$_2$, [Kr$_2$F$_3$]$_2$[SbF$_6$]$_2$·KrF$_2$ and [Kr$_2$F$_3$][AsF$_6$]·[KrF][AsF$_6$] (see section 3.2.2.3).[23] The weak interionic interactions that have been inferred from the crystal structures of the Xe$_2$F$_3$$^+$ salts are supported by their vibrational spectra, which exhibit bands consistent with octahedral anions and V-shaped cations.[35,68,69,91] The absence of strong directional cation-anion interactions is attributed to the coordinatively saturated Xe(II) centres and low charge density of the large cation.

In contrast, the XeF^+ cation exhibits pronounced Lewis acid properties as a consequence of the localization of the positive charge on the coordinatively unsaturated xenon atom. The acidic properties of this cation have been demonstrated by the preparation of strong Lewis acid-base adducts between XeF^+ and a broad range of nitriles,[94-96,98] perfluoro-pyridines,[96] s-trifluorotriazene,[98] and perfluorodiazenes.[97] The Lewis acidity of XeF^+ is also responsible for strong cation-anion interactions that are prevalent among the XeF^+ salts in the solid state, even when the counter anions are derived from extremely strong Lewis acids such as SbF_5 or Sb_2F_{10}. By analogy with the $[KrF][MF_6]$ salts, the Raman spectra of the $[XeF][MF_6]$ salts do not exhibit bands that are characteristic of a diatomic cation and an octahedral anion, but rather exhibit bands consistent with a fluorine bridged ion pair in which the anion is of C_{4v} or lower symmetry.[41,69] Although the vibrational spectra of the $M_2F_{11}^-$ anions are, in themselves, more complex than those of octahedral MF_6^- anions, the strong cation-anion interactions introduce additional complexity to the spectra of the $[XeF][M_2F_{11}]$ salts.[41,64,68,69] The crystal structures of $[XeF][AsF_6]$,[72] $[XeF][RuF_6]$[71] and $[XeF][Sb_2F_{11}]$[73,331] have been determined and confirm the bridged structures propsed by vibrational spectroscopy.

The strong cation-anion bridging interactions in the $[XeF][MF_6]$ and $[XeF][M_2F_{11}]$ salts, and their krypton analogues (see Chapters 3 and 4), provide a unique opportunity to qualitatively assess the fluoride ion acceptor properties of MF_5 and M_2F_{10}. Based on the anticipation that the ionic character and $Xe-F_t$ stretching frequencies of these salts should increase as the fluoride ion acceptor properties of the parent Lewis acids increase, the relative fluoride ion acceptor strengths of the group 15 pentafluorides have been predicted to increase in the order $AsF_5 \approx BiF_5 < SbF_5$.[41] The qualitative results obtained by this method are in general agreement with the enthalpies of fluoride ion attachment recently calculated for the group 15 perfluorides by use of the near local

density functional method,[46] which supercedes an earlier and less extensive scale,[48] and predicts the fluoride ion affinity order $PF_5 < AsF_5 < BiF_5 < SbF_5 < Bi_2F_{10} < Sb_2F_{10}$ (Table 1.2). Although the $Xe\text{-}F_b$ stretching frequency is expected to be more sensitive to variations in the fluoride ion acceptor properties of the parent Lewis acid because of its direct involvement in the cation-anion bridge, the lower frequency and weaker intensity of this vibrational mode often complicates its assignment. The general correlation between stretching frequency and bond length for a given bond type has recently permitted variations among the $Kr\text{-}F_t$ and $Kr\text{-}F_b$ bond lengths of the $[KrF][MF_6]$ (M = As, Sb, Bi, Au) ion pairs to be used to assess the relative fluoride ion affinities of the parent pentafluorides (see Chapters 3 and 4).[23,130] Although the $Kr\text{-}F_t$ bond lengths were not significantly different in these salts, the variations in $Kr\text{-}F_b$ bond lengths indicated that BiF_5 is a weaker fluoride ion acceptor than AsF_5, SbF_5 and AuF_5.[23,130] An earlier comparison of the $Xe\text{-}F_t$ and $Xe\text{-}F_b$ bond lengths and their assigned vibrational frequencies for $[XeF][RuF_6]$ and $[XeF][Sb_2F_{11}]$ has suggested that correlations among the bond lengths, vibrational frequencies and Lewis acidities of the parent Lewis acids also exist for the XeF^+ salts.[68] Unfortunately, the large bond length uncertainties in the reported structures of $[XeF][RuF_6]$[71] and $[XeF][Sb_2F_{11}]$[73,331] and the limited number of species available for comparison at the time prevented the correlation from being firmly established. The crystal structure of $[XeF][AsF_6]$[72] has since been reported, but when considered along with $[XeF][RuF_6]$[71] and $[XeF][Sb_2F_{11}]$,[73,331] the large bond length uncertainties of the latter species still do not allow a qualitative assessment of the fluoride ion acceptor properties of AsF_5, RuF_5 and Sb_2F_{10}.

The correlation between the $Xe\text{-}F_t$ and $Xe\text{-}F_b$ bond lengths and the fluoride ion acceptor properties of the group 15 perfluorides have been investigated in greater detail in the present work by the precise determinations of the X-ray crystal structures of

[XeF][MF$_6$] (M = As, Sb, Bi) and [XeF][M$_2$F$_{11}$] (M = Sb, Bi). The bonding and electronic properties of the [XeF][MF$_6$] (M = As, Sb, Bi) salts have also been investigated by use of electronic structure calculations, which have permitted more detailed vibrational assignments than available in the past and the evaluation of atomic charges, Mayer bond orders and Mayer valencies for these ion pairs.

5.2. Results and Discussion

5.2.1. Syntheses of [XeF][MF$_6$] (M = As, Sb, Bi) and [XeF][M$_2$F$_{11}$] (M = Sb, Bi)

Xenon difluoride acts a fluoride ion donor towards the strong Lewis acids AsF$_5$,[68,69] SbF$_5$,[68] BiF$_5$,[41] Sb$_2$F$_{10}$[68,245] and Bi$_2$F$_{10}$.[41] The [XeF][MF$_6$] (M = As, Sb, Bi) salts described in the present study were prepared by dissolving 1:1 molar ratios of XeF$_2$ and the appropriate pnicogen pentafluoride in anhydrous HF solvent. Crystals of these salts were obtained by slowly cooling the HF solutions, followed by the removal of the solvent as previously described.[130]

The salt, [XeF][Sb$_2$F$_{11}$], was prepared by the direct reaction of XeF$_2$ with excess SbF$_5$.[245] Single crystals of [XeF][Sb$_2$F$_{11}$] were obtained by allowing an SbF$_5$ solution of the salt to cool from 45 °C to ambient temperature over the course of several days. The salt, [XeF][Bi$_2$F$_{11}$], was prepared in a similar fashion by allowing a 1:2 molar ratio of XeF$_2$ and BiF$_5$ to react in anhydrous HF solvent.[41] Crystals suitable for an X-ray structure determination were obtained by slowly removing the solvent under vacuum. An attempt to isolate crystalline [XeF][Bi$_2$F$_{11}$] by slowly cooling a dilute HF solution of 2BiF$_5$:XeF$_2$ resulted in the isolation of [XeF][BiF$_6$], which is consistent with the notion that the equilibrium between Bi$_2$F$_{11}^-$ and BiF$_5$/BiF$_6^-$ (eq 5.1), shifts to the right when the

$$Bi_2F_{11}^- \; \rightleftharpoons \; BiF_5 + BiF_6^- \qquad\qquad (5.1)$$
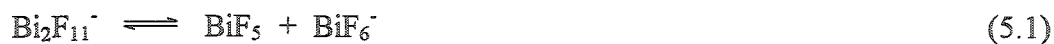
concentration of the solution is low. The isolation of [XeF][BiF$_6$] under dilute conditions is also favoured by its lower solubility relative to that of [XeF][Bi$_2$F$_{11}$].[41]

Attempts to prepare [XeF][As$_2$F$_{11}$] by the reaction of XeF$_2$ with neat AsF$_5$ at ambient temperature or a two-fold excess of AsF$_5$ dissolved in anhydrous HF were unsuccessful. The inability to isolate [XeF][As$_2$F$_{11}$] contrasts with the ability to isolate the analogous [XeF][Sb$_2$F$_{11}$] and [XeF][Bi$_2$F$_{11}$] salts, but may be accounted for by the greater volatility of AsF$_5$ with respect to SbF$_5$ and BiF$_5$, and the weaker Lewis acidity of AsF$_5$ relative to SbF$_5$.[332] Although cryoscopy and conductimetric studies[333] have shown that As$_2$F$_{11}^-$ is the dominant anionic species in HF solution at *ca.* -83 °C, the inability to observe this anion in HF solution by low-temperature ^{19}F NMR spectroscopy implies that the anion undergoes rapid exchange with AsF$_5$ and AsF$_6^-$ according to eq 5.2. Moreover,

$$As_2F_{11}^- \rightleftharpoons AsF_5 + AsF_6^- \qquad\qquad (5.2)$$

the equilibrium shown in eq 5.2 is shifted to the right at higher temperatures.[332] Thus, attempts to crystallize [XeF][As$_2$F$_{11}$] by cooling HF solutions of XeF$_2$ and AsF$_5$ are likely to be unsuccessful owing to early crystallization of [XeF][AsF$_6$]. The larger lattice potential calculated for this salt (558 kJ mol^{-1}) relative to [XeF][As$_2$F$_{11}$] (480 kJ mol^{-1})[309] may also be a contributing factor to the preferential crystallization of [XeF][AsF$_6$]. This explanation also accounts for the inability to prepare [XeF][As$_2$F$_{11}$] by the direct reaction of XeF$_2$ with AsF$_5$, and the stability of As$_2$F$_{11}^-$ salts containing larger counter cations, *i.e.*, (CH$_3$S)$_2$CSH$^+$,[334] Cl$_3$PH$^+$,[335] Br$_3$PH^{+}[335] and (*m*-CF$_3$C$_6$H$_4$)(C$_6$H$_5$)CF$^+$.[336]

5.2.2. X-Ray Crystal Structures of XeF$_2$, [XeF][MF$_6$] (M = As, Sb, Bi) and [XeF][M$_2$F$_{11}$] (M = Sb, Bi)

The single crystal X-ray structures of XeF$_2$ (Figure 5.1) [XeF][AsF$_6$] (Figure 5.2), [XeF][SbF$_6$] (Figure 5.3) [XeF][BiF$_6$] (Figure 5.4), [XeF][Sb$_2$F$_{11}$] (Figure 5.5) and [XeF][Bi$_2$F$_{11}$] (Figure 5.6) were determined at -173 °C. The unit cell parameters and refinement statistics for these species are given in Table 5.1 where they are compared with those reported previously XeF$_2$, [XeF][AsF$_6$], [XeF][RuF$_6$] and [XeF][Sb$_2$F$_{11}$].
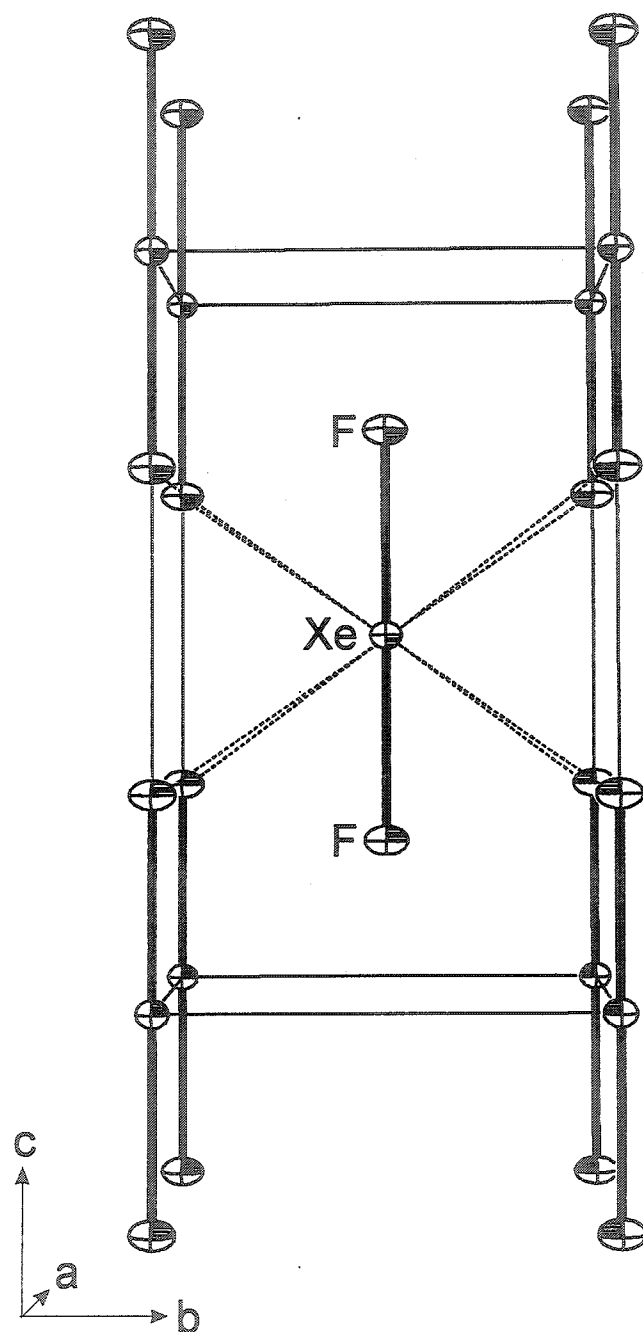
Figure 5.1. Packing diagram of XeF_2 viewed along the a-axis, showing the eight intermolecular $Xe\cdots F$ contacts (dashed lines). Thermal ellipsoids are shown at the 50% probability level.

Figure 5.2. The crystal structure of (a) the structural unit of [XeF][AsF$_6$] and (b) the packing arrangement of this salt viewed along the *b*-axis. Thermal ellipsoids are shown at the 50% probability level.

a

b
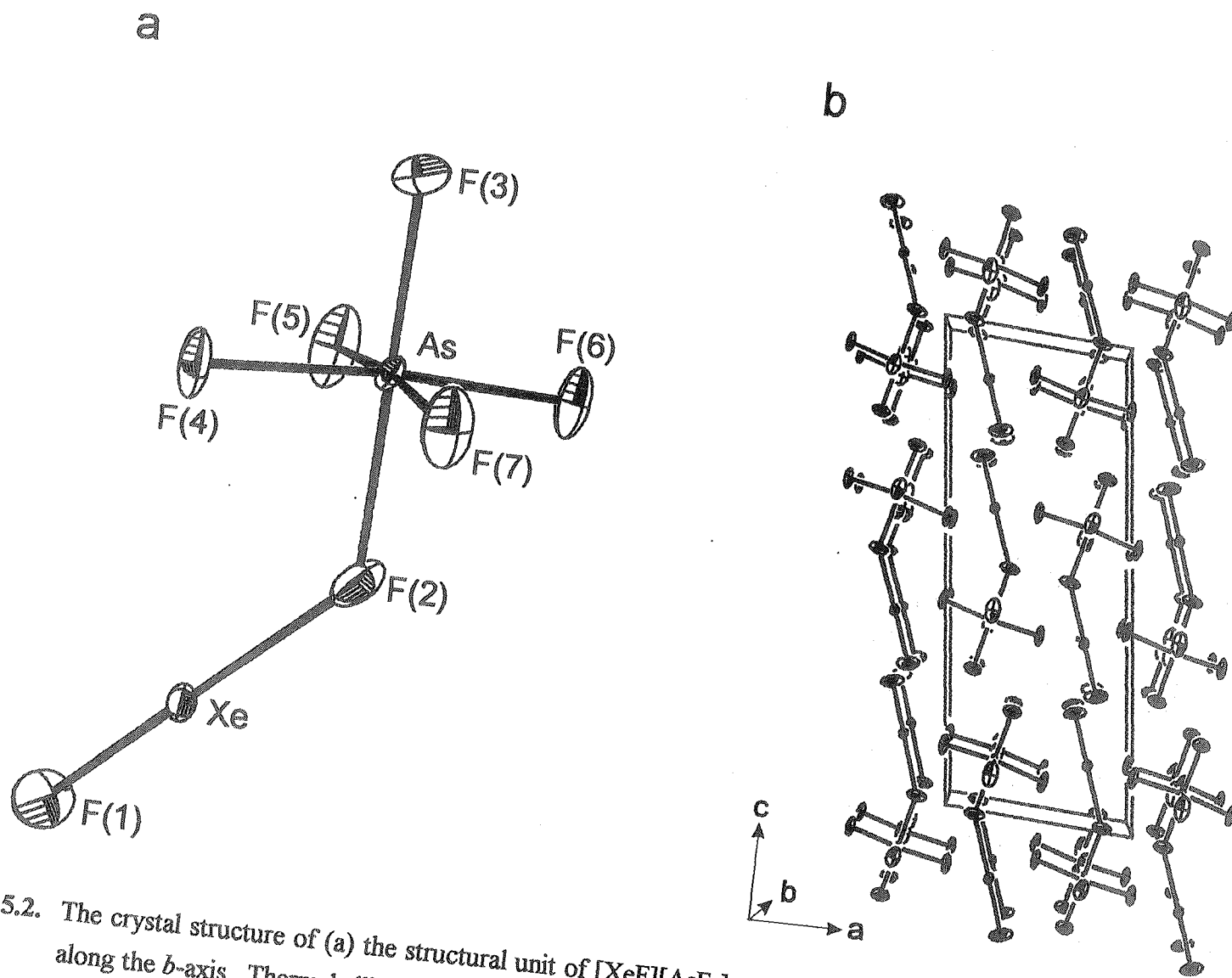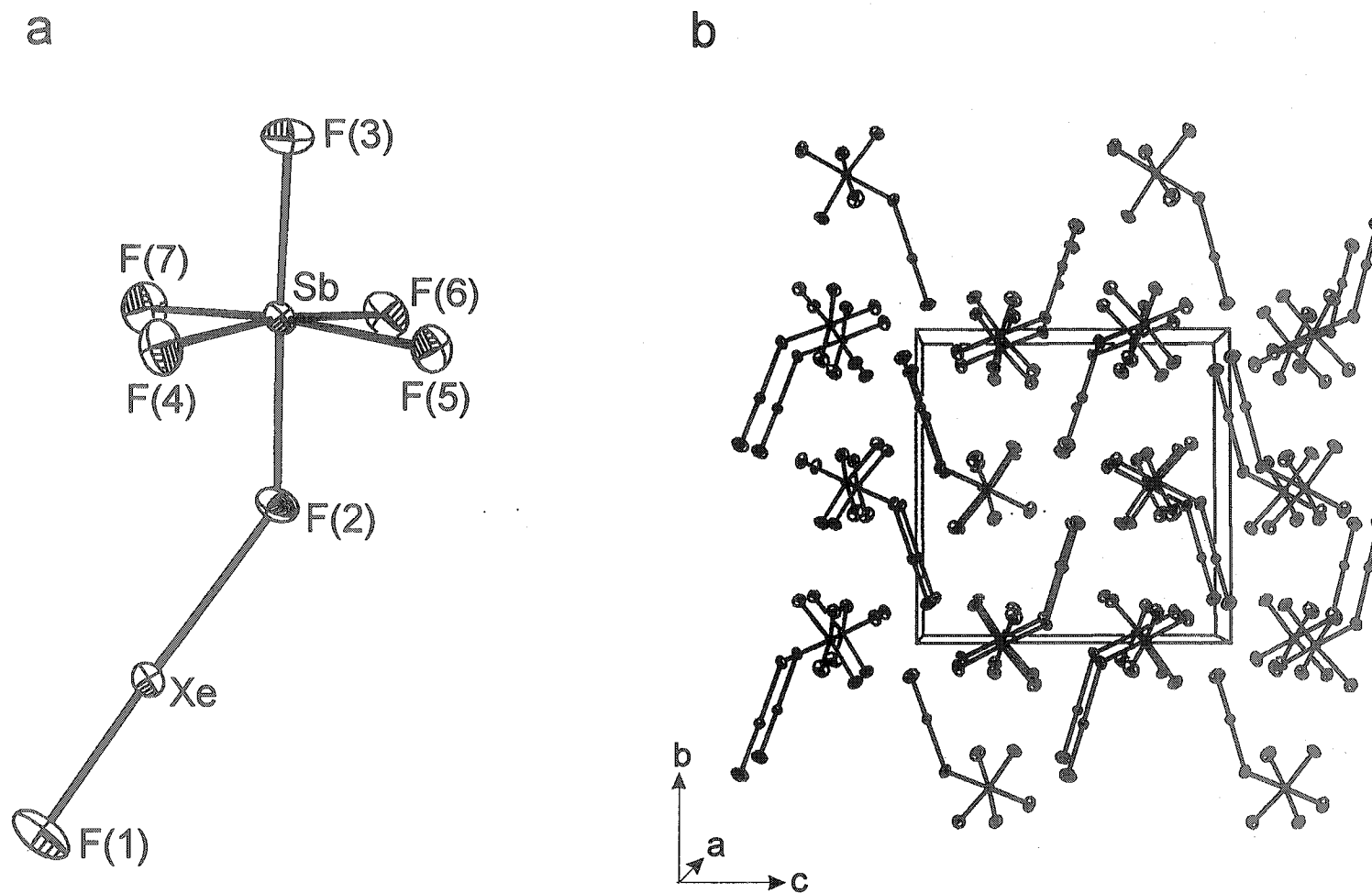
Figure 5.3. The crystal structure of (a) the structural unit of [XeF][SbF$_6$] and (b) the packing arrangement of this salt viewed along the a-axis. Thermal ellipsoids are shown at the 50% probability level.
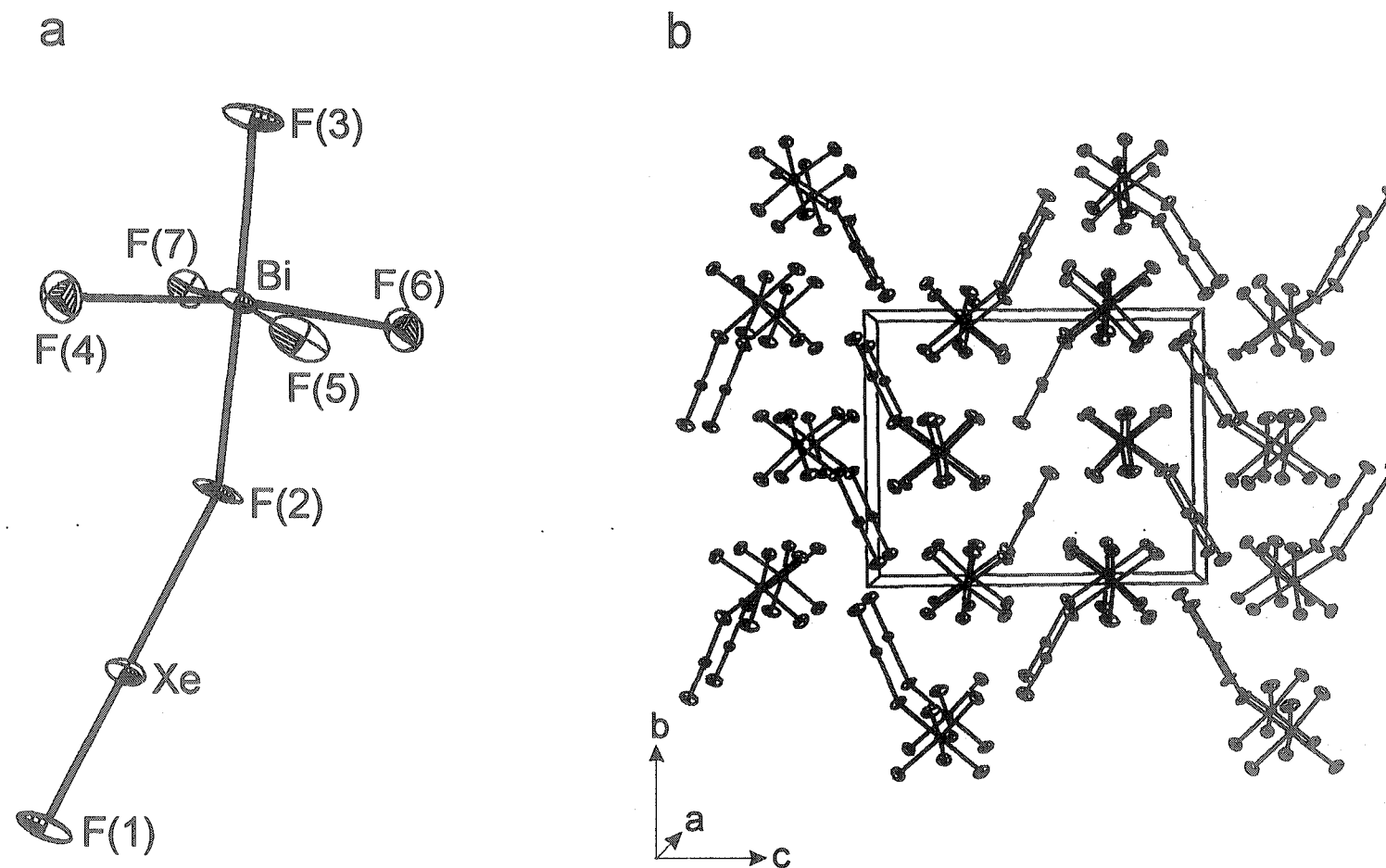
Figure 5.4. The crystal structure of (a) the structural unit of [XeF][BiF$_6$] and (b) the packing arrangement of this salt viewed along the a-axis. Thermal ellipsoids are shown at the 50% probability level.
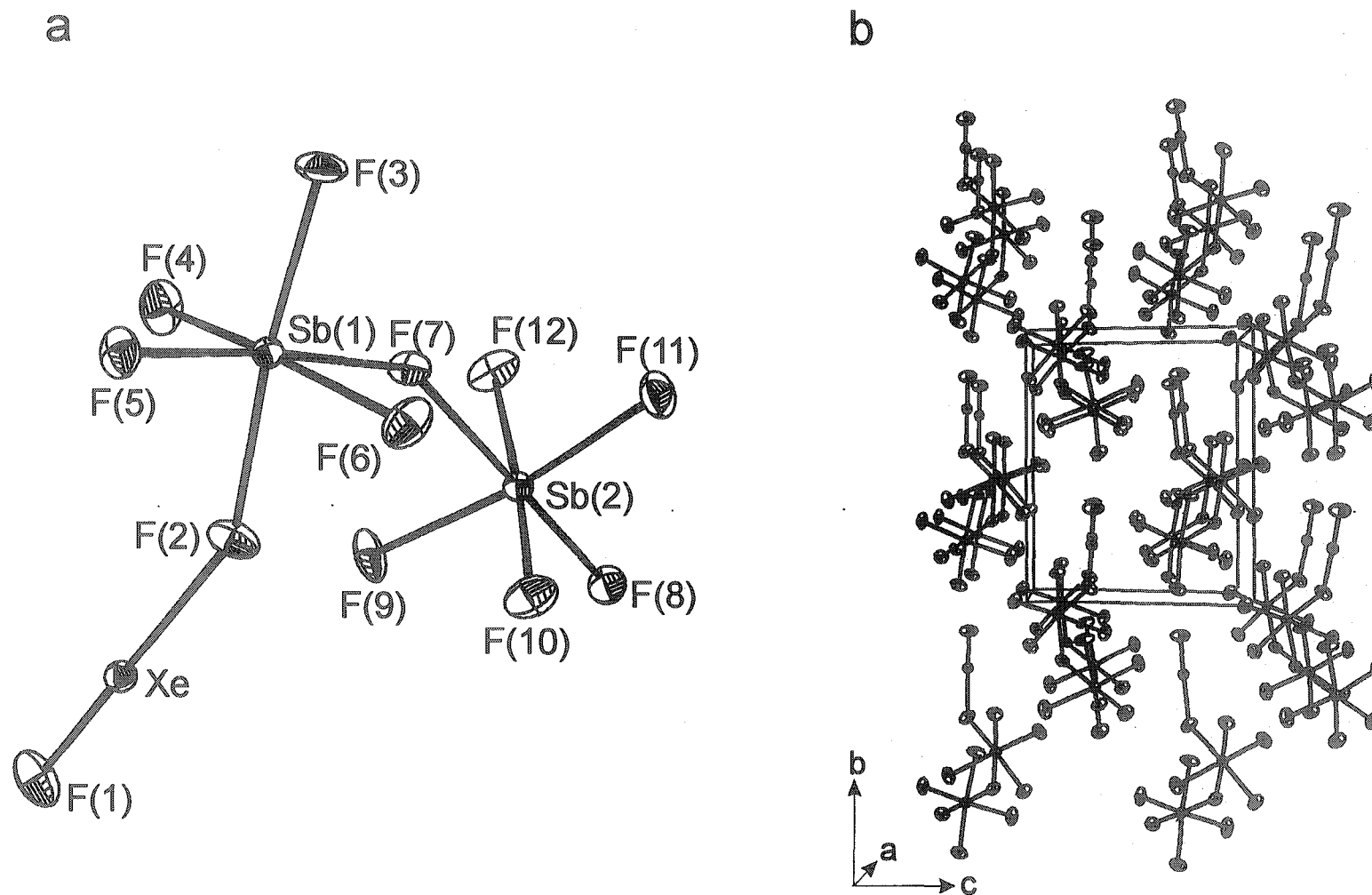
Figure 5.5. The crystal structure of (a) the structural unit of [XeF][Sb$_2$F$_{11}$] and (b) the packing arrangement of this salt viewed along the a-axis. Thermal ellipsoids are shown at the 50% probability level.

a

b

c

a

b
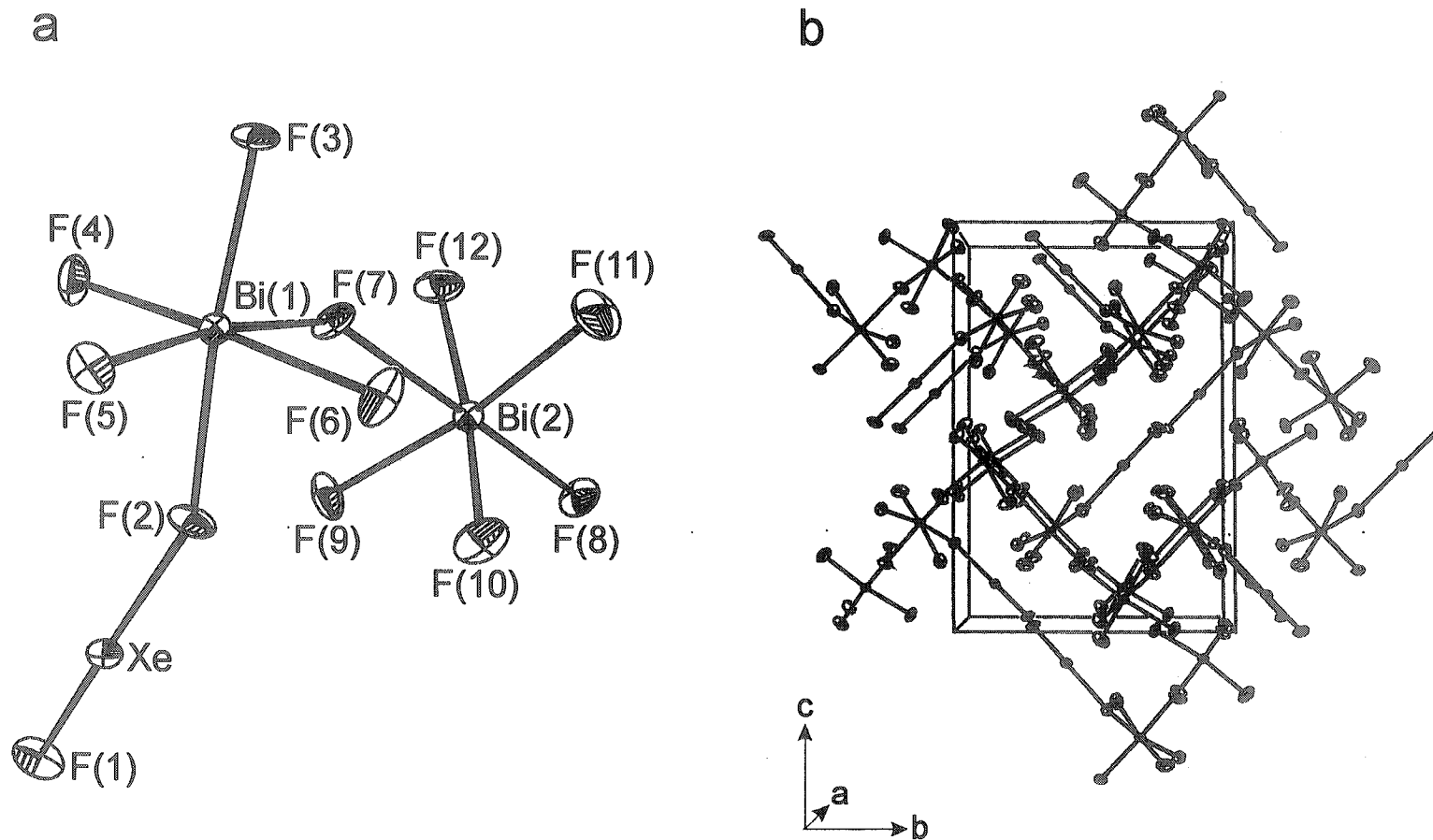
Figure 5.6. The crystal structure of (a) the structural unit of [XeF][Sb$_2$F$_{11}$] and (b) the packing arrangement of this salt viewed along the a-axis. Thermal ellipsoids are shown at the 50% probability level.

Table 5.1 Unit Cell and Refinement Parameters for XeF_2, [XeF][MF_6] (M = As, Sb, Bi) and [XeF][M_2F_{11}] (M = Sb, Bi)

	XeF_2	XeF_2[a]	[XeF][AsF_6]	[XeF][AsF_6][b]	[XeF][SbF_6]	[XeF][BiF_6]	[XeF][RuF_6][c]
Space Group	*I4/mmm*	*I4/mmm*	*P2₁/n*	*P2₁/n*	*P2₁/c*	*P2₁/c*	*P2₁/n*
a (Å)	4.2188(7)	4.315(3)	6.211(1)	6.308(3)	5.356(3)	5.235(2)	7.991(6)
b (Å)	4.2188(7)	4.315(3)	6.169(1)	6.275(3)	10.898(5)	9.946(4)	11.086(6)
c (Å)	6.991(2)	6.990(4)	15.793(3)	16.023(5)	10.926(5)	12.333(6)	7.250(6)
β (deg)	90	90	100.03(3)	99.97(5)	94.055(7)	91.251(6)	90.68(5)
V (Å³)	124.43(5)	130.1(1)	595.8(2)	624.6(5)	636.20(5)	642.01(5)	642.2(8)
Z	2	2	4	4	4	4	4
Mol. mass	169.29	169.29	329.20	329.20	376.03	463.26	365.35
ρ (g cm⁻³)	4.519	4.32	3.782	3.61	4.030	4.896	3.78
T (°C)	-173		-173	24	-173	-173	
μ (mm⁻¹)	13.57		11.36	10.34	9.63	32.71	78.04
R_1[e]	0.0160	0.097	0.0269	0.033	0.0169	0.0409	0.09
wR_2[f]	0.0354		0.0646		0.0365	0.1076	0.11

Table 5.1. continued…

	[XeF][Sb$_2$F$_{11}$]	[XeF][Sb$_2$F$_{11}$][d]	[XeF][Bi$_2$F$_{11}$]
Space Group	*P2$_1$*	*P2$_1$*	*P2$_1$2$_1$2$_1$*
a (Å)	7.225(2)	7.33	7.862(1)
b (Å)	9.392(3)	9.55	9.568(1)
c (Å)	8.070(2)	8.07	13.890(2)
α (deg)	90	90	90
β (deg)	106.734(5)	105.8	90
γ (deg)	90	90	90
V (Å^3)	524.3(3)	543	1044.8(2)
Z	2	2	4
Mol Mass (g/mol)	602.77	602.77	777.23
ρ (g cm^{-3})	3.818	3.69	4.941
T (°C)	-173		-173
μ (mm^{-1})	8.47		36.97
R_1[e]	0.0219	0.104	0.0395
wR_2[e]	0.0491		0.0759

[a] From ref 74 and 339. [b] From ref 72. [c] From ref 71. [d] From ref 73 and 331. [e] $R_1 = \dfrac{\sum \left\| F_o \right| - \left| F_c \right\|}{\sum \left| F_o \right|}$ for $I > 2\sigma(I)$.

[f] $wR_2 = \dfrac{\sum \left| \left(|F_o| - |F_c| \right) w^{\frac{1}{2}} \right|}{\sum \left(|F_o| w \right)}$ for $I > 2\sigma(I)$.

5.2.2.1. XeF$_2$

The single crystal X-ray[75] and neutron diffraction[74] structures of XeF$_2$ have been previously determined. The unit cell determined for XeF$_2$ in the previous X-ray structural study was reported to be tetragonal (*I4/mmm*) with a = 4.315(3) Å and c = 6.990(4) Å, however, the uncertainty in the Xe-F bond length (2.14(14) Å) was high as a result of the strong absorption that resulted from the use of Cu Kα X-rays. The neutron diffraction results were in agreement with the original study, and provided a significant improvement in the precision of the Xe-F bond length (2.00(1) Å).

In light of the present study of the XeF$^+$ salts, which are derived from XeF$_2$, and the fundamental importance of XeF$_2$, the crystal structure of XeF$_2$ has been redetermined (Figure 5.1) to obtain an even more precise Xe-F bond length. Xenon difluoride retains *I4/mmm* crystallographic symmetry at -173 °C, however, a modest contraction of the unit cell occurs along the *a*- and *b*-axes (4.2188(7) Å), whereas the *c*-axis remains unaffected (6.991(2) Å). The more precise Xe-F bond length determined at -173 °C (1.999(4) Å) is in agreement with the earlier crystallographic studies, but shows that the Xe-F bond lengths are significantly longer in the solid state than in the gas phase (1.9791(1),[337] 1.974365(7)[338]). The longer bond length observed in the solid state is attributed to the eight intermolecular Xe$\cdots$F contacts (3.338 Å), which lie within the sum of the xenon (2.16 Å)[286] and fluorine (1.35,[287] 1.47 Å[286]) van der Waals radii and serve to give the xenon and fluorine centres high second-sphere coordination numbers (Figure 5.1).

5.2.2.2. [XeF][AsF$_6$], [XeF][SbF$_6$], [XeF][BiF$_6$], [XeF][Sb$_2$F$_{11}$] and [XeF][Bi$_2$F$_{11}$]

The bond lengths, bond angles and contact distances determined for [XeF][MF$_6$] (M = As, Sb, Bi), and [XeF][M$_2$F$_{11}$] (M = Sb, Bi) are summarized in Tables 5.2 and 5.3, respectively.

Table 5.2. Bond Lengths and Bond Angles of [XeF][MF$_6$] (M = As, Sb, Bi) Determined by X-ray Diffraction and LDF Calculations

| | [XeF][AsF$_6$] | | | [XeF][SbF$_6$] | | [XeF][BiF$_6$] | |
	Expt.	Expt.[a]	Calc.[b]	Expt.	Calc.[b]	Expt.	Calc.[b]
Bond Lengths (Å)							
Xe-F(1)	1.888(3)	1.873(6)	1.991	1.885(2)	1.983	1.913(7)	1.974
Xe--F(2)	2.208(3)	2.212(5)	2.146	2.278(2)	2.170	2.204(7)	2.141
M-F(2)	1.838(3)	1.813(6)	2.087	1.971(2)	2.165	2.108(7)	2.259
M-F(3)	1.683(4)	1.657(6)	1.708	1.857(2)	1.909	1.978(7)	2.025
M-F(4)	1.709(3)	1.690(5)	1.746	1.860(2)	1.931	1.954(7)	2.049
M-F(5)	1.704(3)	1.690(8)	1.726	1.868(2)	1.912	1.953(7)	2.032
M-F(6)	1.698(3)	1.676(5)	1.726	1.866(2)	1.909	1.962(7)	2.032
M-F(7)	1.687(3)	1.813(6)	1.746	1.863(2)	1.920	1.955(6)	2.049
Contact Distances (Å)							
Xe···F(7)'	3.369			3.170		3.343	
Xe···F(7)'	3.489					3.372	
Xe···F(4)	3.491			3.581			
Xe···F(4)'	3.389			3.149		3.110	
Xe···F(4)'	3.489						
Xe···F(4)'	3.580						
Xe···F(6)'	3.376			3.247		3.278	
Xe···F(6)				3.372		3.324	
Xe···F(6)'	3.447						
Xe···F(3)'	3.164			3.118		3.513	
Xe···F(3)'						3.126	
Xe···F(5)	3.490						
Xe···F(5)'	3.438			3.144		3.194	
Xe···F(5)'	3.425			3.366			
Xe···F(2)'				3.565			
Xe···F(1)'	3.350					3.437	
Bond Angles (deg)							
F(1)-Xe-F(2)	179.1(2)	178.9(7)	177.5	177.94(9)	177.3	178.4(3)	178.0
Xe-F(2)-M	133.6(2)	134.8(2)	122.5	136.9(1)	126.0	156.1(4)	126.5
Dihedral Angles (deg)							
Xe-F(2)-M-F(4)	44.2	45.0		18.8	0.0	8.6	45.0

[a] From ref 72. [b] Energy-minimized structures were determined at the MPW1PW91 level of theory using the DZVP (F, As, Sb, Xe) and Stuttgart RLC ECP (Bi) basis sets.

Table 5.3. Bond Lengths and Bond Angles of $[XeF][Sb_2F_{11}]$ and $[XeF][Sb_2F_{11}]$ Determined by Single Crystal X-ray Diffraction

	$[XeF][Sb_2F_{11}]$	$[XeF][Sb_2F_{11}]^b$	$[XeF][Bi_2F_{11}]$
Bond Lengths (Å)			
Xe-F(1)	1.888(4)	1.82(3)	1.909(6)
Xe-F(2)	2.343(4)	2.34(3)	2.253(5)
M-F(2)	1.930(3)	1.91(3)	2.075(6)
M-F(3)	1.855(3)	1.84(4)	1.937(6)
M-F(4)	1.844(3)	1.86(4)	1.930(6)
M-F(5)	1.848(3)	1.81(4)	1.955(5)
M-F(6)	1.856(3)	1.80(4)	1.950(6)
M(1)-F(7)	2.010(3)	1.93(3)	2.092(6)
Sb(2)-F(7)	2.066(3)	2.10(3)	2.195(6)
Sb(2)-F(8)	1.851(4)	1.96(5)	1.956(6)
Sb(2)-F(9)	1.859(3)	1.75(6)	1.959(5)
Sb(2)-F(10)	1.857(3)	1.76(6)	1.958(6)
Sb(2)-F(11)	1.862(4)	1.74(6)	1.970(6)
Sb(2)-F(12)	1.864(3)	1.88(5)	1.954(6)
Contact Distances (Å)			
Xe···F(5)'	3.445		3.380
Xe···F(6)'	3.144		3.064
Xe···F(3)'	3.195		3.131
Xe···F(8)'	3.140		3.123
Xe···F(11)'	3.278		3.439
Xe···F(10)'	3.256		
Xe···F(12)	3.115		3.111
Xe···F(9)	3.174		3.330
Xe···F(9)'	3.592		
Bond Angles (deg)			
F(1)-Xe-F(2)	179.3(2)	176(1)	178.9(3)
Xe-F(2)-M	148.1(2)	149(2)	151.3(3)
Sb-F(7)-Sb(2)	146.0(2)	149(2)	145.3(3)
Dihedral Angles (deg)			
Xe-F(2)-M-F(4)	7.9		5.5

[a] From ref 72. [b] From ref 73 and 331.

The XeF$^+$ cation in the [XeF][MF$_6$] (M = As, Sb, Bi) and [XeF][M$_2$F$_{11}$] (M = Sb, Bi) salts is strongly coordinated to the MF$_6^-$ and M$_2$F$_{11}^-$ anions through a single fluorine bridge. The Xe-F$_t$ (F$_t$, terminal fluorine) bond lengths in [XeF][AsF$_6$] (1.888(3) Å), [XeF][SbF$_6$] (1.885(2) Å) and [XeF][Sb$_2$F$_{11}$] (1.888(4) Å) are not significantly different at the ±3σ (99.7%) level of confidence, but are shorter than those of [XeF][BiF$_6$] (1.913(7) Å) and [XeF][Bi$_2$F$_{11}$] (1.909(6) Å). Excluding the Xe-F$_t$ bond length determined in [XeF][RuF$_6$] (1.872(17) Å),[71] which has a significantly higher uncertainty, the mean Xe-F$_t$ bond length determined from the X-ray crystal structures of the [XeF][MF$_6$] and [XeF][M$_2$F$_{11}$] salts is (1.897(13) Å) and shorter than those of crystalline (1.999(4) Å) and gaseous (1.9791(1),[337] 1.974365(7) Å[338]) XeF$_2$. The same trend is observed between the average Kr-F$_t$ bond length of the [KrF][MF$_6$] (M = As, Sb, Bi, Au) salts (1.766(6) Å), and the Kr-F bond lengths of α-KrF$_2$ (1.894(5) Å),[23] however, the magnitude of the difference is 0.02 Å smaller for the xenon species.

The Xe--F$_b$ and M--F$_b$ (F$_b$, bridging fluorine) bond lengths of the XeF$^+$ salts investigated in the present study are elongated with respect to those of XeF$_2$ and the non-bridging M-F bond lengths of their counter anions. The Xe--F$_b$ bond length differs little among the [XeF][AsF$_6$] (2.208(3) Å), [XeF][BiF$_6$] (2.204(7) Å) and [XeF][RuF$_6$] (2.182(15) Å)[71] salts, but is longer in [XeF][SbF$_6$] (2.278(2) Å). This trend is in general agreement with the fluoride ion affinities of the group 15 pentafluorides, which have most recently been calculated to increase in the order AsF$_5$ (437.9 kJ mol^{-1}) < BiF$_5$ (456.5 kJ mol^{-1}) < SbF$_5$ (472.8 kJ mol^{-1}).[46] The inability to differentiate between the Xe--F$_b$ bond lengths of [XeF][AsF$_6$] and [XeF][BiF$_6$] is consistent with the enthalpies of fluoride ion attachment calculated for AsF$_5$ and BiF$_5$ by the NLDF method,[46] which differ by only 17 kJ mol^{-1}. Although consistent with the expected trend, it is noteworthy that the Xe--F$_b$ bond length of [XeF][SbF$_6$] is significantly longer than that of [XeF][BiF$_6$] despite the 16

173

kJ mol^{-1} difference between the fluoride ion affinities calculated for BiF$_5$ and SbF$_5$ (472.8 kJ mol^{-1}) by the NLDF method.[46] This minor discrepancy may be attributed, in part, to the variable dependencies of the fluoride ion affinities on the computational method utilized, as illustrated by the values obtained for AsF$_5$ (NLDF, 439.7;[46] MP2, 443.1 kJ mol^{-1} [48]) and SbF$_5$ (NLDF, 472.8;[46] MP2, 503.3 kJ mol^{-1} [48]). Unfortunately, the MP2-derived fluoride ion affinity of BiF$_5$ has not been determined and prevents a more comprehensive assessment of the sensitivity of these thermodynamic calculations to the methods used for the group 15 pentafluorides. The stronger fluoride ion affinities of Sb$_2$F$_{10}$ (530.9 kJ mol^{-1}) and Bi$_2$F$_{10}$ (507.5 kJ mol^{-1}),[46] which arise as a consequence of greater dispersal of the negative charge among the fluorine atoms of the M$_2$F$_{11}^-$ anions, are reflected by the longer Xe--F$_b$ bond lengths determined for [XeF][Sb$_2$F$_{11}$] (2.343(4) Å) and [XeF][Bi$_2$F$_{11}$] (2.253(5) Å) when compared with those of [XeF][SbF$_6$] and [XeF][BiF$_6$], respectively. Whereas the Xe--F$_b$ bond lengths of the XeF$^+$ salts imply that the relative fluoride ion affinities of the group 15 perfluorides increase in the order BiF$_5$ ≈ AsF$_5$ < Bi$_2$F$_{10}$ < SbF$_5$ < Sb$_2$F$_{10}$, the ordering inferred from the [KrF][MF$_6$] salts is BiF$_5$ < AsF$_5$ ≈ SbF$_5$.[23] The relative fluoride ion acceptor properties arrived at by the combination of these studies (BiF$_5$ < AsF$_5$ < Bi$_2$F$_{10}$ < SbF$_5$ < Sb$_2$F$_{10}$) is in qualitative agreement with that most recently calculated for the gas-phase species (AsF$_5$ < BiF$_5$ < SbF$_5$ < Bi$_2$F$_{10}$ < Sb$_2$F$_{10}$)[46] with the exception that the bismuth containing species occur at lower relative strengths in the scale derived from the Ng--F$_b$ bond lengths.

The M--F$_b$ bond lengths in [XeF][AsF$_6$] (1.838(3) Å), [XeF][SbF$_6$] (1.971(2) Å), [XeF][BiF$_6$] (2.108(7) Å), [XeF][Sb$_2$F$_{11}$] (1.930(3) Å) and [XeF][Bi$_2$F$_{11}$] (2.075(6) Å) are longer than the average terminal M-F bond lengths of the anions, which are 1.697(12), 1.863(4), 1.960(10), 1.855(6), and 1.952(12) Å, respectively. The shorter M--F$_b$ (M = Sb, Bi) bond lengths determined for the Sb$_2$F$_{11}^-$ and Bi$_2$F$_{11}^-$ salts, when compared with

those of the SbF_6^- and BiF_6^- salts, respectively, are consistent with a greater degree of fluoride ion transfer in the former species as expected based on the higher fluoride ion affinities estimated for the dimeric pnicogen pentafluorides.[46] The difference between the $M\text{--}F_b$ and non-bridging M-F bond lengths is slightly greater for [XeF][AsF_6] (0.14 Å) and [XeF][BiF_6] (0.14 Å) when compared with [XeF][SbF_6] (0.11 Å), and for [XeF][Bi_2F_{11}] (0.15 Å) when compared with [XeF][Sb_2F_{11}] (0.08 Å). These trends are consistent with the relative fluoride ion acceptor properties of the parent Lewis acids arrived at by comparisons of the $Xe\text{--}F_b$ bond lengths (*vide supra*). Although elongation of the $M\text{--}F_b$ bond is expected to shorten M-F(3) bond length as a result of the *trans*-influence, the M-F(3) bond lengths do not significantly differ from the remaining non-bridging bond lengths in [XeF][MF_6] (M = As, Sb, Bi) and [XeF][M_2F_{11}] (M = Sb, Bi).

In contrast to the $F_t\text{-}Xe\text{--}F_b$ bond angles, which show little variation among the XeF^+ salts studied (*vide infra*), the $Xe\text{--}F_b\text{--}M$ bond angles are highly deformable. The $Xe\text{--}F_b\text{--}M$ angles are similar in [XeF][AsF_6] (133.6(2)°) and [XeF][SbF_6] (136.9(1)°) but much larger in [XeF][BiF_6] (156.1(4)°). On the basis of the similar $Xe\text{--}F_b\text{--}M$ bond angles calculated for [XeF][AsF_6] (122.5°), [XeF][SbF_6] (126.0°) and [XeF][BiF_6] (126.5°) (see section 5.3.1), and the similar bond angles determined in the structures of [XeF][Sb_2F_{11}] (146.0(2)°) and [XeF][Bi_2F_{11}] (145.3(3)°), the larger $Xe\text{--}F_b\text{--}M$ bond angle of [XeF][BiF_6] likely arises as a result of solid state packing effects rather than from the electronic properties of this ion pair. The long $Xe\cdots F$ contacts lying within the sum of the van der Waals radii of xenon (2.16 Å)[286] and fluorine (1.35,[287] 1.47 Å[286]) are presumed to be dominant features which give rise to the variation among the $Xe\text{--}F_b\text{--}M$ bond angles in the solid state (Tables 5.2, 5.3). These contacts are most numerous for [XeF][AsF_6], where thirteen $Xe\cdots F$ interactions ranging from 3.164 to 3.580 Å were identified. The structures of [XeF][SbF_6], [XeF][BiF_6] and [XeF][Sb_2F_{11}] each have nine $Xe\cdots F$ contacts

with distances ranging from 3.118 to 3.581 Å, 3.110 to 3.513 Å and 3.115 to 3.592 Å, respectively. The crystal structure of $[XeF][Bi_2F_{11}]$ exhibited only seven Xe···F contacts, with distances ranging from 3.064 to 3.439 Å. The sensitivity of the $Xe-F_b-M$ angle to the Xe···F contacts in these salts is further exacerbated by the low in-plane $Xe-F_b-M$ bending frequencies calculated for the $[XeF][AsF_6]$ (56 cm^{-1}), $[XeF][SbF_6]$ (58 cm^{-1}) and $[XeF][BiF_6]$ (36 cm^{-1}) ion pairs (see section 5.3.2).

The $F-Xe-F_b$ bond angle is slightly bent at the $\pm 3\sigma$ confidence level in the structures of $[XeF][SbF_6]$ (177.94(9)°), $[XeF][AsF_6]$ (179.1(2)°), $[XeF][BiF_6]$ (178.4(3)°), $[XeF][Sb_2F_{11}]$ (197.3(2)°) and $[XeF][Bi_2F_{11}]$ (178.9(3)°), and these bends are reproduced in the calculated structures of the $[XeF][MF_6]$ (M = As, Sb, Bi) salts (see section 5.3.1). Similar non-linear bond angles have been noted for the $[KrF][MF_6]$ salts (see section 3.2.2.2) and have been hypothesized to arise from the repulsive interactions between the lone electron pairs associated with F_b and Kr.

In the absence of packing effects the conformation of the F_t-Xe-F_b moiety with respect to the equatorial fluorine atoms of the anion may be expected to be eclipsed (Structure I), to minimize the distance between the XeF$^+$ cation and the next nearest fluorine atom (F''_e), or staggered (Structure II), to minimize the steric interactions

I   II
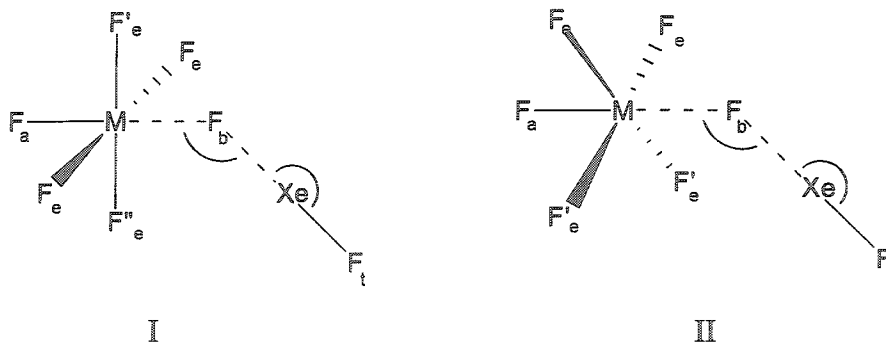
between the cation and the fluorine ligands on the metal centre. Despite the contrastingorigins of these conformational extremes, the Xe-F(2)-M-F(4) dihedral

176

angles of the $[XeF][MF_6]$ salts range from near-staggered (As, 44.2°) to intermediate (Sb, 18.8°) to near-eclipsed (Bi, 8.6°) conformations. The large variation in Xe-F(2)-M-F(4) dihedral angle suggests that the energy difference between the conformational extremes is small, in agreement with the low frequencies calculated for the torsional F_t-Xe--F_b--M wagging motions of these species (see section 5.3.2). Because the $M_2F_{11}^-$ anions (M = As, Sb) are of lower symmetry with respect to the MF_6^- anions, it is difficult to predict a preferred orientation for the F_t-Xe--F_b groups in the $[XeF][M_2F_{11}]$ ion pairs, particularly when long Xe···F contacts are to be taken into account. The F_t-Xe--F_b groups are nearly eclipsed for $[XeF][Sb_2F_{11}]$ and $[XeF][Bi_2F_{11}]$, with Xe--F_b--M-F(4) dihedral angles of 7.9 and 5.5°, respectively.

The $As_2F_{11}^-$ and $Sb_2F_{11}^-$ anions have been structurally characterized in a number of salts, however, the structure of $[XeF][Bi_2F_{11}]$ represents the first crystallographic characterization of the $Bi_2F_{11}^-$ anion. Like its lighter analogues, the $Bi_2F_{11}^-$ anion is comprised of two pseudo-octahedrally coordinated bismuth atoms bridged by a single fluorine atom (F_b'). The four equatorial fluorine atoms at both ends of the $M_2F_{11}^-$ anions in $[XeF][M_2F_{11}]$ are staggered with respect to each other. The interaction between the $M_2F_{11}^-$ anion and the XeF^+ cation is reflected in the asymmetry of the M(1)--F_b'--M(2) bridge bond lengths, where the M--F_b' bond length is shorter for the metal centre that is fluorine bridged to the XeF^+ cation. The asymmetry of the M--F_b bridge bond lengths is less pronounced for the $Sb_2F_{11}^-$ salt (2.010(3), 2.066(3) Å) than it is for the $Bi_2F_{11}^-$ salt (2.092(6), 2.195(6) Å), suggesting a greater degree of ionic character for the former. This trend is in accord with the smaller fluoride ion affinity calculated for Bi_2F_{10} (507.5 kJ mol^{-1}) when compared with that of Sb_2F_{10} (530.9 kJ mol^{-1}).[46] Although the fluoride ion affinity of As_2F_{10} has not been calculated, the value determined for BiF_5 (456.5 kJ mol^{-1}) exceeds that of AsF_5 (439.7 kJ mol^{-1}), suggesting that the fluoride ion affinity of

As_2F_{10} may be less than that of Bi_2F_{10}. If this is true, the M--F_b'--M bridge would be expected to be even more asymmetric in [XeF][As_2F_{11}], and the elongation of the second M--F_b' bond proximate to the Xe--F_b--As bridge could be sufficient enough to destabilize the $As_2F_{11}^-$ anion, favouring the isolation of the [XeF][AsF_6] salt instead.

The Bi--F_b'--Bi bond angle (145.3(3)°) is similar to the Sb--F_b'--Sb (146.0(2)°) bond angle in [XeF][Sb_2F_{11}]. Although [XeF][As_2F_{11}] remains unknown, similar bond angles have recently been reported for the anions in [(m-$CF_3C_6H_4$)(C_6H_5)CF][As_2F_{11}] (156.5(13)°),[336] [($CH_3S)_2CSH$][As_2F_{11}] (159.1(6)°),[334] [Cl_3PH][As_2F_{11}] (148.3(2)°),[335] and [Br_3PH][As_2F_{11}] (145.9(4)°).[335] Despite the similar M--F_b'--M bond angles in these species, a recent theoretical study of the $Sb_2F_{11}^-$ anion by use of the B3LYP method has predicted that the linear fluorine bridged structure with an eclipsed conformation (D_{4h} symmetry) is the minimum energy gas-phase structure. The study also showed that the anion is highly deformable with respect to the conformation of the two sets of equatorial fluorine atoms and the Sb--F_b'--Sb bond angle, with the bent anion (Sb--F_b'--Sb, 160°) being only 1.7 kJ mol^{-1} higher in energy than the linear anion. Thus, it is reasonable to attribute the bent and eclipsed geometries of the $Sb_2F_{11}^-$ and $Bi_2F_{11}^-$ anions in their XeF^+ salts to crystal packing effects of the fluorine ligands. Edwards and coworkers have investigated the effects of close packing arrangements of the light atoms for the polymeric fluorine-bridged species $TcOF_4$,[340] $MoOF_4$,[341] $ReOF_4$[342] and WOF_4.[343] These studies demonstrated that the ideal bridge angle is 132° if the central metal atoms lie within the octahedral interstitial sites of hexagonal close-packed oxygen and fluorine atoms, but is 180° if the metal atoms lie within the octahedral holes of a cubic close-packed lattice of oxygen and fluorine atoms. The packing of the fluorine atoms in the structures of [XeF][Sb_2F_{11}] and [XeF][Bi_2F_{11}] most closely resemble hexagonal close-packed arrangements and are consistent with their bent anion geometries.

The strong interactions between the XeF^+ cation and the MF_6^- and $M_2F_{11}^-$ anions are a consequence of the strong fluoride acceptor properties of XeF^+, MF_5 and M_2F_{10} which can be thought of as competing for the bridging "fluoride ion". For an octahedral MF_6^- anion, each of the fluorine positions is equally basic, and one coordination site is not preferred over another. This is not the case for the $M_2F_{11}^-$ anions, which have two axial positions and eight equivalent equatorial positions if the effects of the $M\text{--}F_b'\text{--}M$ bond angle are ignored. Of the two types of fluorine environments on these anions, the acidic XeF^+ cation is expected to coordinate to the more fluoro-basic site. As a consequence of the $M\text{--}F_b'$ bridge bonds, which induce a *trans*-influence, the axial fluorines are less fluoro-basic than the equatorial fluorines, resulting in *cis*-fluorine bridged structures for the $[XeF][M_2F_{11}]$ salts. The coordination of the cation to an equatorial fluorine position of the $M_2F_{11}^-$ anions is not unique to the XeF^+ salts, but is also observed for $[XeF_3][Sb_2F_{11}]$.[344] An exception to this behaviour is $[XeCl][Sb_2F_{11}]$, for which X-ray crystallography has shown that the xenon atom is bridged to a terminal fluorine atom of the $Sb_2F_{11}^-$ anion.[52] This anomaly reflects the lower bond polarity and Lewis acidity of $XeCl^+$ relative to that of XeF^+, which arises a consequence of the smaller electronegativity difference between chlorine and xenon that is also apparent from the longer $Xe\text{--}F_b$ bond lengths in $[XeCl][Sb_2F_{11}]$ (2.612(4), 2.644(4) Å) relative to that of $[XeF][Sb_2F_{11}]$ (2.278(2) Å).

5.3. Computational Results

5.3.1. Geometries

The energy-minimized gas-phase geometries of the $[XeF][MF_6]$ (M = As, Sb, Bi) ion pairs, calculated by use of the MPW1PW91 method, are summarized in Table 5.2. Whereas the calculated geometries of $[XeF][AsF_6]$ and $[XeF][BiF_6]$ have staggered conformations (Structure I), $[XeF][SbF_6]$ has an eclipsed conformation (Structure II).

The geometries of the [XeF][MF$_6$] (M = As, Sb, Bi) ion pairs obtained by use of the HF method are not reported in the present work, but exhibited C_{4v} symmetries as a result of the linear Xe--F$_b$--M bond angles arrived at by this method. The shortcomings of the HF method at predicting fluorine bridge bond angles has previously been demonstrated for Xe$_2$F$_3^+$ [277] and Kr$_2$F$_3^+$ cations (see section 3.3.2.2),[23] which are calculated to be linear, however, bent Kr--F$_b$--M bond angles have been obtained for the HF optimized structures of [KrF][MF$_6$] (see sections 3.3.1.2 and 4.3.1.1).[23,130]

The calculated Xe-F$_t$ bond lengths for the [XeF][MF$_6$] ion pairs (As, 1.991 Å; Sb, 1.983 Å; Bi, 1.974 Å) are longer than the experimental values by 0.06 (Bi) to 0.10 Å (As, Sb). The Xe--F$_b$ bond lengths are similar in the calculated structures of [XeF][AsF$_6$] (2.146 Å) and [XeF][BiF$_6$] (2.141 Å), but approximately 0.03 Å longer in the structure of [XeF][SbF$_6$] (2.170 Å). These trends reflect the similar fluoride ion acceptor properties of AsF$_5$ and BiF$_5$ inferred from the crystal structures of [XeF][AsF$_6$] and [XeF][BiF$_6$], and the greater fluoride ion affinity of SbF$_5$. The calculated Xe--F$_b$ bond lengths are somewhat shorter than the experimental bond lengths of [XeF][AsF$_6$] (2.208(3) Å), [XeF][SbF$_6$] (2.278(2) Å), [XeF][BiF$_6$] (2.204(7) Å) with the largest difference (0.11 Å) occurring for [XeF][SbF$_6$].

The M--F$_b$ bond lengths calculated for [XeF][AsF$_6$] (2.087 Å), [XeF][SbF$_6$] (2.165 Å) and [XeF][BiF$_6$] (2.259Å) are longer than the average non-bridging M-F bond lengths by 0.36, 0.25 and 0.22 Å, respectively. This is in contrast to the experimental results, for which the differences between the bridging and non-bridging bond lengths are relatively constant for [XeF][AsF$_6$] (0.14 Å), [XeF][SbF$_6$] (0.11 Å) and [XeF][BiF$_6$] (0.14 Å) and smaller in magnitude than the calculated differences. The inability of the calculated structures to reproduce the experimental differences and their trends may be a consequence of the increasing complexity of the electronic structures of these salts with

increasing mass of the central group 15 atom, particularly [XeF][BiF$_6$], for which an effective core potential was required for the bismuth atom. Furthermore, the bond lengths and bond angles involving F$_b$ may be expected to be strongly influenced by the computational method and basis set utilized because of its position between the heavy xenon and group 15 atoms.

As previously noted in the experimental and calculated structures of the [KrF][MF$_6$] (M = As, Sb, Bi, Au) analogues, the F$_t$-Xe--F$_b$ bond angles are slightly bent. Although solid-state packing effects arising from the many intermolecular Xe···F contacts may affect this bond angle in the solid state (see section 5.2.2.2), the calculated gas-phase structures of the [XeF][MF$_6$] (M = As, Sb, Bi) ion pairs also exhibit minor distortions from linearity (As, 177.5°; Sb, 177.3°; Bi, 178.0°), suggesting these angles are intrinsic to the ion-pair geometries.

Although the MPW1PW91 method reproduced the non-linear geometry about the bridging fluorine, the Xe--F$_b$--M bond angles calculated for the [XeF][AsF$_6$] (122.5°), [XeF][SbF$_6$] (126.0°) and [XeF][BiF$_6$] (126.5°) ion pairs are significantly smaller than the experimental values (As, 133.6(2); Sb, 136.9(1); Bi, 156.1(4)°) and exhibit little dependence on the anion. Similar differences have been reported for the [KrF][MF$_6$] salts (see sections 3.2.1.2),[23] and have been attributed to the presence of long Ng···F contacts in the solid state.

5.3.2. Vibrational Frequencies of [XeF][MF$_6$] (M = As, Sb, Bi)

The vibrational assignments of the [XeF][MF$_6$] salts are complicated by the strong interaction between the anion and cation, which introduces additional modes associated with the Xe--F$_b$ stretch and the F-Xe--F$_b$ and Xe--F$_b$--M bends. This interaction also distorts the octahedral geometry of MF$_6^-$, resulting in an elongated M--F$_b$ bond, which removes the degeneracies of the $\nu_2(E_g)$, $\nu_5(F_{2g})$, $\nu_3(F_{1u})$, $\nu_4(F_{1u})$ and $\nu_6(F_{2u})$

vibrational modes. The symmetries of the anions in these salts are often assumed to be C_{4v} for the purposes of vibrational assignments, however, the bent Xe--F_b--M bridge bond angles further reduce the symmetries of the ion pairs to C_s or C_1 depending on the Xe--F_b--M-F_e (F_e, equatorial fluorine) dihedral angle. The Raman spectra of the [KrF][MF$_6$] (M = As, Sb, Bi, Au) salts have recently been reinterpreted in greater detail with the aid of electronic structure calculations by use of the HF and LDF methods (see sections 3.3.2.3 and 4.3.2.1)[23,130] In light of the observation that the vibrational spectra of the krypton-containing species were most accurately determined by use of the LDF method and that the HF method incorrectly predicted the [XeF][MF$_6$] ion pairs to have C_{4v} symmetry, the vibrational frequencies of the [XeF][MF$_6$] ion pairs have been calculated and reassigned using the energy-minimized geometries determined by the MPW1PW91 method. The vibrational frequencies and assignments obtained for the [XeF][MF$_6$] (M = As, Sb, Bi) salts are summarized in Tables 5.4, 5.5 and 5.6, respectively.

The Xe-F_t vibrational frequencies calculated for the AsF$_6^-$ (581 cm^{-1}), SbF$_6^-$ (586 cm^{-1}) and BiF$_6^-$ (568 cm^{-1}) salts are in reasonable agreement with the experimental values (As, 608, 602; Sb, 615; Bi, 608 cm^{-1}), with the slight underestimation being attributed to the overestimation of the Xe-F_t bond lengths. The assignments of the Xe--F_b stretching frequencies in these salts were more difficult. For [XeF][AsF$_6$], the Xe--F_b stretching frequency has been reassigned from 339[68] to 417 cm^{-1} based on the calculated frequency (459 cm^{-1}) and the slight underestimation of the calculated Xe--F_b bond length. The Xe--F_b stretching frequency of [XeF][SbF$_6$] was originally reported to be split (337, 388 cm^{-1}),[68] but has been reassigned to 388 cm^{-1} on the basis of the calculated frequency (440 cm^{-1}) and the underestimated Xe--F_b bond length. The Xe--F_b stretching frequency calculated for [XeF][BiF$_6$] (316 cm^{-1}) is significantly lower than those of the lighter

Table 5.4. Calculated Vibrational Frequencies (cm^{-1}), Assignments and Mode Descriptions for the [XeF][AsF$_6$] Ion Pair

MPW1PW91[a]	Expt.[a,b]	Assignments for [XeF][AsF$_6$] in C_s Point Symmetry[c]
745(5)[142]	731(5)	A" $\nu(AsF_a)$
742(2)[163]		A' $\nu_{as}(AsF_{2e}) - \nu(AsF'_{2e})$
740(17)[162]	724(5)	A' $\nu_{as}(AsF_{2e}) - \nu(AsF'_e)$
657(51)[16]	678(20)	A' $\nu_s(AsF_{2e} + AsF'_{2e})$
	667(4)	
600(7)[3]	586(10)	A' $\nu_{as}(AsF_{2e}) + \nu_{as}(AsF'_{2e})$
581(100)[121]	609(100)	A' $\nu(XeF_t)$ - small $\nu(XeF_b)$
459(63)[106]	417(5)	A' $\nu(XeF_b)$
376(1)[26]	387(6)	A' $\nu(AsF_b)$
369(6)[6]	339(21)	A' $\delta(AsF'_{2e})$
363(1)[51]		A" $\delta(F'_eAsF_e) - \delta(F'_eAsF_e) + \delta(F_bAsF_a)$ o.o.p.
348(2)[15]		A' $\delta(AsF_{2e})$
294(2)[0.4]		A" $\delta(F_bXeF_t)$ o.o.p. - $\delta(F_bXeF_a)$
287(4)[311]		A' $\delta(AsF_{4e})$ wag + $\delta(F_bXeF_t)$ i.p.
266(5)[1]		A" $\delta(F_bAsF_a)$ i.p.
223(<1)[4]		A' $\delta(F_bAsF_a)$ o.o.p.
169(<1)[1]		A" $\delta(F_eAsF_a) - \delta(F_e'AsF_a)$
145(2)[3]	180(2)	A" $\delta(F_bAsF_a)$ o.o.p. - $\delta(F_bXeF_t)$ o.o.p.
140(5)[7]	155(15)	A' $\delta(F_bAsF_a)$ i.p. + $\delta(XeF_bAs)$
138(2)[1]	146(sh)	A' $\delta(F_tXeF_b)$ i.p. $\nu(AsF_b)$ + small $\delta(F_bAsF_a)$
56(2)[<1]	99(1)	A' $\delta(AsF_bXe)$ i.p.
26(3)[<1]		A" XeF$_t$ torsion about As-F$_b$ + (AsF$_5$) rock

[a] Raman intensities are shown in parentheses and are scaled to the most intense band which is given a value of 100. Infrared intensities are shown in brackets, and given in km mol^{-1}. [b] Experimental values are taken from ref 68. A band observed at 443(3) cm^{-1} remains unassigned. [c] The geometry optimization and vibrational frequencies were determined at the MPW1PW91 level of theory in conjunction with the DZVP basis set. The energy-minimized geometry had a staggered orientation and the atom-labeling scheme is given in Structure I. The abbreviations o.o.p. and i.p. denote out-of-plane and in-plane bending modes respectively.

Table 5.5. Calculated Vibrational Frequencies (cm^{-1}), Assignments and Mode Descriptions for the [XeF][SbF$_6$] Ion Pair

MPW1PW91[a]	Expt.[a,b]	Assignments for [XeF][SbF$_6$] in C_s Point Symmetry[c]
671(<1)[113]	685(6)	A" ν_{as}(SbF$_{2e}$)
667(5)[105]	645(15)	A' ν(SbF'$_e$) - ν(SbF"$_e$) - ν(SbF$_a$)
662(15)[95]	645(15)	A' ν(SbF'$_e$) - ν(SbF"$_e$) + ν(SbF$_a$)
609(59)[17]	666(43)	A' ν_s(SbF$_5$) + small ν(SbF$_a$)
586(100)[104]	615(100)	A' ν(XeF$_t$)
580(6)[4]	586(6)	A' ν(SbF"$_e$ + SbF'$_e$) - ν(SbF$_{2e}$)
440(39)[210]	388(4)	A' ν(XeF$_b$) + ν(XeF$_t$)
343(3)[27]	337(6)	A' δ(F$_b$SbF"$_e$) + δ(F$_e$SbF$_e$) along F'$_e$-Sb-F"$_e$
266(7)[34]	290(11)	A" δ(F$_e$SbF"$_e$) - δ(F$_e$SbF"$_e$)
254(2)[62]	267(11)	A" δ(F'$_e$SbF$_e$) - δ(F'$_e$SbF$_e$)
251(1)[115]		A' δ(F$_e$SbF$_e$) + δ(F"$_e$SbF$_b$) along F'$_e$-Sb-F"$_e$
246(1)[55]		A' δ(F$_b$SbF$_e$) + δ(F$_a$SbF$_e$)
233(2)[3]		A' ν(SbF$_b$) + δ(SbF$_{2e}$F'$_e$F"$_e$) o.o.p.
186(4)[5]	180(4)	A' δ(F"$_e$SbF$_a$) + δ(F'$_e$SbF$_b$) + ν(XeF$_b$)
176(<1)[3]		A" δ(F$_t$XeF$_b$) o.o.p. + δ(F$_b$XeF$_a$)
145(4)[4]	141(23)	A' δ(F$_t$XeF"$_e$) i.p. + ν(SbF$_b$)
129(1)[1]		A" δ(F$_e$SbF$_e$) - δ(F"$_e$SbF$_e$')
117(1)[1]		A" δ(F$_t$XeF$_b$) o.o.p. + (SbF$_5$) rock o.o.p.
106(1)[2]		A' δ(F"$_e$SbF$_b$) - δ(F'$_e$SbF$_b$)
58(2)[1]		A' δ(XeF$_b$Sb)
11i(2)[<1]		A" Torsion of XeF$_2$ group about the Sb-F$_b$ bond + rock of SbF$_5$ group towards XeF$_2$

[a] Raman intensities are shown in parentheses and are scaled to the most intense band which is given a value of 100. Infrared intensities are shown in brackets, and given in km mol^{-1}. [b] Experimental values are taken from ref 68. Two bands which were observed at 467(13) and 447(15) cm^{-1} remain unassigned. [c] The geometry optimization and vibrational frequencies were determined at the MPW1PW91 level of theory in conjunction with the DZVP basis set. The energy-minimized geometry had an eclipsed conformation and the atom-labeling scheme is given in Structure II. The abbreviations o.o.p. and i.p. denote out-of-plane and in-plane bending modes respectively.

Table 5.6. Calculated Vibrational Frequencies (cm^{-1}), Assignments and Mode Descriptions for the [XeF][BiF$_6$] Ion Pair

MPW1PW91[a]	Expt.[a,b]	Assignments for [XeF][BiF$_6$] in C_s Point Symmetry[c]	
585(32)[44]		A'	$\nu(BiF_a)$
572(9)[55]	590(12)	A"	$\nu_{as}(BiF_{2e}) - \nu(BiF'_e)$
572(53)[33]		A"	$\nu_{as}(BiF_{2e}) - \nu(BiF'_e)$
568(100)[135]	608(11), 602(48)	A'	$\nu(XeF_t)$ - small $\nu(XeF_b)$
550(94)[13]	588(100)	A'	$\nu_s(BiF_{2e} + BiF'_{2e})$
537(16)[10]	545(4), 541(9)	A"	$\nu_{as}(BiF_{2e}) + \nu_{as}(BiF'_{2e})$
450(27)[239]	439(<1)	A'	$\nu(BiF_b)$
316(6)[21]	417(<1)	A'	$\nu(XeF_b)$
229(1)[27]	242(5)	A"	$\delta(F_bXeF_t)$ o.o.p. - $\delta(F_bXeF_a)$
219(9)[4]	228(4)	A'	$\delta(BiF'_{2e})$
201(1)[114]	207(3)	A'	$\delta(BiF_{2e})$
196(3)[37]	203(1)	A'	$\delta(F'_eBiF_a) - \delta(F'_eBiF_e) - \delta(F'_eBiF_e)$
192(3)[31]	194(<1)	A"	$\delta(F_eBiF'_e) + \delta(F_aBiF_b)$ i.p.
156(9)[4]	186(<1)	A'	$\delta(F_eBiF_a) - \delta(F_eBiF_e)$
153(2)[2]	175(<1)	A"	$\delta(F_eBiF_a) + \delta(F_tKrF_b)$ o.o.p.
138(4)[5]	138(3)	A'	$\delta(F_tXeF_b)$ i.p. + $\nu(F_bBi)$ + small $\delta(F_bBiF_a)$
113(4)[1]	123(1)	A"	$\delta(F_bBiF_a)$ o.o.p.
93(1)[1]	82(3)	A'	$\delta(F_bBiF_a)$ i.p. + $\delta(XeF_bBi)$
86(<1)[<1]	76(2), 72(2)	A"	$\delta(BiF_bXe)$ o.o.p.
36(1)[1]	62(6), 53(3)	A'	$\delta(BiF_bXe)$ i.p.
15(2)[<1]	44(2)	A"	XeF$_t$ torsion about Bi-F$_b$ + (BiF$_5$) rock

[a] Raman intensities are shown in parentheses and are scaled to the most intense band which is given a value of 100. Infrared intensities are shown in brackets, and given in km mol^{-1}. [b] Experimental values are taken from ref 41. Bands observed at 82(3), 76(2), 72(2), 62(6), 53(3), 44(2) cm^{-1} were originally assigned to external modes. [c] The geometry optimization and vibrational frequencies were determined by use of the MPW1PW91 method in conjunction with the DZVP (F, Xe) and Stuttgart RLC ECP (Bi) basis sets. The energy-minimized geometry had staggered conformation and the atom-labeling scheme is given in Structure I. The abbreviations o.o.p. and i.p. denote out-of-plane and in- plane bending modes, respectively.

[XeF][MF$_6$] salts and contrasts with the similar Xe--F$_b$ bond lengths calculated for [XeF][BiF$_6$] and [XeF][AsF$_6$]. The anomalously low Xe--F$_b$ stretching frequency calculated for the bismuth salt is suspected to arise as a result of the location of F$_b$ between the two heavy atoms, Xe and Bi, and the use of an effective core potential for bismuth. For these reasons, the assignment of the Xe--F$_b$ stretching frequency has not been changed from its original value of 417 cm^{-1}.[41]

The variation in the experimental Xe--F$_b$--M bond angles of [XeF][AsF$_6$], [XeF][SbF$_6$] and [XeF][BiF$_6$] is likely a consequence of the long intramolecular Xe$\cdots$F contacts, which vary in length and number from salt to salt (Table 5.2). The influence of packing effects on the Xe--F$_b$--M bond angle is not surprising considering that the in-plane Xe--F$_b$--M bending frequencies calculated for the [XeF][AsF$_6$] (56 cm^{-1}), [XeF][SbF$_6$] (58 cm^{-1}) and [XeF][BiF$_6$] (36 cm^{-1}) ion pairs are low. Even lower vibrational frequencies are calculated for the torsional motion of the XeF$^+$ cation with respect to the F$_b$--M axes in [XeF][AsF$_6$] (26 cm^{-1}), [XeF][SbF$_6$] (11i cm^{-1}) and [XeF][BiF$_6$] (15 cm^{-1}), which is consistent with staggered to nearly eclipsed Xe--F$_b$--M-F(4) dihedral angles observed in the crystal structures of [XeF][AsF$_6$] (44.2°), [XeF][SbF$_6$] (18.8°) and [XeF][BiF$_6$] (8.6°).

5.3.3. Atomic Charges, Mayer Bond Orders, Mayer Valencies

Further insight into the electronic structures of the [XeF][MF$_6$] (M = As, Sb, Bi) ion pairs was obtained by the calculation of their atomic charges, Mayer bond orders and Mayer valencies using the Natural Bond Orbital (NBO) method.[293-296] The Mayer bond orders, Mayer valencies and atomic charges for the [XeF][MF$_6$] ion pairs have been calculated using the electronic structures derived from MPW1PW91 method and are summarized in Table 5.7.

Table 5.7. Atomic Charges, Mayer Valencies and Mayer Bond Orders for [XeF][AsF$_6$], [XeF][SbF$_6$] and [XeF][BiF$_6$]

	[XeF][AsF$_6$]	[XeF][SbF$_6$]	[XeF][BiF$_6$]
Atomic Charges and Valencies[a,b]			
Xe	1.24 (0.52)	1.25 (0.51)	1.21 (0.59)
M	2.75 (2.82)	3.11 (2.41)	2.94 (1.88)
F$_t$	-0.51 (0.32)	-0.49 (0.33)	-0.48 (0.36)
F$_b$	-0.61 (0.35)	-0.63 (0.36)	-0.62 (0.35)
F$_a$	-0.56 (0.48)	-0.63 (0.42)	-0.61 (0.31)
F$_e$	-0.56 (0.45)	-0.65 (0.40)	-0.59 (0.30)
F$'_e$	-0.59 (0.43)	-0.63 (0.40)	-0.63 (0.29)
F$''_e$		-0.67 (0.38)	
Mayer Bond Orders[a]			
Xe-F$_t$	0.32	0.32	0.36
Xe-F$_b$	0.19	0.17	0.21
F$_b$-F$_t$	0.00	0.00	0.00
M-F$_b$	0.21	0.21	0.17
M-F$_a$	0.54	0.45	0.35
M-F$_e$	0.50	0.44	0.35
M-F$'_e$	0.53	0.45	0.33
M-F$''_e$	0.41		

[a] Mayer valencies, Mayer bond orders and atomic charges were obtained by use of the MPW1PW91 method with the DZVP (F, As, Sb, Xe) and Stuttgart RLC ECP (Bi) basis sets. [b] Mayer valencies are given in parentheses.

187

As previously noted for the [KrF][MF$_6$] (M = As, Sb, Bi) series,[23] there is little variation and no clear pattern among the charges of the F$_t$-Xe--F$_b$ groups of the [XeF][AsF$_6$] (F$_t$, -0.51; Xe, 1.24; F$_b$, -0.61), [XeF][SbF$_6$] (F$_t$, -0.49; Xe, 1.25; F$_b$, -0.63) and [XeF][BiF$_6$] (F$_t$, -0.48; Xe, 1.21; F$_b$, -0.62) ion pairs. It is noteworthy that the sum of the F$_t$ (-0.48 to -0.51) and Xe (1.21 to 1.25) charges is approximately +0.8 and is closer to the +1 charge expected for a free NgF$^+$ cation than that found for the [KrF][MF$_6$] ion pairs where the analogous sum is approximately +0.55.[23] The greater cation-anion charge separation in the XeF$^+$ salts implies that the [XeF][MF$_6$] ion pairs are significantly more ionic than the [KrF][MF$_6$] ion pairs, and is consistent with the smaller M--F$_b$ bond length elongation with respect to the non-bridging M-F bonds lengths that is observed for the XeF$^+$ salts (see section 5.2.2.2). Although the electron affinities of XeF$^+$ and KrF$^+$ have not been determined directly, they have been estimated[59,345] to be 10.9[95,346] and 13.2 eV,[59,346] respectively. The lower electron affinity predicted for XeF$^+$, relative to KrF$^+$, undoubtedly limits the amount of electron density that is donated to the cation from the anion through the bridging interaction of the [XeF][MF$_6$] ion pair and accounts for the more ionic character of the xenon salts. The greater ionic character of the xenon(II) salts appears to have a moderating effect on the nature of the anion as indicated by the similar charges calculated for the As (2.75), Sb (3.11), and Bi (2.94) atoms, contrasting with the relatively broad range of values found for the [KrF][MF$_6$] salts (As, 0.90; Sb, 1.45; Bi, 2.23).[23] In accord with the higher positive charge associated with the XeF$^+$ cation, the counterbalancing negative charge on the anion is also higher in the xenon salts than in the krypton salts and is nearly uniformly distributed over the six fluorine atoms ([XeF][AsF$_6$], -0.56 to -0.59; [XeF][SbF$_6$], -0.63 to -0.67; [XeF][BiF$_6$], -0.59 to -0.63). It is noteworthy that the charge on the bridging fluorine atom does not differ significantly

from the non-bridging fluorine atoms of the anion in the XeF^+ salts, providing additional support for a highly ionic cation-anion interaction.

The $Xe-F_t$ and $Xe--F_b$ Mayer bond orders do not vary significantly from one salt to the next. The $Xe-F_t$ bond orders (AsF_6^-, 0.32; SbF_6^- 0.32; BiF_6^-, 0.36) are nearly twice as large as the $Xe--F_b$ bond orders (AsF_6^-, 0.19; SbF_6^- 0.17; BiF_6^-, 0.21), which is consistent with the shorter $Xe-F_t$ bond lengths. The Xe-F bond orders are significantly less than the $Kr-F_t$ (0.76 - 0.79) and $Kr--F_b$ (0.47 - 0.50) bond orders calculated for the $[KrF][MF_6]$ salts.[23] Thus, in addition to exhibiting a greater degree of ionic character with respect to the $Xe--F_b$ bonds (*vide supra*), the $Xe-F_t$ bonds are also more ionic than the $Kr-F_t$ bonds in the $[KrF][MF_6]$ salts, which is consistent with the anticipated greater polarities of the Xe-F bonds based on the relative electronegativities of krypton (2.97),[347] xenon (2.58)[347] and fluorine (4.00)[348] on the Pauling scale. The larger negative charge associated with the MF_6^- anions in the XeF^+ salts also imparts lower M-F bond orders (AsF_6^-, 0.41 - 0.54; SbF_6^-, 0.44 - 0.45; BiF_6^-, 0.33 - 0.35), however, this effect is likely counterbalanced by an increase in ionic bonding, because the non-bridging M-F bond lengths are comparable in the $[KrF][MF_6]$ and $[XeF][MF_6]$ salts. Finally, the reduction of the covalent bonding in the $[XeF][MF_6]$ ion pairs is further illustrated by the absence of F_t--F_b bonding interactions, contrasting with the $[KrF][MF_6]$ ion pairs for which these bond orders range from 0.17 (As) to 0.18 (Sb, Bi).[23]

The differences between the Mayer valencies of the $[XeF][MF_6]$ and $[KrF][MF_6]$ ion pairs parallel their Mayer bond order differences (*vide supra*). The greater ionic character of xenon(II) salts, relative to their krypton(II) analogues, has the effect of lowering the Xe-F, and M-F bond orders, which consequently lowers the valencies of each of the atoms in the $[XeF][MF_6]$ salts. The xenon valence exhibits little variation among the $[XeF][MF_6]$ salts (As, 0.52; Sb, 0.51; Bi, 0.59), but is less than half of that

calculated for the [KrF][MF$_6$] ion pairs (1.31 - 1.32).[23] The pnicogen valencies (As, 2.82; Sb, 2.41; Bi, 1.88) are also approximately half of that calculated for the krypton analogues (As, 5.60, Sb 5.14, Bi, 3.15),[23] with the anomalously low values of the BiF$_6^-$ salts being attributed to the effective core potential used for the bismuth atom.

5.4. Conclusion

The Xe-F bond lengths in crystalline XeF$_2$ have been determined with greater precision at -173 °C, but are consistent with those obtained in earlier crystallographic studies. Despite significant variations in the fluoride ion affinities of the parent pnicogen fluorides, the Xe-F$_t$ bond length does not differ significantly among the structures of [XeF][MF$_6$] (M = As, Sb) and [XeF][Sb$_2$F$_{11}$]. With the exception of the bismuth salts, [XeF][BiF$_6$] and [XeF][Bi$_2$F$_{11}$], where the Xe-F$_t$ bond lengths are slightly longer, this trend is consistent with the absence of Kr-F$_t$ bond length variations in the structures of the [KrF][MF$_6$] (M = As, Sb, Bi, Au) salts, and suggests that the Xe-F$_t$ bond lengths of the [XeF][MF$_6$] (M = As, Sb) and [XeF][Sb$_2$F$_{11}$] salts likely approximate that of the gas-phase XeF$^+$ cation. As noted for the krypton analogues, the experimental Xe--F$_b$ bond lengths in the XeF$^+$ salts show a much stronger anion-dependence, increasing in the order [XeF][BiF$_6$] $\approx$ [XeF][AsF$_6$] < [XeF][Bi$_2$F$_{11}$] < [XeF][SbF$_6$] < [XeF][Sb$_2$F$_{11}$]. This ordering reflects the relative Lewis acidities of the parent MF$_5$ (M = As, Sb, Bi) and M$_2$F$_{11}$ (M = Sb, Bi) species predicted from theoretical calculations with the exception that the Lewis acidities of BiF$_5$ and Bi$_2$F$_{10}$ appear to be slightly weaker than the calculated results imply. Although the M--F$_b$ bond lengths cannot be directly compared among these salts, comparisons among the bridging and non-bridging M-F bond lengths for a given group 15 atom predict the same relative ordering of the MF$_5$ and M$_2$F$_{10}$ fluoride ion affinities as that obtained by comparison of the Xe--F$_b$ bond lengths.

The gas-phase geometries of the [XeF][MF$_6$] ion pairs were determined by use of the MPW1PW91 method and are in reasonable agreement with the structures obtained by X-ray diffraction. Unfortunately, the Xe--F$_b$ and M--F$_b$ bond lengths, which were of particular interest, were consistently underestimated and overestimated, respectively, for the [XeF][MF$_6$] ion pairs. The vibrational spectra obtained from these energy-minimized structures were used to reinterpret the spectra of the [XeF][MF$_6$] (M = As, Sb, Bi) salts in greater detail. Reasonable agreement was obtained for the Xe-F$_t$ stretching frequencies, however, the Xe--F$_b$ stretching frequencies varied widely from one salt to the next, a property that is suspected to be a consequence of the positioning of F$_b$ between the two heavy atoms. The atomic charges, Mayer bond orders and Mayer valencies obtained from the natural bond order (NBO) analysis of calculated structures suggest that the [XeF][MF$_6$] salts are more ionic in terms of both the nature of the cation-anion interaction and the polarities of the Xe-F and M-F bonds than their [KrF][MF$_6$] analogues.

CHAPTER 6

X-RAY CRYSTAL STRUCTURES OF $[XF_6][Sb_2F_{11}]$ (X = Cl, Br, I); ^{35,37}Cl, ^{79,81}Br AND ^{127}I NMR STUDIES AND ELECTRONIC STRUCTURE CALCULATIONS OF THE XF_6^+ CATIONS[349]

6.1. Introduction

The IF_6^+ cation was first prepared as its AsF_6^- and $Sb_3F_{16}^-$ salts by the reaction of IF_7 with AsF_5[218,219] and SbF_5.[219] In contrast, the coordinatively saturated natures of the ClF_6^+ and BrF_6^+ cations require that they be prepared by the oxidative fluorination of ClF_5 (or ClO_2F) and BrF_5. Although PtF_6 oxidizes ClF_5[220-222] or ClO_2F[221,222] to $[ClF_6][PtF_6]$ in approximately 17% yield with respect to PtF_6 (eq 6.1 - 6.3), no means of

$$2ClF_5 + 2PtF_6 \xrightarrow{\text{unfiltered UV}} [ClF_6][PtF_6] + [ClF_2][PtF_6] + F_2 \qquad (6.1)$$

$$2ClF_5 + 2PtF_6 \xrightarrow{\text{filtered UV}} [ClF_6][PtF_6] + [ClF_4][PtF_6] \qquad (6.2)$$

$$6ClO_2F + 6PtF_6 \xrightarrow{-78\,°C} [ClF_6][PtF_6] + 5[ClO_2][PtF_6] + O_2 \qquad (6.3)$$
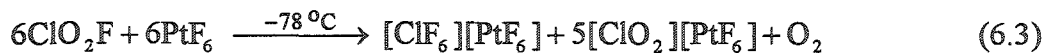
separating $[ClF_6][PtF_6]$ from the chlorine(III) and (V) byproducts has been devised. In contrast, PtF_6 is incapable of oxidizing BrF_5 to BrF_6^+ under similar, or photolytic conditions,[36] which is consistent with the general reluctance of bromine and other late period 4 elements to achieve their highest oxidation states.[350] The salts, $[ClF_6][AsF_6]$[37] and $[BrF_6][AsF_6]$,[36] can be obtained in high purity, but in low yields (ca. 11 and < 20%, respectively), by oxidative fluorination of ClF_5 and BrF_5 with $[KrF][AsF_6]$ or $[Kr_2F_3][AsF_6]$ (eq 6.4, 6.5). The $[ClF_4][AsF_6]$ and $[BrF_4][AsF_6]$ salts are obtained as side

$$XF_5 + [KrF][AsF_6] \rightarrow [XF_6][AsF_6] + Kr \quad (X = Cl, Br) \qquad (6.4)$$

$$XF_5 + [Kr_2F_3][AsF_6] \rightarrow [XF_6][AsF_6] + KrF_2 + Kr \quad (X = Cl, Br) \qquad (6.5)$$
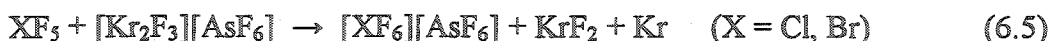
products in these reactions as a consequence of the auto-decomposition of [KrF][AsF$_6$] and [Kr$_2$F$_3$][AsF$_6$] to Kr, F$_2$ and AsF$_5$, and the ensuing reaction of AsF$_5$ with XF$_5$, however, both have significant dissociation vapor pressures at room temperature and can be removed from the non-volatile [XF$_6$][AsF$_6$] (X = Cl, Br) salts under dynamic vacuum.[36,37] The [XF$_6$][AsF$_6$] (X = Cl, Br) salts can be prepared in higher yields (*ca.* 42 and 32%, respectively) using the thermodynamically unstable oxidant, NiF$_3^+$, prepared *in situ* by reaction of NiF$_6^{2-}$ with AsF$_5$ in HF (eq 6.6).[31] Although [XF$_6$][AsF$_6$] (X = Cl, Br)

[Cs]$_2$[NiF$_6$] + 5AsF$_5$ + XF$_5$ →

$$[XF_6][AsF_6] + [Ni][AsF_6]_2 + 2[Cs][AsF_6] \quad (X = Cl, Br) \quad (6.6)$$
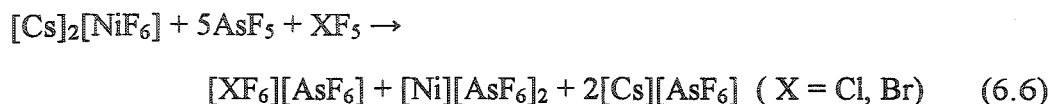
can be separated from [Ni][NiF$_6$] and [Cs][AsF$_6$] based on the solubilities of the products in HF, the salts prepared by this method are generally of lower purity than when prepared using [KrF][AsF$_6$] or [Kr$_2$F$_3$][AsF$_6$].[31]

The vibrational spectra of salts containing the ClF$_6^+$,[31,37,220,221,351] BrF$_6^+$ [31,36,176] and IF$_6^+$ [352-355] cations have been reported and are consistent with octahedral symmetries for each member of the series. The ^{19}F NMR spectra of ClF$_6^+$,[31,37,221,222] BrF$_6^+$ [31,36] and IF$_6^+$ [166,355] and the [127]I NMR spectrum of IF$_6^+$ [166] in anhydrous HF solution exhibit well-resolved halogen-fluorine spin-spin couplings, which are indicative of near-zero electric field gradients at the quadrupolar [35,37]Cl ($I = {}^3/_2$), [79,81]Br ($I = {}^3/_2$) and [127]I ($I = {}^5/_2$) nuclei that arise as a consequence of their octahedral coordination. Spin-spin couplings have also been observed in the ^{19}F and [127]I NMR spectra of powdered [IF$_6$][AsF$_6$],[356] however, minor distortions of the cation in the solid-state result in partial quadrupolar collapse of the signals and much broader line widths. Powder X-ray diffraction studies of [ClF$_6$][AsF$_6$],[37] [BrF$_6$][AsF$_6$][176] and [IF$_6$][AsF$_6$][352,357] have not afforded detailed structural information about the XF$_6^+$ cations, however, the cubic morphologies of these salts (space group, *Pa3*) are consistent with octahedral geometries for the XF$_6^+$ and AsF$_6^-$ ions.

The present study provides the first detailed structural characterization of the XF_6^+ cations by single crystal X-ray diffraction. The solid-state structures of the XF_6^+ cations and their previously reported vibrational frequencies are compared with those calculated using the HF, MP2 and LDF methods. These calculations have been used to assess the electronic structures and bonding of the XF_6^+ (X = Cl, Br, I) cation series. The spectroscopic characterizations of the XF_6^+ cations have been extended to include the ^{35}Cl, ^{37}Cl, ^{79}Br, ^{81}Br and ^{127}I solution NMR spectra of $[ClF_6][AsF_6]$, $[BrF_6][AsF_6]$ and $[IF_6][Sb_3F_{16}]$, and the determination of the spin-lattice relaxation times (T_1) of these central nuclei for the XF_6^+ cations.

6.2. Results and Discussion

The $Sb_2F_{11}^-$ salts of ClF_6^+, BrF_6^+ and IF_6^+ were chosen for investigation by X-ray diffraction over the more easily prepared AsF_6^- salts for two reasons: (1) the electron density of arsenic is very similar to that of bromine and would not allow for easy differentiation between the octahedral BrF_6^+ and AsF_6^- ions in the Fourier difference maps during the refinement of the crystal structure of $[BrF_6][AsF_6]$ (a similar problem would be encountered for $[IF_6][SbF_6]$), and (2) the AsF_6^- salts have been shown by powder diffraction to crystallize in the cubic space group, $Pa3$,[37,176,352] and may be prone to disorder as a result of the high unit cell symmetry. Salts of other octahedral anions, such as SbF_6^-, and PtF_6^-, were avoided for similar reasons. The use of the $Sb_2F_{11}^-$ anion avoids both of the aforementioned problems because of its non-octahedral geometry and the reduced unit cell symmetry of the $[XF_6][Sb_2F_{11}]$ salts (space group, $P2_1/n$). Furthermore, the $Sb_2F_{11}^-$ salts crystallize selectively from anhydrous HF when the mole ratio $SbF_5:[XF_6][SbF_6] \geq 1$.

6.2.1. Syntheses of [ClF$_6$][AsF$_6$], [ClF$_6$][Sb$_2$F$_{11}$], [BrF$_6$][AsF$_6$], [BrF$_6$][Sb$_2$F$_{11}$] and [IF$_6$][Sb$_3$F$_{16}$]

The salts [ClF$_6$][AsF$_6$][37] and [BrF$_6$][AsF$_6$][36] were prepared by oxidation of ClF$_5$ and BrF$_5$ with [KrF][AsF$_6$] at ambient temperature as previously described. The salt, [IF$_6$][Sb$_3$F$_{16}$], was prepared by the reaction of IF$_7$ with excess SbF$_5$ (eq 6.7). These salts

$$IF_7 + 3SbF_5 \rightarrow [IF_6][Sb_3F_{16}] \tag{6.7}$$

were dissolved in anhydrous HF for the NMR studies. The [XF$_6$][Sb$_2$F$_{11}$] (X = Cl, Br) salts, used for the crystallographic studies, were prepared from [XF$_6$][AsF$_6$] by the displacement of AsF$_5$ with SbF$_5$ in anhydrous HF (eq 6.8). Crystals of [XF$_6$][Sb$_2$F$_{11}$]

$$[XF_6][AsF_6] + 2SbF_5 \rightarrow [XF_6][Sb_2F_{11}] + AsF_5 \quad (X = Cl, Br) \tag{6.8}$$
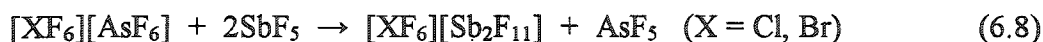
(X = Cl, Br, I) suitable for X-ray crystallography were grown by slowly cooling HF solutions of [XF$_6$][Sb$_2$F$_{11}$] (X = Cl, Br) and [IF$_6$][Sb$_3$F$_{16}$].

6.2.2. X-ray Crystal Structures of [XF$_6$][Sb$_2$F$_{11}$] (X = Cl, Br, I)

The unit cell parameters and refinement statistics for [ClF$_6$][Sb$_2$F$_{11}$], [BrF$_6$][Sb$_2$F$_{11}$] and [IF$_6$][Sb$_2$F$_{11}$] are given in Table 6.1. The bond lengths, contact distances and bond angles determined for [ClF$_6$][Sb$_2$F$_{11}$], [BrF$_6$][Sb$_2$F$_{11}$] and [IF$_6$][Sb$_2$F$_{11}$][358] are summarized in Table 6.2.

The crystal structures of [ClF$_6$][Sb$_2$F$_{11}$] (-130 °C), [BrF$_6$][Sb$_2$F$_{11}$] (-130 °C) and [IF$_6$][Sb$_2$F$_{11}$] (-173 °C) are isomorphous (Figure 6.1), and were solved in the monoclinic $P2_1/n$ space group (Z = 4), whereas the crystal structure of [IF$_6$][Sb$_2$F$_{11}$] (-100 °C)[359] was solved in the monoclinic space group $P2_1/m$ (Z = 4). The structures consist of Sb$_2$F$_{11}^-$ anions, which lie on general positions, and two XF$_6^+$ cations, one of which lies on the origin and the second lies in the centre of the b-c face of the unit cell. The packing of the [XF$_6$][Sb$_2$F$_{11}$] salts is best described in terms of layers of XF$_6^+$ cations and Sb$_2$F$_{11}^-$ anions lying parallel to the b-c face of the unit cell (Figure 1d). It is noteworthy that the unit cell

Table 6.1. Summary of Crystal Data and Refinement Results for $[ClF_6][Sb_2F_{11}]$, $[BrF_6][Sb_2F_{11}]$ and $[IF_6][Sb_2F_{11}]$

	$[ClF_6][Sb_2F_{11}]$	$[BrF_6][Sb_2F_{11}]$	$[IF_6][Sb_2F_{11}]$	$[IF_6][Sb_2F_{11}]^a$
space group	$P2_1/n$	$P2_1/n$	$P2_1/n$	$P2_1/m$
a	11.824(2)	11.931(2)	11.844(1)	11.885(1)
b	8.434(2)	8.492(2)	8.617(1)	8.626(1)
c	12.088(2)	12.103(2)	11.979(2)	12.000(1)
β	97.783(6)	97.558(6)	98.915(2)	98.44(1)
V	1194.3(4)	1215.5(4)	1207.8(3)	1216.9(2)
Z	4	4	4	4
mol. wt. (g mol^{-1})	601.93	646.38	693.40	693.40
ρ_{calcd} (g cm^{-3})	3.348	3.969	3.813	3.785
T (°C)	-130	-130	-173	-100
μ (mm^{-1})	4.95	11.23	7.23	7.181
R_1^b	0.0488	0.0707	0.0217	0.0635
wR_2^c	0.1070	0.1577	0.0601	0.1689

[a] Cell parameters for $[IF_6][Sb_2F_{11}]$ at -100 °C were obtained from ref 359.

$$^b R_1 = \frac{\sum \left| |F_o| - |F_c| \right|}{\sum |F_o|} \text{ for } I > 2\sigma(I). \quad ^c wR_2 = \frac{\sum \left| (|F_o| - |F_c|) w^{\frac{1}{2}} \right|}{\sum (F_o | w)} \text{ for } I > 2\sigma(I).$$

Table 6.2.   Summary of Bond Lengths, Contact Distances and Bond Angles for
[ClF$_6$][Sb$_2$F$_{11}$], [BrF$_6$][Sb$_2$F$_{11}$] and [IF$_6$][Sb$_2$F$_{11}$]

	[ClF$_6$][Sb$_2$F$_{11}$]	[BrF$_6$][Sb$_2$F$_{11}$]	[IF$_6$][Sb$_2$F$_{11}$]	[IF$_6$][Sb$_2$F$_{11}$][a]
bond lengths (Å)				
X(1)-F(1)	1.558(4)	1.684(9)	1.778(8)	1.767(7)
X(1)-F(2)	1.548(4)	1.657(9)	1.779(8)	1.780(10)
X(1)-F(3)	1.548(5)	1.659(8)	1.774(3)	1.771(7)
X(2)-F(4)	1.551(5)	1.664(10)	1.789(7)	1.782(6)
X(2)-F(5)	1.547(4)	1.657(8)	1.773(2)	1.775(9)
X(2)-F(6)	1.550(4)	1.674(9)	1.779(8)	1.769(6)
Sb(1)-F(7)	1.852(4)	1.847(9)	1.865(2)	
Sb(1)-F(8)	1.850(5)	1.838(10)	[b]	
Sb(1)-F(9)	1.841(5)	1.873(10)	[b]	
Sb(1)-F(10)	1.846(5)	1.855(11)	[b]	
Sb(1)-F(11)	1.857(6)	1.844(11)	[b]	
Sb(1)-F(12)	2.045(4)	2.046(9)	2.057(2)	
Sb(2)-F(12)	2.019(4)	2.028(8)	2.033(2)	
Sb(2)-F(13)	1.864(4)	1.858(9)	1.866(2)	
Sb(2)-F(14)	1.852(5)	1.850(9)	1.841(8)	
Sb(2)-F(15)	1.855(5)	1.854(10)	1.854(7)	
Sb(2)-F(16)	1.862(4)	1.864(9)	1.870(8)	
Sb(2)-F(17)	1.843(5)	1.838(9)	1.869(8)	
inter-ligand contact distances for XF$_6$$^+$(Å)[c]				
F(1)···F(2)	2.194	2.362	2.522	
F(1)···F(3)	2.193	2.348	2.503	
F(1)···F(2A)	2.198	2.363	2.510	
F(1)···F(3A)	2.200	2.379	2.521	
F(2)···F(3)	2.199	2.351	2.527	
F(2)···F(3A)	2.180	2.338	2.497	
F(4)···F(5)	2.190	2.352	2.517	
F(4)···F(6)	2.192	2.367	2.554	
F(4)···F(5A)	2.190	2.344	2.520	

Table 6.2.   continued...

	[ClF$_6$][Sb$_2$F$_{11}$]	[BrF$_6$][Sb$_2$F$_{11}$]	[IF$_6$][Sb$_2$F$_{11}$]	[IF$_6$][Sb$_2$F$_{11}$][a]
F(4)···F(6A)	2.193	2.353	2.492	
F(5)···F(6)	2.192	2.356	2.526	
F(5)···F(6A)	2.187	2.355	2.497	
inter-ionic contact distances (Å)[c]				
F(1)···F(8)	2.746	2.777	2.551[d]	
F(1) ···F(13)	2.914	2.911	2.802	
F(2)···F(8)	2.934	[2.959]	2.893[d]	
F(2)···F(13)	2.771	2.801	2.784	
F(2)···F(11)	2.743	2.789	2.704[d]	
F(3)···F(8)	2.877	2.872	2.654[d]	
F(3)···F(9)	2.846	2.871	2.769[d]	
F(4)···F(7)	2.831	2.878	[2.984]	
F(4)···F(16)	2.766	2.757	2.781	
F(4)···F(15)	2.870	2.911	2.882	
F(5)···F(17)	2.688	2.679	[2.974]	
F(5)···F(15)	2.905	2.913	[3.046]	
F(5)···F(13)	[2.998]	[2.946]	2.836	
F(6)···F(7)	2.920	2.901	[2.962]	
F(6)···F(10)	2.599	2.567	2.722[d]	
F(6)···F(16)	2.916	2.914	2.904	
F(6)···F(15)	2.809	2.810	2.732	
X(1)···F(8)	[3.451]	[3.483]	3.401[d]	
X(1)···F(9)	[3.541]	[3.560]	3.412[d]	
X(1)···F(13)	[3.515]	[3.527]	3.435	
X(1)···F(11)	[3.715]	[3.812]	[3.923]	
X(2)···F(7)	[3.522]	[3.547]	[3.579]	
X(2)···F(16)	[3.540]	[3.554]	[3.491]	
X(2)···F(15)	[3.460]	[3.493]	[3.870]	
X(2)···F(13)	[4.061]	[4.059]	[3.499]	

Table 6.2.   continued...

	[ClF$_6$][Sb$_2$F$_{11}$]	[BrF$_6$][Sb$_2$F$_{11}$]	[IF$_6$][Sb$_2$F$_{11}$]	[IF$_6$][Sb$_2$F$_{11}$][a]
bond angles (deg)				
F(1)-X(1)-F(2)	89.9(3)	90.0(5)	90.3(1)	
F(1)-X(1)-F(3)	90.2(3)	89.3(5)	89.6(4)	
F(2)-X(1)-F(3)	90.5(3)	90.3(5)	90.7(4)	
F(4)-X(2)-F(5)	90.0(3)	90.2(5)	89.9(4)	
F(4)-X(2)-F(6)	90.0(3)	90.4(5)	91.4(1)	
F(5)-X(2)-F(6)	90.1(2)	90.0(5)	90.7(4)	
Sb(1)-F(12)-Sb(2)	145.2(3)	144.7(4)	144.1(1)	

[a] The geometric parameters for the two crystallographically non-equivalent Sb$_2$F$_{11}^-$ anions at -100 °C may be found in the supplementary information of ref 360.   [b] The equatorial Sb(1)-F(8-11) bonds of the four-fold disordered -SbF$_5$ group have lengths ranging from 1.72(2) - 1.92(2) Å.   [c] Contact distances given in square brackets exceed the sum of the van der Waals radii, but are provided for comparison.   [d] The F···F and I···F contact distances to F(8-11) correspond to the shortest distances of the modeled disorder.

199

Figure 6.1. The crystal structures of (a) [ClF$_6$][Sb$_2$F$_{11}$] (-130 °C), (b) [BrF$_6$][Sb$_2$F$_{11}$] (-130 °C) and (c) [IF$_6$][Sb$_2$F$_{11}$] (-173 °C). The packing diagram of (d) [ClF$_6$][Sb$_2$F$_{11}$] is representative of the three [XF$_6$][Sb$_2$F$_{11}$] (X = Cl, Br, I) salts. The thermal ellipsoids are shown at the 50% probability level.

volume increases on going from $[ClF_6][Sb_2F_{11}]$ (1194.3(4) $Å^3$) to $[BrF_6][Sb_2F_{11}]$ (1215.5(4) $Å^3$), but decreases slightly from $[BrF_6][Sb_2F_{11}]$ to $[IF_6][Sb_2F_{11}]$ (1207.8(3) $Å^3$). The contraction of the $[IF_6][Sb_2F_{11}]$ unit cell may be attributed, in part, to the lower data acquisition temperature (-173 °C) used for this salt when compared with that used for the lighter halogen analogues (-130 °C), however, at -100 °C, the unit cell volume of $[IF_6][Sb_2F_{11}]$ (1216.9(2) $Å^3$)[359] is comparable to that of $[BrF_6][Sb_2F_{11}]$ at -130 °C. For comparison, the unit cell volumes of $[XF_6][AsF_6]$ obtained at 22 °C increase in the order $[BrF_6][AsF_6]$ (829.0 $Å^3$)[37] < $[ClF_6][AsF_6]$ (849.3 $Å^3$)[176] < $[IF_6][AsF_6]$ (854.7 $Å^3$).[352] Thus, the unit cell volume is not rigorously dependent upon the cation size, but is also influenced by the packing efficiency of the ions in the solid state.

Although the XF_6^+ cations are constrained to local C_i site symmetries by the $P2_1/n$ space group, the cis-F-X-F bond angles were not differentiable from 90° at the ±3σ (99.7%) confidence limit (Table 6.2). The average X-F bond lengths (Cl-F, 1.550(4) Å; Br-F, 1.666(11) Å; I-F, (1.779(6) Å) increase in a near-linear manner with increasing atomic number, Z_X, of the central halogen atom. The ranges of the interligand F···F distances in ClF_6^+ (2.180 - 2.200 Å), BrF_6^+ (2.338 - 2.379 Å) and IF_6^+ (2.492 - 2.554 Å) are small, with the average F···F distance increasing down the group, reflecting the increasing size and ability of the central halogen valence shell to accommodate higher coordination numbers (see section 6.4.2)

The XF_6^+ cations have 13-16 interionic F···F contacts to neighbouring anions that lie within twice the van der Waals radius of fluorine (2.70,[287] 2.94 $Å^{286}$) (Table 6.2). The interionic F···F contact distances are comparable in the three XF_6^+ salts investigated, ranging from 2.60, 2.57 and 2.55 to 2.93, 2.91 and 2.90 Å for $[ClF_6][Sb_2F_{11}]$, $[BrF_6][Sb_2F_{11}]$ and $[IF_6][Sb_2F_{11}]$, respectively. The large number of long contacts and the formal negative charges on the interacting fluorine atoms suggest that these cation-anion

interactions are diffuse and non-directional, consequently, significant distortions of the octahedral XF_6^+ cations are not observed. Although all three XF_6^+ cations have six $F\cdots X$ contacts between the fluorine atoms of the anions and the central halogen atoms that are close to the sum of the fluorine $(1.35,[287]\ 1.47\ \text{Å}[286])$ and central halogen $(Cl:\ 1.80,[287]\ 1.75;[286]\ Br:\ 1.95,[287]\ 1.85;[286]\ I:\ 2.15,[287]\ 1.98\ \text{Å}[286])$ van der Waals radii, the shortest are observed for $[IF_6][Sb_2F_{11}]$ (Table 6.2). The shorter $I\cdots F$ contacts to the $Sb_2F_{11}^-$ anions may account for the smaller unit cell volume of $[IF_6][Sb_2F_{11}]$ relative to that of $[BrF_6][Sb_2F_{11}]$ (Table 6.1).

The equatorial fluorine atoms of the $Sb_2F_{11}^-$ anions of the ClF_6^+ and BrF_6^+ salts have staggered conformations with respect to each other. In contrast, the $Sb_2F_{11}^-$ anion of the IF_6^+ salt exhibits a four-fold rotational disorder of the equatorial fluorine positions of $Sb(1)$ about the $F(7)-Sb(1)-F(12)$ axis (Figure 6.1c). This axis is nearly collinear with the three-fold axis passing through the $(F(4),\ F(5),\ F(6))$ face of the cation. The superposition of the the four-fold symmetry of the $Sb(1)-F(8-11)$ group with the three-fold symmetry of a cation face does not afford an energetically favourable conformation for the fluorine atoms on the anion, and likely accounts for the observed disorder. In contrast, the ordered equatorial $Sb(2)-F(14-17)$ group of this salt is likely a consequence of the $F(12)-Sb(2)-F(13)$ axis not being aligned with a three-fold axis of the cation.

The $Sb(1)-F(12)-Sb(2)$ bond angles lie within a narrow range for the $[XF_6][Sb_2F_{11}]$ salts (Cl, $145.2(3)°$; Br, $144.7(4)°$; I, $144.1(1)°$). A recent computational study of the gas-phase geometry of the $Sb_2F_{11}^-$ anion has shown that the energy-minimized structure of the $Sb_2F_{11}^-$ anion has D_{4h} point symmetry, with a fluorine bridge angle of $180°$ and an eclipsed equatorial fluorine conformation.[361] The fluorine bridge angle was shown to be highly deformable and the potential energy surface of the anion was shown to be insensitive to the relative conformations of equatorial fluorine atoms.

Thus, the conformational geometry and fluorine bridge angle of the $Sb_2F_{11}^-$ anion are expected to be dependent on crystal packing. Edwards and co-workers[340-343] have investigated the effects of the close packing arrangements of the light atoms in fluorine-bridged species. These studies showed that when the metal atoms lie within the octahedral interstitial sites of hexagonal close-packed oxygen and fluorine atoms, the ideal bridge bond angle is 132°. When the metal atom lies within the octahedral interstitial sites of a cubic close-packed lattice of oxygen and fluorine atoms, the ideal bridge bond angle is 180°. The fluorine atom packings and fluorine bridge angles in the $[XF_6][Sb_2F_{11}]$ salts most closely resemble hexagonal close packed arrangements. Thus, the staggered and bent geometries of the anions in these salts may be attributed to solid-state packing effects.[362-364]

6.2.3. $^{35,37}Cl$, $^{79,81}Br$ and ^{127}I NMR Parameters of XF_6^+ (X = Cl, Br, I)

The quadrupolar natures of the $^{35,37}Cl$ ($I = {}^3/_2$), $^{79,81}Br$ ($I = {}^3/_2$) and ^{127}I ($I = {}^5/_2$) nuclides tend to produce extremely broad resonances as a consequence of the highly efficient quadrupolar relaxation mechanism, and generally do not allow the spectra of these nuclei to be exploited for chemical studies. Nevertheless, the few NMR studies in which the $^{35,37}Cl$,[166,365-368] $^{79,81}Br$[166,207,369] and ^{127}I[166,356,366,369-371] nuclides have been employed have clearly demonstrated the usefulness of these nuclides, under certain conditions, for chemical characterization in solution. The relaxation of a quadrupolar nucleus, under the conditions of extreme narrowing, is described by eq 6.9 where $\Delta v_{1/2}$ is

$$\Delta v_{1/2} = \frac{1}{\pi T_1} = \frac{1}{\pi T_2} = \left(\frac{3\pi}{10}\right)\left(\frac{2I+3}{I^2(2I-1)}\right)\left(\frac{eqQ}{h}\right)^2\left(1+\frac{\eta^2}{3}\right)\tau_c \qquad (6.9)$$

the line width at half-height; T_2 is the spin-spin relaxation time; T_1 is the spin-lattice relaxation time; I is the nuclear spin quantum number; Q is the nuclear quadrupole

moment; eq is the electric field gradient (EFG), η is the asymmetry parameter for the EFG; and τ_c is the isotropic rotational correlation time.[372] Equation 6.9 reveals that line widths are dramatically reduced for nuclides having a high value of I, a small value of Q or a combination of the two in accord with the line width factor, $(2I + 3)/[I^2(2I - 1)]Q^2$. The merits of the ^{35,37}Cl, ^{79,81}Br and ^{127}I nuclides with regard to these requirements have been discussed previously.[166] Moreover, narrow line widths are known to arise from quadrupolar nuclei residing at the centre of a highly symmetric ligand environment (e.g., O_h or T_d) for which the values of eq and η are low.[373] The local octahedral environments of the central halogen nuclides in the XF_6^+ (X = Cl, Br, I) cations have consequently allowed the characterization of all three hexafluorocations in anhydrous HF solution by ^{35,37}Cl, ^{79,81}Br and ^{127}I NMR spectroscopy in the present study.

The NMR spectra of the central halogen nuclei of $[^{35,37}ClF_6][AsF_6]$, $[^{79,81}BrF_6][AsF_6]$, and $[^{127}IF_6][Sb_3F_{16}]$ dissolved in anhydrous HF at 27 °C are shown in Figure 6.2. The ^{127}I NMR spectrum of the IF_6^+ cation has previously been reported for $[IF_6][AsF_6]$,[166] but has been obtained for $[IF_6][Sb_3F_{16}]$ in HF solvent in the present study, demonstrating that the anion has little effect on the chemical shift or $^1J(^{127}I-^{19}F)$. The ^{35}Cl, ^{37}Cl, ^{79}Br, ^{81}Br and ^{127}I spectra of the XF_6^+ cations are binomial septets having intensity ratios of 1:6:15:20:15:6:1 as a consequence of coupling to the six chemically equivalent ^{19}F nuclei. The well-resolved $^1J(^{19}F-^mX)$ couplings are consistent with near-zero electric field gradients at the quadrupolar ^{35,37}Cl, ^{79,81}Br and ^{127}I nuclei, and octahedral cation geometries.

6.2.3.1. $^{35,37}ClF_6^+$, $^{79,81}BrF_6^+$ and $^{127}IF_6^+$ Spin-Lattice Relaxation Times

The ^{35,37}Cl, ^{79,81}Br and ^{127}I spin-lattice relaxation times, T_1, for $[ClF_6][AsF_6]$, $[BrF_6][AsF_6]$ and $[IF_6][Sb_3F_{16}]$ in anhydrous HF solutions obtained by the spin-inversion-recovery technique for the ^{19}F-coupled cations are summarized in Table 6.3. The T_1-

Figure 6.2. The (a) ^{35}Cl, (b) ^{37}Cl, (c) ^{79}Br, (d) ^{81}Br and (e) ^{127}I NMR spectra of [ClF$_6$][AsF$_6$], [BrF$_6$][AsF$_6$] and [IF$_6$][Sb$_3$F$_{16}$] in anhydrous HF at 27 °C.

Table 6.3. Spin-Lattice Relaxation Times (T_1), and Isotopic T_1-Ratios for ^{35,37}Cl, ^{79,81}Br and ^{127}I of ClF_6^+, BrF_6^+ and IF_6^+ [a]

cation	T_1 (s)	Q (10^{-28} m^2)	T_1/T_1'	$(Q^2/Q'^2)^{-1}$	$\Delta\nu_{1/2}(X)_{obs}$ [b] (Hz)	$\Delta\nu_{1/2}(X)_{calcd}$ [c] (Hz)	$\Delta\nu_{1/2}(X)_{obs} - \Delta\nu_{1/2}(X)_{calcd}$ [c] (Hz)
$^{35}ClF_6^+$	1.32(3)	-0.08165(80) [d]			3.6	0.2	3.4
			0.51(2)	0.621(9)			
$^{37}ClF_6^+$	2.58(6)	-0.06435(64) [e]			3.2	0.1	3.1
$^{79}BrF_6^+$	0.0246(4)	0.313(3) [f]			25.0	12.9	12.1
			0.69(2)	0.70(1)			
$^{81}BrF_6^+$	0.0354(5)	0.262(3) [f]			16.8	9.0	7.8
$^{127}IF_6^+$	0.00653(1)	-0.710(10) [f]			55.5	48.8	6.7

[a] Data were obtained from the ^{35,37}Cl, ^{79,81}Br and ^{127}I NMR spectra of [ClF$_6$][AsF$_6$], [BrF$_6$][AsF$_6$] and [IF$_6$][Sb$_3$F$_{16}$] recorded in anhydrous HF solvent at 27 °C. [b] The line widths are given for the central line of each spectrum. [c] The line widths are calculated from $\Delta\nu_{1/2} = (\pi T_1)^{-1}$. [d] From ref 374. [e] From ref 374 and 375. [f] From ref 376.

relaxation time obtained for $[IF_6][Sb_3F_{16}]$ is comparable, but slightly smaller, than that previously obtained for $[IF_6][AsF_6]$ (9.7 ms) by use of line fitting techniques.[355,377] The T_1-relaxation times for the ^{35}Cl (1.32(3) s), ^{37}Cl (2.58(6) s), ^{79}Br (24.6(4) ms), ^{81}Br (35.4(5) ms) and ^{127}I (6.53(1) ms) nuclei of the XF_6^+ cations were determined to somewhat longer than those reported for 0.1 to 1.4 M solutions of $[N(C_2H_5)_4][^{35}ClO_4]$ (0.810 - 1.150 s), $[N(C_2H_5)_4][^{79}BrO_4]$ (13.3 - 22.8 ms), $[N(C_2H_5)_4][^{81}BrO_4]$ (18.7 - 31.9 ms) and 1.0 to 0.05 M solutions of $[N(C_2H_5)_4][^{127}IO_4]$ (3.9 - 6.1 ms) in CH_3CN.[166] As expected, the T_1-values decrease as the width factor of the central halogen nuclide increases for the XF_6^+ and XO_4^- ions (X = Cl, Br, I). The similar T_1-relaxation times determined for the central halogen nuclei of the XF_6^+ and XO_4^- ions are not surprising considering that both ions have cubic point symmetries, resulting in near-zero electric field gradients at the central nuclei. In addition to the highly symmetric environment around the central halogen atom, the comparatively large T_1-values of the XF_6^+ and XO_4^- ions are also attributed to the physical shielding of the central nuclei by their respective fluorine and oxygen ligands. Although this effect is not clearly evident when comparing the T_1-relaxation times of XF_6^+ and XO_4^-, the relaxation times of the spherically symmetric $^{35}Cl^-$ (23.8 ms), $^{81}Br^-$ (0.953 ms) and $^{127}I^-$ (0.190 ms) anions are significantly shorter[378] and may be attributed to electric field gradients induced by interactions with the aqueous solvent used in the latter studies and by larger rotational correlation times, τ_c, that result from solvation and ion-pair formation. The concentration dependence of T_1 was not investigated for the XF_6^+ cations, however, with the exception of $[ClF_6][AsF_6]$, the present solutions were more dilute than the most dilute solutions used for the T_1-investigations of the XO_4^- anions.[166] The use of dilute solutions minimizes ion-pairing effects, which, according to eq 6.9, should give rise to smaller τ_c-values and longer T_1-relaxation times as noted in the T_1 determinations of XO_4^-. In addition to the

concentration effect, a comparison of the XF_6^+ and XO_4^- T_1-relaxation times is complicated by the effect different solvent viscosities and dielectric constants have on τ_c and, hence, on T_1 in these studies.

If the T_1-relaxation time is dominated by the quadrupolar mechanism, then it follows from eq 6.9 that the line widths calculated from $\Delta\nu_{1/2} = (\pi T_1)^{-1}$ should equal those measured from the one-dimensional ^{35}Cl, ^{37}Cl, ^{79}Br, ^{81}Br and ^{127}I NMR spectra. A comparison of the line widths obtained by the two methods (Table 6.3) reveals that the observed line widths are greater than those derived from the T_1-relaxation times, however, the differences are small enough to support quadrupole relaxation as the dominant T_1-relaxation mechanism. The ^{127}I line width observed for $[IF_6][Sb_3F_{16}]$ (55.5 Hz) is narrower than those reported for $[IF_6][AsF_6]$ in HF solutions acidified with AsF_5 (170,[355] 70 Hz[166]). The $Sb_3F_{16}^-$ anion is expected to be extensively solvolyzed in HF, generating two mole equivalents of SbF_5, which serve to acidify the solution. This trend is in accord with the fluorine exchange mechanisms proposed by Brownstein and Selig[355] (eq 6.10, 6.11), which are expected to be suppressed as the acidity of the HF solutions

$$IF_6^+ + HF_2^- \quad \rightleftharpoons \quad IF_7 + HF \qquad\qquad (6.10)$$

$$IF_6^+ + 2HF \quad \rightleftharpoons \quad IF_7 + H_2F^+ \qquad\qquad (6.11)$$

increase. The minimal broadening of the central halogen line widths of $[ClF_6][AsF_6]$ and $[BrF_6][AsF_6]$ in HF solution in the absence of excess AsF_5, implies that ligand exchange routes analogous to those proposed in eq 6.12 and 6.13 are unlikely for the ClF_6^+ and BrF_6^+ cations, and is consistent with the fact that ClF_7 and BrF_7 are unknown.

The dominance of the quadrupolar mechanism is further confirmed for the $^{35,37}Cl$ and $^{79,81}Br$ nuclei by considering the $T_1(^{35}Cl)/T_1(^{37}Cl)$ and $T_1(^{79}Br)/T_1(^{81}Br)$ ratios. These ratios should be inversely proportional to the Q^2 ratios of these nuclei multiplied by the spin factors $(f_I = (2I + 3)/(I^2(2I - 1)))$ ratio as illustrated in eq 6.12. The nuclides ^{35}Cl,

$$\frac{T_1(^A X)}{T_1(^B X)} = \left(\frac{f_I(^B X)}{f_I(^A X)}\right)\left(\frac{Q^2(^B X)}{Q^2(^A X)}\right) \qquad\qquad (6.12)$$

^{37}Cl, ^{79}Br and ^{81}Br each have a nuclear spin quantum number of $^3/_2$, which conveniently eliminates the spin-factor terms for these cations. For ClF_6^+, the ratio of the ^{35}Cl and ^{37}Cl T_1-relaxation times is 0.51(2) lower than the value of 0.621(9) estimated from the nuclear quadrupole moments of ^{35}Cl (-0.08165(80) × 10^{-28} m^2 A)[374] and ^{37}Cl (-0.06435(64) × 10^{-28} m^2 A).[374,375] The ratio of the ^{79}Br and ^{81}Br T_1-relaxation times is 0.69(2), and is in excellent agreement with the value of 0.70(1) calculated from the quadrupolar moments of ^{79}Br (0.313(3) × 10^{-28} m^2 A) and ^{81}Br (0.262(3) × 10^{-28} m^2 A).[376]

6.2.3.2. ^{35,37}Cl, ^{79,81}Br and ^{127}I Chemical Shifts

The ^{35,37}Cl, ^{79,81}Br and ^{127}I chemical shifts obtained for the XF_6^+ cations are summarized in Table 6.4. The high-frequency chemical shifts of ^{35}Cl (814.3 ppm), ^{37}Cl (814.7 ppm), ^{79}Br (2079.9 ppm), ^{81}Br (2079.3 ppm) and ^{127}I (3380.6 ppm) are consistent with the high formal oxidation state of the central halogen and formal positive charge of the cation. The ^{127}I NMR chemical shift of $[IF_6][Sb_2F_{11}]$ is slightly higher in frequency than that reported for $[IF_6][AsF_6]$ (3361 ppm).[166] Despite the higher electronegativity of fluorine relative to that of oxygen, even higher frequency halogen chemical shifts are observed for $^{35}ClO_3^-$ (1050 ppm),[365] $^{35}ClO_4^-$ (1009 ppm),[166] $^{79,81}BrO_4^-$ (2489 ppm),[166] and $^{127}IO_4^-$ (4121 ppm),[166] and are presumably a consequence of the high bond orders of the X-O bonds in the latter species.

The tendency for chemical shift ranges to increase with increasing atomic number within a group is well documented and has been correlated with the non-relativistic and relativistic values of the radial terms, $\langle r^{-3}\rangle_{np}$ and $\langle r^{-3}\rangle_{nd}$, for the valence p and d electrons of the free atom.[379] The paramagnetic shielding term, which is proportional to $\langle r^{-3}\rangle_{np}$

Table 6.4.   Chemical Shifts and Coupling Constants for XF_6^+ (X = Cl, Br, I)[a]

cation	$\delta(^mX)$ (ppm)	$^1J(^mX\text{-}^{19}F)$ (Hz)	$^1K(X\text{-}F)$ $(10^{21}\ NA^{-2}m^{-3})$
$^{35}ClF_6^+$	814.3	339	3.057
$^{37}ClF_6^+$	814.7	283	3.065
$^{79}BrF_6^+$	2079.9	1575	5.541·
$^{81}BrF_6^+$	2079.3	1699	5.545
$^{127}IF_6^+$	3380.6	2744	12.046

[a] Parameters were obtained from the $^{35,37}Cl$, $^{79,81}Br$ and ^{127}I NMR spectra of $[ClF_6][AsF_6]$, $[BrF_6][AsF_6]$ and $[IF_6][Sb_3F_{16}]$ recorded in anhydrous HF solvent at 27 °C.

and $<r^{-3}>_{nd}$, dominates the chemical shifts of heavy nuclei as illustrated by the simple atom-in-a-molecule approach (eq 6.13),[379-381] where P_i and D_i represent the degrees of

$$\sigma^P \approx -\left(\frac{\mu_o}{4\pi}\right)\left(\frac{4\mu_B^2}{\Delta E}\right)\left[<r^{-3}>_{np} P_i + <r^{-3}>_{nd} D_i\right] \qquad (6.13)$$

imbalance of valence electrons in the p and d orbitals, ΔE is the average excitation energy, μ_B is the Bohr magneton and μ_o is the permeability of a vacuum. The relationships between the chemical shifts and the atomic numbers of the central halogen nuclei of X^-, XF_6^+ and XO_4^- illustrates that this trend holds for the halogens (Figure 6.3). Excluding the halide ions, X^-, which serve as chemical shift references for chlorine, bromine and iodine, the relationships between chemical shift and Z_X are linear with positive slopes for both series. Both anion series also exhibit linear relationships between Z_X and $<a_o^3/r^3>_{np}$, where $<a_o^3/r^3>_{np}$ have been obtained from the atomic spectra of chlorine (7.16), bromine (13.55) and iodine (18.0).[382]

The dominance of the paramagnetic shielding terms in these species can also be assessed by comparing the ratios of the central halogen chemical shifts, referenced to the highly shielded X^- anions, where the paramagnetic shielding term is minimal, with the corresponding ratios of $<r^{-3}>_{np}$ (Table 6.5). Although the magnitudes of both ratios differ slightly, they exhibit the same periodic trends. It is noteworthy that the chemical shift ratios for the XF_6^+ and XO_4^- ions[383] exceed the $<r^{-3}>_{np}$ ratios, whereas the opposite is found when corresponding ratios are compared for compounds of the heavy group 14 (^{119}Sn and ^{207}Pb)[384] and group 16 (^{77}Se, ^{125}Te)[385] elements. The reversal within the XF_6^+ series may be a consequence of the high oxidation state (+7) of X, the highly ionic natures of their bonds and neglect of the $<r^{-3}>_{nd}$ contribution.[383]

Figure 6.3. Plots of the halogen chemical shifts of XF_6^+, XO_4^- and X^- ions (X = Cl, Br, I) versus atomic number, Z_X.

Table 6.5. Central Halogen Shielding Range Ratios and $<r^{-3}>_p$ Ratios for ClF_6^+, BrF_6^+ and IF_6^+

Central Halogen		Δ_X/Δ_Y [a]	$<r^{-3}>_{pX}/<r^{-3}>_{pY}$ [b]
X	Y		
ClF_6^+	BrF_6^+	0.392	
ClO_4^-	BrO_4^-	0.405[c]	0.528
ClF_6^+	IF_6^+	0.241	
ClO_4^-	IO_4^-	0.244[c]	0.398
BrF_6^+	IF_6^+	0.615	
BrO_4^-	IO_4^-	0.603[c]	0.753

[a] The shielding ratios are defined as $\Delta_X/\Delta_Y = [\delta(XF_6^+) - \delta(X^-)] / [\delta(YF_6^+) - \delta(Y^-)]$ and $\Delta_X/\Delta_Y = [\delta(XO_4^-) - \delta(X^-)] / [\delta(YO_4^-) - \delta(Y^-)]$. [b] The values of $<r^{-3}>_p$ are from ref 382. [c] The ratios of Δ_X/Δ_Y and $<r^{-3}>_{pX}/<r^{-3}>_{pY}$ for the XO_4^- (X = Cl, Br, I) anions were obtained from ref 383.

The ^{127}I chemical shift of the IF_6^+ cation is deshielded relative to that of IF_7 (3095 ppm)[166] and is in accord with the deshieldings exemplified by the ^{77}Se, ^{125}Te and ^{129}Xe chemical shifts of the fluoro-cations of selenium,[386] tellurium[387] and xenon[78,79] relative to those of their neutral parent fluorides.[78,386-388] (also see details in ref 389). Nuclear deshielding upon cation formation is a consequence of the paramagnetic contribution to nuclear magnetic shielding (eq 6.13), which is negative and proportional to $<r^{-3}>_{np}$, the electron imbalance terms (P_i, D_i) and ΔE. Contraction of the valence p-orbitals with increasing charge may be anticipated to be reflected in the X-F bond lengths. With few exceptions, the uncertainties in the average X-F bond lengths of the majority of cationic and neutral fluoro-species do not allow the correlation between deshielding of the central X nucleus and bond length contraction to be verified.[309,344,392-396] Significant bond length contractions do, however, occur for the XeF^+/XeF_2 and XeF_3^+/XeF_4 couples, and support the correlation.[397]. In addition, a change in the symmetry about the central nucleus is expected to result in a change in orbital mixing, when compared with the parent molecule, which leads to increased electron imbalance terms and nuclear deshielding. These interpretations are, at best, qualitative and ignore possible variations in the average excitation term, ΔE.

6.2.3.3. Coupling Constants, $^1J(^mX-^{19}F)$, $^1K(X-F)$ and $^1K(X-F)_{RC}$ of the Group 14 - 18 Hexafluoro-Species

The magnitudes of the isotropic coupling constants ($|^1J(^mX-^{19}F)|$) and reduced isotropic coupling constants ($|^1K(X-F)|$) obtained for the XF_6^+ cations in the present work are summarized in Table 6.4. The $|^1J(^mX-^{19}F)|$ coupling constants measured from the NMR spectra of the central halogen nuclei are in good agreement with those previously obtained from the ^{19}F NMR spectra $[ClF_6][AsF_6]$ ($|^1J(^{35}Cl-^{19}F)|$, 338 - 340; $|^1J(^{37}Cl-^{19}F)|$, 283 - 285.3 Hz),[31,37] $[ClF_6][SbF_6]$ ($|^1J(^{35}Cl-^{19}F)|$, 340; $|^1J(^{37}Cl-^{19}F)|$, 283 Hz),[37]

$[ClF_6][PtF_6]$ $(|^1J(^{35}Cl-^{19}F)|,$ 337; $|^1J(^{37}Cl-^{19}F)|,$ 281 Hz),[221] $[BrF_6][AsF_6]$ $(|^1J(^{79}Br-^{19}F)|,$ 1587; $|^1J(^{81}Br-^{19}F)|,$ 1709 Hz),[36] $[BrF_6][Sb_2F_{11}]$ $(|^1J(^{79}Br-^{19}F)|,$ 1575; $|^1J(^{81}Br-^{19}F)|,$ 1697 Hz),[36] and $[IF_6][AsF_6]$ $(|^1J(^{127}I-^{19}F)|,$ 2730 Hz)[166,355] in anhydrous HF solution. The value of $|^1J(^{127}I-^{19}F)|$ for $[IF_6][AsF_6]$ (2740 Hz),[166] in anhydrous HF, has also been determined from the ^{127}I NMR spectrum.[355] Although seldom extolled in the literature, J-couplings are more accurately determined from the NMR spectra of the high-spin quadrupolar nuclei than from the NMR spectrum of the spin-½ nucleus coupled to ^mX owing to the shorter relaxation times of ^mX relative to ^{19}F.[373,398] Thus, the $|^1J(^mX-^{19}F)|$ coupling constants determined from the spectra of the central high-spin ^mX nuclides in the present work, and previously for $[IF_6][AsF_6]$[166] are somewhat larger than those obtained from the ^{19}F NMR spectra.

6.2.3.3.1. Dominant Contributions to $^1J(^mX-^{19}F)$

The magnitudes and signs of $^1J(^mX-^{19}F)$ $(^mX = {}^{35}Cl, {}^{79}Br, {}^{127}I)$ for the XF_6^+ cations have recently been calculated using relativistic density functional theory (the ZORA-DFT method).[399] The magnitudes of the calculated isotropic J-coupling constants, $^{35}ClF_6^+$ (344 Hz), $^{79}BrF_6^+$ (1398 Hz) and $^{127}IF_6^+$ (2793 Hz), are in good agreement with the experimental values (*vide supra*). The signs of the calculated coupling constants were found to be negative in each case and are in accord with a previous empirical prediction (*vide infra*) that the signs of $^1K(X-F)$ for the isoelectronic hexafluoro-species of groups 14 - 17 are all negative.[36]

Ramsey's non-relativistic formalism[400] describes the indirect coupling of nuclear spins in terms of three coupling mechanisms, which contribute to the isotropic J-coupling: the Fermi-contact (FC) term and non-contact terms consisting of the spin-orbit (SO) mechanism, which is subdivided into diamagnetic (DSO) and paramagnetic (PSO) contributions, and the spin-dipolar (SD) contribution. The FC mechanism is customarily

assumed to be the dominant coupling term, however, the remaining non-contact terms can also make significant contributions.[399] For example, the PSO term is dominant for XF (X = Cl, Br, I) and XeF[+].[399] Both non-contact terms are dependent on $<r^{-3}>_{np}$, the expectation value of the inverse cube of the electron-nuclear distance of the valence p orbitals, which have a periodic dependence and are relatively large for the halogens.[382]

The indirect nuclear spin-spin coupling tensors of the XF_6^+ cations calculated using the ZORA-DFT method[399] did not separate the FC and SD terms, however, the FC + SD contributions dominated the isotropic indirect spin-spin coupling. The PSO term was shown to be highly dependent upon the number of electron lone pairs on the central heavy atom and was minimal for the XF_6^+ cations, which displayed low PSO/(FC + SD) ratios for ClF_6^+ (14/86), BrF_6^+ (24/76) and IF_6^+ (18/82).[399] In the ensuing discussion, the relative roles of the FC term and of the non-contact terms, SD and PSO, are assessed, semi-empirically, for the hexafluoro-species of groups 14 - 17 by examining trends among their isotropic reduced coupling constants.

The present discussion of the FC contributions to the $^1J(^mX-^{19}F)$ coupling constants of the XF_6^+ cations and isovalent species of groups 14 - 17 and periods 3 - 6 makes use of the formalism developed by Pople and Santry.[401] The FC term is given by eq 6.14, where all undefined symbols have their usual meanings and values, $|\Psi_{ns,X}(0)|^2$

$$J(^mX-^{19}F) = -\frac{4\mu_o\mu_B^2}{9\pi}\gamma_X\gamma_F|\Psi_{ns,X}(0)|^2|\Psi_{2s,F}(0)|^2\,\Pi_{XF} \qquad (6.14)$$

and $|\Psi_{2s,F}(0)|^2$ are the s electron densities of the ns valence orbitals at the nuclei of the X and F atoms and Π_{XF} is the mutual polarizability of the ns orbitals of X and F and is equivalent to the $P^2_{nsX/2sF}\,(^3\Delta E)^{-1}$ terms in the formalism of McConnell,[402] where $P_{nsX/2sF}$ is the s bond order term and $^3\Delta E$ is an average triplet excitation energy. For closely

related series, the magnitudes of the coupling constants are expected to be proportional to the s electron densities at the spin-coupled nuclei and to $P^2_{nsX/2sF}$.

6.2.3.3.2. Periodic Trends in $^1K(X\text{-}F)$

The spin-spin coupling constants of the XF_6^+ series are not directly comparable because $^1J(^mX\text{-}^{19}F)$ is also proportional to the product of the gyromagnetic ratios of ^mX and ^{19}F. The reduced coupling constant, $K(X\text{-}F)$, (eq 6.15) removes the nuclear

$$K(X-F) = \frac{4\pi^2 J(^mX - {}^{19}F)}{h\gamma_X\gamma_F} \tag{6.15}$$

dependence of the spin-spin coupling by factoring out the gyromagnetic ratios of the spin-coupled nuclei,[157,403] allowing comparisons to be made among spin-spin coupling constants of different nuclides of the same element and nuclides of different elements. The γ-values are positive for the naturally occurring spin-active nuclides of groups 14, 16 and 17, but are negative for those of group 15. Thus, the sign of $^1K(X\text{-}F)$ is also dependent on the group that X belongs to.

The substitution of eq 6.14 into eq 6.15 gives eq 6.16, which shows that $^1K(X\text{-}F)$

$$K(^mX - {}^{19}F) = -\frac{16}{9}\pi\mu_o\mu_B^2|\Psi_{ns,X}(0)|^2|\Psi_{2s,F}(0)|^2\Pi_{XF} \tag{6.16}$$

is proportional to the products of $|\Psi_{ns,X}(0)|^2$ and Π_{XF} when it is dominated by the FC mechanism. The Π_{XF} and $|\Psi_{2s,F}(0)|^2$ terms, to a first approximation, may be treated as constants for the structurally related and isovalent group 14 - 17 hexafluoro-species, so that plots of $^1K(X\text{-}F)$ versus $|\Psi_{ns,X}(0)|^2$ are expected to yield linear relationships having slopes that are proportional to $|\Psi_{ns,F}(0)|^2\Pi_{XF}$. The s electron densities of the valence orbitals at the nuclei of the main-group elements have been calculated for their free atoms,[404] and can be used as estimates of $|\Psi_{ns,X}(0)|^2$ and $|\Psi_{2s,F}(0)|^2$ for the group 14 - 17

hexafluoro-species assuming that bonding has a negligible effect on the valence s orbital electron densities at the spin-coupled nuclei. Relativistic corrections have been applied to $|\Psi_{ns,X}(0)|^2$ of the main-group elements of periods 4 - 6,[404] with the corrected values denoted by $|\Psi_{ns,X}(0)|^2_{rel}$, but have not been applied to the period 1 - 3 elements where relativistic effects are negligible. Relativistic effects for the heavier elements result in contraction of the valence s orbitals such that $|\Psi_{ns,X}(0)|^2_{rel}$ is invariably greater than $|\Psi_{ns,X}(0)|^2$. The relationship between $|^1K(\text{X-F})|$ and $|\Psi_{ns,X}(0)|^2_{rel}$ for the group 14 - 17 hexafluoro-species is shown in Figure 6.4. The correlations for groups 14 - 16 are nearly linear with positive slopes that intersect near the origin. Although the XF_6^+ cations exhibit a non-linear relationship, with a line of best fit having a slope that is intermediate with respect to those of the group 14 and 15 species, the general observation that $|^1K(\text{X-F})|$ increases with increasing $|\Psi_{ns,X}(0)|^2_{rel}$ and approaches zero as $|\Psi_{ns,X}(0)|^2_{rel}$ approaches zero is also consistent with the overall dominance of the FC term for these octahedral species and is consistent with the smaller PSO contributions that have been calculated for the XF_6^+ cations.[399]

The relationship between $|^1K(\text{X-F})|^{1/2}$ and Z_X has been previously described for the isovalent hexafluorides of periods 14 - 17.[36] Similar trends are noted in the present work when $|^1K(\text{X-F})|$ is plotted against Z_X (Figure 6.5), where the value of $|^1K(\text{X-F})|$ increases, within each group, in a near-linear fashion with increasing Z_X for the periods 3 - 5 species. The plots also increase, with positive slopes, from left to right across the periodic table within each isovalent series, intersecting near the origin. The increase in $|\Psi_{ns,X}(0)|^2_{rel}$ with increasing Z_X across each period is also an established trend,[405] and is reflected in plots of $|^1K(\text{X-F})|$ versus Z_X, however, the halogen series deviates from the near-linear trends observed for groups 14, 15 and 16. The most notable deviations occur for ClF_6^+ and BrF_6^+, where the value of $|^1K(\text{Cl-F})|$ for ClF_6^+ is similar to $|^1K(\text{S-F})|$ of SF_6
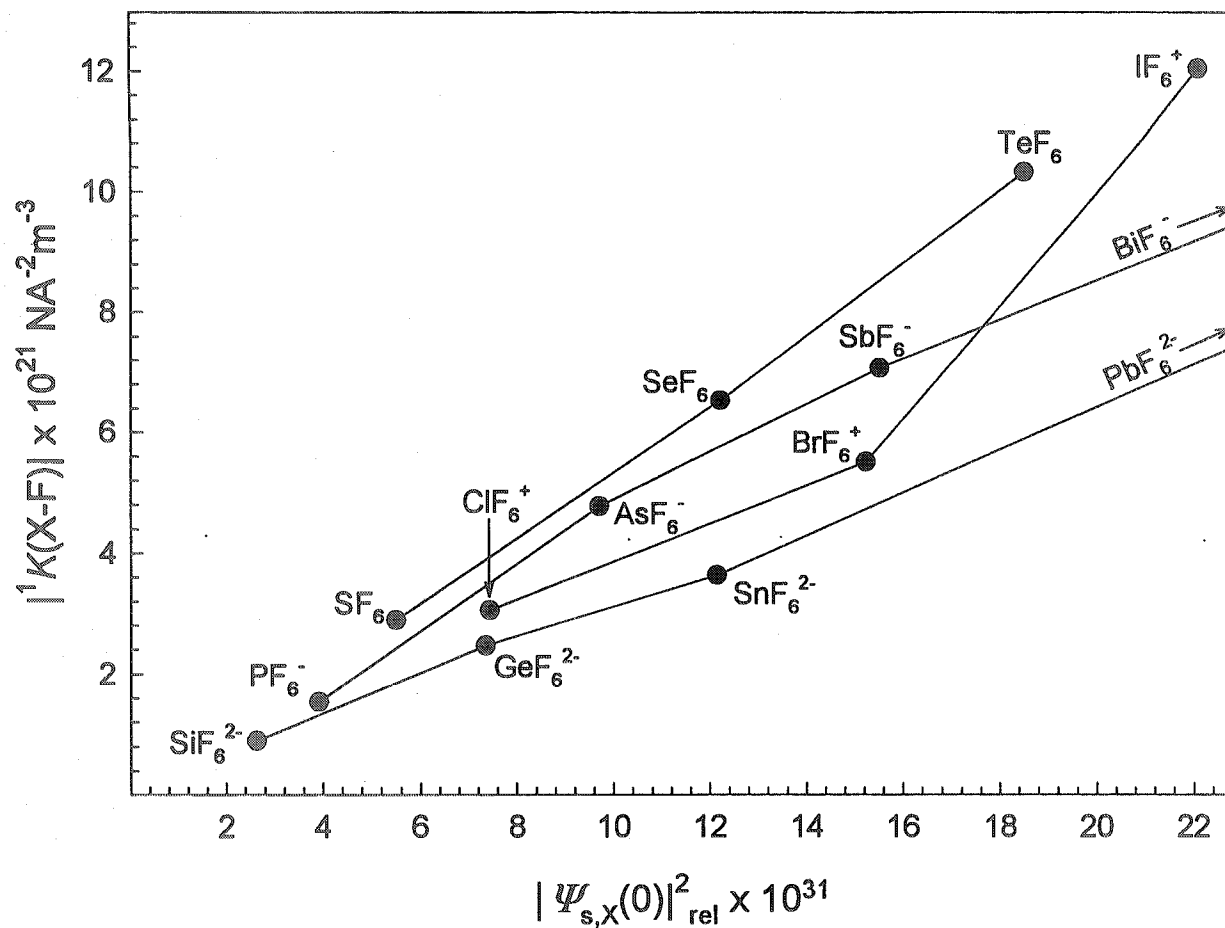
Figure 6.4. Plots of the reduced coupling constants, $|^1K(X\text{-}F)|$, of the XF_6^+, XF_6, XF_6^- and XF_6^{2-} series versus $|\Psi_{ns,X}(0)|^2_{rel}$. The coordinates for the period 6 hexafluoro-anions are: BiF_6^- ($|^1K(X\text{-}F)|$, 20.60; $|\Psi_{ns,X}(0)|^2_{rel}$ 56.54) and PbF_6^{2-} ($|^1K(X\text{-}F)|$, 14.01; $|\Psi_{ns,X}(0)|^2_{rel}$, 40.99).
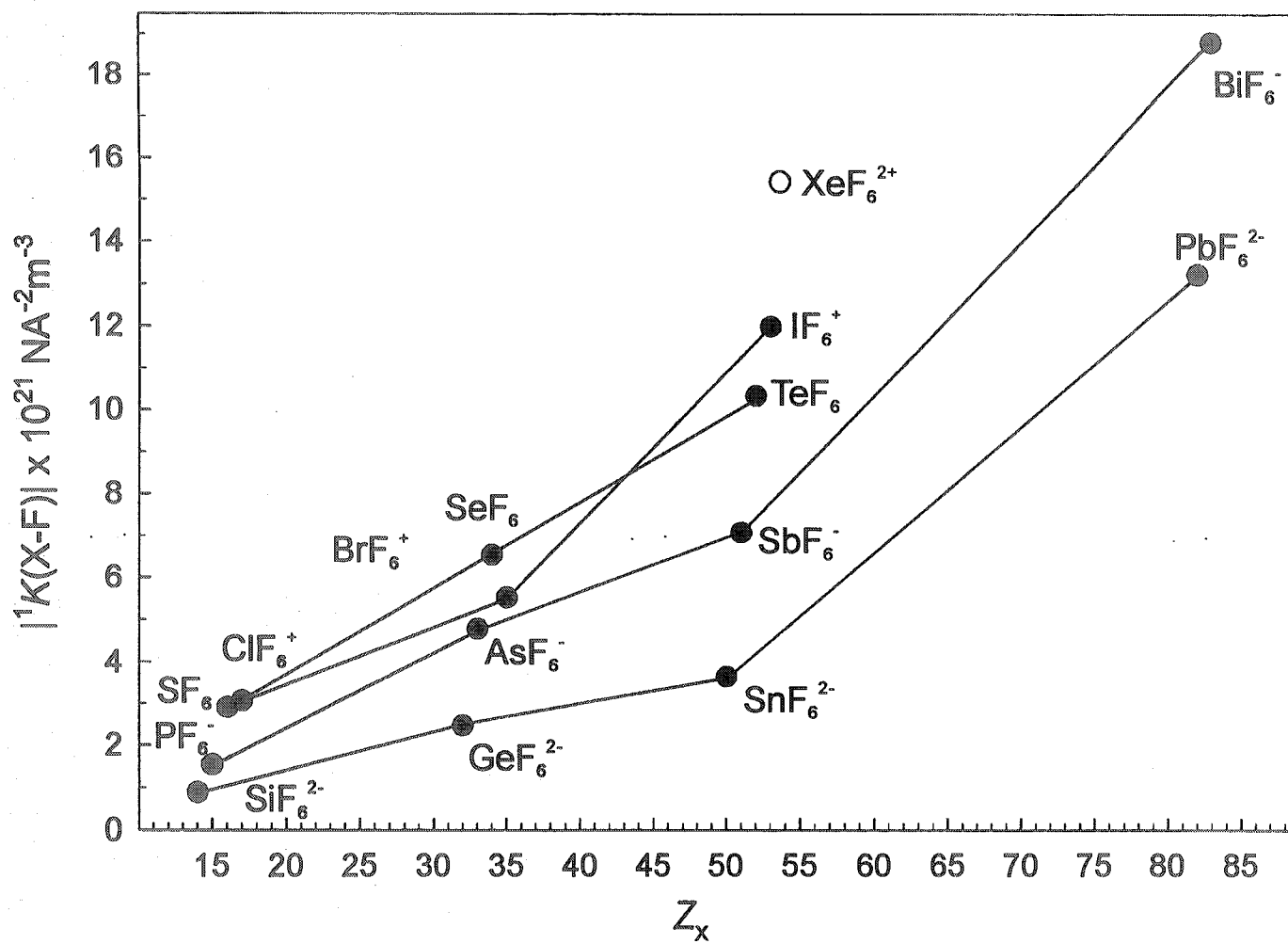
Figure 6.5. Plots of the reduced coupling constants, $|^1K(X\text{-}F)|$ versus atomic number, Z_X, for the isovalent group 14 - 17 hexafluoro-species.

and $|^1K(\text{Br-F})|$ of BrF_6^+ is lower than $|^1K(\text{Se-F})|$ of SeF_6. This anomaly may be attributable to the non-contact contributions identified in the previous theoretical study of the XF_6^+ cations, where the PSO terms accounted for 14% (ClF_6^+), 24% (BrF_6^+) and 18% (IF_6^+) of $|^1K(\text{X-F})|$.[399] Although the anomalous behaviors of BrF_6^+ and, to a more limited extent, ClF_6^+ are noteworthy and may result from different relative contributions from the contact and non-contact terms, it is not possible to comment further on these anomalies in the absence of the PSO/(FC + SD) ratios for the hexafluoro-species of groups 14 - 16.

A plot of $|^1K(\text{X-F})|$ versus X-F bond length exhibits a positive slope within each group (Figure 6.6), but of greater interest, is the relationship between $|^1K(\text{X-F})|$ and the X-F bond lengths across each period. Plots of $|^1K(\text{X-F})|$ for isoelectronic members of periods 3 and 4 versus their X-F bond lengths exhibit significant deviations from linearity when compared with the plot for the period 5 species. Although the PSO contribution is expected to be small when there are no electron lone pairs on the central atom,[399] it is clear from lines of best-fit that $|^1K(\text{X-F})|$ increases with decreasing bond length within each period, suggesting a dependence on $\langle r^{-3}\rangle_{np}$ and significant contributions from non-contact terms. The observed trends, however, are also consistent with $|\Psi_{ns,\text{X}}(0)|^2_{rel}$ and s bond order trends, which increase across each period and down each group, and provide significant contributions to the FC mechanism.

6.2.3.3.3. Absolute Signs of $^1J(^m\text{X-}^{19}\text{F})$ and $^1K(\text{X-F})$

The relative signs of the $^1K(\text{X-F})$ coupling constants involving main-group elements have been surveyed by Jameson,[405] but definitive assignments of the absolute signs for the majority of spin-spin couplings have not been made. On the basis of the similar trends observed for $|^1K(\text{X-F})|$, when plotted against Z_X, X-F bond length and $|\Psi_{s,\text{X}}(0)|^2_{rel}$ for the hexafluoro-species of groups 14 - 17 (Figures 6.4 - 6.6) and recent confirmation that the isotropic coupling constants of the XF_6^+ cations are negative,[399] it
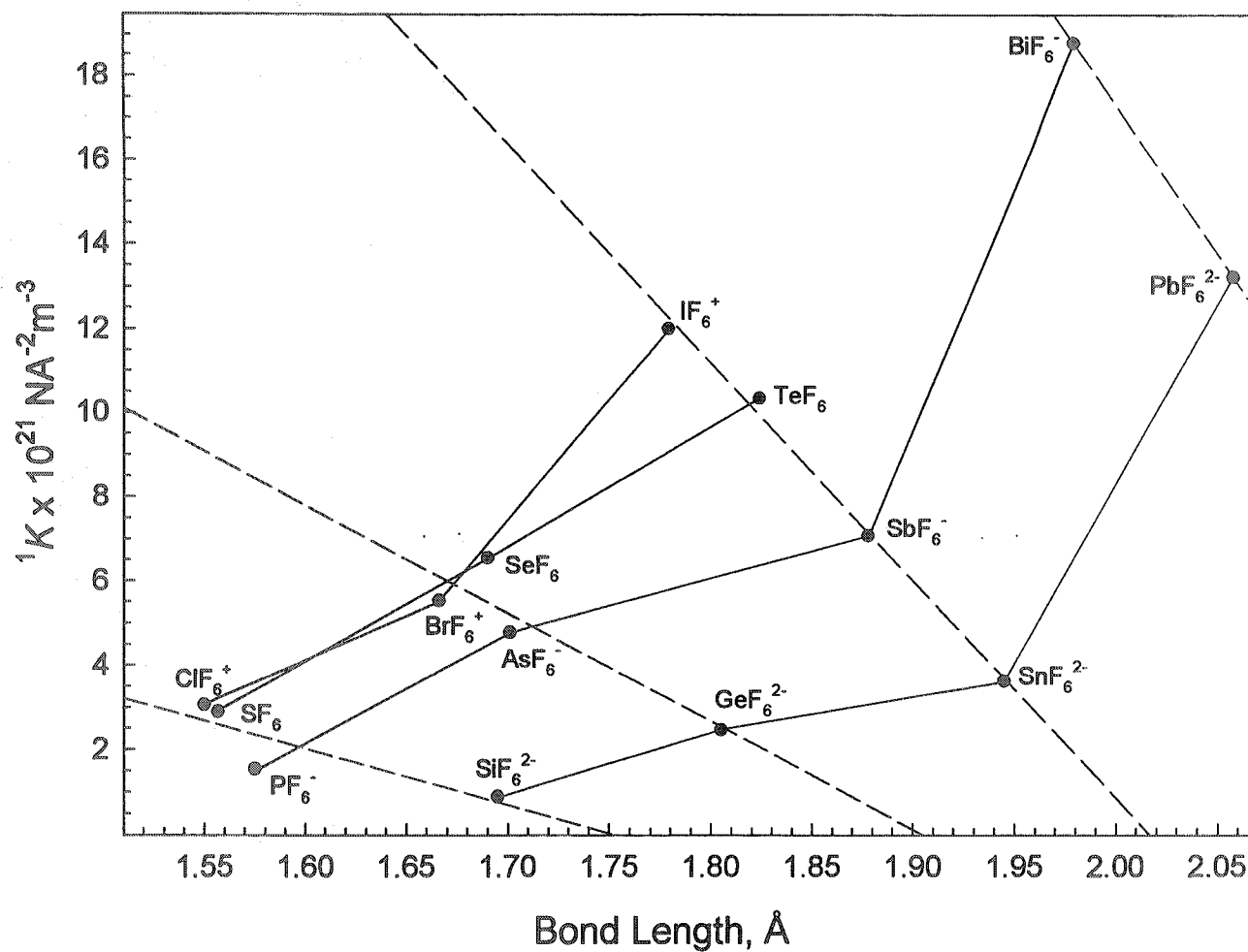
Figure 6.6. Plots of the reduced coupling constants, $|{}^{1}K(\text{X-F})|$, of the isoelectronic group 14 - 17 hexafluoro-species versus the average X-F bond length.

may be inferred that the signs of the reduced coupling constants of the hexafluoro-species of groups 14 - 17 are all negative. In contrast, the γ-values of the group 15 nuclides are all negative, suggesting that the trends depicted in Figures 4 - 6 are preserved because the $^1J(^mX-^{19}F)$ couplings of PF_6^-, AsF_6^-, SbF_6^- and BiF_6^- are positive.

The established trends among groups 14 - 17 hexafluoro-species also have implications relating to the signs of $^1J(^{129}Xe-^{19}F)$ and $^1J(^{131}Xe-^{19}F)$ for known xenon fluoride species and the hypothetical octahedral Xe(VIII) species, XeF_6^{2+}. Because ^{129}Xe ($I = \frac{1}{2}$) has a negative γ-value and that of ^{131}Xe ($I = \frac{3}{2}$) a positive value, $^1J(^{129}Xe-^{19}F)$ and $^1J(^{131}Xe-^{19}F)$ will have opposite signs. The previously discussed trends indicate that $^1K(Xe-F)$ is negative and from the assumption that all $^1K(X-F)$ values in Figures 4 - 6 are negative, $^1J(^{129}Xe-^{19}F)$ for XeF_6^{2+}, which is isoelectronic with the period 5 hexafluoro-species, is predicted to be positive with an estimated magnitude of 4800 ±930 Hz. The predicted sign is also in accord with the relative signs predicted from plots of experimental ^{19}F chemical shifts versus $^1J(^{129}Xe-^{19}F)$ for the known Xe-F bonded derivatives of xenon.[104] The latter relationship indicates that all $^1J(^{129}Xe-^{19}F)$ couplings involving Xe(II) and Xe(IV) have negative signs whereas those of Xe(VI) have the smallest magnitudes and can have either negative or positive signs. The relationship assigns positive and negative signs to the axial and equatorial $^{129}Xe-^{19}F$ couplings, respectively, of the XeF_5^+ cation. These empirical relationships also predict a positive value for the $^1J(^{129}Xe-^{19}F)$ coupling of XeO_3F_2 (991-1015 Hz),[78] which is the only Xe(VIII) species for which a $^{129}Xe-^{19}F$ coupling constant has been determined. These empirical trends have been recently supported by ZORA-DFT calculations,[69] which also assigned positive signs to the axial and equatorial $^1J(^{129}Xe-^{19}F)$ coupling constants of the unknown XeF_7^+ cation but did not consider either the XeF_6^{2+} cation or XeO_3F_2.

6.3. Computational Results

6.3.1. Geometries

The energy-minimized structures of the ClF_6^+, BrF_6^+ and IF_6^+ cations, have been calculated with O_h symmetry using the HF, MP2 and LDF methods (Table 6.6). The ClF_6^+, BrF_6^+ and IF_6^+ bond lengths calculated by the HF method provided the best agreement with the average experimental value. In the case of each XF_6^+ cation, the X-F bond lengths determined by MP2 and LDF methods were found to be similar, but were consistently longer than the experimental values.

6.3.2. Vibrational Frequencies

The infrared and Raman frequencies of the ClF_6^+,[31,37,220-222,351] BrF_6^+[31,36,176] and IF_6^+[353-355] cations have been previously determined. These octahedral cations are expected to have 15 normal modes of vibration, $A_{1g} + E_g + F_{2g} + 2F_{1u} + F_{2u}$, where the $\nu_1(A_{1g})$, $\nu_2(E_g)$, and $\nu_5(F_{2g})$ modes are Raman-active, the $\nu_3(F_{1u})$ and $\nu_4(F_{1u})$ modes are infrared active and the $\nu_6(F_{2u})$ mode is both Raman and infrared-inactive. The previously reported experimental frequencies and intensities of the ClF_6^+, BrF_6^+ and IF_6^+ cations are listed in Table 6.7, where they are compared with those calculated by HF, MP2 and LDF methods. The unscaled vibrational frequencies of the XF_6^+ cations were consistently overestimated by the HF calculations and underestimated by the MP2 and LDF calculations. The application of the recommended 0.8953 scaling factor to the HF frequencies improved the fit significantly, however, these frequencies remained slightly overestimated.

The inactive $\nu_6(F_{2u})$ mode of ClF_6^+ was previously assigned at 353 cm^{-1} on the basis of the first overtone of $\nu_6(F_{2u})$ $(A_{1g} + E_g + F_{2g})$ at 706 cm^{-1} in the infrared spectrum,[37] and is bracketed by the calculated frequencies (HF, 383 cm^{-1}; MP2, 308 cm^{-1}; LDF, 296 cm^{-1}). The $\nu_6(F_{2u})$ modes of BrF_6^+ and IF_6^+ have never been directly or

Table 6.6. Comparison of the Experimental and Calculated Bond Lengths (Å) for ClF_6^+, BrF_6^+ and IF_6^+

Cation[a]	Expt. (ave)	HF	MP2	LDF
ClF_6^+	1.550(4)	1.547	1.623	1.612
BrF_6^+	1.666(11)	1.663	1.731	1.730
IF_6^+	1.779(6)	1.811	1.874	1.869

[a] The geometries of the XF_6^+ cations were optimized with O_h symmetries and the DZVP basis set was used for each calculation.

Table 6.7. Experimental and Calculated Vibrational Frequencies for ClF_6^+, BrF_6^+ and IF_6^+

cation	assignment (O_h)	description[a]	expt.[a,b,c]	HF[d]	scaled HF[e]	MP2[d]	LDF[d]
ClF_6^+	$v_1(A_{1g})$	νsym. in phase	688(100)	746(100)[0]	668	599(100)[0]	628(100)[0]
	$v_2(E_g)$	νsym. out of phase	631(27)	703(78)[0]	629	556(64)[0]	565(51)[0]
	$v_3(F_{1u})$	νas	890[ms]	1017(0)[1002]	911	804(0)[867]	840(0)[867]
	$v_4(F_{1u})$	δumbrella	590[m]	631(0)[111]	565	518(0)[39]	506(0)[54]
	$v_5(F_{2g})$	δscissor	517(40)	550(24)[0]	492	452(45)[0]	440(32)[0]
	$v_6(F_{2u})$	δpucker	353	383(0)[0]	343	308(0)[0]	296(0)[0]
BrF_6^+	$v_1(A_{1g})$	νsym. in phase	658(100)	739(100)[0]	662	616(100)[0]	623(100)[0]
	$v_2(E_g)$	νsym. out of phase	668(28)	746(64)[0]	668	622(51)[0]	614(147[0]
	$v_3(F_{1u})$	νas	775[ms]	885(0)[420]	792	733(0)[396]	736(0)[363]
	$v_4(F_{1u})$	δumbrella	427, 433[m]	472(0)[183]	423	400(0)[108]	377(0)[90]
	$v_5(F_{2g})$	δscissor	405(34)	435(24)[0]	389	365(44)[0]	345(31)[0]
	$v_6(F_{2u})$	δpucker		306(0)[0]	274	248(0)[0]	231(0)[0]
IF_6^{+c}	$v_1(A_{1g})$	νsym. in phase	708(100)	806(100)[0]	722	622(100)[0]	623(100)[0]
	$v_2(E_g)$	νsym. out of phase	732(20)	811(38)[0]	726	651(39)[0]	614(39)[0]
	$v_3(F_{1u})$	νas	797, 790[ms]	892(0)[357]	790	719(0)[276]	736(0)[363]
	$v_4(F_{1u})$	δumbrella	343[m]	378(0)[231]	338	301(0)[141]	377(0)[90]
	$v_5(F_{2g})$	δscissor	340(40)	366(18)[0]	328	278(38)[0]	344(29)[0]
	$v_6(F_{2u})$	δpucker		234(0)[0]	210	179(0)[0]	231(0)[0]

[a] Abbreviations denote symmetric (sym), asymmetric (asym), medium (m) and medium strong. [b] The observed Raman and infrared intensities are relative values and are given in parentheses, and brackets, respectively. [c] Experimental vibrational frequencies and intensities are from ref 37 for [ClF6][AsF6], ref 36 (Raman) and ref 176 (infrared) for [BrF6][AsF6] and ref 352 for [IF6][AsF6]. [d] The calculated infrared intensities are given in parentheses and have units of km mol^{-1}. The calculated Raman intensities are scaled relative to their most intense feature, which is given a value of 100. [e] A scaling factor of 0.8953 was applied as recommended in ref 323.

indirectly observed, however, the calculations predict that their frequencies lie between 231 to 306 cm^{-1} and 179 to 234 cm^{-1}, respectively.

In contrast to the ClF_6^+ cation, where $v_1(A_{1g})$ is at higher frequency than $v_2(E_g)$, the frequency order of these vibrational modes is reversed for BrF_6^+ ($v_1(A_{1g})$, 658 cm^{-1}; $v_2(E_g)$, 668 cm^{-1}) and IF_6^+($v_1(A_{1g})$, 708 cm^{-1}; $v_2(E_g)$, 732 cm^{-1}). The frequency orders of these bands are correctly predicted by the HF and MP2 calculations, but not by the LDF calculations, whereas the frequency orders of the remaining bands are correctly predicted by all three methods.

The calculated infrared and Raman intensities for the XF_6^+ cations are in semi-quantitative agreement with the relative experimental intensities. Although the experimental absolute extinction coefficients of the infrared-active $v_3(F_{1u})$ and $v_4(F_{1u})$ bands of the XF_6^+ cations have not been determined, it is clear that the experimental transition moment of $v_3(F_{1u})$ is greater than that of $v_4(F_{1u})$. The experimental intensities are consistent with the intensities calculated by HF, MP2 and LDF methods, which provided $v_3(F_{1u})$: $v_4(F_{1u})$ intensity ratios of 9.0, 22.2 and 16.1 for ClF_6^+, 2.3, 3.7 and 4.0 for BrF_6^+ and 1.5, 2.0 and 4.0 for IF_6^+. The experimental Raman intensity of $v_1(A_{1g})$ is invariably greater than those of $v_2(E_g)$ and $v_5(F_{2g})$ and this trend is reproduced by the calculated intensities.

6.3.3. Natural Bond Orbital (NBO) Analyses

The atomic charges and Mayer bond orders calculated for the XF_6^+ cations using the energy-minimized geometries determined from HF, MP2 and LDF calculations are summarized in Table 6.8. The NBO analyses of the XF_6^+ cations is reflective of the highly polar covalent X-F bonds anticipated for the halogen(VII)-fluorine bonds.

The X-F bond orders calculated for ClF_6^+ (0.454 to 0.517), BrF_6^+ (0.477 to 0.519) and IF_6^+ (0.464 to 0.485) are similar for the three cations and exhibit a minimal

Table 6.8. Atomic Charges, Valencies and Mayer Bond Orders for the XF_6^+ Cations

		HF	MP2	LDF
atomic charges and valencies[a]				
ClF_6^+	Cl	2.91 (3.10)	2.60 (2.72)	2.51 (2.93)
	F	-0.32 (0.37)	-0.27 (0.32)	-0.25 (0.36)
BrF_6^+	Br	3.35 (3.11)	3.03 (2.86)	2.86 (2.95)
	F	-0.39 (0.40)	-0.34 (0.37)	-0.31 (0.39)
IF_6^+	I	4.14 (2.91)	3.73 (2.78)	3.50 (2.85)
	F	-0.52 (0.40)	-0.46 (0.40)	-0.42 (0.40)
bond orders				
ClF_6^+	Cl-F	0.517	0.454	0.488
	$F–F_{cis}$	-0.039	-0.034	-0.034
	$F–F_{trans}$	0.008	0.004	0.004
BrF_6^+	Br-F	0.519	0.477	0.492
	$F–F$	-0.031	-0.026	-0.027
	$F–F_{trans}$	0.003	0.001	0.001
IF_6^+	X-F	0.485	0.464	0.475
	$F–F_{cis}$	-0.022	-0.018	-0.019
	$F–F_{trans}$	0.001	0.000	0.000

[a] Valencies are given in parentheses.

dependence on the computational method. In contrast, the atomic charge distributions show a clear increase in the ionic character of the X-F bonds down the group, reflecting the relative electronegativities[406] of the central halogens (Cl, 2.83; Br, 2.74; I, 2.21) and the fluorine (4.10) ligands. Although the negative F--F bond orders calculated for the cations may be interpreted as being anti-bonding in nature, their small magnitudes imply that the ligand-ligand interactions are more aptly described as non-bonding. Consequently, the repulsive F⋯F interactions, which account for the octahedral geometries of the XF_6^+ cations can be attributed to the Coulombic forces acting among the negatively charged fluorine ligands.

6.4. Structural Trends Among the XF_6^+ Cations and Related Fluoride Species

6.4.1. Nature of X-F Bonding in the XF_6^+ Cations

The calculated atomic charges and Mayer bond orders for the XF_6^+ cations suggest that the X-F bond are partially ionic in nature, with the degree of ionic character increasing as the electronegativity of the central halogen decreases. The combination of these bonding contributions leads to X-F bond lengths that are among the shortest known for the neutral and charged binary halogen fluorides. The covalent component of these octahedral cations may be described in terms of the classic sp^3d^2 hybridization model,[407] or by a more preferred model, which utilizes the three p-orbitals of the central atom and avoids the use of d-orbitals.[408] In the latter model, the six symmetry-adapted fluorine orbitals contributing to the bonding combine with available orbitals on the central X atom. Four symmetry-adapted fluorine orbitals combine with the s and p orbital of the central atom to generate four filled bonding orbitals (one A_{1g} and three T_{1u}). The remaining two filled fluorine-ligand orbitals are non-bonding with E_g symmetry, and are fluorine only in character if there is no central d-orbital participation. This bonding model ensures that the X-F bonds will have appreciable polarities.

6.4.2. Assessment of Ligand Close Packing Among the Isovalent Hexafluoro-Species of Groups 14 - 17

Bond length contraction with increasing central halogen oxidation state is likely offset by increases in the magnitudes of the inter-ligand $F\cdots F$ repulsive interactions when the halogen atom is in a high oxidation state (+5 or +7), has a high coordination number and a net positive charge. Significant ligand-ligand repulsions, which are a consequence of the smaller size of the central halogen atom, can account for the inability of chlorine and bromine to exhibit coordination numbers that exceed six. This hypothesis is supported by the negative Mayer bond orders between *cis*-fluorine atoms, which decrease in the order $ClF_6^+ > BrF_6^+ > IF_6^+$, and the increase in the average experimental inter-ligand $F\cdots F$ distances, ClF_6^+ (2.192(5) Å) < BrF_6^+ (2.356(11) Å) < IF_6^+ (2.516(17) Å). The present experimental findings are in accord with the views of Robinson and Gillespie[409] who have recently investigated the role of ligand close packing (LCP) in octahedral main-group fluorides of periods 3, 4 and 5 and concluded from the experimental inter-ligand $F\cdots F$ distances[410] that the fluorine ligands of ClF_6^+ are close packed whereas those of BrF_6^+ and IF_6^+ are not. They go on to point out that although the F ligands of period 4 species, such as BrF_6^+, are not close packed because of the larger sizes of period 4 atoms, the central atoms are not large enough to accommodate more than six ligands, contrasting with the period 5 elements which can accommodate as many as seven or eight small ligand atoms.

Comparisons among the isovalent main-group hexafluoro-species, XF_6^+ (X = Cl, Br, I), XF_6 (X = S, Se, Te), XF_6^- (X = P, As, Sb) and XF_6^{2-} (X = Si, Ge, Sn) also reveal several relationships among their net charges, X-F bond lengths (Figure 6.7) and $F\cdots F$ contact distances. With the exception of the dianions, SiF_6^{2-} (1.695(5)/*2.40* Å)[411] and GeF_6^{2-} (1.80(4)/*2.55* Å),[412] the X-F bond lengths and $F\cdots F$ contact distances (values in
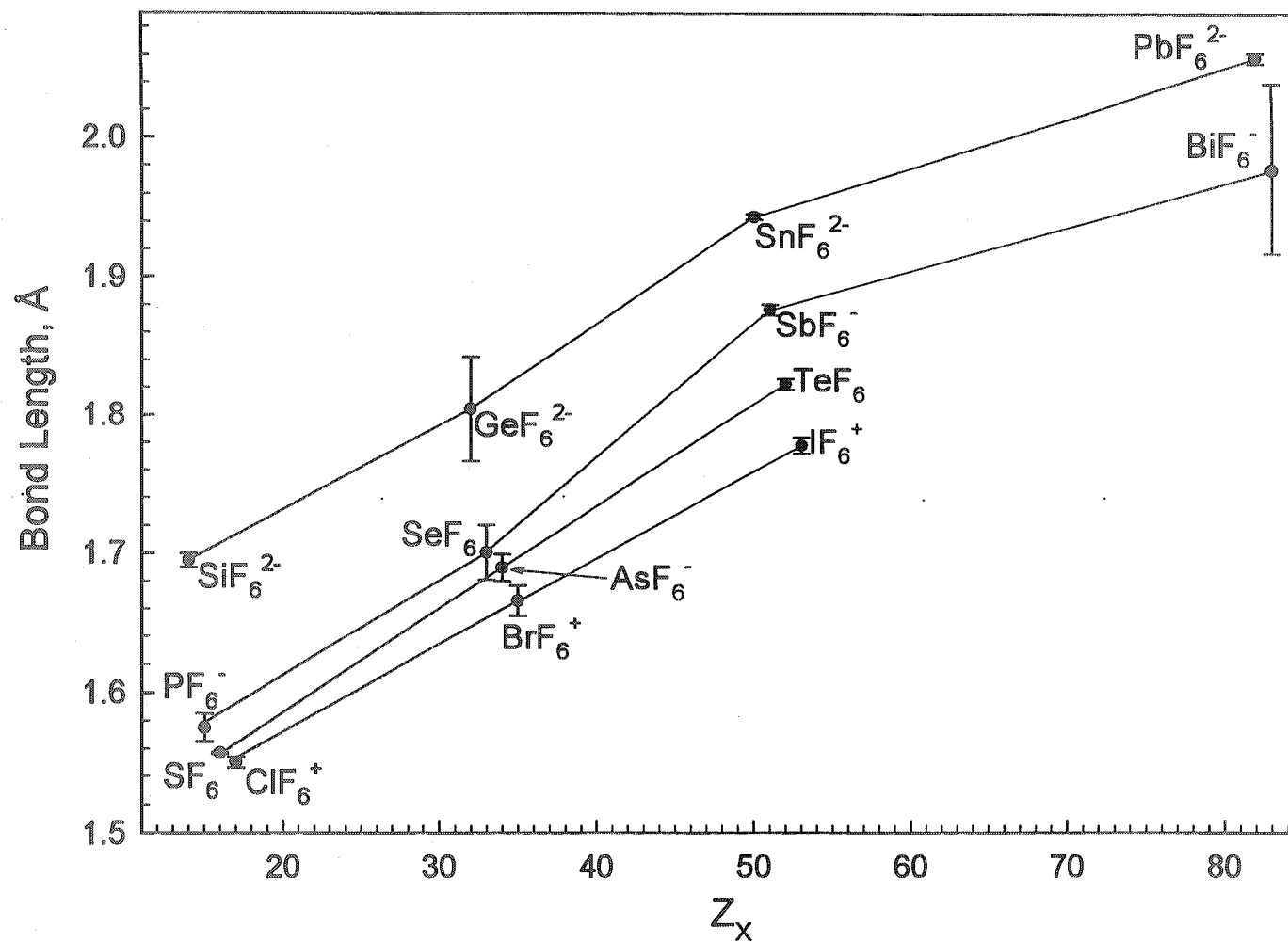
Figure 6.7. Plots of the average X-F bond lengths of the isovalent group 14 - 17 hexafluorides versus atomic number, Z_X.

italics) do not differ significantly among the period 3 (ClF_6^+, 1.550(4)/2.19 Å; SF_6, 1.5568(6)/2.202 Å;[413] PF_6^- 1.58(1)/2.23 Å[414]) and period 4 (BrF_6^+, 1.666(11)/2.36 Å; SeF_6, 1.69(1)/2.39 Å;[415] AsF_6^- 1.70(2)/2.40 Å[23]) hexafluoro-species. The absence of a significant dependence of the X-F bond lengths on net charge suggests that the bond contraction expected with increasing oxidation state along each period is counter-balanced by F···F ligand-ligand interactions in periods 3 and 4. Repulsive interactions of this kind are not surprising considering that the F···F contacts are significantly less than twice the sum of the van der Waals radius of fluorine (2.70,[287] 2.94 Å[286]). This is not the case for period 5 and 6 hexafluo-species, where the X-F bond lengths clearly exhibit a contraction as the net charge becomes more positive (SnF_6^{2-}, 1.945(2)/2.75 Å;[416] SbF_6^-, 1.878(4)/2.66 Å;[23] TeF_6, 1.824(4)/2.58 Å;[417] IF_6^+, 1.779(6)/2.52 Å and PbF_6^{2-}, 2.058(4)/2.91 Å;[418] BiF_6^-, 1.98(5)/2.80[419]) and the F···F contact distances approach the van der Waals sum for the anionic species. The reduced ligand-ligand interactions among the period 5 and 6 hexafluoro-species is also consistent with the ability of their central atoms to exhibit coordination numbers as high as seven (IF_7,[420] TeF_7^-,[421] SbF_7^{2-}[422]) and eight (TeF_8^{2-},[421] IF_8^{2-}[423]).

6.5. Conclusion

The X-ray crystal structures of the XF_6^+ (X = Cl, Br, I) cations have been determined for the first time as their isomorphous $Sb_2F_{11}^-$ salts. The XF_6^+ cations display among the shortest X-F bond lengths known for the neutral and charged binary halogen fluorides. The atomic charges and Mayer bond orders calculated for the XF_6^+ cations suggest that the bond length trends observed among the series reflect the degree of ionic character in the X-F bonds, which increases as the electronegativity of the central halogen decreases. The vibrational frequencies and intensities of the XF_6^+ cations, derived from

electronic structure calculations, were also used to confirm the previous assignments of their infrared and Raman spectra.

The $^{35,37}Cl$, $^{79,81}Br$ and ^{127}I NMR spectra of the ClF_6^+, BrF_6^+ and IF_6^+ cations and their T_1-relaxation times reflect the octahedral geometries of these cations in HF solution. The central halogen chemical shifts of XO_4^- and XF_6^+ increase significantly when descending the halogen group, reflecting the dominance of the paramagnetic shielding terms for the heavier nuclei, paralleling the larger values of $<r^{-3}>_{np}$ associated with these elements. Trends in isotropic reduced coupling constants, $|^1K(X-F)|$, with $|\Psi_{ns,X}(0)|^2$ and Z_X for the period 3 - 5 hexafluoro-species have near-linear relationships across each period that are consistent with the dominant role of the Fermi contact spin-spin coupling mechanism. The anomalous behaviors of BrF_6^+ and, to a lesser extent, ClF_6^+ within these relationships may result from different relative contributions from the contact and non-contact terms. The $|^1K(X-F)|$ couplings increase linearly across a period from left to right as the X-F bond length decreases, with the best correlation being observed for period 5 hexafluoro-species where inter-ligand F⋯F repulsions are minimized. From the similar behaviors of $|^1K(X-F)|$ with respect to $|\Psi_{ns,X}(0)|^2$, Z_X and the X-F bond lengths of the group 14 - 17 hexafluoro-species of periods 3 - 5, it is inferred that $^1K(X-F)$ coupling constants have the same sign. Furthermore, the recently established negative signs for $^1J(^mX-^{19}F)$ of the XF_6^+ cations also imply that the signs of $^1J(^mX-^{19}F)$ are negative for the group 14 and 16 hexafluoro-species, but positive for the group 15 analogues and for the presently unknown $^{129}XeF_6^{2+}$ cation.

CHAPTER 7

FLUORIDE ION ACCEPTOR PROPERTIES OF
BrO_3F AND ClO_3F; SYNTHESIS AND CHARACTERIZATION OF SALTS
CONTAINING THE $BrO_3F_2^-$ ANION

7.1. Introduction

Prior to the present work, the only Br(VII) species that had been prepared in macroscopic quantities were $HBrO_4$,[167,205] BrO_3F[162] and salts containing the BrF_6^+ [36,137] and BrO_4^- ions.[161,167,167,205] The difficulties associated with the syntheses of bromine(VII) compounds are consistent with the general reluctance of late period four elements to attain their highest oxidation states. As previously illustrated by the nearly quantitative syntheses of alkali metal perbromate salts from $HBrO_4$[161,167] (eq 7.1) and BrO_3F from

$$HBrO_4 + MOH \rightarrow [M][BrO_4] + H_2O \qquad (7.1)$$

$$[K][BrO_4] + 2SbF_5 + 3HF \rightarrow BrO_3F + [H_3O][SbF_6] + [K][SbF_6] \qquad (7.2)$$
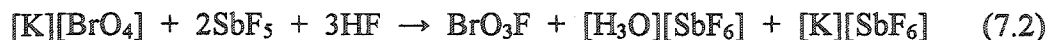
$[K][BrO_4]$[162] (eq 7.2), the syntheses of new Br(VII) species from existing ones are of particular interest because the need to oxidize a lower valent bromine species is circumvented.

The ability of main-group and transition metal fluorides and oxide fluorides to undergo fluoride ion transfer reactions (eq 7.3, 7.4) is well known and provides relatively

$$MO_mF_n + F^- \rightarrow MO_mF_{n+1}^- \qquad (7.3)$$

$$MO_mF_n \rightarrow MO_mF_{n-1}^+ + F^- \qquad (7.4)$$
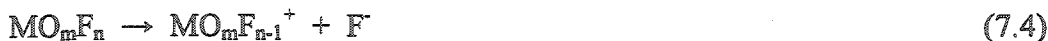
straight forward routes to anionic and cationic derivatives of BrF_3 (BrF_2^+,[211,212] BrF_4^-[424]), BrF_5 (BrF_6^-,[425] BrF_4^+ [362,426]), BrO_2F ($BrO_2F_2^-$,[244] BrO_2^+ [207,213]), and $BrOF_3$ ($BrOF_4^-$,[427,428]

$BrOF_2^{+}$ [215,216]), but has not been used for the interconversion of Br(VII) species. Of the known Br(VII) species, BrF_6^{+} and BrO_3F might be expected to undergo fluoride ion transfer reactions leading to BrF_7, $BrO_3F_2^{-}$ and BrO_3^{+}. Although a high-temperature synthesis of BrF_7 has been reported,[177] the existence of BrF_7 is doubtful in view of the fact that reaction of BrF_6^{+} with NOF at -78 °C results in the reduction to BrF_6^{-} with the evolution of fluorine gas,[36] and that attempts to oxidize BrF_5 with F_2 under photolytic conditions at -40 to -60 °C have also been unsuccessful.[226] The inability to prepare BrF_7 likely reflects the strong steric interactions that would exist among the fluorine ligands and is consistent with other period four elements, which fail to exhibit coordination numbers in excess of six.[409]

Perbromyl fluoride was first prepared by analogy with the preparation of ClO_3F.[206] The reaction of [K][BrO_4] with the strong Lewis acid, SbF_5, in anhydrous HF produces BrO_3F in nearly quantitative yield (97%) at ambient temperature (eq 7.2),[162] and has also been shown to proceed when AsF_5,[207] BrF_5,[207] [BrF_6][AsF_6],[207] or XeF_6[208] are used in place of SbF_5. In contrast to ClO_3F, which is thermodynamically stable (ΔH_f°, -21.422 kJ mol^{-1})[429] and exhibits remarkable kinetic stability, BrO_3F is unstable (ΔH_f°, 137(1) kJ mol^{-1})[175] and acts as a potent oxidative fluorinating agent.[172] The fluoride ion donor properties of BrO_3F have been assessed in anhydrous HF solvent by monitoring solutions of BrO_3F and SbF_5 by Raman spectroscopy, and solutions of BrO_3F and AsF_5 by ^{19}F NMR spectroscopy.[207] The absence of vibrational frequency shifts or changes in the ^{19}F NMR chemical shift of BrO_3F in these studies indicates that interactions between the fluorine or oxygen ligands of BrO_3F and the Lewis acids are likely to be weak to negligible. The fluoride-ion acceptor properties of BrO_3F have not been explicitly investigated, however, the failure of BrO_3F to react with NaF, which is used to remove HF from BrO_3F (eq 7.5) after its synthesis in this solvent,[162] indicates that BrO_3F is not a

$$NaF + (n+1)HF \rightarrow [Na][HF_2 \cdot HF] \tag{7.5}$$

strong fluoride ion acceptor. The observation that CsF^{217} and NO_2F^{217} do not behave as fluoride ion donors towards ClO_3F has also lead to the prediction that BrO_3F is a poor fluoride ion acceptor,[207] however, recent theoretical calculations suggest that BrO_3F may react with strong fluoride ion donors.[46]

The present work investigates the fluoride-ion acceptor behaviour of BrO_3F towards fluoride-ion donors of varying strength, and reinvestigates the fluoride-ion acceptor properties of ClO_3F by monitoring its reaction with $[N(CH_3)_4][F]$. The VSEPR model predicts that the $BrO_3F_2^-$ and $ClO_3F_2^-$ anions should possess trigonal bipyramidal geometries (D_{3h} symmetry) in which the three oxygen atoms occupy the equatorial positions and the two fluorine atoms occupy axial positions. Although vibrational spectroscopy has verified that this geometry is common among neutral and anionic inorganic pentahalides such as MF_5 (M = V, Mo, As, Sb, Bi), MCl_5 (M = Nb, Ta, Mo, P, As, Sb), MBr_5 (M = Nb, Ta), MF_5^- (M = Si), MCl_5^- (M = Ti, Si, Ge), $SnBr_5^-$, and MCl_5^{3-} (M = Cu, Cd),[430] the only trigonal bipyramidal species that have equatorial oxygen ligands are OsO_3F_2[431,432] and XeO_3F_2.[433] Moreover, OsO_3F_2 polymerizes as a *cis*-fluorine bridged chain structure in the solid state and only displays D_{3h} symmetry when isolated in a matrix.[431,432] The challenging synthesis of XeO_3F_2, by the reaction of XeO_4 with XeF_6, has yet to yield bulk quantities of XeO_3F_2 in the solid state, however, ^{19}F NMR spectroscopy of SO_2ClF, HF and BrF_5 solutions of XeO_3F_2,[104,43]4 and vibrational spectroscopy (Raman, IR) of XeO_3F_2 isolated in argon and neon matrices[433] have confirmed the predicted geometry.[435] Consequently, the preparation of salts containing the $BrO_3F_2^-$ or $ClO_3F_2^-$ anions would not only significantly extend the chemistries of Br(VII) and Cl(VII), but would also provide the first anionic oxide fluorides having D_{3h} symmetries.

7.2. Results and Discussion

7.2.1.1. Syntheses of α-[Cs][BrO₃F₂], β-[Cs][BrO₃F₂], [Rb][BrO₃F₂], [K][BrO₃F₂], [N(CH₃)₄][BrO₃F₂] and [NO]₂[BrO₃F₂][F]

The fluoride ion acceptor properties of BrO_3F were investigated by monitoring its reactions with $[N(CH_3)_4][F]$, NOF and MF (M = K, Rb, Cs) by means of Raman spectroscopy. An initial attempt to prepare $[Cs][BrO_3F_2]$ in anhydrous HF failed to provide Raman spectroscopic evidence for fluoride ion transfer to BrO_3F, suggesting that the transfer of fluoride ion from CsF to BrO_3F is thermodynamically less favourable than fluoride ion transfer to HF (eq 7.6). Consequently, the use of HF as a solvent was

$$BrO_3F + (x+1)HF + CsF \rightarrow BrO_3F + [Cs][HF_2 \cdot xHF] \qquad (7.6)$$

abandoned for the remainder of these studies.

Although violent detonations occasionally occurred when BrO_3F was brought into contact with CH_3CN, the high first adiabatic ionization potential (13.59 eV),[436] favourable liquid range, and resistance to fluoride ion attack at low temperature[236,246] makes CH_3CN an ideal solvent for the synthesis of anions derived from strong oxidative fluorinators.[51,95] Consequently, the $N(CH_3)_4^+$, K^+, Rb^+ and Cs^+ salts of $BrO_3F_2^-$ could be prepared and handled in CH_3CN solvent for prolonged periods at low temperatures (< -30 °C) and at ambient temperatures for short periods of time. The slow oxidation of the solvent at room temperature does, however, prevent NMR spectroscopic studies from being carried out at ambient temperatures (see section 7.2.4). The $N(CH_3)_4^+$, K^+, Rb^+, and Cs^+ salts of $BrO_3F_2^-$ were prepared by the reaction of BrO_3F with finely divided $[N(CH_3)_4][F]$, KF, RbF and CsF, respectively, in CH_3CN solvent (eq 7.7, 7.8). Raman spectroscopy was used to verify the formation of the salts prior to solvent removal under

$$[N(CH_3)_4][F] + BrO_3F \rightarrow [N(CH_3)_4][BrO_3F_2] \qquad (7.7)$$

$$MF + BrO_3F \rightarrow [M][BrO_3F_2] \quad (M = K, Rb, Cs) \qquad (7.8)$$

dynamic vacuum at -40 °C, and was used to monitor the progress of the reaction. The reactivities of [N(CH$_3$)$_4$][F] and CsF towards BrO$_3$F were similar, and the formation of [N(CH$_3$)$_4$][BrO$_3$F$_2$] and [Cs][BrO$_3$F$_2$] was nearly instantaneous with adequate mixing at -40 to -48 °C. The low-temperature phase (α-) of [Cs][BrO$_3$F$_2$] was isolated when the reaction and solvent removal were completed at, or below, -40 °C, whereas the high-temperature phase (β-) of [Cs][BrO$_3$F$_2$] was isolated when the reaction was carried out at -35 °C. Samples of β-[Cs][BrO$_3$F$_2$] may alternatively be prepared by allowing [Cs][BrO$_3$F$_2$] to stand at 0 °C for 35 hr in the absence of a solvent, however, the phase change is not reversible at -78 oC over period of four days. The reactions of KF and RbF with BrO$_3$F were slow at -40 °C when compared with the nearly instantaneous formations of [N(CH$_3$)$_4$][BrO$_3$F$_2$] and α-[Cs][BrO$_3$F$_2$], but proceeded over the period of 1 hr at -30 to -35 °C. In the case of [Rb][BrO$_3$F$_2$], Raman spectroscopy was used to follow the progress of the reaction by monitoring the intensities of the strong RbF bands at 3144(100), 3160(87), 3338(4), 3357(2) and 3396(21) cm^{-1}. The slower reaction rates of KF and RbF at temperatures below -40 °C likely reflect the higher lattice energies and resulting lower solubilities of KF (821 kJ mol^{-1})[185] and RbF (785 kJ mol^{-1})[185] when compared with that of CsF (740 kJ mol^{-1}).[185]

Samples of [NO]$_2$[BrO$_3$F$_2$][F] were prepared by the reaction of BrO$_3$F with neat NOF at -78 °C (eq 7.9) for 5 min followed by rapid (*ca.* 30 s) removal of the excess NOF

$$2NOF + BrO_3F \rightarrow [NO]_2[BrO_3F_2][F] \tag{7.9}$$
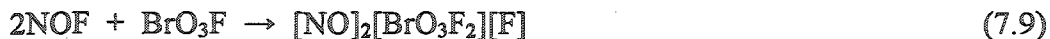
under dynamic vacuum at -78 °C. The colourless product had a significant dissociation vapour pressure at -78 °C and was crystallized by allowing the solid to sublime under 1000 Torr of argon over a period of several weeks at -78 °C. The Raman spectrum of the initial and crystalline products were identical, and single-crystal X-ray diffraction was used to establish the product stoichiometry in eq 7.9.

238

7.2.1.2. Attempted Preparation of $[N(CH_3)_4]_2[BrO_3F_3]$

A sample of $[N(CH_3)_4][BrO_3F_2]$ was prepared by reaction of $[N(CH_3)_4][F]$ with a stoichiometric excess of BrO_3F in CH_3CN solvent. After solvent removal and verification by Raman spectroscopy that $[N(CH_3)_4][BrO_3F_2]$ had been obtained, a stoichiometric amount of $[N(CH_3)_4][F]$ was weighed into the vessel at -160 °C and sufficient CH_3CN was condensed onto the reactants to solubilize them at 0 °C. The Raman spectrum of the colourless solid remaining after removal of the solvent at -40 °C showed that it was $[N(CH_3)_4][BrO_3F_2]$ and provided no evidence for $[N(CH_3)_4]_2[BrO_3F_3]$ formation.

7.2.1.3. Attempted Preparation of $[N(CH_3)_4][ClO_3F_2]$

A CH_3CN solution of ClO_3F and $[N(CH_3)_4][F]$ was allowed to react at -40 °C for 1 hr prior to removing the solvent under dynamic vacuum at -40 °C. The remaining solid was determined to be $[N(CH_3)_4][F]$ by Raman spectroscopy indicating that $[N(CH_3)_4][ClO_3F_2]$ was not produced or dissociated during the removal of the solvent.

The reaction of $[N(CH_3)_4][F]$ with liquid ClO_3F was monitored by Raman spectroscopy after warming the mixture to -40 °C for 1 hr. Prior to the removal of the excess ClO_3F, the Raman spectrum (-163 °C) of the mixture exhibited bands consistent with those of ClO_3F and $[N(CH_3)_4][F]$, providing no evidence for the formation of $[N(CH_3)_4][ClO_3F_2]$. The Raman spectrum (-163 °C) of the solid remaining after the removal of the ClO_3F under vacuum at -120 °C, was consistent with that of $[N(CH_3)_4][F]$, providing additional evidence that fluoride ion is not transferred to ClO_3F.

7.2.1.4. Attempted Preparation of $O_3Br-OTeF_5$ and $[N(CH_3)_4][BrO_3F(OTeF_5)]$

The Pauling electronegativity of the $-OTeF_5$ group (3.87,[79] 3.88[79,437]) is estimated to be similar to that of fluorine (4.00), and the oxidative resistance of the former ligand has allowed the preparation of numerous $-OTeF_5$ analogues of the main-group fluorides

and oxide fluorides (e.g., $O_2BrOTeF_5$,[438] $Xe(OTeF_5)_2$,[439] $BrOTeF_5$,[440] $B(OTeF_5)_3$[441]). The existence of such species has prompted the attempted synthesis of the unknown $-OTeF_5$ derivative of BrO_3F (i.e., $O_3Br-OTeF_5$) in the present work.

The preparation of $O_3Br-OTeF_5$ was attempted by the reaction of $B(OTeF_5)_3$ with BrO_3F (eq 7.10). The reaction of $B(OTeF_5)_3$ with a stoichiometric excess of neat BrO_3F

$$3BrO_3F + B(OTeF_5)_3 \rightarrow 3O_3Br-OTeF_5 + BF_3 \qquad (7.10)$$

was monitored by Raman spectroscopy at -90 °C, after allowing the reagents to mix at -78 (2 hr), -52 (5 min), -40 (25 min), and 0 °C (2 hr). Although $B(OTeF_5)_3$ exhibited limited solubility in BrO_3F at temperatures below -40 °C, it was completely soluble at 0 °C. Only bands associated with $B(OTeF_5)_3$ and BrO_3F were observed in the Raman spectrum of the solid at -95 °C (Table 7.1), indicating that displacement of fluoride by the $-OTeF_5$ group did not occur.

The preparation of $[N(CH_3)_4][F_5TeO-BrO_3F]$ was attempted by the reaction of $[N(CH_3)_4][OTeF_5]$ with BrO_3F (eq 7.11). The low solubility of $[N(CH_3)_4][OTeF_5]$ in

$$BrO_3F + [N(CH_3)_4][OTeF_5] \rightarrow [N(CH_3)_4][BrO_3F(OTeF_5)] \qquad (7.11)$$

BrO_3F at 0 °C prevented the reaction of these reagents in the absence of a solvent, however, the addition of 0.02 mL of CH_3CN was sufficient to solubilize the $[N(CH_3)_4][OTeF_5]$ at -32 °C. The Raman spectrum (-42 °C) of a CH_3CN solution of $[N(CH_3)_4][OTeF_5]$ and BrO_3F was acquired, however, only bands which could be assigned to BrO_3F and CH_3CN were observed. The solid remaining after the removal of the volatile components of the mixture under vacuum at -40 °C was identified as $[N(CH_3)_4][OTeF_5]$ by use of low-temperature (-163 °C) Raman spectroscopy (Table 7.2), indicating that $[N(CH_3)_4][BrO_3F(OTeF_5)]$ is not formed or readily dissociates to its starting reagents at -40 °C.

Table 7.1. Raman Frequencies and Vibrational Mode Assignments of Mixtures of $B(OTeF_5)_3$ and BrO_3F

Mixture of $B(OTeF_5)_3$ and BrO_3F [a]	$B(OTeF_5)_3$ [b]	BrO_3F [c]	Assignment [b,c]
1050 (3)	1050(6)		$\nu_1(E')$
970(5)		971(5)	$\nu_4(E)$
870(100)		868(100)	$\nu_1(A_1)$
754(3)	755(5)		$\nu_{23}(E')$
733(19)	732(5)		$\nu_2(A') + FEP$
716(60)	716(96)		$\nu_3(A')$
702(8)	702(16)		$\nu_{25}(E')$
673(68)	673(100)		$\nu_4(A')$
661(10)	660(18)		$\nu_{34}(E'')$
599(11)		596(13)	$\nu_2(A_1)$
499(21)	500(44)		$\nu_5(A')$
382(12)		378(9)	$\nu_5(E)$
356(6)		355(6)	$\nu_3(A_1)$
337(4)	338(7)		$\nu_6(A')$
332(2)	332(3)		$\nu_{35}(E'')$
324(8)	325(15)		$\nu_{27}(E')$
318(11)	318(17)		$\nu_8(A')$
311(14)	311(18)		$\nu_{36}(E'')$
291(15)		289(13)	$\nu_6(E)$
	254(3)		$\nu_9(A')$
245(3)	246(7)		$\nu_{30}(E')$
	140(3)		$\nu_{10}(A')$

[a] Recorded at -95 °C in a 4-mm o.d. FEP tube after dissolving $B(OTeF_5)_3$ in BrO_3F at 0 °C for 2 hr. [b] Vibrational frequencies and mode assignments for $B(OTeF_5)_3$ (C_{3h}) are from ref 442, and were rerecorded in a glass sample tube at -146 °C. [c] Vibrational frequencies and mode assignments for BrO_3F (C_{3v}) are from ref 207, and were obtained in a FEP sample tube at -72 °C.

Table 7.2. Raman Frequencies and Vibrational Mode Assignments for the Solid Remaining after Reaction of $[N(CH_3)_4][OTeF_5]$ with BrO_3F in CH_3CN

$[N(CH_3)_4][OTeF_5]$[a] Prior to Reaction	Product[b]	$[N(CH_3)_4][OTeF_5]$	Assignment $N(CH_3)_4{}^{+}$ [c]	$OTeF_5{}^{-}$ [d]
3045(24)	3045(28)	3045(8)		
3031(22)	3032(24)	3030(7)		
3004(5, br)	3005(4, br)		$\nu_5(E)$,	
2986(8, br)	2984(6, br)		$\nu_{14}(F_2)$,	
2966(15)	2965(10)	2968(2)	$\nu_1(A_1)$	
2927(11)	2934(7)	2931(2)	+ combination	
	2929(15)		bands	
2820(10)	2820(11)	2820(3)		
1473(24)	1474(27)	1477(10)	$\nu_2(A_1)$, $\nu_6(E)$	
1460(22)	1460(21)	1465(7)		
1417(5)	1418(5)	1421(2)	$\nu_{16}(F_2)$	
1287(3)	1288(3)	1288(1)	$\nu_{17}(F_2)$	
1181(2)	1184(2)			
1173(3)	1173(3)	1175(1)	$\nu_7(E)$	
951(24)	951(26)	952(18)	$\nu_{18}(F_2)$	
855(15)	855(38)	858(35)		$\nu_1(A_1)$
755(9)	756(11)	758(12)	$\nu_3(A_1)$	
743(sh)	745(7)	748(7)		
654(sh)	655(8)			$\nu_2(A_1)$
651(100)	650(100)	652(100)		
592(20)	593(18)	594(22)		$\nu_3(A_1)$, $\nu_5(B_1)$
590(14)	591(15)			
458(6)	458(6)	459(7)	$\nu_{19}(F_2)$	
379(4, br)	378(5)	375(4)	$\nu_8(E)$	
347(12)	348(12)	347(9)		$\nu_9(E)$
329(52)	330(44)	329(40)		$\nu_{10}(E)$
283(8)	284(8)	283(6)		$\nu_7(B_2)$
194(2)		196(3)		$\nu_{11}(E)$

[a] Recorded at -80 °C in 4-mm o.d. FEP. Bands from the FEP sample tube were observed at 294(4), 387(3), 733(12), 1305(2), 1383(2) cm^{-1}. [b] Recorded at -163 °C in 4-mm o.d. FEP after dissolving $[N(CH_3)_4][OTeF_5]$ in BrO_3F in 0.02 mL of CH_3CN at -32 °C, and removal of the volatile material at -40 °C. Bands from the FEP sample tube were observed at 294(3), 387(3), 733(10), 1306(2), 1384(2) cm^{-1}. [c] The vibrational bands were assigned with the aid of the Raman spectrum of $[N(CH_3)_4][OTeF_5]$ reported at -150 °C, ref 443.

7.2.2. X-ray Crystal Structures of [N(CH$_3$)$_4$][BrO$_3$F$_2$] and [NO]$_2$[BrO$_3$F$_2$][F]

Crystals of [N(CH$_3$)$_4$][BrO$_3$F$_2$] were grown by slowly cooling a CH$_3$CN solution of the salt from 10 to -25 °C. The solvent was then decanted from the crystalline product, which was dried under dynamic vacuum at -40 °C. Crystalline [NO]$_2$[BrO$_3$F$_2$][F] was obtained by allowing the salt to sublime under an argon atmosphere at -78 °C over a period of several weeks. The unit cell parameters and refinement statistics for [N(CH$_3$)$_4$][BrO$_3$F$_2$] and [NO]$_2$[BrO$_3$F$_2$][F] at -173 °C are summarized in Table 7.3.

7.2.2.1. [N(CH$_3$)$_4$][BrO$_3$F$_2$]

The crystal structure of [N(CH$_3$)$_4$][BrO$_3$F$_2$] (Figure 7.1) exhibits well-separated and weakly interacting cations and anions, consistent with its ionic description. While the N(CH$_3$)$_4^+$ cations are fully ordered, the BrO$_3$F$_2^-$ anions exhibit a two-fold rotational disorder along the Br-O(1) axis. The disorder reflects the solid state packing arrangement of the salt, which is best described in terms of columns of cations and anions which run parallel to the c-axis, but are staggered with respect to each other in this dimension (Figure 7.1b). The Br-O(1) bond axis is parallel to the c-axis of the tetragonal unit cell, such that the Br-F bonds would be expected to be orientated perpendicular to this axis. The comparatively long interanionic Br⋯O(1A) contact distances (4.21 Å) along the c-axis do not provide a preferred orientation of the Br-F bonds nor of the two remaining Br-O bonds in the a-b plane. Therefore, two equally populated orientations of the anion lying orthogonal to each other are observed. The disorder does not allow the extraction of meaningful bond lengths and bond angles for the oxygen and fluorine atoms involved in the disorder because the electron densities of oxygen and fluorine ligands are similar and the difference between their positions in superimposed model (0.64(1) Å) approaches the theoretical resolution (0.35 Å)[444] attainable with the molybdenum Kα X-ray radiation used for the experiment. Consequently, the Br-O(1) bond length (1.600(3) Å, Table 7.4)

Table 7.3. Summary of Crystal Data and Refinement Results for $[NO]_2[BrO_3F_2][F]$ and $[N(CH_3)_4][BrO_3F_2]$

	$[NO]_2[BrO_3F_2][F]$	$[N(CH_3)_4][BrO_3F_2]$
Space Group	$C2/c$	$P4/nmm$
a (Å)	9.892(3)	8.5718(7)
b (Å)	12.862(4)	8.5718(7)
c (Å)	10.141(4)	5.8117(6)
β (deg)	105.38(2)	90
V (Å^3)	1246.0(7)	427.02(7)
Z	4	2
Mol. wt. (g mol^{-1})	244.88	240.03
ρ_{calcd} (g cm^{-3})	2.616	1.867
T (°C)	-173	-173
μ (mm^{-1})	6.66	4.81
$R_1{}^a$	0.0671	0.0314
$wR_2{}^b$	0.1813	0.0761

$$^a R_1 = \frac{\sum \left\| F_o \right| - \left| F_c \right\|}{\sum \left| F_o \right|} \text{ for } I > 2\sigma(I). \quad ^b wR_2 = \frac{\sum \left| \left(\left| F_o \right| - \left| F_c \right|\right) w^{\frac{1}{2}} \right|}{\sum \left(F_o \left| w \right. \right)} \text{ for } I > 2\sigma(I).$$

a

I

II
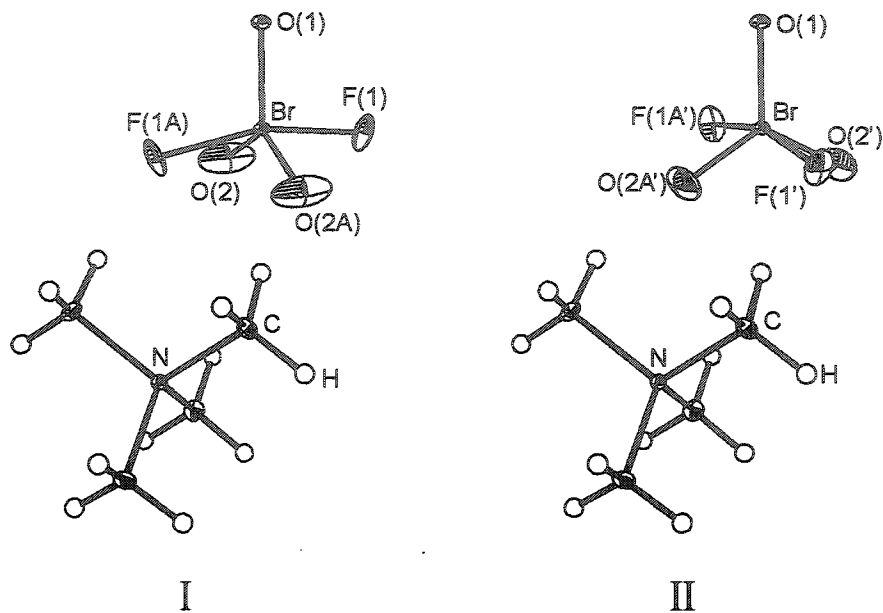
b
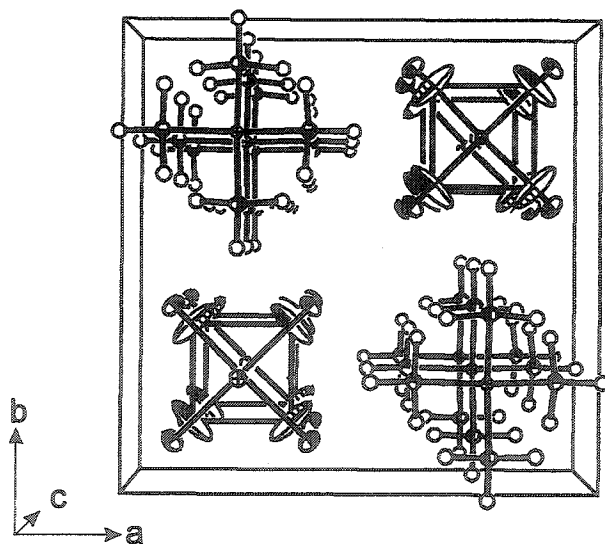
Figure 7.1.   (a) The structural unit of $[N(CH_3)_4][BrO_3F_2][F]$ showing the two orientations, I and II, of the $BrO_3F_2^-$ anion. (b) The packing diagram of $[N(CH_3)_4][BrO_3F_2][F]$ viewed along the c-axis. Thermal ellipsoids are shown at the 50% probability level.

Table 7.4. Summary of the Bond Lengths and Bond Angles for $[N(CH_3)_4][BrO_3F_2]$

Bond Lengths (Å)[a]		Bond Angles (deg)[a]	
Br-O(1)	1.600(3)	O(1)-Br-O(2)	118.7(5)
Br-O(2)	1.44(1)	O(1)-Br-F(1)	98.5(3)
Br-F(1)	1.77(6)	O(2)-Br-F(1)	85.9(4)
N-C	1.496(2)	C-N-C(A)	109.2(1)
C-H(1)	0.924[b]	C-N-C(B)	110.0(2)
C-H(2)	0.908[b]		
BrO(1)···Br(B)	4.21		

[a] A two-fold disorder of $[N(CH_3)_4][BrO_3F_2]$ occurs along the Br-O(1) C_2-axis of the anion such that O(2) and F(1) effectively exchange positions. As a result, the Br-O(2), and Br-F(1) bond lengths and the bond angles determined for the anion are not reliable. The Br-O(1), N-C and C-H bond lengths and the bond angles of the cation are not affected by the disorder. [b] The H positions were refined isotropically.

is the only reliable anion parameter, but is in excellent agreement with the Br-O distances of $[NO]_2[BrO_3F_2][F]$ (see section 7.2.2.2). Although two distinct positions associated with the oxygen and fluorine positions involved in the disorder can be identified, the Br-O(2) (1.44(1) Å) and Br-F (1.77(6) Å) bond lengths are artificially contracted and are shorter than those of $[NO]_2[BrO_3F_2][F]$ and those determined by electronic structure calculations. The O(1)-Br-O(2) and O(1)-Br-F(1) bond angles, which should be 120 and 90°, respectively, are likewise averaged to intermediate values of 118.7(5) and 98.5(3)°. Attempts to constrain the bond angles and/or bond lengths of the anion did not lower the residual agreement factor (R_1) or the uncertainties of the geometric parameters, and therefore were not utilized in the refinement of the reported structure.

7.2.2.2. $[NO]_2[BrO_3F_2][F]$

In contrast to the crystal structure of $[N(CH_3)_4][BrO_3F_2]$, the structure of $[NO]_2[BrO_3F_2][F]$ (Figure 7.2) is ordered, providing accurate geometric parameters for the $BrO_3F_2^-$ anion (Table 7.5). The asymmetric unit of this salt is best described in terms of two crystallographically unique $BrO_3F_2^-$ and NO^+ ions and a single F^- anion, which are well separated from each other and consistent with the salt's ionic description. Each NO^+ and F^- ion has a symmetry-related position, such that the empirical formula of the salt ($[NO]_2[BrO_3F_2][F]$) is half that of the asymmetric unit ($[NO]_4[BrO_3F_2]_2[F]_2$). For convenience, the empirical formula of the salt is used in the ensuing discussion.

The geometry of the $BrO_3F_2^-$ anion is based upon a trigonal bipyramidal AX_3Y_2 VSEPR arrangement in which the larger steric demands of the double bond pair domains of the oxygen ligands, require that they occupy the equatorial positions. The minor distortions of the O-Br-O (118.2(2) - 123.5(5)°) and O-Br-F (89.4(3) - 90.7(2)°) bond angles are attributed to solid state packing effects. The position of the Br-O(3) bond on the two-fold axis results in each anion having two unique Br-O bonds and two equivalent
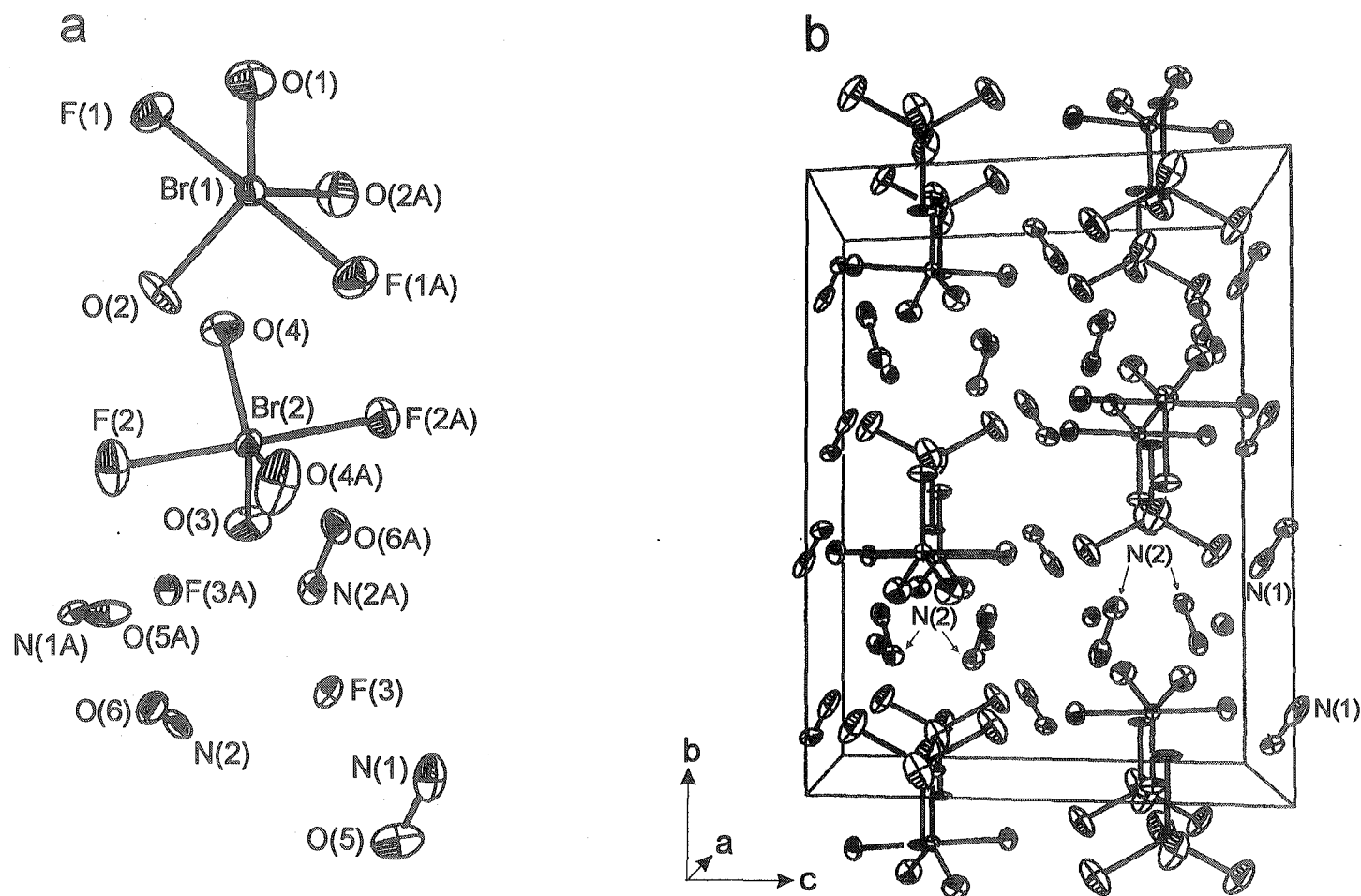
Figure 7.2. (a) Structural unit and (b) packing diagram of $[NO]_4[BrO_3F_2]_2[F]_2$. Thermal ellipsoids are shown at the 50% probability level.

Table 7.5. Summary of the Geometric Parameters for $[NO]_2[BrO_3F_2][F]$

Bond Lengths (Å)		Bond Angles (deg)	
Br(1)-O(1)	1.599(7)	O(1)-Br(1)-O(2)	119.7(2)
Br(1)-O(2)	1.602(5)	O(1)-Br(1)-F(1)	90.4(1)
Br(1)-F(1)	1.872(4)	F(1)-Br(1)-F(1A)	179.3(3)
Br(2)-O(3)	1.593(7)	O(2)-Br(1)-F(1)	89.9(3)
Br(2)-O(4)	1.610(6)	O(3)-Br(2)-O(4)	118.2(3)
Br(2)-F(2)	1.849(5)	O(3)-Br(2)-F(2)	90.8(2)
N(1)-O(5)	1.038(9)	O(4)-Br(2)-F(2)	89.8(3)
N(2)-O(6)	1.066(8)	F(2)-Br(2)-F(2A)	178.5(3)
O(5A)···F(1)	2.746	N(1A)-O(5A)···F(1)	132.1
O(6A)···F(1)	2.854	N(2B)-O(6A)···F(1)	143.8
O(6B)···F(1)	2.852	O(6B)-N(2A)···F(1)	90.8
N(2A)···F(1)	2.631	N(1B)-O(5B)···F(2)	136.3
O(5B)···F(2)	2.847	O(6A)-N(2A)···F(2)	116.3
O(5A)···F(2)	3.000	O(5A)-N(1A)···F(2)	105.9
O(6A)···F(2)	2.827	O(5)-N(1)···F(3)	105.5
N(1)···F(2)	2.544	O(5A)-N(1A)···F(3)	114.4
N(2)···F(2)	2.631	O(6)-N(2)···F(3)	103.4
N(1)···F(3)	2.032	O(6A)-N(2A)···F(3)	102.3
N(2)···F(3)	2.216		
N(1A)···F(3)	2.412		
N(2A)···F(3)	2.214		
O(6)···F(3)	2.672		
O(6A)···F(3)	2.654		
O(5)···F(3)	2.517		
O(5A)···F(3)	2.954		

Br-F bonds. The four unique Br-O bond lengths are the same at the $\pm3\sigma$ (99.7%) level of confidence, with a range of 1.593(7) - 1.610(5) Å and an average value of 1.601(7) Å. The Br-F bond lengths are significantly different for the two crystallographically independent anions at this level of confidence, with values of 1.872(4) and 1.849(5) Å for Br(1)-F(1) and Br(2)-F(2), respectively. The Br-F bond length variation likely arises from different contacts between the NO^+ cations and the fluorine ligands of the crystallographically distinct $BrO_3F_2^-$ anions (Figure 7.3a, 7.3b). Each fluorine atom of the $BrO_3F_2^-$ anions has three NO^+ cation contacts such that the Br-F$\cdots$[NO]$_3$ coordination is pseudo-tetrahedral, however, the contacts to F(1) and F(2) differ. Two cation contacts to F(1) are of the N-O$\cdots$F type, with F$\cdots$O distances of 2.746 and 2.854 Å, and N-O$\cdots$F angles of 132.1 and 143.8°, respectively. The remaining contact to F(1) occurs between both atoms of the cation with N$\cdots$F and O$\cdots$F distances of 2.631 and 2.852 Å, respectively, and an O-N$\cdots$F angle of 90.8°. For F(2), only one of the cation interactions is of the N-O$\cdots$F type, with an O$\cdots$F distance of 2.847 Å and an N-O$\cdots$F angle of 136.3°. The remaining two contacts to F(2) are to the nitrogen atom of the cation, having N$\cdots$F distances of 2.544 and 2.827 Å, and O-N$\cdots$F angles of 105.9 and 116.3°, respectively. The O$\cdots$F contacts to both anions are less than the sum of the fluorine (1.35,[287] 1.47 Å[286]) and oxygen (1.40,[287] 1.52 Å[286]) van der Waals radii, but these interactions are expected to be weak in view of the negative atomic charges on the oxygen and fluorine ligands. Although there are two N$\cdots$F contacts to F(2), with the shorter of these being nearly 0.10 Å less than the single N$\cdots$F(1) contact, the Br-F(1) bond is significantly longer than the Br-F(2) bond. The difference may result from the $\sigma_g^2\sigma_u^{*2}\sigma_g^2\pi_u^4\pi_g^*$ electronic configuration of the NO^+ cation. Transfer of electron density from the anion to the cation is expected when the LUMO (π_g^*) is directed towards the electron donor. The ideal π-acceptor orientation of NO^+ is only observed for F(1) (O-N$\cdots$F, 90.8°), resulting in
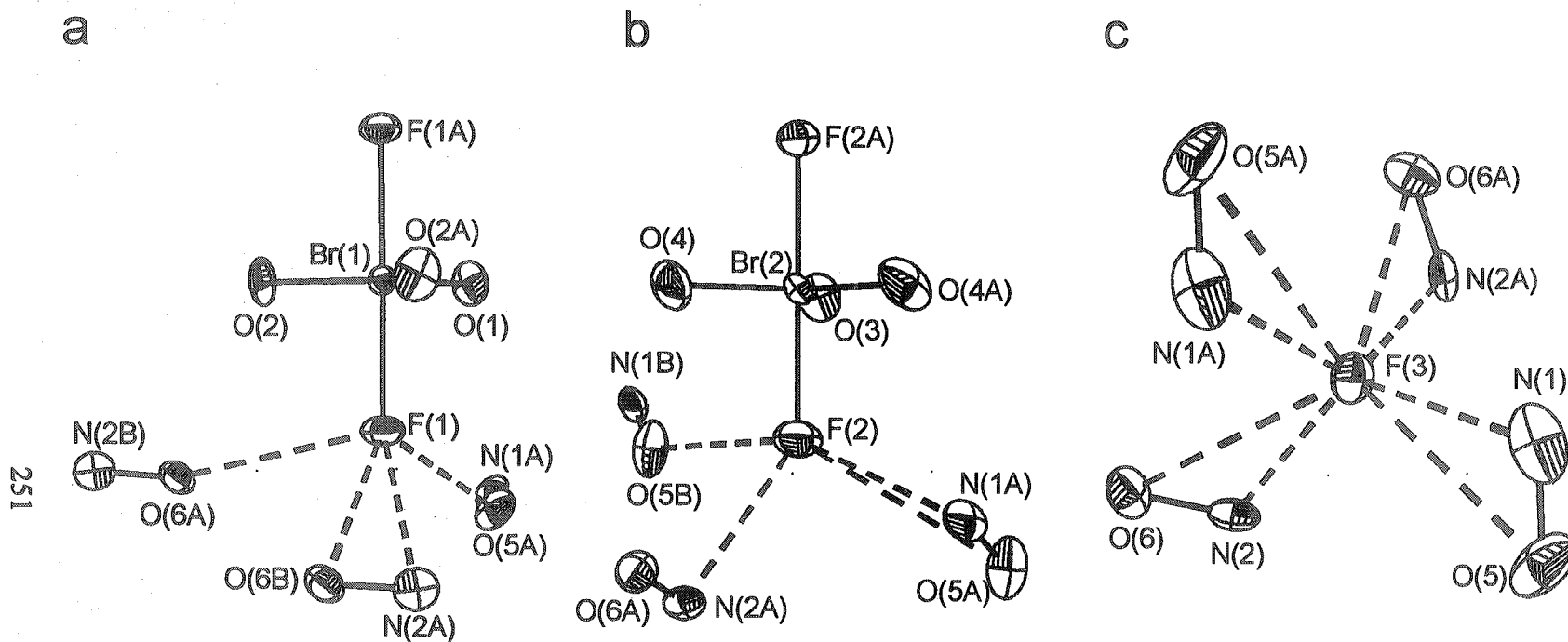
Figure 7.3. The cation-anion coordination environments of (a) F(1), (b) F(2) and (c) F(3) for $[NO]_2[BrO_3F_2][F]$. Thermal ellipsoids are shown at the 50% probability level.

elongation of the Br-F(1) bond. The N(1)-O(5) (1.038(9) Å) and N(2)-O(6) (1.066(8) Å) bond lengths are equivalent at the ±3σ confidence limit and cannot be used to verify O-N···F interactions leading to Br-F(1) bond elongation, however, the uniqueness of the two NO^+ positions is apparent from the two N-O stretching frequencies observed in the Raman spectrum of the salt (see section 7.2.3.5).

The fluoride ion (F(3)) in $[NO]_2[BrO_3F_2][F]$ is tetrahedrally coordinated to four NO^+ cations by means of long contacts (Figure 7.3c; 2.216 - 2.412 Å), which are significantly longer than the N-F bond length in NOF (1.52 Å).[445,446] The four N···F(3) distances are shorter than the N···F contacts to the $BrO_3F_2^-$ anions (2.544 - 2.631 Å), reflecting the stronger Lewis basicity of the fluoride ion. Although none of the O-N···F contact angles display the ideal 90° angle that serves to maximize the π-acceptor character of the cation, the cations are coordinated side-on to the fluoride ion, with O-N···F angles of 102.3 to 111.4° and O···F(3) contact distances (2.517 - 2.945 Å) that lie within the sum of the van der Waals radii for oxygen and fluorine (2.75,[287] 2.99 Å[286]). Coordination of the NO^+ cations to the fluoride ion presumably serves to stabilize the $[NO]_2[BrO_3F_2][F]$ salt by reducing the cation interactions with the fluorine ligands of the $BrO_3F_2^-$ anions. This contrasts with the unknown $[NO][BrO_3F_2]$ salt which, in the absence of a fluoride ion, may be expected to result in stronger ON^+···F-BrO_3F contacts and destabilization with respect to $[NO]_2[BrO_3F_2][F]$ and BrO_3F formation (eq 7.12).

$$2[NO][BrO_3F_2] \rightarrow [NO]_2[BO_3F_2][F] + BrO_3F \qquad (7.12)$$
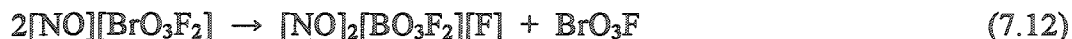
7.2.2.3. Comparison of Bond Lengths for the Known Br(VII) Species

Accurate geometric parameters are now available for BrO_4^-,[170,447,448] BrO_3F,[174] BrF_6^+ [360] (see section 6.2.2) and $BrO_3F_2^-$ (see section 7.2.2), allowing the effects of net charge and coordination number on their Br-F and Br-O bond lengths to be assessed.

The average, non-disordered, Br-O bond length obtained from the crystal structures of $[N(CH_3)_4][BrO_3F_2]$ and $[NO]_2[BrO_3F_2][F]$ is 1.602(6) Å, and is very similar to the average bond length of BrO_4^- (1.603(16) Å) obtained from the weighted X-ray structures of $[M][BrO_4]$ (M = K,[170] Cs,[447] Tl[448]) despite the higher coordination number of $BrO_3F_2^-$. On the basis of the negligible effect coordination number has on the Br-O bond lengths of $BrO_3F_2^-$ and BrO_4^-, the shorter Br-O bond length of BrO_3F (1.582(1) Å)[174] may be attributed to its net zero charge, which results in higher bond orders and less polar bonds (see section 7.3.5). These trends also imply that the longer interligand O···O distances of $BrO_3F_2^-$ (2.775 Å), when compared with those of BrO_4^- (2.618 Å)[170,447,448] and BrO_3F (2.660 Å),[174] reflect the larger O-Br-O bond angle of the $BrO_3F_2^-$ anion.

Despite the absence of a clear contraction of the average bond lengths for AsF_6^- (1.70(2) Å),[23] SeF_6 (1.69(1) Å)[415] and BrF_6^+ (1.666(11) Å; see section 6.2.2)[360] with increasing positive charge, the F···F bond orders (see section 6.3.3) and ligand-packings of the XF_6^+ (X = Cl, Br, I) cations[409] indicate that the fluorine ligands of BrF_6^+ are not close packed and that the ligand-ligand repulsive interactions of this cation are intermediate with respect to those of ClF_6^+ and IF_6^+. Although ligand-ligand repulsions may have some effect on the Br-F bond lengths of the coordinatively saturated BrF_6^+ cation, such interactions do not appear to strongly affect the bond lengths of lower coordinate Br(VII) species (*vide supra*). Consequently, the anticipated trend of decreasing Br-F bond length with increasing net positive charge is apparent for $BrO_3F_2^-$ (1.861(16) Å), BrO_3F (1.708(3) Å),[174] and BrF_6^+ (1.666(11) Å).

7.2.3. Vibrational Spectra of α-$[Cs][BrO_3F_2]$, β-$[Cs][BrO_3F_2]$, $[Rb][BrO_3F_2]$, $[K][BrO_3F_2]$, $[N(CH_3)_4][BrO_3F_2]$ and $[NO]_2[BrO_3F_2][F]$

Whereas main-group and transition metal pentahalides having trigonal bipyramidal geometries are common, oxide halides having the AO_3X_2 (D_{3h} symmetry)

VSEPR arrangement are rare and have been previously limited to XeO_3F_2 and matrix isolated OsO_3F_2. Of the twelve fundamental modes of vibration ($\Gamma_{vib} = 2A_1' + 2A_2'' + 3E' + E''$) expected for these species (Figure 7.4), $\nu_1(A_1')$, $\nu_2(A_1')$, $\nu_5(E')$, $\nu_6(E')$, $\nu_7(E')$ and $\nu_8(E'')$ are Raman-active and $\nu_3(A_2'')$, $\nu_4(A_2'')$, $\nu_5(E')$, $\nu_6(E')$ are infrared-active.

The Raman spectra of α-[Cs][BrO_3F_2] (Figure 7.5), β-[Cs][BrO_3F_2] (Figure 7.6), [Rb][BrO_3F_2] (Figure 7.7), [K][BrO_3F_2] (Figure 7.8), [N(CH$_3$)$_4$][BrO_3F_2] (Figure 7.9) and [NO]$_2$[BrO_3F_2][F] (Figure 7.10) were recorded at -163 °C. The infrared spectrum of β-[Cs][BrO_3F_2] (Figure 7.11) was obtained at ambient temperature and was used to verify the frequencies of both A_2'' modes, which are formally Raman-inactive but are often rendered Raman-active because of site-symmetry lowering and/or vibrational coupling within the unit cell. The vibrational mode assignments for the $BrO_3F_2^-$ anion (Table 7.6) were made with the assistance of electronic structure calculations (see section 7.3.3) and by comparison with the reported vibrational spectra of XeO_3F_2[433] and OsO_3F_2.[431,432]

7.2.3.1. α-[Cs][BrO_3F_2]

The low-temperature phase (α-) of [Cs][BrO_3F_2] exhibits six Raman-active bands, consistent with group theoretical prediction and D_{3h} symmetry. The most intense band in the spectrum at 802 cm^{-1}, was assigned to the symmetric $\nu_1(A_1')$ BrO_3 stretch, and the band at 896 cm^{-1} to the $\nu_5(E')$ asymmetric BrO_3 stretch. These assignments are supported by the calculated frequencies and the general trend that $\nu_{sym} < \nu_{asym}$, although the order of the $\nu_1(A_1')$ and $\nu_5(E')$ frequencies was found to be reversed for OsO_3F_2.[431,432] The lowest vibrational frequency of $BrO_3F_2^-$ is at 229 cm^{-1} and is assigned to the axial BrF_2 bending mode, $\nu_7(E')$, by analogy with those reported for PF_5 (300 cm^{-1}),[452] AsF_5 (123 cm^{-1}),[453] SbF_5 (90 cm^{-1}),[454] VF_5 (200 cm^{-1}),[455,456] MoF_5 (112 cm^{-1}),[457] XeO_3F_2 (190 cm^{-1})[433] and monomeric OsO_3F_2 (206 cm^{-1}).[431] The remaining bands at 383, 414 and 433 cm^{-1} were assigned to $\nu_6(E')$, $\nu_8(E'')$ and $\nu_2(A_1')$, respectively.
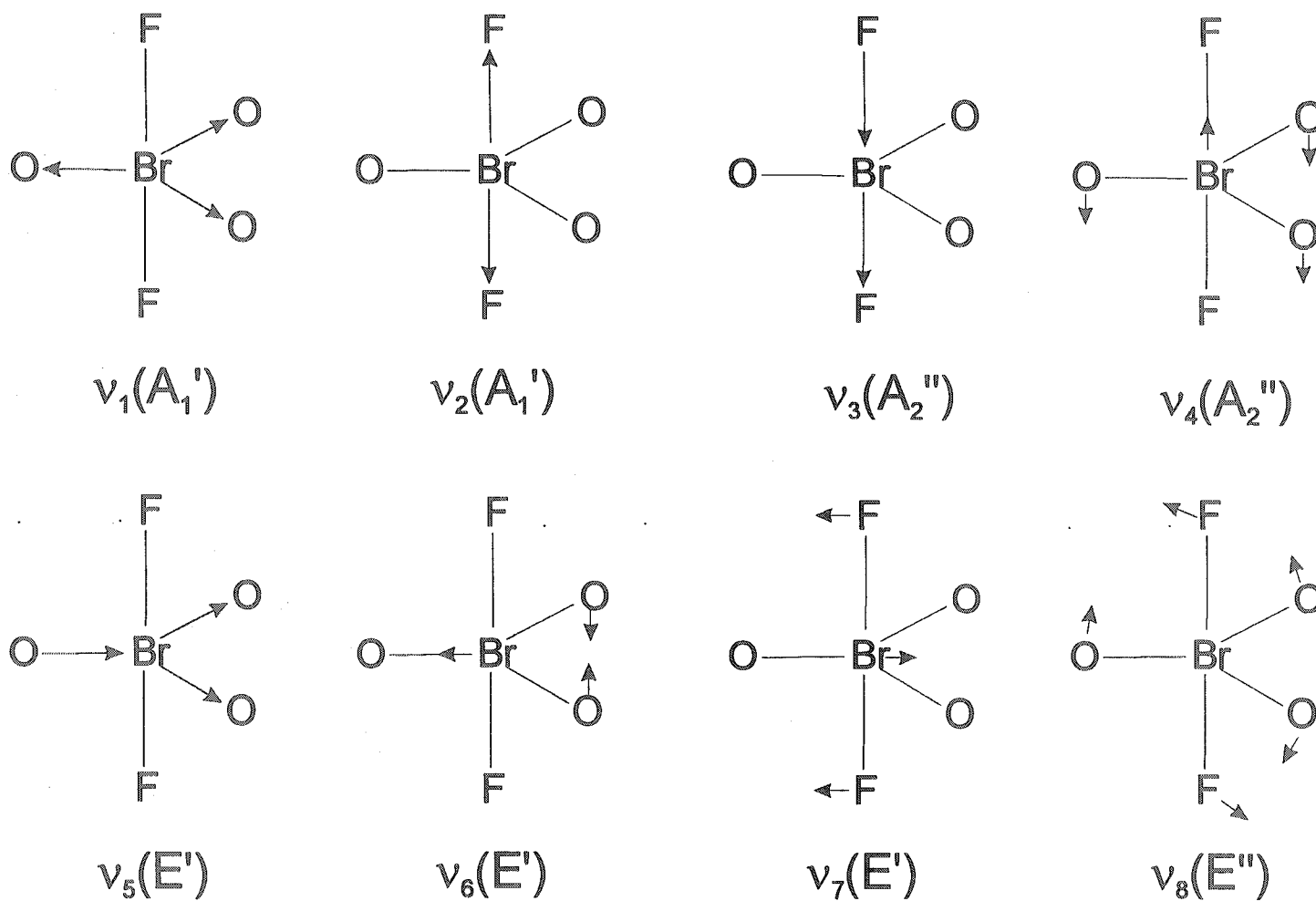
Figure 7.4. The displacement vectors for the fundamental vibrational modes of the $BrO_3F_2^-$ anion and their assignments under D_{3h} symmetry.
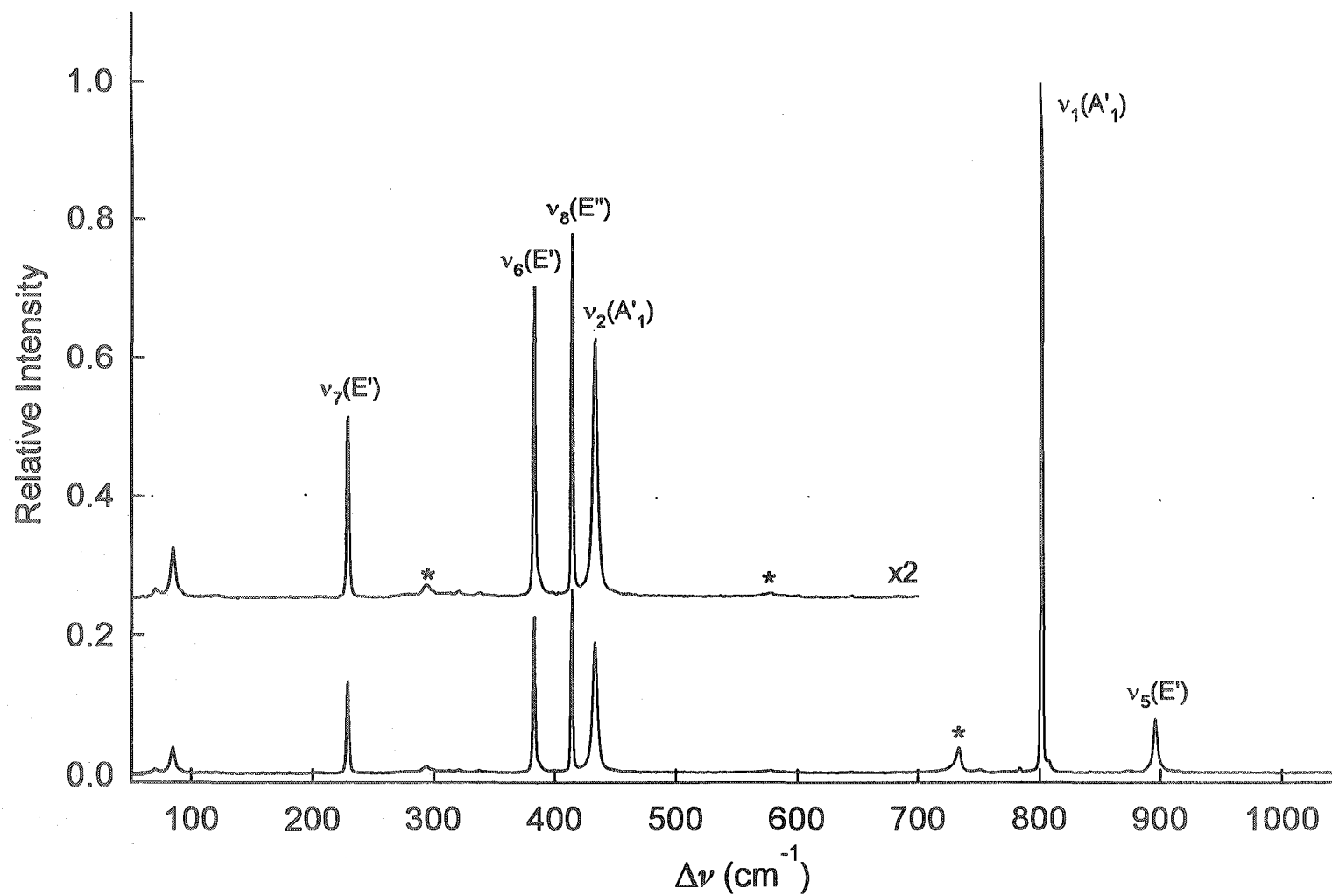
Figure 7.5. Raman spectrum of α-[Cs][BrO₃F₂] recorded at -163 °C using 1064-nm excitation. Asterisks denote bands arising from the FEP sample tube.
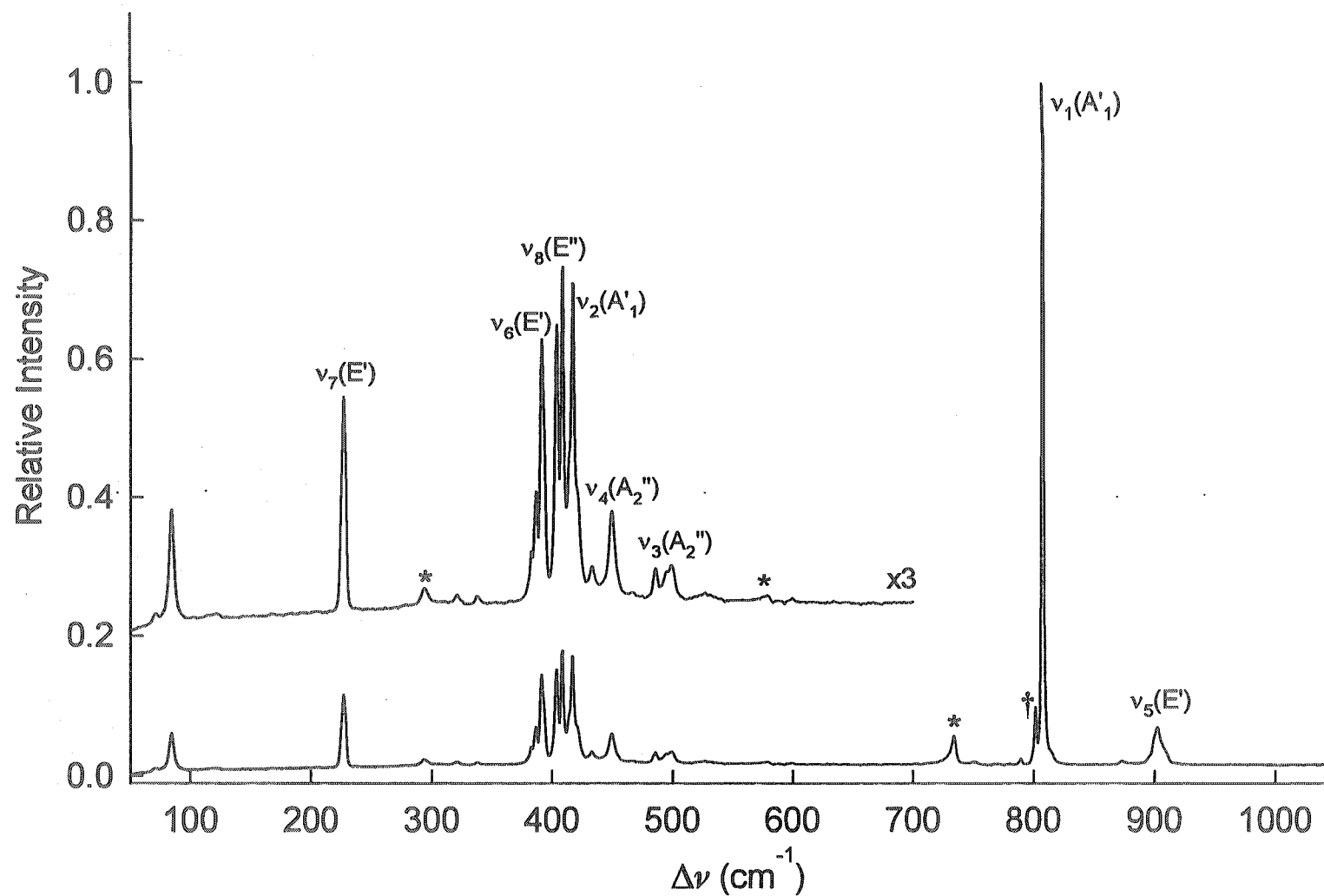
Figure 7.6. Raman spectrum of β-[Cs][BrO$_3$F$_2$] recorded at -163 $^\circ$C using 1064-nm excitation. Asterisks denote bands arising from the FEP sample tube. The band at 802 cm^{-1} (†) arises from residual α-[Cs][BrO$_3$F$_2$].
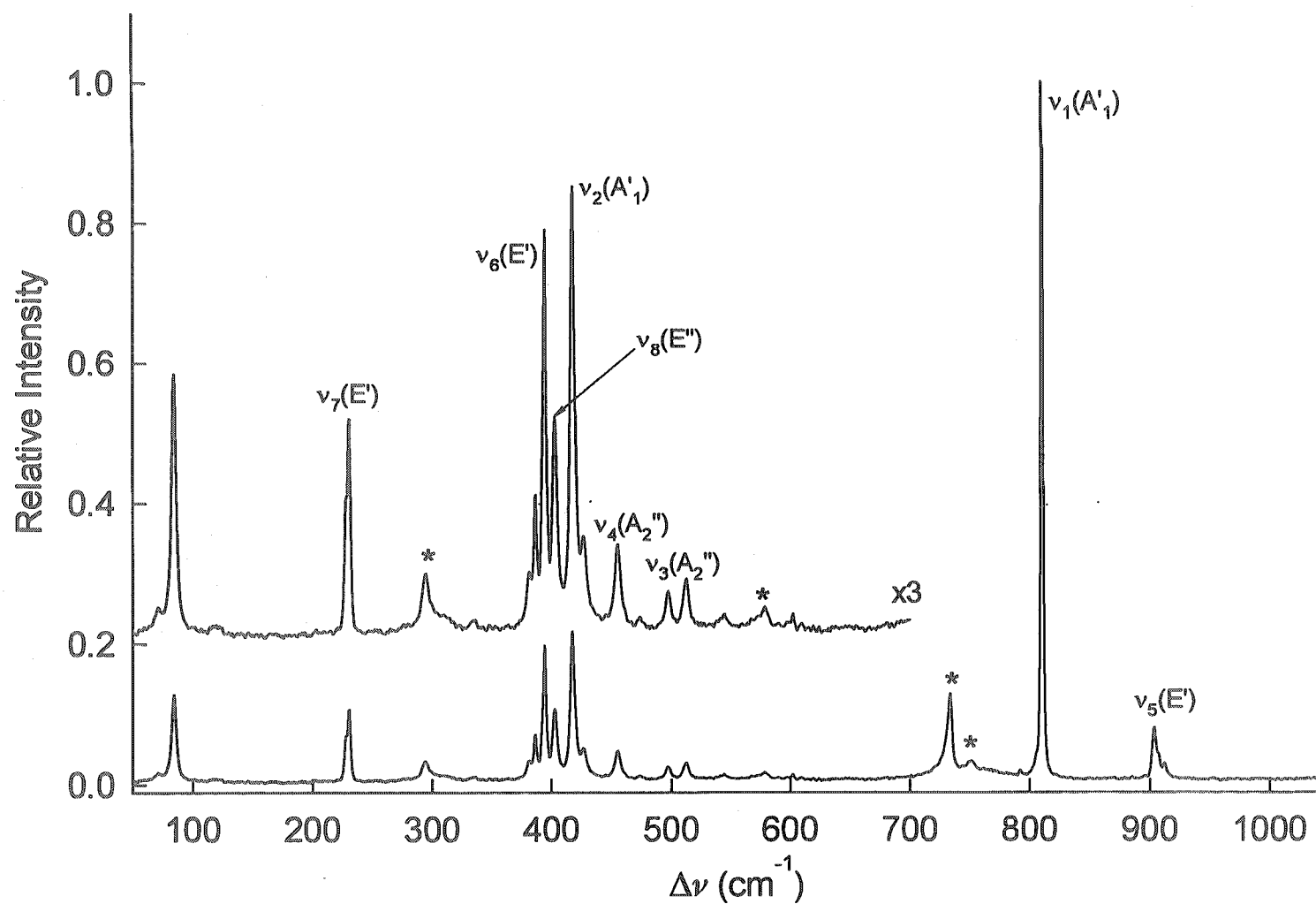
Figure 7.7. Raman spectrum of [Rb][BrO$_3$F$_2$] recorded at -163 °C using 1064-nm excitation. Asterisks denote bands arising from the FEP sample tube.
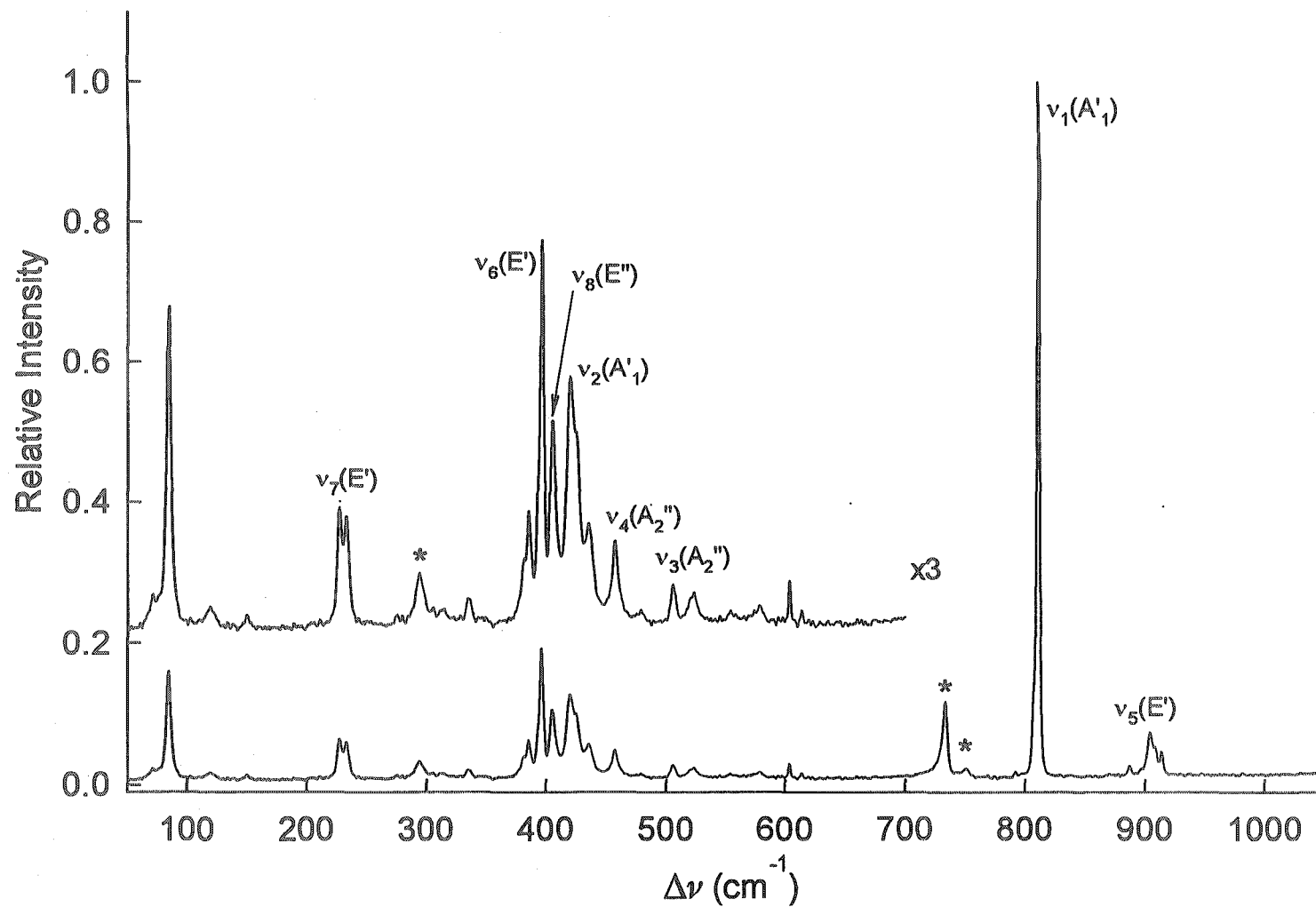
Figure 7.8. Raman spectrum of [K][BrO$_3$F$_2$] recorded at -163 °C using 1064-nm excitation. Asterisks denote bands arising from the FEP sample tube.
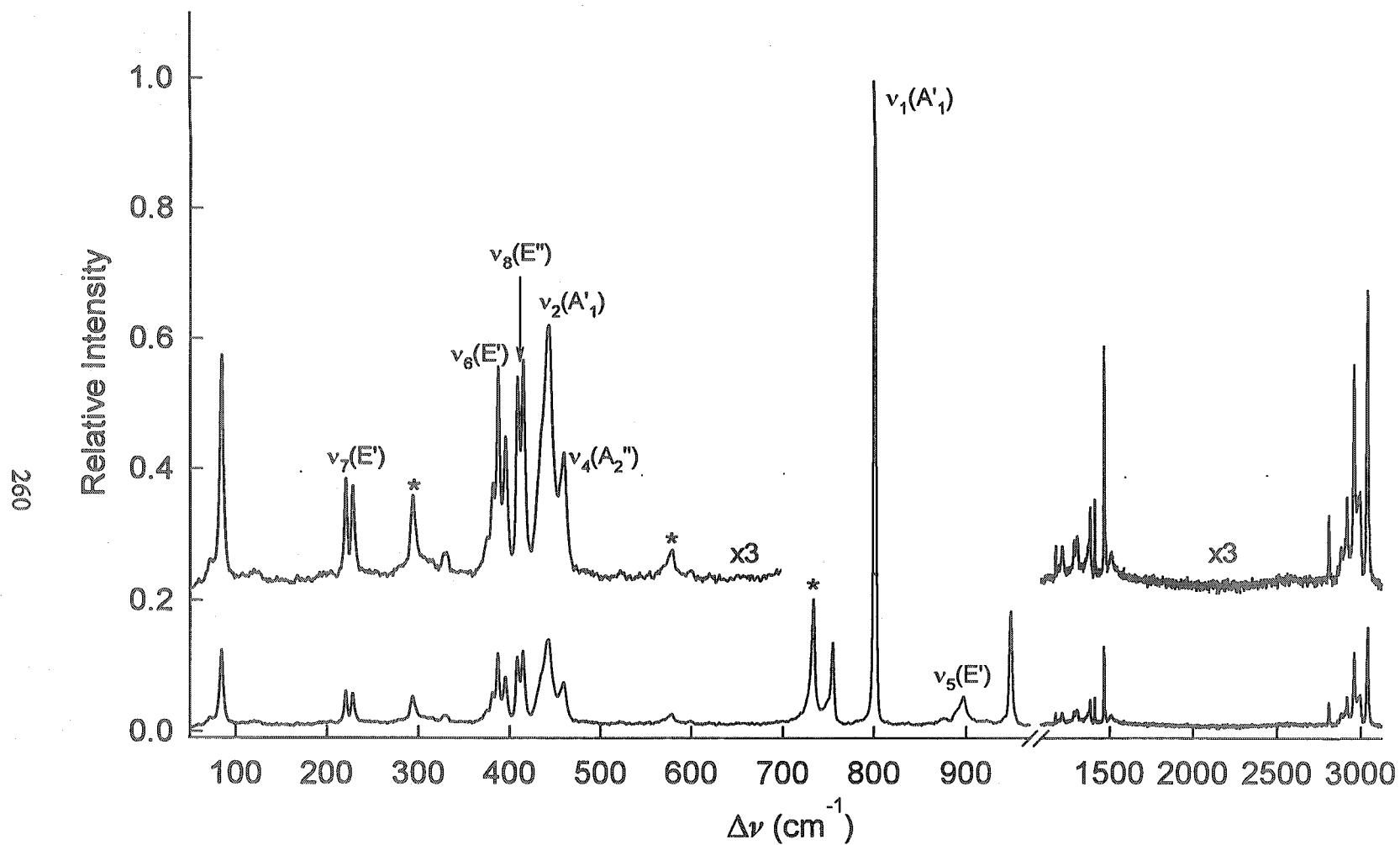
Figure 7.9. Raman spectrum of $[N(CH_3)_4][BrO_3F_2]$ recorded at -163 °C using 1064-nm excitation. Asterisks denote bands arising from the FEP sample tube.
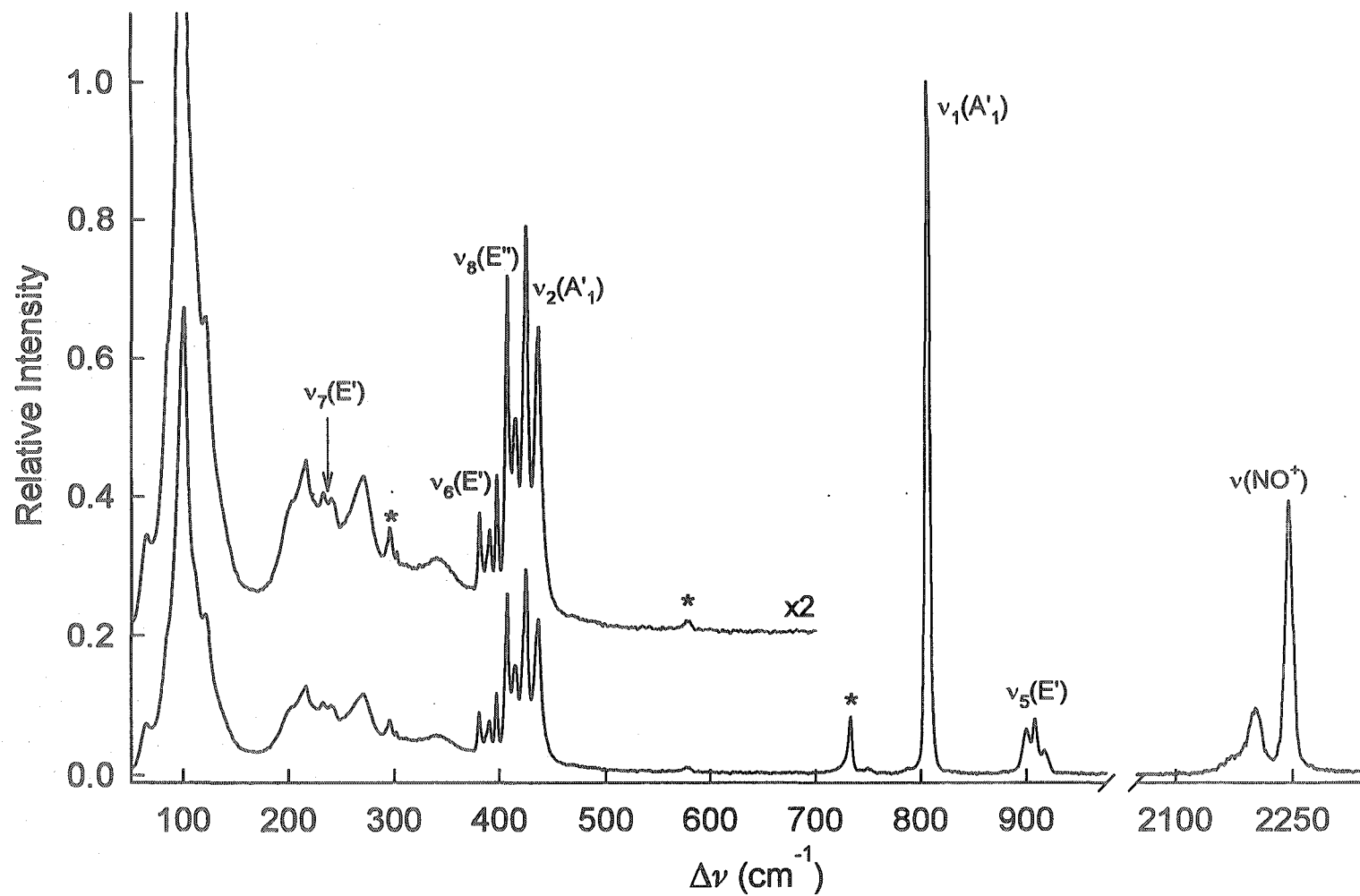
Figure 7.10. Raman spectrum of $[NO]_2[BrO_3F_2][F]$ recorded at -163 °C using 1064-nm excitation. Asterisks denote bands arising from the FEP sample tube.
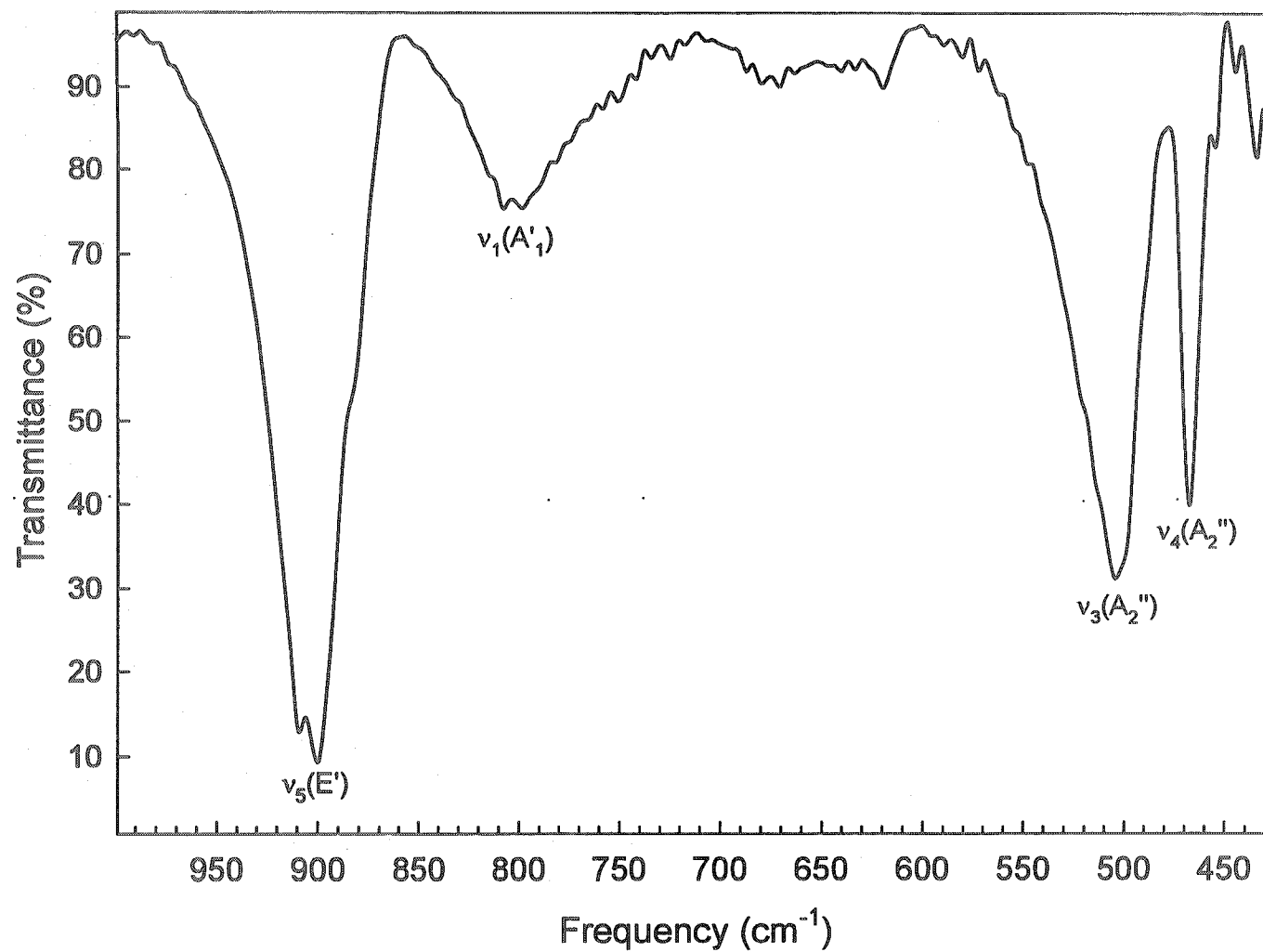
Figure 7.11. Infrared spectrum of β-[Cs][BrO$_3$F$_2$] recorded in a AgCl pellet at ambient temperature.

Table 7.6. Raman Frequencies, Intensities and Vibrational Assignments of Salts Containing the $BrO_3F_2^-$ Anion[a]

Assignment	[K][BrO₃F₂]	[Rb][BrO₃F₂]	α-[Cs][BrO₃F₂]	β-[Cs][BrO₃F₂][b]	[NO]₂[BrO₃F₂][F][c]	[N(CH₃)₄][BrO₃F₂][d]
$\nu_1(A_1')$	811(100)	810(100)	802(100)	807(100)	806(100)	801(100)
$\nu_2(A_1')$	435(6)	427(5)	433(19)	421(sh)	436(21)	434(sh)
	420(13)	417(22)		417(17)	425(28)	442(14)
$\nu_3(A_2'')$	523(2)	512(3)		497(3)		
	506(3)	497(3)		485(3)		
$\nu_4(A_2'')$	457(5)	455(5)		449(6)		460(6)
				433(3)		
$\nu_5(E')$	914(5)	912(3)	896(8)	908(sh)	917(3)	896(5)
	908(5)	907(sh)		903(7)	908(7)	
	904(7)	904(8)		899(sh)	900(6)	
$\nu_6(E')$	397(19)	394(20)	383(23)	392(14)	397(10)	395(3)
	393(sh)	386(7)		386(7)	390(5)	389(4)
		381(3)		383(sh)	381(7)	382(2)
$\nu_7(E')$	227(6)	228(sh)	229(13)	227(12)	240(sh)	228(1)
	233(6)	231(11)			233(sh)	222(1)
$\nu_8(E'')$	406(11)	403(11)	414(27)	409(18)	415(14)	414(12)
				404(15)	407(25)	408(11)

[a] All spectra were recorded at -163 °C in ¼-in or 4-mm o.d. FEP sample tubes. Frequencies are given in cm⁻¹. The intensities, given in parenthesis, are scaled relative to the intensity of the ν_1 band, which is assigned an value of 100. The abbreviation, sh, denotes a shoulder. [b] The infrared spectrum of β-[Cs][BrO₃F₂] was obtained in a AgCl pellet at ambient temperature. The ν_1 (800(w, br) cm⁻¹), ν_5 (909(s), 900(s), 881(sh) cm⁻¹), ν_3 (504(m) cm⁻¹) and ν_4 (468(m) cm⁻¹) vibrational modes were observed in the infrared spectrum of β-[Cs][BrO₃F₂], where the abbreviations w, m, s, and br denote weak, medium, strong, and broad, respectively. [c] The NO⁺ stretching modes were observed at 2203(8) and 2246(31) cm⁻¹. [d] Bands at 3042(16), 2995(6), 2919(5), 2881(3), 2866(2), 2809(5), 1469(11), 1466(13), 1412(5), 1286(3), 1184(2), 1177(3), 949(19), 329(2) cm⁻¹ were assigned to N(CH₃)₄⁺ by comparison with the assignments given for this cation in refs 246, 449-451.

7.2.3.2. β-[Cs][BrO₃F₂]

The high-temperature phase (β-) of [Cs][BrO₃F₂] is easily differentiated from the α-phase on the basis of frequency shifts, splittings of the Raman-active modes, and additional weak bands in the Raman spectrum, which are assigned to the formally Raman-inactive A_2'' vibrational modes. The $v_1(A_1')$ (807 cm^{-1}) and $v_5(E')$ (903 cm^{-1}) BrO₃ stretches are at higher frequencies in the β-phase than in the α-phase. The $v_5(E')$ band is also broadened with shoulders at 899 and 908 cm^{-1}, which are presumed to arise from site-symmetry lowering of the anion that leads to removal of the E' degeneracy. The well-resolved splittings of the $v_6(E')$ (386, 392 cm^{-1}) and $v_8(E'')$ (404, 409 cm^{-1}) modes are also consistent with the latter assumption. The reduced symmetry, inferred from the splitting of the degenerate BrO₃ stretches and bends, also permits the observation of the $v_3(A_2'')$ and $v_4(A_2'')$ modes, which are formally Raman-inactive under D_{3h} symmetry. With the aid of the calculated vibrational frequencies, the asymmetric BrF₂ stretch ($v_4(A_2'')$) was assigned to the band at 449 cm^{-1}, while the higher frequency bands (485, 497 cm^{-1}) were assigned to the BrO₃ umbrella bend ($v_3(A_2'')$). These modes were observed at 468 and 504 cm^{-1} in the infrared spectrum of β-[Cs][BrO₃F₂] along with $v_1(A_1')$ (800 cm^{-1}) and $v_5(E')$ (881, 900, 909 cm^{-1}) modes (Figure 7.11).

7.2.3.3. [K][BrO₃F₂] and [Rb][BrO₃F₂]

The spectra of [K][BrO₃F₂] and [Rb][BrO₃F₂] were similar to that of β-[Cs][BrO₃F₂], and were assigned accordingly. In contrast to [Cs][BrO₃F₂], only single phases were observed for [K][BrO₃F₂] and [Rb][BrO₃F₂], which may reflect the higher temperatures required for their syntheses. The symmetric and asymmetric BrO₃ stretching frequencies of the K⁺ and Rb⁺ salts are slightly higher in frequency than in β-[Cs][BrO₃F₂] and exhibited larger splittings for $v_5(E')$. The band splittings for $v_2(A_1')$, $v_6(E')$ and $v_8(E'')$ (390 - 430 cm^{-1}) are somewhat more complex in the K⁺ and Rb⁺ salts

than for the corresponding modes of β-[Cs][BrO$_3$F$_2$], and the possibility of overlapping bands cannot be ruled out as suggested by the apparent absence of splitting on v_8(E"). Splitting of the axial fluorine bending mode, v_7(E'), appears as a shoulder in the spectrum of [Rb][BrO$_3$F$_2$] but is well resolved for [K][BrO$_3$F$_2$]. The splittings of the degenerate E' bands may be attributed to site-symmetry lowering of the anion in the solid state, however, the splittings of the non-degenerate v_2(A$_1$') mode in the K$^+$ (420, 425 cm^{-1}) and Rb$^+$ (417, 427 cm^{-1}) salts indicate that vibrational coupling within the unit cell must also be occur. The formally Raman-inactive A$_2$" modes appear as weak bands in the spectra of [K][BrO$_3$F$_2$] and [Rb][BrO$_3$F$_2$]. The band contours of the higher frequency v_3(A$_2$") BrO$_3$ bend are similar in the spectra of [K][BrO$_3$F$_2$] (506, 523 cm^{-1}), [Rb][BrO$_3$F$_2$] (497, 512 cm^{-1}) and β-[Cs][BrO$_3$F$_2$] (485, 497 cm^{-1}). The asymmetric BrF$_2$ stretch, v_4(A$_2$"), was a single band in [K][BrO$_3$F$_2$] (457 cm^{-1}) and [Rb][BrO$_3$F$_2$] (455 cm^{-1}) and is less sensitive to the nature of the counter ion.

7.2.3.4. [N(CH$_3$)$_4$][BrO$_3$F$_2$]
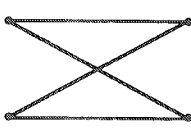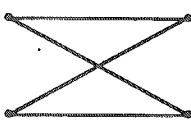
The Raman spectrum of [N(CH$_3$)$_4$][BrO$_3$F$_2$] is characteristic of a BrO$_3$F$_2^-$ anion exhibiting minor distortions and displays minimal overlap of the cation and anion bands. The disordered BrO$_3$F$_2^-$ anions in the crystal structure of [N(CH$_3$)$_4$][BrO$_3$F$_2$] prevents an unambiguous correlation between the free ion, site and crystallographic symmetries of the anions, however, broadening or splitting of the v_2(A$_1$'), v_3(A$_2$"), v_5(E'), v_6(E') and v_7(E') modes is indicative of factor-group splitting. The two high-frequency BrO$_3$ stretches occur at 801 cm^{-1} (v_1(A$_1$')) and 896 cm^{-1} (v_5(E')), with the former again being the most intense feature in the spectrum and the latter exhibiting minor broadening. The frequencies of the remaining modes and their relative intensities are consistent with those of the alkali metal salts. The two formally Raman-inactive A$_2$" bands were not observed, but may overlap with the broad v_{19}(F$_2$) cation band at 460 cm^{-1}.[451]

7.2.3.5. $[NO]_2[BrO_3F_2][F]$

The Raman spectrum of $[NO]_2[BrO_3F_2][F]$ is similar to those of the alkali metal and $N(CH_3)_4^+$ salts, with the exception that the low-frequency region (175 - 375 cm^{-1}) is dominated by broad bands of medium intensity. These bands are tentatively assigned to the ON$\cdots$F(3) stretching and O-N$\cdots$F(3) bending modes, which are expected to be significantly lower in frequency than those of ONF (735, 492 cm^{-1}, respectively)[458] as a result of the long N$\cdots$F contact distances, and are broadened because there are several such contacts (see section 7.2.2.2). The presence of two bands in the N-O stretching region (2203, 2246 cm^{-1}) is consistent with two crystallographically unique cation positions (Figure 7.2). Although the N-O stretching frequencies are more similar to that of NO$^+$ (2273 cm^{-1})[459] than to that of ONF (1843 cm^{-1}),[460-462] the shift to lower frequency is consistent with significant cation interactions with the anions.

The splittings of the $\nu_2(A_1')$, $\nu_5(E')$, $\nu_6(E')$ $\nu_7(E')$ and $\nu_8(E')$ modes of $BrO_3F_2^-$ in the Raman spectrum of $[NO]_2[BrO_3F_2][F]$ are consistent with factor group splitting. Correlation of the free anion symmetry (D_{3h}) with the site symmetries of the two crystallographically unique $BrO_3F_2^-$ anions (C_{2v}) and, in turn, with the unit cell symmetry (C_{2h}) predict the following components for each vibrational mode: ν_1 and $\nu_2 \rightarrow 4A_g + 4A_u$; ν_3 and $\nu_4 \rightarrow 4B_g + 4B_u$; ν_5, ν_6, ν_7 and $\nu_8 \rightarrow 4A_g + 4A_u + 4B_g + 4B_u$ (Table 7.7). Because the unit cell is centrosymmetric, only the A_g and B_g components are Raman-active, whereas the A_u and B_u components are infrared active. Thus, the maximum number of vibrational components expected in the Raman spectrum is four for ν_1 - ν_4 and eight for ν_5 - ν_8. The inability to observe all 48 Raman-active modes is attributed to the experimental resolution (1 cm^{-1}) and the small energy differences expected among the factor group split components of the vibrational modes.

Table 7.7. Factor-Group Analysis of the $BrO_3F_2^-$ Anion in $[NO]_2[BrO_3F_2][F]$[a]

Symmetry of Free $BrO_3F_2^-$		Site-Symmetry of $BrO_3F_2^-$	Crystal Symmetry of $[NO]_2[BrO_3F_2][F]$	
D_{3h}		C_{2v}	C_{2h}	

$4v_1$, $4v_2$	A_1'			
		$20\,A_1$	A_g	$2v_1$, $2v_2$, $2v_5$, $2v_6$, $2v_7$, $2v_8$, 2T, 2R (Raman-active)
$4R$	A_2'			
		$4\,A_2$	A_u	$2v_1$, $2v_2$, $2v_5$, $2v_6$, $2v_7$, $2v_8$, 2T, 2R (Infrared-active)
$4v_3$, $4v_4$, 4T	A_2''			
		$12\,B_1$	B_g	$2v_3$, $2v_4$, $2v_5$, $2v_6$, $2v_7$, $2v_8$, 4R, 4T (Raman-active)
$4v_5$, $4v_6$, $4v_7$, 4T	E'			
		$12\,B_2$	B_u	$2v_3$, $2v_4$, $2v_5$, $2v_6$, $2v_7$, $2v_8$, 4R, 4T (Infrared-active)
$4v_8$, 4R	E''			

[a] The two unique $BrO_3F_2^-$ anions in the asymmetric unit of $[NO]_2[BrO_3F_2][F]$ have C_{2v} site-symmetries. The factor-group analysis has been carried out for one of these anions in the monoclinic space group $C2/c$, with $Z = 4$. Consequently, the number of modes for each symmetry description should be doubled to account for the coupled vibrational modes of the eight $BrO_3F_2^-$ anions in the unit cell.

7.2.3.6. Variations in the $BrO_3F_2^-$ Stretching Frequencies

Among the $BrO_3F_2^-$ salts studied in this work, the frequency of the symmetric BrO_3 stretch $\nu_1(A_1')$ follows the trend: $[N(CH_3)_4][BrO_3F_2]$ (801 cm^{-1}) < $[Cs][BrO_3F_2]$ (α-phase 802 cm^{-1}; β-phase 807 cm^{-1}) $\approx$ $[NO]_2[BrO_3F_2][F]$ (806 cm^{-1}) < $[Rb][BrO_3F_2]$ (810 cm^{-1}) $\approx$ $[K][BrO_3F_2]$ (811 cm^{-1}], which is paralleled by the frequency trends observed for the asymmetric BrO_3 stretching mode, $\nu_5(E')$: $[N(CH_3)_4][BrO_3F_2]$ (896 cm^{-1}) $\approx$ $[Cs][BrO_3F_2]$ (α-phase 896 cm^{-1}; β-phase 903 cm^{-1}) < $[NO]_2[BrO_3F_2][F]$ (908 cm^{-1}) $\approx$ $[Rb][BrO_3F_2]$ (908 cm^{-1}) < $[K][BrO_3F_2]$ (910 cm^{-1}). The BrO_3 stretching frequency trends reflect the relative fluoride-ion donor strengths of the parent fluoride salts, which are expected to decrease in the order $[N(CH_3)_4][F]$ > CsF > RbF > KF based on the increase in charge-to-radius ratios over ionic fluorides.[463] The correlation between the BrO_3 stretching frequencies and the fluoride ion donor properties can be rationalized in terms of the resonance structures (I - III), which delocalize the negative charge over the
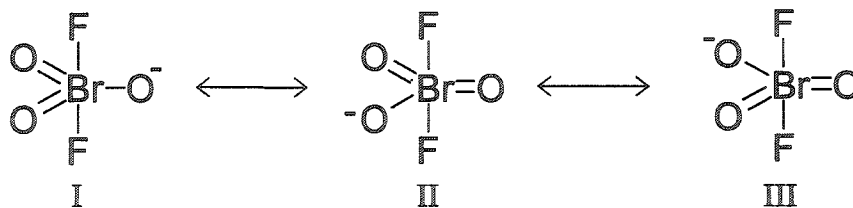
three oxygen atoms. For the strongest fluoride ion donor, $[N(CH_3)_4][F]$, the interactions between the cation and the fluorine ligands of the anion are expected to be minimal and the formal Br-O bond order is expected to be close to the ideal value of 1.66. As the donor strength of the fluoride ion source decreases (i.e., the F$^-$ ion affinity of the cation increases) the interaction between the cation and the anion through the fluorine ligands is expected to increase. Such interactions would reduce the net negative charge on the anion, resulting in an increase in the Br-O bond order and the BrO_3 stretching frequencies. In the extreme case of complete fluoride ion abstraction, BrO_3F (C_{3v}) is

obtained, increasing the formal bond order to 2 and the Br-O stretching frequency to 876 cm^{-1} [172,173].

The trends among the BrF_2 stretching frequencies of these salts are complicated by splittings observed for their $v_2(A_1')$ and $v_3(A_2'')$ modes in addition to the low intensities of their formally Raman-inactive $v_3(A_2'')$ modes. For $[K][BrO_3F_2]$, $[Rb][BrO_3F_2]$ and β-$[Cs][BrO_3F_2]$, the Br-F stretching frequencies and splittings are similar, suggesting that these species are isomorphous. The asymmetric BrF_2 stretch, $v_3(A_2'')$, was not observed in the spectra of α-$[Cs][BrO_3F]$, $[NO]_2[BrO_3F_2][F]$ or $[N(CH_3)_4][BrO_3F_2]$, however, the symmetric stretching frequencies, $v_2(A_1')$, are higher in these salts than in the lighter alkali metal salts and β-$[Cs][BrO_3F_2]$. The $v_2(A_1')$ frequency trend correlates with the lower BrO_3 stretching frequencies of these salts (*vide supra*) and is consistent with more complete fluoride ion transfer to the anion.

7.2.4. NMR Spectroscopy

The ^{19}F, ^1H and ^{13}C NMR spectra of $[N(CH_3)_4][BrO_3F_2]$ dissolved in CH_3CN at -40 °C were obtained from a sample which had been stored at -196 °C and had not been previously warmed above -40 °C. The ^{19}F NMR spectrum was recorded between -500 and 580 ppm and exhibited a single resonance at 237.0 ppm ($\Delta v_{1/2}$, 360 Hz) which is assigned to the magnetically equivalent fluorines of the $BrO_3F_2^-$ anion (Figure 7.12). The ^{19}F chemical shift of $BrO_3F_2^-$ is significantly more shielded than those of BrF_6^+ (337 - 339 ppm)[31,36] and BrO_3F (269 - 274 ppm),[207] with the general trend of increased deshielding with increasing formal charge being adhered to for these Br(VII) species. The broad line width is attributed to the nearly completely quadrupole-collapsed $^1J(^{79,81}Br-^{19}F)$ spin-spin coupling, which was previously invoked to account for the broad ^{19}F line widths observed for BrO_3F ($\Delta v_{1/2}$, 70 - 217 Hz).[207] Quadrupolar collapse in these lower symmetry species contrasts with that of the highly symmetric BrF_6^+ cation, for
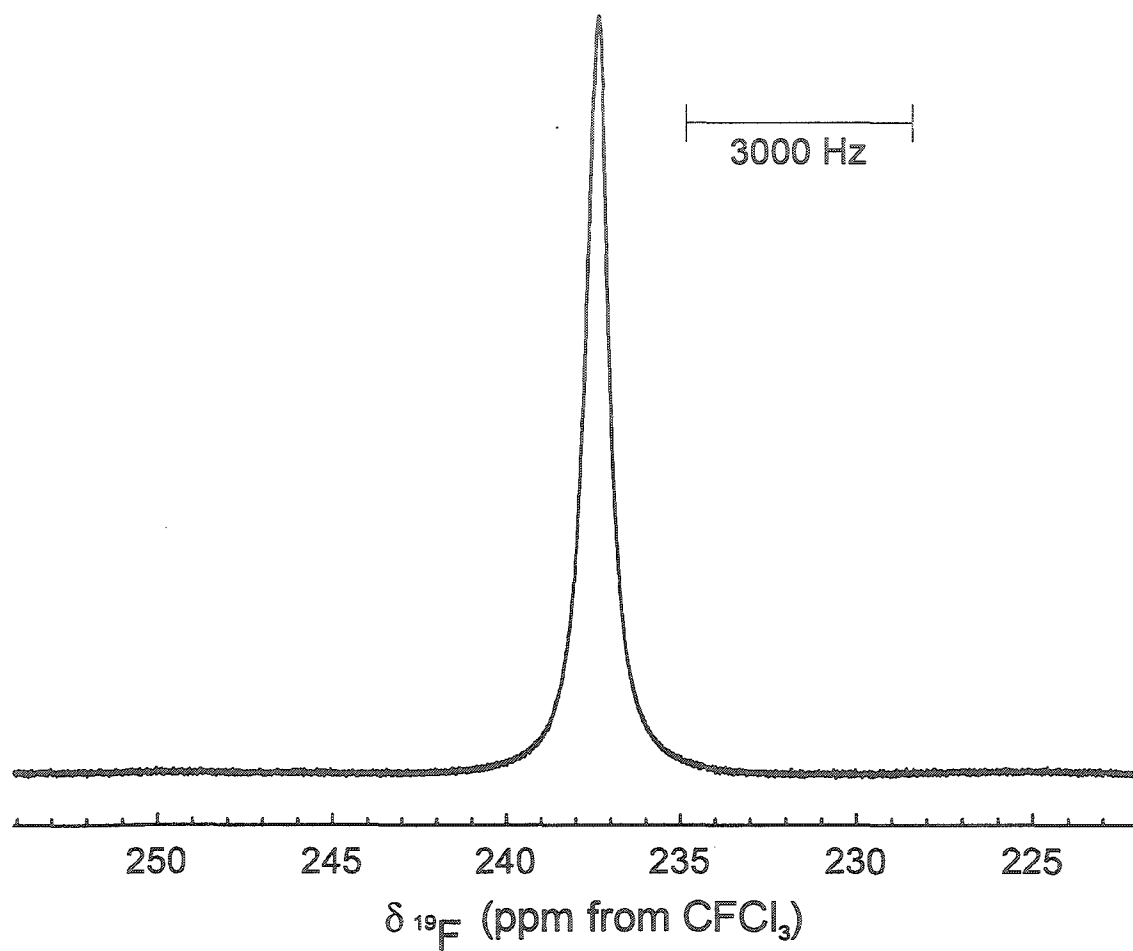
Figure 7.12. The ^{19}F NMR spectrum of the $BrO_3F_2^-$ anion for $[N(CH_3)_4][BrO_3F_2]$ in CH_3CN solvent at -40 °C.

which the near-zero electric field gradient at the octahedrally coordinated bromine nuclei slows quadrupolar relaxation rate so that the $^1J(^{79,81}Br-^{19}F)$ couplings can be resolved (see section 6.2.3).[36] The ^1H and ^{13}C resonances arising from the $N(CH_3)_4^+$ cation were observed at 3.0[236] and 55.4 ppm, respectively, with a $^1J(^{13}C-^1H)$ coupling constant of 143 Hz (measured in the ^{13}C spectrum).

A second sample of $[N(CH_3)_4][BrO_3F_2]$ that had been prepared for study by NMR spectroscopy, but warmed to ambient temperature for 2 hr did not exhibit the characteristic ^{19}F resonance of the anion at -40 °C. Instead, the pale yellow solution exhibited ^{19}F resonances at 396.5, 49.0, 15.0 and -36.7 ppm. The resonances at 396.5 (1:1:1 triplet; $^3J(^{19}F-^{14}N)$ = 115 Hz) and 49.0 ppm (1:1:1:1 quartet; $^3J(^{19}F-^1H)$ = 7.2 Hz) are assigned to NO_2F[464] and CH_3COF,[465] respectively. The resonances at 15.0 and - 36.7 ppm had relative integrated intensities of 0.14 and 0.20 with respect to CH_3COF (1.00) and could not be assigned. In addition to the CH_3CN solvent (1.9 ppm) and $N(CH_3)_4^+$ cation (3.5 ppm) resonances, the ^1H NMR spectrum exhibited a broad resonance (10 Hz) at 10.4 ppm. The CH_3COF identified in the ^{19}F NMR spectrum was not observed in the ^1H spectrum, but is likely coincident with the intense solvent signal. Although ^{79}Br and ^{81}Br NMR spectroscopy does not afford an unambiguous determination of the bromine-containing species in the absence of $J(^{79,81}Br-^{19}F)$ coupling, as a result of quadrupolar relaxation, ^{79}Br NMR spectroscopy established the presence of BrO_4^- (2482 ppm)[166] and the absence of Br^- (ca. 0 ppm), when referenced to infinitely dilute KBr(aq). The ^{19}F, ^1H and ^{79}Br NMR spectra may be accounted for the by the partial reaction of $BrO_3F_2^-$ with adventitious water to form BrO_4^- and HF (eq 7.13). The HF generated by this reaction

$$[N(CH_3)_4][BrO_3F_2] + H_2O \rightarrow [N(CH_3)_4][BrO_4] + 2HF \qquad (7.13)$$
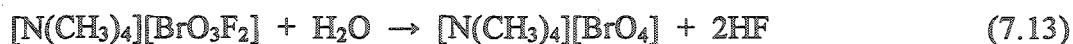
likely undergoes rapid fluoride ion exchange with the remaining $BrO_3F_2^-$ in solution (eq 7.14), accounting for the inability to observe $BrO_3F_2^-$ or BrO_3F in the ^{19}F NMR spectrum

$$HF + BrO_3F_2^- \rightleftharpoons BrO_3F + HF_2^- \qquad (7.14)$$

and the resonance at 10.4 ppm in the ^{1}H NMR spectrum, which is at lower chemical shift than that reported for HF_2^- (16.3 ppm).[466] The BrO_3F produced by this exchange mechanism is a more aggressive oxidizing agent than the $BrO_3F_2^-$ anion and likely reacts with CH_3CN to produce CH_3COF and NO_2Br (eq 7.15). The latter of these species was not observed but may undergo halide exchange with HF to produce the observed product, NO_2F (eq 7.16).

$$BrO_3F + CH_3CN \rightarrow CH_3COF + (NO_2Br) \qquad (7.15)$$

$$(NO_2Br) + HF \rightarrow HBr + NO_2F \qquad (7.16)$$
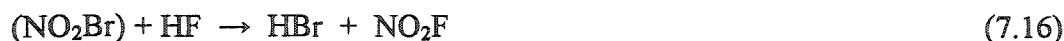
7.3 Computational Results

7.3.1. Geometries of BrO_3F, ClO_3F, $BrO_3F_2^-$, $ClO_3F_2^-$, and *fac/mer*-$BrO_3F_3^{2-}$

The energy-minimized gas-phase structures of BrO_3F, ClO_3F, $BrO_3F_2^-$, and $ClO_3F_2^-$, *fac*-$BrO_3F_3^{2-}$ and *mer*-$BrO_3F_3^{2-}$ were determined by use of the HF, MP2 and MPW1PW91 methods (Table 7.8). The geometries of the parent oxide fluorides, BrO_3F and ClO_3F, are not explicitly discussed, but were calculated so that the effects of fluoride ion coordination on the X-O and X-F (X = Cl, Br) bond lengths could be compared.

7.3.1.1. $BrO_3F_2^-$ and $ClO_3F_2^-$

The geometry of the $BrO_3F_2^-$ anion determined by X-ray diffraction (see section 7.2.2) exhibited only small distortions from D_{3h} symmetry, justifying the calculation of $BrO_3F_2^-$ and $ClO_3F_2^-$ under this constraint. The Br-O bond length, which has average values of 1.600(3) and 1.603(7) Å in the structures of $[N(CH_3)_4][BrO_3F_2]$ and $[NO]_2[BrO_3F_2][F]$, respectively, was overestimated by 0.03 to 0.04 Å by the MPW1PW91 (1.639 Å) method but was better determined by the HF (1.590 Å) and MP2 (1.601 Å) methods. The Br-O bond lengths were calculated to be 0.02 (MP2) to 0.04 Å (HF) longer than those calculated for BrO_3F, and similar to the differences obtained from

Table 7.8. Geometric Parameters of $BrO_3F_2^-$, $ClO_3F_2^-$, and $BrO_3F_3^{2-}$

	Bond/Angle[a]	HF[b,c]	MP2[b,c]	MPW1PW91[c,d]	Expt. (ave.)
BrO_3F[e]	Br-O	1.553	1.580	1.612	1.582(1)
	Br-F	1.703	1.809	1.806	1.708(3)
	O-Br-F	102.2	101.5	101.8	103.3(3)
	O-Br-O	115.6	116.2	116.0	114.9(3)
ClO_3F[f]	Cl-O	1.392	1.429	1.438	1.404(2)
	Cl-F	1.582	1.714	1.685	1.619(4)
	O-Cl-F	102.7	101.7	102.0	116.6(5)
	O-Cl-O	115.3	116.0	115.8	100.8(8)
$BrO_3F_2^-$[g]	Br-O	1.590	1.601	1.639	1.602(6)
	Br-F	1.806	1.896	1.905	1.861(16)
$ClO_3F_2^-$	Cl-O	1.431	1.447	1.465	
	Cl-F	1.760	1.911	1.881	
fac-$BrO_3F_3^2$	Br-O	1.632	1.648	1.684	
	Br-F	1.877	1.973	1.998	
	O-Br-O	102.2	102.6	102.4	
	O-Br-F$_{cis}$	88.8	88.5	88.5	
	F-Br-F	77.4	77.4	77.9	
mer-$BrO_3F_3^{2-}$	Br-O	1.619	1.650	1.676	
	Br-O'	1.643	1.641	1.688	
	Br-F	2.064	1.999	2.078	
	Br-F'	1.838	1.959	1.974	
	O'-Br-O	99.5	97.9	98.6	
	O'-Br-F	80.5	82.1	81.4	
	O'-Br-F'	89.4	89.3	89.4	
	O-Br-F'	93.7	94.8	93.8	
	F'-Br-F	86.3	85.2	86.2	

[a] The symmetry-equivalent oxygen and fluorine atoms in mer-$BrO_3F_3^{2-}$ are denoted by O' and F', respectively. [b] Calculations were performed using a 6-311G(d) basis set. [c] Bond lengths and bond angles are given in Å and degrees, respectively. [d] Calculations were performed using a DZVP basis set. [e] Gas phase experimental parameters are from ref 174. [f] Gas phase experimental parameters are from ref 467.

experiment (0.01 - 0.03 Å). The average Br-F bond length determined from the structure of $[NO]_2[BrO_3F_2][F]$ (1.86(2) Å) is intermediate with respect those calculated by use of the HF (1.806 Å), MP2 (1.896 Å) and MPW1PW91 (1.905 Å) methods, with no one method clearly outperforming the others. The smaller difference between the calculated Br-F bond lengths of BrO_3F and $BrO_3F_2^-$ (0.09 - 0.10 Å), when compared with the average experimental difference (0.15 Å), is attributed to the ON···F-BrO_3F contacts present in the solid state (Figure 7.3), which are expected to lengthen the Br-F bonds.

Although attempts to prepare $[N(CH_3)_4][ClO_3F_2]$ were unsuccessful, the anion is predicted to be thermodynamically stable with respect to dissociation to ClO_3F and F^- in the gas phase (see section 7.3.2). The weak fluoride ion acceptor properties of ClO_3F are reflected in the Cl-F bond lengths of the anion, which were calculated to be *ca.* 0.19 Å longer than that for ClO_3F, contrasting with the smaller difference (*ca.* 0.10 Å) found for the bromine analogues. Additional elongation and destabilization of the Cl-F bonds of $ClO_3F_2^-$ relative to ClO_3F would be expected in the solid state, where contacts between the fluorine ligands and counter cation are likely, and may account, in part, for the inability to prepare salts of this anion. The difference between the Cl-O bond lengths calculated for $ClO_3F_2^-$ and ClO_3F is *ca.* 0.03 Å, and is comparable with the bond length difference calculated for $BrO_3F_2^-$ and BrO_3F.

7.3.1.2. *fac*-$BrO_3F_3^-$ and *mer*-$BrO_3F_3^-$

The energy-minimized geometries of *fac*-$BrO_3F_3^-$ and *mer*-$BrO_3F_3^-$ exhibit local minima, however, both isomers are predicted to be thermodynamically unstable towards the fluoride ion loss (see section 7.3.2). The more stable facial isomer (C_{3v} symmetry) is predicted to have Br-O bond lengths that are *ca.* 0.04 Å longer than those calculated for $BrO_3F_2^-$. The higher Br(VII) coordination number and increased net negative charge of the dianion has a greater effect on the Br-F bond lengths, which are predicted to be 0.07

to 0.09 Å longer for *fac*-$BrO_3F_3^{2-}$ than for $BrO_3F_2^-$, reflecting the instability of the dianion towards fluoride ion loss. Despite significant distortions from 90°, the O-Br-O (102.2 - 102.6°), O-Br-F (88.5 - 88.6°) and F-Br-F (77.4 - 77.9°) bond angles of *fac*-$BrO_3F_3^{2-}$ are relatively insensitive to the computational method used, suggesting that they are constrained by ligand-ligand close-packing effects.

The *mer*-$BrO_3F_3^{2-}$ dianion possesses C_{2v} symmetry with two geometrically equivalent oxygen (O') and fluorine (F') atoms, which are perpendicular to each other, and unique fluorine (F) and oxygen atoms (O), which lie trans to each other. The Br-O and Br-O' bond lengths are similar for *mer*-$BrO_3F_3^{2-}$, and are *ca.* 0.04 Å longer than those calculated for the $BrO_3F_2^-$ anion. As expected, the difference between the Br-F bond lengths of $BrO_3F_2^-$ and *mer*-$BrO_3F_3^{2-}$ is greater than the difference between the Br-O bond lengths, reflecting the instability of *mer*-$BrO_3F_3^{2-}$ towards fluoride ion loss. In contrast to the *fac*-isomer, where the C_{3v} symmetry constraint has the effect of elongating the Br-F bond lengths equally with respect to those of $BrO_3F_2^-$, the unique Br-F bond of the *mer*-isomer is predicted to be 0.04 to 0.23 Å longer than the Br-F' bond lengths, suggesting loss of this ligand as fluoride ion is preferred over the loss of one of the F' ligands. Like *fac*-$BrO_3F_3^{2-}$, the bond angles of *mer*-$BrO_3F_3^{2-}$ are distorted from 90°, but to a lesser extent. The location of the three oxygen atoms in the same molecular plane reduces the number of *cis*- O-Br-O bond angles from three in the *fac*-isomer to two in the *mer*-isomer, which is reflected by the more open O-Br-O' bond angle (97.9 - 99.5°). Likewise, the F-Br-F' bond angles are more closed in the *mer*-isomer (85.2 - 86.3°) than they are in the *fac*-isomer.

7.3.2. Enthalpies of Fluoride Ion Attachment to BrO₃F and ClO₃F

The gas-phase fluoride ion affinities of 170 main-group fluorides and oxide fluorides have recently been calculated by the near-local density functional (NLDF)

method,[46] expanding upon the fluoride ion affinities of 31 species calculated earlier by the MP2/PDZ method.[48] In the present study, the enthalpies of fluoride ion attachment for BrO_3F, $BrO_3F_2^-$ and ClO_3F have been determined by the G2 method (Table 7.9), which includes configuration interaction energy corrections (MP4, QCISD). The validity of this method was verified by the determination of the enthalpies of fluoride ion attachment for HF, COF_2, SO_2, BF_3 and AlF_3, for which experimental values are known and which have been used as benchmarks in the earlier computational studies (Table 7.9). The enthalpies of fluoride ion attachment calculated for the test species by the use of the G2 method were in good agreement with those obtained by the CCST(T) method, and the close correlation of both methods to the experimental values implies that the values obtained for BrO_3F, $BrO_3F_2^-$ and ClO_3F are also reliable.

Perbromyl fluoride and ClO_3F are both predicted to exhibit fluoride ion acceptor properties in the gas-phase, however, the enthalpy of fluoride ion attachment is significantly more exothermic for BrO_3F (-261.1 kJ mol^{-1}) than it was for ClO_3F (-132.3 kJ mol^{-1}). The enthalpy of fluoride ion attachment to BrO_3F, determined in the present study, is 11% smaller than that reported earlier (-292 kJ mol^{-1}),[46] and is bracketed by the values calculated for $XeOF_4$ (-267 kJ mol^{-1}), TeF_6 (-257 kJ mol^{-1}), and XeF_4 (-239 kJ mol^{-1}).[46] Considering the experimentally established stabilities of $XeOF_5^-$,[468] TeF_7^- [421] and XeF_5^- [473] it is not surprising that salts containing the $BrO_3F_2^-$ anion have proven to be isolable.

The enthalpy of fluoride ion attachment to ClO_3F determined by the G2 method is also lower than that obtained by the NLDF method (180 kJ mol^{-1}).[46] The present study indicated that the fluoride ion acceptor strength of ClO_3F is intermediate with respect to those of PF_3 (-187.9 kJ mol^{-1}), HF (-154.0 kJ mol^{-1}), NO_2F (-80.3 kJ mol^{-1}) and NOF (-72.8 kJ mol^{-1}) in the gas phase.[48] Although salts of PF_4^-,[474,475] and HF_2^- [476] are known,

Table 7.9. Calculated Enthalpies of Fluoride Ion Attachment

Reaction[a]	Calculated ΔH°_{react} (kJ mol^{-1})[b]				Expt. ΔH°_{react} (kJ mol^{-1})
	G2	MP2/PDZ[c]	NLDFT[d]	CCSD(T)/CBS[d]	
$HF + F^- \rightarrow HF_2^-$	-188.7	-154.0	-181.2	-188.3	-164(4)[e]
$BF_3 + F^- \rightarrow BF_4^-$	-341.4	-347.7	-324.7	-341.0	-331(8)[f]
$COF_2 + F^- \rightarrow COF_3^-$	-210.5	-208.8	-208.8	-211.3	-208.8[c]
$AlF_3 + F^- \rightarrow AlF_4^-$	-479.7	-481.2	-461.9	-485.3	-488(8)[g]
$SO_2 + F^- \rightarrow SO_2F^-$	-218.5		-208.8	-224.3	-225[h]
$BrO_3F + F^- \rightarrow BrO_3F_2^-$ [c]	-261.1		-292.5		
$BrO_3F_2^- + F^- \rightarrow mer\text{-}BrO_3F_3^{2-}$	367.8				
$BrO_3F_2^- + F^- \rightarrow fac\text{-}BrO_3F_3^{2-}$	362.1				
$ClO_3F^a + F^- \rightarrow ClO_3F_2^-$	-132.3		-179.9		

[a] The calculated geometries were constrained to the point groups predicted by the VSEPR model. [b] Enthalpies of reaction were determined by use of the absolute enthalpies of formation calculated for the gas phase products and reagents. [c] From ref 48. [d] From ref 46. [e] From ref 469. [f] From ref 470. [g] From ref 471. [h] From ref 472.

those of $NO_2F_2^-$,[477] and NOF_2^- remain unknown. The ranking of $ClO_3F_2^-$ within this series is consistent with the minimum enthalpy of fluoride ion attachment (-126 to -146 kJ mol^{-1})[46] generally required for the formation of a stable salt, and the inability to prepare $[N(CH_3)_4][ClO_3F_2]$.

To date, the only known hexacoordinate compounds of bromine are BrF_6^- and BrF_6^+. Given the favourable enthalpy of fluoride ion attachment of BrO_3F and the ability to prepare several salts containing the $BrO_3F_2^-$ anion, the stabilities of the mer-$BrO_3F_3^{2-}$ and fac-$BrO_3F_3^{2-}$ dianions were also calculated (eq 7.17). The enthalpies of fluoride ion

$$BrO_3F_2^- + F^- \rightarrow mer/fac\text{-}BrO_3F_3^{2-} \qquad (7.17)$$

attachment to $BrO_3F_2^-$ are endothermic for the formation of fac- (362.1 kJ mol^{-1}) and mer-$BrO_3F_3^{2-}$ (366.8 kJ mol^{-1}) and consistent with the inability to prepare these dianions by reaction of $[N(CH_3)_4][F]$ with $[N(CH_3)_4][BrO_3F_2]$. Interestingly, the stabilities of both isomers were similar, with fac-$BrO_3F_3^{2-}$ being only 4.7 kJ mol^{-1} more stable than mer-$BrO_3F_3^{2-}$.

7.3.3. Vibrational Frequencies of $BrO_3F_2^-$ and $ClO_3F_2^-$

The vibrational spectra of $BrO_3F_2^-$ (Table 7.10) and $ClO_3F_2^-$ (Table 7.11) were calculated by use of the HF, MP2 and MPW1PW91 methods, and assisted in the the assignment of the experimental spectra of the $BrO_3F_2^-$ salts (see section 7.2.3).

Although comparisons among the experimental and calculated Br-O and Br-F bond lengths of BrO_3F and $BrO_3F_2^-$ did not reveal any anomalous trends, the HF and MP2 methods exhibit irregular behaviour with respect to their Br-O stretching frequencies. For the HF method, the unscaled symmetric and asymmetric BrO_3 stretching frequencies correlate well with the experimental frequencies, contrasting with the frequencies of remaining modes which are overestimated even after the application of a 0.8953 scaling factor.[323] For the MP2 method, the symmetric and asymmetric BrO_3

Table 7.10. Calculated Vibrational Frequencies and Intensities of the $BrO_3F_2^-$ Anion

Symmetry and Mode Description[a]		Calculated Frequencies and Intensities[b]				Experimental[b,c]
		HF[b]	HF (scaled)[d]	MP2	MPW1PW91	
$v_1(A_1')$	sym. BrO_3 stretch	819(100)[0]	733	913(100)[0]	788(100)[0]	802(100)[w]
$v_2(A_1')$	sym. BrF_2 stretch	539(37)[0]	482	437(74)[0]	435(45)[0]	433(19)
$v_3(A_2'')$	asym. BrF_2 stretch	613(0)[455]	548	555(0)[382]	529(0)[389]	504[m]
$v_4(A_2'')$	o.o.p. BrO_3 wag	543(0)[106]	486	489(0)[23]	447(0)[17]	468[m]
$v_5(E')$	asym. BrO_3 stretch	926(28)[240]	829	1011(20)[434]	883(32)[304]	896(8)[s]
$v_6(E')$	sym. O-Br-O bend	459(28)[144]	411	415(38)[102]	378(26)[76]	383(23)
$v_7(E')$	sym. O-Br-F bend	258(6)[<1]	231	223(6)[<1]	207(6)[<1]	229(13)
$v_8(E'')$	asym. O-Br-F bend	475(22)[0]	425	417(36)[0]	384(24)[0]	414(27)

[a] "Out of plane" is denoted by o.o.p.. [b] Frequencies are given in cm^{-1}. Raman intensities are given in parentheses, and are scaled to the most intense peak, which is assigned a value of 100. Infrared intensities are given in brackets, and are given in km mol^{-1} for the calculated spectra. The intensities of the experimental infrared bands are denoted by weak (w), medium (m) or strong (s). [c] The Raman-active frequencies are given for α-[Cs][BrO$_3$F$_2$] at -163 °C. The $v_3(A_2'')$ and $v_4(A_2'')$ frequencies were obtained from the infrared spectrum of β-[Cs][BrO$_3$F$_2$] at ambient temperature. [d] Values were scaled by 0.8953 as recommended in ref 323.

Table 7.11. Calculated Vibrational Frequencies and Intensities of the $ClO_3F_2^-$ Anion

Symmetry and Mode Description[a]		Calculated Frequencies and Intensities[b]			
		HF[b]	HF (scaled)[c]	MP2	MPW1PW91
$\nu_1(A_1')$	sym. ClO_3 stretch	899(100)[0]	805	972(100)[0]	862(100)[0]
$\nu_2(A_1')$	sym. ClF_2 stretch	412(32)[0]	369	368(91)[0]	383(38)[0]
$\nu_3(A_2'')$	o.o.p. ClO_3 wag	735(0)[370]	658	649(0)[482]	625(0)[415]
$\nu_4(A_2'')$	asym. ClF_2 stretch	530(0)[656]	475	486(0)[202]	474(0)[157]
$\nu_5(E')$	asym. ClO_3 stretch	1146(8)[678]	1026	1273(13)[740]	1137(15)[286]
$\nu_6(E')$	sym. O-Cl-O bend	513(30)[94]	458	529(33)[60]	485(15)[22]
$\nu_7(E')$	sym. O-Cl-F bend	307(5)[2]	274	248(2)[6]	235(2)[1]
$\nu_8(E'')$	asym. O-Cl-F bend	574(19)[0]	514	457(24)[0]	435(10)[0]

[a] "Out of plane" is denoted by o.o.p.. [b] Frequencies are given in cm^{-1}. Raman intensities are given in parentheses, and are scaled to the most intense peak, which is assigned a value of 100. The infrared intensities are given in brackets, and are in km mol^{-1}. [c] Values were scaled by 0.8953 as recommended in ref 323.

stretching frequencies are overestimated by *ca.* 110 cm^{-1}, contrasting with the reasonable agreements obtained for the remaining vibrational frequencies when no scalings are applied. Although $ClO_3F_2^-$, BrO_2F_3, $BrO_2F_2^+$ and $BrO_2F_4^-$ remain unknown, a comparison of the Br-O stretching frequencies calculated by use of the HF and MP2 methods reveals that these trends are common among the oxide fluorides of chlorine (*vide infra*) and bromine (see section B.3.2). Interestingly, these anomalies are not encountered for the XO_3^+ and XO_2^+ (X = Cl, Br) cations (see section 8.3.3), suggesting they are only manifested among the oxide fluoride species.

In contrast to the irregular results obtained by the HF and MP2 methods, the MPW1PW91 method reproduced the vibrational frequencies of the $BrO_3F_2^-$ anion with reasonable accuracy. The errors in the MPW1PW91 frequencies ranged from -30 cm^{-1} for $v_8(E'')$ to +25 cm^{-1} for $v_3(A_2'')$ with an average error of only -10 cm^{-1}. In addition to providing accurate vibrational frequencies, the relative Raman and infrared intensities calculated by use of the MPW1PW91 method were also in qualitative agreement with those observed for α-[Cs][BrO$_3$F$_2$] and β-[Cs][BrO$_3$F$_2$], respectively.

Although the calculated vibrational frequencies of $ClO_3F_2^-$ cannot be compared with experimental values, similar trends are noted among the HF, MP2 and MPW1PW91 methods for the $BrO_3F_2^-$ and $ClO_3F_2^-$ anions. As a consequence of the inaccurate symmetric ($v_1(A_1')$) and asymmetric ($v_5(E')$) ClO_3 stretching frequencies anticipated for the HF and MP2 methods (*vide supra*), the MPW1PW91 method is believed to provide the most reliable vibrational frequencies for the $ClO_3F_2^-$ anion and is exclusively referred to in the ensuing discussion. The symmetric (862 cm^{-1}) and asymmetric (1137 cm^{-1}) Cl-O stretching frequencies occur at higher frequencies than the Br-O stretching frequencies, which is consistent with both the higher force constants associated with the Cl-O stretches (see section 7.3.4) and the smaller reduced masses associated with the

chlorine species. This contrasts with the symmetric and asymmetric ClF_2 stretching frequencies, which have lower frequencies than their BrF_2 counterparts. The low ClF_2 stretching frequencies are inconsistent with the shorter bond lengths and lower reduced mass, but are accounted for by the low Cl-F stretching force constant (see section 7.3.4), which reflects the weaker fluoride ion acceptor properties of ClO_3F when compared with those of BrO_3F (see section 7.3.2).

7.3.4. Force Constants for $BrO_3F_2^-$, $ClO_3F_2^-$, XeO_3F_2 and OsO_3F_2

Internal force constants have been previously determined for XeO_3F_2[433,478-480] and OsO_3F_2[479-481] from their experimental vibrational spectra and estimated bond lengths by use of the Wilson FG-matrix method.[482] The acquisition of the vibrational spectra and X-ray crystal structure of the $BrO_3F_2^-$ anion have permitted the determination of the internal force constants for this anion in the present work by the same method, allowing comparisons of force constants to be made among these isostructural oxide fluorides. To complement these studies, and to allow for comparisons with the unknown $ClO_3F_2^-$ anion, the symmetry force constants of $BrO_3F_2^-$, $ClO_3F_2^-$, XeO_3F_2 and OsO_3F_2 have been calculated by the B-matrix method,[483] which provides a fully determined force field, including the off-diagonal components, by use of the second derivative matrices determined during the optimization (MPW1PW91/SVWN) of these species.

7.3.4.1. Internal Force Constants Derived From General Valence Force Field Analyses

The internal force constants and potential energy distributions of $BrO_3F_2^-$, XeO_3F_2, and OsO_3F_2 determined by the FG-matrix method are summarized in Tables 7.12, 7.13 and 7.14, respectively. With the exception of OsO_3F_2, for which $v_2(A_1')$ was underestimated by 11 cm^{-1} and $v_3(A_2'')$ was overestimated by 9 cm^{-1}, the fits between the experimental vibrational frequencies and those obtained from the optimized force

Table 7.12. Force Constants of $BrO_3F_2^-$ Derived From General Valence Force Field (NCT) and B-Matrix Analyses

	General Valence Force Field Analysis					B-Matrix Analysis		
Mode	Freq.[a]		P.E.D.[b,c]	Internal Force Constants[d]	Freq.[a]	P.E.D.[b,f]	Symmetry Force Constants[c,d,f]	
	Expt.	Fit			DFT[e]			
$v_5(E')$	896	896	$100f_D$	f_D 5.86	887	$66F_{55} + 21F_{66} + 13F_{77}$	$F_{11} = f_D + 2f_{DD}$	5.83
$v_1(A_1')$	802	802	$97f_D + 3f_{DD}$	f_d 2.09	787	$95F_{11} + 5F_{22}$	$F_{22} = f_d + 2f_{dd}$	2.09
$v_3(A_2'')$	504	504	$80f_d + 20f_\beta$	f_α 0.64	530	$66F_{33} + 34F_{44}$	$F_{33} = f_d - f_{dd}$	1.65
$v_4(A_2'')$	468	468	$63f_d + 14f_{\beta\beta} + 8f_d$	f_β 1.55	430	$17F_{33} + 83F_{44}$	$F_{12} = 6^{\frac{1}{2}}f_{Dd}$	0.28
			$+ 8f_{d\beta} + 7f_{d\beta}'$	f_{DD} 0.10			$F_{44} = f_\beta - f_{\beta\beta} - 2f'_{\beta\beta} - 2f''_{\beta\beta}$	2.19
$v_2(A_1')$	433	433	$100f_d$	f_{Dd} 0.00	423	$94F_{22} + 6F_{11}$	$F_{34} = (3(f_{d\beta} - f'_{d\beta}))^{\frac{1}{2}}$	0.41
$v_8(E'')$	409	409	$100f_\beta$	$f_{D\alpha}$ 0.04	361	$100F_{88}$	$F_{55} = f_D - f_{DD}$	5.64
$v_6(E')$	383	383	$54f_\alpha + 20f_\beta$	$f_{D\beta}$ 0.04	357	$4F_{55} + 63F_{66} + 32F_{77}$	$F_{66} = f_\alpha - f_{\alpha\alpha}$	0.59
			$+ 15f_{\alpha\beta} + 11f_{\alpha\alpha}$	$f_{d\alpha}$ 0.00			$F_{77} = f_\beta + f_{\beta\beta} - f'_{\beta\beta} - f''_{\beta\beta}$	1.36
$v_7(E')$	229	229	$72f_\beta + 24f_\alpha + 4f_{\alpha\alpha}$	$f_{d\beta}$ 0.18	193	$2F_{55} + 56F_{66} + 42F_{77}$	$F_{56} = f'_{D\alpha} - f_{D\alpha}$	0.00
							$F_{57} = 2^{\frac{1}{2}}(f_{D\beta} - f'_{D\beta})$	-0.01
							$F_{67} = -2^{\frac{1}{2}}(f_{\alpha\beta} - f'_{\alpha\beta})$	0.00
							$F_{88} = f_\beta - f_{\beta\beta} - f'_{\beta\beta} - f''_{\beta\beta}$	1.14

[a] Frequencies are given in cm^{-1}. [b] Potential energy distributions (P.E.D.) are given in percent. [c] f_D, and f_d denote Br-O and Br-F stretches, respectively. f_α and f_β denote O-Br-O and O-Br-F bending motions, respectively. f_{xy} denotes interaction force constants of f_x and f_y, where x and y are D, d, α, or β. [d] Force constants for bond stretches and bends are given in mdyne $Å^{-1}$ and mdyne $Å$ rad^{-2}, respectively. [e] The vibrational frequencies, and second derivative matrix used for the determination of the symmetry force constants were calculated by use of the SVWN method in conjunction with the DZVP basis set. The energy minimized Br-F and Br-O bond lengths were 1.916 and 1.646 Å, respectively. [f] The force constants, F_{ii} ($i = 1 \cdots 8$), correspond to the normal modes, v_i. The force constants F_{ij} correspond to the off-diagonal interactions between v_i and v_j, where $i \neq j$.

Table 7.13. Force Constants of XeO₃F₂ Derived From General Valence Force Field (NCT) and B-Matrix Analyses

| Mode | General Valence Force Field Analysis | | | | | | | | | B-Matrix Analysis | | | |
| | Freq.[a,b] | | P.E.D.[c,d] | Internal Force Constants[d,e] | | | | | | Freq.[a] | P.E.D.[c,e] | Symmetry Force Constants[d,e] | |
	Expt.	Fit			f	g	h	i	j	DFT[k]			
$v_5(E')$	896	896	$98f_D$	f_D	6.27	6.24	6.20	6.33	6.32	845	$76F_{55}+15F_{66}$ $+9F_{77}$	$F_{11}=f_D+2f_{DD}$	5.45
				f_d	3.66	3.11	3.05	3.57	3.57			$F_{22}=f_d+2f_{dd}$	2.92
$v_1(A_1')$	807	807	$100f_D$	f_a	0.53			0.37		761	$97F_{11}+3F_{22}$	$F_{12}=6^{\frac{1}{2}}f_{Dd}$	-0.09
$v_3(A_2'')$	632	633	$100f_d$	f_β	1.30			0.07		595	$79F_{33}+21F_{44}$	$F_{33}=f_d-f_{dd}$	1.28
$v_2(A_1')$	567	565	$100f_d$	$-f_{DD}$	0.06	0.15	0.03	0.10	0.09	510	$96F_{22}+4F_{11}$	$F_{44}=f_\beta-f_{\beta\beta}-2f'_{\beta\beta}-2f''_{\beta\beta}$	3.04
$v_4(A_2'')$	375	375	$85f_\beta+15f_{\beta\beta}$	f_{Dd}	0.00	0.39	0.00		0.00	326	$8F_{33}+92F_{44}$	$F_{34}=(3(f_{d\beta}-f'_{d\beta}))^{\frac{1}{2}}$	0.11
$v_8(E'')$	361	361	$100f_\beta$	f_{Da}	0.01			0.04		291	$100F_{88}$	$F_{55}=f_D-f_{DD}$	5.64
$v_6(E')$	316	316	$48f_a+24f_\beta$	$f_{D\beta}$	0.00			0.01		276	$3F_{55}+61F_{66}$ $+36F_{77}$	$F_{66}=f_a-f_{aa}$	0.43
			$21f_{a\beta}+6f_{aa}$	f_{da}	0.00			0.04				$F_{77}=f_\beta+f_{\beta\beta}-f'_{\beta\beta}-f''_{\beta\beta}$	1.10
$v_7(E')$	190	190	$64f_\beta+32f_a$	$f_{d\beta}$	0.15					157	$61F_{66}+39F_{77}$	$F_{56}=f'_{Da}-f_{Da}$	0.00
			$+4f_{aa}$									$F_{57}=2^{\frac{1}{2}}(f_{D\beta}-f'_{D\beta})$	-0.04
												$F_{67}=-2^{\frac{1}{2}}(f_{a\beta}-f'_{a\beta})$	0.00
												$F_{88}=f_\beta-f_{\beta\beta}-f'_{\beta\beta}-f''_\beta$	0.85

[a] Frequencies are given in cm^{-1}. [b] Experimental values are from ref 433. [c] Potential energy distributions (P.E.D.) are given in percent. [d] Force constants for bond stretches and bends are given in mdyne $Å^{-1}$ and mdyne Å rad^{-2}, respectively. f_D, f_d, f_a and f_β denote Xe-O and Xe-F stretches and O-Xe-O and O-Xe-F bending motions, respectively. f_{xy} denotes interaction force constants of f_x and f_y, where x and y are D, d, a, or β. [e] The force constants, F_{ii} ($i = 1 \cdots 8$), corresponds to the normal modes, v_i. The force constants F_{ij} correspond to the off-diagonal interactions between v_i and v_j, where $i \neq j$. [f] This work. [g] From ref 433. [h] From ref 478. [i] From ref 479. [j] From ref 480. [k] The vibrational frequencies (cm^{-1}), and second derivative matrix used for the determination of the symmetry force constants were calculated by use of the SVWN method in conjunction with the DZVP basis set. The energy minimized Xe-F and Xe-O bond lengths were 1.983 and 1.802 Å, respectively.

Table 7.14. Force Constants of OsO_3F_2 Derived From General Valence Force Field (NCT) and B-Matrix Analyses

	General Valence Force Field Analysis								B-Matrix Analysis			
Mode	Freq.[a,b]		P.E.D.[c]	Internal Force Constants[d]					Freq.[a]	P.E.D.[c,e]	Symmetry Force Constants[d,e]	
	Expt.	Fit			I	g	h	i	LDF[j]			
$v_1(A_1')$	947	943	$90f_D + 9f_{DD}$	f_D	7.57	6.52	7.67	7.64	965	$93F_{11} + 7F_{22}$	$F_{11} = f_D + 2f_{DD}$	8.73
$v_5(E')$	929	930	$100f_D$	f_d	4.09	3.25	4.11	2.87	957	$80F_{55} + 12F_{66} + 8F_{77}$	$F_{22} = f_d + 2f_{dd}$	4.30
$v_3(A_2'')$	646	655	$100f_d$	f_a	0.49	0.12	0.35		655	$95F_{33} + 5F_{44}$	$F_{33} = f_d - f_{dd}$	0.85
$v_2(A_1')$	619	608	$100f_d$	f_β	1.10	-0.03	0.08		616	$9F_{11} + 91F_{22}$	$F_{12} = 6^{\frac{1}{2}}f_{Dd}$	0.49
$v_8(E'')$	348	348	$100f_\beta$	f_{DD}	0.39	0.42	0.37	0.40	353	$100F_{88}$	$F_{44} = f_\beta - f_{\beta\beta} - 2f'_{\beta\beta} - 2f''_{\beta\beta}$	4.13
$v_6(E')$	317	317	$84f_\beta + 8f_d$	f_{Dd}	0.00	0.67	0.00	0.00	312	$3F_{55} + 68F_{66} + 29F_{77}$	$F_{34} = (3(f_{d\beta} - f'_{d\beta}))^{\frac{1}{2}}$	0.61
			$+ 8f_{\beta\beta}$	f_{Da}	0.02		0.06				$F_{55} = f_D - f_{DD}$	7.63
$v_4(A_2'')$	258	258	$62f_\beta + 33f_a$	$f_{D\beta}$	0.02		0.03		261	$12F_{33} + 88F_{44}$	$F_{66} = f_a - f_{aa}$	0.64
			$+ 5f_{a\beta}$	f_{da}	0.00		0.01				$F_{77} = f_\beta + f_{\beta\beta} - f'_{\beta\beta} - f''_{\beta\beta}$	1.18
$v_7(E')$	206	206	$63f_\beta + 37f_a$	$f_{d\beta}$	0.21		0.14		189	$3F_{55} + 49F_{66} + 48F_{77}$	$F_{56} = f'_{Da} - f_{Da}$	0.00
											$F_{57} = 2^{\frac{1}{2}}(f_{D\beta} - f'_{D\beta})$	-0.08
											$F_{67} = -2^{\frac{1}{2}}(f_{a\beta} - f'_{a\beta})$	0.00
											$F_{88} = f_\beta - f_{\beta\beta} - f'_{\beta\beta} - f''_{\beta\beta}$	1.14

[a] Frequencies are given in cm^{-1}. [b] Experimental values are from ref 431. [c] Potential energy distributions (P.E.D.) are given in percent. [d] Force constants for bond stretches and bends are given in mdyne $Å^{-1}$ and mdyne $Å$ rad^{-2}, respectively. f_D, f_d, f_a and f_β denote Os-O and Os-F stretches and O-Os-O and O-Os-F bending motions, respectively. f_{xy} denotes interaction force constants of f_x and f_y, where x and y are D, d, a, or β. [e] The force constants, F_{ii} ($i = 1 \cdots 8$), corresponds to the normal modes, v_i. The force constants F_{ij} correspond to the off diagonal interactions between v_i and v_j, where $i \neq j$. [f] This work. [g] From ref 481. [h] From ref 479. [i] From ref 480. [j] The vibrational frequencies (cm^{-1}), and second derivative matrix used for the determination of the symmetry force constants were calculated by use of the SVWN method in conjunction with the DZVP basis set. The energy minimized Os-F and Os-O bond lengths were 1.897 and 1.717 $Å$, respectively.

constants were within ± 2 cm^{-1}. The Xe-O and Os-O stretching force constants (f_D) obtained in this work (6.27 and 7.57 mdyne Å^{-1}, respectively) are in good agreement with those reported earlier for XeO$_3$F$_2$ (6.20 - 6.33 mdyne Å^{-1})[478-480] and OsO$_3$F$_2$ (6.52 - 7.67 mdyne Å^{-1}),[479-481] with the exception of one low value reported for OsO$_3$F$_2$.[481] The f_D-value is lower for BrO$_3$F$_2^-$ (5.86 mdyne Å^{-1}) than for XeO$_3$F$_2$, and may be attributed to the higher formal oxidation state of xenon, which reduces the polarity of it's A-O bonds. Although net charge and oxidation state effects may be used to account for the higher f_D-value determined for OsO$_3$F$_2$ when compared with that of BrO$_3$F$_2^-$, f_D is significantly larger for OsO$_3$F$_2$ than for XeO$_3$F$_2$ despite the neutral charges and formal +8 oxidation states of the central atoms in both species. The difference likely reflects the relative degrees of dπ-pπ bonding between the central atom and the oxygen ligands, which is expected to be significant for d^0 species, but negligible for the main-group species.[484] Stronger A-O bonds for OsO$_3$F$_2$ are also supported by the Os-O bond length (1.717 Å), which is calculated to be $ca.$ 0.09 Å shorter than the Xe-O bond length of XeO$_3$F$_2$ (1.802 Å) despite xenon being from period five and osmium being from period six.

The Xe-F and Os-F stretching force constants (f_d) obtained for XeO$_3$F$_2$ (3.66 mdyne Å^{-1}) and OsO$_3$F$_2$ (4.09 mdyne Å^{-1}) are in good agreement with the most recently reported values determined by the FG-matrix method for XeO$_3$F$_2$ (3.57 mdyne Å^{-1})[479,480] and OsO$_3$F$_2$ (4.11 mdyne Å^{-1}),[479] but are greater than those reported in earlier studies.[480,481] The trends among the f_d-values for BrO$_3$F$_2^-$ (2.09 mdyne Å^{-1}), XeO$_3$F$_2$ and OsO$_3$F$_2$ are similar to those noted for f_D, and may also be attributed to net charge effects, formal oxidation state of the central atom and relative degrees of dπ-pπ bonding. The smaller difference between f_d-values of XeO$_3$F$_2$ and OsO$_3$F$_2$ (0.43 mdyne Å^{-1}) when compared with the difference in f_D-values (1.30 mdyne Å^{-1}) is consistent with

significantly lower Os-F $d\pi$-$p\pi$ bonding interaction as is expected from the reluctance of fluorine to form multiple bonds.

Considering that bending force constants are typically an order of magnitude less than stretching force constants, the O-A-F bending force constants, f_β, of $BrO_3F_2^-$ (1.55 mdyne Å rad^{-2}), XeO_3F_2 (1.30 mdyne Å rad^{-2}) and OsO_3F_2 (1.10 mdyne Å rad^{-2}) are relatively large. The repulsive interligand O···F interactions in these species may account, in part, for the magnitudes of these force constants, but the observation that f_β is greater for XeO_3F_2 than it is for OsO_3F_2, despite the shorter bond lengths and ligand-ligand contact distances calculated for OsO_3F_2, implies that other factors are involved. The observation that f_β decreases as the principal quantum number of the central element increases over the series suggests that f_β is correlated with the diffuseness of the valence orbitals. Similar, although less pronounced, trends occur for the O-A-O bending force constants, F_α, of $BrO_3F_2^-$ (0.64 mdyne Å rad^{-2}), XeO_3F_2 (0.53 mdyne Å rad^{-2}) and OsO_3F_2 (0.49 mdyne Å rad^{-2}), whose lower values may be attributed to the large O-A-O bond angles (120°) that give rise to minimal interligand O···O interactions.

7.3.4.2. Symmetry Force Constants Derived From B-Matrix Analyses

The unscaled symmetry force constants and potential energy distributions of $BrO_3F_2^-$, XeO_3F_2, OsO_3F_2 and the unknown $ClO_3F_2^-$ anion determined by the B-matrix method are summarized in Tables 7.12, 7.13, 7.14 and 7.15, respectively. The relationships between the symmetry force constants and the internal force constants of trigonal bipyramidal molecules have been derived earlier[485] and are also summarized in these tables. A complete comparison of the force constants obtained by the two methods is not possible because the FG-matrix method does not take into account all of the off-diagonal terms, however, the values of F_{11} and F_{55} obtained for $BrO_3F_2^-$, XeO_3F_2 and OsO_3F_2 are in reasonable agreement for both methods.

Table 7.15. Force Constants of $ClO_3F_2^-$ Derived from B-Matrix Analysis

Mode	Freq.[a]	P.E.D.[b]	Symmetry Force Constants[c]	
$\nu_5(E')$	1133	$57F_{55} + 27F_{66} + 16F_{77}$	$F_{11} = f_D + 2f_{DD}$	6.98
$\nu_1(A_1')$	862	$94F_{11} + 6F_{22}$	$F_{22} = f_d + 2f_{dd}$	1.68
$\nu_4(A_2'')$	621	$35F_{33} + 65F_{44}$	$F_{12} = 6^{\frac{1}{2}}f_{Dd}$	0.43
$\nu_6(E')$	484	$9F_{55} + 65F_{66} + 26F_{77}$	$F_{33} = f_d - f_{dd}$	2.04
$\nu_3(A_2'')$	474	$91F_{33} + 9F_{44}$	$F_{44} = f_\beta - f_{\beta\beta} - 2f'_{\beta\beta} - 2f''_{\beta\beta}$	1.73
$\nu_8(E'')$	434	$100F_{88}$	$F_{34} = (3(f_{d\beta} - f'_{d\beta}))^{\frac{1}{2}}$	0.78
$\nu_2(A_1')$	383	$7F_{11} + 93F_{22}$	$F_{55} = f_D - f_{DD}$	6.97
$\nu_7(E')$	235	$51F_{66} + 49F_{77}$	$F_{66} = f_\alpha - f_{\alpha\alpha}$	0.85
			$F_{56} = f'_{D\alpha} - f_{D\alpha}$	0.00
			$F_{57} = 2^{\frac{1}{2}}(f_{D\beta} - f'_{D\beta})$	-0.08
			$F_{67} = -2^{\frac{1}{2}}(f_{\alpha\beta} - f'_{\alpha\beta})$	0.00
			$F_{77} = f_\beta + f_{\beta\beta} - f'_{\beta\beta} - f''_{\beta\beta}$	1.57
			$F_{88} = f_\beta - f_{\beta\beta} - f'_{\beta\beta} - f''_{\beta\beta}$	1.40

[a] Frequencies are given in cm^{-1}. The vibrational frequencies, and second derivative matrix used for the determination of the symmetry force constants were calculated by use of the SVWN method in conjunction with the DZVP basis set. The energy-minimized Cl-F and Cl-O bond lengths were 1.878 and 1.477 Å, respectively. [b] Potential energy distributions (P.E.D) are given in percent. [c] Force constants for bond stretches and bends are given in mdyne $Å^{-1}$ and mdyne Å rad^{-2}, respectively. f_D, and f_d denote Cl-O and Cl-F stretches, respectively. f_α and f_β denote O-Cl-O and O-Cl-F bending motions, respectively. f_{xy} denotes interaction force constants of f_x and f_y, where x and y are D, d, α, or β. Force constants for bond stretches are given in mdyne $Å^{-1}$. The force constants, F_{ii} ($i = 1 \cdots 8$), correspond to the normal modes ν_i. The force constants F_{ij} correspond to the off diagonal interactions between ν_i and ν_j, where $i \neq j$.

The potential energy distributions determined from the analyses of $ClO_3F_2^-$, $BrO_3F_2^-$, XeO_3F_2 and OsO_3F_2 demonstrate that there is some mixing of the symmetry force constants for vibrational modes having the same symmetry. The amount of mixing is minor for the A_1' modes, with 91 to 97% of $\nu_1(A_1')$ and $\nu_2(A_1')$ being described by F_{11} and F_{22}, respectively. Considerable mixing of the asymmetric AF_2 stretches, $\nu_3(A_2'')$, and the out-of-plane umbrella bends, $\nu_4(A_2'')$, results in these fundamental vibrations having similar atomic motions. This is especially true for $BrO_3F_2^-$ where the contribution of F_{44} to $\nu_3(A_2'')$ is 34%, and the contribution of F_{33} to $\nu_4(A_2'')$ is 17%. Each of the three E' modes has contributions from F_{55}, F_{66} and F_{77} with the degree of mixing being greatest for $\nu_5(E')$, for which the F_{55} contribution ranged from 57% for $ClO_3F_2^-$ to 80% for OsO_3F_2. The $\nu_6(E')$ and $\nu_7(E')$ modes are dominated by F_{66} and F_{77}, and contain only minor contributions from F_{55} (0 - 9%). The only mode having E'' symmetry is the F-A-F bend (ν_8) and accordingly has F_{88} as its sole contributor.

Despite the stronger A-O bonds expected for XeO_3F_2 relative to those of $BrO_3F_2^-$, the symmetric (F_{11}) and asymmetric (F_{55}) BrO_3 stretching force constants are similar for both species. This may, in part, arise from the greater underestimation of the AO_3 stretching frequencies of XeO_3F_2 (ca. 49 cm^{-1}) relative to those of $BrO_3F_2^-$ (ca. 12 cm^{-1}), however, the opposite signs of the off-diagonal terms (f_{DD}) for XeO_3F_2 and $BrO_3F_2^-$ and their contributions to F_{11} ($f_D + 2f_{DD}$) and F_{55} ($f_D - f_{DD}$) are also likely to be significant. These main-group species contrast with OsO_3F_2, which has significantly higher F_{11} and F_{55} values and may be attributed to stronger Os-O bonds arising from dπ-pπ bonding. A comparison of the AO_3 stretching force constants reveals that F_{11} and F_{55} are 1.15 and 1.33 mdyne Å^{-1} higher, respectively, for $ClO_3F_2^-$ when compared with $BrO_3F_2^-$. This trend is in accord with the calculated Cl-O bond order of $ClO_3F_2^-$, which is 7% greater than the Br-O bond order of $BrO_3F_2^-$ (see section 7.3.5), and with the weaker fluoride ion

acceptor properties of ClO_3F. It is noteworthy that F_{11} is similar to F_{55} for $ClO_3F_2^-$, $BrO_3F_2^-$ and XeO_3F_2, but is significantly greater than F_{55} for OsO_3F_2. The difference likely accounts for the occurrence of the symmetric AO_3 stretch, $v_1(A_1')$ at higher frequency than the asymmetric AO_3 stretch, $v_5(E')$.[431]

The dominance of the internal force constant f_d towards the symmetric (F_{22}) and asymmetric (F_{33}) AF_2 stretching force constants results in similar trends being arrived at by the two methods. It is noteworthy that the symmetric AF_2 stretch is larger than the asymmetric AF_2 stretch for $BrO_3F_2^-$ (2.09, 1.65 mdyne $\mathring{A}^{-1}$), XeO_3F_2 (2.92, 1.28 mdyne $\mathring{A}^{-1}$) and OsO_3F_2 (4.30, 0.85 mdyne $\mathring{A}^{-1}$), whereas the opposite trend occurs for $ClO_3F_2^-$ (1.68, 1.73 mdyne $\mathring{A}^{-1}$). The reversal of the AF_2 stretching force constants for $ClO_3F_2^-$ likely reflects the strengthening of a Cl-F bond as the anion takes on more ClO_3F character during the asymmetric stretch. With this in mind, it is not surprising the species with the largest values of F_{22} exhibit the smallest values for F_{33}.

Although the atomic motions associated with the asymmetric AF_2 stretch ($v_3(A_2'')$) and the AO_3 umbrella deformation ($v_4(A_2'')$) are made similar by the significant degrees of vibrational coupling for these modes, the latter has more O-A-F bending character and less A-F stretching character than the former. The F_{44} values decrease along the series: $ClO_3F_2^-$ (2.04 mdyne $\mathring{A}$ rad^{-2}) > $BrO_3F_2^-$ (1.65 mdyne $\mathring{A}$ rad^{-2}) > XeO_3F_2 (1.28 mdyne $\mathring{A}$ rad^{-2}) > OsO_3F_2 (0.85 mdyne $\mathring{A}$ rad^{-2}), reflecting the decreasing resistance to angular distortions with increasing valence orbital diffuseness.

7.3.5. Atomic Charges and Bond Orders

The atomic charges, valencies and bond orders of XO_4^-, XO_3F, and $XO_3F_2^-$ (X = Cl, Br) are summarized in Table 7.16, and were calculated by use of the Natural Bond Orbital (NBO) method in conjunction with the energy-minimized geometries determined by the MPW1PW91 method.

Table 7.16. Atomic Charges, Mayer Valencies and Mayer Bond Orders for XO_4^-, XO_3F and $XO_3F_2^-$ ($X = Cl$, Br)[a]

	ClO_4^-	ClO_3F	$ClO_3F_2^-$	BrO_4^-	BrO_3F	$BrO_3F_2^-$
Mayer Atomic Charges and Valencies[b]						
X	2.49 (3.46)	2.45 (3.25)	2.43 (3.10)	2.75 (3.28)	2.71(3.09)	2.78 (3.20)
O	-0.87 (0.66)	-0.67 (0.78)	-0.77 (0.72)	-0.93 (0.68)	-0.74(0.78)	-0.85 (0.71)
F		-0.44 (0.26)	-0.67 (0.14)		-0.49(0.30)	-0.62 (0.22)
Mayer Bond Order						
X-O	0.86	0.95	0.91	0.82	0.90	0.85
X-F		0.38	0.22		0.40	0.32
O--O	-0.07	-0.07	-0.06	-0.05	-0.05	-0.03
O--F		-0.04	-0.04		-0.03	-0.03

[a] Results were obtained using the MPW1PW91/DZVP energy-minimized structure. [b] Atomic valencies are given in parentheses.

The charges on the bromine (2.71 - 2.78) and chlorine (2.43 - 2.49) atoms exhibit little variation among the oxygen rich species, XO_4^-, XO_3F and $XO_3F_2^-$ (X = Br, Cl), and are similar to those reported for BrF_6^+ (2.86) and ClF_6^+ (2.51) using the same computational method. The charges on the chlorine atoms are *ca.* 0.3e less than those on bromine atoms in the analogous species, and are attributed to the higher electronegativity of chlorine. The relative invariance of the central halogen charge means that the atomic charges on the oxygen and fluorine ligands must vary accordingly to balance the net charges of these species. Interestingly, the charge distributions among the oxygen and fluorine ligands of XO_3F (82% O, 18% F) and $XO_3F_2^-$ (67% O, 33% F) are identical for X = Cl and Br, indicating that they are strongly correlated with the relative electronegativities of the ligand atoms.

A comparison of the X-F bond orders for XO_3F and $XO_3F_2^-$ (X = Br, Cl) shows that they are correlated with the relative fluoride ion affinities of BrO_3F and ClO_3F. Whereas the Br-F bond order of $BrO_3F_2^-$ is 73% of that calculated for BrO_3F, the Cl-F bond orders of $ClO_3F_2^-$ are only 58% of that determined for ClO_3F. With the exception of the slightly higher (*ca.* 5%) X-O bond orders calculated for the chlorine species, the X-O bond orders are not strongly influenced by the relative X-F bond strengths as indicated by their limited variation and consistent ordering among the XO_4^-, XO_3F and $XO_3F_2^-$ species. Similar trends may be derived from the ligand valencies of these species, but are somewhat complicated by the small repulsive ligand-ligand interactions.

The O--O and O--F bond orders of XO_4^-, XO_3F and $XO_3F_2^-$ are in agreement with the expected trends derived from their geometries and relative X-O and X-F bond lengths, being small and negative in all cases. The O--O bond orders are more negative for the (pseudo)tetrahedral species, XO_4^- and XO_3F, than for the $XO_3F_2^-$ species, which is attributed to their smaller O-X-O bond angles. The magnitudes of the O--F interactions

are not affected by the contraction of the O-X-F bond angles in $XO_3F_2^-$ ($90°$) relative to those calculated for BrO_3F ($116.0°$) and ClO_3F ($115.8°$), however, doubling the number of such interactions in the $XO_3F_2^-$ anions likely promote fluoride ion dissociation.

7.4. Conclusion

Perbromyl fluoride reacts with MF (M = K, Rb, Cs), NOF and $[N(CH_3)_4][F]$ to form salts containing the $BrO_3F_2^-$ anion. With the exception of $[NO]_2[BrO_3F_2][F]$, which has a significant dissociative vapour pressure at temperatures as low at -78 °C, the $BrO_3F_2^-$ salts studied are all stable under dynamic vacuum at -40 °C. Moreover, it has proved possible to handle β-$[Cs][BrO_3F_2]$ for several hours under inert conditions at ambient temperature. The vibrational spectra of $BrO_3F_2^-$ has been assigned under D_{3h} symmetry in the aforementioned salts with the aid of electronic structure calculations and comparisons with the vibrational spectra of XeO_3F_2 and OsO_3F_2. Although the vibrational spectra of these salts are indicative of well-separated cations and anions, small Br-O and Br-F frequency shifts occur and can be correlated to the relative fluoride ion donor strengths of the alkali metal fluorides, NOF and $[N(CH_3)_4][F]$. The structures of $[N(CH_3)_4][BrO_3F_2]$ and $[NO]_2[BrO_3F_2][F]$ have been determined by use of low-temperature single crystal X-ray diffraction. Although the anion is disordered in the former salt, the anion exhibits trigonal bipyramidal geometries as predicted by the VSEPR model.

Attempts to prepare salts containing the $ClO_3F_2^-$ and $BrO_3F_3^{2-}$ anions by the reactions of ClO_3F and $[N(CH_3)_4][BrO_3F_2]$ with $[N(CH_3)_4][F]$ have been unsuccessful. Failure to prepare the $BrO_3F_3^{2-}$ dianion has been attributed to the thermodynamic instabilities of the *fac-* and *mer-* isomers with respect to fluoride ion dissociation, as determined by theoretical calculations at the G2 level of theory. Similar calculations have predicted $ClO_3F_2^-$ and $BrO_3F_2^-$ to be thermodynamically stable with respect to

fluoride ion loss, however, the enthalpy of fluoride ion attachment for ClO_3F (-132 kJ mol^{-1}) is considerably less exothermic than that of BrO_3F (-261 kJ mol^{-1}) and comparable to the minimum value typically required for the formation of a stable anion (-126 to - 146 kJ mol^{-1}) when lattice and solvation energies are taken into account.

The atomic charges, bond orders and valencies of $BrO_3F_2^-$ and $ClO_3F_2^-$ have been determined using NBO analyses and have been compared with those of the halogen(VII) species XO_4^-, XO_3F and XF_6^+ (X = Cl, Br). The central halogen charges are nearly invariant among Cl(VII) and Br(VII) species, and the net charges on these species are dispersed among the highly electronegative oxygen and fluorine ligands. A comparison of the calculated bond orders of $BrO_3F_2^-$ and $ClO_3F_2^-$ leads to the prediction that $ClO_3F_2^-$ has stronger X-O bonds but weaker X-F bonds than $BrO_3F_2^-$. This prediction is consistent with the force constant analyses of these anions and the greater fluoride ion affinity of BrO_3F relative to that of ClO_3F.

CHAPTER 8

FLUORIDE ION DONOR PROPERTIES OF BrO₃F AND ClO₃F AND THE STRUCTURAL CHARACTERIZATION OF [ClO₂][SbF₆] AND [BrO₂][SbF₆] BY SINGLE CRYSTAL X-RAY DIFFRACTION AND RAMAN SPECTROSCOPY

8.1 Introduction

The fluoride ion donor and acceptor properties of the fluorides and oxide fluorides of bromine and chlorine in the +3 and +5 oxidation states have been investigated in detail and have lead to the syntheses of cationic and anionic derivatives of ClF_3 (ClF_2^{+},[486-489] ClF_4^{-}[490-495]), BrF_3 (BrF_2^{+},[211,212,353,488,489] BrF_4^{-}[424]), ClF_5 (ClF_4^{+},[496-500] ClF_6^{-}[501]), BrF_5 (BrF_4^{+},[210,362,499,502] BrF_6^{-}[425,503-505]), ClO_2F (ClO_2^{+},[145,222,506-508] $ClO_2F_2^{-}$[509,510]), BrO_2F (BrO_2^{+},[207,213] $BrO_2F_2^{-}$[244,509]), $ClOF_3$ ($ClOF_2^{+}$,[511,512] $ClOF_4^{-}$[511,513]), and $BrOF_3$ ($BrOF_2^{+}$,[215,216] $BrOF_4^{-}$[427,428]). In contrast to the lower oxidation states of bromine and chlorine, fluoride ion transfer reactions involving Br(VII) and Cl(VII) species have only been studied in the context of the syntheses of $BrO_3F_2^{-}$ (see Chapter 7) and ClO_2F_3[514-516] from BrO_3F (eq 8.1) and $ClO_2F_2^{+}$ (eq 8.2), respectively. The exploitation of similar

$$BrO_3F + F^- \rightarrow BrO_3F_2^- \tag{8.1}$$

$$ClO_2F_2^+ + F^- \rightarrow ClO_2F_3 \tag{8.2}$$

Lewis acid-base reactions for the preparation of new Br(VII) and Cl(VII) cations and anions is complicated by several factors, including the stronger ligand-ligand repulsions encountered for the high coordinate neutral and anionic halogen (VII) oxide fluorides[409] and the inability to prepare their neutral precursors $ClOF_5$,[517] $BrOF_5$[207,226] and BrO_2F_3[244] (also see Appendix B). Perbromyl fluoride[207] and ClO_3F[217,518] fail to exhibit fluoride ion

donor properties towards the strong Lewis acids AsF_5 and SbF_5 in anhydrous HF, preventing the isolation of salts containing the BrO_3^+ and ClO_3^+ cations. The observation of BrO_3^+ and ClO_3^+ in the mass spectra of BrO_3F[162] and ClO_3F[519] suggests these cations may have some inherent stability and could be isolated as stable salts if an extremely strong Lewis acid was used to abstract fluoride from the parent perhalyl fluorides and the resulting anion was resistant to oxidation by the XO_3^+ cation.

In contrast, BrO_2F and ClO_2F behave as fluoride ion donors, reacting with strong Lewis acids to form BrO_2^+ and ClO_2^+ salts. The vibrational spectra of the chloryl[145,222,507,508,520] and bromyl[207,213] cations have been obtained for several salts, and are consistent with the symmetric V-shaped geometries predicted by the VSEPR[521] model of molecular geometry for an AX_2E arrangement of electron bond pairs and lone pairs. Single crystal X-ray diffraction has been used to obtain accurate Cl-O bond lengths and O-Cl-O bond angles for the $Sb_2F_{11}^-$,[522] BF_4^-,[523] ClO_4^-,[520] and RuF_6^-[508] salts of ClO_2^+, however, the geometric parameters of BrO_2^+ have only been estimated from the photoelectron spectrum of the $BrO_2\cdot$ radical using an iterative Franck-Condon analysis (IFCA).[524,525] Modern computational methods have been used to investigate the structure and vibrational frequencies of BrO_2^+,[524,526] but surprisingly have not been employed for the characterization of ClO_2^+.

In the present study, the reactions of BrO_3F and ClO_3F with neat SbF_5 were investigated with the anticipation that this highly acidic medium may enable the syntheses of BrO_3^+ and ClO_3^+ salts. In the course of this study, the crystal structures of $[BrO_2][SbF_6]$ and $[ClO_2][SbF_6]$ were determined by low-temperature X-ray diffraction. Electron structure calculations have been used to model the structures and vibrational frequencies of the XO_3^+ and XO_2^+ cations (X = Br, Cl), and to assess the thermodynamic stabilities of the XO_3^+, and XO_2^+ salts in conjunction with empirical relationships.

8.2. Results and Discussion

8.2.1. Reactions of BrO_3F with SbF_5 and AsF_5

The reaction of BrO_3F with SbF_5 proceeded vigorously at 0 °C, with the evolution of O_2 and the formation of a red-orange solid, which was identified by Raman spectroscopy as $[BrO_2][Sb_nF_{5n+1}]$ from the intense Br-O stretching modes of the bromyl cation at 937 and 870 cm^{-1}.[213] Other oxygen containing species of bromine were not observed in the Raman spectrum of the products, suggesting that reaction proceeds quantitatively according to eq 8.3. A similar reaction does not occur at -78 °C when neat

$$BrO_3F + nSbF_5 \xrightarrow{\quad SbF_5, \ 0°C \quad} [BrO_2][Sb_nF_{5n+1}] + \frac{1}{2}O_2 \qquad (8.3)$$

AsF_5 is used in place of SbF_5, however, $[BrO_2][Sb_nF_{5n+1}]$ can be prepared at temperatures as low as -45 °C if SbF_5 is dissolved in AsF_5, suggesting that $(SbF_5)_n$ (n > 1) is required to initiate the reaction. The red-orange salt, $[BrO_2][SbF_6]$, was obtained by recrystallization of $[BrO_2][Sb_nF_{5n+1}]$ from anhydrous HF and was determined to be pure by low-temperature Raman spectroscopy (see section 8.2.4).

8.2.2. Reactions of ClO_3F and ClO_2F with SbF_5

In contrast to BrO_3F, ClO_3F does not react with neat SbF_5 at temperatures as high as 20 °C. The inertness of ClO_3F towards neat SbF_5 is consistent with its inability to form adducts with BF_3, PF_5, AsF_5, SbF_5 and SO_3.[217] The chloryl salt, $[ClO_2][SbF_6]$, was prepared by analogy with $[ClO_2][MF_6]$ (M = As,[507] Ru,[508] Au[145]) and $[ClO_2][BF_4]$[507] by the reaction of ClO_2F with SbF_5 in HF solvent (eq 8.4), and was obtained in high purity by recrystallizing the crude material from anhydrous HF solution.

$$ClO_2F + SbF_5 \xrightarrow{\quad HF \quad} [ClO_2][SbF_6] \qquad (8.4)$$

8.2.3. Crystal Structures of $[BrO_2][SbF_6]$ and $[ClO_2][SbF_6]$

The unit cell parameters and refinement statistics for $[BrO_2][SbF_6]$ and $[ClO_2][SbF_6]$ are summarized in Table 8.1. Both salts crystallize in the monoclinic space

Table 8.1. Summary of Crystal Data and Refinement Results for $[BrO_2][SbF_6]$ and $[ClO_2][SbF_6]$

	$[BrO_2][SbF_6]$	$[ClO_2][SbF_6]$
Space Group	$P2/n$	$P2/n$
a (Å)	7.251(3)	7.194(5)
b (Å)	5.779(2)	5.682(4)
c (Å)	7.328(3)	7.270(4)
α (deg)	90	90
β (deg)	92.897(4)	90.02(1)
γ (deg)	90	90
V (Å^3)	306.7(2)	297.1(3)
Z	2	2
Mol. mass (g mol^{-1})	347.63	303.18
ρ_{calcd} (g cm^{-3})	3.765	3.389
T (°C)	-173	-173
μ (mm^{-1})	11.08	5.16
$R_1{}^a$	0.0142	0.0558
$wR_2{}^b$	0.0331	0.1385

$^a R_1 = \dfrac{\sum \left| |F_o| - |F_c| \right|}{\sum |F_o|}$ for $I > 2\sigma(I)$. $\quad ^b wR_2 = \dfrac{\sum \left| (|F_o| - |F_c|)w^{\frac{1}{2}} \right|}{\sum (|F_o|w)}$ for $I > 2\sigma(I)$.

group $P2/n$ and are isostructural and isomorphous with $[ClO_2][RuF_6]$.[508] The structures of the $[XO_2][MF_6]$ (X = Cl, Br) salts are simplified by the symmetry of the unit cell, which constrains the point symmetries of the cations and anions to C_{2v} and C_i, respectively. Consequently, each salt exhibits only one crystallographically unique X-O bond and three unique M-F bonds. The bond lengths, bond angles and the relevant cation-anion contact distances are summarized in Table 8.2.

The packing of the $[XO_2][SbF_6]$ (X = Cl, Br) salts is best described in terms of alternating layers of cations and anions lying parallel to the ac-plane (Figure 8.1). The cations and anions are coplanar in the ab-plane, but are staggered along the bc-plane such that each cation exhibits four long interionic X⋯F contacts lying within the sum of the van der Waals radii of Br (1.95,[287] 1.85 Å[286]), Cl (1.80,[287] 1.75 Å[286]) and F (2.70,[287] 2.94 Å[286]). The XO_2^+ cations are ideally oriented in these salts, with the X-E axis (E = lone pair) bisecting the angles subtended by the X⋯F contacts (*i.e.*, F(1)⋯X⋯F(1A), F(3)⋯X⋯F(3A)). The structurally equivalent X⋯F(1) and X⋯F(3) contact distances in $[BrO_2][SbF_6]$ (2.590, 2.685 Å) and $[ClO_2][SbF_6]$ (2.516, 2.742 Å) are significantly different, however, the average X⋯F distances are very similar in these salts (Br, 2.638; Cl, 2.629 Å) despite the larger size of the BrO_2^+ cation. The similar average chlorine-anion contact distances determined in the structures of $[ClO_2][RuF_6]$ (2.614 Å),[508] $[ClO_2][Sb_2F_{11}]$ (2.680 Å),[522] $[ClO_2][ClO_4]$ (2.669 Å)[520] and $[ClO_2][BF_4]$ (2.600 Å)[523] suggest that these interactions are not coincidental, but play an important role in orientating the comparatively small XO_2^+ cations within the large interstitial holes produced by the anions.

The Br-O bond lengths of $[BrO_2][SbF_6]$ (1.595(2) Å) are moderately shorter, but comparable to those estimated for the gas-phase BrO_2^+ cation (1.6135 Å) from the photoelectron spectrum of the $BrO_2\cdot$ radical.[524] The bond lengths of the BrO_2^+ cation are

Table 8.2. Bond Lengths and Bond Angles Determined for $[XO_2][SbF_6]$ (X = Br, Cl)

	$[BrO_2][SbF_6]$	$[ClO_2][SbF_6]$
Bond Lengths (Å)		
X-O	1.595(2)	1.381(7)
Sb-F(1)	1.884(2)	1.881(4)
Sb-F(2)	1.888(1)	1.871(4)
Sb-F(3)	1.869(1)	1.858(6)
X···F(1)	2.590	2.516
X···F(3)	2.685	2.742
Bond Angles (deg)		
O-X-O	112.0(1)	117.7(5)
F(1)-Sb-F(2)	90.05(6)	91.5(3)
F(1)-Sb-F(3)	90.84(6)	89.5(3)
F(2)-Sb-F(3)	90.46(7)	89.5(3)
O(1)···X···F(1)	101.3	102.1
O(1)···X···F(1A)	105.8	102.0
O(1)···X···F(3)	81.4	80.7
O(1)···X···F(3A)	166.4	161.6
O(2)···X···F(1)	105.8	102.0
O(2)···X···F(1A)	101.3	102.1
O(2)···X···F(3)	166.4	161.6
O(2)···X···F(3A)	81.4	80.7
F(1)···X···F(1A)	130.5	132.3
F(1)···X···F(3)	72.4	72.0
F(1)···X···F(3A)	71.7	72.2
F(3)···X···F(3A)	85.2	80.8

a
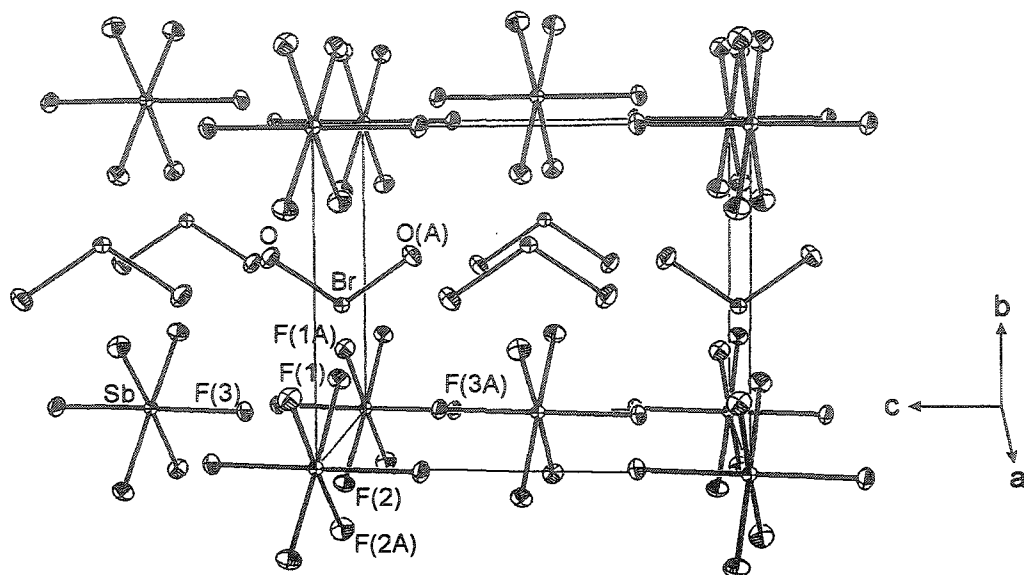
b
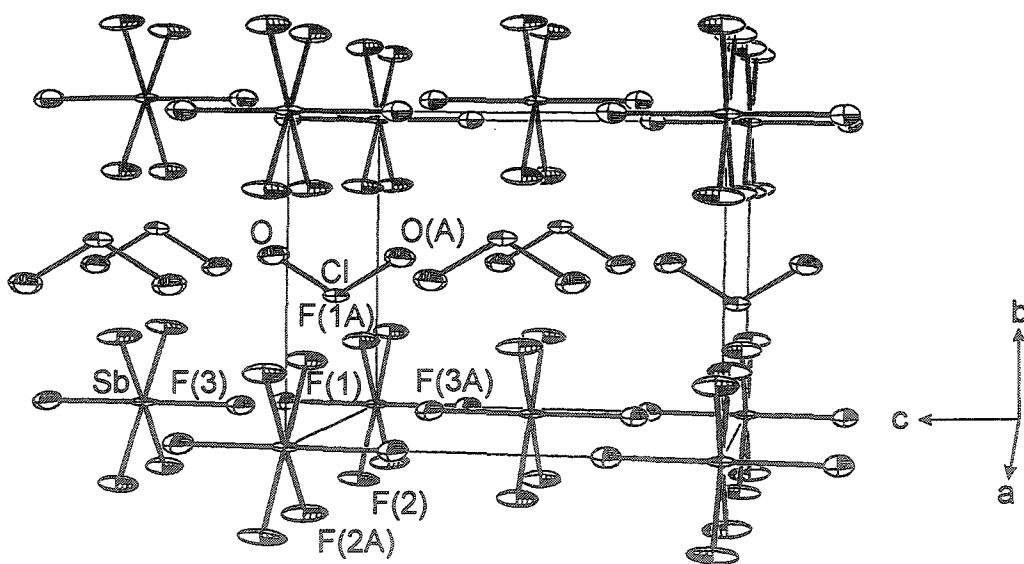
Figure 8.1. Packing diagrams of (a) [BrO₂][SbF₆] and (b) [ClO₂][SbF₆] at -173 °C viewed along the *a*-axis. The thermal ellipsoids are shown at the 50% probability level.

similar to the Br(V)-O double bonds of $[NO_2][BrF_4]\cdot2BrOF_3$ (1.569, 1.606 Å)[527] and the non-bridging Br-O bonds in $O_2BrOBrO_2$ (1.606(12), 1.611(2), 1.613(2), 1.606(2) Å)[528] and $O_2BrOTeF_5$ (1.595(4), 1.608(3) Å).[438] Unfortunately, comparisons among the bond lengths of the cation and its parent oxide fluoride, BrO_2F, cannot be made because the structure of the latter species is disordered.[438] The Br-O double bonds in these species are shorter than those of BrO_3^- (1.648(4) Å),[529] which has a slightly smaller formal Br-O bond order ($^5/_3$), but are comparable to that reported for the $BrOF_4^-$ anion (1.575(3) Å),[527] suggesting the Br(V)-O bond lengths are also geometry dependent. The bond lengths of BrO_2^+ are significantly shorter than those of the structurally related $BrO_2\cdot$ radical (1.6491(15) Å),[530] which is attributed to the unpaired electron in the bromine valence shell and resulting lower formal oxidation state of bromine.

The Cl-O bond lengths in $[ClO_2][SbF_6]$ (1.381(7) Å) cannot be differentiated from those determined for the ClO_2^+ cations in the BF_4^- (1.405(1), 1.408(1) Å),[523] ClO_4^- (1.406(2), 1.410(2) Å)[520] RuF_6^- (1.379(9) Å),[508] and $Sb_2F_{11}^-$ (1.28(3), 1.31(4) Å)[522] salts at the $\pm3\sigma$ (99.7%) level of confidence, however, at the $\pm2\sigma$ (95.5%) limit the Cl-O bond lengths contract with increasing anion size. The origin of this trend is uncertain, but may reflect a reduction in electron density transfer from the anion to the cation as the charge density of the anion decreases. Charge transfers of this type would be expected to increase the $ClO_2\cdot$ radical character of ClO_2^+, and are reflected in the structures of $[ClO_2][BF_4]$ and $[ClO_2][ClO_4]$ for which the Cl-O bond lengths approach those of the $ClO_2\cdot$ radical (1.475(3) Å).[531] Although the partial radical character proposed for the ClO_2^+ salts is not reflected in the colours of these salts, which are all colourless, a similar phenomenon may account for the intense red-orange colour of $[BrO_2][SbF_6]$. The bond lengths of ClO_2^+ are similar to the Cl(V)-O double bond lengths of gaseous ClO_2F (1.419(9) Å)[532] and $ClOF_3$ (1.405(3),[533] but are significantly shorter than those of ClO_3^-

(1.502(3) Å),[534] in accord with the lower formal Cl-O bond order of the anion ($^5/_3$) and the trends noted for the Br(V) analogues.

The O-Br-O bond angle in $[BrO_2][SbF_6]$ (112.0(1)°) is moderately smaller than the O-Cl-O bond angles determined in the structures of $[ClO_2][SbF_6]$ (117.7(5)°), $[ClO_2][RuF_6]$ (117.2(9)°),[508] $[ClO_2][ClO_4]$ (118.9(2)°),[520] $[ClO_2][BF_4]$ (118.47(6)°)[523] and $[ClO_2][Sb_2F_{11}]$ (122(2)°).[522] The bond angles of both XO_2^+ cations are consistent with the VSEPR model, which predicts a trigonal-planar AX_2E arrangement, having an O-X-O bond angle slightly less than 120° as a consequence of the larger electron lone pair domain when compared with the more localized bonding pairs. On the basis of the narrow range of bond angles obtained for the ClO_2^+ salts and the similar bond angles obtained for the gaseous $BrO_2\cdot$ (114.44(25)°)[530] and $ClO_2\cdot$ (117.7(1.7)°)[531] radicals, the interionic contacts observed in the solid state structures of the XO_2^+ salts (*vide supra*) do not appear to have a strong influence on the O-X-O bond angles.

8.2.4. Vibrational Spectra of $[BrO_2][SbF_6]$ and $[ClO_2][SbF_6]$

The vibrational frequencies of $[BrO_2][SbF_6]$ obtained by Raman spectroscopy (Figure 8.2) are summarized in Table 8.3, where they are compared with those previously reported for $[BrO_2][Sb_{2.24}F_{12.2}]$,[213] $[BrO_2][AsF_6]$[214] and $[BrO_2][BF_4]$.[214] The Raman vibrational frequencies of $[ClO_2][SbF_6]$ (Figure 8.3) are summarized in Table 8.4, where they are compared with those previously reported for $[ClO_2][MF_6]$ (M = As,[507] Ru,[508] Pt,[222] Ir,[222] Au[145]), $[ClO_2][BF_4]$[507] and $[ClO_2][ClO_4]$.[520] The three fundamental vibrations ($\Gamma_{vib} = 2A_1 + B_2$) of the BrO_2^+ and ClO_2^+ cation exhibit minor anion dependencies, which are greatest for $v_1(A_1)$ (Br, 862 - 884; Cl, 1039 - 1065 cm^{-1}), and $v_3(B_2)$ (Br, 931 - 947; Cl, 1280 - 1308 cm^{-1}) and least for $v_2(A_1)$ (Br, 372 - 382; Cl, 518 - 521 cm^{-1}). These anion-dependent shifts do not correlate with the size or Lewis basicity of the anion, however, the similar frequency shifts observed among the chlorine and bromine
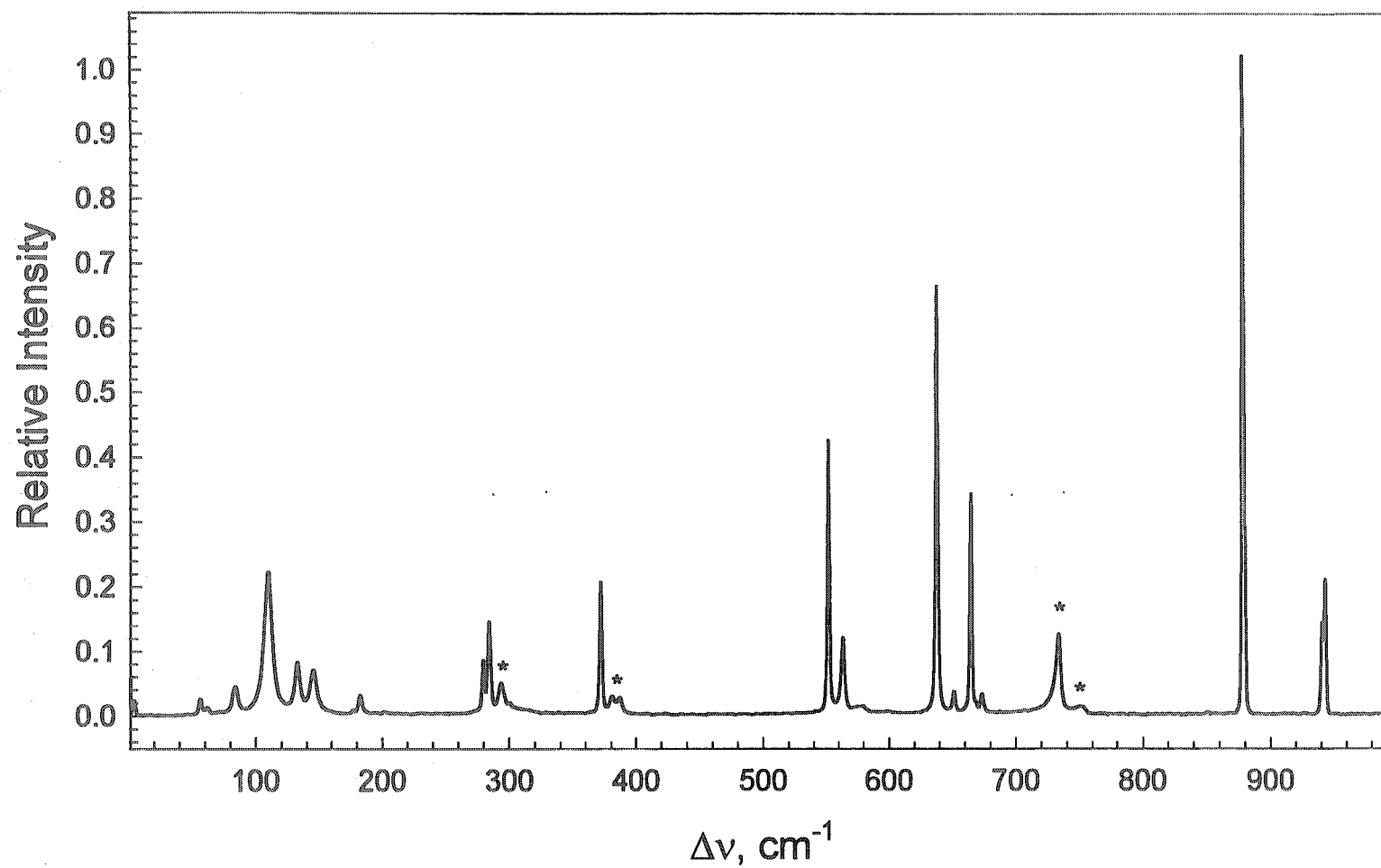
Figure 8.2. Raman spectrum of crystalline [BrO$_2$][SbF$_6$] recorded at -163 °C in a FEP vessel using 1064-nm excitation. Bands from the FEP sample tube are denoted by asterisks (*).

Table 8.3. Vibrational Frequencies[a] for Salts of the BrO_2^+ Cation

Assignment	$[BrO_2][SbF_6]$[b]	$[BrO_2][Sb_nF_{5n+1}]$[c]	$[BrO_2][AsF_6]$[d]	$[BrO_2][BF_4]$[e]
$\nu_1(A_1)\ BrO_2^+$	877.9(100)	865(s)[vw]	862(100)	884(100)
$\nu_2(A_1)\ BrO_2^+$	371.9(21)	375(m)[s]	382(6)	379(11)
$\nu_3(B_2)\ ^{79}BrO_2^+$	942.8(21)	932(m)[s]	931(20)	947(13)
$^{81}BrO_2^+$	940.5(15)			
$\nu_1(A_{1g})\ MF_6^-$	664.5(35)		685(60)	
	637.7(67)			
$\nu_2(E_g)\ MF_6^-$	563.4(12)		576(18)	
	551.1(43)		552(28)	
$\nu_3(F_{1u})\ MF_6^-$	673.2(3)			
	651.1(4)			
$\nu_5(F_{2g})\ MF_6^-$	284.2(15)		368(15)	
	279.7(8)			
$\nu_1(A_1)\ MF_4^-$				771(4)

[a] Frequencies are given in cm^{-1}. Raman intensities are given in parentheses and are scaled such that $\nu_1(A_1)$ has an intensity of 100. [b] Raman frequencies obtained in the present work. [c] Infrared frequencies obtained from ref 213. The abbreviations vw and vs denote "very weak" and "very strong", respectively. [d] Raman frequencies obtained from ref 214. [e] Raman frequencies obtained from ref 214.
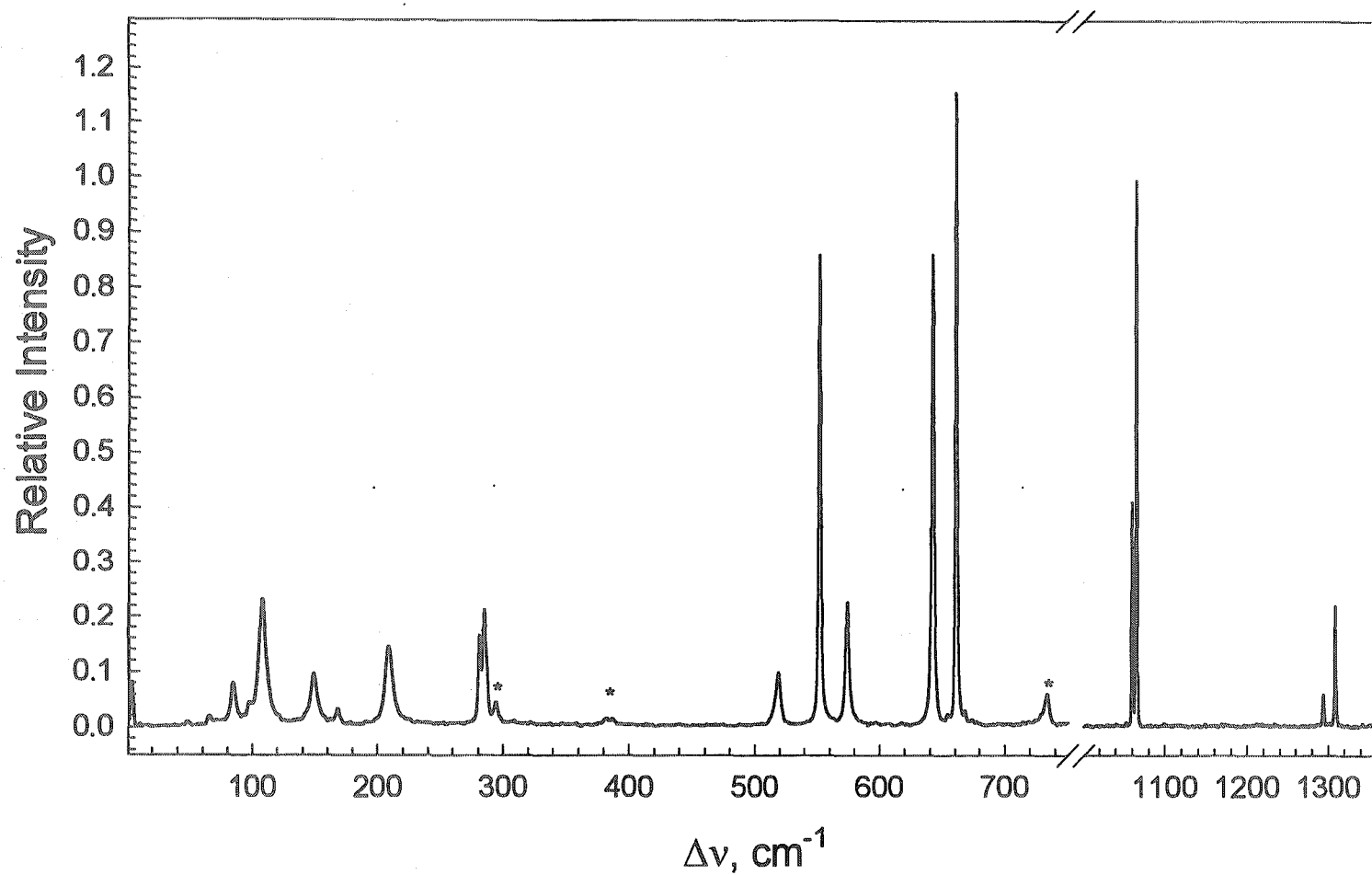
Figure 8.3. Raman spectrum of crystalline [ClO$_2$][SbF$_6$] recorded at -163 °C in a FEP vessel using 1064-nm excitation. Bands from the FEP sample tube are denoted by asterisks (*).

Table 8.4. Vibrational Frequencies[a] for Salts of the ClO_2^+ Cation

Assignment	[SbF$_6$][b]	[AsF$_6$][c]	[RuF$_6$][d]	[PtF$_6$][e]	[IrF$_6$][f]	[AuF$_6$][g]	[ClO$_4$][h]	[BF$_4$][j]
$\nu_1(A_1)$ $^{35}ClO_2^+$	1064.7(100)	1044.4(100)	1058(100)	1054(100)	1057(100)	1055(100)	1055(vs)	990 - 1100[vs]
$^{37}ClO_2^+$	1059.4(42)	1039.1(40)				1043(27)		
$\nu_2(A_1)$ ClO_2^+	518.9(10)	521.3(30)	518(26)	518(30)	519(18)	519(36)	520(s)	518[m]
$\nu_3(B_2)$ $^{35}ClO_2^+$	1308.3(22)	1296.4(10)	1300(18)	1299(15)	1301(10)	1296(36)	1295(w)	1308[m]
$^{37}ClO_2^+$	1293.5(6)		1285(5)	1287(3)	1280(18)	1230(w)	1294[mw]	
$\nu_1(A_{1g})$ MF$_6^-$	660.7(116)	684(80)	663(263)	644(500)	670(164)	595(909)		
	641.9(86)							
$\nu_2(E_g)$ MF$_6^-$	573.8(22)	570(50)	570(74)	569(90)	561(41)	589(791)		
	551.9(86)		551(111)	554(125)	549(79)			
$\nu_3(F_{1u})$ MF$_6^-$	667.9(3)							
	653.9(2)							
$\nu_5(F_{2g})$ MF$_6^-$	284.6(21)	372(50)	266(176)	240(225)	248(139)	233(sh)		
	280.9(16)				224(336)			
$\nu_1(A_1)$ MY$_4^-$							914(s)	
$\nu_2(E)$ MY$_4^-$							474(m), 432(m)	
$\nu_3(F_2)$ MY$_4^-$							1145(w)	990 - 1100[vs]
$\nu_4(F_2)$ MY$_4^-$							615(m)	532[w], 521[w]

[a] Frequencies are given in cm^{-1}. Raman intensities are given in parentheses and are scaled such that $\nu_1(ClO_2^+)$ has an intensity of 100. Infrared intensities are given in brackets using the abbreviations w (weak), m (medium), mw (medium weak), s (strong), and vs (very strong). [b] Raman frequencies obtained in the present work. [c] Raman frequencies obtained from ref 507. [d] Raman frequencies obtained from ref 508. [e] Raman frequencies obtained from ref 222. [f] Raman frequencies obtained from ref 222. [g] Raman frequencies obtained from ref 145. [h] Raman frequencies obtained from ref 520. [i] The abbreviations vs, s, m, mw and w, denote "very strong", "strong", "medium", "medium weak" and "weak", respectively. [j] Infrared frequencies obtained from ref 507.
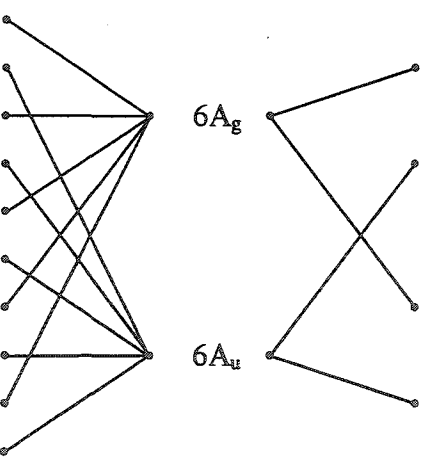
analogues of the $[XO_2][SbF_6]$ and $[XO_2][AsF_6]$ salts imply that they are closely related to the cation-anion packing arrangements and $X\cdots F$ contacts.

The Raman spectra of the BrO_2^+ and ClO_2^+ salts frequently exhibit splittings of their cation and anion bands. The crystal structure determinations of the isomorphous $[XO_2][SbF_6]$ (X = Br, Cl) salts have allowed a factor-group analysis to be carried out for these species (Table 8.5). Under the unit cell symmetry, C_{2h}, the $v_1(A_1)$ and $v_2(A_1)$ modes of the cation are each split into two components of A_g and A_u symmetry, whereas the $v_3(B_2)$ mode is split into components of B_g and B_u symmetry. The factor-group splitting of these modes does not, however, account for the splittings observed in the Raman spectra because the A_u and B_u modes are Raman-inactive. The splitting of cation bands is therefore attributed to the two naturally occurring bromine isotopes, ^{79}Br (50.7%) and ^{81}Br (49.3%), and chlorine ^{35}Cl (75.8%) and ^{37}Cl (24.2%). This assignment is consistent with the similar peak heights of the split $v_1(A_1)$ band of $[BrO_2][SbF_6]$, and the *ca.* 3:1 peak height ratios observed for the $v_1(A_1)$ and $v_3(B_2)$ bands of many ClO_2^+ salts, where the more intense band is always higher in frequency and is assigned to $^{35}ClO_2^+$. The larger splittings observed for $[ClO_2][SbF_6]$ ($\Delta v_1 = 5.3$ cm^{-1}; $\Delta v_3 = 14.8$ cm^{-1}) when compared with $[BrO_2][SbF_6]$ ($\Delta v_3 = 2.3$ cm^{-1}) are in excellent agreement with the magnitude of the splittings calculated for the gas-phase ClO_2^+ ($\Delta v_1 = 5.5$ cm^{-1}; $\Delta v_3 = 14.3$ cm^{-1}) and BrO_2^+ ($\Delta v_1 = 1.2$ cm^{-1}; $\Delta v_3 = 2.8$ cm^{-1}) cations by use of the QCISD method (see section 8.3.3) and reflect the greater difference in reduced masses for the chlorine isotopes.

In contrast to the splittings observed for the vibrational modes for the cations of $[XO_2][SbF_6]$, the splittings of the $v_1(A_{1g})$ Raman-active modes of the SbF_6^- anions (Br, 27; Cl, 19 cm^{-1}) cannot be attributed to isotopic effects because this symmetric vibration does not involve displacement of the central antimony atoms. The splittings observed for

308

Table 8.5. Factor Group Analyses for $[XO_2][SbF_6]$ (X = Br, Cl)[a]

Symmetry of Free XO_2^+		Site Symmetry of XO_2^+		Crystal Symmetry of $[XO_2][SbF_6]$	
C_{2v}		C_{2v}		C_{2h}	
$2v_1, 2v_2, 2T$	A_1	A_1		A_g	v_1, v_2, R, T
$2R$	A_2	A_2		B_g	$v_3, 2R, 2T$
$2R, 2T$	B_1	B_1		A_u	v_1, v_2, R, T
$2v_3, 2R, 2T$	B_2	B_2		B_u	$v_3, 2R, 2T$

Symmetry of Free SbF_6^-		Site Symmetry of SbF_6^-		Crystal Symmetry of $[XO_2][SbF_6]$	
O_h		C_i		C_{2h}	
$2v_1$	A_{1g}			A_g	$v_1, 2v_2, 3v_5, 3R$
	A_{1u}			A_u	$3v_3, 3v_4, 3v_6, 2T$
	A_{2g}	$6A_g$			
	A_{2u}				
$2v_1$	E_g				
	E_u				
$2R$	F_{1g}			B_g	$v_1, 2v_2, 3v_5, 3R$
$2v_3, 2v_4, 2T$	F_{1u}	$6A_u$			
$2v_5$	F_{2g}			B_u	$3v_3, 3v_4, 3v_6, 2T$
$2v_6$	F_{2u}				

[a] The $[XO_2][SbF_6]$ (X = Br, Cl) salts crystallize in the monoclinic space group *P2/n* with $Z = 2$.

the Raman-active bands of the anion are, however, explained by the factor group analyses of these salts (Table 8.5), which predict each of the A_{1g} ($A_g + B_g$), E_g ($2A_g + 2B_g$) and F_{1g} ($3A_g + 3B_g$) to be split into Raman-active bands under the C_{2h} symmetry of the unit cell. Likewise, the triply degenerate $v_3(F_{1u})$, $v_4(F_{1u})$ and $v_6(F_{2u})$ modes are predicted to be split into infrared-active bands of $3A_u$ and $3B_u$ symmetry. In contradiction with the selection rules for the point (O_h; F_{1u}),, site (C_i; A_u) and crystal (C_{2h}; A_u, B_u) symmetries, which predict $v_3(F_{1u})$ to be Raman-inactive, this band is observed in the Raman spectra of the $[XO_2][SbF_6]$ salts, although its weak relative intensity (< 4) reflects its forbidden nature.

8.3. Calculations

8.3.1. Fluoride Ion Donor Properties of BrO_3F and ClO_3F and the Stabilities of BrO_3^+ and ClO_3^+

Attempts to prepare $[BrO_3][Sb_nF_{5n+1}]$ by the reaction of SbF_5 with BrO_3F were unsuccessful, resulting in the reduction of the Br(VII) centre and the isolation of BrO_2^+ salts. This contrasts with ClO_3F, which fails to react with SbF_5 at ambient temperature. To account for the different reactivities of these species, electronic structure calculations and established empirical methods[535-537] were used in conjunction with known thermodynamic quantities to estimate $\Delta H°$, $\Delta S°$, and $\Delta G°$ for eq 8.5 and 8.6.

$$XO_3F + (MF_5)_n \rightarrow [XO_3][M_nF_{5n+1}] \quad (M = As, Sb) \tag{8.5}$$

$$XO_3F + (MF_5)_n \rightarrow [XO_2][M_nF_{5n+1}] + \tfrac{1}{2}O_2 \quad (M = As, Sb) \tag{8.6}$$
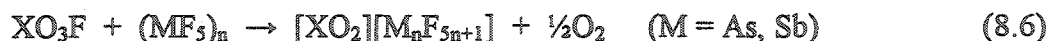
The standard enthalpies for these reactions were determined by analysis of their Born-Haber cycles (Figure 8.4). The enthalpy change for the gas-phase fluoride ion transfer reactions between a halogen oxide fluoride and a Lewis acid were calculated by use of eq 8.7, where the enthalpies of fluoride ion abstraction ($\Delta H°_{-F^-}$) from the perhalyl

$$\Delta H°_{F^-} = \Delta H°_{-F^-} + \Delta H°_{+F^-} \tag{8.7}$$

fluorides were calculated by the Gaussian-2 (G2) method and the enthalpies of fluoride

ion attachment ($\Delta H^{\circ}_{+F^-}$) to the Lewis acids are those reported by Christe *et al.*[46,48] (Table

8.6). The G2 method was also used to calculate the gas-phase enthalpies of reduction for

the XO_3^+ cations corresponding to eq 8.8 (Table 8.6). The enthalpy of vapourization

$$XO_3^+ \rightarrow XO_2^+ + \tfrac{1}{2}O_2 \tag{8.8}$$

term (ΔH°_{vap}) is zero for AsF_5 because it is a gas under standard conditions, but must be

accounted for in reactions involving SbF_5, which is a viscous liquid at ambient

temperature. The determination of ΔH°_{vap} for $(SbF_5)_n$ (n = 1 - 3) is complicated by the

polymeric nature of liquid SbF_5 and the predominance of the $(SbF_5)_3$ trimer in the gas

phase at ambient temperature.[538] Using the enthalpy of vapourization for $(SbF_5)_3$ (43.4 kJ

mol^{-1})[539] and the dissociation energy reported for $\tfrac{1}{4}(SbF_5)_4$ to SbF_5 (18.5 kJ mol^{-1}),[540] the

enthalpy of vapourization for monomeric SbF_5 has previously been estimated to be 30.9

kJ mol^{-1}.[541] A similar approach has been used to estimate the enthalpy of vapourization

for Sb_2F_{10} (38.1 kJ mol^{-1}). The lattice enthalpies of the proposed XO_3^+ and XO_2^+ salts

(Table 8.7) were estimated by use of the empirical volume-based method[542] recently

generalized by Jenkins *et al.*[535,536] in eq 8.9, where R is the gas constant (8.314 J K^{-1}

$$H^{\circ}_{L} = 2I\left(\frac{\alpha}{\sqrt[3]{V_m}} + \beta\right) + nRT \tag{8.9}$$

I is the ionicity of the salt and the constants α, β and n depend on the nature of the salt.[543]

In this formalism, H°_{L} is the lattice enthalpy and is defined as the energy required to

break the crystalline lattice, and therefore has a positive value. This approach is

generally accurate to 4% for salts with H°_{L} less than 5000 kJ mol^{-1},[536] and is particularly

useful because the unit molar volume (V_m) of an unknown salt can be estimated with

reasonable accuracy using several methods.[536,544] Furthermore, errors in V_m are

dampened by the inverse dependence of H°_{L} on the cube root of V_m. The net enthalpies

$$SbF_5(g) \quad + \quad BrO_3^+(g) + F^-(g) \xrightarrow{\Delta H^\circ_{+F^-}} SbF_6^-(g) + BrO_3^+(g)$$

$$\Big\uparrow \Delta H^\circ_{vap} \qquad\qquad \Big\uparrow \Delta H^\circ_{-F^-} \qquad\qquad\qquad\qquad \Big\downarrow \Delta H^\circ_L$$

$$SbF_5(l) \quad + \quad BrO_3F(g) \xrightarrow{\quad \Delta H^\circ \quad} [BrO_3][SbF_6](s)$$

$$SbF_5(g) \quad + \quad BrO_3^+(g) + F^-(g) \xrightarrow{\Delta H^\circ_{+F^-}} SbF_6^-(g) + BrO_3^+(g)$$

$$\Big\downarrow \Delta H^\circ_{red}$$

$$SbF_6^-(g) + \\ BrO_2^+(g) + \tfrac{1}{2}O_2(g)$$

$$\Big\uparrow \Delta H^\circ_{vap} \qquad\qquad \Big\uparrow \Delta H^\circ_{-F^-} \qquad\qquad\qquad\qquad \Big\downarrow \Delta H^\circ_L$$

$$SbF_5(l) \quad + \quad BrO_3F(g) \xrightarrow{\quad \Delta H^\circ \quad} [BrO_2][SbF_6](s) \\ + \tfrac{1}{2}O_2(g)$$
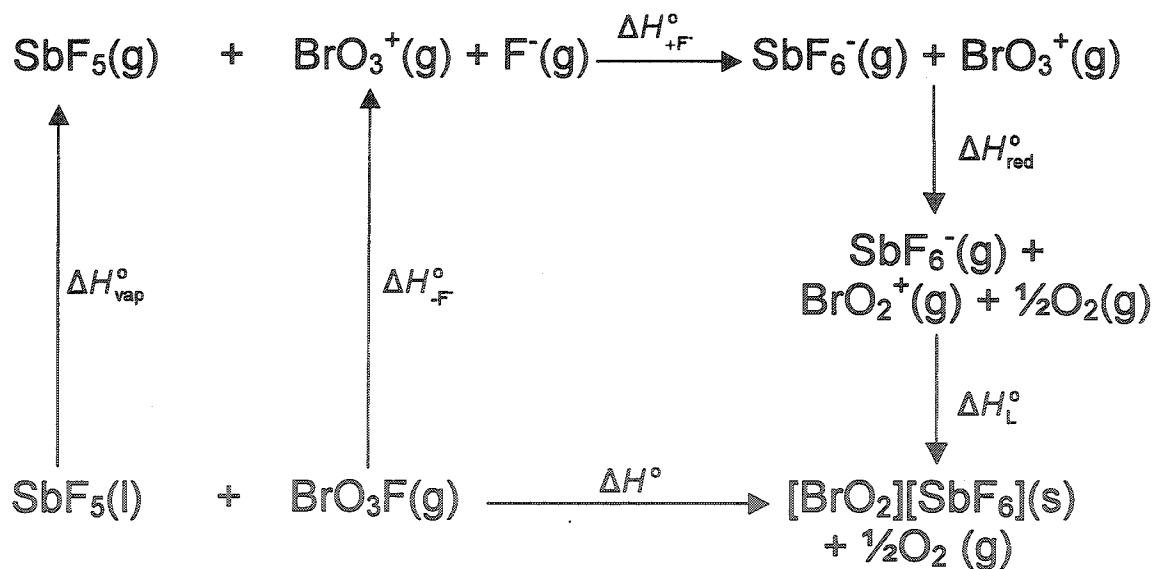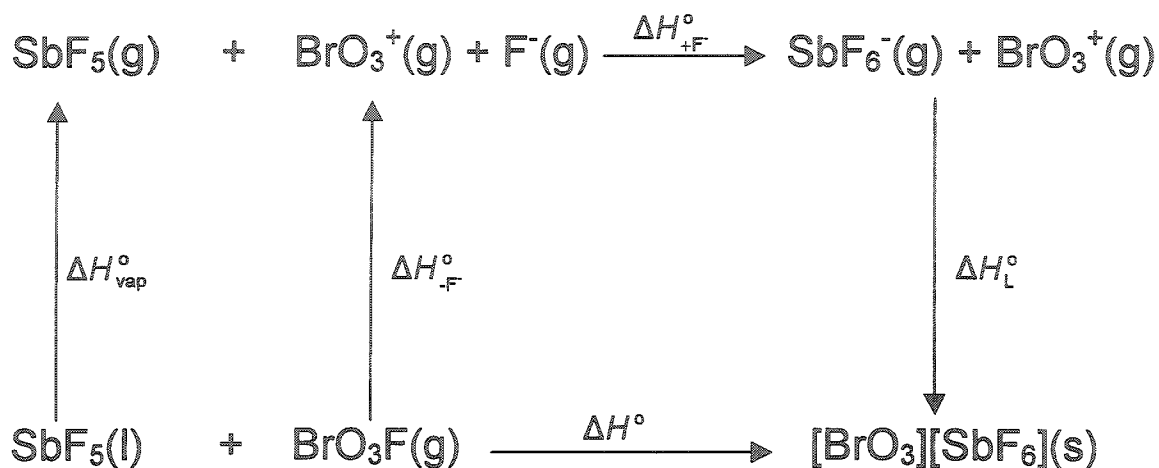
Figure 8.4. Thermochemical cycles that describe the reactions of BrO_3F with SbF_5 and that lead to the formation of $[BrO_3][SbF_6]$ and $[BrO_2][SbF_6]$.

Table 8.6. Enthalpies of Reaction Determined for Gas-Phase Fluoride Ion Transfer Reactions Involving BrO_3F, ClO_3F, BrO_2F, ClO_2F, AsF_5 and Sb_nF_{5n}

	$\Delta H^\circ_{\pm F^-}$ (kJ mol^{-1})
Enthalpies of F$^-$ Detachment	
$BrO_3F(g) \rightarrow BrO_3^+(g) + F^-(g)$	1005[a]
$ClO_3F(g) \rightarrow ClO_3^+(g) + F^-(g)$	999[a]
$BrO_2F(g) \rightarrow BrO_2^+(g) + F^-(g)$	903[a]
$ClO_2F(g) \rightarrow ClO_2^+(g) + F^-(g)$	895[a]
Enthalpies of F$^-$ Attachment	
$AsF_5(g) + F^-(g) \rightarrow AsF_6^-(g)$	-443[b]
$SbF_5(g) + F^-(g) \rightarrow SbF_6^-(g)$	-503[b]
$Sb_2F_{10}(g) + F^-(g) \rightarrow Sb_2F_{11}^-(g)$	-531[c]
$Sb_3F_{15}(g) + F^-(g) \rightarrow Sb_3F_{16}^-(g)$	-551[c]
Enthalpies of Reduction	
$BrO_3^+(g) \rightarrow BrO_2^+(g) + \frac{1}{2}O_2(g)$	-215[a]
$ClO_3^+(g) \rightarrow ClO_2^+(g) + \frac{1}{2}O_2(g)$	-145[a]

[a] Calculated using the Gaussian-2 method. [b] From ref 48. [c] From ref 46.

Table 8.7. Estimated[a] Lattice Enthalpies of Salts Containing the BrO_3^+, ClO_3^+, BrO_2^+ and ClO_2^+ Cations

Salt	V_m $(nm^3)^a$	ΔH_L° $(kJ\ mol^{-1})^b$	S° $(J\ mol^{-1}\ K^{-1})^c$
$[BrO_3][AsF_6]$	0.151	545	220
$[BrO_3][SbF_6]$	0.162	539	235
$[BrO_3][Sb_2F_{11}]$	0.268	473	379
$[BrO_3][Sb_3F_{16}]$	0.374	434	524
$[ClO_3][AsF_6]$	0.147	553	215
$[ClO_3][SbF_6]$	0.158	543	230
$[ClO_3][Sb_2F_{11}]$	0.264	475	374
$[ClO_3][Sb_3F_{16}]$	0.370	436	518
$[BrO_2][AsF_6]$	0.142	558	208
$[BrO_2][SbF_6]$	0.153	547	223
$[BrO_2][Sb_2F_{11}]$	0.259	477	367
$[BrO_2][Sb_3F_{16}]$	0.365	437	511
$[ClO_2][AsF_6](s)$	0.138	563	203
$[ClO_2][SbF_6](s)$	0.149	551	218
$[ClO_2][Sb_2F_{11}](s)$	0.255	479	362
$[ClO_2][Sb_3F_{16}](s)$	0.361	438	506

[a] The formula unit volume, V_m, for $[ClO_2][SbF_6]$ (0.149 nm^3) and $[BrO_2][SbF_6]$ (0.153 nm^3) were obtained from their crystallographic unit cells. The volumes of ClO_2^+ (0.028 nm^3) and BrO_2^+ (0.032 nm^3) were estimated by substitution of the volume of the SbF_6^- anion (0.121 nm^3, ref 536), from V_m. The estimated volume of ClO_3^+ (0.037 nm^3) was obtained from ref 544. The average difference in volumes of NO_x^+ (n = 1, 2) and ClO_x^+ (n = 2, 3) is 0.009 nm^3 and was used to estimate the volume of BrO_3^+ (0.041 nm^3) from the volume of BrO_2^+. The values of V_m for the remaining XO_2^+ and XO_3^+ salts were estimated from the sums of the cation and anion volumes (AsF_6^-, 0.110 nm^3, ref 536; $Sb_2F_{11}^-$, 0.227 nm^3, ref 309; $Sb_3F_{16}^-$, 0.333 nm^3, ref 309). [b] The lattice enthalpies (ΔH_L°) were calculated as described in ref 535. [c] The standard entropies were calculated as described in ref 537.

of reaction (eq 8.10) calculated for the formation of the XO_3^+ and XO_2^+ salts by the

$$\Delta H^\circ = \Delta H^\circ_{vap} + \Delta H^\circ_{F^-} + \Delta H^\circ_{red} - H^\circ_L \qquad (8.10)$$

reaction of the perhalyl fluorides with AsF_5 and $(SbF_5)_n$ (n = 1 - 3) are summarized in Table 8.8.

A method for estimating the absolute standard entropy of a salt from its unit volume has recently been reported by Jenkins and Glasser (eq 8.11).[537] The entropies of

$$S^\circ([XO_3][MF_6]) = kV_m + c \qquad (8.11)$$

the XO_2^+ and XO_3^+ salts under investigation are summarized in Table 8.7. When coupled with the known standard entropies of $BrO_3F(g)$ (299 J mol^{-1} K^{-1}),[175] $ClO_3F(g)$ (279 J mol^{-1} K^{-1}),[429] $AsF_5(g)$ (487 J mol^{-1} K^{-1}),[545] $SbF_5(l)$ (265 J mol^{-1} K^{-1})[545] and $O_2(g)$ (206 J mol^{-1} K^{-1}),[429] this method allows ΔS° (eq 8.12, 8.13) and ΔG° (eq 8.14) to be calculated

$$\Delta S^\circ = S^\circ([XO_3][MF_6]) - S^\circ(MF_5) - S^\circ(XO_3F) \qquad (8.12)$$

$$\Delta S^\circ = S^\circ([XO_2][MF_6]) + \tfrac{1}{2}S^\circ(O_2) - nS^\circ(MF_5) - S^\circ(XO_3F) \qquad (8.13)$$

$$\Delta G^\circ = \Delta H^\circ - T\Delta S^\circ \qquad (8.14)$$

for the reactions of interest. The values of ΔS° and ΔG° obtained for these reactions are summarized in Table 8.8. The large calculated enthalpies of fluoride ion abstraction from BrO_3F and ClO_3F are nearly counterbalanced by the large enthalpies of fluoride ion attachment to the Lewis acids and the lattice energies of the products, resulting in net reaction enthalpies that approach thermal neutrality (-16 to +63 kJ mol^{-1}), but are generally weakly endothermic.

It is noteworthy that the entropy term, which is often assumed to have a small effect on ΔG°, increases the endothermicity of these reactions by 94 to 170 kJ mol^{-1}. Consequently, the inability to prepare salts containing BrO_3^+ and ClO_3^+ by the reaction of the perhalyl fluoride with strong fluoride ion acceptors is consistent with the positive values of ΔG° calculated for the reactions of BrO_3F (92 - 233 kJ mol^{-1}) and ClO_3F

315

Table 8.8. Values of ΔH°, ΔS°, and ΔG° Calculated for Selected Reactions of XO_3F and XO_2F (X = Cl, Br) with AsF_5, SbF_5, Sb_2F_{10}, and Sb_3F_{15}

	ΔH° (kJ mol^{-1})	ΔS° (J mol^{-1} K^{-1})	ΔG° (kJ mol^{-1})
Formation of BrO_3^+ Salts:			
$BrO_3F(g) + AsF_5(g) \rightarrow [BrO_3][AsF_6](s)$	16	-566	185
$BrO_3F(g) + SbF_5(l) \rightarrow [BrO_3][SbF_6](s)$	-6	-329	92
$BrO_3F(g) + 2SbF_5(l) \rightarrow [BrO_3][Sb_2F_{11}](s)$	39	-450	173
$BrO_3F(g) + 3SbF_5(l) \rightarrow [BrO_3][Sb_3F_{16}](s)$	63	-570	233
Formation of ClO_3^+ Salts:			
$ClO_3F(g) + AsF_5(g) \rightarrow [ClO_3][AsF_6](s)$	6	-551	170
$ClO_3F(g) + SbF_5(l) \rightarrow [ClO_3][SbF_6](s)$	-16	-314	78
$ClO_3F(g) + 2SbF_5(l) \rightarrow [ClO_3][Sb_2F_{11}](s)$	31	-435	161
$ClO_3F(g) + 3SbF_5(l) \rightarrow [ClO_3][Sb_3F_{16}](s)$	55	-556	221
Formation of BrO_2^+ Salts:			
$BrO_3F(g) + AsF_5(g) \rightarrow [BrO_2][AsF_6](s) + \frac{1}{2}O_2(g)$	-208	-475	-66
$BrO_3F(g) + SbF_5(l) \rightarrow [BrO_2][SbF_6](s) + \frac{1}{2}O_2(g)$	-229	-238	-158
$BrO_3F(g) + 2SbF_5(l) \rightarrow [BrO_2][Sb_2F_{11}](s) + \frac{1}{2}O_2(g)$	-183	-359	-76
$BrO_3F(g) + 3SbF_5(l) \rightarrow [BrO_2][Sb_3F_{16}](s) + \frac{1}{2}O_2(g)$	-155	-480	-12
Formation of ClO_2^+ Salts:			
$ClO_3F(g) + AsF_5(g) \rightarrow [ClO_2][AsF_6](s) + \frac{1}{2}O_2(g)$	-149	-460	-12
$ClO_3F(g) + SbF_5(l) \rightarrow [ClO_2][SbF_6](s) + \frac{1}{2}O_2(g)$	-170	-223	-104
$ClO_3F(g) + 2SbF_5(l) \rightarrow [ClO_2][Sb_2F_{11}](s) + \frac{1}{2}O_2(g)$	-117	-344	-1
$ClO_3F(g) + 3SbF_5(l) \rightarrow [ClO_2][Sb_3F_{16}](s) + \frac{1}{2}O_2(g)$	-92	-465	47
Stabilities of $[XO_2][SbF_6]$:			
$BrO_2F(g) + SbF_5(l) \rightarrow [BrO_2][SbF_6](s)$	-116	-335	-16
$ClO_2F(g) + SbF_5(l) \rightarrow [ClO_2][SbF_6](s)$	-129	-340	-28

316

(78 - 221 kJ mol^{-1}) with AsF$_5$(g) and SbF$_5$(l). Moreover, there are distinctive minima in $\Delta H°$, $\Delta S°$ and $\Delta G°$ for the reactions that lead to the [XO$_3$][SbF$_6$] salts, indicating that the benefits of using the stronger fluoride ion affinities of Sb$_2$F$_{10}$ and Sb$_3$F$_{16}$ are offset by the lower lattice energies and greater entropies of the proposed Sb$_2$F$_{11}^-$ and Sb$_3$F$_{16}^-$ salts.

With the exception of the reaction of ClO$_3$F with Sb$_3$F$_{15}$, which is predicted to be mildly endothermic ($\Delta G°$, 47 kJ mol), reactions involving the reduction of the perhalyl fluorides and the formation of the BrO$_2^+$ (-12 to -158 kJ mol^{-1}) and ClO$_2^+$ (47 to -194 kJ mol^{-1}) salts are predicted to be exothermic. The differences between the $\Delta G°$ values corresponding to the formation of the XO$_3^+$ and XO$_2^+$ salts is primarily a result of the large gas-phase enthalpies of reduction calculated for BrO$_3^+$ (-215 kJ mol^{-1}) and ClO$_3^+$ (-145 kJ mol^{-1}), however, the higher lattice energies calculated for the XO$_2^+$ salts and smaller entropy changes associated with the formation of these salts also make significant contributions. The larger magnitude of $\Delta H°_{red}$ for BrO$_3^+$ compared with that of ClO$_3^+$ is in agreement with the observation that ClO$_3$F fails to react with SbF$_5$(l), whereas the reaction of BrO$_3$F with SbF$_5$(l) is spontaneous and rapid. The failure of BrO$_3$F to undergo reductive elimination of O$_2$ in the presence of SbF$_5$ dissolved in HF or in AsF$_5$(l) and the general inertness of ClO$_3$F suggests that a kinetic barrier likely impedes reductive elimination of O$_2$ from the perhalyl fluorides. These trends also suggest that the barrier is only overcome or reduced in the presence of (SbF$_5$)$_n$ (n > 1), producing [BrO$_2$][Sb$_n$F$_{5n+1}$], which can subsequently be converted to the more stable [BrO$_2$][SbF$_6$] salt. The observation that ClO$_3$F does not undergo a similar reaction may be attributed to the near-zero free energy change calculated for the formation of [ClO$_2$][Sb$_2$F$_{11}$] and to the likelihood that the kinetic barrier is higher for ClO$_3$F than it is for BrO$_3$F. The latter hypothesis is consistent with the remarkable inertness of ClO$_3$F, as illustrated by its

failure to react with metallic sodium at temperatures below 300 °C[547] and strong fluoride ion donors such as [N(CH$_3$)$_4$][F] (see Chapter 7), NO$_2$F[217] and CsF.[217]

Given the high enthalpies of fluoride abstraction calculated for XO$_3$F, which contributed to the inability to prepare salts containing the XO$_3^+$ cations, the stabilities of the [XO$_2$][SbF$_6$] salts with respect to dissociation (eq 8.15) are also of interest. The

$$[XO_2][MF_6] \rightarrow XO_2F + SbF_5 \qquad\qquad (8.15)$$

thermochemistries of these reactions (Table 8.8) were investigated by analogy with the method used to investigate the formation of the [XO$_3$][SbF$_6$] salts using the known standard entropies of BrO$_2$F (294 J mol^{-1} K^{-1})[548] and ClO$_2$F (279 J mol K^{-1}).[548] The calculated free energies of dissociation for [BrO$_2$][SbF$_6$] (16 kJ mol^{-1}) and [ClO$_2$][SbF$_6$] (28 kJ mol^{-1}) are moderately positive indicating that both salts are stable under standard conditions. The relative stabilities predicted for [BrO$_2$][SbF$_6$] and [ClO$_2$][SbF$_6$] are in qualitative agreement with the stabilities of [BrO$_2$][SbF$_6$], [BrO$_2$][Sb$_{22.4}$F$_{12.2}$],[213] [ClO$_2$][SbF$_6$], [ClO$_2$][Sb$_2$F$_{11}$],[522] [ClO$_2$][RuF$_6$][508] and [ClO$_2$][AsF$_6$][507] at ambient temperature, and the instabilities noted for [BrO$_2$][AsF$_6$],[207,214] [BrO$_2$][BF$_4$],[214] and [ClO$_2$][BF$_4$].[507,523] The XO$_2^+$ salts contrast to the unknown XO$_3^+$ salts in this respect, because the latter salts are enthalpically unstable with respect to dissociation to XO$_3$F and the parent Lewis acid, and therefore are not stabilized by reduction of the TΔS° term.

8.3.2. Geometries of the XO$_2^+$ and XO$_3^+$ Cations (X = Cl, Br)

The energy-minimized geometries of the XO$_2^+$ and XO$_3^+$ cations were calculated by use of the HF, MP2, MPW1PW91 and QCISD methods and are summarized in Table 8.9. A comparison of the calculated geometries of BrO$_2^+$ and ClO$_2^+$ with those obtained from the crystal structures of the [XO$_2$][SbF$_6$] salts (Tables 8.2) reveals similar trends between the two species. The experimental X-O bond lengths of the XO$_2^+$ cations are bracketed by the HF and MPW1PW91 methods, which underdetermined and

Table 8.9. Calculated Bond Lengths (Å) and Bond Angles (deg) of the BrO_3^+, ClO_3^+, BrO_2^+ and ClO_2^+ Cations

Method	XO_2^+				XO_3^+			
	Br-O	O-BrO	Cl-O	O-Cl-O	Br-O	O-Br-O	Cl-O	O-Cl-O
HF/6-311G(d)	1.529	116.1	1.372	119.9	1.537	120	1.537	120
MP2/6-31G*	1.656[a]	117.5[a]	1.492	122.4				
MP2/6-311G(d)	1.635	118.6	1.478	121.8	1.601	120	1.478	120
MP2/TZ2P	1.630[b]	117.6[b]						
MP4/TZ2P	1.679[b]	122.0[b]						
MPW1PW91/DZVP	1.607	116.3	1.435	120.4	1.609	120	1.434	120
QCISD/6-31G*	1.638[a]	116.0[a]	1.460	120.2				
QCISD/6-311G(2d)	1.603[a]	116.1[a]	1.426	121.0	1.595	120	1.416	120
QCISD/6-311+G(3df)	1.584[a]	115.6[a]						
CCSD(T)/TZ2P	1.619[b]	115.8[b]						
CCSD(T)/6-311G(2df)	1.607[b]	115.6[b]						
CCSD(T)/6-311+G(3df)	1.605[a]	115.5[a]						
Expt. (min)	1.595(2)	112.0(1)	1.28(3)	117.2(9)				
Expt. (max)	1.6135	117.5	1.405(1)	122(2)				

[a] From ref 524. [b] From ref 526.

overdetermined the bond lengths, respectively. The MP2 method provided poorer agreement with the experimental bond lengths of the BrO_2^+ cation than the HF and MPW1PW91 methods, and even longer bond lengths were predicted using the computationally more expensive MP4 method.[526] The anomalously long Cl-O bond lengths calculated for the ClO_2^+ cation by use of the MP2/6-31G* and MP2/6-311G(d) methods suggests that the MP2 and MP4 perturbation methods are also less than ideal for this cation. Detailed studies of the BrO_2^+ cation have revealed that the Br-O bond length can be accurately calculated when the CCSD(T)[524,526] and QCISD[526] methods are used. Although the choice of basis set used with these methods has a minor effect on the bond lengths of the BrO_2^+ cation, the calculations utilizing the 6-311G basis set with a polarization function provided similar results and were within an acceptable range of the experimental value. Interestingly, the Cl-O bond lengths obtained by use of the QCISD method (1.426 - 1.460 Å) were moderately longer than the experimental values (1.28(3) - 1.405(1) Å), contrasting with the seemingly excellent agreement obtained for the BrO_2^+ cation when the same method was used. The bond angles of the XO_2^+ cations were overestimated by 2 to 5° by each of the computational methods used in the present and previous studies, however, the small ranges among the calculated O-Br-O (116.1 - 118.6°) and O-Cl-O (119.9 - 121.8°) angles suggests that this parameter is largely insensitive to the computational method used.

The inability to prepare and structurally characterize salts containing the XO_3^+ cations prevents a direct assessment of the calculated bond lengths of these trigonal planar cations. However, on the basis of the trends noted for the XO_2^+ cations (*vide supra*), the Br-O bond lengths of BrO_3^+ are predicted to be within the range defined by the HF (1.537 Å) and MPW1PW91 (1.609 Å) methods and are likely very similar to the value obtained using the QCISD method (1.595 Å). By the same argument, the Cl-O

bond lengths of ClO_3^+ are predicted to lie within the range defined by the HF (1.372 Å) and MPW1PW91 (1.451 Å) methods and close to, although perhaps slightly less than, the value obtained with the QCISD method (1.416 Å). It is noteworthy that the bond lengths predicted for the XO_3^+ cations are consistently shorter than those of the $BrO_3F_2^-$ (HF, 1.590; MPW1PW91, 1.639 Å) and $ClO_3F_2^-$ (HF, 1.431; MPW1PW91, 1.465 Å) anions determined by the same method (see section 7.3.1.1). The shorter bond lengths predicted for the XO_3^+ cations, relative to those of the $XO_3F_2^-$ anions, which also have trigonal planar oxygen arrangements, are attributed to their positive charges, which result in shorter and less polar bonds.

8.3.3. Vibrational Frequencies of the XO_2^+ and XO_3^+ Cations (X = Cl, Br)

Two prior studies have investigated the vibrational frequencies of the BrO_2^+ cation using the MP2, MP4, QCISD and CCSD(T) methods with various basis sets,[524,526] however, these studies did not include the use of the computationally less demanding HF and density functional methods. Despite the extensive structural characterization of several salts containing the ClO_2^+ cation, the vibrational frequencies of this cation have not been modeled using modern computational methods. The present study remedies these omissions by the calculation of the vibrational frequencies of the BrO_2^+ cation by use of HF and MPW1PW91 methods, and of the ClO_2^+ cation by use of HF, MP2, MPW1PW91 and QCISD methods (Table 8.10).

As is usually the case,[323] the HF frequencies are significantly higher than the experimental values and reflect the short X-O bond lengths that are generally obtained by use of this method. The application of a 0.8953 scaling factor[323] improves the correlation of the $v_2(A_1)$ frequencies considerably for both XO_2^+ cations, however, the $v_1(A_1)$ and $v_3(B_2)$ frequencies remain overestimated by an average of 113 and 135 cm^{-1}, respectively.

Table 8.10. Calculated Vibrational Frequencies[a] of the BrO_2^+ and ClO_2^+ Cations

Method	BrO_2^+			ClO_2^+		
	$v_1(A_1)$	$v_2(A_1)$	$v_3(B_2)$	$v_1(A_1)$	$v_2(A_1)$	$v_3(B_2)$
HF/6-311G(d)	1116.2(100)[3]	433.3(3)[35]	1224.4(18)[57]	1312.8(100)[18]	610.0(4)[54]	1597.4(17)[139]
Scaled HF	999	388	1096	1176	546	1429
MP2/6-31G*	870[b]	325[b]	1161[b]	915.9(100)[<1]	439.9(0)[18]	1188.3(1)[169]
MP2/6-311G(d)	844.0(100)[2]	325.9(0)[10]	1072.9(5)[758]	901.4(100)[<1]	446.9(0)[20]	1173.1(1)[136]
MP2/TZ2P	854[c]	323[c]	992[c]			
MP4/TZ2P	788[c]	270[c]	1014[c]			
MPW1PW91/DZVP	939.6(100)[<1]	348.7(14)[14]	1016.4(33)[28]	1097.7(100)[5]	503.1(14)[27]	1340.4(31)[71]
QCISD/6-31G*	812[b]	330[b]	899[b]	964.6[<1]	472.5[24]	1226.9[44]
QCISD/6-311G(2d): (^{79}Br, ^{35}Cl)	865.7[2][b]	349.6[13][b]	968.4[21][b]	1019.5[3]	503.7[22]	1290.4[53]
(^{81}Br, ^{37}Cl)	864.5[2]	348.8[13]	965.6[20]	1014.0[3]	499.9[21]	1276.1[50]
QCISD/6-311+G(3df)	928[b]	369[b]	1029[b]			
CCSD(T)/TZ2P	822[c]	332[c]	910[c]			
CCSD(T)/6-311+G(3df)	862[b]	350[b]	955[b]			
expt. range	862 - 884	372 - 382	931 - 947	1039 - 1065	518 - 521	1230 - 1308

[a] Frequencies are given in cm^{-1}. Relative Raman intensities are given in parentheses and are scaled such that the most intense band has value of 100. Absolute infrared intensities (km mol^{-1}) are given in square brackets. [b] From ref 524. [c] From ref 526.

The vibrational frequencies obtained for the XO_2^+ cations using the MPW1PW91 method were in reasonable agreement with the range of frequencies obtained experimentally. Using this method, the $v_1(A_1)$ and $v_3(B_2)$ stretching frequencies of BrO_2^+ were overestimated by 56 and 69 cm^{-1}, respectively, while the $v_2(A_1)$ bending mode was underestimated by 23 cm^{-1}. The same trends were observed for ClO_2^+ using the MPW1PW91 method, however, the errors were approximately 50% smaller than those of BrO_2^+, reflecting the less complex electronic structure of ClO_2^+.

The MP2 vibrational frequencies of the BrO_2^+ cation have been determined with a variety of basis sets.[524,526] The frequencies of the $v_1(A_1)$ and $v_2(A_1)$ modes do not exhibit strong basis set dependencies and were calculated with reasonable accuracy, whereas the frequency of $v_3(B_2)$ decreased substantially as the quality of the basis set improved, and only came within 45 cm^{-1} of the experimental range when the TZVP basis set was used. Interestingly, the vibrational frequencies of the BrO_2^+ cation obtained using the MP4/TZVP method[526] were less accurate than those obtained using the MP2/TZVP method.[526] The vibrational frequencies of the ClO_2^+ cation exhibited little variation for the two basis sets that were investigated (6-31G*, 6-311G(d)) with the MP2 method, and surprisingly exhibited poorer agreement with the experimental spectra, than obtained for BrO_2^+.

The computational methods that accounted for the accessible excited electronic states, (i.e., QCISD and CCSD(T)) provided the best overall modeling of vibrational frequencies for the BrO_2^+ cation.[524,526] Both methods exhibited minor basis set dependencies resulting in positive frequency shifts for each of the three vibrational modes of BrO_2^+ as the quality of the basis set improved. The best correlation for the BrO_2^+ cation was obtained from the QCISD/6-31G(2d) method, which provided $v_1(A_1)$ and $v_3(B_2)$ stretching frequencies within the experimental range and underestimated the

$\nu_2(A_1)$ frequency by only 22 cm^{-1}. The calculated frequency shifts for $^{79,81}BrO_2^+$ isotopomers are in excellent agreement with the experimental spectrum of $[BrO_2][SbF_6]$, in which splitting of cation bands is only observed for the asymmetric stretch (see section 8.2.4). On the basis of the results obtained for the BrO_2^+ cation, the vibrational frequencies of the ClO_2^+ cation were calculated by use of the QCISD method. The use of the 6-311G(2d) basis set again provided the best correlation with experimental spectra, with $\nu_1(A_1)$ and $\nu_2(A_1)$ being underestimated by 19 and 14 cm^{-1} respectively, and $\nu_3(B_2)$ lying within the observed range. As anticipated from the larger relative mass difference of ^{35}Cl and ^{37}Cl, when compared with ^{79}Br, and ^{81}Br, the isotopic frequencies shifts determined by use of the QCISD/6-311G(2d) method are larger for ClO_2^+. The calculated isotopic splittings for the $\nu_1(A_1)$ and $\nu_3(B_2)$ stretching modes are in good agreement with those observed experimentally, however, the 4 cm^{-1} splitting calculated for $\nu_2(A_2)$ is not resolved in the Raman spectra of the ClO_2^+ salts (see section 8.2.4).

Each of the computational methods correctly predicts the $\nu_1(A_1)$ band to be the most intense feature in the Raman spectra of the XO_2^+ cations. The correspondence is not as good for the two weaker modes, for which the calculations predict $\nu_3(B_2)$ to be more intense than $\nu_2(A_1)$, whereas these bands are generally have similar peak heights in the experimental spectra.

The trigonal planar XO_3^+ cations have six fundamental modes of vibration (Γ_{vib} = $A_1' + A_2'' + 2E'$) corresponding to three Raman-active bands (A_1', $2E'$) and three infrared active bands (A_2'', $2E'$). The vibrational frequencies of the XO_3^+ cations have been determined by use of the HF, MPW1PW91, MP2 and QCISD methods (Table 8.11). The frequencies of the XO_3^+ cations obtained using the QCISD/6-311G(2d) method are expected to provide the most reliable frequencies based on the results for the XO_2^+ cations (*vide supra*). The observation that the $\nu_1(A_1)$ and $\nu_3(B_2)$ X-O stretching

Table 8.11. Vibrational Frequencies[a] Calculated for the Unknown BrO_3^+ and ClO_3^+ Cations

Mode	Description	HF[b,c]	scaled HF[d]	MP2[b,c]	MPW1PW91[b,c]	QCISD
BrO_3^+						
$\nu_1(A_1')$	$\nu_s(BrO_3)$	964.6(100)[0]	863.7	908.0(34)[0]	855.4(100)[0]	824.8[0]
$\nu_2(A_2'')$	δ(o.o.p. BrO_3)	292.7(0)[24]	262.1	272.8(0)[6]	251.2(0)[8]	241.0[7]
$\nu_3(E')$	$\nu_{as}(BrO_3)$	1054.1(19)[94]	943.8	1251.4(100)[14]	974.9(49)[46]	920.3[22]
$\nu_4(E')$	δ(i.p. O-Br-O)	390.3(19)[56]	349.5	334.3.(8)[24]	319.3(26)[24]	331.6[26]
ClO_3^+						
$\nu_1(A_1')$	$\nu_s(ClO_3)$	1125.1(100)[0]	1007.4	910.0(28)[0]	964.3(100)[0]	949.5[0]
$\nu_2(A_2'')$	δ(o.o.p. ClO_3)	508.8(0)[40]	455.6	427.5(0)[10]	433.3(0)[14]	467.8[12]
$\nu_3(E')$	$\nu_{as}(ClO_3)$	1441.9(26)[372]	1291.1	1390.0(100)[28]	1278.0(47)[160]	1258[136]
$\nu_4(E')$	δ(i.p. O-Cl-O)	580.2(18)[78]	519.5	462.1(13)[42]	484.0(27)[42]	510.4[20]

[a] Frequencies are given in cm^{-1}. [b] Raman intensities are given in parentheses and are scaled to the most intense mode, which is given a value of 100. [c] Absolute infrared intensities (km mol^{-1}) are in square brackets. [d] Scaled by 0.8953 as recommended in ref 323.

frequencies, obtained using the scaled HF and unscaled MPW1PW91 methods are moderately higher than those obtained with the QCISD method suggests correlations between the experimental and theoretical frequencies are consistent for the XO_2^+ and XO_3^+ cations. The consistencies of these computational trends are further supported by the MP2 calculations, which predict higher frequencies for the asymmetric X-O stretches $(v_3(B_2))$ and lower frequencies for the symmetric X-O stretches $(v_1(A_1))$ when compared with those obtained from the QCISD method. Although the XO_2^+ cations do not have bending modes resembling the out-of-plane bends $(v_2(A_2''))$ of the XO_3^+ cations, the limited variations of the $v_2(A_2'')$ and $v_4(E')$ bending modes observed among the scaled HF and unscaled MPW1PW91, MP2 and QCISD methods $(i.e., < 31 \text{ cm}^{-1})$ imply that these modes are not strongly dependent on the method used and provide reasonable estimates for the frequencies of these modes. The ordering of the vibrational frequencies predicted for the XO_3^+ cations are in qualitative agreement with other trigonal planar AX_3 species,[549] exhibiting asymmetric $v_3(E')$ stretches that are higher in energy than the symmetric $v_1(A_1')$ stretches, and $v_2(A_2'')$ out-of-plane bending frequencies that are lower in energy than the in-plane $v_4(E')$ bends. The HF and MPW1PW91 methods predict the symmetric XO_3 stretching mode to be the most intense feature in the Raman spectra of these cations as is commonly the case, however, the relative intensities of $v_1(A_1')$ and $v_3(E'')$ obtained by the MP2 method are reversed.

8.4. Conclusion

The fluoride ion donor properties of BrO_3F and ClO_3F have been investigated by their reactions with neat SbF_5. The inability to form salts containing the BrO_3^+ or ClO_3^+ cations is in qualitative agreement with the positive values of ΔG° estimated for these reactions, and is strongly related to the high enthalpy of fluoride ion detachment from the parent perhalyl fluorides $(ca. 1000 \text{ kJ mol}^{-1})$. The spontaneous reaction of BrO_3F with

neat SbF_5 or SbF_5 dissolved in AsF_5 to form $[BrO_2][Sb_nF_{5n+1}]$ contrasts with the inertness of ClO_3F towards neat SbF_5. Although estimates of $\Delta G°$ for the reactions of BrO_3F and ClO_3F with SbF_5 to form the $[XO_2][SbF_6]$ salts with the evolution of O_2 suggest both reactions should be spontaneous, the reaction is 53 kJ mol^{-1} more exothermic for BrO_3F than it is for ClO_3F. Comparisons of $\Delta G°$ for reactions involving $(SbF_5)_n$ (n = 1 - 3) and the observation that BrO_3F only reacts with polymeric SbF_5 suggest that the contrasting behaviours of BrO_3F and ClO_3F are kinetic in origin.

The X-ray crystal structures of $[BrO_2][SbF_6]$ and $[ClO_2][SbF_6]$ were determined for the first time, and the former structure represents the first crystallographic characterization of the BrO_2^+ cation. The earlier theoretical analyses of the structure and vibrational frequencies of the BrO_2^+ cation have been extended to include the HF and MPW1PW91 methods, and the modeling of these properties for the ClO_2^+ cation have been completed for the first time by use of the HF, MPW1PW91, MP2, and QCISD methods. Of these methods, the QCISD/6-311G(2d) calculations provided the most reliable correlations with the experimental structures and vibrational frequencies of the BrO_2^+ and ClO_2^+ cations and likely to provide reliable estimates of the geometric parameters and vibrational frequencies of the BrO_3^+ and ClO_3^+ cations.

CHAPTER 9

CONCLUSIONS AND DIRECTIONS FOR FUTURE WORK

9.1. Conclusions

Prior to the present work, Kr(II) compounds were predominately studied by spectroscopic techniques, and the only compound of krypton for which accurate geometric parameters were known was KrF_2.[127-129,279] The present work has significantly extended the structural characterization of Kr(II) compounds by the determination of the low-temperature single crystal X-ray structures of α-KrF_2, and several salts containing the KrF^+ and $Kr_2F_3^+$ cations. The precision of the geometric parameters obtained for the fluorine-bridged KrF^+ salts, exceeded those of the analogous $[XeF][MF_6]$ (M = Ru,[71] As[72]) and $[XeF][Sb_2F_{11}]$ salts,[73] and prompted a more extensive and precise study of the XeF^+ salts. In the present study, the crystal structures of $[XeF][MF_6]$ (M = As, Sb, Bi) and $[XeF][M_2F_{11}]$ (M = Sb, Bi) were determined with precisions comparable to their krypton analogues. The determination of the crystal structure of $[XeF][Bi_2F_{11}]$ is particularly noteworthy because it represents the first crystallographic study of the $Bi_2F_{11}^-$ anion.

Previous studies have indicated that the relative fluoride ion affinities of the pnicogen pentafluorides and their dimers may be ranked by comparison of the $Ng-F_t$ stretching frequencies of the fluorine-bridged $[NgF][MF_6]$ (Ng = Kr, Xe) and $[NgF][M_2F_{11}]$ salts. The present work has extended this concept by comparison of the $Ng-F_t$ and $Ng--F_b$ bond lengths determined for the KrF^+ and XeF^+ salts. In general, the $Ng-F_t$ bond lengths were insensitive to the counter anion and were a poor indicator of the

Lewis acid strength of the NgF^+ cation or of the fluoride ion acceptor properties of the pentafluoride. The $Ng\text{--}F_b$ bond length is a more reliable indicator of Lewis acid strength and indicates that the fluoride ion affinity of the fluorides investigated increases in the order $BiF_5 < AsF_5 < Bi_2F_{10} < SbF_5 \approx AuF_5 < Sb_2F_{10}$.

Several significant contributions to the limited chemistry of bromine(VII) have also been made in the present work. The octahedral geometries of the XF_6^+ (X = Cl, Br, I) cations had previously been determined by vibrational spectroscopy[36,220,221,352] and multi-NMR (^{19}F, ^{127}I)[36,166,221] spectroscopy. The present work has extended the characterizations of these cations in HF solution by the acquisition of the previously unreported $^{35,37}Cl$, and $^{79,81}Br$ NMR spectra, and the determination of their $^{35,37}Cl$, $^{79,81}Br$ and ^{127}I spin-lattice relaxation times. The bond lengths of the XF_6^+ cations have also been measured for the first time, by the X-ray structure determinations of $[XF_6][Sb_2F_{11}]$ (X = Cl, Br, I).

The previously unknown fluoride ion acceptor properties of BrO_3F have been investigated in detail and have permitted the synthesis of several salts containing the $BrO_3F_2^-$ anion. The $BrO_3F_2^-$ anion is the first Br(VII) species to be isolated since the discoveries of BrO_4^- (1968),[161] BrO_3F (1969)[162] and BrF_6^+ (1974),[36,137] and is only the fourth species of Br(VII) to have been isolated in significant quantities. The trigonal bipyramidal geometry and geometric parameters of the $BrO_3F_2^-$ anion have been unambiguously determined by use of Raman, infrared, and ^{19}F NMR spectroscopies and by single crystal X-ray diffraction. Furthermore, of the three oxide fluorides known to possess D_{3h} symmetry (i.e., XeO_3F_2, OsO_3F_2, $BrO_3F_2^-$), $BrO_3F_2^-$ is the only one for which bond lengths have been determined.

The poor fluoride ion donor properties BrO_3F[207] have been reaffirmed in the present work, which demonstrates that $[BrO_3][SbF_6]$ cannot be synthesized by reaction of

BrO_3F with liquid SbF_5. Instead, the reaction yields $[BrO_2][SbF_6 \cdot nSbF_5]$, contrasting with the inertness of BrO_3F towards MF_5 (M = As, Sb) in HF solution,[207] and the inertness of ClO_3F towards liquid SbF_5. A combination of electronic structure calculations and volume-based empirical relationships have been used to investigate the thermodynamics of these reactions, and account for the inability to prepare salts containing the XO_3^+ cations, and the spontaneous reduction of BrO_3F by liquid SbF_5.

A fully ordered low-temperature modification of $[O_2][AuF_6]$ has also been identified for the first time by the use of single crystal X-ray diffraction and variable temperature Raman spectroscopy. In concert with the calculated vibrational frequencies of the gas-phase AuF_6^- anion, the low-temperature Raman spectrum of α-$[O_2][AuF_6]$ has been used to reassign the $\nu_2(E_g)$ stretching frequency of the anion.

Throughout this work, electronic structure calculations have been used to model the geometries, vibrational frequencies, atomic charges, bond orders and thermodynamic stabilities of the compounds studied experimentally. These studies have reaffirmed the general shortcomings of the HF method, and have identified anomalous X-O stretching frequency trends for the oxide fluorides of bromine and chlorine at the HF and MP2 levels of theory. The best correlations to the experimental results were generally obtained with the density functional and configuration interaction based methods. The continual refinement of these methods and the use of larger and more accurate basis sets are expected to increase their accuracies, and will enhance their usefulness in the study of fluorides and oxide fluorides.

9.2. Directions for Future Work

The successful characterization of KrF_2, KrF^+ and $Kr_2F_3^+$ by single crystal X-ray diffraction warrants the use of this technique for the study of additional Kr(II) compounds. The Lewis base properties of KrF_2 should be investigated in greater detail to

establish a stronger relationship between the Kr-F bond lengths and the fluoride ion acceptor properties of the parent Lewis acid. The crystal structures of $[KrF][Sb_2F_{11}]$, which is predicted to be the most ionic KrF^+ salt known, and the covalent $KrF_2 \cdot MOF_4$ (M = Cr, Mo, W) adducts[81,124] would contribute significantly to this relationship, as would the syntheses and characterizations of the presently unknown adducts of KrF_2 with divalent metal cations (eq 9.1). By analogy with the xenon analogues, for which n ranges from 2.5 to 4,[85,86,88-90] the Kr-F bonds of the A^{2+} adducts are anticipated to be highly

$$[A][MF_6]_2 + KrF_2 \xrightarrow{HF} [A(KrF_2)_n][MF_6]_2$$

$$(A = Pb, Sr, Ca, Ba, Cd; M = As, Sb) \qquad (9.1)$$
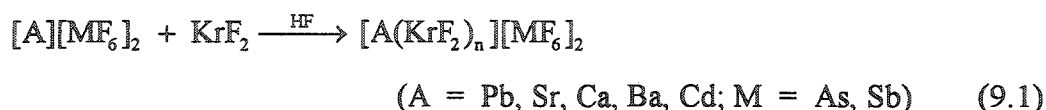
symmetric and similar to those of KrF_2. The characterizations of $Kr(OTeF_5)_2$[136] and salts containing the $RCN-KrF^+$ (R = H, CF_3, C_2F_5, $n-C_3F_7$)[51,98] cations by low-temperature X-ray diffraction should also be attempted to establish accurate experimental Kr-O and Kr-N bond lengths for the first time. These studies are expected to be very challenging because of the thermal sensitivity of these species, particularly $Kr(OTeF_5)_2$, which has yet to be isolated in the solid state and rapidly decomposes at temperatures above -78 °C.[136]

Attempts should be made to establish the dimorphism of $[Cs][BrO_3F_2]$ by single crystal X-ray diffraction. The absence of vibrational mode splitting in the Raman spectrum of $\alpha-[Cs][BrO_3F_2]$ suggests that this morphology crystallizes in a highly symmetric space group and that the number of anions in the unit cell is small, whereas the β-phase likely has a lower symmetry unit cell and a larger value of Z. The determinations of both morphologies would assist in establishing whether the vibrational splittings observed for $\beta-[Cs][BrO_3F_2]$ and the lighter alkali metal salts are related to minor distortions of the anion or to vibrational coupling withing the unit cell.

High-level electronic structure calculations have indicated that the preparation of BrO_2F_3 should be feasible by the oxidative fluorination of BrO_2F (see Appendix B).

Although KrF_2, KrF^+, and $Xe_2F_{11}^+$ do not oxidize BrO_2F to BrO_2F_3 or $BrO_2F_2^+$, and the fluorination of BrO_2F at elevated temperatures can be ruled out on account of the limited stability of BrO_2F, the use of the potent low-temperature oxidative fluorinating agent O_2F_2 may provide a straightforward route to BrO_2F_3 at low temperature (eq 9.2). The

$$BrO_2F + O_2F_2 \rightarrow BrO_2F_3 + O_2 \qquad (9.2)$$

synthesis of BrO_2F_3 should also be attempted by the low-temperature oxidative fluorination of BrO_2F under photolytic conditions (eq 9.3), however, the viability of this

$$BrO_2F + F_2 \xrightarrow{\text{UV}} BrO_2F_3 \qquad (9.3)$$

approach will depend on the photo-stabilities of BrO_2F and BrO_2F_3. Preliminary electronic structure calculations in the present work predict that BrO_2F_3 should behave both as a fluoride ion donor and as a fluoride ion acceptor. The Lewis base properties predicted for BrO_2F_3 would parallel those already demonstrated for ClO_2F_3, suggesting that salts containing the $BrO_2F_2^+$ cation may be prepared according to eq 9.4. Although

$$BrO_2F_3 + SbF_5 \xrightarrow{\text{HF}} [BrO_2F_2][SbF_6] \qquad (9.4)$$
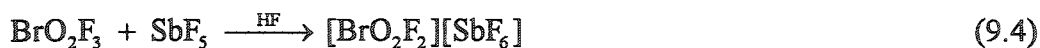
the $ClO_2F_4^-$ anion remains unknown, the favourable fluoride ion acceptor properties predicted for BrO_2F_3 indicate that the fluoride ion acceptor properties of this oxide fluoride may parallel those of IO_2F_3.[550-556] Consequently, $HOBrOF_4$ may be isolable by reaction of BrO_2F_3 with HF (eq 9.5), whereas $BrO_2F_4^-$ containing salts could be prepared by the reaction of BrO_2F_3 with suitable sources of fluoride (eq 9.6). Unambiguous

$$BrO_2F_3 + HF \rightarrow HOBrOF_4 \qquad (9.5)$$

$$BrO_2F_3 + [M][F] \xrightarrow{\text{CH}_3\text{CN}} [M][BrO_2F_4] \quad (M = N(CH_3)_4, Cs, Rb, K) \qquad (9.6)$$

characterization of BrO_2F_3, which may exist as a dimer by analogy to IO_2F_3,[553,557-559] and its $HBrO_2F_4$, $BrO_2F_2^+$, and $BrO_2F_4^-$ derivatives should be possible by means of standard spectroscopic techniques (Raman, infrared, ^{19}F NMR) and low-temperature single crystal X-ray diffraction.

REFERENCES

1. Blondel, C.; Cacciani, P.; Delsart, D.; Trainham, R., *Phys. Rev. A*, **1989**, *40*, 3698.
2. Drzaic, P. S.; Marks, J.; Brauman, J. I., In *Gas Phase Ion Chemistry*, Browers, M. T. ed.; Academic Press: Orlando, **1984**, *Vol. 3*, p. 167.
3. Determined from the free energies of formation of F_2 and F^- provided In *NIST JANAF Thermochemical Tables 4th Ed.*, Chase, M. W., ed.; American Chemical Society: New York, **1998**, pp. 1053, 1099.
4. Colbourn, E. A.; Dagenais, M.; Douglas, A. E.; Raymonda, J. W., *Can. J. Phys.*, **1976**, *54*, 1343.
5. Mercier, H. P. A.; Sanders, J. C. P.; Schrobilgen, G. J.; Tsai, S. S., *Inorg. Chem.*, **1993**, *32*, 386.
6. Malm, J. G.; Chernick, C. L., *Inorg. Synth.*, **1966**, *88*, 254.
7. Chernick, C. L.; Malm, J. G., *Inorg. Synth.*, **1966**, *8*, 258.
8. Lutar, K.; Šmalc, A., *Eur. J. Solid State Inorg. Chem.*, **1991**, *28*, 631.
9. Šmalc, A.; Lutar, K.; Slivnik, J., *J. Fluorine Chem.*, **1975**, *6*, 287.
10. Malone, T. J.; McGee, H. A. Jr., *J. Phys. Chem.*, **1965**, *69*, 4338.
11. Gunn, S. R., *J. Am. Chem. Soc.*, **1966**, *8*, 254.
12. Gunn, S. R., *J. Phys. Chem.*, **1967**, *71*, 2934.
13. Streng, L. V.; Streng. A. G., *Inorg. Chem.*, **1966**, *5*, 328.
14. Slivnik, J.; Šmalc, A.; Lutar, K.; Žemva, B.; Frlec, B., *J. Fluorine Chem.*, **1975**, *5*, 273.
15. Šmalc, A.; Lutar, K.; Žemva, B., *Inorg. Synth.*, **1992**, *29*, 11.
16. Kinkead, S. A.; FitzPatrick, J. R.; Foropoulos Jr., J., Kissane, R. J.; Purson, J. D., *ACS Symp. Ser.*, **1994**, *555*, 40.
17. Artyukhov, A. A.; Legasov, V. A.; Makeev, G. N.; Smirnov, B. M.; Chaivanov, B. B., *Khim, Vys,. Energ.*, **1976**, *10*, 512.; *High Energy Chem.*, **1976**, *10*, 450.
18. Artyukhov, A. A.; Legasov, V. A.; Makeev, G. N.; Chaivanov, B. B., *Khim. Vys. Energ.*, **1977**, *11*, 89; *High Energy Chem.*, **1977**, *11*, 70.
19. Schreiner, F.; Malm, J. G.; Hindman, J. C., *J. Am. Chem. Soc.*, **1965**, *87*, 25.
20. Sessa, P. A.; McGee, H. A. Jr., *J. Phys. Chem.*, **1969**, *73*, 2078.
21. Frlec, B.; Holloway, J. H., *Inorg. Chem.*, **1976**, *15*, 1263.
22. Bezmel'nitsyn, V. N.; Legasov, V. A.; Chaivanov, B. B., *Dokl. Akad. Nauk. SSSR*, **1977**, *235*, 96; *Dokl. Chem.*, **1977**, *235*, 365.
23. Lehmann, J. F.; Dixon, D. A.; Schrobilgen, G. J., *Inorg. Chem.*, **2000**, *40*, 3002.
24. MacKenzie, D. R., *Science*, **1963**, *141*, 1171.
25. MacKenzie, D. R.; Fajer, J., *Inorg. Chem.*, **1966**, *5*, 699.
26. Court, T. L.; Dove, M. F. A., *J. Chem. Soc., Chem. Comm.*, **1971**, 726.
27. Court, T. L.; Dove, M. F. A., *J. Chem. Soc., Dalton Trans.*, **1973**, 1995.
28. Christe, K. O., *Inorg. Chem.*, **1986**, *25*, 3721.

29. Christe, K. O.; Wilson, R. D., *Inorg. Chem.*, 1987, *26*, 2554.
30. Lucier, G.; Shen, C.; Casteel, W. J. Jr.; Chacón, L.; Bartlett, N., *J. Fluorine Chem.*, 1995, *72*, 157.
31. Schroer, T.; Christe, K. O., *Inorg. Chem.*, 2001, *40*, 2415.
32. Christe, K. O.; Dixon, D. A., *J. Am. Chem. Soc.*, 1992, *114*, 2978.
33. Christe, K. O.; Wilson, W. W.; Wilson, R. D., *Inorg. Chem.*, 1984, *23*, 2058.
34. McKee, D. E.; Adams, C. J.; Zalkin, A.; Bartlett, N., *J. Chem. Soc., Chem. Comm.*, 1973, 26.
35. Holloway, J. H.; Schrobilgen, G. J., *J. Chem. Soc., Chem. Comm.*, 1975, 623.
36. Gillespie, R. J.; Schrobilgen, G. J., *Inorg. Chem.*, 1974, *13*, 1230.
37. Christe, K. O.; Wilson, W. W.; Curtis, E. C., *Inorg. Chem.*, 1983, *22*, 3056.
38. Christe, K. O.; Wilson, R. D.; Wilson, W. W.; Bau, R.; Sukuar, S.; Dixon, D. A., *J. Am. Chem. Soc.*, 1991, *113*, 3795.
39. Bartlett, N.; Lucier, G.; Shen, C.; Casteel Jr., W. J.; Chacón, L.; Munzenberg, J.; Žemva, B., *J. Fluorine Chem.*, 1995, *71*, 163.
40. Gillespie, R. J.; Schrobilgen, G. J., *Inorg. Chem.*, 1976, *15*, 22.
41. Gillespie, R. J.; Martin, D.; Schrobilgen, G. J., *J. Chem. Soc. Dalton Trans.*, 1980, 1898.
42. Dean, P. A; Gillespie, R. J.; Hulme, R.; Humphries, D. A., *J. Chem. Soc. A*, 1971, 341.
43. Gillespie, R. J.; Peel, T. E., *J. Am. Chem. Soc.*, 1973, *95*, 5173.
44. Fabre, P. L.; Devynck, J.; Tremillon, B., *Chem. Rev.*, 1982, *82*, 591.
45. Gillespie, R. J.; Ouchi, K.; Pez, G. P., *Inorg. Chem.*, 1969, *8*, 63.
46. Christe, K. O.; Dixon, D. A., 16th Winter Fluorine Conference, St. Petersburg, Fl., Jan. 12 - 17, 2003.
47. Hwang, I. C.; Seppelt, K., *Angew. Chem., Int. Ed. Engl.*, 2001, *40*, 3690; *Angew. Chem.*, 2001, *113*, 3808
48. Christe, K. O.; Dixon, D. A.; McLemore, D.; Wilson, W. W.; Sheehy, J. A.; Boatz, J. A., *J. Fluorine Chem.*, 2000, *101*, 151.
49. Larson, J. W.; McMahon, T. B., *Inorg. Chem.*, 1987, *26*, 4018.
50. Chernick, C. L.; Claassen, H. H.; Fields, P. R.; Hyman, H. H.; Malm, J. G.; Manning, W. M.; Matheson, M. S.; Quarterman, L. A.; Schreiner, F.; Selig, H. H.; Sheft, I.; Siegel, S.; Sloth, E. N.; Stein, L.; Studier, M. H.; Weeks, J. L.; Zirin, M. H., *Science*, 1962, *138*, 136.
51. Schrobilgen, G. J., *J. Chem. Soc., Chem. Comm.*, 1988, 863.
52. Seidel, S.; Seppelt, K., *Angew. Chem., Int. Ed. Engl.*, 2001, *40*, 4225; *Angew. Chem.*, 2001, *113*, 4318.
53. Drews, T.; Seidel, S.; Seppelt, K., *Angew. Chem., Int. Ed. Engl.*, 2002, *41*, 454; *Angew. Chem.*, 2002, *114*, 470.
54. Frohn, H. J.; Jakobs, S., *J. Chem. Soc., Chem. Comm.*, 1989, 625.
55. Naumann, D.; Tyrra, W., *J. Chem. Soc., Chem. Comm.*, 1989, 47.
56. Hwang, I. C.; Seidel, S.; Seppelt, K., *Angew. Chem., Int. Ed. Engl.*, 2003, *42*, 4392; *Angew. Chem.*, 2003, *115*, 4528.

57. Drews, T.; Seppelt, K., *Angew. Chem., Int. Ed. Engl.*, **1997**, *36*, 273; *Angew. Chem.*, **1997**, *109*, 264.

58. *Noble Gas Compounds*, Hyman, H. H., ed.; University of Chicago Press, Chicago, **1963**.

59. Bartlett, N.; Sladky, F. O., In *Comprehensive Inorganic Chemistry*, Bailer, J. C. Jr.; Emeléus, H. J.; Nyholm, S. R.; Trotman-Dickenson A. F., eds.; Pergamon Press: New York, **1973**, *Vol. 1*, p. 213 - 330.

60. Hawkins, D. T.; Falconer, W. E.; Bartlett, N., In *Noble Gas Compounds: A Bibliography*, Plenum Press Inc.: New York, **1978**, p. 1962 - 1976.

61. Seppelt, K.; Lentz, D., *Prog. Inorg. Chem.*, **1982**, *29*, 167.

62. Selig, H.; Holloway, J. H., *Top. Curr. Chem.*, **1984**, *124*, 33.

63. Žemva, B., *Croat. Chem. Acta*, **1988**, 61, 163.

64. Bartlett, N., *Proc. Chem. Soc.*, **1962**, 218.

65. Bartlett, N.; Jha, N. K., In *Noble-Gas Compounds*, Hyman, H. H., ed.; University of Chicago Press, Chicago, **1963**, p. 23 - 34.

66. Graham, L.; Graudejus, O.; Jha, N. K.; Bartlett, N., *Coord. Chem. Rev.*, **2000**, *197*, 321.

67. Botkovitz, P.; Lucier, G. M.; Rao, R. P.; Bartlett, N., *Acta Chim. Slov.*, **1999**, *46*, 141.

68. Gillespie, R. J.; Landa, B., *Inorg. Chem.*, **1973**, *12*, 1383.

69. Sladky, F. O.; Bulliner, P. A.; Barlett, N., *J. Chem. Soc. A.*, **1969**, 2179.

70. Sokolov, V. B.; Prusakov, V. N.; Ryzhhov, A. V.; Dobyshevskii, Y. V.; Khoroshev, S. S., *Dokl. Akad. Nauk SSSR*, **1976**, *229*, 887; *Dokl. Chem. Proc. Acad. Sci. USSR*, **1976**, *229*, 525.

71. Bartlett, N.; Gennis, M.; Bibler, D. D.; Morrell, B. K.; Zalkin, A., *Inorg. Chem.*, **1973**, *12*, 1717.

72. Zalkin A.; Ward, D. L.; Biagioni, R. N.; Templeton, D. H.; Bartlett, N., *Inorg. Chem.*, **1978**, *17*, 1318.

73. McRae, V. M.; Peacock, R. D.; Russell, D. R., *J. Chem. Soc., Chem. Comm.*, **1969**, 62.

74. Levy, H. A.; Agron, P. A., *J. Am. Chem. Soc.*, **1963**, *85*, 241.

75. Agron, P. A.; Begun, G. M.; Levey, H. A.; Mason, A. A.; Jones, C. G.; Smith, D. F., *Science*, **1963**, *139*, 842.

76. Gillespie, R. J.; Netzer, A.; Schrobilgen, G. J., *Inorg. Chem.*, **1974**, *13*, 1455.

77. Gillespie, R. J.; Schrobilgen, G. J., *Inorg. Chem.*, **1974**, *13*, 2370.

78. Schrobilgen, G. J.; Holloway, J. H.; Granger, P.; Brevard, C., *Inorg. Chem.*, **1978**, *17*, 980.

79. Birchall, T.; Myers, R. D.; de Ward, H.; Schrobilgen, G. J., *Inorg. Chem.*, **1982**, *21*, 1068.

80. Keller, N.; Schrobilgen, G. J., *Inorg. Chem.*, **1981**, *20*, 2118.

81. Holloway, J. H.; Schrobilgen, G. J., *Inorg. Chem.*, **1981**, *20*, 3363.

82. Holloway, J. H.; Schrobilgen, G. J., *Inorg. Chem.*, **1980**, *19*, 2632.

83. Tsao, P.; Cobb, C. C.; Claassen, H. H., *J. Chem. Phys.*, **1971**, *54*, 5247.

84. Tucker, P. A.; Taylor, P. A.; Holloway, J. H.; Russell, D. R., *Acta Crystallogr.*, **1975**, *B31*, 906.
85. Tramšek, M.; Benkič, P.; Žemva, B., *Solid State Sciences*, **2002**, *4*, 9.
86. Benkič, P.; Tramšek, M.; Žemva, B., *Solid State Sciences*, **2002**, *4*, 1425.
87. Matsumoto, K.; Hagiwara, R.; Ito, Y.; Tamada, O., *Solid State Sciences*, **2002**, *4*, 1465.
88. Turičnik, A.; Benkič, P.; Žemva, B., *Inorg. Chem.*, **2002**, *41*, 5521.
89. Tramšek, M; Benkič, P.; Žemva, B., *Inorg. Chem.*, **2004**, *43*, 699.
90. Tavčar, G.; Benkič, P.; Žemva, B., *Inorg. Chem.*, **2004**, *43*, 1452.
91. Fir, B. A.; Gerken, M.; Pointner, B. E.; Mercier, H. P. A.; Dixon, D. A.; Schrobilgen, G. J., *J. Fluorine Chem.*, **2000**, *105*, 159.
92. Bartlett, N.; DeBoer, B. G.; Hollander, F. J.; Sladky, F. O.; Templeton, D. H.; Zalkin, A., *Inorg. Chem.*, **1974**, *13*, 780.
93. Sladky, F. O.; Bulliner, P. A.; Bartlett, N.; Deboer, B. G.; Zalkin, A., *Chem. Comm.*, **1968**, 1048.
94. Emara, A. A. A.; Schrobilgen, G. J., *J. Chem. Soc., Chem. Comm.*, **1987**, 1644.
95. Emara, A. A. A.; Schrobilgen, G. J., *Inorg. Chem.*, **1992**, *31*, 1323.
96. Emara, A. A. A.; Schrobilgen, G. J., *J. Chem. Soc., Chem. Comm.*, **1988**, 257.
97. Koppe, K., Undergraduate Research Project, McMaster University, Hamilton, Canada, **2000**.
98. Schrobilgen, G. J., *J. Chem. Soc. Chem. Comm.*, **1988**, 1506.
99. Fir, B. A., M.Sc. Thesis, McMaster University, Hamilton, Ontario, **1999**, pp. 101 - 156.
100. Schrobilgen, G. J., In *Synthetic Fluorine Chemistry*, Olah, G. A.; Prakash, G. K. S.; Chambers, R. D., eds.; Wiley: New York, **1992**, Chapter 1, p. 1 - 30.
101. Žemva, B., In *Encyclopedia of Inorganic Chemistry*, King, R. B., ed.; Wiley: Chichester, **1994**, *vol. 5*, pp. 2660 - 2680.
102. Schrobilgen, G. J.; Whalen, J. M., In *Kirk-Othmer Encyclopedia of Chemical Technology 4th ed.*; Wiley: New York, **1994**, Chapter 13, pp. 38 - 53.
103. Holloway, J. H.; Hope, E. G., *Adv. Inorg. Chem.*, **1998**, *46*, 51.
104. Gerken, M.; Schrobilgen, G. J., *Coord. Chem. Rev.*, **2000**, *197*, 335.
105. G. J. Schrobilgen, In *NMR and the Periodic Table*, Harris, R. K; Mann, B. E., eds.; Academic Press: London, **1978**, Chapter 14.
106. Gillespie, R. J.; Landa, B.; Schrobilgen, G. J., *J. Inorg. Nucl. Chem.*, H. H. Hyman Mem. Vol., Katz, J. J.; Sheft, I., eds.; Pergamon Press: Oxford, **1976**, p. 179.
107. Schrobilgen, G. J., In *The Encyclopedia of Nuclear Magnetic Resonance*, Grant, D. M.; Harris, R. K., eds.; John Wiley and Sons: New York, **1996**, p. 3251.
108. Gerken, M.; Mercier, H. P. A.; Schrobilgen, G. J., In *Advanced Inorganic Fluorides: Synthesis, Characterization and Applications*, Nakajima, T.; Tressaud, A.; Žemva, B., eds.; Elsevier Science: Zurich, **1999**, Chapter 5.
109. Schrobilgen, G. J., In *Encyclopedia of Physical Science and Technology 3rd Ed.*, Hawthorn, M. F., ed.; Academic Press: San Diego, **2002**, *10*, 449.
110. Moran, M. D.; Schrobilgen, G. J.; In *Kirk-Othmer Encyclopedia of Chemical Technology (online)*, **2004**.

111. Lehmann, J. F.; Mercier, H. P. A.; Schrobilgen, G. J., *Coord. Chem. Rev.*, 2002, *233*, 1.
112. Khriachtchev, L.; Petterson, M.; Runeberg, N.; Lundell, J.; Räsänen, M., *Nature*, 2000, 406, 874.
113. Khriachtchev, L.; Pettersson, M.; Lignell, A.; Räsänen, M., *J. Am. Chem. Soc.*, 2001, *123*, 8610.
114. Falconer, W. E.; Morton, J. R.; Streng, A. G., *J. Chem. Phys.*, 1964, *41*, 902.
115. Tiee, J. J.; Quick, C. R.; Hsu, A. H.; Hof, D. E, *Phys. Scr.*, 1990, *41*, 71.
116. Grosse, A. V.; Kirshenbaum, A. D.; Streng, A. G.; Streng, L. V., *Science*, 1963, *139*, 1047.
117. Streng, A. G.; Kirshenbaum, A. D.; Streng, L. V.; Grosse, A. V., In *Noble Gas Compounds*, Hyman, H. H., ed.; University Chicago Press: Chicago, 1963, p. 73.
118. Turner, J. J.; Pimentel, G. C., In *Noble Gas Compounds*, Hyman, H. H., ed.; University Chicago Press: Chicago, 1963, p. 101.
119. Turner, J. J.; Pimentel, G. C., *Science*, 1963, 140, 974.
120. Claassen, H. H.; Goodman, G. L.; Malm, J. G.; Schreiner, F., *Chem. Phys.*, 1965, *42*, 1229.
121. MacKenzie, D. R., unpublished results.
122. Turner, J. J; Pimentel, G. C., *Science*, 1964, *143*, 974.
123. Al-Mukhtar, M.; Holloway, J. H.; Hope, E. G.; Schrobilgen, G. J., *J. Chem. Soc., Dalton Trans.*, 1991, 2831.
124. Christe, K. O.; Wilson, W. W.; Bougon, R. A., *Inorg. Chem.*, 1986, *25*, 2163.
125. Ruby, S. L.; Selig, H., *Phys. Rev.*, 1966, *147*, 348.
126. Holloway, J. H.; Schrobilgen, G. J.; Bukshpan, S.; Hilbrants, W.; de Waard, H., *J. Chem. Phys.*, 1977, *66*, 2627.
127. Harshberger, W.; Bohn, R, K.; Bauer, S. H., *J. Am. Chem. Soc.*, 1967, *89*, 6466.
127. Bürger, H.; Ma, S.; Winnewisser, B. P., *J. Mol. Spectrosc.*, 1994, *164*, 84.
129. Burbank, R. D.; Falconer, W. E.; Sunder, W. A., *Science*, 1972, *178*, 1285.
130. Lehmann, J. F.; Schrobilgen, G. J., *J. Fluorine Chem.*, 2003, *119*, 109.
131. Lutar, K.; Jesih, A.; Žemva, B., *Polyhedron*, 1988, 7, 1217.
132. Hillier, I. H.; Vincent, M. A., *J. Chem. Soc., Chem. Comm.*, 1989, 30.
133. Koch, W., *J. Chem. Soc., Chem. Comm.*, 1989, 215.
134. Wong, M. W.; Radom, L., *J. Chem. Soc., Chem. Comm.*, 1989, 719.
135. Dixon, D. A.; Arduengo, A. J. III, *Inorg. Chem.*, 1990, *29*, 970.
136. Sanders, J. C. P.; Schrobilgen, G. J., *J. Chem. Soc. Chem. Comm.*, 1989, 1576.
137. Gillespie, R. J.; Schrobilgen, G. J., *J. Chem. Soc., Chem. Comm.*, 1974, 90.
138. Gold can be dissolved in *aqua regia*, a 3:1 mixture of concentrated HCl and HNO_3.
139. Bartlett, N., *Gold Bull.*, 1998, *31*, 22.
140. Moore, C. E., *Atomic Energy Levels*, Natl. Bur. Stand. (U.S.) Circ. 467, U.S Govt. Print. Off., Washington, D. C., 1958.
141. Puddephatt, R. J., In *The Chemistry of Gold*, Clark, R. J. H., ed.; Elsevier, New York, 1978, p. 31-37, 63-65, 90-93.
142. Edwards, A. J.; Falconer, W. E.; Griffiths, J. E.; Sunder, W. A.; Vasile, M. J., *J. Chem. Soc., Dalton Trans.*, 1974, 1129.

143. Vasile, M. J.; Richardson, T. J.; Stevie, F. A.; Falconer, W. E., *J. Chem. Soc., Dalton, Trans.*, **1976**, 351.

144. Leary, K.; Bartlett, N., *J. Chem. Soc., Chem. Comm.*, **1972**, 903.

145. Nabiev, S. S., *Russ. Chem. Bull.*, **1999**, *48*, 711.

146. Bartlett, N.; Leary, K., *Rev. Chim. Miner.*, **1976**, *13*, 82.

147. Popov, A. I.; Val'kovskii, M. D.; Kiselev, Y. M.; Chumaevskii, N. A.; Sokolov, V. B.; Spirin, S. N., *Zh. Neorg. Khim.*, **1990**, *35*, 1970; *Russ. J. Inorg. Chem.*, **1990**, *35*, 1122.

148. Leary, K.; Zalkin, A.; Bartlett, N., *J. Chem. Soc., Chem. Comm.*, **1973**, 131.

149. Graudejus, O.; Elder, S. H.; Lucier, G. M.; Shen, C.; Bartlett, N., *Inorg. Chem.*, **1999**, *38*, 2503.

150. Lehmann, J. F.; Schrobilgen, G. J., unpublished results.

151. Timakov, A. A.; Prusakov, V. N.; Drobyshevskii, Y. V., *Dokl. Akad. Nauk. SSSR*, **1986**, 291, 125; *Dokl. Chem.*, **1986**, *291*, 442.

152. Graudejus, O.; Wilkinson, A. P.; Chacón, L. C.; Bartlett, N., *Inorg. Chem.*, **2000**, *39*, 2794.

153. Buslaeva, T. M.; Malynov, I. V.; Koteneva, N. A.; Sinitsyn, N. M.; Kravchenko, V. V., *Russ. J. Inorg. Chem.*, **1990**, *35*, 1127.

154. Leary, K.; Zalkin, A.; Bartlett, N., *Inorg. Chem.*, **1974**, *13*, 775.

155. Graudejus, O.; Müller, B. G., *Z. Anorg. Allg. Chem.*, **1996**, *622*, 1076.

156. Seppelt, K.; Bartlett, N., *Z. Anorg. Allg. Chem.*, **1977**, *436*, 122.

157. Mason, J., In *Multinuclear NMR*, Mason, J., ed.; Plenum Press: New York, **1987**; Appendix, pp. 623 - 629.

158. Sokolov, V. B.; Tsinov, V. G.; Ryzhkov, A. V., *Theor. Eksp. Khim.*, **1980**, *16*, 345; *Theor. Exp. Chem.*, **1980**, *16*, 270.

159. Kiselev, Y. M.; Popov, A. I.; Goryunov, A.. V.; Chumaevskii, N. A.; Savinova, L. N.; Sokolov, V. B.; Spirin, S. N., *Russ. J. Inorg. Chem.*, **1990**, *3*, 35.

160. Brunvoll, J.; Ischenko, A. A.; Ivanov, A. A.; Romanov, G. V.; Sokolov, V. B.; Spiridonov, V. P.; Strand, T. G., *Acta Chem. Scand.*, **1982**, *36A*, 705.

161. Appelman, E. H., *J. Am. Chem. Soc.*, **1968**, *90*, 1900.

162. Appelman, E. H.; Studier, M. H., *J. Am. Chem. Soc.*, **1969**, *91*, 4561.

163. Sloth, E. N.; Stein, L.; Williams, C. W., *J. Phys. Chem.*, **1969**, *73*, 279.

164. Greenwood, N. N.; Earnshaw, *Chemistry of the Elements 2nd Ed.*, Butterworth Heinemann, Oxford, **1998**, p. 552, 561, 755, 780, 872.

165. Cotton, F. A.; Wilkinson, G., *Advanced Inorganic Chemistry 56th Ed.*, Wiley Interscience, New York, **1988**, p. 395, 569.

166. Dove, M. F. A.; Sanders, J. C. P.; Appelman, E. H., *Magn. Reson. Chem.*, **1995**, *33*, 44.

167. Appelman, E. H., *Inorg. Chem.*, **1969**, *8*, 223.

168. Brown, L. C.; Begun, G. M.; Boyd, G. E., *J. Am. Chem. Soc.*, **1969**, *91*, 2250.

169. Johnson, G. K.; Smith, P. N.; Appelman, E. H.; Hubbard, W. N., *Inorg. Chem.*, **1970**, *9*, 119.

170. Siegel, S.; Tani, B.; Appelman, E., *Inorg. Chem.*, **1969**, *8*, 1190.

171. Keith, J. N.; Solomon, I. J., *Inorg. Chem.*, **1970**, *9*, 1560.

172. Claassen H. H.; Appelman, E. H., *Inorg. Chem.*, 1970, *9*, 622.
173. Bürger, H.; Pawelke, G.; Appelman, E. H., *J. Mol. Spectrosc.*, 1990, *144*, 201.
174. Appelman, E. H.; Beagley, B.; Cruickshank, D. W. J.; Foord, A.; Rustad, S.; Ulbrecht, V., *J. Mol. Struct.*, 1976, *35*, 139.
175. Johnson, G. K.; O'Hare, P. A. G.; Appelman, E. H., *Inorg. Chem.*, 1972, *11*, 800.
176. Christe, K. O.; Wilson, R. D., *Inorg. Chem.*, 1975, *14*, 694.
177. Fogle, C. E.; Rewick, R. T., U. S. Patent 3,615,260.
178. Urch, D. S., *J. Inorg. Nucl. Chem.*, 1963, *25*, 771.
179. Hugus, Z. Z. Jr., *J. Am. Chem. Soc.*, 1952, *74*, 1076.
180. Bancroft, G. M.; Gesser, H. D., *J. Inorg. Nucl. Chem.*, 1965, *27*, 1545.
181. Nyholm, R. S., *Proc. Chem. Soc.*, 1961, 273.
182. Dasent, W. E., *J. Chem. Ed.*, 1963, *40*, 130.
183. Seppelt, K., *Angew. Chem., Int. Ed. Engl.*, 1976, *15*, 377; *Angew. Chem.*, 1976, *88*, 410.
184. Cartmell, E.; Fowles, G. W. A., *Valency and Molecular Structure*, Butterworths, London, 1977, p. 39.
185. Wagman, D. D.; Evans, W. H.; Parker, V. B.; Schumm, R. H.; Halow, I.; Bailey, S. M.; Churney, K. L.; Nuttal, R. L., *J. Phys. Chem. Ref. Data*, 1982, *11*, Suppl. 2.
186. Woolf, A. A., *J. Fluorine Chem.*, 1975, *5*, 172.
187. O'Hare, P. A. G., *J. Chem. Thermodyn.*, 1992, *24*, 1009.
188. Johnson, G. K; Papatheodorou, G. N.; Johnson, C. E., *J. Chem. Thermodyn.*, 1981, *13*, 745.
189. Carre, J.; Germain, P.; Kollmannsberger, M.; Perachon, G.; Thourey, J., *J. Fluorine Chem.*, 1979, *13*, 365.
190. Carre, J.; Kollmannsberger, M.; Thourey, J.; Perachon, G.; Bousquet, J., *J. Fluorine Chem.*, 1976, *8*, 401.
191. Cordfunke, E. H. P.; Ouweltjes, W.; Prins, G., *J. Chem. Thermodyn.*, 1987, *19*, 369.
192. Özgen, T., *Int. J. Mass Spectrometry Ion Phys.*, 1983, *48*, 427.
193. Seppelt, K., *Z. Anorg. Allg. Chem.*, 1977, *434*, 5.
194. Cook, E. H., *J. Chem. Soc.*, 1894, *65*, 1894.
195. Decoursey, W. F., Ph.D. Thesis, Iowa State College, Iowa, U.S.A.. 1953. pp. 16 - 25.
196. Duke, F. R.; Shute, E. A., *J. Phys. Chem.*, 1962, *66*, 2114.
197. Jach, J., *J. Phys. Chem. Solids*, 1963, *24*, 63.
198. Kämmerar, H., *J. Prakt. Chem.*, 1863, *90*, 190.
199. MacIvor, E., *Chem. News*, 1876, *33*, 35.
200. Muir, M. M. P., *J. Chem. Soc.*, 1876, *30*, 469.
201. Wolfram, G., *Liebigs's Ann.*, 1879, *198*, 95.
202. Michael, A.; Conn, W. T., *Am. Chem. J.*, 1901, *23*, 89.
203. Robertson, P. W., *Chem. News*, 1912, *108*, 50.
204. DeCoursey, W. F., Ph.D. Thesis, Iowa State College, Iowa, U.S.A., 1953, pp. 28 - 48.
205. Appelman, E. H., *Inorg. Synth.*, 1972, *13*, 1.
206. Engelbrecht, A. F., U.S. Patent 2942947, June 28, 1960.

207. Gillespie, R. J.; Spekkens, P. H., *Isr. J. Chem.*, **1978**, *17*, 11.
208. Gerken, M.; Schrobilgen, G. J., unpublished results.
209. Spekkens, P. H., Ph.D. Thesis, McMaster University, Hamilton, Ontario, Canada, **1977**, Chapter 7.
210. Schmeisser, M.; Pammer, E., *Angew. Chem.*, **1957**, *69*, 781.
211. Woolf, A., A.; Emeleus, H. J., *J. Chem. Soc.*, **1949**, 2865.
212. Brown, D. H.; Dixon, K. R.; Sharp, D. W. A, *Chem. Comm.*, **1966**, 654.
213. Jacob, E., *Angew. Chem., Int. Ed. Engl.*, **1976**, *15*, 158.; *Angew. Chem.*, **1976**, *88*, 189.
214. Spekkens, P. H., Ph.D. Thesis, McMaster University, Hamilton, Ontario, Canada, **1977**, Chapter 5.
215. Adelhelm, E.; Jacob, E., *Angew. Chem., Int. Ed. Engl.*, **1977**, *16*, 461; *Angew. Chem.*, **1977**, *89*, 476.
216. Bougon, R. Huy, T. B.; Charpin, P.; Gillespie, R. J.; Spekkens, P. H., *J. Chem., Soc., Dalton Trans.*, **1979**, 6.
217. Christe, K. O.; Schack, C. J., Adv. *Inorg. Chem. Radiochem.*, **1976**, *18*, 319.
218. Seel, F.; Detmer, O., *Angew. Chem.*, **1958**, *70*, 163.
219. Seel, F.; Detmer, O., *Z. Anorg. Allg. Chem.*, **1959**, *301*, 113.
220. Roberto, F. Q., *Inorg. Nucl. Chem. Letters*, **1972**, *8*, 737.
221. Christe, K. O., *Inorg. Nucl. Chem. Letters*, **1972**, *8*, 741.
222. Christe, K. O., *Inorg. Chem.*, **1973**, *12*, 1580.
223. Jacob, E., *Z. Anorg. Allg. Chem.*, **1977**, *433*, 255.
224. Christe, K. O., *Inorg. Nucl. Chem. Lett.*, **1972**, *8*, 453.
225. Christe, K. O.; Wilson, R. D., Curtis, E. C., *Inorg. Chem.*, **1973**, *12*, 1358.
226. Pilipovich, D.; Rogers, H. H.; Wilson, R. D., *Inorg. Chem.*, **1972**, *11*, 2192.
227. Spekkens, P. H., Ph.D. Thesis, McMaster University, Hamilton, Ontario, Canada, **1977**, Chapter 4.
228. Bougon, R. A.; Christe, K. O.; Wilson, W. W., *J. Fluorine Chem.*, **1985**, *30*, 237.
229. McKee, D. E.; Bartlett, N., *Inorg. Chem.*, **1973**, *12*, 2738.
230. Griffiths, J. E.; Sunder, W. A.; Falconer, W. E., *Spectrochim. Acta*, **1975**, *31A*, 1207.
231. Ibers, J. A.; Hamilton, W. C., *J. Chem. Phys.*, **1966**, *44*, 1748.
232. Bertolini, J. C., *J. Emerg. Med.*, **1992**, *10*, 163.
233. Peters, D.; Mietchen, R., *J. Fluorine Chem.*, **1996**, *79*, 161.
234. Segal, E. B., *Chem. Health Saf.*, **2000**, 19.
235. Winfield, J. M., *J. Fluorine Chem.*, **1984**, *25*, 91.
236. Christe, K. O.; Wilson, W. W., *J. Fluorine Chem.*, **1990**, *47*, 117.
237. Casteel, W. J. Jr.; Kolb, P.; Leblond, N.; Mercier, H. P. A.; Schrobilgen, G. J., *Inorg. Chem.*, **1996**, *35*, 929.
238. Mazej, Z.; Žemva, B., personal communication.
239. Kinkead, S. A., personal communication.
240. Chernick, C. L.; Malm, J. G., *Inorg. Synth.*, **1966**, *8*, 259.
241. Seppelt, K., *Acc. Chem. Res.*, **1997**, *30*, 111.
242. Christe, K. O.; Wilson, R. D.; Schack, C. J., *Inorg. Synth.*, **1986**, *24*, 3.

243. Gillespie, R. J.; Spekkens, P. H., *J. Chem. Soc., Chem. Comm.*, **1975**, 314.

244. Gillespie, R. J.; Spekkens, P. H., *J. Chem. Soc., Dalton Trans.*, **1977**, 1539.

245. Edwards, A. J.; Holloway, J. H.; Peacock, R. D., *Proc. Chem. Soc.*, **1963**, 275.

246. Christe, K. O.; Wilson, W. W.; Wilson, R. D.; Bau, R.; Feng, J., *J. Am. Chem. Soc.*, **1990**, *112*, 7619.

247. Bougon, R.; Bui, H. T., *Compt. Rendu. Acad. Sciences, Paris*, **1976**, *283C*, 461.

248. Gillespie, R. J.; Landa, B.; Schrobilgen, G. J., *Inorg. Chem.*, **1976**, *15*, 1256.

249. Adams, C. J.; Bartlett, N., *Isr. J. Chem.*, **1978**, *17*, 114.

250. Claassen, H. H.; Chernick, C. L.; Malm, J. G., *J. Am. Chem. Soc.*, **1963**, *85*, 1927.

251. SMART, Version, 5.054, Siemens Energy and Automation Inc., Madison, WI, **1999**.

252. SAINT+, Version 6.01, Siemens Energy and Automation Inc., Madison, WI, **1999**.

253. Sheldrick, G. M., SADABS (Siemens Area Detector Adsorption Corrections), **1998**, personal communication.

254. Sheldrick, G. M., SHELXTL, Version 5.1, Siemens Analytical X-ray Instruments Inc.: **1998**.

255. Par, R. G.; Yang, W., *Density-Functional Theory of Atoms and Molecules*; Oxford University Press: New York, **1989**.

256. Andzelm, J.; Wimmer, E.; Salahub, D. R., In *The Challenge of d and f Electrons: Theory and Computation*, Salahub, D. R., Zerner, M.C., eds.: ACS Symposium Series, No. 394, American Chemical Society: Washington D. C., **1989**, p. 228.

257. Andzelm, J., In *Density Functional Theory in Chemistry*, Labanowski, J.; Andzelm, J., eds.; Springer-Verlag: New York, **1991**, p. 155.

258. Andzelm, J. W.; Wimmer, E. J., *J. Chem. Phys.*, **1992**, *96*, 1280. DGauss is a density functional program which is part of UniChem and is available from Oxford Molecular. Versions 4.1 and 5.0 were used.

259. Gaussian 98, Revision A.4, Frisch, M. J.; Trucks, G. W.; Schlegel, H. B.; Scuseria, G. E.; Robb, M. A.; Cheeseman, J. R.; Zakrzewski, V. G.; Montgomery J. A. Jr.; Stratmann, R. E.; Burant, J. C.; Dapprich, S.; Millam, J. M.; Daniels, A. D.; Kudin, K. N.; Strain, M. C.; Farkas, O.; Tomasi, J.; Barone, V.; Cossi, M.; Cammi, R.; Mennucci, B.; Pomelli, C.; Adamo, C.; Clifford, S.; Ochterski, J.; Petersson, G. A.; Ayala, P. Y.; Cui, Q.; Morokuma K.; Malick D. K.; Rabuck A. D.; Raghavachari, K.; Foresman, J. B.; Ciosloski, J.; Ortiz, J. V.; Stefanov, B. B.; Lui, G.; Liashenko, A.; Piskorz, P.; Komaromi, I.; Gomperts, R.; Martin, R. L.; Fox, D. J.; Keith T.; Al-Laham, M. A.; Peng, C. Y.; Nanayakkara, A.; Gonzalez, C.; Challacombe, M.; Gill P. M. W.; Johnson, B.; Chen, W.; Wong, M. W.; Andres, J. L.; Gonzalez, C.; Head-Gordon, M.; Replogle, E. S.; Pople, J. A., Gaussian, Inc., Pittsburgh, PA, **1998**.

260. Basis sets were obtained from the Extensible Computational Chemistry Environment Basis Set Database, Version 6/19/03, as developed and distributed by the Molecular Science Computing Facility, Environmental and Molecular Sciences Laboratory which is part of the Pacific Northwest Laboratory, P.O. Box 999, Richland, Washington 99352, USA, and funded by the U.S. Department of Energy. The Pacific Northwest Laboratory is a multi-program laboratory operated by

Battelle Memorial Institute for the U.S. Department of Energy under contract DE-AC06-76RLO 1830.

261. Komornicki, A.; Fitzgerald, G. J., *J. Chem. Phys.*, **1993**, *98*, 1398.

262. Hay, P. J.; Wadt, W. R., *J. Chem. Phys.*, **1982**, *82*, 271.

263. Hay P. J.; Wadt, W. R., *J. Chem. Phys.*, **1982**, *82*, 285.

264. Hay P. J.; Wadt, W. R., *J. Chem. Phys.*, **1982**, *82*, 299.

265. Godbout, N.; Salhub, D. R.; Andzelm, J.; Wimmer, E., *Can. J. Chem.*, **1992**, *70*, 560.

266. Vosko, S. H.; Wilk, L.; Nusair, M., *Can. J. Phys.*, **1980**, *58*, 1200.

267. Adamo, C.; Barone, V., *J. Chem. Phys.*, **1998**, *108*, 664.

268. Reprinted with permission from Lehmann, J. F.; Dixon, D. A.; Schrobilgen, G. J., *Inorg. Chem.*, **2001**, *40*, 3002. Copyright 2001 American Chemical Society.

269. Prusakov, V. N.; Sokolov, V. B., *At. Energ.*, **1971**, *31*, 259.

270. Selig, H.; Peacock, R. D., *J. Am. Chem. Soc.*, **1964**, *86*, 3895.

271. Frlec, B.; Holloway, J. H., *J. Chem, Soc., Chem. Commun.*, **1973**, 370.

272. Frlec, B.; Holloway, J. H., *J. Chem, Soc., Chem. Commun.*, **1974**, 89.

273. Žemva, B.: Slivnik; J.; Šmalc, A., *J. Fluorine Chem.*, **1975**, *6*, 191.

274. Christe, K. O.; Dixon, D. A.; Mack, H. G.; Oberhammer, H.; Pagelot, A.; Sanders, J. C. P.; Schrobilgen, G. J., *J. Am. Chem. Soc.*, **1993**, *115*, 11279.

275. LeBlond, N.; Mercier, H. P. A.; Dixon, D. A.; Schrobilgen, G. J., *Inorg. Chem.*, **2000**, *39*, 4494.

276. Siegel, S.; Gebert, E., *J. Am. Chem. Soc.*, **1964**, *86*, 3896.

277. Dixon, D. A.; Arduengo, A. J. III; Farnham, W. B., *Inorg. Chem.*, **1989**, *28*, 4589.

278. Levy, H. A.; Agron, P. A., In *Noble-Gas Compounds*; Hyman H. H., ed.; University of Chicago Press: Chicago, **1963**, p. 221 - 225.

279. Murchison, C.; Reichman, S.; Anderson, D.; Overend, J.; Schreiner, F., *J. Am. Chem. Soc.*, **1968**, *90*, 5690.

280. Minkwitz, R.; Broechler, R.; Ludwig, R., *Inorg. Chem.*, **1997**, *36*, 4280.

281. Christe, K. O.; Wilson, W. W.; Drake, G. W.; Petrie, M. A.; Boatz, J. A., *J. Fluorine Chem.*, **1998**, *88*, 185.

282. Smolyar, A. E.; Charkin, O. P.; Klimenko, N. M., *Zh. Strukt. Khim.*, **1974**, *15*, 993; *J. Struc. Chem.*, **1974**, *15*, 885.

283. Bancroft, G. M.; Bristow, D. J.; Tse, J. S.; Schrobilgen, G. J., *Inorg. Chem.*, **1983**, *22*, 2673.

284. Boldrini, P.; Gillespie, R. J.; Ireland, P. R.; Schrobilgen, G. J., *Inorg. Chem.*, **1974**, *13*, 1690.

285. Gillespie, R. J.; Martin, D.; Schrobilgen, G. J.; Slim, D. R., *J. Chem. Soc., Dalton Trans.*, **1977**, 2234.

286. Bondi, A., *J. Phys. Chem.*, **1964**, *68*, 441.

287. Pauling, L., *The Nature of the Chemical Bond and the Structure of Molecules and Crystals, 3rd Ed.*; Cornell University Press: Ithica, NY, 1960, p. 260.

288. Bhagavantam, S.; Venkatarayudu, R., *Proc. Indian Acad. Sci.*, **1939**, *9A*, 224.

289. The effects of secondary contacts on the geometries of the $Kr_2F_3^+$ cations are difficult to assess. The number of $Kr\cdots F$ contacts to the $Kr_2F_3^+$ cations range from 6

to 8 per krypton atom with Kr···F contact distances ranging from 2.902 to 3.489 Å. There are also 6 to 8 long Kr···F contacts to the adducted KrF_2 molecules, and they vary from 3.104 to 3.473 Å. Of the 58 ($Kr_2F_3^+$) and 14 (KrF_2) Kr···F contacts observed in the structures of $[Kr_2F_3][SbF_6]\cdot KrF_2$, $[Kr_2F_3]_2[SbF_6]_2\cdot KrF_2$, and $[Kr_2F_3][AsF_6]\cdot[KrF][AsF_6]$, 50 ($Kr_2F_3^+$) and 12 ($KrF_2$) contacts have F_t-Kr···F angles falling in the ranges 52-80° and 100-122°, while the remaining long contact angles fall between 80 and 100°. The angular distribution of long contacts is generally consistent with the avoidance of the valence lone pair domains of Kr.

290. Heyns, A. M., *Spectrochim. Acta*, **1977**, *33*, 315.
291. Naulin, C.; Bougon, R. J., *J. Chem. Phys.*, **1976**, *64*, 4155.
292. Griffiths, J. E.; Sunder, W. A., *J. Chem. Phys.*, **1982**, *77*, 1087.
293. Mayer, I., *Chem. Phys. Lett.*, **1983**, *97*, 270.
294. Mayer, I., *Theoret. Chim. Acta*, **1985**, *67*, 315.
295. Mayer, I., *J. Quantum Chem.*, **1986**, *29*, 73.
296. Mayer, I., *J. Quantum Chem.*, **1986**, *29*, 477.
297. Dixon, D. A.; Schrobilgen, G. J., unpublished results.
298. Reprinted with permission from *J. Fluorine Chem.*, **2003**, *119*, 109. Copyright 2003 Elsevier.
299. Kiselev, Y. M.; Popov, A. I.; Sokolov, V. B.; Spirin, S. N., *Zh. Neorg. Khim.*, **1989**, *34*, 434; *Russ. J. Inorg. Chem.*, **1989**, *34*, 243.
300. Bartlett, N.; Yeh, S.; Kourtakis, K. Mallouk, T., *J. Fluorine Chem.*, **1984**, *26*, 97.
301. Yeh, S. M.; Bartlett, N., *Rev. Chim. Miner.*, **1986**, *23*, 676.
302. Schrobilgen, G. J.; Fir, B. A.; Gerken, M.; Koppe, K.; Lehmann, J. F.; Pointner, B. E.; Mercier, H. P. A., Pacifichem 2000 (invited oral presentation), Honolulu, Hawaii, December 14 - 19, 2000.
303. Müller, B. G., *J. Fluorine Chem.*, **1981**, *17*, 489.
304. Bartlett, N.; Lohmann, D. H., *J. Chem. Soc.*, **1962**, 5253.
305. Shamir, J. Binenboym, J.; Claassen, H. H., *J. Am. Chem. Soc.*, **1968**, *90*, 6223.
306. Christe, K. O.; Wilson, R. D.; Goldberg, I. B., *Inorg. Chem.*, **1976**, *15*, 1271.
307. Loos, K. R.; Campanile, V. A.; Goetschel, C. T., *Spectrochim. Acta*, **1970**, *26A*, 365.
308. Schomaker, V., Trueblood, K. N., *Acta Crystallogr.*, **1968**, *B24*, 63.
309. Elliott, H. S.; Jenkins, H. D. B.; Lehmann, J. F.; Schrobilgen, G. J., unpublished results.
310. Young A. R. II, Hirata, T.; Morrow, S. I., *J. Am. Chem. Soc.*, **1964**, *86*, 20.
311. Shamir, J. Binenboym, J., *Inorg. Chim. Acta*, **1968**, *2*, 37.
312. Beal, J. B. Jr., Pupp, C.; White, W. E., *Inorg. Chem.*, **1969**, *8*, 829.
313. Bartlett, N.; Lohmann, D. H., *Proc. Chem. Soc.*, **1962**, 115.
314. Schrobilgen, G. J.; Fir, B. A.; Gerken, M.; Koppe, K..; Lehmann, J. F.; Pointner, B. E.; Mercier, H. P. A., 16th International Symposium of Fluorine Chemistry, University of Durham, United Kingdom, July 16 - 20, 2000.
315. Graudejus, O.; Wilkinson, A. P.; Chacón, L. C.; Bartlett, N., *Inorg. Chem.*, **2000**, *39*, 2794.
316. Müller, B. G., *J. Fluorine Chem.*, **1981**, *17*, 409.

317. Hertzberg, G.; *Molecular Spectra and Molecular Structure I. Spectra of Diatomic Molecules*, Van Nostrand Co. Inc.: Toronto, **1950**, p. 560.

318. Brant, A.; Kiselev, Y. M.; Martynenko, L. I., *Z. Anorg. Allg. Chem.*, **1981**, *474*, 233.

319. Brant, A.; Kiselev, Y. M.; Martyknenko, L. I., *Zh. Neorg. Khim.*, **1983**, *28*, 2806; *Russ. J. Inorg. Chem.*, **1983**, *28*, 1593.

320. Sladky, F. O.; Bulliner, P. A.; Bartlett, N., *J. Chem. Soc. A.*, **1969**, 2180.

321. Babcock, H. D.; Herzberg, L., *Astrophys. J.*, **1948**, *108*, 167.

322. Chandrasekher, C. A.; Griffith, K. S.; Gellene, G. I., *Int. J. Quant. Chem.*, **1996**, *58*, 29.

323. Pople, J. A.; Scott, A. P.; Wong, M. W.; Radom L., *Isr. J. Chem.*, **1993**, *33*, 345.

324. Nabiev, S. S., Preprint IAE No. 5310/12, Kurchatov Institute of Nuclear Energy, Moscow, Moscow, **1991**, 87.

325. Bartlett, N.; Beaton, S. P.; Jha, N. K., *J. Chem. Soc., Chem. Commun.*, **1966**, 168.

326. Korobov, M. V.; Kuznetsov, S. V.; Sidorov, L. N., *Int. J. Mass Spectrometry and Ion Processes*, **1989**, *87*, 13.

327. Gutsev, G. I.; Boldyrev, A. I., *Mol. Phys.*, **1984**, *53*, 23.

328. Vasile, M. J.; Falconer, W. E., *J. Chem. Soc., Dalton Trans.*, **1975**, 316.

329. Vasile, M. J.; Richardson, T. J., Stevie, F. A.; Falconer, W. E., *J. Chem. Soc., Dalton Trans.*, **1776**, 351.

330. Griffiths, J. E.; DiStefano, D.; Sunder, W. A., *J. Raman Spectrosc.*, **1980**, *9*, 67.

331. Burgess, J.; Fraser, C. J. W.; McRae, V. M.; Peacock, R. D.; Russell, D. R., *J. Inorg. Nucl. Chem., Suppl.*, **1976**, 183.

332. Barraclough, C. G.; Besida, J.; Davies, P. G.; O'Donnell, T. A., *J. Fluorine Chem.*, **1988**, *38*, 405.

333. Dean, P. A. W.; Gillespie, R. J.; Hulme, R.; Humphreys, D. A., *J. Chem. Soc. A.*, **1971**, 341.

334. Minkwitz, R.; Neikes, F., *Inorg. Chem.*, **1999**, *38*, 5960.

335. Minkwitz, R.; Dzyk, M., *Eur. J. Inorg. Chem.*, **2002**, 569.

336. Christe, K. O.; Zhang, X.; Bau, R.; Hegge, J.; Olah, G. A.; Prakash, G. K. S.; Sheehy, J. A., *J. Am. Chem. Soc.*, **2000**, *122*, 481.

337. Brassington, N. J.; Edwards H. G. M.; Long, D. A., *J. Chem. Soc., Faraday Trans. 2*, **1978**, *74*, 1208.

338. Bürger, H.; Kuna, R.; Ma, S.; Breidung, J.; Thiel, W., *J. Chem., Phys.*, **1994**, *101*, 1.

339. Siegel, S.; Gerbert, E., *J. Am. Chem. Chem. Soc.*, **1963**, *85*, 240.

340. Edwards, A. J.; Jones, G. R.; Sills, R, J. C., *J. Chem. Soc., A*, **1970**, 2521

341. Edwards, A. J.; Steventon, B. R., *J. Chem. Soc. A*, **1968**, 2503.

342. Edwards, A. J.; Jones, G. R., *J. Chem. Soc. A*, **1968**, 2511.

343. Edwards, A. J.; Jones, G. R., *J. Chem. Soc. A*, **1968**, 2074.

344. McKee, D. E.; Zalkin, Z.; Bartlett, N., *Inorg. Chem.*, **1973**, *12*, 1713.

345. EA(NgF$^+$) = IP(Ng) + BE(NgF$\cdot$) - BE(NgF$^+$), where BE(XeF$\cdot$)

346. Schrobilgen, G. J., *J. Chem. Soc., Chem. Comm.*, **1998**, 863.

347. Allen, L. C., *J. Am. Chem. Soc.*, **1989**, *111*, 9003.

348. Pauling, L., *The Nature of the Chemical Bond and the Structure of Molecules and Crystals, 3rd Ed.*; Cornell University Press: Ithica, NY, 1960, p. 93.

349. Reprinted with permission from Inorganic Chemistry, 2004, in press. Copyright 2004 American Chemical Society.

350. Huheey, J. E., *Inorganic Chemistry, 4th Ed.*; HarperCollins College Publishers: New York, 1993, pp. 876 - 877.

351. Christe, K. O.; Wilson, W. W., *Inorg. Chem.*, 1983, *22*, 1950.

352. Christe, K. O.; Sawodny, W., *Inorg. Chem.*, 1967, *6*, 1783.

353. Christe, K. O.; Schack, C. J., *Inorg. Chem.*, 1970, *9*, 2801.

354. Christe, K. O.; Sawodny, W., *Inorg. Chem.*, 1968, *7*, 1685.

355. Brownstein, M.; Selig, H., *Inorg. Chem.*, 1972, *11*, 656.

356. Hon, J. F.; Christe, K. O., *J. Chem. Phys.*, 1970, *52*, 1960.

357. Beaton, S., Ph.D. Thesis, University of British Columbia, 1966. The I-F bond length was estimated to be 1.75 Å from powder diffraction data.

358. The structure of $[IF_6][Sb_2F_{11}]$ at -100 °C was solved in the space group $P2_1/m$, but exhibited higher thermal parameters for the equatorial fluorine positions of the anion and significantly higher values of R_1 and wR_2. For these reasons, the discussion of the geometric parameters of $[IF_6][Sb_2F_{11}]$ is limited to those determined at -173 °C.

359. The crystal structure of $[IF_6][Sb_2F_{11}]$ at -100 °C was obtained in collaboration with Dr. K. O. Christe, and A. Kornath, Loker Hydrocarbon Research Institute, University of Southern California.

360. Lehmann, J. F.; Schrobilgen, G. J.; Christe, K. O.; Kornath, A.; Suontamo, R. J., *Inog. Chem.*, 2004, in press.

361. Sham, I. H. T.; Patrick, B. O.; von Ahsen, B.; von Ahsen, S.; Willner, H.; Thompson, R. C.; Aubke, F., *Solid State Sciences*, 2002, *4*, 1457.

362. Vij, A.; Tham, F. S.; Vij, V.; Wilson, W. W.; Christe, K. O., *Inorg. Chem.*, 2002, *41*, 6397.

363. Minkwitz. R.; Reinemann, S.; Seelbinder, R.; Konikowski, D.; Hartl, H.; Brüdgam, I.; Hegge, J.; Hoge, B.; Sheehy, J. A.; Christe, K. O., *Inorg. Chem.*, 2001, *40*, 4404.

364. Vij, A.; Wilson, W. W.; Vij, V., Tham, F. S.; Sheehy, J. A.; Christe, K. O., *J. Am. Chem. Soc.*, 2001, *123*, 6308.

365. Saito, Y., *Can. J. Chem.*, 1965, *43*, 2530.

366. Lindeman, B.; Forsén, S., In *NMR, Basic Principles and Progress*; Diehl, P.; Fluck, E; Kosfeld, R., eds.; Springer-Verlag, New York, 1976, Vol. 12, p. 326.

367. Drakenberg, T.; Forsén, S., In *The Multinuclear Approach to NMR Spectroscopy*; Lambert, J. B.; Riddell., F. G., eds.; NATO ASI Series C, Reidel: Boston, 1983, p. 405.

368. Lindeman, B.; In *NMR of Newly Accessible Nuclei*, Laszlo, P., ed.; Academic Press: London, 1983, Vol. 1, p. 233.

369. Levason, W.; Ogden, J. S.; Spicer, M. D.; Young, N. A., *J. Chem. Soc., Dalton, Trans.*, 1990, 349.

370. Kren, R. M.; Dodgen, H. W.; Nyman, C. J., *Inorg. Chem.*, 1968, *7*, 446.

371. Evans, J.; Levason, W.; Spicer, M. D., *J. Chem. Soc., Dalton Trans.*, 1990, 2307.

372. Abragam, A., *The Principles of Nuclear Magnetism*; Oxford University Press: London, 1978, Chapter 8.

373. Sanders, J. C. P.; Schrobilgen, G. J., In *Multinuclear Magnetic Resonance in Liquids and Solids - Chemical Applications*; Granger, P.; Harris, R. K., eds.; Kluwer Academic Press: Netherlands, 1990, pp. 157 - 186.

374. Sundholm, D.; Olsen, J., *J. Chem. Phys.*, 1993, *98*, 7152.

375. Legon, A. C.; Thorn, J. C., *Chem. Phys. Lett.*, 1993, *215*, 554.

376. Bieroń, J.; Pyykoö, P.; Sundholm, D.; Kellö, V.; Sadlej, A. J. *Phys. Rev. A*, 2001, *64*, 052507.

377. Suzuki, M.; Kubo, R., *Mol. Phys.*, 1963, *7*, 201.

378. Hertz, H. G.; Holz, M.; Klute, R.; Stalidis, G.; Versmold, H., *Ber. Bunsen-Ges. Phys. Chem.*, 1974, *78*, 24.

379. Jameson, C. J.; Gutowsky, H. S., *J. Chem. Phys.*, 1964, *40*, 1714.

380. Griffith, J. S.; Orgel, L. E., *Trans. Faraday Soc.*, 1957, *53*, 601.

381. Schneider, W. G.; Buckingham, A. D., *Discuss. Faraday Soc.*, 1962, *34*, 147.

382. Barnes, R. G.; Smith, W. V., *Phys. Rev.*, 1954, *93*, 95.

383. Sanders, J. C. P., Ph.D. Thesis, University of Nottingham, Nottingham, UK, 1986, p. 82.

384. Kennedy, J. D.; McFarlane, W.; Pyne, G. S., *J. Chem. Soc., Dalton Trans.*, 1977, 2332.

385. McFarlane, H. C. E; McFarlane, W., *J. Chem. Soc., Dalton, Trans.*, 1973, 2416.

386. Damerius, R.; Huppmann, P.; Lentz, D.; Seppelt, K., *J. Chem. Soc., Dalton Trans.*, 1984, 2821.

387. Collins, M. J.; Schrobilgen, G. J., *Inorg. Chem.*, 1985, *24*, 2608.

388. Schumacher, G. A.; Schrobilgen, G. J., *Inorg. Chem.*, 1984, *23*, 2923.

389. The ^{77}Se, ^{125}Te and ^{129}Xe chemical shifts of SeF_3^+ (1135 ppm, SO_2ClF),[386] TeF_3^+ (671.2 ppm, SO_2),[387] XeF^+ (-574 ppm, SbF_5),[78,79] XeF_3^+ (595 ppm, SbF_5),[78] and XeF_5^+ (12.7 ppm, HF)[78] are all significantly deshielded with respect to; SeF_4 (1083 ppm, CH_3F),[386] TeF_4 (606.6 ppm, SO_2),[387] XeF_2 (-2009 ppm, $CFCl_3$),[78] XeF_4 (202.9 ppm, $CFCl_3$)[388] and XeF_6 (-60.8 ppm, a tetramer in CF_2Cl_2/SO_2ClF).[78]

390. Edwards, A. J.; Jones, G. R., *J. Chem. Soc. A*, 1970, 1891.

391. Edwards, A. J.; Taylor, P., *J. Chem. Soc., Dalton Trans.*, 1973, 2150.

392. Burbank, R. D., *Acta Crystallogr.*, 1962, *15*, 1207.

393. Bowater, I. C.; Brown, R. D.; Burden, F. R., *J. Mol. Spectrosc.*, 1968, *28*, 454.

394. Edwards, A. J.; Hewaidy, F. I., *J. Chem. Soc. A*, 1968, 2977.

395. Reichman, S.; Schreiner, F., *J. Chem. Phys.*, 1969, *51*, 2355.

396. Burns, J. H.; Agron, P. A.; Levy, H. A., *Science*, 1963, *139*, 1208.

397. The differences between the bond lengths of the cation and the neutral species are not significant at the $\pm\sigma$ level for IF_6^+ (1.779(6) Å, $Sb_2F_{11}^-$ salt; this work), SeF_3^+ (1.73(4) Å, $Nb_2F_{11}^-$ salt),[390] TeF_3^+ (1.84(2) Å, $Nb_2F_{11}^-$ salt)[391] when compared with those of the neutral parent fluorides IF_7 (1.87(7) Å)[392] SeF_4 (1.72(5) Å),[393] TeF_4 (1.86(6) Å).[394] Significant Xe-F bond length contractions occur for XeF^+ (1.888(4) Å, $Sb_2F_{11}^-$ salt),[309] and XeF_3^+ (weighted average: 1.87(5) Å, $Sb_2F_{11}^-$ salt)[344] when compared with those of XeF_2 1.9773(15) Å, and XeF_4 1.953(4) Å.[396]

346

398. Chevalier, Y., *Magn. Res. Chem.*, **1986**, *24*, 404.

399. Bryce, D. L.; Wasylishen, R. E., *Inorg. Chem.*, **2002**, *41*, 3091.

400. Ramsey, N. F., *Phys. Rev.*, **1953**, *91*, 303.

401. Pople, J. A.; Santry, D. P., *Mol. Phys.*, **1964**, *8*, 1.

402. McConnell, H. M., *J. Chem. Phys.*, **1956**, *24*, 460.

403. The values of the gyromagnetic ratios used in this study are ^{19}F (25.1815×10^7 rad s^{-1} T^{-1}), ^{35}Cl (2.6242×10^7 rad s^{-1} T^{-1}), ^{37}Cl (2.1844×10^7 rad s^{-1} T^{-1}), ^{79}Br (6.7256×10^7 rad s^{-1} T^{-1}), ^{81}Br (7.2498×10^7 rad s^{-1} T^{-1}) and ^{127}I (5.3896×10^7 rad s^{-1} T^{-1}).

404. Pyykkö, P.; Wiesenfeld, L., *Mol. Phys.*, **1981**, *43*, 557.

405. Jameson, C. J. In *Multinuclear NMR*; Mason, J., ed.; Plenum Press: New York, **1987**; Chapter 4, p. 92 - 100.

406. Allred, A. L.; Rochow, E. G., *J. Inorg. Nucl. Chem.*, **1958**, *5*, 264.

407. Holleman, A. F.; Wiberg, E., In *Inorganic Chemistry*, Wiberg, N.; Aylett, B. J., eds.; Academic Press: San Diego, **2001**, pp. 331 - 337.

408. Kutzelnigg, W., *Angew. Chem. Int. Ed. Engl.*, **1984**, *23*, 272; *Angew. Chem.*, **1984**, *96*, 262.

409. Robinson, E. A.; Gillespie, R. J., *Inorg. Chem.*, **2003**, *42*, 3865.

410. The Br-F bond length (1.55 Å) and inter-ligand F···F contact distance (2.19 Å) cited for the BrF_6^+ cation in Table 4 of ref 409 are erroneous; the values should be 1.666(11) and 2.356(11) Å, respectively.

411. Zalkin, A.; Forrester, J. D.; Templeton, D. H., *Acta Crystallogr.*, **1964**, *17*, 1408.

412. Popov, D. Y.; Kavun, V. Y.; Gerasimenko, A. V.; Sergienko, V. I.; Antokhina, T. F., *Russ. J. Inorg. Chem.*, **1999**, *44*, 97; *Zh. Neorg. Khim.*, **1999**, *44*, 103.

413. Ischenko, A.; Ewbank, J. D.; Schäfer, L., *J. Phys. Chem.*, **1994**, *98*, 4287.

414. Wang, Y.; Calvert, L. D.; Brownstein, S. K., *Acta Crystallogr.*, **1980**, *B36*, 1523.

415. Ewing, V. C.; Sutton, L. E., *Trans. Faraday Soc.*, **1963**, *59*, 1241.

416. Benghalem, A.; Leblanc, M.; Calage, Y., *Acta Crystallogr.*, **1990**, *C46*, 2453.

417. Seip, H. M.; Stølevik, R., *Acta Chem. Scand.*, **1966**, *20*, 1535.

418. Brock, D.; Mercier, H. P. A.; Schrobilgen, G. J. Unpublished results.

419. Lucier, G.; Münzenberg, J.; Casteel Jr., W. J.; Bartlett, N., *Inorg. Chem.*, **1995**, *34*, 2692.

420. Ruff, O.; Keim, R., *Z. Anorg. Chem.*, **1931**, *201*, 245.

421. Selig, H.; Sarig, S.; Abramowitz, S., *Inorg. Chem.*, **1974**, *13*, 1508.

422. Drake, G. W.; Dixon, D. A.; Sheehy, J. A.; Boatz, J. A.; Christe, K. O., *J. Am. Chem. Soc.*, **1998**, *120*, 8392.

423. Christe, K. O.; Sanders, J. C. P.; Schrobilgen, G. J.; Wilson, W. W., *J. Chem. Soc., Chem. Comm.*, **1991**, *13*, 837.

424. Siegel, S., *Acta Crystallogr.*, **1956**, *9*, 493.

425. Bougon, R.; Charpin, P.; Soriano, J. C. R., Hebd. *Seánces Acad. Sci., Ser.* **1971**, *C272*, 565.

426. Lind, M. D.; Christe, K. O., *Inorg. Chem.*, **1972**, *11*, 608.

427. Gillespie, R. J.; Spekkens, P. H., *J. Chem. Soc., Dalton Trans.*, **1976**, 2391.

428. Bougon, R.; Joubert, P.; Tantot, G., *J. Chem. Phys.*, **1977**, *66*, 1562.

429. *NIST JANAF Thermochemical Tables 4th Ed.*, Chase, M. C. Jr., ed.; American Institute of Physics; New York, 1998, pp. 775, 1745.

430. Nakamoto, K., *Infrared and Raman Spectra of Inorganic and Coordination Compounds 5th Ed.*, John Wiley and Sons: New York, 1997, pp. 209 - 211.

431. Beattie, I. R.; Blayden, H. E.; Crocombe, R. A.; Jones, P. J.; Ogden, J. S., *J. Raman Spectrosc.*, 1976, *4*, 313.

432. Hope, E. G.; Levason, W.; Ogden, J. S., *J. Chem. Soc., Dalton Trans.*, 1988, 61.

433. Claassen, H. H.; Juston, J. L., *J. Chem. Phys.*, 1971, *55*, 1505.

434. Gerken, M. Ph.D., Thesis, McMaster University, Hamilton, Ontario, Canada, 2000, Chapter 5.

435. Gillespie, R. J., In *Noble-Gas Compounds*; Hyman, H. H., ed.; University of Chicago Press, Chicago, 1963, pp. 333 - 339.

436. Dibeler, V. H.; Liston, S. K., *J. Chem. Phys.*, 1968, *48*, 4765.

437. Sladky, F.; Kropshofer, *Inorg. Nucl. Chem. Lett.*, 1972, *8*, 195.

438. Hwang, I. C.; Kuschel, R.; Seppelt, K., *Z. Anorg. Allg. Chem.*, 1997, *623*, 379.

439. Sladky, F. O., *Angew. Chem., Int. Ed. Engl.*, 1969, *8*, 523; *Angew. Chem.*, 1969, *81*, 536.

440. Gerken, M.; Kolb, P.; Wegner, Mercier, H. P. A.; Borrmann, H.; Dixon, D. A.; Schrobilgen, G. J., *Inorg. Chem.*, 2000, *39*, 2813.

441. Sladky, F.; Kropshofer, H.; Leitzke, O., *J. Chem. Soc., Chem. Comm.*, 1973, 134.

442. Mercier, H. P. A.; Moran, M. D,; Schrobilgen, G. J.; Steinberg, C.; Suontamo, R. J., *J. Am. Chem. Soc.*, 2004, *126*, 5533.

443. Christe, K. O.; Dixon, D. A.; Sanders, J. C. P.; Schrobilgen, G. J.; Wilson, W. W., *Inorg. Chem.*, 1993, *32*, 4089.

444. Stout, C. H.; Jensen, L. H., *X-Ray Structure Determination 2nd Ed.*, John Wiley and Sons; New York, 1989, p. 12.

445. Magnuson, D. W., *J. Chem. Phys.*, 1951, *19*, 1071.

446. Stephenson, C. V.; Jones, E. A., *J. Chem. Phys.*, 1952, *20*, 135.

447. Gerbert, E.; Peterson, S. W.; Reis, A. H.; Appelman, E. H., *J. Inorg. Nucl. Chem.*, 1981, *43*, 3085.

448. Gallucci, J. C.; Gerkin, R. E.; Reppart, W. J., *Acta Crystallogr.*, 1989, *C45*, 701.

449. Berg, R. W., *Spectrochim. Acta*, 1978, *34A*, 655.

450 Kabisch, G.; Close, M., *J. Raman Spectrosc.*, 1978, *21*, 1708.

451. Mercier, H. P. A.; Sanders, J. C. P.; Schrobilgen, G. J., *J. Am. Chem. Soc.*, 1994, *116*, 2921.

452. Beattie, I. R.; Livingston, K. M. S.; Reynolds, D. J., *J. Chem. Phys.*, 1969, *51*, 4269.

453. Hoskins, L. C.; Lord, R. C., *J. Chem. Phys.*, 1967, *46*, 2402.

454. Gaunt, J.; Ainscough, J. B., *Spectrochim. Acta*, 1957, *10*, 57.

455. Claassen, H. H.; Selig, H., *J. Chem. Phys.*, 1966, *44*, 4039.

456. Hope, E. G., *J. Chem. Soc., Dalton Trans.*, 1990, 723.

457. Acquista, N.; Abramowitz, S., *J. Chem. Phys.*, 1973, *58*, 5484.

458. Smardzewski, R. R.; Fox, W. B., *J. Am. Chem. Soc.*, 1974, *96*, 304.

459. Babaeva, V. P.; Rosolovskii, V. Y., *Russ. J. Inorg. Chem.*, 1971, *16*, 471.

460. Jones, E. A.; Woltz, P. J. H., *J. Chem. Phys.*, 1950, *18*, 1516.

461. Magnuson, D. W., *J. Chem. Phys.*, **1952**, *20*, 380.

462. Jones, L. H., *J. Chem. Phys.*, **1967**, *47*, 3371.

463. Christe, K. O.; Jenkins, H. D. B., *J. Am. Chem. Soc.*, **2003**, *125*, 9457.

464. Mason, J.; Van Bronswijk, W., *J. Chem. Soc., Chem. Comm.*, **1969**, 357.

465. Schaumburg, K., *J. Magn. Res.*, **1972**, *7*, 177.

466. Martin, J. S.; Fujiwara, F. Y., *Can. J. Chem.*, **1971**, *49*, 3071.

467. Clark, A. H.; Beagley, B.; Cruickshank, D. W. J.; Hewitt, T. G., *J. Chem. Soc. A*, **1970**, 872.

468. Christe, K. O.; Dixon, D. A.; Sanders, J. C. P.; Schrobilgen, G. J.; Tsai, S. S.; Wilson, W. W., *Inorg. Chem.*, **1995**, *34*, 1868.

469. Largon, J. W.; McMahon, T. B., *J. Am., Chem. Soc.*, **1983**, *105*, 2944.

470. Veljkovic, M.; Neskovic, O.; Zmbov, K. F.; Borshchevskii, A. Y.; Vaisberg, V. F.; Sidorov, L. N., *Rapid Comm. Mass Spectrom.*, **1991**, *5*, 37.

471. Nikitin, M. I.; Igolkina, H. A.; Skokan, E. V.; Sorokin, I. D.; Sidorov, L. N., *Zh. Fiz. Khim.*, **1986**, *60*, 39.

472. Lobring, K. C.; Check, C. E.; Sunderlin, L. S., *Int. J. Mass. Spec.*, **2003**, *22*, 221.

473. Christe, K. O.; Curtis, E. C.; Dixon, D. A.; Mercier, H. P. A.; Sanders, J. C. P.; Schrobilgen, G. J., *J. Am. Chem. Soc.*, **1991**, *113*, 3351.

474. Wermer, P.; Ault, B. S., *Inorg. Chem.*, **1981**, *20*, 970.

475. Christe, K. O.; Dixon, D. A.; Mercier, H. P. A.; Sanders, J. C. P.; Schrobilgen, G. J.; Wilson, W. W., *J. Am. Chem. Soc.*, **1994**, *116*, 2850.

476. Gilbert, A. S.; Sheppard, N., *Spectrochim. Acta*, **1976**, *32A*, 923.

477. Lawlor, L.; Passmore, J., *Inorg. Chem.*, **1979**, *18*, 2923.

478. Natarajan, A.; Chockalingam, K., *Pramana*, **1977**, *9*, 573.

479. Gnanasekaran, S.; Ranganayaki, S.; Gnanasekaran, P., *Asian J. Chem.*, **1989**, *1*, 173.

480. Mohan, S.; Vasuki, G., *Proc. Nat. Acad. Sci. India*, **1989**, *59A*, 163.

481. So, S. P., *Z. Phys. Chem., Neue Folge*, **1978**, *109*, 157.

482. Wilson, E. B., *J. Chem. Phys.*, **1941**, *9*, 76.

483. Komornicki, A; BMATRIX Version 2.0; Polyatomics Research Institute: Palo Alto, CA, **1996**.

484. Reed, A. E.; Schleyer, P. v. R., *J. Am. Chem. Soc.*, **1990**, *112*, 1434.

485. Levin, I. W, *J. Mol. Spectrosc.*, **1970**, *33*, 61.

486. Christe, K. O.; Sawodny, W., *Inorg. Chem.*, **1967**, *6*, 313.

487. Lynron, H.; Passmore, J., *Can. J. Chem.*, **1971**, 2539.

488. Edwards, A. J.; Sills, R. J. C., *J. Chem. Soc., A*, **1969**, 1467.

489. Carter, H. A.; Aubke, F., *Can. J. Chem.*, **1970**, *48*, 3456.

490. Asprey, L. B.; Margarave, J. L.; Silverthorn, M. E., *J. Am. Chem. Soc.*, **1961**, *83*, 2955.

491. Kelly, D. H.; Post, B.; Mason, R. W., *J. Am. Chem. Soc.*, **1963**, *85*, 307.

492. Whitney, E.; MacLaren, R.; Fogle, C.; Hurely, T., *J. Am. Chem. Soc.*, **1964**, *86*, 2583.

493. Whitney, E.; MacLaren, Hurtley, T.; Fogle, C., *J. Am. Chem. Soc.*, **1964**, *86*, 4340.

494. Christe, K. O.; Guertin, J. P., *Inorg. Chem.*, **1966**, *5*, 473.

495. Zhang, X.; Seppelt, K., *Z. Anorg. Allg. Chem.*, **1997**, *623*, 491.

496. Bantov, D. V.; Dzevitskiy, B. E.; Konstantinov, T. S.; Ustynyuk, Y. A.; Sukhoverkhov, V. F., *Dokl. Akad. Nauk. SSSR*, **1968**, *186*, 851.

497. Roberto, F. Q.; Mamantov, G., *Inorg. Chim. Acta*, **1968**, *2*, 317.

498. Chrsite, K. O.; Pilipovich, D., *Inorg. Chem.*, **1969**, *8*, 391.

499. Christe, K. O.; Sawdony, W., *Inorg. Chem.*, **1973**, *12*, 2879.

500. Christe, K. O.; Zhang. X.; Sheehy, J. A.; Bau, R., *J. Am. Chem. Soc.*, **2001**, *123*, 6338.

501. Christe, K. O.; Wilson, W. W.; Chirakel, R. V.; Sanders, J. C. P.; Schrobilgen, G. J., *Inorg. Chem.*, **1990**, *29*, 3506.

502. Surles, T.; Perkins, A.; Quarterman, L. A.; Hyman, H. H.; Popov, A. I., *J. Inorg. Nucl. Chem.*, **1972**, *34*, 3561.

503. Mahjoub, A. R.; Zhang, X.; Seppelt, K., *Chem. Eur. J.*, **1995**, *1*, 261.

504. Christe, K. O., *Inorg. Chem.*, **1989**, *28*, 3275.

505. Mahjoub, A. R.; Hoser, A.; Fuchs, J.; Seppelt, K., *Angew. Chem., Int. Ed. Engl.*, **1989**, *28*, 1526; *Angew. Chem.*, **1989**, *101*, 1528.

506. Schmeisser, M.; Brändle., K., *Adv. Inorg. Chem. Radiochem.*, **1963**, *5*, 41.

507. Christe, K. O.; Schack, C. J.; Pilpovich, D.; Sawdony, W., *Inorg. Chem.*, **1969**, *8*, 2489.

508. Bougon, R.; Cicha, W. V.; Lance, M.; Meublat, L.; Nierlich, M.; Vigner, J., *Inorg. Chem.*, **1991**, *30*, 102.

509. Grihapati, M., *Z. Anorg. Allg. Chem.*, **1965**, *340*, 110.

510. Christe, K. O.; Curtis, E. C., *Inorg. Chem.*, **1972**, *11*, 35.

511. Christe, K. O.; Schack, C. J.; Pilipovich, D., *Inorg. Chem.*, **1972**, *11*, 2205.

512. Christe, K. O.; Curtis, E. C.; Schack, C. J., *Inorg. Chem.*, **1972**, *11*, 2212.

513. Christe, K. O.; Curtis, E. C., *Inorg. Chem.*, **1972**, *11*, 2209.

514. Christe, K. O., *Inorg. Nucl. Chem., Lett.*, **1972**, *8*, 457.

515. Christe, K. O.; Wilson, R. D., *Inorg. Chem.*, **1973**, *12*, 1356.

516. Christe, K. O.; Curtis, E. C., *Inorg. Chem.*, **1973**, *12*, 2245.

517. Schack, C. J.; Lindahl, C. B.; Pilipovich, D.; Christe, K. O., *Inorg. Chem.*, **1972**, *11*, 2201.

518. Wamser, C. A.; Fox, W. B.; Gould, D.; Sukornick, B., *Inorg. Chem.*, **1968**, *7*, 1933.

519. Alekseev, V. I.; Fedorova, L. I.; Baluev, A. V., *Bull. Acad. Sci. USSR Chem. Sci.*, **1983**, *32*, 980; *Izvestiya Akad. Nauk. SSSR Khim*, **1983**, *5*, 1084.

520. Tobias, K. M.; Jansen, M., *Z. Anorg. Allg. Chem.*, **1987**, *550*, 16.

521. Gillespie, R. J.; Hargittai, I., In *The VSEPR Model of Molecular Geometry*, Boston: Allyn and Bacon, **1991**.

522. Edwards, A. J.; Sills, R. J. C., *J. Chem. Soc., Dalton Trans.*, **1974**, 1726.

523. Antipin, M. Y.; Ellern, A. M.; Sukhoverkhov, Y. T.; Buslaev, Y. A., *Dokl. Akad. SSSR, Engl.*, **1987**, *293*, 354; *Dokl. Akad. Nauk. SSSR*, **1987**, *293*, 1152.

524. Dyke, J. M.; Gamblin, S. D.; Hooper, N.; Lee, E. P. F.; Morris, A.; Mok, D. K. W.; Chau, F. T., *J. Chem. Phys.*, **2000**, *112*, 6262.

525. Chau, F. T.; Dyke, J. M.; Lee, E. P. F.; Wang, D, C., *J. Elect. Spec. Rel. Phen.*, **1998**, *7*, 33.

526. Fransisco, J. S., *Chem. Phys. Lett.*, **1998**, *288*, 307.

527. Ellern, A.; Boatz, J. A.; Christe, K. O.; Drews, T.; Seppelt, K., *Z. Anorg. Allg. Chem.*, **2002**, *628*, 1991.

528. Leopold, D.; Seppelt, K., *Angew. Chem., Int. Ed. Engl.*, **1994**, *33*, 975; *Angew. Chem.*, **1994**, *106*, 1043.

529. Adams, S. C.; Bernstein, Z. L., *Acta Crystallogr.*, **1977**, *B33*, 3601.

530. Müller, H. S. P.; Miller, C. E.; Cohen, E. A., *Angew. Chem., Int. Ed. Engl.*, **1996**, *35*, 2129; *Angew. Chem.*, **1996**, *35*, 2285.

531. Tobias, K. M.; Jansen, M., *Angew. Chem., Int. Ed. Engl.*, **1986**, *25*, 993; *Angew. Chem.*, **1986**, *98*, 994.

532. Robiette, A. G.; Parent, C. R.; Gerry, M. C. L., *J. Mol. Spectrosc.*, **1981**, *86*, 455.

533. Oberhammer, H.; Christe, K. O., *Inorg. Chem.*, **1982**, *21*, 273.

534. Burke-Laing, M. E.; Trueblood, K. N., *Acta Crystallogr.*, **1977**, *B33*, 2698.

535. Jenkins, H. D. B.; Tudela, D.; Glasser, L., *Inorg. Chem.*, **2002**, *41*, 2364.

536. Jenkins, H. D. B.; Roobottom, H. K.; Passmore, J.; Glasser, L., *Inorg. Chem.*, **1999**, *38*, 3609.

537. Jenkins, H. D. B.; Glasser, L, *Inorg. Chem.*, **2003**, *42*, 8702. In this equation, V_m is the unit volume of the salt in nm^3, $k = 1360$ J K^{-1} mol^{-1} nm^{-3} and $c = 15$ J K^{-1} mol^{-1}

538. Brunvoll, J.; Ischenko, A. A.; Miakshin, I. N.; Romanov, G. V.; Spiridonov, V. P.; Strand, T. G.; Sukoverkhov, V. F., *Acta Chem. Scand.*, **1980**, *A34*, 733.

539. Shair, R. C.; Schurig, W. F., *Ind. Eng. Chem.*, **1951**, *43*, 1624.

540. Fawcett, J.; Holloway, J. H.; Peacock, R. D.; Russell, D. K., *J. Fluorine Chem.*, **1982**, *20*, 9.

541. Bougon, R.; Huy, T. B.; Burgess, J.; Christe, K. O.; Peacock, R. D., *J. Fluorine Chem.*, **1982**, *19*, 263.

542. Mallouk, T. E.; Rosenthal, G. L.; Muller, G.; Busaco, R.; Bartlett, N., *Inorg. Chem.*, **1984**, *23*, 3167.

543. For salts composed of singly charged and non-liner ions, such as those in the present study: $I = 1$, $\alpha = 117.3$ nm kJ mol^{-1}, $\beta = 51.9$ kJ mol^{-1} and $n = 2$.

544. Jenkins, H. D. B.; Glasser, L.; Klapotke, T. M.; Crawford, M. J.; Lee, J.; Sunderlin, L. S.; Liebman, J. F., *Inorg. Chem.*, **2004**, (in press).

545. O'Hare, P. A. G., *J. Chem. Thermodyn.*, **1993**, *25*, 391.

546. Liass, S.G.; Bartmess J.E.; Liebmann, J.F.; Holmes, J.L.; Levin, R.D.; Mallard, W.G., *J. Phys. Chem. Ref. Data Suppl. 1*, **1988**, *17*.

547. Engelbrecht, A.; Atzwanger, H., *J. Inorg. Nucl. Chem.*, **1956**, *2*, 348.

548. Christe, K. O.; Curtis, E. C.; Jacob, E:, *Inorg. Chem.*, **1978**, *17*, 2744.

549. Nakamoto, K., In *Infrared and Raman Spectra of Inorganic and Coordination Compounds 5th Ed.*, John Wiley and Sons: Toronto, **1997**, pp. 180 - 182.

550. Engelbrecht, A.; Mayr, O.; Ziller, G.; Schandara, E., *Monatsh. Chemie*, **1974**, *105*, 796.

551. Carter, H. A.; Ruddick, J. N.; Sams, J. R.; Aubke, F., *Inorg. Nucl. Chem. Lett.*, **1975**, *11*, 29.

552. Gillespie, R. J.; Krasznai, J. P., *Inorg. Chem.*, **1977**, *16*, 1384.

553. Syvret, R. G., Ph.D. Thesis, McMaster University, **1987**, Chapters 3 - 7.

554. Boatz, J. A.; Christe, K. O.; Dixon, D. A.; Fir, B. A.; Gerken, M.; Gnann, R. Z.; Mercier, H. P. A.; Schrobilgen, G. J., *Inorg. Chem.*, 2003, *42*, 5282.

555. Syvret, R. G.; Schrobilgen, G. J., *J. Chem. Soc., Chem. Comm.*, 1985, *21*, 1529.

556. Syvret, R. G.; Schrobilgen, G. J., *Inorg. Chem.*, 1989, *28*, 1564.

557. Beattie, I.; Crobombe, R.; German, A.; Jones, P.; Marsden, C.; Van Schalkwyk, G.; Bukovszky, A., *J Chem. Soc., Dalton Trans.*, 1976, 1380.

558. Smart, L., *Chem. Comm.*, 1977, 519.

559. Pointner, B. E.; Schrobilgen, G. J., personal communication.

560. Sloth, E. N.; Stein, L.; Williams, C. W. W., *J. Phys. Chem.*, 1969, *73*, 278.

561. Žemva, B,; Lutar, K.; Chacón, L.; Fele-Beuermann, M.; Allman, J.; Shen, C.; Bartlett, N., *J. Am. Chem., Soc.*, 1995, *117*, 10025.

562. Muetteries, E. L.; Phillips, W. D., *J. Am. Chem. Soc.*, 1959, *81*, 1084.

563. Dungan, C. H.; Van Wazer, J. R., *Compilation of Reported F^{19} NMR Chemical Shifts*, Wiley-Interscience, New York, NY, 1970.

564. Gillespie, R. J.; Schrobilgen, G. J., *Inorg. Chem.*, 1974, *13*, 765.

565. Gutowsky, H. S.; Hoffman, C. J., *J. Chem. Phys.*, 1951, *19*, 1259.

566. Schack, C. J.; Lindahl, C. B.; Pilipovich, Christe, K. O., *Inorg. Chem.*, 1972, *11*, 9.

567. Christe, K. O.; Bougon, R., *J. Chem. Soc., Chem. Comm.*, 1992, 1056.

568. Bougon, R.; Ban, B.; Seppelt, K., *Chem. Ber.*, 1993, *126*, 1331.

569. LeBlond, N.; Schrobilgen, G. J., *Chem. Comm.*, 1996, 2479.

570. Liebman, J. F., *J. Fluorine Chem.*, 1977, *9*, 147.

571. The XF_6^+ cations were investigated using the HF, MP2 and SVWN methods with the DZVP basis set. The vibrational frequencies of ClF_6^+ cation obtained using the HF/6-311G(d), MP2/6-311G(d) and MPW1PW91/DZVP methods were shifted by an average of -6, +12 and +19 cm^{-1}, respectively. The vibrational frequencies of BrF_6^+ cation obtained using the HF/6-311G(d), MP2/6-311G(d) and MPW1PW91/DZVP methods were shifted by an average of +1, +21 and +20 cm^{-1}, respectively.

572. Oesterling, R. E.; Tyczkowski, E. A., *J. Am. Chem. Soc.*, 1958, *80*, 5286.

573. Johnson, G. K.; Malm, J. G.; Hubbard, W. N., *J. Chem. Thermodyn.*, 1972, *4*, 879.

574. Gunn, S. R., *J. Am. Chem. Soc.*, 1965, *87*, 2290.

575. Kudchadker, S. A.; Kudchadker, A. P., *Proc. Indian Acad. Sci.*, 1971, *73A*, 261.

576. Kirshenbaum, A. D.; Grosse, A. V.; Aston, J. G., *J. Am. Chem. Soc.*, 1959, *81*, 6398.

577. Kirshenbaum, A. D.; Grosse, A. V., *J. Am. Chem. Soc.*, 1959, *81*, 1277.

APPENDIX A
ATOMIC COORDINATES, SITE OCCUPANCIES AND EQUIVALENT ISOTROPIC DISPLACEMENT PARAMETERS FOR:

α-KrF$_2$, [KrF][MF$_6$] (M = As, Sb, Bi), [Kr$_2$F$_3$][SbF$_6$]·KrF$_2$,
Kr$_2$F$_3$]$_2$[SbF$_6$]$_2$·KrF$_2$,[Kr$_2$F$_3$][AsF$_6$]·[KrF][AsF$_6$], XeF$_2$, [XeF][MF$_6$] (M = As, Sb, Bi),
[XeF][M$_2$F$_{11}$] (X = Sb, Bi), [KrF][AuF$_6$], α-[O$_2$][AuF$_6$], [XF$_6$][Sb$_2$F$_{11}$] (X = Cl, Br, I),
[N(CH$_3$)$_4$][BrO$_3$F$_2$], [NO]$_2$[BrO$_3$F$_2$][F], and [XO$_2$][SbF$_6$] (X = Cl, Br)

Atom	x	y	z	S.O.F	U$_{eq}$
			α-KrF$_2$		
Kr	0.00000	0.00000	0.00000	0.0625	0.03169
F	0.00000	0.00000	0.29168	0.1250	0.04097
			β-[KrF][AsF$_6$]		
Kr	0.46804	0.72625	0.47023	1.0000	0.01835
As	0.09572	0.48544	0.27227	1.0000	0.01730
F1	0.62808	0.87243	0.52090	1.0000	0.03547
F2	0.28829	0.54413	0.41669	1.0000	0.02811
F3	-0.07902	0.42815	0.14086	1.0000	0.03416
F4	0.23464	0.60729	0.19267	1.0000	0.03133
F5	0.35284	0.38490	0.25180	1.0000	0.02960
F6	-0.01840	0.36951	0.36873	1.0000	0.03231
F7	-0.14089	0.59117	0.30878	1.0000	0.03740
			[KrF][SbF$_6$]		
Sb	0.40256	0.48700	0.22753	1.0000	0.01804
Kr	0.01928	0.73354	0.02528	1.0000	0.01956
F1	-0.13951	0.87544	-0.02432	1.0000	0.03595
F2	0.19941	0.55756	0.08322	1.0000	0.02790
F3	0.59007	0.41688	0.36376	1.0000	0.03568
F4	0.26804	0.61408	0.32122	1.0000	0.03534
F5	0.12445	0.38299	0.24910	1.0000	0.02869
F6	0.50857	0.36670	0.11570	1.0000	0.03504
F7	0.66146	0.59644	0.18910	1.0000	0.03630

Appendix A.   continued...

Atom	x	y	z	S.O.F	U_{eq}
			$[KrF][BiF_6]$		
Bi	0.40054	0.48769	0.22991	1.0000	0.02217
Kr	0.01423	0.73492	0.02473	1.0000	0.02391
F1	-0.14938	0.87571	-0.02225	1.0000	0.04883
F2	0.19019	0.56372	0.07711	1.0000	0.03518
F3	0.58364	0.40824	0.36940	1.0000	0.04033
F4	0.25646	0.62417	0.32268	1.0000	0.04118
F5	0.10275	0.38191	0.24749	1.0000	0.03580
F6	0.50077	0.36659	0.11077	1.0000	0.03957
F7	0.67004	0.60096	0.19170	1.0000	0.04163
			$[Kr_2F_3][SbF_6]\cdot KrF_2$		
Sb1	0.29012	0.67814	0.77958	1.0000	0.01696
Kr1	0.23448	0.16519	0.77950	1.0000	0.02025
Kr2	0.68954	0.32873	0.72682	1.0000	0.02346
Kr5	0.80852	-0.14759	0.70707	1.0000	0.02184
F1	-0.00403	0.11588	0.84436	1.0000	0.03120
F2	0.85735	0.43921	0.73642	1.0000	0.04172
F3	0.50869	0.20159	0.70278	1.0000	0.04093
F7	0.93764	-0.21134	0.50628	1.0000	0.03491
F8	0.68186	-0.07572	0.90547	1.0000	0.03686
F9	0.26138	0.88098	0.62333	1.0000	0.02989
F10	0.22401	0.56057	0.67102	1.0000	0.03119
F11	0.32511	0.47581	0.93161	1.0000	0.02997
F12	0.04233	0.68393	0.93419	1.0000	0.02647
F13	0.36063	0.79495	0.88609	1.0000	0.02891
F14	0.54210	0.67894	0.62217	1.0000	0.02922
			$[Kr_2F_3]_2[SbF_6]_2\cdot KrF_2$		
Sb2	0.78981	0.07581	0.94253	1.0000	0.01874
Sb1	1.31493	0.32405	0.96179	1.0000	0.01876
Kr1	1.24253	0.02975	1.49194	1.0000	0.02524
Kr2	1.34178	0.05885	1.10222	1.0000	0.02491
Kr3	0.75338	0.22000	1.01920	1.0000	0.02254
Kr4	1.14574	0.19517	0.90389	1.0000	0.02202

Appendix A.   continued...

Atom	x	y	z	S.O.F	U_{eq}
Kr5	0.80366	0.37603	0.95542	1.0000	0.02345
F1	1.10989	0.02939	1.62843	1.0000	0.04587
F2	1.29854	0.08387	0.89048	1.0000	0.04135
F3	1.39921	0.02879	1.34411	1.0000	0.03497
F4	0.62593	0.21763	1.15935	1.0000	0.04023
F5	1.35698	0.17098	0.93344	1.0000	0.03739
F6	0.90241	0.22377	0.86280	1.0000	0.03186
F7	0.74230	0.43413	0.88948	1.0000	0.03917
F8	0.86562	0.31759	1.01819	1.0000	0.03815
F9	1.22023	0.36893	1.05525	1.0000	0.03252
F10	1.09671	0.31944	0.76693	1.0000	0.03673
F11	1.23142	0.28320	1.08372	1.0000	0.02890
F12	1.39136	0.36515	0.83445	1.0000	0.04444
F13	1.40657	0.27903	0.86586	1.0000	0.04292
F14	1.53546	0.32723	1.15241	1.0000	0.02872
F15	0.98181	0.07311	1.16321	1.0000	0.03053
F16	0.60136	0.07751	0.72076	1.0000	0.03271
F17	0.66614	0.03223	1.01267	1.0000	0.03256
F18	0.91333	0.11958	0.87476	1.0000	0.03994
F19	0.90374	0.03351	0.85506	1.0000	0.03619
F20	0.68029	0.11789	1.03431	1.0000	0.02967
		$[Kr_2F_3][AsF_6] \cdot [KrF][AsF_6]$			
As1	0.76554	0.68056	0.48673	1.0000	0.02611
As2	0.73651	0.47225	0.22394	1.0000	0.02951
Kr1	0.69331	0.63465	0.98389	1.0000	0.03201
Kr2	0.29063	0.72093	0.79665	1.0000	0.03310
Kr3	0.73820	0.43098	0.60522	1.0000	0.03213
F1	0.95877	0.61231	1.02281	1.0000	0.06361
F2	0.19988	0.77273	0.66811	1.0000	0.05140
F3	0.38627	0.66187	0.94462	1.0000	0.04016
F4	0.71014	0.38541	0.75986	1.0000	0.04941
F5	0.77665	0.48758	0.42976	1.0000	0.04909
F6	0.69738	0.45837	0.03952	1.0000	0.03838
F7	0.80784	0.40744	0.26992	1.0000	0.05245

Appendix A.   continued...

Atom	x	y	z	S.O.F	U_{eq}
F8	0.99610	0.48914	0.20450	1.0000	0.05188
F9	0.66680	0.53936	0.20763	1.0000	0.04800
F10	0.48059	0.45819	0.26845	1.0000	0.05156
F11	0.75271	0.74884	0.48327	1.0000	0.10871
F12	0.72421	0.67989	0.29687	1.0000	0.08477
F13	0.77881	0.61105	0.48852	1.0000	0.08268
F14	1.03821	0.68148	0.47098	1.0000	0.07312
F15	0.50001	0.67530	0.50597	1.0000	0.10297
F16	0.80572	0.68219	0.67795	1.0000	0.05708
		$[KrF][AuF_6]$			
Au	0.97045	0.04623	0.51746	1.0000	0.01913
Kr	0.99332	-0.39008	0.69898	1.0000	0.02312
F1	0.94354	-0.55812	0.80485	1.0000	0.05197
F2	1.06985	-0.19978	0.56730	1.0000	0.08169
F3	0.87234	0.28220	0.46501	1.0000	0.07342
F4	0.78534	-0.01834	0.58986	1.0000	0.03006
F5	1.09638	0.14671	0.67931	1.0000	0.06128
F6	1.15816	0.10574	0.44759	1.0000	0.03227
F7	0.84495	-0.05352	0.35765	1.0000	0.06752
		$\alpha\text{-}[O_2][AuF_6]$			
Au1	0.50000	0.50000	0.50000	0.5000	0.02323
F1	0.41481	0.73095	0.81846	1.0000	0.03363
F2	0.19751	0.54065	0.29692	1.0000	0.03298
F3	0.27363	0.17819	0.59243	1.0000	0.03718
O1	-0.03734	0.06956	0.94706	1.0000	0.03336
		XeF_2			
Xe	0.00000	0.00000	0.00000	0.0625	0.00853
F	0.00000	0.00000	0.28592	0.1250	0.01505
		$[XeF][AsF_6]$			
Xe	0.26243	0.19605	0.62195	1.0000	0.01044
As	0.23650	0.29602	0.38801	1.0000	0.00862
F1	0.19787	0.07647	0.72471	1.0000	0.04375

Appendix A.   continued...

Atom	x	y	z	S.O.F	U_{eq}
F2	0.34035	0.34040	0.50293	1.0000	0.03619
F3	0.14189	0.25483	0.28279	1.0000	0.03589
F4	-0.01897	0.29494	0.41427	1.0000	0.02387
F5	0.25322	0.02590	0.41062	1.0000	0.03099
F6	0.50128	0.29752	0.37388	1.0000	0.02398
F7	0.22677	0.56829	0.37788	1.0000	0.02488
		[XeF][SbF₆]			
Xe	0.47150	0.23554	0.47672	1.0000	0.01015
Sb	0.09768	-0.01171	0.27217	1.0000	0.00943
F1	0.63352	0.38269	0.52627	1.0000	0.02590
F2	0.28881	0.05400	0.41842	1.0000	0.01680
F3	-0.07649	-0.07809	0.13485	1.0000	0.02163
F4	0.22790	0.11805	0.18630	1.0000	0.02126
F5	0.38029	-0.10655	0.24780	1.0000	0.01774
F6	-0.00713	-0.13376	0.37684	1.0000	0.02071
F7	-0.16654	0.08828	0.31237	1.0000	0.02485
		[XeF][BiF₆]			
Bi	0.39149	0.51722	0.21886	1.0000	0.01007
Xe	-0.00637	0.23560	0.02310	1.0000	0.01163
F1	-0.20099	0.09170	-0.04004	1.0000	0.02505
F2	0.20939	0.40550	0.09419	1.0000	0.02310
F3	0.54596	0.62635	0.33727	1.0000	0.02057
F4	0.24450	0.38934	0.32028	1.0000	0.02444
F5	0.68828	0.40121	0.20033	1.0000	0.02378
F6	0.50721	0.63229	0.10043	1.0000	0.02145
F7	0.07650	0.62266	0.22149	1.0000	0.01639
		[XeF][Sb₂F₁₁]			
Xe	0.31982	1.21939	0.70777	1.0000	0.01129
Sb1	-0.04859	0.94848	0.85814	1.0000	0.00937
Sb2	0.30907	0.71376	0.69615	1.0000	0.00981
F1	0.51370	1.35184	0.70021	1.0000	0.02565
F2	0.07750	1.05699	0.71864	1.0000	0.01811

Appendix A.   continued...

Atom	x	y	z	S.O.F	U_{eq}
F3	-0.14853	0.82468	0.98974	1.0000	0.01945
F4	0.14610	1.00763	1.04836	1.0000	0.02412
F5	-0.21145	1.09930	0.86234	1.0000	0.01803
F6	-0.20654	0.87561	0.65202	1.0000	0.01986
F7	0.13382	0.79270	0.83671	1.0000	0.01479
F8	0.46581	0.64496	0.56878	1.0000	0.01982
F9	0.42803	0.89093	0.74012	1.0000	0.02220
F10	0.12602	0.79039	0.50615	1.0000	0.02268
F11	0.16212	0.54841	0.67600	1.0000	0.02204
F12	0.46491	0.64746	0.90822	1.0000	0.02223
		$[XeF][Bi_2F_{11}]$			
Bi1	0.09758	0.33859	0.74005	1.0000	0.00864
Bi2	0.39849	0.10286	0.91726	1.0000	0.00998
Xe	0.40294	0.60505	0.90611	1.0000	0.01102
F1	0.49669	0.73212	0.99782	1.0000	0.02175
F2	0.29618	0.45637	0.79577	1.0000	0.01647
F3	-0.07812	0.20677	0.70385	1.0000	0.01529
F4	-0.04706	0.42304	0.83611	1.0000	0.02069
F5	0.05603	0.47993	0.64118	1.0000	0.01664
F6	0.26764	0.24704	0.65959	1.0000	0.02283
F7	0.17776	0.19951	0.84699	1.0000	0.01621
F8	0.60024	0.01917	0.97606	1.0000	0.01956
F9	0.40237	0.27871	0.98945	1.0000	0.02099
F10	0.52628	0.19398	0.81384	1.0000	0.02526
F11	0.35661	-0.05529	0.82963	1.0000	0.02978
F12	0.23141	0.02419	1.00625	1.0000	0.02257
		$[ClF_6][Sb_2F_{11}]$			
Sb1	0.72513	0.00852	0.64441	1.0000	0.02190
Sb2	0.80865	0.02424	0.34522	1.0000	0.01919
Cl1	1.00000	0.00000	1.00000	0.5000	0.02093
Cl2	0.50000	0.00000	1.00000	0.5000	0.01998
F1	1.01035	0.10783	0.89724	1.0000	0.02878
F2	0.97676	0.14808	1.06913	1.0000	0.03063

Appendix A.   continued...

Atom	x	y	z	S.O.F	U_{eq}
F3	1.12993	0.01711	1.03743	1.0000	0.03286
F4	0.59315	0.12167	0.97924	1.0000	0.02921
F5	0.43819	0.02912	0.88056	1.0000	0.03171
F6	0.42947	0.13464	1.04495	1.0000	0.02950
F7	0.64876	0.03154	0.76751	1.0000	0.04222
F8	0.67576	-0.19593	0.60983	1.0000	0.04133
F9	0.85481	-0.06911	0.72839	1.0000	0.04394
F10	0.78821	0.20903	0.65105	1.0000	0.06061
F11	0.60513	0.08671	0.54423	1.0000	0.05469
F12	0.81090	-0.01970	0.50972	1.0000	0.02617
F13	0.80622	0.05852	0.19261	1.0000	0.03221
F14	0.73644	0.21269	0.37159	1.0000	0.03328
F15	0.94680	0.12675	0.38601	1.0000	0.03535
F16	0.88729	-0.16692	0.34426	1.0000	0.02952
F17	0.67071	-0.08084	0.32628	1.0000	0.03125
		$[BrF_6][Sb_2F_{11}]$			
Sb1	0.72664	0.00216	0.64334	1.0000	0.02202
Sb2	0.80970	0.02153	0.34413	1.0000	0.01856
Br1	1.00000	0.00000	1.00000	0.5000	0.02054
Br2	0.50000	0.00000	1.00000	0.5000	0.01749
F1	1.00858	0.11553	0.88835	1.0000	0.02680
F2	0.97669	0.15748	1.07458	1.0000	0.02981
F3	1.13827	0.02027	1.03601	1.0000	0.02987
F4	0.59978	0.12886	0.97806	1.0000	0.03113
F5	0.43681	0.02748	0.87114	1.0000	0.03139
F6	0.42243	0.14494	1.04507	1.0000	0.02876
F7	0.64864	0.01736	0.76501	1.0000	0.04210
F8	0.68297	-0.20046	0.60547	1.0000	0.04814
F9	0.85420	-0.07265	0.72882	1.0000	0.05306
F10	0.78580	0.20443	0.65378	1.0000	0.07739
F11	0.60948	0.07986	0.54370	1.0000	0.06524
F12	0.81539	-0.01522	0.51030	1.0000	0.02674
F13	0.80391	0.05001	0.19127	1.0000	0.02878
F14	0.73296	0.20566	0.36662	1.0000	0.03380

Appendix A.   continued...

Atom	x	y	z	S.O.F	U_{eq}
F15	0.94461	0.12985	0.37926	1.0000	0.03499
F16	0.89217	-0.16494	0.34507	1.0000	0.02860
F17	0.67554	-0.08765	0.33098	1.0000	0.02888
		$[IF_6][Sb_2F_{11}]$			
Sb2	0.81184	0.00010	0.33736	1.0000	0.00880
Sb1	0.72758	0.00005	0.63862	1.0000	0.01158
I1	1.00000	0.00000	1.00000	0.5000	0.01104
I2	0.50000	0.00000	1.00000	0.5000	0.00787
F1	1.01484	0.14561	0.89807	1.0000	0.02714
F2	0.98297	0.14563	1.10137	1.0000	0.02937
F3	1.15022	0.00144	1.04293	1.0000	0.03044
F4	0.59943	0.14627	0.97271	1.0000	0.01338
F5	0.44141	-0.00284	0.85456	1.0000	0.01708
F6	0.39896	0.14289	1.02626	1.0000	0.01780
F7	0.64470	-0.00200	0.75893	1.0000	0.02351
F8_a	0.70419	-0.20777	0.59232	0.2500	0.00479
F8_b	0.65312	-0.17544	0.58449	0.2500	0.00498
F8_c	0.62314	-0.11452	0.54842	0.2500	0.00739
F8_d	0.59458	-0.02607	0.51574	0.2500	0.00449
F9_a	0.86157	-0.05257	0.73100	0.2500	0.00720
F9_b	0.84774	-0.12783	0.71532	0.2500	0.00443
F9_c	0.80536	-0.19796	0.67113	0.2500	0.00453
F9_d	0.74342	-0.22019	0.62756	0.2500	0.00582
F10_a	0.76504	0.20662	0.65679	0.2500	0.00449
F10_b	0.82659	0.17116	0.69728	0.2500	0.00353
F10_c	0.86225	0.09417	0.72362	0.2500	0.00526
F10_d	0.85537	0.02648	0.72688	0.2500	0.00447
F11_a	0.60017	0.06590	0.52744	0.2500	0.00439
F11_b	0.62994	0.12999	0.55834	0.2500	0.00698
F11_c	0.67328	0.17624	0.57556	0.2500	0.00425
F11_d	0.70741	0.21139	0.61210	0.2500	0.00484
F12	0.82210	0.00139	0.50837	1.0000	0.01176
F13	0.80093	-0.00008	0.18025	1.0000	0.01716
F14	0.70131	0.15010	0.33823	1.0000	0.02123

Appendix A.   continued...

Atom	x	y	z	S.O.F	U_{eq}
F15	0.92528	0.15017	0.35949	1.0000	0.01636
F16	0.92639	-0.15108	0.35916	1.0000	0.01985
F17	0.70189	-0.15536	0.33790	1.0000	0.02273
		$[N(CH_3)_4][BrO_3F_2]$			
Br1	0.25000	0.25000	0.56626	0.1250	0.01948
F	0.10573	0.39427	0.61113	0.2500	0.08214
O1	0.25000	0.25000	0.29088	0.1250	0.02756
O2	0.14561	0.35439	0.68544	0.2500	0.19060
N	0.75000	0.25000	0.00000	0.1250	0.01690
C	0.75000	0.39301	-0.14765	0.5000	0.02943
H1	0.75000	0.48150	-0.05591	0.5000	0.01069
H2	0.83578	0.38664	-0.23462	1.0000	0.00614
		$[NO]_2[BrO_3F_2][F]$			
Br1	0.00000	0.38475	0.75000	0.5000	0.01213
Br2	0.00000	0.05114	0.75000	0.5000	0.01331
F1	0.12589	0.38388	0.92420	1.0000	0.02354
F2	0.18702	0.05304	0.75046	1.0000	0.03406
F3	-0.12345	-0.27005	0.62832	1.0000	0.01801
O1	0.00000	0.50904	0.75000	0.5000	0.02554
O2	0.11182	0.32315	0.69073	1.0000	0.02604
O3	0.00000	-0.07273	0.75000	0.5000	0.02634
O4	0.03866	0.11033	0.89504	1.0000	0.03991
O5	-0.23300	-0.42399	0.48649	1.0000	0.03146
O6	0.13761	-0.22324	0.62078	1.0000	0.02202
N1	-0.28055	-0.36707	0.53136	1.0000	0.02806
N2	0.10317	-0.29564	0.65139	1.0000	0.01931
		$[ClO_2][SbF_6]$			
Sb	0.75000	0.52589	0.75000	0.5000	0.00968
Cl	0.75000	0.89319	0.25000	0.5000	0.01173
F1	0.93009	0.28583	0.74642	1.0000	0.02492
F2	0.93380	0.75876	0.74630	1.0000	0.02921
F3	0.74791	0.52569	0.49449	1.0000	0.03442
O	0.75151	1.01892	0.08744	1.0000	0.02748

Appendix A.   continued...

Atom	x	y	z	S.O.F	U_{eq}
			$[BrO_2][SbF_6]$		
Sb	0.25000	0.45891	0.75000	0.5000	0.00618
Br	0.75000	0.88202	0.75000	0.5000	0.00731
F1	0.07089	0.69426	0.71683	1.0000	0.01286
F2	0.06776	0.23275	0.71224	1.0000	0.01490
F3	0.21367	0.45985	1.00269	1.0000	0.01279
O	0.78720	1.03643	0.92850	1.0000	0.01606

APPENDIX B

ATTEMPTED PREPARATION OF BrO_2F_3 AND SALTS CONTAINING THE $BrO_2F_2^+$ CATION

B.1. Introduction

A detailed review of the oxide fluoride chemistry of Br(VII), including the attempted syntheses of BrO_2F_3 and $BrOF_5$ was published by Gillespie and Spekkens in 1978.[207] Although the plausible neutral oxide fluorides of Br(VII) include BrO_3F, BrO_2F_3 and $BrOF_5$, only BrO_3F[162] has been prepared and isolated in significant quantities. Despite the general reluctance of bromine to achieve the +7 oxidation state, the chemistries of bromine and chlorine generally parallel one another and the ability to isolate ClO_2F_3[514-516] and several salts containing the $ClO_2F_2^+$ cation suggests the syntheses of BrO_2F_3 and $BrO_2F_2^+$ are more likely than the synthesis of $BrOF_5$. Accordingly, there is no evidence for the existence of $BrOF_5$,[207,226] however, BrO_2F_3 has been observed by mass spectrometry as a hydrolysis product of BrF_5.[560] The formation of BrO_2F_3 by the hydrolysis of BrF_5 is presumed to proceed according to eq B.1, however, attempts to prepare larger quantities of BrO_2F_3 by this method have not been

$$2BrF_5 + 2H_2O \rightarrow 2BrO_2F_3 + BrF_3 + 4HF \qquad (B.1)$$

$$BrF_5 + 2H_2O \xrightarrow{\text{excess } BrF_5} BrO_2F + 4HF \qquad (B.2)$$

successful, producing BrO_2F (eq B.2) in nearly quantitative yields (>90 %).[223,227] These observations suggest that BrO_2F_3 is only produced in low yields, or that BrO_2F_3 may undergo rapid hydrolysis to form BrO_2F (eq B.3).

$$BrO_2F_3 + H_2O \rightarrow BrO_2F + 2HF + \frac{1}{2}O_2 \qquad (B.3)$$
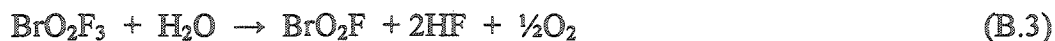
The preparations of BrO_2F_3 or salts containing the $BrO_2F_2^+$ cation also have been attempted by the oxidation of BrO_2F and by ligand exchange reactions involving BrO_3F. Although PtF_6 is capable of oxidizing ClO_2F to $[ClO_2F_2][PtF_6]$,[224,225] it is incapable of oxidizing BrO_2F, forming the Br(V) salts, $[BrO_2][PtF_6]$ and $[BrOF_2][PtF_6]$, instead[215] (eqs B.4, B5). This behaviour parallels the ability of PtF_6 to oxidize ClF_5 to ClF_6^+,[220-222]

$$BrO_2F + PtF_6 \rightarrow [BrO_2][PtF_6] + \frac{1}{2}O_2 \tag{B.4}$$

$$2BrO_2F + 5PtF_6 \rightarrow 2[BrOF_2][PtF_6] + [O_2][PtF_6] + 2PtF_5 \tag{B.5}$$
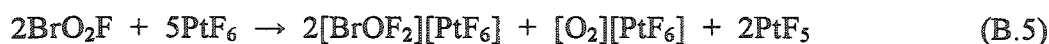
and its inability to oxidize BrF_5 to BrF_6^+.[36] Krypton difluoride also fails to oxidize BrO_2F, but efficiently oxidizes the oxygen ligands of BrO_2F to form $BrOF_3$ (eq B.6) followed by BrF_5 (eq B.7).[244] The synthesis of BrO_2F_3 by the ligand exchange reaction

$$BrO_2F + KrF_2 \xrightarrow{\text{HF}} BrOF_3 + \frac{1}{2}O_2 + Kr \tag{B.6}$$

$$BrOF_3 + KrF_2 \xrightarrow{\text{HF}} BrF_5 + \frac{1}{2}O_2 + Kr \tag{B.7}$$
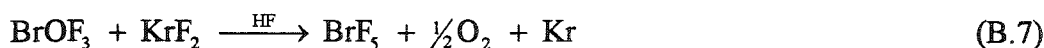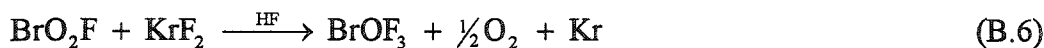
between BrO_3F and the strong fluorinating agent SbF_5 has been unsuccessful,[209] however, the use of XeF_6 as a fluorinating agent has recently provided some evidence that BrO_2F_3 may be produced by metathesis (eq B.8).[208] Unfortunately, this system has not been fully

$$BrO_3F + XeF_6 \rightarrow BrO_2F_3 + XeOF_4 \tag{B.8}$$

investigated and the formation of BrO_2F_3 by this method remains speculative.

The present work re-examines the ligand exchange reaction proposed for XeF_6 and BrO_3F, and investigates the preparation of salts containing the $BrO_2F_2^+$ cation by the reactions of BrO_2F with the oxidative fluorinating agents XeF_3^+, $Xe_2F_{11}^+$ and KrF^+. The properties of BrO_2F_3 have also been assessed in terms of its structure, vibrational frequencies, thermodynamic stability and Lewis acid-base properties with the aid of electronic structure calculations and thermochemical data derived from these calculations.

B.2. Results and Discussion

B.2.1. Reaction of XeF$_6$ with [K][BrO$_4$]

The reaction of [K][BrO$_4$] with XeF$_6$ in HF has been previously shown to produce BrO$_3$F and XeOF$_4$, however, in the presence of excess XeF$_6$, a weak singlet (275.1 ppm) at slightly higher frequency than that of BrO$_3$F (270.0 ppm) was also observed in the ^{19}F NMR spectrum.[208] In the present work, 1:2.3 and 1:5.2 molar ratios of [K][BrO$_4$] and XeF$_6$ were monitored by ^{19}F NMR spectroscopy at -80 °C after warming the HF solutions to temperatures ranging from -78 to 23 °C. Perbromyl fluoride (269.7 ppm),[207] XeOF$_4$ (91.2 ppm; $^1J(^{129}$Xe-^{19}F), 1150 Hz),[104] XeF$_6$ (107.7 ppm)[104] and small amounts of XeF$_4$ (-25.4 ppm; $^1J(^{129}$Xe-^{19}F), 1930 Hz),[104] were identified by their chemical shifts and coupling constants, however, no evidence for the formation of BrO$_2$F$_3$ was obtained. The reaction of XeF$_6$ with [K][BrO$_4$] likely proceeds according to eq B.9 and occurs at

$$\text{XeF}_6 + [\text{K}][\text{BrO}_4] + \text{HF} \xrightarrow{\text{HF}} \text{XeOF}_4 + [\text{K}][\text{HF}_2] + \text{BrO}_3\text{F} \qquad \text{(B.9)}$$

temperatures as low as -78 °C. This reaction contrasts with the subsequent ligand exchange reaction proposed for XeF$_6$ and BrO$_3$F (eq B.8) in that it is likely driven, in part, by the formation of HF$_2^-$. The failure of XeF$_6$ to react with BrO$_3$F is in qualitative agreement the calculated thermochemical data for this system (see section B.3.6), which predict that the ligand exchange is an endothermic process ($\Delta G°$, 130 kJ mol^{-1}).

B.2.2. Attempted Oxidation of BrO$_2$F with [XeF$_3$][AsF$_6$]

The oxidation of BrO$_2$F with [XeF$_3$][AsF$_6$] (eq B.10) was attempted by the

$$[\text{XeF}_3][\text{AsF}_6] + \text{BrO}_2\text{F} \rightarrow [\text{XeF}][\text{AsF}_6] + \text{BrO}_2\text{F}_3 \qquad \text{(B.10)}$$
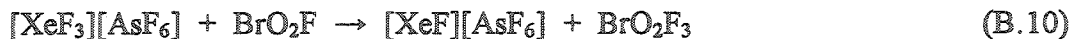
addition of AsF$_5$ to HF solutions of XeF$_4$ and BrO$_2$F. Although this reaction is predicted to be only mildly endothermic ($\Delta G°$, 10 kJ mol^{-1}; see section B.3.7.), the Raman spectrum the solid precipitated at -78 °C revealed that the metered addition of AsF$_5$ to the solution only produced [XeF$_3$][AsF$_6$] after all of the BrO$_2$F had been converted to [BrO$_2$][AsF$_6$].

Consequently, the stronger oxidizing properties of the XeF_3^+ cation relative to those of XeF_4 (which failed to oxidize BrO_2F at -30 °C) could not be used to oxidize BrO_2F. Similar problems arise when attempting to oxidize fluoro-basic species with acidic oxidizing agents, as exemplified by the reactions of XeF_6 with NiF_4 (eq B.11)[561] or NiF_3^+

$$2XeF_6 + NiF_4 \rightarrow [XeF_5]_2[NiF_6] \tag{B.11}$$

$$2XeF_6 + [NiF_3][AsF_6] \rightarrow [XeF_5][NiF_6] + AsF_5 \tag{B.12}$$

$$[NiF_3][AsF_6] + ClO_2F \rightarrow [ClO_2][AsF_6] + NiF_4 \tag{B.13}$$
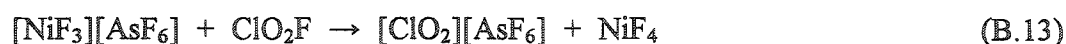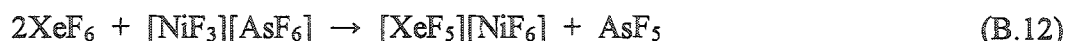
(eq B.12),[31] and ClO_2F with the $[NiF_3][AsF_6]$ (eq B.13),[31] and reflect the general reluctance of cations to be oxidized.[31] For these reasons, and because BrO_2F failed to react with XeF_4, the oxidation of $[BrO_2][AsF_6]$ with XeF_4 was not pursued further.

Anhydrous HF solutions of $[BrO_2][AsF_6]$ and $[XeF_3][AsF_6]$ were prepared by the further acidification of the $XeF_4/[BrO_2][AsF_6]$ mixtures with AsF_5. Warming these solutions to temperatures ranging from -35 to 45 °C failed to provide visual or spectroscopic (Raman) evidence for a chemical reaction between these species. The remarkable stability of this solution is not surprising considering that the interaction of the XeF_3^+ cation with the already oxidatively resistant BrO_2^+ cation is further inhibited by the Coulombic repulsion between the cations.

B.2.3. Attempted Oxidation of BrO_2F with $[Xe_2F_{11}][AsF_6]$

The reaction of $[Xe_2F_{11}][AsF_5]$ with a stoichiometric excess of BrO_2F (*ca.* 1 : 1.7) in anhydrous HF was monitored by Raman spectroscopy. The Raman spectrum of the colourless solid obtained after mixing the reagents at -50 °C for one hour, contained bands that were characteristic of BrO_2F (270, 294, 308, 387, 500, 909, 943 cm^{-1}),[207] $Xe_2F_{11}^+$ (358, 580, 584, 594, 604, 645, 653, 656, 665 cm^{-1})[249] AsF_6^- (367, 564, 722 cm^{-1})[249] and a small amount of XeF_4 (504, 508, 545 554 cm^{-1}),[250] confirming that "Xe_2F_{12}" is a stronger fluoride ion donor than BrO_2F and XeF_4.[106] The reaction between

BrO_2F and $[Xe_2F_{11}][AsF_6]$, or $[XeF_5][AsF_6]$ which is likely the predominant Xe(VI) species in solution, was slow below -40 °C, but proceeded smoothly at -30 °C, at which temperature a colourless gas was evolved and the solution took on a pale yellow colour. The Raman spectrum of the colourless precipitate was monitored periodically, and was shown to exhibit XeF_4 bands that progressively increased in intensity, while those of $[Xe_2F_{11}][AsF_6]$ decreased and had all but disappeared after a total of 20 hr at -30 °C. The only oxygen-containing bromine species observed in the Raman spectrum after this period was BrO_2F, indicating that the bromine species produced during the reduction of $Xe_2F_{11}^+$ is very soluble and a better fluoride ion donor than XeF_4 and BrO_2F.

The reaction of $[Xe_2F_{11}][AsF_6]$ with BrO_2F (*ca.* 1 : 0.21 molar ratio) in HF was monitored by ^{19}F NMR spectroscopy (-70 °C) prior to, and after warming the sample to -30 °C for 1.5 and 18 hr (Table B.1). The pale yellow solution evolved a colourless gas during the first five minutes of warming, but did not exhibit further visible signs of reaction after this period, indicating that all of the BrO_2F had been consumed. In addition to the fluorine-exchange broadened resonances of XeF_5^+, XeF_6 and AsF_5/AsF_6^-, the ^{19}F NMR spectrum of the solution acquired after the initial 1.5 hr warming period exhibited 4.2- and 2.7-fold increases in the relative molar quantities of $XeOF_4$ and XeF_4, when compared with the integrated intensities of the XeF_5^+(eq) and AsF_5 resonances, respectively. The relative intensities of the $XeOF_4$:XeF_5^+ and XeF_4:AsF_5 resonances did not change significantly after the second warming period, indicating that the reaction had proceeded to completion. The formation of $XeOF_4$ and XeF_4 could not be correlated with the formation of a fluorine or oxide fluoride of bromine, suggesting that the product undergoes rapid fluorine exchange with the HF solvent. By analogy with reactions of KrF_2[244] and KrF^+ (see section B.2.4) with BrO_2F, $BrOF_3$ is a plausible reaction product and may account for the formation of $XeOF_4$ (eq B.14) and XeF_4 (eq B.15). Moreover,

Table B.1. ^{19}F NMR Parameters for the Reaction of $2XeF_6$:AsF_5 with BrO_2F in HF Solution at -30 °C[a]

Assignment[b]	Chemical Shift (ppm)	Multiplicity	$^2J(^{19}F-^{19}F)$ (Hz)	$^1J(^{19}F-^{129}Xe)$ (Hz)	Line Width[c] (Hz)	Reference
BrF$_5$ {	267.6, F$_{ax}$	quintet	74.4		36	[562, 563]
	131.9, F$_{ex}$	doublet	74.4		31	[562, 563]
XeF$_5^+$	229.7, F$_{ax}$	broad singlet			9650	[564]
XeF$_5^+$ }	104.9[d]	broad singlet			5550	[564] [156]
(XeF$_6$)$_4$						
XeOF$_4$	91.3	singlet/doublet		1147.0	29	[79]
XeF$_4$	-25.1	singlet/doublet		3874.9	28	[473]
AsF$_6^-$ }						[562, 563]
AsF$_5$	-68.3	singlet			1690	[562, 563]
HF (solvent)	-193.5	singlet			1020	[565]

[a] Spectra were recorded in a 4-mm FEP sample tube at -70 °C. [b] Weak, unassigned singlets were observed at -166.5, -152.0, -74.7, -72.9, -58.5, -21.3 and 142.4 ppm. [c] The line widths of the central lines are reported for BrF$_5$, XeOF$_4$ and XeF$_4$. [d] The rapid fluorine exchange, broad line widths and similar chemical shifts of (XeF$_6$)$_4$ and F$_{eq}$ of XeF$_5^+$ prevents an absolute assignment. [e] The rapid ligand exchange, broad line widths and similar chemical shifts of AsF$_5$ and AsF$_6^-$ prevents an absolute assignment.

$$[Xe_2F_{11}][AsF_6] + BrO_2F \rightarrow BrOF_3 + XeOF_4 + [XeF_5][AsF_6] \qquad (B.14)$$

$$[Xe_2F_{11}][AsF_6] + BrO_2F \rightarrow BrOF_3 + XeF_4 + \tfrac{1}{2}O_2 + [XeF_5][AsF_6] \qquad (B.15)$$
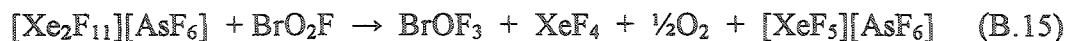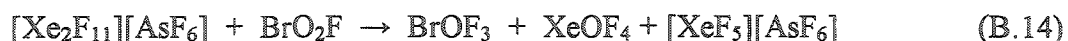
previous studies have demonstrated that $BrOF_3$ is very soluble in HF and that rapid fluorine exchange prevents its ^{19}F resonances from being observed in this solvent.[247] The evolution of XeF_4 could alternatively be accounted for by the oxidative fluorination of Br_2 (eq B.16) arising from the limited stability of BrO_2F in HF (eq B.17),[207] however, the

$$3[Xe_2F_{11}][AsF_6] + Br_2 \rightarrow 2BrF_3 + 3XeF_4 + 3[XeF_5][AsF_6] \qquad (B.16)$$

$$3BrO_2F \rightarrow Br_2 + BrF_3 + 3O_2 \qquad (B.17)$$
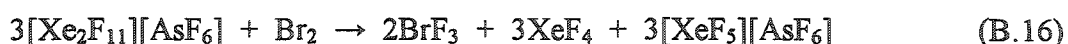
cessation of gas evolution after five minutes at -30 °C suggests that this reaction pathway is less likely than those that result in the formation of $BrOF_3$. The likelihood that BrF_3 is produced during the course of the reaction is also not favoured because the weak ^{19}F resonances of BrF_5 (*ca.* 3 mol% with respect to $XeOF_4$) do not increase in intensity between the 1.5 and 18 hr warming periods as a result of the oxidation of BrF_3 by the excess $[Xe_2F_{11}][AsF_6]$ (eq B.18).

$$[Xe_2F_{11}][AsF_6] + BrF_3 \rightarrow [XeF_5][AsF_6] + XeF_4 + BrF_5 \qquad (B.18)$$
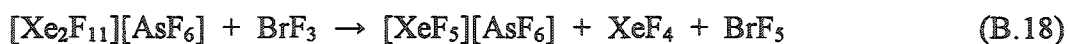
Although the bromine-containing species produced by the reaction of BrO_2F with $[Xe_2F_{11}][AsF_6]$ could not be identified by Raman or ^{19}F NMR spectroscopy, the formation of BrO_2F_3 appears unlikely on the basis of the positive value of $\Delta G°$ (88 kJ mol^{-1}) calculated for the oxidative fluorination of BrO_2F by $[XeF_5][AsF_6]$ (see section B.3.7).

B.2.4. Reactions of KrF_2 with $[BrO_2][SbF_6]$, and $[KrF][AsF_6]$ with $[BrO_2][AsF_6]$

An earlier attempt to oxidatively fluorinate BrO_2F with KrF_2, was unsuccessful, but resulted in the sequential formation of $BrOF_3$ and BrF_5 at 2 °C.[244] Unfortunately, it is unclear from these reactions whether the loss of oxygen results from oxidation of the central bromine atoms and subsequent decomposition of BrO_2F_3 or $BrOF_5$, or from the

oxidation of the electron-rich oxygen ligands of BrO_2F and $BrOF_3$. If the oxidation proceeds at the bromine centre, the use of the more potent oxidizer KrF^+ may permit the reaction to be carried out at lower temperatures where the decompositions of the desired BrO_2F_3 or $BrO_2F_2^+$ products are expected to be slower. Conversely, if KrF_2 oxidizes the oxygen ligands, the use of the Lewis acid KrF^+ is not expected to be beneficial in the preparation of higher valent oxide fluorides of bromine from BrO_2F as a consequence of its Lewis basic oxygen sites.

The reaction of $[BrO_2][SbF_6]$ with a 20% molar excess of KrF_2 in anhydrous HF at -30 °C proceeded vigorously with the evolution of krypton and oxygen gas. The spontaneity of the reaction suggests that KrF_2 is a stronger fluoride ion donor than BrO_2F and that the reaction is initiated by the displacement of BrO_2F from $[BrO_2][SbF_6]$ (eq B.19). The pale yellow-orange product was characterized by low-temperature Raman

$$[BrO_2][SbF_6] + KrF_2 \rightarrow BrO_2F + [KrF][SbF_6] \tag{B.19}$$

spectroscopy, and was shown to be a mixture of O_2^+ (1865 cm^{-1}),[230] BrO_2^+ (372, 878, 943 cm^{-1}),[207,213] $BrOF_2^+$ (318, 657, 1059 cm^{-1})[215,216,511,566] and BrF_4^+ (714, 718 cm^{-1})[499] salts. The formation of the $BrOF_2^+$ cation (eq B.20) parallels the oxidation of an oxygen ligand

$$BrO_2F + KrF^+ \rightarrow BrOF_2^+ + \frac{1}{2}O_2 \tag{B.20}$$

when BrO_2F is allowed to react with KrF_2 (eq B.6),[244] and the observation of O_2^+ salts is explained by the subsequent oxidation of the O_2 by KrF^+ (eq B.21).[40] Given the instability of $[BrF_4][SbF_6]$,[248] the BrF_4^+ salt is likely in the form of $[BrF_4][Sb_2F_{11}]$, which may be formed by the further oxidation of $[BrOF_2][SbF_6]$ (eq B.22). This reaction also

$$KrF^+ + O_2 \rightarrow O_2^+ + Kr + \frac{1}{2}F_2 \tag{B.21}$$

$$2[BrOF_2][SbF_6] + 3[KrF][SbF_6]$$

$$\rightarrow 2[BrF_4][Sb_2F_{11}] + 2Kr + [O_2][SbF_6] + \frac{1}{2}F_2 \tag{B.22}$$

accounts for the coexistence of the SbF_6^- (282, 562, 664 cm^{-1})[248] and $Sb_2F_{11}^-$ (657, 665, 686, 701, 705 cm^{-1})[248] anion bands in spectrum, however, the weak fluoride ion donor properties of BrF_5[499] likely permit anion exchange reactions to proceed and prevents the counter anions of the BrO_2^+, BrO_2F^+ and O_2^+ cations from being assigned with certainty (eq B.23).

$$\tfrac{1}{2}[BrF_4][Sb_2F_{11}] + [A][SbF_6]$$

$$\rightarrow \tfrac{1}{2}BrF_5 + [A][Sb_2F_{11}] \quad (A = BrO_2^+, BrOF_2^+, O_2^+) \qquad (B.23)$$
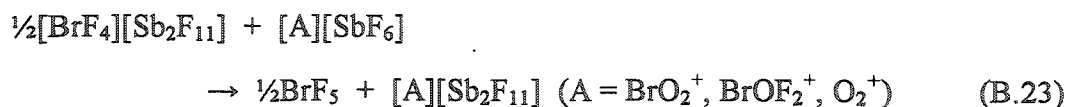
In a second experiment, BrO_2F and KrF_2 were combined in BrF_5 solvent followed by a 30% molar excess of AsF_5 (with respect BrO_2F and KrF_2) in an attempt to lower the basicity of the oxygen ligands by completely converting BrO_2F to BrO_2^+. In spite of the greater resistance to oxidation expected for the BrO_2^+ cation, the reaction proceeded smoothly at -30 °C, suggesting that an equilibrium exists between $[BrO_2][AsF_6]$ and BrO_2F in BrF_5 solution (eq B.24). The Raman spectrum of the product was obtained

$$[BrO_2][AsF_6] \rightleftharpoons BrO_2F + AsF_5 \qquad (B.24)$$

after the gas evolution had ceased, however, the only oxygen-containing bromine species observed were $[BrO_2][AsF_6]$ and $[BrOF_3][AsF_6]$, which were identified by their characteristic Br-O stretching frequencies at 1062 cm^{-1} [215,216] and 865 and 932 cm^{-1}, [207] respectively. It is difficult to assess the extent to which KrF^+ reacts with $[BrOF_2][AsF_6]$ to form $[BrF_4][AsF_6]$ and O_2^+ because BrF_5 solvent was used, however, the oxidation of oxygen ligands of BrO_2^+ or $BrOF_2^+$ was verified by the intense O_2^+ stretching frequency of $[O_2][AsF_6]$ (1857 cm^{-1})[230] observed in the Raman spectrum.

The oxidation of oxygen ligands by KrF_2 or KrF^+ is not unique to BrO_2F, but has also been observed in attempts to oxidize $XeOF_4$ with $[KrF][SbF_6]$ (eq B.25)[35] and for

$$[KrF][SbF_6] + 2XeOF_4 \rightarrow [XeOF_4 \cdot XeF_5][SbF_6] + Kr + \tfrac{1}{2}O_2 \qquad (B.25)$$

$$CrO_2F_2 + KrF_2 \rightarrow CrOF_4 + Kr + \tfrac{1}{2}O_2 \qquad (B.26)$$

$$OsO_4 + 2KrF_2 \rightarrow cis\text{-}OsO_2F_2 + 2Kr + O_2 \qquad (B.27)$$

$$TcO_2F_3 + KrF_2 \rightarrow TcOF_5 + Kr + \tfrac{1}{2}O_2 \qquad (B.28)$$
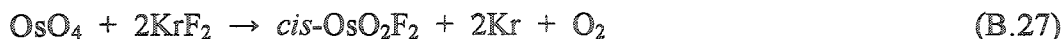
the reactions of CrO_2F_2 (eq B.26)[124] OsO_4 (eq B.27)[274,567,568] and TcO_2F_3 (eq B.28)[275,569]

with KrF_2. A complex reaction mechanism for the oxidation of $XeOF_4$ by $[KrF][SbF_6]$

reaction has been proposed by Liebman,[570] and postulates the formation of F_4XeOF^+ and

F_4XeOOF^+ as intermediates that lead to XeF_4, which is subsequently re-oxidized to

XeF_5^+. Although a similar mechanism can be proposed for the displacement of oxygen

from BrO_2F, the reaction of this low-coordinate species with KrF^+ could also proceed

through a much simpler pathway involving the concerted oxidation of an oxygen ligand

and the transfer of a fluorine ligand from KrF^+ to the "$BrOF^+$" moiety. In this

mechanism, KrF^+ initially coordinates to BrO_2F as shown in eq B.29, which is in accord
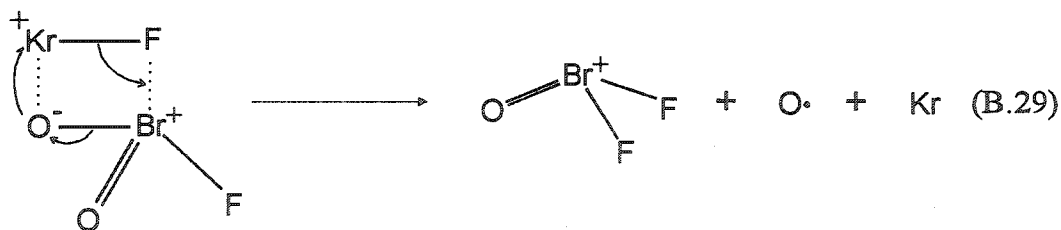
with the $^{\delta+}Kr\text{-}F^{\delta-}$ and $^{\delta+}Br\text{-}O^{\delta-}$ bond polarities of the parent species. The $F\cdots Br$

coordination is further supported by the Lewis acidity of BrO_2F, which has been

demonstrated by the preparation of salts containing the $BrO_2F_2^-$ anion.[244] The oxygen

radical produced by this mechanism is expected to be short lived in solution, recombining

to form O_2, which is subsequently oxidized to O_2^+ by any remaining KrF^+. Provided

$[BrOF_2][AsF_6]$ is in equilibrium with its parent oxide fluoride ($BrOF_3$) in solution, a

similar mechanism can account for the oxidation of the remaining oxygen ligand to form

BrF_5. Furthermore, the polarities of the Kr-F bonds in KrF_2 (see section 3.3.3.1) also

allow this mechanism to be adapted for the oxidative displacement of O_2 from BrO_2F and

$BrOF_3$ by KrF_2.

372

B.3. Calculations

B.3.1. Geometries of BrO_2F_3, $BrO_2F_2^+$, and $BrO_2F_4^-$

The energy-minimized gas-phase geometries of BrO_2F_3, $BrO_2F_2^+$ and $BrO_2F_4^-$ were determined by the HF, MP2 and MPW1PW91 methods and are summarized in Table B.2. With the exception of $BrO_2F_4^-$, which has a calculated MP2 Br-O bond length that is shorter than that obtained by use of the HF method, the Br-O and Br-F bond lengths of the title species increase in the order HF < MP2 < MPW1PW91. The bond angles of these species do not vary by more than 1° among the computational methods used, suggesting they are tightly constrained irrespective of the relative Br-O and Br-F bond lengths. As expected, a comparison among these species reveals a general elongation of the Br-O and Br-F bond lengths at a given level of theory as the net negative charge on the species increases.

B.3.2. Vibrational Frequencies of BrO_2F_3, $BrO_2F_2^+$ and $BrO_2F_4^-$

The vibrational frequencies of BrO_2F_3, $BrO_2F_2^+$ and $BrO_2F_4^-$ were determined by the HF, MP2 and MPW1PW91 methods and are summarized in Table B.3. It is apparent from the Br-O stretching frequencies determined by the HF and MP2 methods that the general frequency trends noted for the XF_6^+ (see section 6.3.2)[571] and XO_2^+ (see section 8.3.3) cations do not apply to BrO_2F_3 or to its ionic derivatives. The Br-O stretching frequencies are clearly overestimated by the MP2 method and underestimated by the HF method, which is reminiscent of the trends noted for the $BrO_3F_2^-$ and $ClO_3F_2^-$ anions (see section 7.3.3). Consequently the MPW1PW91 method is believed to provide the best representation of the vibrational frequencies for BrO_2F_3, $BrO_2F_2^+$ and $BrO_2F_4^-$. The origin of this anomalous behaviour, which appears to selectively arise in cases where oxygen and fluorine ligands are both present, is not apparent from a comparison of the Br-O bond lengths determined by the HF and MPW1PW91 methods, however, the Br-O

Table B.2. Calculated Geometries of BrO_2F_3, $BrO_2F_2^+$ and $BrO_2F_4^-$

Species	Bond /Angle	HF[a,b]	MP2[a,b]	MPW1PW91[a,c]
BrO_2F_3	Br-O	1.558	1.572	1.609
(C_{2v})	Br-F_{ax}	1.732	1.804	1.809
	Br-F_{eq}	1.690	1.786	1.784
	F_{ax}-Br-F_{eq}	82.7	82.0	82.7
	O-Br-O	129.8	130.3	130.2
	O-Br-F_{eq}	115.1	114.8	114.9
	O-Br-F_{ax}	93.1	93.3	93.1
$BrO_2F_2^+$	Br-O	1.525	1.552	1.584
(C_{2v})	Br-F	1.653	1.735	1.736
	O-Br-O	93.7	127.6	126.3
	O-Br-F	108.1	107.8	108.1
	F-Br-F	93.7	92.7	93.1
$BrO_2F_4^-$	Br-O	1.615	1.602	1.648
(D_{4h})	Br-F	1.768	1.850	1.863
	O-Br-F	90.0	90.0	90.0

[a] Bond lengths and bond angles are given in Å and degrees, respectively. [b] Calculated using 6-311G(d) basis set. [c] Calculated using a DZVP basis set.

Table B.3. Calculated Vibrational Frequencies of BrO_2F_3, $BrO_2F_2^+$ and $BrO_2F_4^-$

Species	Symmetry and Mode Description[a]	HF[b,c]	Scaled HF	MP2[b,c]	MPW1PW91[b,d]
BrO_2F_3	$\nu_1(A_1)$ $\nu_s(BrO_2)$	912(58)[51]	817	1035(98)[40]	885(84)[37]
(C_{2v})	$\nu_2(A_1)$ $\nu_s(BrF_3)$	751(100)[75]	672	593(100)[99]	609(100)[87]
	$\nu_3(A_1)$ $\nu_{as}(BrF_3)$	638(60)[0]	571	529(75)[0]	534(64)[1]
	$\nu_4(A_1)$ δ(i.p. BrO_2/BrF_{2ax})	433(16)[55]	388	380(26)[25]	357(16)[22]
	$\nu_5(A_1)$ δ(o.o.p. BrO_2/BrF_{2ax})	249(10)[1]	223	215(12)[1]	202(9)[0]
	$\nu_6(A_2)$ $\delta(BrO_2$ scissor)	477(21)[0]	427	423(34)[0]	397(22)[0]
	$\nu_7(B_1)$ $\nu_{as}(BrO_2)$	992(11)[87]	888	1138(16)[153]	958(21)[92]
	$\nu_8(B_1)$ δ(o.o.p. BrF_3 wag)	449(10)[59]	402	392(16)[42]	370(10)[32]
	$\nu_9(B_1)$ δ(o.o.p. BrF_{eq} wag)	219(5)[1]	196	175(8)[0]	167(7)[0]
	$\nu_{10}(B_2)$ $\nu_{as}(BrF_{2ax})$	743(3)[315]	665	641(4)[223]	636(3)[258]
	$\nu_{11}(B_2)$ $\delta(BrF_{2eq}O_2$ umbrella)	521(3)[90]	466	470(8)[43]	435(4)[36]
	$\nu_{12}(B_2)$ δ(i.p. BrF_3 wag)	472(10)[1]	423	395(13)[1]	377(10)[1]
$BrO_2F_2^+$	$\nu_1(A_1)$ $\nu_s(BrO_2)$	1011(53)[42]	905	1127(100)[26]	959(84)[28]
(C_{2v})	$\nu_2(A_1)$ $\nu_s(BrF_2)$	786(100)[48]	704	642(69)[79]	657(100)[56]
	$\nu_3(A_1)$ $\delta(BrO_2$ scissor)	396(16)[45]	355	351(21)[19]	326(19)[16]
	$\nu_4(A_1)$ $\delta(BrF_2)$	314(11)[0]	281	264(14)[1]	248(13)[0]
	$\nu_5(A_2)$ $\delta(BrO_2F_2$ torsion)	300(15)[0]	269	263(21)[0]	234(18)[0]
	$\nu_6(B_1)$ $\nu_{as}(BrO_2)$	1082(13)[56]	969	1249(24)[82]	1032(26)[41]
	$\nu_7(B_1)$ δ(i.p. BrO_2 wag)	403(14)[44]	361	354(21)[29]	324(16)[22]
	$\nu_8(B_2)$ $\nu_{as}(BrF_2)$	806(41)[81]	722	658(23)[93]	671(41)[78]
	$\nu_9(B_2)$ δ(o.o.p. BrO_2 wag)	375(14)[37]	336	338(14)[15]	307(15)[13]

Species	Symmetry and Mode Description[a]	HF[b,c]	Scaled HF	MP2[b,c]	MPW1PW91[b,d]
$BrO_2F_4^-$	$\nu_1(A_{1g})$ $\nu_s(BrO_2)$	734(100)[0]	657	900(71)[0]	757(100)[0]
$(D_{4h})^e$	$\nu_2(A_{1g})$ $\nu_s(BrF_4)$	602(75)[0]	539	485(100)[0]	489(87)[0]
	$\nu_3(A_{2u})$ $\delta(BrF_4$ umbrella)	809(0)[69]	724	1025(0)[243]	402(0)[43]
	$\nu_4(A_{2u})$ $\nu_{as}(BrO_2)$	501(0)[86]	449	435(0)[56]	840(0)[125]
	$\nu_5(B_{1g})$ $\nu_{as}(BrF_4)$	576(45)[0]	516	463(55)[0]	450(48)[0]
	$\nu_6(B_{2g})$ $\delta(BrF_2)$	334(6)[0]	299	271(11)[0]	252(9)[0]
	$\nu_7(B_{2u})$ δ(o.o.p. BrF_4 scissor)	326(0)[0]	292	279(0)[0]	263(0)[0]
	$\nu_8(E_g)$ δ(FBrO scissor)	500(45)[0]	448	457(53)[0]	415(39)[0]
	$\nu_9(E_u)$ $\nu_{as}(BrF_2)$	672(0)[904]	602	602(0)[640]	572(0)[704]
	$\nu_{10}(E_u)$ δ(i.p. BrO_2)	523(0)[108]	468	483(0)[52]	435(0)[36]
	$\nu_{11}(E_u)$ $\delta(BrF_2$ wag)	233(0)[2]	209	189(0)[0]	181(0)[0]

[a] In-plane and out-of-plane bending modes are denoted by i.p and o.o.p, respectively. [b] Raman intensities are given in parentheses and scaled such that the most intense peak is given an arbitrary value of 100. Infrared intensities are given in square brackets in units of km mol^{-1}. Values were scaled by 0.8953 as recommended in ref 323. [c] Calculated using the 6-311G(d) basis set. [d] Calculated using the DZVP basis set. [e] The *trans*-isomer of $BrO_2F_4^-$ (D_{4h}) is calculated to be 8 kJ mol^{-1} more stable than *cis*-$BrO_2F_4^-$.

bond lengths obtained by use of the MP2 method are consistently shorter than those obtained using the MPW1PW91 method, and provides some insight into the overestimation of the Br-O stretching frequencies by the MP2 method.

The calculated (MPW1PW91) Br-O and Br-F stretching frequencies decrease significantly as the net charge on the species becomes more negative, which is consistent with the associated elongation of the bromine-ligand bond lengths and increase of the bromine-ligand bond polarities with increasing negative charge. For ν_s(Br-O) and ν_{as}(Br-O), the magnitude of this shift is approximately 75 cm^{-1} when comparing $BrO_2F_2^+$ and BrO_2F_3, but is significantly greater (*ca.* 120 cm^{-1}) for BrO_2F_3 and $BrO_2F_4^-$. The frequency shifts of ν_s(Br-F) and ν_{as}(Br-F) are calculated to be similar (*ca.* 42 cm^{-1}) for $BrO_2F_2^+$ and BrO_3F_2, however, a comparison of BrO_2F_3 with $BrO_2F_4^-$ reveals the change in ν_s(Br-F) (120 cm^{-1}) to be significantly less than the change in ν_{as}(Br-F) (186 cm^{-1}). The symmetric Br-F and Br-O stretches are predicted to be the most intense features in the Raman spectra of BrO_2F_3, $BrO_2F_2^+$ and $BrO_2F_4^-$ (Table B.3), with the relative intensities of these two bands being within 13 to 16% of each other in each of the three species. When coupled with the selection rules and calculated intensities, the significant Br-O and Br-F shifts predicted by MPW1PW91 calculations suggest vibrational spectroscopy should provide a simple means of identifying and differentiating between these species, should they prove isolable.

B.3.3. Thermodynamic Stability of BrO_2F_3

The observation of $BrO_2F_3^+$ and $BrO_2F_2^+$ by mass spectrometry[560] implies that BrO_3F_2 has some inherent stability, however, it is unclear whether it is thermodynamic or kinetic in nature. Given the current inability to isolate BrO_2F_3 and the absence of experimental thermodynamic data for this oxide fluoride, its stability with respect to O_2 (eq B.30) and F_2 loss (eq B.31) has been assessed by the G2 method. The calculated

$$BrO_2F_3 \rightarrow BrOF_3 + \tfrac{1}{2}O_2 \qquad\qquad\qquad (B.30)$$

$$BrO_2F_3 \rightarrow BrO_2F + F_2 \qquad\qquad\qquad (B.31)$$

enthalpies (ΔH°), entropies (ΔS°) and Gibbs free energies (ΔG°) of these reactions are summarized in Table B.4, where they are compared with the analogous values calculated for ClO_2F_3. It is apparent from both ΔH° and ΔG° that BrO_2F_3 is unstable with respect to O_2 loss (ΔG°, -51 kJ mol^{-1}), but stable with respect to F_2 loss (ΔG°, 77 kJ mol^{-1}). Furthermore, it is implied from the reversal of these reactions that BrO_2F_3 is more likely to be prepared by the oxidative fluorination of BrO_2F than by the oxidation of $BrOF_3$. This is in contrast to ClO_2F_3, which is predicted to be unstable towards the loss of both O_2 (ΔG°, -120 kJ mol^{-1}) and F_2 (ΔG°, -21 kJ mol^{-1}), but is reported to be stable at ambient temperature.[514,515] By analogy with ClO_3F,[572] the observed stability of ClO_2F_3 has been attributed to kinetic factors, which likely include steric protection of the Cl(VII) centre by the comparatively short Cl-O and Cl-F bonds. The general inertness of ClO_3F is in contrast to the aggressive fluorinating properties of BrO_3F,[162,175] suggesting that BrO_2F_3 is unlikely to exhibit the same degree of kinetic stabilization proposed for its chlorine analogue. For this reason, and because the likely precursor, BrO_2F, is also unstable,[210,244] the synthesis and isolation of BrO_2F_3 is most likely to be achieved under low-temperature conditions.

B.3.4. Fluoride Ion Donor Properties of BrO_2F_3

With the aid of electronic structure calculations and empirical relationships, the fluoride-ion donor properties of BrO_2F_3 have been quantitatively assessed to determine the likelihood of isolating salts containing the $BrO_2F_2^+$ cation. A study of the reactions of XO_3F (X = Br, Cl) with AsF_5 and $(SbF_5)_n$ (n = 1 - 3) has revealed that the enthalpies and free energies of reaction exhibit a sharp minimum when "monomeric" SbF_5 is used as the Lewis acid (see section 8.3.1). Given the similarities of the Born-Haber cycles

Table B.4. Thermodynamic Parameters of BrO_2F_3, ClO_2F_3 and Related Compounds

	V_m (nm³)[a]	$H_L^°$ (kJ mol⁻¹)	$\Delta H^°$ (kJ mol⁻¹)	$\Delta S^°$ (J mol⁻¹ K⁻¹)	$\Delta G^°$ (kJ mol⁻¹)
Decomposition Reactions					
$BrO_2F_3(g) \rightarrow BrOF_3(g) + \frac{1}{2}O_2(g)$[b]			-51	97	-80
$BrO_2F_3(g) \rightarrow BrO_2F(g) + F_2(g)$[b]			78	171	27
$ClO_2F_3(g) \rightarrow ClOF_3(g) + \frac{1}{2}O_2(g)$[b]			-120	101	-150
$ClO_2F_3(g) \rightarrow ClO_2F(g) + F_2(g)$[b]			-21	174	-73
$[XeF_5][AsF_6] \rightarrow [XeF_3][AsF_6](s) + F_2(g)$[e]			163	161	115
$[XeF_5][AsF_6] \rightarrow [XeF_3][AsF_6](s) + F_2(g)$[e]			91	181	37
$[KrF][AsF_6] \rightarrow Kr(g) + AsF_5(g) + F_2(g)$[e]			-48	486	-193
Fluoride Ion Transfer Reactions					
$BrO_2F_3 + F^- \rightarrow$ *trans*-$BrO_2F_4^-$[b]			-279		
$BrO_2F_3 + F^- \rightarrow$ *cis*-$BrO_2F_4^-$[b]			-271		
$BrO_2F_3 \rightarrow BrO_2F_2^+ + F^-$[b]			914		
$ClO_2F_3 + F^- \rightarrow ClO_2F_4^-$[b]			-149		
$ClO_2F_3 + F^- \rightarrow ClO_2F_4^-$[b]			-151		
$ClO_2F_3 \rightarrow ClO_2F_2^+ + F^-$[b]			804		
$SbF_5 + F^- \rightarrow SbF_6^-$[f]			-503		
Lewis Acid-Base Reactions					
$BrO_2F_3(g) + SbF_5(l) \rightarrow [BrO_2F_2][SbF_6]$[c,g]	0.177	527	-85	-308	7
$ClO_2F_3(g) + SbF_5(l) \rightarrow [ClO_2F_2][SbF_6]$[d,g]	0.177	527	-195	-288	-109

Table B.4. continued...

Reactions Leading to BrO_2F_3	V_m $(nm^3)^a$	H_L^o (kJ mol^{-1})	ΔH^o (kJ mol^{-1})	ΔS^o (J mol^{-1} K^{-1})	ΔG^o (kJ mol^{-1})
$XeF_6(s) + \frac{1}{2}O_2(g) \rightarrow XeOF_4(g) + F_2(g)$			313	232	244
$BrO_3F(g) + F_2(g) \rightarrow BrO_2F_3(g) + \frac{1}{2}O_2(g)^c$			-180	288	-94
$XeF_6(s) + BrO_3F(g) \rightarrow BrO_2F_3(g) + XeOF_4(g)^c$			133	10	130
$[XeF_5][AsF_6](s) + BrO_2F(g) \rightarrow BrO_2F_3(g) + [XeF_3][AsF_6](s)^{c,e}$			85	-10	88
$[XeF_3][AsF_6](s) + BrO_2F(g) \rightarrow BrO_2F_3(g) + [XeF][AsF_6](s)^{c,e}$			13	315	10
$[KrF][AsF](s) + BrO_2F(g) \rightarrow BrO_2F_3(g) + Kr(g) + AsF_5(g)^{c,e}$			-126	681	-220

^{a} The unit volumes of $[BrO_2F_2][SbF_6]$ and $[ClO_2F_2][SbF_6]$ were estimated by adding the volume of two fluorine ligands to the unit volumes of $[BrO_2][SbF_6]$ and $[ClO_2][SbF_6]$, respectively. The volume of the two fluorine ligands were estimated from the average differences of the BrF_2^+, BrF_4^+ and BrF_6^+ cation volumes (0.024 nm^3) for $BrO_2F_2^+$, and the ClF_2^+, ClF_4^+, and ClF_6^+ cations (0.028 nm^3) for $ClO_2F_2^+$. ^{b} Calculated using the G2 method. ^{c} The average standard entropies of BrO_3F (299 J mol^{-1} K^{-1}) and BrO_2F (294 J mol^{-1} K^{-1}) were used as a estimate of $S^o(BrO_2F_3)$. ^{d} The average standard entropies of ClO_3F (279 J mol^{-1} K^{-1}) and ClO_2F (279 J mol^{-1} K^{-1}) were used as a estimate of $S^o(ClO_2F_3)$. ^{e} The values of ΔH^o, and ΔG^o were calculated using the values of ΔH_f^o and ΔG_f^o calculated for $[XeF_5][AsF_6]$ (ΔH_f^o, -1663; ΔG_f^o, -1354 kJ mol^{-1}) $[XeF_3][AsF_6]$ (ΔH_f^o, -1500; ΔG_f^o, -1239 kJ mol^{-1}), $[XeF][AsF_6]$ (ΔH_f^o, -1409; ΔG_f^o, -1202 kJ mol^{-1}) and $[KrF][AsF_6]$ (ΔH_f^o, -1186; ΔG_f^o, -976 kJ mol^{-1}) in ref 309 and the enthalpy and free energy of fluorination calculated for BrO_2F (see above). ^{f} The enthalpy of fluoride ion attachment to SbF_5 was obtained from ref 48. ^{g} The values of ΔH_{vap}^o (30.9 kJ mol^{-1}) and S^o (265 J mol^{-1} K^{-1}) for SbF_5 were obtained from refs 541 and 546, respectively.

constructed for the formation of the BrO_3^+ (Figure 8.4) and $BrO_2F_2^+$ (Figure B.1) salts, for which the overall spontaneities of the reactions rely heavily on ΔH_L° and $\Delta H_{F^-}^\circ$, a similar energy minimum in energy is anticipated for $[BrO_2F_2][SbF_6]$.

The determination of the enthalpy change for the reaction of BrO_2F_3 with SbF_5 (eq B.32) can be accomplished as previously described for BrO_3F (see section 8.3.1.), but

$$BrO_2F_3 + SbF_5 \rightarrow [BrO_2F_2][SbF_6] \tag{B.32}$$

requires the assumption that BrO_2F_3 is a monomeric gas under standard conditions. This assumption is likely valid given that all of the known bromine oxide fluorides are gases under standard conditions, but would result in the omission of $\Delta H_{vap}^\circ(BrO_2F_3)$ if BrO_2F_3 proves to be a liquid or solid. The reaction of BrO_2F_3 with SbF_5 to form $[BrO_2F_2][SbF_6]$ is predicted to be enthalpically favourable (ΔH°, -85 kJ mol^{-1}, Table B.4), which may be attributed to the stronger fluoride ion donor properties of BrO_2F_3 ($\Delta H_{-F^-}^\circ$, 914 kJ mol^{-1}) relative to that of BrO_3F (1005 kJ mol^{-1}).

Although the entropy of $SbF_5(l)$ (265 J mol^{-1} K^{-1})[546] is known, those of BrO_2F_3 and $[BrO_2F_2][SbF_6]$ must be estimated if ΔS° and ΔG° are to be determined for this reaction. The entropy of $BrO_2F_3(g)$ is estimated to be 297 J mol^{-1} K^{-1} based on the average of the values previously determined for $S^\circ(BrO_2F)$ (294 J mol^{-1} K^{-1})[548] and $S^\circ(BrO_3F)$ (299 J mol^{-1} K^{-1}).[175] The absolute entropy of the $[BrO_2F_2][SbF_6]$ (174 J mol^{-1} K^{-1}) was calculated by use of the volume-based approach recently reported by Jenkins and Glasser[537] (eq B.33), employing an estimated unit volume of (V_m) of 0.177 nm^3. As

$$S^\circ(XO_3][MF_6]) = kV_m + c \tag{B.33}$$

previously noted for the formations of the BrO_3^+ and BrO_2^+ salts, the entropy term makes a significant contribution towards ΔG° for the reaction of BrO_2F_3 with SbF_5 (-TΔS°, 92 kJ mol^{-1}). The slightly positive value of ΔG° (7 kJ mol^{-1}) suggests $[BrO_2F_2][SbF_6]$ is prone to dissociation at 298 K, but should be isolable at lower temperatures (*ca.* <2 °C) where

$$SbF_5(g) \quad + \quad XO_2F_2^+(g) \xrightarrow{\quad \Delta H^\circ_{+F^-} \quad} SbF_6^-(g)$$

$$+ F^-(g) \qquad\qquad\qquad\qquad\qquad\quad + XO_2F_2^+(g)$$

$$\Big\uparrow \Delta H^\circ_{vap} \qquad\qquad \Big\uparrow \Delta H^\circ_{-F} \qquad\qquad\qquad \Big\downarrow \Delta H^\circ_L$$

$$SbF_5(l) \quad + \quad XO_2F_3(g) \xrightarrow{\quad \Delta H^\circ \quad} [XO_2F_2][SbF_6](s)$$
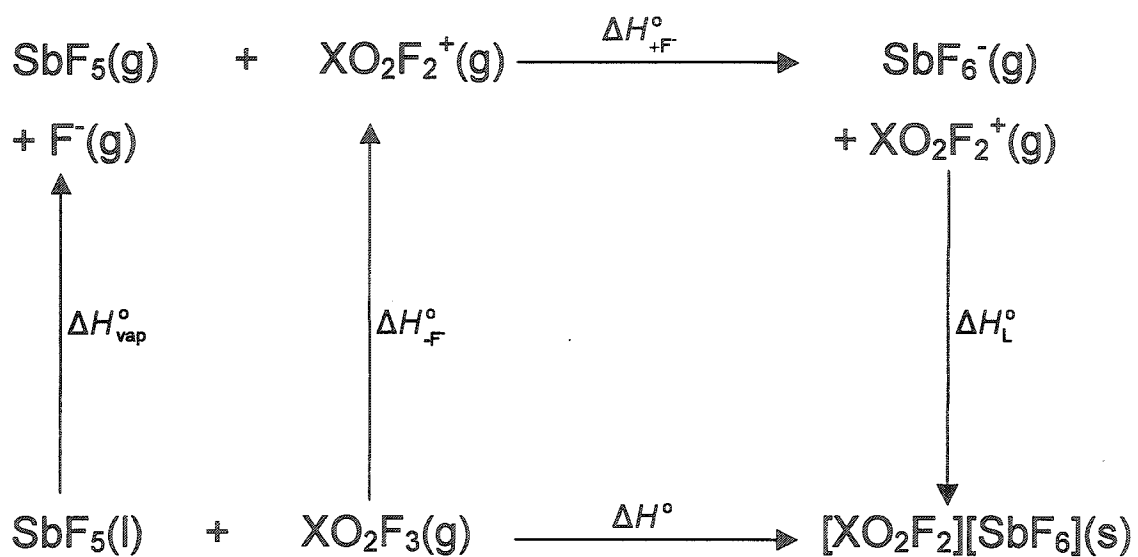
Figure B.1. Thermochemical cycle for the formation of $[XO_2F_2][SbF_6]$ (X = Br, Cl) by reaction of XO_2F_3 with SbF_5.

the destabilizing entropy contribution is reduced. This contrasts with the reaction of ClO_2F_3 with SbF_5 to form $[ClO_2F_2][SbF_6]$ (Table B.4), which is predicted to be significantly more exothermic ($\Delta G°$, -109 kJ mol^{-1}) and is consistent with the ability to isolate several salts containing the $ClO_2F_2^+$ cation.[224,225] The difference in the predicted stabilities of these salts is attributed to the stronger fluoride ion donor properties predicted for ClO_2F_3 ($\Delta H°_{-F^-}$, 804 kJ mol^{-1}) relative to BrO_2F_3 ($\Delta H°_{-F^-}$, 914 kJ mol^{-1}) and may contribute to the experimental difficulties associated with attempts to isolate salts containing the $BrO_2F_2^+$ cation.[207,215,244]

The isolation of $[BrO_2F_2][SbF_6]$ may also be problematic because BrO_2F_3 is thermodynamically unstable with respect to O_2 loss ($\Delta G°$, -80 kJ mol^{-1}) and because eq 8.9[535,536] predicts $[BrOF_2][SbF_6]$ to have a higher lattice energy than $[BrO_2F_2][SbF_6]$. By analogy with the BrO_3^+ systems investigated (see section 8.3.1.), these driving forces can be expected to be sufficient to favour the formation of $[BrOF_2][SbF_6]$ and O_2 unless impeded by a kinetic barrier.

B.3.5. Fluoride Ion Acceptor Properties of BrO$_2$F$_3$

The Lewis acidity of BrO_2F_3 has been evaluated by the determination of the gas-phase enthalpy of fluoride ion attachment ($\Delta H°_{+F^-}$) to this oxide fluoride (eq B.34) by use

$$BrO_2F_3 + F^- \rightarrow \textit{cis/trans-}BrO_2F_4^- \qquad (B.34)$$

of the G2 method (Table B.4). The values of $\Delta H°_{+F^-}$ calculated for the formations of *cis-* (-271 kJ mol^{-1}) and *trans-*$BrO_2F_4^-$ (-279 kJ mol^{-1}) imply that the *trans* isomer is 8 kJ mol^{-1} more stable than the *cis* isomer. Although the relative stabilities of the isomers are reversed for $BrO_2F_4^-$, the small energy difference between them is in accord with the 1 kJ mol^{-1} difference in $\Delta H°_{+F^-}$ calculated for the chlorine analogues, and the observation of both *cis-* and *trans-*HIO_2F_4 in a variety of solvents by ^{19}F NMR spectroscopy.[553] Surprisingly, the formation of *trans-*$BrO_2F_4^-$ by transfer of fluoride to the parent oxide

fluoride is calculated to be slightly more exothermic than the formation $BrO_3F_2^-$ ($\Delta H^{\circ}_{+F^-}$, -261 kJ mol^{-1}; see section 7.3.2.) despite the saturated coordination of the $BrO_2F_4^-$ anion. The successful isolation of several salts containing the $BrO_3F_2^-$ anion (see Chapter 7) implies that similar salts of the $BrO_2F_4^-$ anion (*i.e.*, K^+, Rb^+, Cs^+, NO^+, $N(CH_3)_4^+$) should be isolable if BrO_2F_3 can be prepared and isolated on a laboratory scale. Although a similar trend is noted between the enthalpies of fluoride ion attachment to ClO_3F (-132 kJ mol^{-1}) and *trans*-ClO_2F_3 (-149 kJ mol^{-1}), these values are significantly smaller than those of their bromine analogues and neither ClO_3F[217] (see section 7.2.1.3) nor ClO_2F_3[514,515] are known to behave as fluoride ion acceptors.

B.3.6. Thermochemistry of the Ligand Exchange Reaction Between XeF₆ and BrO₃F

The failure of XeF_6 and BrO_3F to undergo ligand exchange reactions resulting in the formation of $XeOF_4$ and BrO_2F_3 (eq B.8) is difficult to assess from a thermodynamic viewpoint because of the absence of thermodynamic data for $XeOF_4$ in its standard liquid state. A preliminary evaluation of the thermodynamics of this reaction can, however, be made using the thermodynamic information available for gaseous $XeOF_4$, by evaluating ΔG° for eq B.35 and B.36 (Table B.4). The free energy of the former reaction (eq B.35)

$$BrO_3F + F_2 \rightarrow BrO_2F_3 + \tfrac{1}{2}O_2 \tag{B.35}$$

$$XeF_6 + \tfrac{1}{2}O_2 \rightarrow XeOF_4 + F_2 \tag{B.36}$$

has been calculated using the G2 method and is predicted to be moderately exothermic (ΔG°, -94 kJ mol^{-1}). Using the reported enthalpies of formation and standard entropies of solid XeF_6 (ΔH_f°, -338.2; S°, 210.4)[573] and gaseous $XeOF_4$ (ΔH_f°, -25.1; S°,[574] 340.8 [575]), F_2 (S°, 202.8)[185] and O_2 (S°, 205.1),[185] which are given in units of kJ mol^{-1} and J mol^{-1} K^{-1}, respectively, the change in the free energy for the second reaction (eq B.36) is estimated to be 244 kJ mol^{-1}. The sum of the free energy changes calculated for eq B.35 and B.36, which is equivalent to ΔG° for eq B.8, predicts the ligand exchange reaction between

XeF_6 and BrO_3F to be endothermic ($\Delta G°$, 130 kJ mol^{-1}) and therefore a non-spontaneous process. Although this treatment neglects the condensation of $XeOF_4$ to its standard state, the free energy change of this process is unlikely to be large enough in magnitude to reverse the sign of $\Delta G°$. These predictions are in qualitative agreement with the non-reactivity of XeF_6 and BrO_3F in HF solution (see section B.2.1.).

B.3.7. Thermochemistry of the Reactions of BrO_2F With [XeF$_5$][AsF$_6$], [XeF$_3$][AsF$_6$] and [KrF][AsF$_6$]

The nearly neutral free energy of reaction calculated for the reaction of BrO_2F_3 with SbF_5 to form $[BrO_2F_2][SbF_6]$ at 298 K (see section B.3.4) implies that the energetics for the oxidative fluorination of BrO_2F by salts containing the XeF_3^+, XeF_5^+ and KrF^+ cations can be estimated from the sum of the free energies of eq B.37 and B.38 (or B.39).

$$BrO_2F + F_2 \rightarrow BrO_2F_3 \qquad\qquad (B.37)$$

$$[XeF_n][AsF_6] \rightarrow [XeF_{n-2}][AsF_6] + F_2 \quad (n = 3, 5) \qquad (B.38)$$

$$[KrF][AsF_6] \rightarrow Kr + AsF_5 + F_2 \qquad\qquad (B.39)$$
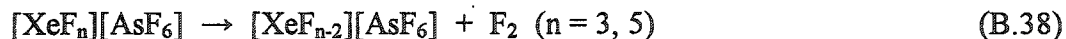
Although this approach ignores the stabilization of the $BrO_2F_2^+$ salts predicted at lower temperatures (see section B.3.4), the positive values of $\Delta S°$ predicted for the oxidation of BrO_2F by these fluorocations (Table B.4) mediates the overall temperature dependence of the reaction and prevents the fluoride ion donor properties of BrO_2F_3 from becoming a strong thermodynamic driving force.

The standard free energies of formation have recently been estimated for $[XeF_5][AsF_6]$ ($\Delta G_f°$, -1354 kJ mol^{-1})[309] and $[XeF_3][AsF_6]$ ($\Delta G_f°$, -1239 kJ mol^{-1})[309] using a combination of experimental data, electronic structure calculations, and empirical methods, and allows the free energy of reduction among these Xe(VI) and Xe(IV) fluorocation salts (eq B.40) to be calculated. It is clear from this simplified approach that

$$[XeF_5][AsF_6] \rightarrow [XeF_3][AsF_6] + F_2 \qquad\qquad (B.40)$$

the reduction of $[XeF_5][AsF_6]$ is an endothermic process (ΔG°, 115 kJ mol) and is expected to proceed only when coupled with a significantly exothermic oxidative process. Although the stability of BrO_2F_3 with regards to the loss of F_2 (see section B.3.3.) indicates that the oxidative fluorination of BrO_2F (eq B.37) is an exothermic process (ΔG°, -27 kJ mol^{-1}), its change in free energy is not large enough to compensate for the energy required for the reduction of $[XeF_5][AsF_6]$ (Table B.4). Consequently, the net reaction (eq B.41) is predicted to be endothermic (ΔG°, 88 kJ mol^{-1}), and is not

$$BrO_2F + [XeF_5][AsF_6] \rightarrow BrO_2F_3 + [XeF_3][AsF_6] \quad (B.41)$$
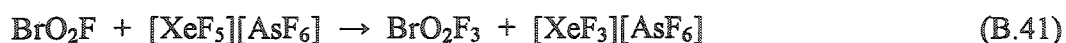
expected to proceed spontaneously. This prediction is in qualitative agreement with the inability of $[Xe_2F_{11}][AsF_6]$ to oxidize BrO_2F to BrO_2F_3 (see section B.2.3).

A similar comparison of the free energies of formation estimated for $[XeF_3][AsF_6]$ (-1239 kJ mol^{-1})[309] and $[XeF][AsF_6]$ (-1202 kJ mol)[309] predicts the oxidation of BrO_2F to BrO_2F_3 (eq B.42) to be mildly endothermic (ΔG°, 10 kJ mol^{-1};

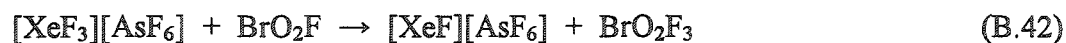$$[XeF_3][AsF_6] + BrO_2F \rightarrow [XeF][AsF_6] + BrO_2F_3 \quad (B.42)$$

Table B.4). The non-spontaneity of the reaction predicted from these calculations is further impeded in practice by the stronger Lewis base character of BrO_2F relative to XeF_4, which results in the preferential formation of the oxidatively resistant salt $[BrO_2][AsF_6]$ rather than the oxidant $[XeF_3][AsF_6]$ (see section B.2.2).

The unfavourable energetics encountered in the oxidation of BrO_2F by use of XeF_3^+ and XeF_5^+ are avoided if the thermodynamically unstable KrF^+ cation is used as the oxidant. Using the free energies of formation recently determined and estimated for AsF_5 (ΔG_f°, -1169 kJ mol^{-1})[545] and $[KrF][AsF_6]$ (ΔG_f°, -976 kJ mol^{-1}),[309] respectively, the free energy of reduction for $[KrF][AsF_6]$ (eq B.39) is calculated to be -193 kJ mol^{-1}. Not surprisingly, the oxidation of BrO_2F by $[KrF][AsF_6]$ (eq B.43) is predicted to be an

$$[KrF][AsF_6] + BrO_2F \rightarrow BrO_2F_3 + Kr + AsF_5 \quad (B.43)$$

exothermic (ΔG°, -220 kJ mol^{-1}), and therefore a spontaneous process. Although the BrO$_2$F$^+$ and O$_2$$^+$ salts obtained during attempts to oxidize BrO$_2$F or BrO$_2$$^+$ with the KrF$^+$ cation may be postulated to arise form the decomposition of BrO$_2$F$_3$ to BrOF$_3$ and O$_2$ followed by reaction with AsF$_5$ and KrF$^+$ to give BrOF$_2$$^+$ and O$_2$$^+$ salts, respectively, these products may alternatively be explained by a concerted oxidation of an oxygen ligand and transfer of a fluorine ligand to the bromine centre (see section B.2.4). Assuming this is the case, the oxidative fluorination of BrO$_2$F is expected to be more favourable if a less polar and non-acidic oxidizing agent is used. The potent low-temperature fluorinating properties of O$_2$F$_2$ meet these criteria, however, the thermodynamic instability of O$_2$F$_2$ (ΔH_f°, 20 kJ mol^{-1})[576] and its low kinetic stability make it very difficult to handle, even under cryogenic conditions.[577]

B.4. Conclusion

The preparation of BrO$_2$F$_3$ and salts containing the BrO$_2$F$_2$$^+$ cation were unsuccessful when a ligand exchange reaction between XeF$_6$ and BrO$_3$F, or oxidation of BrO$_2$F by the fluoro-cations XeF$_3$$^+$, Xe$_2F_{11}$$^+$ and KrF$^+$ were attempted. When coupled with the experimental observations, the investigation of the thermochemistry of these reactions exposes the diverse obstacles that must be overcome for the preparation of BrO$_2$F$_3$ or its ionic derivatives. Although the ligand exchange reaction between XeF$_6$ and BrO$_3$F, and the oxidation of BrO$_2$F with Xe$_2$F$_{11}$$^+$ and XeF$_3$$^+$ were simply predicted to be thermodynamically unfavourable, the failure of KrF$^+$ to oxidize BrO$_2$F to BrO$_2$F$_2$$^+$ demonstrates the importance of finding an oxidant that will oxidize the Br(V) centre rather than the oxygen ligands.

The thermodynamic stability of BrO$_2$F$_3$ was investigated using the G2 method, which predicted BrO$_2$F$_3$ to be unstable towards the loss of O$_2$ and the formation of BrOF$_3$, but stable with respect to the loss of F$_2$. Evaluation of the thermodynamic

parameters associated with the Lewis base properties of BrO_2F_3 using a combination of electronic structure calculations and empirical relationships suggest that this oxide fluoride is a weak fluoride ion donor and that the isolation of $[BrO_2F_2][SbF_6]$ is thermodynamically unfavourable at 298 K but favourable at lower temperatures. The Lewis acid properties of BrO_2F_3 are predicted to be similar to those of BrO_3F, and salts containing the *cis*- and/or *trans*-$BrO_2F_4^-$ anion should be isolable provided a synthetic route to BrO_2F_3 can be achieved. The fluoride ion donor and acceptor properties of BrO_2F_3 are in contrast to those of ClO_2F_3, which is predicted and observed to be a moderate fluoride ion donor but too weak a fluoride ion acceptor to form $ClO_2F_4^-$.

The calculated vibrational frequencies of BrO_2F_3, the $BrO_2F_2^+$ cation and the $BrO_2F_4^-$ anion reveal complex trends when HF and MP2 methods are used and which are reminiscent of those for BrO_3F and $BrO_3F_2^-$. Consequently, the use the HF and MP2 methods in conjunction with the 6-311G(d) basis set is cautioned for the investigation of related oxide fluorides. The MPW1PW91 method did not exhibit such irregularities for mixed F/O ligand systems, and is believed to provide the most reliable predictions for the vibrational frequencies of BrO_2F_3, $BrO_2F_2^+$ and *trans*-$BrO_2F_4^-$. When coupled with the selection rules, the significant shifts predicted for the Br-O and Br-F vibrational frequencies among these three species should allow for their unambiguous identification by vibrational spectroscopy.